Silent Functional MRI with Looping Star
A Novel Approach to Imaging Brain Function in Health and Disease

Damestani, Nikou

Awarding institution:
King's College London

Silent Functional MRI with Looping Star: A Novel Approach to Imaging Brain Function in Health and Disease

Nikou Louise Damestani

King's College London

A thesis submitted for the degree of

Doctor of Philosophy in Neuroimaging Physics

30th September 2021

Abstract

Functional magnetic resonance imaging (fMRI) is conventionally performed using echo-planar imaging (EPI)-based acquisition methods. These acquisition methods produce high acoustic noise during scanning, which presents significant limitations to fMRI studies. For example, the loud scanning noise affects the comfort and anxiety levels of study participants, which can lead to those with a particularly low tolerance for loud noise requesting removal from the scanning environment. Higher anxiety levels can also lead to higher participant motion, corrupting the acquired data.

Furthermore, high acoustic noise during scanning has been shown to confound fMRI results across numerous paradigms, limiting the interpretability and generalisability of fMRI studies. This especially affects studies investigating auditory processing due to the interaction of the scanner acoustic noise with auditory stimuli. As fMRI indirectly measures neural activity, eliminating any external confound is essential to improving the reliability and specificity of the technique. As a result, conventional auditory fMRI studies typically require complex workflows or advanced equipment, often unique to each study site, to circumvent the acoustic noise and present auditory stimuli.

Recently, a new fMRI acquisition technique has been developed known as Looping Star. Looping Star is a three-dimensional, non-Cartesian, multi-echo, T_2*-weighted pulse sequence that reduces the acoustic noise of scanning to ambient level. The acoustic noise is minimised at its source by reducing the gradient switching, without requiring advanced adaptations to the scanner hardware such as vacuum isolation of the gradients. As it is an entirely novel technique, in-depth investigations of its characteristics have

been limited. Additionally, the capabilities of Looping Star as a multi-echo fMRI modality had not been explored prior to the initiation of this project.

This thesis characterises the Looping Star pulse sequence in phantoms and participant cohorts, evaluating its use as an acoustically silent, multi-echo, fMRI acquisition method. The image quality and temporal stability produced by Looping Star were explored across a range of acquisition parameters, as was the functional sensitivity of Looping Star to neural activity in response to a variety of fMRI paradigms. Crucially, Looping Star was compared with both single-echo and multi-echo gradient-recalled echo echo-planar imaging (GRE-EPI) acquisitions, which are the standard techniques for fMRI investigations.

Ultimately it was found that Looping Star is not only functionally sensitive to the detected neural responses to a range of task-based paradigms, but can also be used for the identification of core resting-state networks. It was also established that Looping Star is compatible with conventional analysis methods. Looping Star produced adequate results relative to GRE-EPI, although differences between modalities were also found. These differences present interesting avenues for further research, including exploring methods for disentangling the impact of acoustic noise from the impact of the pulse sequence.

Finally, potential future directions for further optimisation of Looping Star were investigated. These ranged from its application to quantitative susceptibility mapping to improvements in image reconstruction that could benefit its spatial and temporal resolution. These areas of optimisation will further facilitate the translation and application of Looping Star to a wide range of fMRI studies across cohorts, improving the accessibility and scope of fMRI research.

Dedication

For my parents

جز نـقـش تو در نـظر نیامد ما را
جز کوی تو رهـگذر نیامد ما را

The only vision I have is your sight.

The only thing I follow is your light.

- Rubaiyat 1 by Mohammad Hafez-e Shirazi, translated by Shahriar Shahriari*

You are always my guiding light. Thank you for everything.

* Shahriar Shahriari, 1999 - 2005, Los Angeles, CA, http://www.hafizonlove.com/divan/rubaiyat/1.htm, Accessed 29th September 2021.

Acknowledgements

To my supervisors (and academic parents), Dr Fernando Zelaya and Dr David J Lythgoe: you consistently prioritised my development as an independent researcher and supported me through incredibly difficult moments over the past four years, for which I will always be grateful. I couldn't have asked for better supervisors; thank you for all you have taught me and for treating me as your equal during this journey.

To my colleagues at GE Healthcare, especially Dr Anabea Solana and Dr Florian Wiesinger: it was a pleasure and a privilege to develop this project with you. Thank you for your encouragement and for the excellent suggestions of Christmas markets during my visits to Munich! To the students and staff from the NIHR Maudsley Biomedical Research Centre, the funding body that made this research possible: it has been a joy being part of the community. Thank you for the incredible opportunities you provided that have formed my foundation as a researcher. I am incredibly proud to have been a member of the 2017 - 2021 studentship cohort. I'd also like to add a special thank you to Julia Wootley for always supporting our cohort.

I have also been so fortunate to have been surrounded by the most inspirational researchers, who I am proud to call my "PhD family". Dr Emil Ljungberg, it was a privilege to work with you throughout our PhDs and I am so lucky to have you as a lifelong friend. Emily Clements, I cannot thank you enough for being there for me and believing in me and I look forward to all our future dog walks! Sonia Medina-Hernandez and Dr Olivia Kowalczyk, I appreciate you both for always being ready with a glass of wine and a chat. Harriet Fawsitt-Jones, Julia Schubert, Dr Nuria Mackes, Diana Rotaru, and many more,

thank you all for making this journey memorable. I can't wait to see what you all achieve!

To my fellow members of "Team Silent", Dr Tobias Wood and Professor Gareth Barker: I'll always treasure our mutual appreciation for ABBA and Eurovision! To Professor Steve Williams, Dr Vincent Giampietro, and Milena Rodriguez: I wouldn't be where I am today without the fantastic MSc Neuroimaging course and your encouragement. The Neuroimaging Department has been the most incredible environment to work in. Thank you to everyone who helped me develop as a scientist, including (but of course not limited to): Dr Owen O'Daly, Dr Rosalyn Moran, Professor Federico Turkheimer, Dr Po-Wah So, and Professor Mitul Mehta.

To my "GCH + Debra" girls, I am blessed to have you in my life. Our regular meetups have meant I've never lost touch with who I am, and I have you all to thank for that. To my undergraduate physics team, especially Maryam Reisjalali, your positivity and TV series suggestions always keep me smiling. To my bestie across the pond, Michael Coffel, you have always rooted for me and your visits to London have meant so much to me. Thank you for being available despite the time difference!

To Alastair Roberts, my best friend, partner, and the person who has been my rock every day of this journey. There aren't enough "thank yous" for articulating how grateful I am to have been on this journey with you. I can't wait for our next adventure. To my brother and sister-in-law, Kian and Kirsty Damestani: thank you for always being (literally) around the corner when I need you, and for bringing my nephew Artan into this world this year - he brings us so much joy. Buffy, my beloved toy poodle, thanks for the cuddles! To Nannipops, I miss you every day and you are always in my heart.

And last, but most importantly, to my parents: Tracy and Peyman Damestani. You have been by my side through every part of this rollercoaster. You have only ever shown me love and support, be it through keeping me well fed or by printing my first publication for me to treasure. You are my motivation every day, and I love you both so very much. I will always strive to make you proud. Thank you for being you.

COVID-19 Impact Statement

During the years 2020/21, as a result of the global COVID-19 pandemic, research at King's College London was suspended. This meant that our centre, the Centre for Neuroimaging Sciences, was closed for twelve months and MRI research with healthy volunteers could not take place. The collection of additional data for the following chapters was limited:

- Chapter 10: Coherence-resolved Looping Star
- Chapter 11: Taking Looping Star Further

In addition, a pilot investigation in participants with autism spectrum disorder who are averse to intense sounds had to be suspended.

Declaration

I, Nikou Louise Damestani, author of this thesis, declare that this thesis contains original work conducted only by myself unless referenced otherwise. Any work performed collaboratively is explicitly stated in the text of this thesis.

Academic Outputs

Publications

- Damestani, N.L. et al. 2021. Revealing the mechanisms behind novel auditory stimuli discrimination: An evaluation of silent functional MRI using Looping Star. Human Brain Mapping.

- Ljungberg, E., Damestani, N.L., Wood, T.C. et al. 2021. Silent Zero TE MR Neuroimaging: Current State-of-the-Art and Future Directions. Progress in Nuclear Magnetic Resonance Spectroscopy.

- Wood, T.C., Damestani, N.L. et al. 2020. Silent myelin-weighted magnetic resonance imaging. Wellcome Open Research.

Conference Presentations

- Damestani, N.L. et al. 2021. Coherence-resolved Looping Star (CRLS): Improvements to image quality for silent structural and functional neuroimaging. In Proc. ISMRM Virtual Conference. Abstract 2677

- Leynes, A.P., Damestani, N.L. et al. 2021. Extreme Looping Star: Quiet fMRI at high spatiotemporal resolution. In Proc. ISMRM Virtual Conference. Abstract 458.

- Wood. T.C and Damestani, N.L. 2021. Bold-free fMRI? In Proc. ISMRM Virtual

Conference. Poster 1252.

- Damestani, N.L. et al. 2020. Silent fMRI of auditory and motor functions using coherence-resolved Looping Star. In Proc. Virtual OHBM Annual Meeting. Poster 2022

- Damestani, N.L. et al. 2020. Silent functional MRI for novel sound discrimination using the auditory oddball paradigm. In Proc. Virtual ISMRM Annual Meeting. Abstract 3894

- Damestani, N.L. et al. 2019. Looping Star silent fMRI: a platform for improving studies of auditory processing. In Proc. 27th ISMRM Annual Meeting. Abstract 363.

- Damestani, N.L. et al. 2019. Identifying functional resting state networks in silence using Looping Star. In Proc. 25th OHBM Annual Meeting. Poster W364.

- Damestani, N.L. and Ljungberg, E. 2019. Silent MRI: an improved scanning environment for studying the brain. Invited talk. NIHR BRC Annual Conference.

- Damestani, N.L. 2019. First Round Heats, 3-Minute Thesis Competition. Institute of Psychiatry, Psychology and Neuroscience, King's College London.

- Damestani, N.L. and Ljungberg, E. 2018. ZTE MRI: fast, functional, quiet and quantitative. Presentation at University of Nottingham, NIHR IVSA Award.

- Damestani, N.L. et al. 2018. Looping Star - a novel silent approach to imaging brain function in health and disease. Oral Presentation. British Chapter of ISMRM Annual Meeting.

- Damestani, N.L. and Ljungberg, E. 2018. Silent MRI. European Brain Council: Enhanced engagement through public-private partnerships.

Contents

List of Tables

List of Figures

List of Abbreviations

2D two-dimensional

3D three-dimensional

ANC Active Noise Cancellation

ASL Arterial Spin Labelling

BOLD blood oxygen level dependent

BURST burst of short RF pulses

BW readout bandwidth

CBF cerebral blood flow

COV coefficient of variation

CRLS coherence-resolved Looping Star

CSF cerebrospinal fluid

CVA Clustered Volume Acquisition

DDAs dummy acquisitions

EPI echo-planar imaging

FA flip angle

FID free-induction decay

fMRI functional magnetic resonance imaging

FOV field of view

FWD framewise displacement

FWE family-wise error

FWHM full-width at half-maximum

GLM general linear model

GM grey matter

GRE first gradient echo

GRE2 second gradient echo

GRE3 third gradient echo

GRE-EPI gradient-recalled echo echo-planar imaging

GSF gradient smoothing factor

HASTE Half Fourier Acquisition Single Shot Turbo Spin Echo

HRF haemodynamic response function

ICA Independent Component Analysis

ICC intra-class correlation

ILSQR iterative least squares

IR-SPGR inversion-recovery prepared spoiled gradient echo

ISMRM International Society for Magnetic Resonance in Medicine

ISSS Interleaved Silent Steady State

LS Looping Star

ME multi-echo

ME-ICA multi-echo independent component analysis

MRI magnetic resonance imaging

MNI Montreal Neurological Institute

NMR nuclear magnetic resonance

OHBM Organisation for Human Brain Mapping

PCA Principal Component Analysis

PETRA Pointwise Encoding Time Reduction with Radial Acquisition

PRESTO PRinciples of Echo-Shifting with a Train of Observations

PSC percentage signal change

PSD percentage signal drift

PSF percentage signal fluctuation

QSM quantitative susceptibility mapping

RARE Rapid Acquisition with Relaxation Enhancement

ReML Restricted Maximum Likelihood

RF radiofrequency

RDC radius of decorrelation

ROI region of interest

RUFIS Rotating Ultra-fast Imaging Sequence

SAR specific absorption rate

SE single-echo

SEPIA SuscEptibility mapping PIpeline tool for phAse images

SHARP sophisticated harmonic artifact reduction for phase data

SNR signal-to-noise ratio

spl spokes per loop

SSN static spatial noise

STI susceptibility tensor imaging

SWAN susceptibility-weighted acquisition

SWI susceptibility-weighted imaging

SWIFT SWeep Imaging with Fourier Transformation

TE echo time

TEDANA TE Dependent ANAlysis

TI inversion time

TR repetition time

tSNR temporal signal-to-noise ratio

VASO Vascular Space Occupancy

WASPI Water and Fat Suppressed Proton Projection MRI

WM white matter

ZTE zero echo time

Chapter 1

Introduction: Fundamental Concepts for Functional Magnetic Resonance Imaging

Summary

This chapter presents an introduction to:

- The physical principles of magnetic resonance imaging (MRI) relevant to functional neuroimaging.
- Image encoding and formation of MRI.
- The physiological basis of the functional magnetic resonance imaging (fMRI) signal.
- Conventional fMRI using gradient-recalled echo echo-planar imaging (GRE-EPI).
- The core concepts of fMRI analysis and statistical inference.
- Multi-echo GRE-EPI and its application to fMRI.
- Limitations and advances of conventional fMRI with GRE-EPI.

Overview

In this chapter, the key concepts and physical principles that form the basis of this thesis are detailed. General terminology that will assist with the understanding of this thesis will also be introduced.

1.1 The Static Magnetic Field and Particle Physics

The key components of an MRI scanner are the static magnetic field, the gradient coils and the RF coils. The static magnetic field strength of the scanners used in this thesis is 3 Tesla (3 T), with appropriate spatial uniformity across the centre of the bore. Spatial uniformity, or spatial homogeneity, of this large static magnetic field is vital to ensure that there are no dramatic signal changes within the region under investigation (Bushberg et al., 2012; Dale et al., 2015; Huettel et al., 2014).

Some subatomic particles possess a property known as angular momentum. In the case of protons, angular momentum is composed of the spin angular momentum and orbital angular momentum. For MRI, the spin angular momentum is crucial as this property interacts with electromagnetic fields (Bushberg et al., 2012; Dale et al., 2015; Huettel et al., 2014). These particles also have a finite magnetic dipole moment, meaning they have their own inherent magnetisation. Classical mechanics dictates that a magnetic dipole with spin angular momentum, in the presence of a large magnetic field, will precess at the Larmor frequency (ω). This precession is of the spin axis, about the magnetic field direction, and its dependency on the magnetic field strength (B_0) is described by Equation (1.1).

$$\omega_0 = \gamma B_0 \tag{1.1}$$

This equation is known as the Larmor equation, where a constant known as the gyromagnetic ratio (γ) scales the Larmor frequency ω_0, and the value of γ is specific to each nuclear species (Dale et al., 2015).

According to the Zeeman effect, particles with a spin value equal to 1/2 will split into either spin-up or spin-down energy states when subject to an external magnetic field

(Brown et al., 2014; Dale et al., 2015). Protons are one such particle, and they are abundant in the human body. Assuming no interactions between protons, there will be a tendency for a net number of protons to exist in the lower energy state, which is aligned parallel to the static magnetic field (Hanson, 2008). The collection of protons that form the small majority are referred to as the net magnetisation, as seen in Figure 1.1

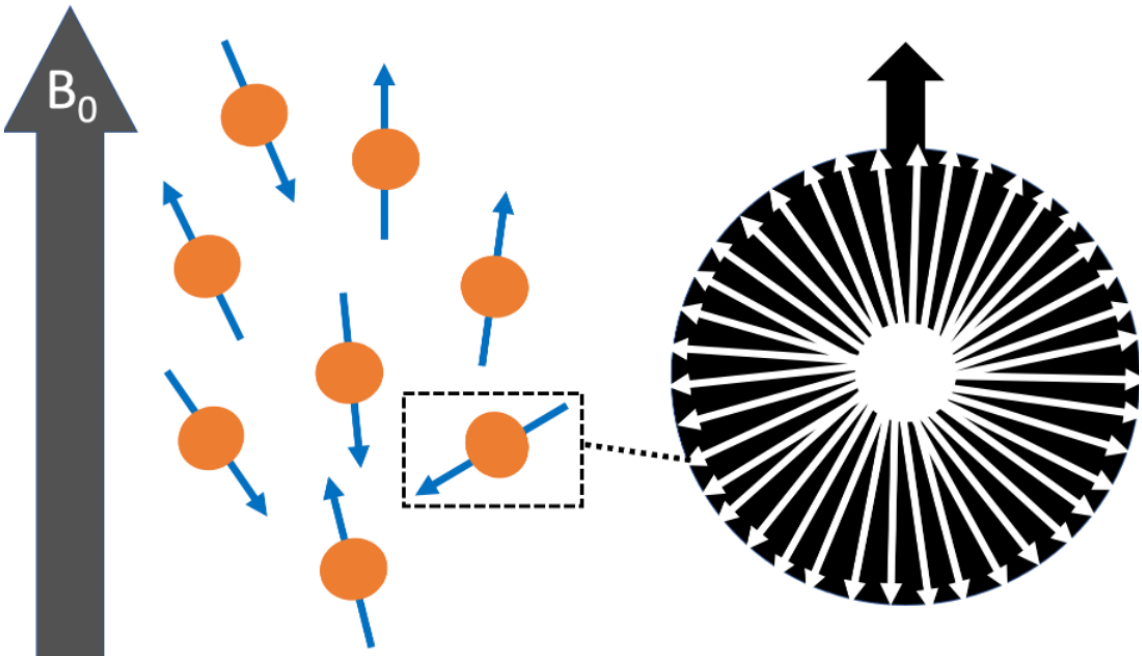

Figure 1.1: (left) Individual spins randomly distributed, where blue arrow indicates magnetic moment and orange circle represents proton. (right) 2D visual representation of a small majority of protons, where white arrows indicate direction of magnetic moments and black arrow indicates net magnetisation. Direction of main static magnetic field B_0 indicated by large dark grey arrow. Inspired by Hanson (2008).

Specifically, the number of spins in excess (N_e) compared with the number of spins in the total sample (N_s) is approximately

$$N_e = N_s \frac{\hbar\omega_0}{2kT} \tag{1.2}$$

where $\hbar$ is the reduced Planck constant, ω_0 is the Larmor precession frequency, T is the temperature, and k is the Boltzmann constant. The net magnetisation ($< \mu >$) can be derived (Hanson, 2008) and approximately equals to

$$< \mu > \approx \frac{\hbar^2 \gamma^2 B_0}{4kT} \tag{1.3}$$

To produce an image in MRI, this net precessing magnetisation must be detected by an external coil and made spatially dependent. Once detected, it will produce a current in said coil via the electromotive force, therefore producing a signal (Huettel et al., 2014). One of the most convenient ways for signal detection to occur is to excite the net magnetisation into a different plane from the large static magnetic field using magnetic resonance (Section 1.2).

1.2 Origins of Magnetic Resonance

Resonance in MRI occurs when the frequency of the applied electromagnetic radiation is equal to the natural frequency of the precessing proton (i.e. the Larmor frequency). A convenient way to do this is in the form of a pulse at RF because the Larmor frequency of a proton in a static magnetic field of strength 3 T falls within the RF field range. Applying an RF field waveform with equal frequency to the proton Larmor frequency in the static magnetic field will lead to energy deposition and absorption, i.e. resonance (Brown et al., 2014; Dale et al., 2015; Huettel et al., 2014).

In the case of a collection of protons, the RF field excitation bandwidth must encompass the range of Larmor frequencies of the distribution of protons. This then causes a rotation of the collective spin distribution out of alignment with the static magnetic field, referred to as excitation, facilitating their detection with external coils (Hanson, 2008). The spins continue to precess after this excitation is turned off, however in the interest of relevance to this thesis the rotating frame of reference is adopted, which is a coordinate system rotating at the Larmor frequency (Brown et al., 2014). The degree at which the excitation occurs can be characterised by the FA and is calculated based on the pulse shape, amplitude and time duration of the RF pulse.

Once the net magnetisation has been excited into a different plane from the static magnetic field, all of the protons (for a given magnetic field strength) will precess in phase ϕ_0 and with a particular frequency ω_0, equal to the phase and frequency induced by the RF field. The magnetisation at time t after application of the RF field (i.e. once excitation stops) in the x-y plane is defined as in Equation (1.4) (Brown et al., 2014) .

$$M_+(t) \equiv M_x(t) + iM_y(t) = M_0 e^{-i\omega_0 t + i\phi_0} \tag{1.4}$$

When the RF field is no longer applied, interactions between protons occur that lead the net magnetisation to dephase and return to its low-energy state: in alignment with the static magnetic field. This is known as relaxation (Section 1.3).

1.3 Spin Relaxation Properties

Relaxation occurs through multiple interaction mechanisms, though in general the processes are different for the transverse (perpendicular to the static magnetic field and described by time constant T_2) and longitudinal magnetisation (described by time constant T_1).

The relaxation properties of protons are of particular importance to fMRI, as will become apparent in Sections 1.4 and 1.7, and are unique to the tissue under investigation. T_1 and T_2 can be mathematically defined by a semi-classical approximation known as the Bloch equation (Bloch, 1946), shown in Equation (1.5), where $\vec{M}$ is the magnetisation vector in three-dimensions, $\vec{B}$ is the magnetic field vector in three-dimensions and t is the time point.

$$\frac{d\vec{M}(t)}{dt} = \vec{M}(t) \times \gamma\vec{B}(t) \tag{1.5}$$

The full phenomena of relaxation in both transverse and longitudinal dimensions is given as

$$\frac{d\vec{M}(t)}{dt} = \gamma\vec{M} \times \vec{B} + \frac{1}{T_1}(\vec{M}_0 - \vec{M}_z) - \frac{1}{T_2}(\vec{M}_x + \vec{M}_y) \tag{1.6}$$

In living systems, T_1 recovery often occurs on a much longer time scale than T_2 relaxation and involves the interaction of spins with their environment (Brown et al., 2014). These interactions stimulate the protons to lose energy and return into alignment with the static magnetic field, known as thermal equilibrium (Buxton, 2013). Energy deposition is induced by the local magnetic field perturbations of neighbouring protons. T_1 recovery for a single spin species is defined to a first approximation by the following solution of the Bloch equation (Equation (1.7))

$$M_z(t) = M_0 - (M_0 - M_z(t = 0))e^{-\frac{t}{T_1}} \tag{1.7}$$

Any mechanism that affects T_1 relaxation can also affect T_2 relaxation, though T_2 relaxation can also occur independently of T_1 as it is independent of energy transfer. Instead, T_2 relaxation is dependent, at first, on dephasing of the protons induced by disturbances in the local magnetic field (Buxton, 2013). The impact of T_2 on the evolution of the net magnetisation is given (to a first approximation) by the following solution of the Bloch equation (Equation (1.8))

$$M(t)_{x,y} = M_0(e^{-\frac{t}{T_2}}) \tag{1.8}$$

Proton dephasing also occurs due to external magnetic field inhomogeneities. For example, magnetic susceptibility differences in tissues, particularly at air-tissue interfaces, can impose further local magnetic field changes. This effect causes a faster T_2 relaxation, which is referred to as T_2*. In fMRI, tissues with additional inflow of oxygenated blood,

induced by neural activity, produce a different extent of T_2* -induced decay than tissues with reduced blood inflow (Huettel et al., 2014). T_2* is therefore a core mechanism exploited in fMRI, whereby image contrast is produced as a result of changes in regional oxygenation of the blood. This is discussed in more depth in Section 1.7 and 1.8.

The relationship between T_2*, T_2 and the relaxation rate due to field inhomogeneities (T_2') is given by

$$\frac{1}{T_{2*}} = \frac{1}{T_2} + \frac{1}{T_2'} \tag{1.9}$$

where T_2' is reversible signal decay. Therefore, the time at which the signal decay is sampled is vital for ensuring as much signal is acquired as possible. The decay immediately after excitation (in the absence of the gradients) is known as the FID, and due to the speed at which the signal decays it is usually very challenging to acquire an image of this initial decay.

From the Bloch equations above (Equations (1.7) and (1.8)), the T_1 of a tissue is quantified as the time point at which the longitudinal component of the magnetisation recovers to $1 - 1/e$ (approximately 63 %) of its initial value, whereas the T_2 is the time point at which the signal (transverse component of the magnetisation) decays to $1/e$ (approximately 37 %) of its initial value (Dale et al., 2015). In cerebral tissues at 3 T, the T_1 and T_2 values are shown in Table 1.1, adapted from Stanisz et al. (2005), Lu et al. (2005), Wright et al. (2008), and Piechnik et al. (2009).

These relaxation times are critical as they affect the choice of imaging parameters, discussed in Section 1.4.

Table 1.1: Average T_1 and T_2 values at 3T for different brain tissues from the literature (Lu et al., 2005; Piechnik et al., 2009; Stanisz et al., 2005; Wright et al., 2008).

Tissue	$\mathbf{T_1(ms)}$	$\mathbf{T_2(ms)}$
Grey matter	1607 $\pm$ 112	99 $\pm$ 7
White matter	838 $\pm$ 50	69 $\pm$ 3
Cerebrospinal fluid	3817 $\pm$ 424	503 $\pm$ 64
Blood	1932 $\pm$ 85	275 $\pm$ 50

1.4 Image Acquisition and Contrast

To acquire images using only the FID, an acquisition method with sufficient speed of RF and magnetic field gradient application would be required to collect the signal prior to substantial decay. This method would have very limited contrast between tissues, given the speed of decay across tissues (Table 1.1). To achieve the best image contrast between tissues at a more convenient timescale in relation to the relaxation times, a concept known as echo-based imaging can be employed. There are two forms of echo-based imaging, known as spin echo and gradient echo.

Spin echo imaging involves applying an RF pulse, known as the refocusing pulse, ideally of flip angle π (180°), after the initial, usually $\pi/2$ (90°), RF excitation (Hahn, 1950). The first RF pulse excites the net magnetisation into the transverse plane, which begins to decay (i.e. FID) after excitation stops. The phases of the proton spins that accumulate during decay are then inverted by the second RF pulse, refocusing the spins to their initial phase to recover the signal lost from the initial dephasing. Since the phase dispersion induced by external field inhomogeneities is refocused, this is referred to as a T_2, rather than T_2*, based technique (Huettel et al., 2014).

The time between the application of the initial RF excitation and the time the recovered "echo" signal reaches a maximum is known as the echo time (TE). Since the rate at

which the "new" phase is accumulated is the same as the rate of initial decay, all of the spins will return approximately to the original phase at the echo time, maximising the signal (Brown et al., 2014). The echo time is selected during image acquisition and is double the time between the application of the exciting RF pulse and the refocusing RF pulse. The TE selection must consider the tissue contrast desired as different tissues have distinct T_2 decay values, and so they will produce different signal intensities at different echo times (Figure 1.2). However, the amplitude of the signal at the echo time will still be lower than the initial signal (M_0). This loss of signal originates from the local magnetic field distortions, which are effectively randomly varying fields. These distortions lead to spin-spin interactions, such that spins partially cancel each other out (Buxton, 2013).

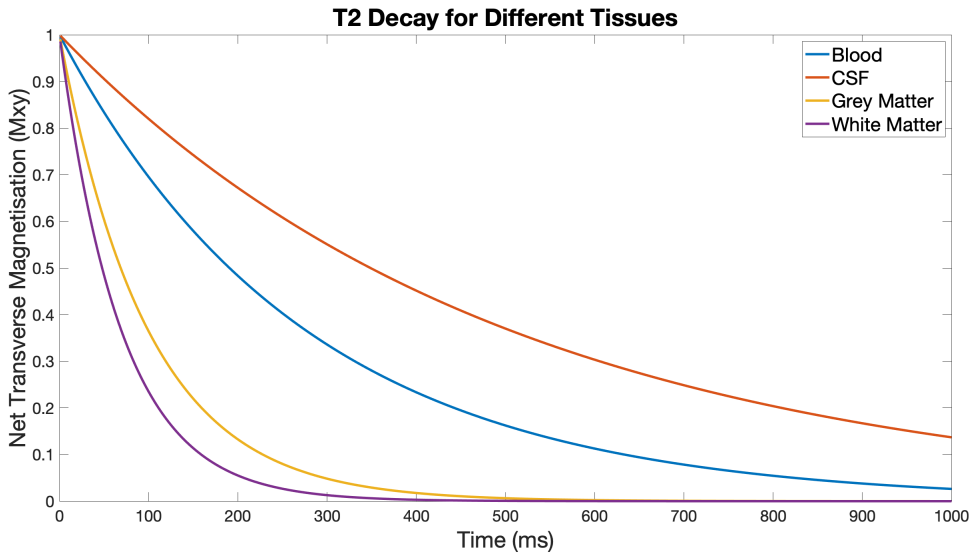

Figure 1.2: Net transverse magnetisation (M_{xy}) decay plots in time for blood (blue), grey matter (yellow), white matter (purple) and CSF (orange), using the average T_2 values from Table 1.1.

When multiple cycles of exciting RF pulses are applied (i.e. $\pi/2$ - $\pi/2$ - $\pi/2\ldots$), the repetition time (TR) must also be considered. This is the time between the RF pulses that excite the net magnetisation into the transverse plane (i.e. $\pi/2$ - $\pi/2$). The selection of TR also contributes to the extent of FID signal decay after a series of excitation cycles, and can therefore affect the image contrast, as described by Equation (1.10) (Brown et al., 2014).

$$M_{x,y}(t_n) = M_0(1 - e^{-\frac{TR}{T_1}})e^{\frac{-t_n}{T_2}} \tag{1.10}$$

where $M_{x,y}(t_n)$ is the evolution of the net magnetisation in the transverse plane in the nth cycle, and t_n is the time after n echoes. For an excitation-refocusing cycle, the transverse magnetisation at the time of a given echo can then be derived in terms of TR and TE (Brown et al., 2014)

$$M_{x,y}(TE) = M_0(1 - e^{-\frac{TR}{T_1}})e^{\frac{-TE}{T_2}} \tag{1.11}$$

Where TE is the time at which the echo occurs.

For gradient echo imaging, the same concepts of echo time and repetition time apply. To visualise a gradient echo in its simplest form, consider only two consecutive gradients. A gradient echo is produced by applying a gradient pulse that creates additional phase dispersion, followed by applying a refocusing gradient (i.e. of the same net amplitude but opposite sign) to recover the induced dispersion of the first gradient pulse (Buxton, 2013). This means any further decay (i.e. not induced by the gradient) will not be recovered, hence its sensitivity to T_2*.

The effect of the refocusing gradient is best explained mathematically, as described by Brown et al. (2014). Consider a constant negative gradient lobe applied in the time interval (t_1, t_2), followed by a second positive gradient lobe during the time interval (t_3, t_4). The phase behaviour after application of these gradients (ϕ_G) can be described as

$$\phi_G(z,t) = +\gamma G_z(t_2 - t_1) - \gamma G_z(t - t_3) \tag{1.12}$$

where G_z is the gradient lobe and γ is the gyromagnetic ratio of the nuclear species. The induced additional phase will therefore return to its original value, as if no gradient

pulse had been applied, at the specified time t (Equation (1.13))

$$t = t_3 + t_2 - t_1 \tag{1.13}$$

Inserting this time t into the phase dispersion equation, Equation (1.12)

$$\phi_G(z, t_3 + t_2 - t_1) = +\gamma G_z(t_2 - t_1) - \gamma G_z(t_2 - t_1) = 0 \tag{1.14}$$

Therefore the phase returns to where the decay of the FID would have been at that point, as if no gradient pulses had been applied.

Both spin echo and gradient echo techniques have been employed in functional imaging as reviewed across numerous studies, for example Boyacioğlu et al. (2014); Halai et al. (2014); Norris (2012); Zhao et al. (2004), however gradient echo imaging is generally preferred due to its greater sensitivity to changes in blood oxygenation on T_2* , as explained in Sections 1.7 and 1.8.

1.5 Basics of Image Encoding

Translating the MR signals described previously into images requires spatial encoding of the MR signal. Signal encoding in conventional MRI begins with "slice" selection. Based on the Larmor frequency equation (Equation (1.1)), a range of magnetic field strengths for the same nuclear species will produce a range of Larmor frequencies. This range of magnetic field strengths can be produced in MRI, by means of a magnetic field gradient, i.e. increasing or decreasing field amplitude as a function of position across space (Figure 1.3). By selecting an RF excitation bandwidth encompassing only a range of frequencies, a specific portion of the object of interest can be excited (Brown et al., 2014; Huettel

et al., 2014).

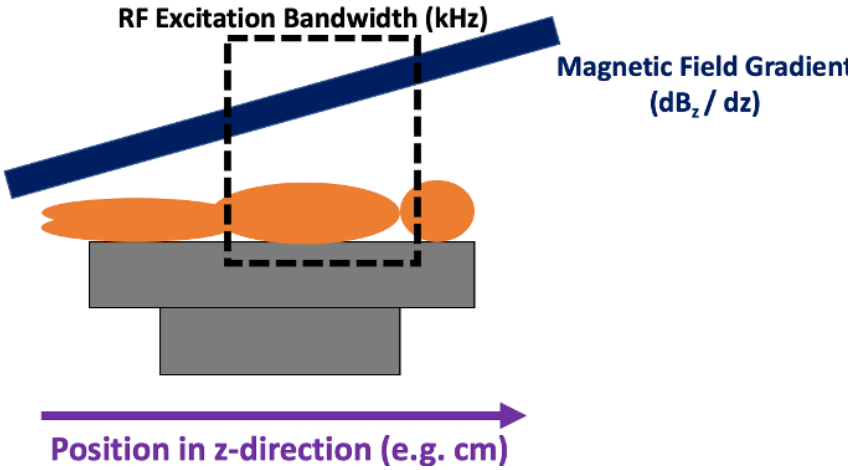

Figure 1.3: Simplified example of 2D slice selection for spatial encoding along the z-direction in k-space. Dark blue diagonal angle represents magnetic field gradient along z, defined by $\frac{dB_z}{dz}$. The dotted black line represents the RF excitation bandwidth. The excited protons (i.e. those within the dotted black lines, forming a large "slice") will resonate at different Larmor frequencies, due to the presence of the magnetic field gradient.

Producing a range of frequencies across space distinguishes the spins across a given direction. To encode signals for a three-dimensional (3D) image, it follows that gradients must be produced for all three Cartesian dimensions. To achieve this, conventional imaging involves selecting a thin "slice" along a single direction (e.g. in the z-direction), then applying two additional magnetic field gradients in the x- and y-directions, known as the phase and frequency encoding gradients. This procedure will produce a unique combination of x-, y-, and z- encoding gradients for a specific position in space (Bushberg et al., 2012; Dale et al., 2015; McRobbie et al., 2017).

To demonstrate this mathematically, consider the following derivation by Brown et al. (2014). A spatially varying field in the z-direction is added to the large static field (B_0). This field affects the overall gradient in the z-direction as given by

$$B_z(z,t) = B_0 + zG_z(t) = B_0 + z\frac{dB_z}{dz} \tag{1.15}$$

Where the time dependency refers to any time-dependent changes in the gradient. This translates to frequencies as

$$\omega(z,t) = \omega_0 + \omega_{G_z(t)} \tag{1.16}$$

Adding a second gradient, but in the x-direction that previously has not experienced any static gradients

$$B_x(x,t) = x\frac{dB_x}{dx} \tag{1.17}$$

Such that the overall frequencies in these two dimensions become

$$\omega(x,z) = \omega_0 + \omega_{G_z} + \omega_{G_x} \tag{1.18}$$

Where $\omega_{G_z} = \gamma z G_z$ and $\omega_{G_x} = \gamma x G_x$. This combination of frequencies will encode a specific plane in space. The encoding gradients are applied in different planes and for different durations, depending on the acquisition technique used. In echo-planar imaging, the most commonly used pulse sequence for fMRI, the phase encoding gradient is usually applied for a short period. When switched off, the frequencies will retain the imposed phase, which provides another unique identifier for the position in the slice (McRobbie et al., 2017). This is discussed specifically for conventional fMRI in Section 1.8.

1.6 K-space and Image Reconstruction

Different gradients generate different distinguishing phases and frequencies in an object, and the application of these gradients can be visualised using a concept known as k-space. K-space can be considered a "map" of the gradients applied to generate the image, and each point in k-space represents the inverse domain of the object that is being imaged. In other words, points in k-space correspond to spatial frequency components in the image,

and can also be viewed as the frequency encoding produced by the time integrals of the gradients (Bernstein et al., 2004; Huettel et al., 2014).

To visualise this, consider a 2D Cartesian grid of perpendicular gradient (or k-space) directions k_x, k_y, which is at a particular selected slice in the z-direction (Figure 1.4). By exciting the sample, signal is encoded at the centre of k-space. Application of the appropriate pre-phasing gradients for a period of time after slice selection generates a trajectory in k-space to a chosen location in one of the corners of the k-space domain, as shown in Figure 1.4. An encoding gradient along the x-direction in space can then be applied for a period, and the signal from the slice during its application is collected; filling the first line of the k-space Cartesian grid.

To move through the second (perpendicular) dimension, y, of the Cartesian grid, a perpendicular encoding gradient can be applied. Once again, the signal received whilst applying the gradient in the perpendicular direction is collected and fills the perpendicular line of k-space. In Figure 1.4, this is applied for a shorter period of time; hence a shorter distance in k-space is encoded. The pattern of x- and y- dimension signal encoding can then be repeated to encode signals for the entire Cartesian plane of the slice.

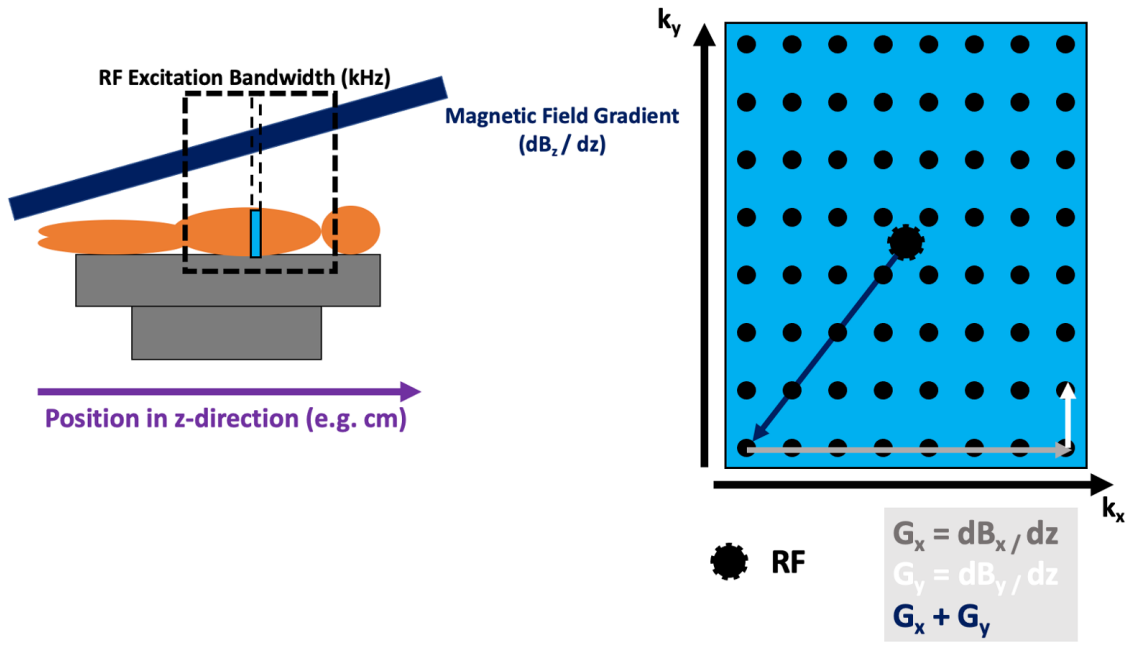

Figure 1.4: Simple example of 2D encoding for a single slice in k-space, whereby a thin slice is selected in the z-direction consisting of an x-y plane (blue). After slice selective RF excitation (dotted central sphere), application of pre-phasing gradient lobes in both the x and y direction directs the k-space trajectory to one of the corners of the k-space domain (dark blue arrow). The x-direction encoding gradient then samples along k_x for a time period (grey arrow) and the y-direction encoding gradient samples along k_y (white arrow) for a time period. The length of the arrow indicates the duration of the gradient applied, as k-space represents time integrals of the gradients.

Though k-space can be used to visualise the result of frequency encoding by magnetic field gradients in a sequence, it is not trivial how this relates to image space as the signal from the entire object is constantly collected under different applied gradients. Explicitly, under the assumption of no relaxation and diffusion effects, the MR signal is the phase-dependent sum of all the signals from all positions and dependent on the product of the net magnetisation and coil component in the transverse plane (Buxton, 2013). This is described by Bernstein et al. (2004), whereby the signal is defined in Equation (1.19)

$$S(t) = \int M(\vec{r})B(\vec{r})e^{-i\phi(\vec{r},t)}d^3r \tag{1.19}$$

where $S(t)$ is the signal received at time point t, M is the net transverse magnetisation, and B is the component of the receive coil B_1 field in the transverse plane, across all directions $\vec{r}$. ϕ is the accumulated phase at a given position and time point, defined as

$$\phi(\vec{r},t) = \gamma \int \vec{r} \cdot \vec{G}(t')dt' \tag{1.20}$$

where $\vec{G}$ is the gradient amplitude vector. Using the relationship of accumulated phase and frequency $\phi(\vec{r},t) = 2\pi\vec{k}(t)$, k-space can then be defined as

$$\vec{k}(t) = \frac{\gamma}{2\pi} \int \vec{G}(t')dt' \tag{1.21}$$

One point in k-space can therefore be interpreted as the change in phase produced by the gradients across all points in space and after a time period (Buxton, 2013). The signal can therefore be represented as the Fourier transform of the transverse magnetisation in real space

$$S(t) = \int M(\vec{r})B(\vec{r})e^{-i2\pi\vec{k}(t)\vec{r}}d^3r \tag{1.22}$$

Equation (1.22) demonstrates that k-space is the Fourier conjugate of image space, requiring a Fourier transformation to produce images from the data. As a result of this inverse relationship, one point in k-space equates to a signal contribution from the complete image, not one point in image space. Signals near the centre of k-space represent contributions from lower spatial frequencies, containing information on the image intensity, whereas signals in the outer edges of k-space represent contributions to higher spatial frequencies, related to fine details in the image. The centre of k-space is the time point at which the signals from all voxels have identical phase, representing all of the transverse magnetisation within the slice (Huettel et al., 2014). If no gradients were applied, all of the data would be encoded in the centre point of the k-space domain. By sampling k-space at an appropriate distance between k-space points, translating to appropriate times in acquisition space, a resolved image containing high and low spatial frequency will be created after Fourier transformation. K-space can therefore be considered a map of spatial frequencies, inversely proportional to the 'spatial wavelength'

(Buxton, 2013).

A fully sampled k-space relates to the FOV such that $\Delta k = 1/FOV$ and the coverage of k-space determines the theoretical spatial resolution. The only way to change the field of view is therefore to change the spacing between k-space points. For example, if the maximum length of k-space traversed is preserved but alternate phase encoding steps are removed, the FOV will be halved in the direction that the phase encoding steps are missed (Bernstein et al., 2004; Hollingsworth, 2015). K-space is also linked to the spatial resolution, whereby if the maximum distance of k-space traversed by the gradients is halved but Δk is preserved, the resultant image will have half the spatial resolution (i.e. a larger pixel size).

Given that Δk is a time interval that is also proportional to the gradient amplitude, stronger gradients will sample k-space faster. However, they must also be able to be rapidly reversed in the case of fast acquisition schemes such as those used in conventional fMRI (Section 1.8). The ability of magnetic field gradients to change their amplitude can be quantified by the slew rate (Brown et al., 2014; Buxton, 2013), i.e. their maximum rate of change of amplitude. Manipulating the gradients in this manner creates a trajectory in k-space, and the speed of trajectory traversal in k-space is determined by the change in the gradient amplitude (Bernstein et al., 2004).

When collecting the data, all of k-space may not be sampled by the encoding gradient, but the trajectory defined by the gradient will be traversed. Assuming constant spacing between samples, the time between samples (Δt, or the "dwell time") is given by the inverse of the readout bandwidth (or bandwidth of the frequency encoding gradient). For example, the readout bandwidth might be $\pm$31.25 kHz, meaning that a sample of the MR signal from the entire object will be taken every 16 μs. If this bandwidth is increased, the time between samples will decrease. The relationship of this timing with the distance between samples in k-space (Δk) for a constant readout gradient (G_x) can therefore be given as (Bernstein et al., 2004)

$$\Delta k_x = \frac{\gamma G_x \Delta t}{2\pi} \tag{1.23}$$

These concepts of k-space are crucial for understanding the relationship between the series of gradients, or "pulse sequence", applied and the images produced in MRI.

1.7 Physiological Principles of Functional MRI

The goal of fMRI is to detect changes in neuronal activity and their overall communicative structure. This neural activity can be related to the presence or absence of a given stimulus. MRI cannot directly measure neuronal activity; this would require measurements of highly localised and rapid changes in electromagnetic fields (Huettel et al., 2014). Alternatively, the MR signal is sensitive to the local rate of blood flow (or cerebral blood flow (CBF)) and the oxygen extraction fraction in the tissue.

This relationship was first determined by Ogawa et al. (1990), who found that when a rat breathed CO_2-enriched air, which increases brain blood flow while keeping oxygen metabolism constant, there was less signal loss near the blood vessels in the brain (Buxton, 2013). This reduced signal loss was explained by the oxygenation level of the venous blood: the venous blood was more oxygenated as a result of a disproportionate increase in blood flow, reducing the relative concentration of deoxyhaemoglobin in the venous domain. Given that deoxyhaemoglobin is paramagnetic (Pauling and Coryell, 1936), it changes the magnetic susceptibility of blood, speeding up the T_2* decay. MR signal is then lost at a faster rate when more deoxyhaemoglobin is present in a tissue.

As a result, if a series of MR images are collected rapidly through time, changes in signal intensity are observed during neural activity as activity triggers changes in the level of blood oxygenation. The change in signal observed is referred to as the blood oxygen level dependent (BOLD) response, which produces a contrast of around 1-5% difference between the active tissues during rest and active tissues in response to a stimulus. The

BOLD response has been shown to evolve on the order of seconds in response to tasks (Kwong et al., 1992; Ogawa et al., 1992).

What continues to be debated are the biological and physiological underpinnings, and therefore the interpretability, of the BOLD signal. For example, blood oxygen changes detected in fMRI can be accentuated by the presence of large draining veins, which are downstream of the initial neural activity (Chen and Cohen-Adad, 2019; McRobbie et al., 2017) but it has also been shown that both local field potentials and single-unit activity are highly correlated with the BOLD signal (Berens et al., 2010; Logothetis et al., 2001; Logothetis and Wandell, 2004; Mukamel et al., 2005). This topic is discussed in depth by Buxton (2013) and Attwell and Iadecola (2002).

The accepted view on the origins of the BOLD signal is that it is facilitated by neurovascular coupling, as reviewed by Phillips et al. (2015): oxygen is delivered to the brain via arterial blood when activity occurs, in order to facilitate enhanced metabolism of oxygen to support the neural activity. As metabolism occurs, the amount of deoxyhaemoglobin increases, potentially reducing the MR signal. However, a surplus of oxygenated blood is delivered due to increases in metabolism, which reduces the decay of the signal after depletion as oxyhaemoglobin is diamagnetic, producing a signal contrast. The temporal characteristics of the MR signal change can be modelled by the HRF, which is discussed in Section 1.11.

The BOLD response incorporates both intravascular and extravascular components, though the extent to which each contributes to the signal depends on the magnetic field strength and acquisition method employed (Chen and Cohen-Adad, 2019). For spin echo EPI, particularly at field strengths above 4T, intravascular contributions can be detected due to the suppression of magnetic field-induced inhomogeneities as discussed in Section 1.4 (Boxerman et al., 1995; Duong et al., 2003). These contributions arise from dynamic dephasing induced by the paramagnetic field changes produced by deoxyhaemoglobin. The susceptibility differences in this case produce a reduction in T_2 localised to the capillaries, venules and veins, constituting up to 70 % of the total BOLD signal (Chen and Cohen-Adad, 2019).

For GRE-EPI at 3 T, the BOLD response is primarily sensitive to downstream effects of neural activity, i.e. in large draining veins. These involve static dephasing produced by the susceptibility differences between tissue and deoxygenated blood, which induce T_2* shortening. Despite its lower specificity to the location of neural activity, the functional sensitivity of this technique is much higher than spin echo EPI (Chen and Cohen-Adad, 2019). The technicalities of this method are discussed in more depth in Section 1.8.

1.8 Conventional Functional MRI with Echo-Planar Imaging

The most popular acquisition method to date for fMRI is GRE-EPI. EPI (Mansfield, 1977) involves encoding multiple gradient echoes in the course of one RF excitation, hence allowing rapid acquisition of images. Pre-phasing gradients are applied prior to the series of both frequency and phase encoding gradients to move to the bottom corner of k-space (Bernstein et al., 2004; Brown et al., 2014). GRE-EPI is performed using a bipolar oscillating readout gradient, where a series of readout gradient lobes are applied with alternating polarity. Between each gradient lobe, a short phase encoding gradient, or "blip" (Stehling et al., 1991), is applied to transition the sampling across k-space (Figure 1.5). An exemplar GRE-EPI pulse sequence is shown in Figure 1.5 with trapezoidal waveforms, though sinusoidal waveforms can also be used (Stehling et al., 1991).

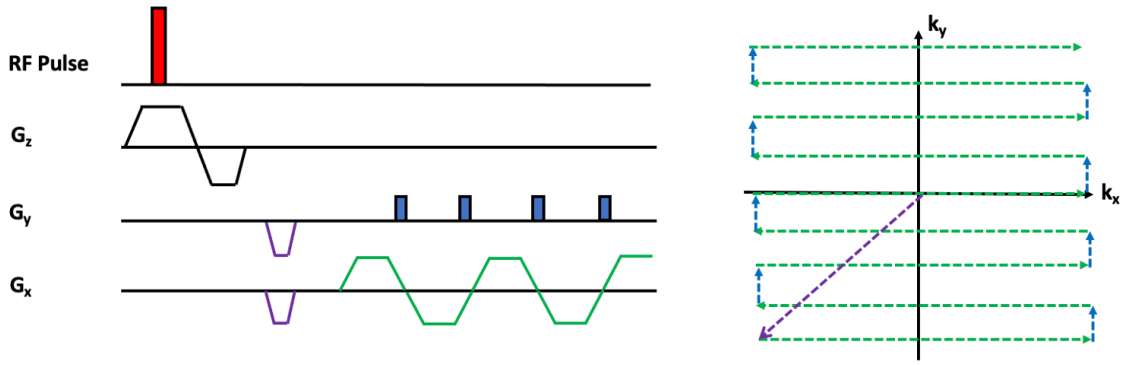

Figure 1.5: (left) Simple example of the GRE-EPI pulse sequence, where G_x, G_y, G_z are the gradient waveforms in the x-, y- and z-directions. The x-direction involved the bipolar oscillating readout, the y-direction indicates the phase encoding blips, and the z-direction in combination with the RF pulse produces slice selection. (right) Simple example of a slice in k-space, where k_x, k_y are the k-space encoding directions colour-coordinated with the pulse sequence.

GRE-EPI acquisitions for fMRI are often 'single-shot', encoding multiple lines of k-space after one RF excitation. Each line of k-space is encoded by an echo, produced by the oscillating bipolar gradient. However, the echoes produced decrease in amplitude with time, affecting the signal contribution to the portion of k-space encoded. For example, the final echo in the "echo train" could be at a later echo time, where the signal will have decayed substantially (see Figure 1.2 and Equation (1.11)). Less signal will therefore contribute to the designated portion of k-space, affecting image contrast (Bernstein et al., 2004; Brown et al., 2014).

The time at which the k-space sampling passes through the centre of k-space in GRE-EPI determines the extent of T_2* weighting of the image, which directly relates to the sensitivity of the technique to the BOLD response (Ogawa et al., 1992); hence this is the echo time of interest for fMRI (Brown et al., 2014; Dale et al., 2015). In other words, the TE is the time delay between excitation and the data collection at the centre of k-space (Buxton, 2013; Huettel et al., 2014; Ljungberg et al., 2021a). The T_2* of the tissue of interest must therefore be carefully considered when determining the TE employed by the GRE-EPI acquisition.

GRE-EPI can collect an entire 2D k-space slice using one RF excitation, therefore the total time to acquire a volume is simply a product of the number of slices and the time to acquire one slice. One slice is acquired on the order of tens of milliseconds in order to collect the data before significant T_2* decay, typically producing a TR on the order of 2-3 seconds (Huettel et al., 2014). The main sacrifice is that of spatial resolution, as the size of the k-space matrix must be lower to traverse k-space so quickly. Standard GRE-EPI acquisitions involve a 64 x 64 matrix size, with approximately 3 mm resolution, though numerous advances have improved the spatial and temporal resolution of GRE-EPI (Section 1.9).

1.9 Advances in Functional MRI

Methods to circumvent the spatiotemporal limitations of GRE-EPI have ranged from novel sampling schemes to advanced image reconstruction techniques. Parallel imaging has accelerated GRE-EPI acquisitions, as it does not require full k-space coverage to acquire an image of appropriate spatial resolution (Brown et al., 2014). Instead, image reconstruction incorporates the sensitivity patterns from the elements of the receive coils to compensate for missing k-space data, producing high quality images across techniques (Hamilton et al., 2017). For example, this technique has been used for spin echo fMRI with Half Fourier Acquisition Single Shot Turbo Spin Echo (HASTE), yielding fewer artefacts and accelerating acquisition (Ye et al., 2010).

Single-shot GRE-EPI is typically a 2D slice-selective technique, meaning a 3D image is formed through "stacking" the acquired slices. Timing differences between the slices are then addressed in post-processing. Single-shot approaches to 3D imaging, whereby the whole volume is excited, have been applied with EPI (Mansfield et al., 1989) and then extended to fMRI studies (Mansfield et al., 1995b; Van Der Zwaag et al., 2006). The core limitations have been lower spatial resolution and longer sampling times, though these have been circumvented using numerous techniques such as integration with parallel imaging and multi-band acquisitions (Narsude et al., 2016; Posse et al., 2012; Rabrait et al., 2008). Multi-band acquisitions in particular are gaining widespread popularity in fMRI, as they can substantially reduce acquisition time (Feinberg and Yacoub, 2012; Kundu et al., 2017; Preibisch et al., 2015; Yang et al., 2020). These techniques acquire different portions of k-space data through using multiple RF excitations, followed by combining the images at the reconstruction stage, which benefits spatial resolution in both 2D and 3D (Graedel et al., 2017; Jorge et al., 2013; Krämer et al., 2012; Menon et al., 1997; Van Der Zwaag et al., 2012).

Methods for 3D GRE-EPI with alternative sampling techniques have also been developed with success. For example, hybrid methods that segment the acquired trajectories have been shown to improve the temporal resolution (Beckett et al., 2020; Goerke et al., 2005;

Graedel et al., 2017; Stenger et al., 1998). Radial 2D GRE-EPI acquisition schemes (Silva et al., 1998) have been extended to 3D by incorporating multi-shot functionality, i.e. segmenting the acquisition, demonstrating repetition times of 400 ms per volume at 3.75 mm isotropic resolution (Lee et al., 2010). More recently, such techniques have been applied at as short as 22 ms per volume (Rettenmeier et al., 2021), though fluctuations in aliasing patterns were of concern. Temporal acceleration of 3D GRE-EPI is an exciting area of development, particularly as it could better disentangle the contributions of physiological noise from neural activity, especially at high magnetic field strengths ($>$ 3 T) (Bollmann and Barth, 2020; Francis and Panchuelo, 2014; Jorge et al., 2013; Narsude et al., 2014; van der Zwaag et al., 2016).

Despite these excellent advances in implementing 3D GRE-EPI, many of the technical developments have been tailored to specific sites, paradigms, or mechanisms behind the BOLD response, and can also be computationally demanding (Bollmann and Barth, 2020). This limits the accessibility of these advances for widespread fMRI research; hence 2D single-shot GRE-EPI remains the most common fMRI acquisition method. One of the more widely used developments of GRE-EPI has been multi-echo fMRI, as discussed in Section 1.10.

1.10 Multi-echo Functional MRI

Multi-echo fMRI with GRE-EPI is a simple extension that produces a separate time series for different echo times, sampling the k-space domain at multiple time points within one RF excitation (Posse et al., 1999). This procedure means that the volumes acquired from each echo will have a different amount of T_2* weighting but consistent T_1 weighting, allowing better identification of non-BOLD-related noise sources in the fMRI signal (Posse, 2012; Speck and Hennig, 2005). The method of extracting these noise sources is described by Kundu et al. (2012), whereby the signal S at echo time TE_n can be described as

$$S(TE_n) = S_0 \exp(-R_2 * TE_n) \tag{1.24}$$

where $R_2* = 1/T_2*$ and S_0 is the initial signal intensity at TE = 0. Changes in signal can then be defined by a simple two-component model (Equation (1.25))

$$\frac{\Delta S}{S} = \frac{\Delta S_0}{S_0} - \Delta R_2 * \cdot TE \tag{1.25}$$

where ΔS is the signal change for a given echo time, ΔS_0 represents non-BOLD signal changes and ΔR_2* represents BOLD-related signal changes. The change in signal overall will increase with TE for the BOLD signal changes, but non-BOLD signal changes will be relatively constant across echo times or not show an exponential dependence (Figure 1.6). Non-BOLD signal changes typically include motion, fluctuations in MR hardware (known as thermal noise) and physiology (Kundu et al., 2017).

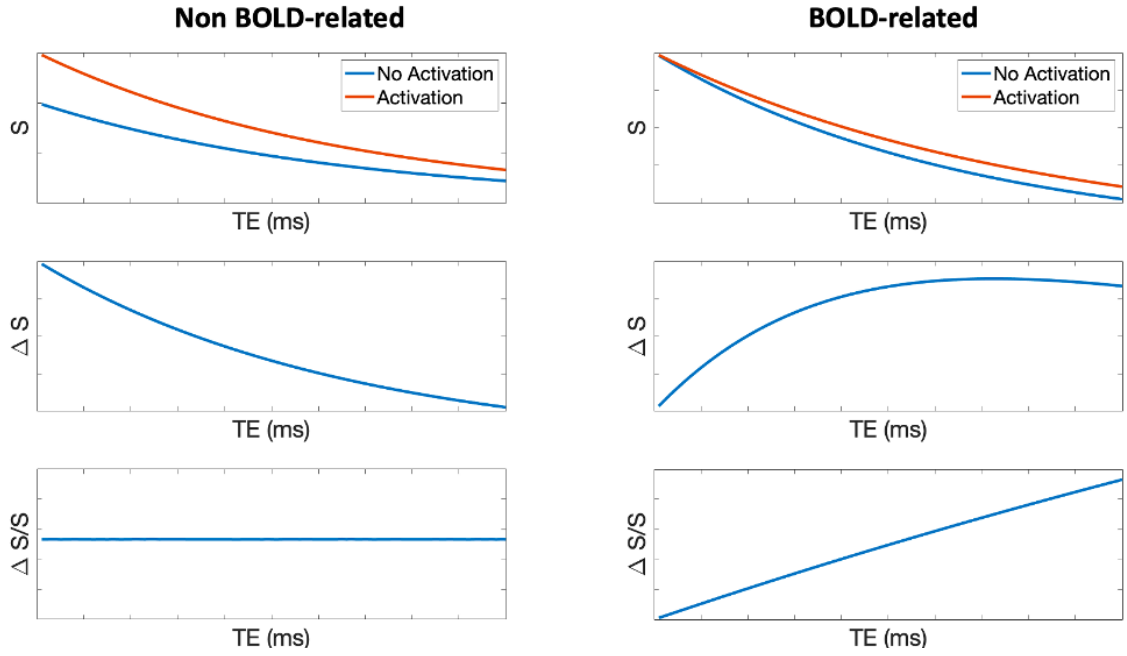

Figure 1.6: Example of signal dependence in multi-echo fMRI. (top) For non-BOLD-related signals, the signal amplitude (S) will decay in a similar manner during the state of activation (orange) or the state of no activation (blue). (middle) The difference between these states (ΔS) shows that the change in signal decays exponentially in time, whereas the percentage signal change ($\frac{\Delta S}{S}$) will be constant with increasing echo time. (bottom) Alternatively, BOLD related signals will evolve differently between the two states, leading to an increase in percentage signal change with increasing echo time. The T_2* values employed for this simulation were 66 ms for no activation and 80 ms for activation states, derived from Table 1.1. Based on Figure 1 by Kundu et al. (2012).

Multi-echo fMRI not only enables separate statistical maps to be created for each echo, but the echoes can also be combined to maximise the BOLD contrast-to-noise ratio (Poser et al., 2006; Posse et al., 1999). Producing a weighted summation of the T_2* images allows modelling of the noise in the BOLD time course without making any assumptions about its characteristics (Gowland and Bowtell, 2007; Kundu et al., 2012). One of the most accepted strategies to date is an optimal combination weighting (Kundu et al., 2012; Posse et al., 1999).

After optimal echo combination, Independent Component Analysis (ICA) is often used as a de-noising strategy to extract or remove non-BOLD components (Evans et al., 2015; Kundu et al., 2012). ICA can be used both for task-based (Gonzalez-Castillo et al., 2016; Moia et al., 2021) and resting-state data (Lynch et al., 2020; Olafsson et al., 2015; Waltmann et al., 2019). Alternatively, sparse paradigm-free mapping is a novel deconvolution technique applied to multi-echo fMRI, which can be used to extract ΔR_2*-related signal changes for tasks where event timing may not be known (Caballero-Gaudes et al., 2019).

In single-echo acquisitions, the echo time is selected to be close to the T_2* of grey matter in the region of interest to maximise functional contrast. For multi-echo fMRI, the choice of the range of echo times of multi-echo fMRI is important to optimise BOLD sensitivity, and a lower receiver bandwidth should be used to maximise SNR (Gowland and Bowtell, 2007).

Other considerations for multi-echo fMRI are highlighted by Kundu et al. (2017), including the impact of the unmet assumption that noise is isotropic and homogeneous in multi-echo data and whether global signals should be removed. The employment of multi-band multi-echo imaging has also overcome temporal limitations the technique (Boyacioğlu et al., 2015; Olafsson et al., 2015), and the benefits of multi-echo fMRI have also been demonstrated at 7 T (Poser and Norris, 2009).

1.11 Functional MRI Experiment Design

At this stage the physics behind conventional fMRI has been detailed, highlighting that the technique involves collecting an entire brain volume image (or, for multi-echo fMRI, a group of images) as rapidly as possible (i.e. using a short TR). Rapid sampling ensures that the signal evolution for the duration of the experiment can be acquired. Each voxel will then contain a time-dependent signal, or time series, sampled every TR (e.g. 2-3 seconds). These time-evolving signals are influenced by the BOLD response: when neural activity occurs, the blood-oxygen-level phenomenon leads to variations in the time-dependent signal, relative to regions of reduced activity. It is now important to highlight the practicalities of fMRI experiment design.

The most common fMRI experiment design, or task-related paradigm, is a simple block-periodic design stimulation. This design involves a stimulus (A) presented for approximately 15 - 30 seconds, followed by a period of either no stimulus presentation or a 'control' stimulus (B). This is repeated in an A-B-A-B manner. With this design, periodic signal changes in the time series are (in theory) generated in response to the stimulation in areas of the brain engaged in the execution of the paradigm. Even the briefest stimulation will induce a response, and this can be characterised in a linear manner (Boynton et al., 1996, 2012). Linearity in this context means that the amplitude of the response scales with the intensity of the stimulus, and if two stimuli are applied in quick order they will superimpose. However, Vazquez and Noll (1998) found that the amplitude can only be predicted in this manner for stimuli of at least 6 seconds.

Event-related designs differ from block designs as they involve presenting short stimuli (a few seconds), usually in a 'jittered' order (Watanabe et al., 2013). Event-related designs enable probing of more specific cognitive mechanisms, such as episodic memory (Buxton, 2013). The key consideration for such studies is the timing between stimuli, particularly considering the impact of non-linear contributions to the BOLD signal (Monti, 2011). A full review of study design considerations is given by Amaro and Barker (2006) and Poldrack et al. (2011), with some of the pitfalls of particular designs outlined by Haller

and Bartsch (2009).

1.12 Functional MRI Analysis

1.12.1 Haemodynamic Response Function

In order to interpret which brain regions are active (i.e. those that are demonstrating the BOLD response), a model is used to represent the expected change in signal. The most common model used is the convolution of the input stimulus paradigm and the hypothesised HRF, which is often modelled by a Volterra or Gamma-variate function (Friston et al., 2000b; Uludağ et al., 2015). At times, the haemodynamic response function (HRF) is used interchangeably with the BOLD response, though it should be noted that the HRF is a linear impulse function used to describe the MR signal changes from the initiation of a stimulus (Poldrack et al., 2011). The HRF consists of the following key components: the initial dip of the signal amplitude, the rise to the peak, the fall, and the undershoot (Figure 1.7).

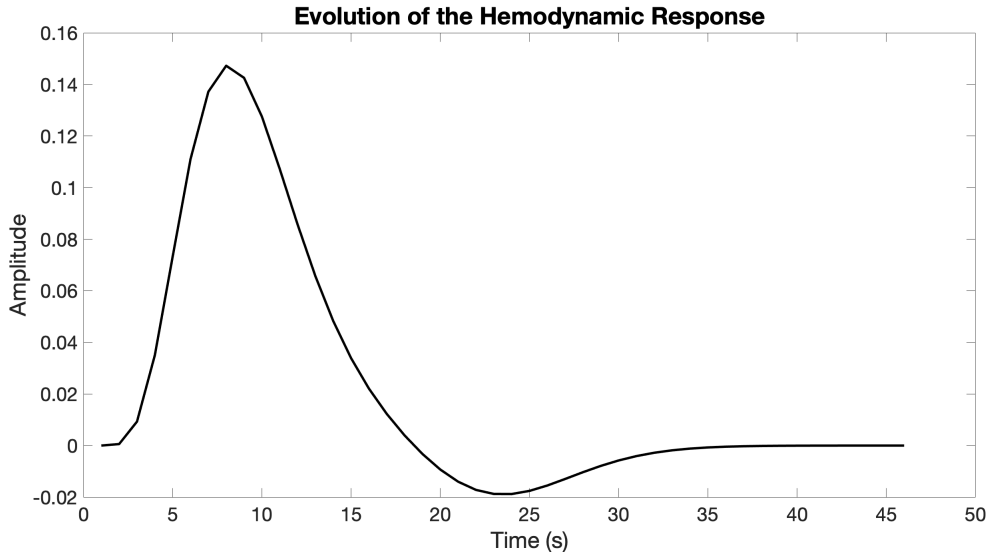

Figure 1.7: Example of the haemodynamic response function, generated with 'spm _hrf' function (FIL Methods Group, 2020) using TR = 0.7, number of time bins used to generate function = 16, response delay 6 s, delay of undershoot 16 s, dispersion of response = 1, dispersion of undershoot = 0.5, ratio of response to undershoot = 6, onset of activation at 0 s and length of kernel 32 s.

Different models have been used to interpret these dynamics on a physiological basis (Buxton, 2013; Poldrack et al., 2011). The initial dip is a 1 - 2 second interval before the positive rise in signal, where it is thought that there is an increase in the concentration of deoxygenated haemoglobin without an increase in regional blood flow; hence a signal reduction is seen. This initial dip, however, is not always easily observed, and the physiological interpretation of this has not been straightforward (Ances, 2004).

Following the initial dip, there is an increased inflow of oxygenated blood which leads to signal recovery and rise to the signal peak as more oxygenated blood is delivered than extracted, peaking at around 5 seconds after the initial stimulus (Huettel et al., 2014). After the response to the stimulus stops, the blood outflows and the signal decreases to baseline. However, it produces a post-stimulus undershoot thought to be related to venous expansion or the maintenance of increased neuronal activity in the absence of reactive hyperaemia (Buxton et al., 1998; Friston et al., 2000b).

Characterisation of the haemodynamic response is an ongoing field of research, varying from identifying activity in cortical columns at increasing field strengths, enabling techniques such as Vascular Space Occupancy (VASO) (Huber et al., 2018; Lu et al., 2003) which indirectly measures cerebral blood volume, to using high spatiotemporal resolution across the cortex to refine modelling (Taylor et al., 2018). The shape and dynamics of the haemodynamic response can also vary not only between individuals (Badillo et al., 2013; Handwerker et al., 2012) but between stimuli (Haigh et al., 2015) and brain regions (Handwerker et al., 2012). Furthermore, the coupling between neural activity and haemodynamic signals can vary in strength and pattern (Drew, 2019). These are vital considerations for fMRI analysis.

1.12.2 General Linear Model

The most common framework used to model the fMRI time series, upon selection of an appropriate haemodynamic response function, is known as the general linear model (GLM). The GLM involves correlating the measured time series for each voxel with a reference

model, which is defined by a design matrix including the stimulus pattern and selected regressors (Poldrack et al., 2011). Voxels with signals that are tightly correlated (i.e. statistically significant) with the model used are considered "active". As described by Pernet (2014), the GLM is defined by the following matrix equation (Equation 1.26)

$$y = X\beta + \epsilon \tag{1.26}$$

where y is the column vector of the time series from each voxel, X is the experimental design matrix convolved with the haemodynamic response function, and β represents the coefficients (or weightings) of each of the experimental conditions contained in the design matrix. The β coefficients are needed to fit the design matrix to the signal, minimising the difference between the design and the measured signal. ϵ is the error term. Figure 1.8 demonstrates the fMRI design matrix.

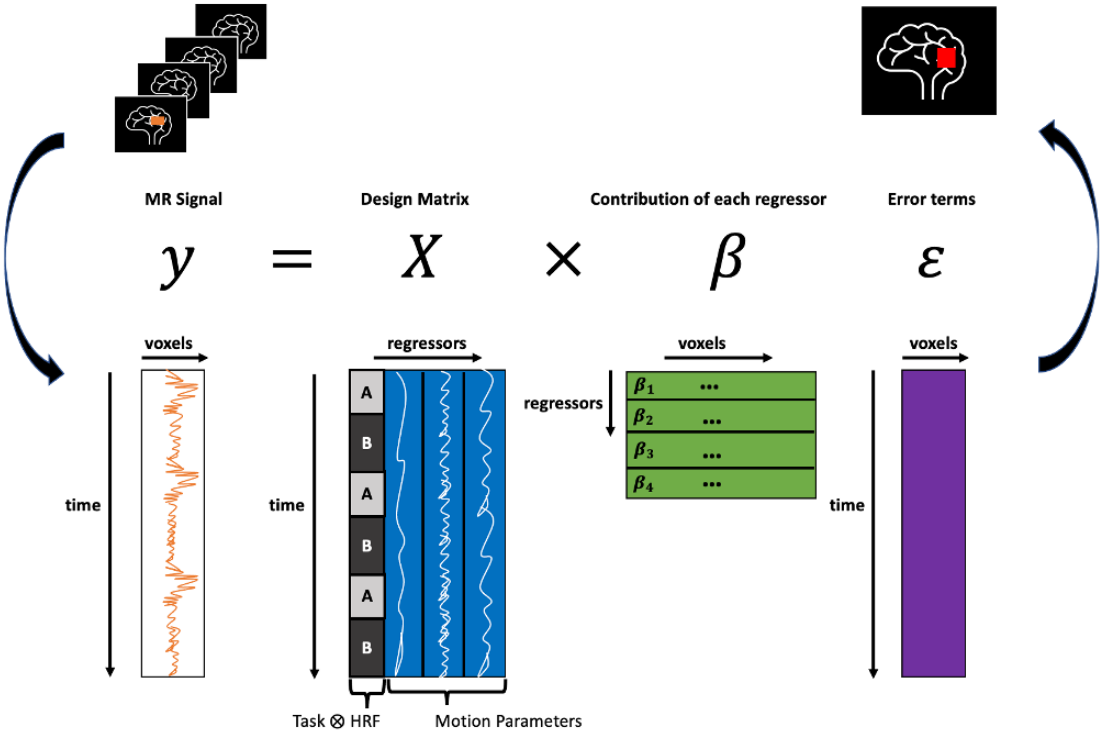

Figure 1.8: Visualisation of the fMRI design matrix format. The time series per voxel is modelled using a design matrix containing the model and regressors that are weighted in contribution according to their β parameters. The first component of the design matrix is the task convolved with the appropriate HRF, with the following components being motion regressors. An error term is also included in the model. Inspired by Jenkinson et al. (2017).

The set of model β parameters can therefore be obtained by matrix inversion:

$$\hat{\beta} = (X^T X)^{-1} X^T y \tag{1.27}$$

where X is the design matrix, X^T is the transpose of the design matrix, y is the vector of the time series, and $\hat{\beta}$ is the predicted beta values. The variance in the data $\hat{\sigma}^2$ is then given by

$$\hat{\sigma}^2 = \frac{\hat{e}^T \hat{e}}{n - rank(X)} \tag{1.28}$$

where n is the number of dimensions of the matrix and $\hat{e}$ are the estimated residuals. The model for a given contrast of interest c is deemed significant through the use of the Students t-distribution, whereby

$$t = \frac{c^T \hat{\beta}}{\sqrt{\hat{\sigma}^2 c^T (X^T X)^{-} 1 c}} \tag{1.29}$$

The T-statistic is not a direct measure of neural activity but is proportional to the ratio of the BOLD signal change evaluated by the contrast vector and the variance. The T-statistic is influenced by the variance in the noise characteristics; hence the HRF used to model the BOLD signal must be appropriate (Chen and Cohen-Adad, 2019). In terms of statistical inference, either voxel-level or cluster-level interpretations can be made from the statistical T-maps produced, each with their own conditions for appropriate use (Poldrack et al., 2011).

Once the t-value, or T-statistic, has been determined, statistical significance can be computed. At this stage, it is vital to consider the thresholds used for significance testing, which must be justified (Constable, 2006), and the correction for multiple comparisons as many thousands of voxels are simultaneously activated. Correction for multiple

comparisons is described in depth by numerous sources (Eklund et al., 2016; Lindquist and Mejia, 2015; Loring et al., 2002; Poldrack et al., 2008; Woo et al., 2014), though in brief: as many hundreds of thousands of voxels are present and simultaneously tested in fMRI GLM analysis, assuming that all voxels with a p-value < 0.05 are significant would imply that 5 % of the voxels are false positives; hence the threshold for statistical significance must be controlled for the number of related tests (Poldrack et al., 2011).

Other regressors can be included to model the signal drift and motion parameters, to further account for variability in the model. There are other contributions to the signal variance, which arise from thermal noise, from the electronics of the system, and physiological noise, which usually falls within the frequency range of the TR, i.e. 0.3 - 0.5 Hz (cardiac 1 Hz, vasomotion 0.1 Hz, breathing 0.3 Hz, as described by Chen et al. (2019). Equally, however, it is important not to overparametrise the model (i.e. add too many regressors) as this can change the statistical outputs of the model (Pernet, 2014).

Methods to enable flexibility in modelling are reviewed by (Monti, 2011) and can include using temporal derivatives to account for variability in the haemodynamic response function. Nonparametric statistics have also been implemented for fMRI to address a few of the assumptions that are not valid for fMRI (Eklund et al., 2016; Winkler et al., 2016), and although they can improve the accuracy some paradigms, they cannot be a universal solution (Brown and Behrmann, 2017; Kessler et al., 2017).

'Resting-state' fMRI, i.e. in the absence of an applied stimulus, involves an alternative analysis technique from the GLM presented above. In this case, an explicit model is not used as there is no contrast of interest for the design matrix; the participant is 'at rest' (Huettel et al., 2014). The interest lies in the spontaneous fluctuation of neural activity and the characterisation of networks based on intrinsic correlations between the time series of the different brain regions (Poldrack et al., 2011). Regressors are used to de-noise the signals to give rise to the inherent correlations induced by the haemodynamic response, though various methods can be used to analyse this data that range from model-based to model-free techniques (Lee et al., 2013).

1.13 Limitations of Conventional Functional MRI with Echo-Planar Imaging

Conventional fMRI with GRE-EPI is highly advantageous as it can acquire volumes at a fast rate. Furthermore, the sensitivity of the static dephasing mechanism is substantially higher at conventional field strengths (3 T) than that of other methods sensitive to functionally-induced changes, such as VASO or Arterial Spin Labelling (ASL). However, there are several technical considerations to address when using EPI. The first is that of image aliasing in the phase encoding dimension. The distance between samples in k-space corresponds to the inverse of the length of the field of view. If the field-of-view selected is too small, a "wrapped" image will appear at the edges of the field of view (Brown et al., 2014). Nyquist ghosting is another form of aliasing which originates from phase shifts produced in the time-reversal application between phase-encoding steps in EPI for image reconstruction. These phase shifts produce an overlapping "ghost" in the image (Bushberg et al., 2012; Dale et al., 2015).

Phase shifts between data acquisition steps can arise from numerous sources, including local field inhomogeneities, eddy currents, subject movement or temporal changes in signal amplitude (Bernstein et al., 2004). Phase shifts can also be induced by different tissues in the brain, as different molecules may shift the frequency of precession relative to the receiver frequency. These phase shifts are known as chemical shifts, which can manifest as another artefact in the direction associated with the lowest gradient amplitude (Brown et al., 2014). Chemical shift is particularly prevalent in the presence of fatty tissues. Signal dropout is also common, where the neighbouring magnetic susceptibility of different tissues can cause rapid signal decay or spin cancellation (Bushberg et al., 2012; Huettel et al., 2014), and dynamic changes in local field gradients will be incompletely refocused (Logothetis, 2008).

GRE-EPI is especially sensitive to local field inhomogeneities that cause image distortions, originating from phase shifts that translate to spatial misregistration of spins (Brown et al.,

2014; Huettel et al., 2014). Such inhomogeneities are often caused by the susceptibility differences between, for example, bone, tissue, and air. In the case where the full background gradient is inhomogeneous, these distortions can translate as stretching or shearing in the image, though this can almost be resolved by post-processing methods (Jezzard and Balaban, 1995). Spin-history artefacts are another misregistration artefact, whereby spins with different magnetisation levels are introduced into incorrect slices via through-plane motion, producing exaggerated signals that could be task-correlated (Yancey et al., 2011).

Of particular importance to GRE-EPI for fMRI is the echo-shift effect, where if the phase dispersion occurs to a greater extent during the dephasing gradient lobe than expected, due to magnetic field inhomogeneities, then the time point at which these phases fully refocus upon application of the rephasing gradient lobe will be affected (Brown et al., 2014). Given the dependence of the BOLD signal on the T_2* of a tissue, an incorrect echo refocusing time would limit the signal received at the selected echo time on the scanner interface. This effect is visible in the k-space data as the centre of k-space will appear shifted. If the temporal shift is substantial, signal dropout will occur as the signal will fall outside the acquisition window.

Another limiting factor to MRI in general, but especially to fMRI with GRE-EPI, is inflow effects. These effects originate from the regional blood flow, where the incoming or outgoing blood in an MRI slice effectively carries magnetisation states from other areas (Gao and Liu, 2012). For fMRI, signal fluctuation can confound the localisation of functionally induced signal changes. It can also lead to modulation of the BOLD signal amplitude and interfere with the temporal characteristics of the signal. The specificity of the BOLD signal is also affected in GRE-EPI, as increases in neural activity will produce oxygenation changes in all vessels, with exceptionally high magnitude in the larger draining vessels, that may mask the changes specific to capillary beds (Logothetis, 2008).

Though EPI is generally a very efficient method for traversing k-space rapidly, the raw data requires substantial sorting prior to reconstruction that can lead to ghosting if performed incorrectly (Huettel et al., 2014). Advances using spiral imaging have been

implemented that can address this, however these schemes remain prone to distortion artefacts (Glover et al., 2012). The critical limitation of interest to this thesis is the acoustic noise of GRE-EPI, which is discussed in the next part of the introduction.

Chapter 2

Introduction: Acoustic Noise and Functional Imaging

Summary

This chapter covers the following topics:

- The origin of acoustic noise in conventional fMRI.
- Safety concerns of scanner acoustic noise.
- The impact of acoustic noise across studies and cohorts.
- Alternative strategies for reducing acoustic noise.
- Principles of zero echo time (ZTE) and radial imaging.

Overview

The origins of acoustic noise in GRE-EPI are discussed in depth in this chapter, as this forms one of the key phenomena under consideration in this thesis. The limitations imposed by the scanner acoustic noise across studies and participant cohorts are highlighted. The background of acoustic noise reduction techniques for fMRI is outlined, and the core principles behind the development of Looping Star are introduced.

2.1 Origins of Acoustic Noise in MRI

Acoustic noise is measured using the sound pressure level in the air, in units of decibel (dB, Pulkki and Karjalainen (2014)). Sound pressure level measurements are commonly used as they account for environmental contributions to acoustic noise. This level can be weighted towards specific frequencies to better relate to the frequencies heard by the human ear, as the sensitivity profile of human hearing across frequencies is not uniform (McJury, 2021)

Explicitly, human hearing sensitivity is highest between 3 - 4 kHz and lower for less than 250 Hz and higher than 5 kHz (Pulkki and Karjalainen, 2014). A-weighting is used to weight the sound pressure level towards mid-range sound frequencies, i.e. attenuating the low and high frequencies, therefore better representing human hearing (Pulkki and Karjalainen, 2014). This measurement is referred to as LA_{eq} with units of A-weighted decibels, dB(A). The C-weighted sound pressure level is weighted towards lower frequencies to represent what humans hear during loud noise, with the absolute peak written as LC_{peak} with units of dB(C). As described by McJury (2021), the loudness of a sound is a mental response to the sound intensity and is approximately proportional to the intensity over several orders of magnitude; hence the use of the decibel, which is a log-scale based measure.

The acoustic noise of MRI pulse sequences such as GRE-EPI originates from Lorentz forces. The Lorentz force is a physical principle whereby a force is generated by a time-varying current in a coil within a magnetic field (Grant and Phillips, 1990). For a small element of the coil, it is described by Equation (2.1)

$$F = B_0 \times Idl \tag{2.1}$$

where B_0 is the static magnetic field strength and I is the gradient current through wire

element of length dl. The total force on the coil is the integral of the above equation over the entire coil.

As rapid gradient switching occurs in GRE-EPI, forces are repetitively produced in a short period, manifesting as vibrations of the gradient coil. Given that these coil vibrations are occurring within the housing of the scanner and that sound is simply the projection of vibrations through the air, these vibrations manifest as loud acoustic noise (Shellock et al., 1998). Other sources of noise in the MR facility include that of the cryopump and influences of the RF radiation, the latter of which is known as RF hearing (McJury and Shellock, 2000), but this section will focus on the scanner noise produced by the vibrations induced from gradient switching only.

Acoustic scanner noise, particularly in GRE-EPI, is periodic due to the repetitive structure of MR pulse sequences (Counter et al., 1997). The periodicity in the acoustic profile of EPI is related to the acquisition time per slice, and reducing the time between gradient amplitude changes will increase the noise (Rizzo Sierra et al., 2008). The acoustic noise also increases with decreases in slice thickness, FOV and echo time, as these all lead to more rapidly occurring changes in gradient amplitude within the pulse sequence (McJury, 2021). The gradient slew rate also affects the acoustic noise, with faster gradient slew rates increasing the acoustic noise. This is because faster switching occurs, which increases the forces produced (Ott et al., 2016). Moelker et al. (2003) also showed that the acoustic noise increases with magnetic field strength, supported by Equation (2.1).

Table 2.1 shows the range of recorded sound pressure levels of EPI-based acquisitions across a few studies at 3 T. The methodology is not consistent, and different manufacturers and decibel weightings are used. The more recent GRE-EPI acquisitions indicated in Table 2.1 produce lower acoustic noise levels due to technological advances in scanner technology, such as improved gradient performance.

Table 2.1: EPI-based acquisitions and reported sound pressure level across studies

Authors	Sound Pressure Level	Decibel Weighting	Acquisition Type
Peelle et al. (2010)	90.2	dB(A)	Siemens 3 T Tim Trio (Siemens Medical Systems, Erlangen, Germany). GRE-EPI: TR = 2.8 s, TE = 30 ms, Bandwdith = 2230 Hz/Px, 284 scans, 19.2 cm FOV, 64 x 64 mm matrix
Solana et al. (2016)	114.0	dB(A)	GE 3 T MR750w (GE Healthcare, Waukesha, Wisconsin, USA). GRE-EPI: TR = 2.5 s, TE = 30 ms, 22 cm FOV, 3.4 x 3.4 x 3 mm voxel size
Rizzo Sierra et al. (2008)	102	dB	Philips Intera 3 T. EPI: TR = 3 s, TE = 35 ms, 46 slices, 64 x 64 matrix, 22.4 cm FOV, 925 Hz dominant readout train
Price et al. (2001)	118.3	dB(A)	Varian 3.0 3 T (Varian Inc., Palo Alto, USA). GRE-EPI: TR = 3 s, TE = 5 ms, Slice width = 5 mm, matrix size 64 x 64, 25 cm FOV
Foster et al. (2000)	127	dB	3 T 100-cm-bore Oxford Magnet Technology. EPI (MBEST) Clustered Volume Acquisition. (exact parameters not specified in detail)
Zapp et al. (2012)	88.7	dB	Manufacturer and field strength not specified. Conventional EPI: matrix size 64 x 64, readout 725 Hz, TE = 50 ms, FOV 22 cm, slice thickness 4 mm.

Andoh et al. (2017)	74.8	dB	3 T Siemens Tim Trio (Siemens Medical Systems, Erlangen, Germany). GRE-EPI: Slice thickness 3.5 mm, 36 slices, 22.4 cm FOV, 64x64 matrix size, in plane resolution 3.5 x 3 x 5 mm, acquisition bandwidth 2442 Hz, TR = 2.79 s, TE = 30 ms
Ravicz et al. (2000)	131	dB	GE Signa 3 T. Spin echo EPI: TR = 2 s, slice thickness = 5 mm, matrix size 128 x 64

2.2 Safety Concerns of Acoustic Noise in MRI

The range of human hearing frequencies is between 20 Hz - 20 kHz, with the majority of energy in EPI scanning within the audible range (i.e. up to 1 kHz) (Hall et al., 2009; Talavage and Hall, 2012). Given that hearing sensitivity increases for the audible range of frequencies, hearing ability is susceptible to damage if loud noise occurs in this frequency range (McJury, 2021; Pulkki and Karjalainen, 2014). As earphones and earplugs tend to perform better at higher frequencies than lower frequencies (Brunnquell et al., 2020; McJury et al., 1997), they are the preferred method of dampening acoustic noise and are mandatory for participants being scanned in the United Kingdom (Published by the Medicines and Healthcare products Regulatory Agency, 2021).

However, despite the use of earplugs and earphones being compulsory, the concern regarding participant safety remains. Foster et al. (2000) explored the acoustic noise generated during an EPI acquisition at 3 T and performed five measurement sessions, finding that the sound pressure level ranged from 123 to 132 dB(A). This study highlighted that these sound levels could cause hearing damage without sufficient hearing protection, based on the noise limitations outlined by international guidelines. Sheppard et al. (2018) also reviewed two studies that indicated temporary hearing loss after scanning, stating

that regular MR scanning and absence of earplugs could significantly increase the risk of permanent damage. This supported the findings of Brummett et al. (1988), who found distinct differences in hearing loss between participants wearing earplugs and those that were not.

Sheppard et al. (2018) also stress the importance of appropriate earplug fitting, which is further supported by Viallet et al. (2015) who highlighted the variability of sound attenuation with earplugs. McJury (2021) also describes the importance of earplug application, as well as considerations regarding hidden hearing loss. Radomskij et al. (2002) showed that MRI noise affected otoacoustic emissions, which quantify the operation of the inner ear, with the value decreasing after exposure to MR noise. Govindaraju et al. (2011) also presented a case study of hearing loss and tinnitus post-MRI in a patient case study, and Bongers et al. (2017) showed that acoustic noise exposure increases the rate of change of hearing threshold level, producing some hearing loss.

Another safety concern is that anxiety is a common response to the MR environment (Quirk et al., 1989), with advice in place suggesting the use of music during scanning to lower this effect (Oztek et al., 2020). However, this remains difficult to implement effectively in the noisy scanning environment. Furthermore, although a foetus is protected by surrounding tissues, low-frequency energy levels of sound can penetrate tissue, which could be of concern (Gerhardt and Abrams, 2000). However, no evidence for safety concerns has been recorded to date (Jabehdar Maralani et al., 2021). Shifts in hearing have also been seen in preclinical studies, with interaction effects observed with cisplatin injection (Laurell, 1992) indicating that caution may be advised for studies involving certain drugs.

Finally, the companions and workers in the MR environment must also be considered. For example, Lauer et al. (2012) highlighted that animals (which may be present for assistive needs of patients) could experience hearing damage due to MRI scanner noise. Radiographers also spend a long period in the scanning facility, which could also pose safety concerns (Price et al., 2001).

2.3 Impact of Acoustic Noise: Non-auditory fMRI Tasks

The acoustic noise in fMRI is generally constant across the duration of a scan. For task-based paradigms, it has been assumed that the constant scanning noise is common to both the active and the reference conditions and can therefore be ignored in analysis. This is based on the principle of "pure insertion", whereby contrasting fMRI conditions is considered a simple additive process, which may not be the case when background acoustic noise is present (Di Salle et al., 2003). Studies have shown across various tasks that the acoustic scanning noise interacts with the functional sensitivity of the study. This has been seen in tasks that do not explicitly require auditory recruitment, as discussed in this section.

Tomasi et al. (2005) identified increased BOLD-related responses in the cerebellum, multiple frontal gyri and the fusiform and lingual gyri when implementing a working memory task during periods of increased scanner noise, achieved by deliberately changing the resonant vibration modes of the gradient coil. Another example was produced by Cho et al. (1998b), who investigated the impact of acoustic noise by producing a silent condition with an acoustic shield for the ears and a noisy condition by playing a recording of the scanner noise through the shield. They found that when comparing the silent condition of a visual task compared with the noisy condition, there was reduced visual activation for the noisy condition. They also investigated the impact on motor activation, which was increased during the noisy condition.

Other studies have employed sparse scanning techniques to explore the impact of acoustic noise on the neural response to a variety of tasks, which involve applying a stimulus in blocks without MRI acquisition (i.e. in silence) followed by acquiring the signal changes rapidly after the stimulus ends (Hall et al., 1999). Explicitly, the amplitude of the scanner noise is the same as conventional fMRI when scanning occurs, but acquisition occurs in short blocks after stimulus presentation in silence. This is described in more depth in

Section 2.6.2.2. Contrary to Cho et al. (1998b), Elliott et al. (1999) demonstrated no impact of acoustic noise on both visual and motor tasks using sparse sampling, though decreased activation was seen during an auditory task for the sparse sampling method.

Identification of resting-state networks has also been affected when comparing their characteristics between sparse and continuous acquisitions (Yakunina et al., 2015). A method of sparse sampling known as Interleaved Silent Steady State (ISSS) has also shown that the connectivity between resting-state networks is affected by acoustic noise (Andoh et al., 2017). Another method of adapting the fMRI scanner noise is presented by Haller et al. (2005). In this case, the scanner noise is, again, of the same amplitude as conventional fMRI, however the EPI noise is tuned to be either continuous or pulsed. They found differential activation across the cortex between techniques, although differences in the sampling schemes between techniques may have affected the results.

One method to address the scanner acoustic noise volume is to employ noise-cancelling headphones (described in Section 2.6.1.3). These headphones can be also be used to simultaneously cancel the scanning noise and play auditory stimuli. Such hardware has demonstrated interesting behavioural effects from the acoustic noise from fMRI. For example, recorded acoustic scanner noise played through noise-cancelling headphones affected the olfactory detection threshold score in an olfactory task (Fjaeldstad et al., 2019). However, the acoustic noise of fMRI did not affect taste perception in a separate study using similar methodology (Lorentzen et al., 2021). Playing recorded acoustic scanner noise through insert earphones has also been shown to significantly reduce unpleasantness ratings in a heat-related pain paradigm (Boyle et al., 2006).

The scanner noise itself has also been integrated as part of the fMRI paradigm, where Zhang et al. (2005) suggested that gradient acoustic noise reduced activity in the visual cortex using a cross-modal paired stimuli paradigm. This paradigm involved presenting a flashing light after the scanner acoustic noise with a varying delay. They found that the visual activity differed based on the duration of the delay, with significant signal reduction in the visual cortex occurring when the flashing light was presented 300 ms after the acoustic noise. In this case, a conventional multi-slice fMRI acquisition was

used with a 1.35 second delay applied between volumes. These studies suggest that the interpretability of many tasks may be affected by the acoustic background noise.

2.4 Impact of Acoustic Noise: Auditory Processing fMRI Studies

Although scanner acoustic noise can affect other regions of interest as described in Section 2.3, the region that is predominantly affected by acoustic noise is the auditory cortex, as highlighted by the following studies. The methodological challenges of auditory fMRI are reviewed by Peelle (2014).

Bandettini et al. (1998) demonstrated the impact of acoustic noise by mapping the regions of the brain that are reactive to acoustic scanner noise. The study was performed by creating a contrast between one sequence which collected the EPI signal, as normal, and another sequence that applied only the gradients initially then applied the RF excitation after some time. Based on changes in the steady-state MR signal, they found auditory regions with enhanced BOLD contrast induced by the noise of the gradient pulses. Talavage et al. (1999) also demonstrated that the spatial extent and the z-scores of regions activated by an auditory paradigm decreased with a longer duration of gradient noise from the scanner using a GRE-EPI acquisition. Extended durations of acoustic noise were applied using gradient switching without slice excitation.

In a two-part study, Gaab et al. (2007b) first showed increased signal within Heschl's gyrus for a word-processing task when employing clustered-volume and sparse temporal sampling acquisitions in comparison with continuous scanning. Gaab et al. (2007a) then showed that during the same word-processing task, but with different levels of scanner background noise, there was an interaction effect of the acoustic noise that impacted the contrasts of the experimental and baseline conditions. Both studies primarily detected changes within Heschl's gyrus, though they comment on effects seen in other auditory-related brain regions.

Acoustic noise can also have behavioural effects in response to auditory paradigms. For example, Pripfl et al. (2006) demonstrated that participants with a low tolerance for fMRI acoustic noise performed worse during a mental reasoning task, using an EEG acquisition with fMRI background noise applied. Shah et al. (2000) also showed that scanner noise affected task performance when acquisition involved short repetition times, likely due to significant acoustic masking from the background noise. Jäncke et al. (1998) also showed that increasing auditory stimulus intensity, when avoiding masking effects using appropriate acquisition and paradigm timing, can increase the spatial extent of the fMRI response.

PET is an interesting technique to use in combination with recorded fMRI noise as PET acquisition is silent. Using ^{15}O labelled water, PET can measure radionuclide uptake due to increased cerebral blood flow induced by neural activity. Mazard et al. (2002) used PET during a visual mental imagery task with fMRI-like noise applied during acquisition, demonstrating that the acoustic noise increased the regional cerebral blood flow in the anterior cingulate cortex and Wernicke's area. Furthermore, they found that more errors in the task took place during acoustic noise condition. Chonde et al. (2013) also showed that MR acoustic noise was related to a specific increase in FDG uptake in the primary auditory cortex. Magnetoencephalography (MEG) has also been used as another silent acquisition technique to explore the impact of recorded fMRI noise. Novitski et al. (2006) showed that fMRI acoustic noise reduced the amplitude of the MEG responses to different acoustic tones, especially for higher frequency tones.

Further studies of the auditory cortex include that of Peelle et al. (2010), who compared a quieter EPI sequence, which employed sinusoidal readout gradients to produce a narrow-band acoustic frequency spectrum, with conventional EPI and found that the quieter sequence provided more robust activation in the auditory regions. Similarly, Mueller et al. (2011) compared sparse temporal sampling, ISSS and conventional continuous scanning of the same acquisition length and found that ISSS had the best sensitivity to more subtle activity in subcortical brain regions in response to music. This study was further supported by Schmidt et al. (2008), who compared conventional fMRI and clustered sparse acquisition and found more robust functional responses across the superior temporal

plane during sparse acquisition during an auditory language comprehension task.

Not only does the acoustic noise affect the amplitude of the response in the auditory cortex, but also Langers et al. (2005b) showed that the shape of the haemodynamic response was affected by the scanner noise. They found that interactions were more substantial and more complex in shape when the spectral content of the tone stimulus and scanner noise were more similar. This interaction was also shown by Ranaweera et al. (2011), as the haemodynamic response changed for different temporal patterns of background scanning noise. The impact of acoustic noise on subcortical structures linked to auditory processing has also been explored: Sigalovsky and Melcher (2006) found increased activation with increasing sound level for the cochlear nucleus, superior olive, inferior colliculus and auditory cortical areas using sparse sampling.

The impact of auditory noise, applied in bursts using sparse temporal sampling, has also demonstrated an effect on the time course of the BOLD response in the auditory cortex (Hall et al., 2000). Longer TRs are recommended for such acquisitions to reduce the interaction of the scanner noise on any tasks, as scanner noise could affect the effect of interest in the auditory cortex. Tamer et al. (2009) also characterised the haemodynamic response to a single block of fMRI scanning noise and found an estimate for the peak magnitude change from baseline in the auditory cortex of around 0.29 % in the right hemisphere and 0.48 % in the left hemisphere. Ulmer et al. (1998) demonstrated that large auditory and language cortices are bilaterally activated by scanner noise using a task that included an audio recording of scanner noise overlaid on spoken texts.

2.5 Impact of Acoustic Noise: Participant and Patient Cohorts

Acoustic noise from MRI scanning can also significantly impact the participant experience and inclusion in MR research, ultimately limiting the inferences that can be made and therefore limiting investigations of biomarkers that could be crucial for treatment

development.

In particular, participants who demonstrate sound aversive symptoms such as hyperacusis (Baguley, 2003; Baguley and McFerran, 2011) will typically be excluded from fMRI studies, limiting the inferences that can be made of such cohorts (Davies et al., 2014; Golm et al., 2013). Koops and van Dijk (2021) recently demonstrated that participants with hyperacusis can experience significant discomfort during fMRI scanning. Hyperacusis is particularly prevalent in disorders such as the Tullio phenomenon (Watson et al., 2000) and tinnitus (Baguley, 2003; Chen et al., 2015). Another sound aversive trait is misophonia, which is defined as autonomic arousal to innocuous or repetitive sounds (Cavanna and Seri, 2015; Edelstein et al., 2013). Such sounds are indeed present in MRI scanning, which then limits the investigations that can be performed with this cohort.

Participants with autism spectrum disorder are another cohort that commonly reports hypersensitivity to acoustic noise, though its prevalence is likely to differ across individuals (Stiegler and Davis, 2010). Such hypersensitivity is also supported by non-MRI based studies that highlight that noise can significantly affect children with autism spectrum disorder (Kanakri et al., 2017). Children without diagnoses of autism spectrum disorder have also demonstrated inhomogeneous symptoms of sensitivity to sound (Rosing et al., 2016).

Furthermore, although there is theoretically no damage to the foetus in pregnancy (Mervak et al., 2019), there are concerns regarding the scanning of neonates. Neonates can experience detrimental effects as a result of high acoustic noise (Graven and Browne, 2008a,b) so acoustic noise reduction is vital. Philbin et al. (1996) also demonstrated that MRI scanning might alter the vital signs of neonates, signalling potential distress. Tkach et al. (2014) devised an MR system to reduce this noise level in one example, and acoustic hoods have been developed to reduce acoustic noise impact on this cohort (Nordell et al., 2009).

It is important also to address that even participants without a formal diagnosis of a sound aversive condition can be affected by acoustic noise. For example, Sartoretti et al.

(2020) showed that reduced acoustic noise reduced patient discomfort, which is supported by McNulty and McNulty (2009) who demonstrated that participants were far more tolerant, via an acceptability rating questionnaire, of quieter scanning systems. Dewey et al. (2007) also showed that reduced scanner acoustic noise correlated with a reduced incidence of claustrophobia in a cohort study of 55,000 patients. Quirk et al. (1989) demonstrated that anxiety in patients during an MRI scan was affected by scanner noise. The fMRI environment, including the loud acoustic noise, can also exacerbate anxiety in the most vulnerable patient groups, demonstrated by Mutschler et al. (2014) in carriers of genetic polymorphism for anxiety vulnerability.

2.6 Strategies to Reduce Acoustic Noise using GRE-EPI

It is clear from the previous section that conventional fMRI with GRE-EPI produces concerns regarding interpretability of results and accessibility of MR research to all cohorts. However, GRE-EPI-based adaptations to reduce acoustic noise remain preferable given its sensitivity to the BOLD response. Numerous techniques have been applied, both in terms of hardware and software adaptations, to reduce acoustic noise. Gradient acoustic noise is dependent both on the position in the scanner and the forces applied to the gradient coils, as well as the shape and timing of pulses (Hedeen and Edelstein, 1997), hence both software and hardware are important to consider. Given that EPI and fMRI are of interest for this thesis, this section will focus on techniques applicable in these contexts.

2.6.1 Hardware Modifications

The most commonly applied hardware is that of earplugs, earmuffs and helmets to reduce the impact of acoustic scanning noise (Ravicz and Melcher, 2001). However, acoustic noise can be conducted through body tissues to the middle ear; therefore this hardware

may not always provide sufficient attenuation (Di Salle et al., 2003). Additionally, as mentioned previously, appropriate attenuation relies on correct application of earplugs (Sheppard et al., 2018).

Scanner architecture is a critical component for understanding and resolving the acoustic noise that originates from vibrations in the gradient structures (Edelstein et al., 2002). For example, open MRI scanners are low field and also have a very different gradient coil mounting design, both of which contribute to lower acoustic noise (McJury, 2021; Price et al., 2001). Scanner structure can also generate standing acoustic waves in the bore. These standing waves can then vary the sound pressure levels across the different directions within the bore (More et al., 2006).

2.6.1.1 Gradient Isolation

One hardware-based technique to reduce the acoustic noise of the scanner is gradient shielding, which aims to prevent the propagation of vibrations that constitute sound. Air vacuums and separate gradient supports can also significantly dampen acoustic noise. Edelstein et al. (2002) explored various pathways for noise propagation across scanner components, testing different strategies for noise reduction such as vibration isolation, vacuum isolation and damping. In a standard scanner, they found that a substantial contributor to acoustic noise was the vibration in the gradient supports. They addressed this by sealing the gradient assembly in an airtight enclosure.

However, upon isolation of these vibrations, Edelstein et al. (2002) also found further contributions to acoustic noise. Electromagnetism-based noise was identified, including eddy-current induced vibrations within the cryostat inner bore, RF body coil and patient tube. These were addressed using low-eddy-current RF coils, constrained-layer damping and acoustic absorption. They demonstrated noise reduction in the cryostat bore for spin echo EPI of 16 dB(A). The same group later developed further electromagnetic shielding produced by eddy currents induced by "warm bore" cylinder, suggesting the installation of passive copper shielding Edelstein et al. (2005). A model for computation of the vibration

modes of these "warm bore" cylinders was studied in depth by Taracila et al. (2005).

Gradient vibration isolation through the use of vacuum chambers for spin echo EPI was also explored by Katsunuma et al. (2002). They also built a separate support for the gradient coil and employed similar methods for reducing electromagnetic induction in the RF coils to achieve, overall, a 33.5 dB reduction in acoustic noise. Acoustic barriers and sound-absorbing foam have also been used to isolate gradients. For example, one study showed the use of acoustic absorbers in the scanner bore, which reduced the acoustic noise in the acoustic frequency range of an MPRAGE sequence (i.e. above 1100 Hz) (Li and Mechefske, 2010). The same group had previously also demonstrated that an acoustic liner could reduce the sound pressure level for EPI by more than 20 dB (Mechefske et al., 2002). However, the implementation of these gradient isolation systems, as well as any retrofitting to reduce coil vibration (Lin et al., 2009; Mechefske et al., 2002), can be costly and cannot necessarily be applied to installed scanners (Okada and Nakai, 2003); hence these procedures are limited across applications.

2.6.1.2 Gradient Coil Design

Gradient coils can be designed to reduce acoustic noise by devising the coil loop such that the Lorentz forces are coupled and balanced (Bowtell and Mansfield, 1991; Haywood et al., 2007; Mansfield et al., 1994, 2001, 1995a; Roozen et al., 2008). These gradient coil systems have been successfully applied for EPI acquisitions at 3 T, although there are limitations to their efficiency as reviewed by Hidalgo-Tobon (2010).

Alsop and Connick (1996) also designed gradient coils that balanced the torque on a cylindrical coil. Where force is dependent on the current density, element area and magnetic field, the torque also considers angular and rotational effects. This method demonstrated benefits to the performance compared to force-balanced acoustic screening, though there are no comments on whether it significantly reduced acoustic noise. More recently, a low cryogen compact 3 T scanner with an asymmetric force and torque-balanced gradient head coil and sinusoidal gradient pulses has been employed for diffusion

imaging with EPI, which not only improved efficiency but also lowered acoustic noise by 8.5 dB(A) - 15.6 dB(A) relative to whole-body MRI (Tan et al., 2018). It has not, however, been extended for use with fMRI.

Forbes et al. (2007) computed an analytical method to aid the design of coil windings in order to reduce the acoustic noise. At 7 T, Lorentz forces can become of great concern for acoustic noise amplification (see Equation (2.1)). However, the gradient coil geometry can be designed to cancel net forces and effectively dampen the impact (Winkler et al., 2018). Another approach to gradient coil design was presented by Cho et al. (1998a), who demonstrated a rotating direct current gradient coil to remove acoustic noise, though it was limited by its need for projection image reconstruction.

2.6.1.3 Active Noise Cancellation

Active Noise Cancellation (ANC) involves the development of a waveform that destructively interferes with the acoustic noise produced by the scanner. One of the first examples of this technique is demonstrated by (McJury et al., 1997), who produced an antiphase waveform to the noise recorded at the scanner bore centre. This waveform was played through an error microphone (essentially a loudspeaker) in the scanner bore to generate a quiet region produced by destructive sound interference. Different algorithms can be used to generate the optimal antiphase waveform given the complexity of scanner noise, as well as the variability across sequences (Chen et al., 1999; Kannan et al., 2011; Lee et al., 2017; Reddy et al., 2011). Li et al. (2011a) review the history of active noise control in their study, and also demonstrate an active noise control system with a magnetic compatible headset optimised for higher acoustic frequencies.

A recent study by Dewey et al. (2020) used ANC headphones during fMRI scanning to explore lifetime noise exposure levels of individuals and their relationship to neural responses using an auditory paradigm, and found that lifetime noise exposure may be associated with central hyperactivity in young adults with normal hearing thresholds. The same group also published a study demonstrating differences between the results of

continuous and sparse sampling during an auditory processing study when using ANC in both cases (Dewey et al., 2021). Interestingly, although ANC should theoretically benefit the interpretation of auditory studies (Hall et al., 2009), significant improvements in activity maps across studies have not been observed (Blackman and Hall, 2011; Talavage et al., 2014). Reviews suggest that this may indicate the importance of stimulus parameter selection or could suggest that there remains a presence of sub-threshold acoustic energy that interacts with neural activity (Blackman and Hall, 2011; Hall et al., 2009; Talavage et al., 2014).

2.6.2 Software Modifications

Hardware-based modifications for removing or reducing acoustic noise can be costly and challenging to implement across sites; hence software-based (i.e. pulse sequence-related) approaches are preferred. These can vary from adapting timings in the pulse sequence to different gradient waveform applications. Software methods for reducing acoustic noise in structural imaging have not significantly affected image quality, so they are of great interest (Fuelkell et al., 2018; Matsuo-Hagiyama et al., 2016).

2.6.2.1 Gradient Pulse Shapes

One of the pulse sequence modifications employed is the "soft tone parameter", or soft gradient pulses, which decreases the gradient slew rate. Soft gradient pulses were first devised by Hennel et al. (1999) for gradient echo, spin echo and Rapid Acquisition with Relaxation Enhancement (RARE) acquisitions. The trapezoidal pulse waveforms of the gradients are band-limited to lower acoustic frequencies and convolved with a cosine window to smoothen the gradients, reducing the acoustic noise. Rondinoni et al. (2013) used a soft-tone parameter technique with EPI for exploring differences between rest conditions in noisy and quieter scans. The insula, left middle frontal gyrus and right precentral and left inferior parietal lobules showed significant differences between resting-state networks depending on the noise condition. Loenneker et al. (2001) also

used soft gradient pulses with simultaneous multi-slice gradient echo imaging to maximise volume coverage, retaining low acoustic noise and T_2* sensitivity.

Alternatively, Schmitter et al. (2008) developed an EPI sequence where narrow-band acoustic frequencies are produced using a sinusoidal readout echo train. This implementation leads to a low acoustic noise sequence as smoother transitions between gradient directional switching are produced. This technique was evaluated by Peelle et al. (2010) for suitability in an auditory task in comparison with three other sequences. They found that the quieter sequence produced robust activation in response to a sentence listening task in some regions, though loss of activation in others. Zapp et al. (2012) also demonstrated the benefits of sinusoidal readout gradients for fMRI, not only reducing the acoustic noise by 11.1 dB but also improving the temporal resolution. Rather than reduce the acoustic noise of scanning, another technique is to "tune" the pulse sequence to produce a less distracting sound characteristic. For example, Seifritz et al. (2006) presented a technique that produced continuous rather than pulsed sound with the same acoustic amplitude that enhanced the BOLD response for a range of tasks.

2.6.2.2 Sparse Sampling and Clustered Volume Acquisition

The primary alternative for auditory fMRI is sparse temporal sampling, also referred to as Clustered Volume Acquisition (CVA). The principle of these techniques is to apply the stimulus in silent blocks followed by the conventional noisy image acquisition during the peak of the haemodynamic response. This method is feasible as the haemodynamic response peak is approximately 3 - 5 seconds after the stimulus onset. The terminology of "sparse temporal sampling" was initially developed by Hall et al. (1999), whereas clustered volume acquisition was devised by Edmister et al. (1999). The origins of the techniques are discussed in depth by Talavage and Hall (2012), with the main difference between them being that sparse sampling tends to involve longer interscan intervals.

Sparse sampling has also been incorporated with multi-band acquisition, facilitating longer periods of silence between acquisitions (De Martino et al., 2015). The benefits

of sparse sampling-based techniques for BOLD signal detection have been highlighted across numerous studies (Di Salle et al., 2001; Eden et al., 1999; Edmister et al., 1999; Gaab et al., 2003; Langers and Van Dijk, 2012; MacSweeney et al., 2000; Schmithorst and Holland, 2004; Skouras et al., 2013; Yang et al., 2000). Crucially, interval timing must be taken into account with sparse sampling; for example, Liem et al. (2012) demonstrated that the interval timing between periods of scanner noise with short cluster-onset asynchrony produced better results than those with longer cluster-onset asynchrony. Perrachione and Ghosh (2013) summarised the considerations of sparse-sampling fMRI, highlighting the intricacies and limitations of the technique.

Another important consideration is the inter-subject variability of the time to peak of the haemodynamic response, as this can affect the peak BOLD signal received. Furthermore, as the acoustic noise produced by the readout will initiate a BOLD response, the readout duration must be short to avoid contaminating the response to the stimulus of interest. (Di Salle et al., 2003). Andoh et al. (2017) recently evaluated an evolution of sparse sampling known as ISSS (Schwarzbauer et al., 2006) by comparing resting-state results with conventional fMRI. This technique involved the rapid acquisition of a set of echo-planar imaging volumes following silent periods, during which steady-state longitudinal magnetisation was maintained with a train of relatively silent slice-selective excitation pulses. They found high reproducibility across days and increased connectivity between and within a variety of networks.

2.6.2.3 Other Software-Based Techniques

The standard parameters of EPI can also be used to reduce the acoustic noise. For example, McJury (2021) suggests the use of spin echo sequences with 2D functionality and low gradient amplitude to reduce acoustic noise. Parallel imaging techniques such as SENSE can also be employed for acoustic noise reduction as they can facilitate reduced slew rates, given that fewer lines of k-space are required (De Zwart et al., 2002). Tomasi and Ernst (2003) also demonstrated the importance of considering the frequency of the EPI readout trains and frequency of the gradient coil vibrations, as resonant modes

can induce vibrations. Counter et al. (1997) also showed that for a range of MRI pulse sequences, slice thickness and sound pressure level were inversely related.

As will be discussed in more depth in the following section, gradient trajectories can also be adapted to reduce acoustic noise. For example, spiral readouts have inherently lower acoustic noise levels (Oesterle et al., 2001) but produce inhomogeneity artefacts that are more difficult to correct (Graedel et al., 2019). BURST is another example of an alternative acquisition technique, whereby a train of excitation pulses is followed by a train of echoes, therefore not requiring rapidly switched gradients and thus reducing acoustic noise, though producing images with lower signal to noise (Di Salle et al., 2003; Hennig and Hodapp, 1993). Another recent development is that of supersonic EPI, where gradient switching exceeds the acoustic threshold for human hearing (Versteeg et al., 2020).

Other pulse sequence design methods have also been applied across different manufacturers for a range of imaging techniques beyond GRE-EPI, including ComforTone by Phillips (Yamashiro et al., 2019), Piannissimo ™ by Toshiba (Toshiba America Medical Systems, 2014), Silenz by GE Healthcare (Alibek et al., 2014) and the Quiet Suite by Siemens (Aida et al., 2016; Ida et al., 2015), the details of which are not widely available.

2.7 Acoustic Noise Reduction via Radial fMRI

A fundamental limitation to the range of acoustic noise reduction techniques employed for GRE-EPI is that no single technique is employed accessibly across sites and paradigms. A useful solution would be a pulse sequence-based technique that eliminates acoustic noise at its source, as this could be used across sites without requiring advanced or costly setups. This aspiration was one of the factors that reignited the interest in ZTE techniques, as they inherently reduce the acoustic noise of scanning since rapid gradient switching is not used. Instead, small incremental changes in the gradient direction are applied with the net amplitude of the gradient remaining constant. A complete overview

of silent ZTE techniques is presented in a review that I co-authored (Ljungberg et al., 2021a); therefore, this section focuses on specific highlights relevant for fMRI.

The application of the RF pulses in combination with a readout gradient produces three-dimensional sampling "spokes" in k-space that sample the FID. Zero echo-time refers to the time at which the signal sampling crosses the centre of k-space, which is effectively zero since RF excitation and readout bandwidths are applied simultaneously. Considering k-space, the delay between the centre of the RF pulse and the time at which the centre of k-space is sampled is directly related to the T_2* weighting (Section 1.8); hence the term "zero echo-time" is used to describe these sequences (Ljungberg et al., 2021a).

ZTE acquisition schemes were initially established with the intention of imaging flow, as they avoid the timing delays of slice-by-slice images that can give rise to motion artefacts (Jezzard and Clare, 1999; Madio and Lowe, 1995). Furthermore, 3D radial ZTE-based methods are robust to phase distortions induced by motion as artefacts manifest as image blur rather than phase wrapping. These sampling schemes also require short, hard pulses, which produce very low flip angles, in order to produce large excitation bandwidths that uniformly excite the full readout bandwidth (Weiger and Pruessmann, 2012), meaning they are also robust to slice profile effects (Ljungberg et al., 2020).

RUFIS was devised over 20 years ago (Madio and Lowe, 1995) and it is widely accepted as one of the simplest ZTE acquisition schemes. The RUFIS pulse sequence is detailed in-depth in Section 3.1. In brief: as the RF excitation is applied simultaneously with the readout gradient, image encoding begins immediately, barring the brief dead time where no data collection takes place between the coil switching from transmit to receive (Weiger and Pruessmann, 2012). Solana et al. (2016) developed a adaptation to the RUFIS pulse sequence, incorporating a T_2 preparation module before the RUFIS acquisition. This method weighted the signal towards T_2 decay and provided comparable sensitivity to spin echo EPI in a motor fMRI paradigm.

Multi-band SWeep Imaging with Fourier Transformation (SWIFT) is another ZTE-based development applied mainly in preclinical scanners thus far. A 9.4 T scanner produced

32 dB reduction in peak sound pressure level and 20 dB reduced average sound pressure levels than EPI with typical fMRI parameters (Idiyatullin et al., 2015). The key difference relative to T_2 prepared RUFIS is its use of sweeping RF pulses, with multi-band referring to the multiple sidebands of the excitation profile in the readout dimension used to achieve a high bandwidth (Idiyatullin et al., 2015). Multi-band SWIFT has been applied in EEG-fMRI (Paasonen et al., 2020) and alongside deep brain stimulation (Lehto et al., 2017) in rats, producing similar activation levels to that of spin echo EPI. Another preclinical application is that of contrast agent-enhanced ZTE, though this is an invasive technique and hence not preferable for human use (MacKinnon et al., 2020).

The limitation of both SWIFT and T_2 prepared-RUFIS is functional sensitivity, as GRE-EPI is significantly more sensitive to changes in T_2*. It is for this reason that ZTE-based techniques that produce a later echo were developed. One such technique is a ZTE method using a burst of short RF pulses (BURST), which has been applied structurally (Crémillieux et al., 1997; Jakob et al., 1997) and recently extended to fMRI (Lancione et al., 2019; Schulte et al., 2019). BURST involves reversing the direction of k-space traversal after the excitation, returning to the centre of k-space by retracing the steps out of k-space. BURST has demonstrated high quality T_2* and T_2 weighted images, though its functional extension has been limited due to the long repetition times (Lancione et al., 2019; Schulte et al., 2019).

Looping Star, the method of interest for this project, was developed from these principles and is discussed in depth in Section 3.1. To briefly introduce the technique: where BURST involves refocusing by repeating the trajectory, effectively "rewinding" the sequence, Looping Star involves a time-multiplexed gradient refocusing mechanism that produces loops in k-space (Wiesinger et al., 2019). These loops can then be repeated in time, producing multi-echo images. Given that only incremental changes in gradient direction are required to fulfil the refocusing criteria, the silent acquisition is retained.

Chapter 3

Introduction: Theory of Looping Star

Summary

This chapter covers the following topics:

- An introduction to Looping Star via RUFIS.
- Looping Star pulse sequence, k-space trajectory and technical considerations.
- Bloch simulations and point spread functions of Looping Star.
- Implications of under-sampling on the image quality of Looping Star data.
- Computations of spatial profile, Ernst angle and signal-to-noise efficiency of Looping Star.

Overview

This chapter details the key concepts of the Looping Star pulse sequence, including the physics and technical implementation involved in the method. The parameters involved in the Looping Star pulse sequence are described. The impact of under-sampling and signal decay on the point spread function of Looping Star are also shown. Simplified Bloch simulations of the pulse sequence are also presented, and the signal-to-noise ratio (SNR) efficiency is explored.

3.1 RUFIS and Looping Star Pulse Sequences

Looping Star is based on a ZTE sequence known as RUFIS (Madio and Lowe, 1995). RUFIS involves applying a non-selective RF excitation after the gradient has been ramped to a constant value. The gradient direction is then changed by a small amount after the initial signal decay, and the next excitation is performed at a new gradient step (Figure 3.1A). It is this minimal directional gradient change that leads to significant acoustic noise reduction, as reduced gradient switching minimises the vibrations produced by the Lorentz forces that manifest as sound in the scanner (see Section 2.1).

The signal from the entire volume of interest is received, as the excitation bandwidth of the RF pulse encompasses the readout bandwidth (Weiger and Pruessmann, 2012). The excitation bandwidth is the range of frequencies encompassed by the RF field, whereas the readout bandwidth is the range of frequencies encoded by the gradient within the volume of interest. The readout bandwidth is also usually broader than the range of frequencies of interest to avoid wrapping artefacts (Bernstein et al., 2004). The excitation bandwidth encompasses the full receiver bandwidth by means of the excitation employing a short, hard RF pulse, with very low flip angle ($< 5°$). These pulses have been compared with swept frequency pulses, and their ease of use has been highlighted (Weiger et al., 2011). The spatial profile of the RF excitation pulse is described in further detail in Section 3.6.

As previously mentioned, the echo time can be defined as the time between the initial signal excitation and when it is sampled through the centre of k-space (Boss et al., 2015; Ljungberg et al., 2021a; Weiger and Pruessmann, 2012). In RUFIS, this time is effectively zero as the excitation is applied after the gradient is ramped. Sampling therefore begins very close to the centre of k-space (Section 3.9.3). The cumulative trajectory (i.e. the trajectory after applying all gradients 'steps' in the series) extends outwards in k-space, beyond the matrix for the field of view specified (k_{max}), and does not return to the centre of k-space (Figure 3.1B); hence refocusing of the magnetisation is never achieved, and an echo is not produced. Instead, only the initial signal decay is sampled, referred to as the FID despite the gradient presence (Section 1.3), and an image is produced with

predominantly proton density-weighted contrast.

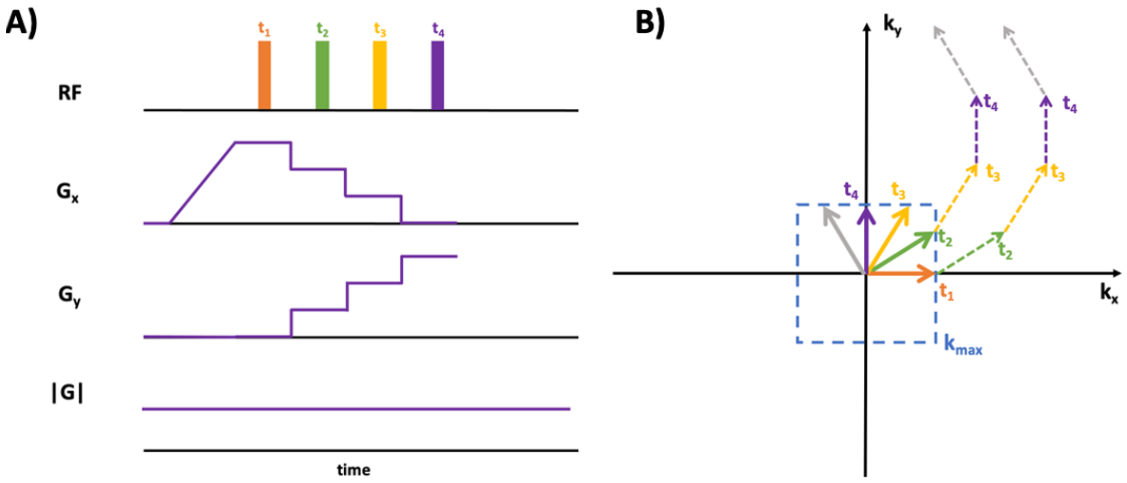

Figure 3.1: A) Diagram of RUFIS pulse sequence across time with hard block RF pulses, and gradients in two dimensions (G_x, G_y). The data is continuously sampled (i.e. the analogue-to-digital converter (ADC) is on) during the gradient directional changes. The net gradient amplitude is also shown ($|G|$). The time points of the first four RF excitations are indicated as t_1, t_2, t_3, t_4 B) Cumulative trajectory in k-space after the first four excitations, colour coordinated to match the RUFIS pulse sequence, with the four time points labelled. Arrows indicate direction of cumulative trajectory. k_{max} is the maximum extent of k-space sampled, depending on the matrix size and spacing.

As described in Sections 1.7 - 1.8, conventional functional imaging (i.e. based on the static dephasing phenomenon) requires a T_2*-weighted echo, therefore the RUFIS scheme described above is largely insensitive to changes in neuronal activity. Either a magnetisation preparation pulse needs to be applied before RUFIS readout, as performed by Solana et al. (2016), or the cumulative sampling trajectory needs to be modified to return the transverse magnetisation component to the centre of k-space to refocus the transverse magnetisation and collect an echo. The Looping Star pulse sequence, developed by our collaborators at GE Healthcare (Wiesinger et al., 2019), achieves the latter by building on RUFIS, modifying the gradient directions so that the k-space trajectory returns to the centre of k-space after a number of gradient steps (Figure 3.2).

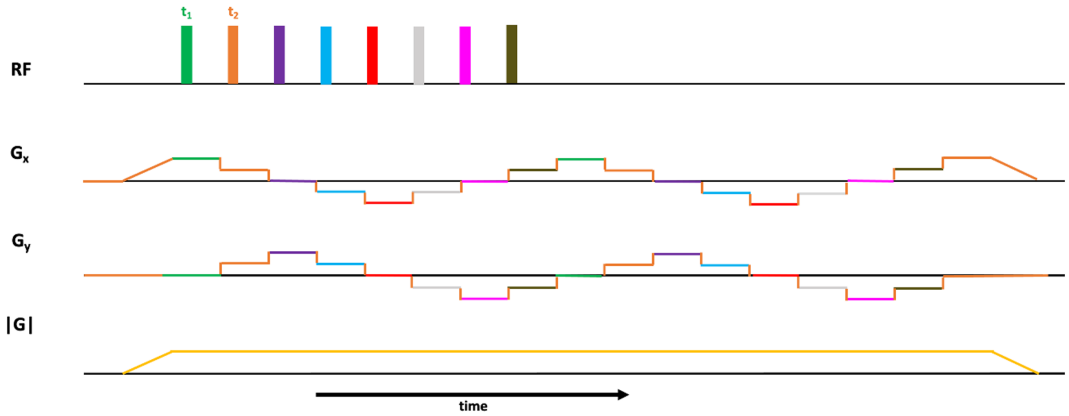

Figure 3.2: Diagram of the Looping Star pulse sequence across time with hard block RF pulses, and gradients in two dimensions (G_x, G_y). The net gradient amplitude is also shown ($|G|$). The first portion of the pulse sequence is RUFIS-like, with eight gradient steps encoding the FID. The gradients are applied such that the cumulative trajectory returns to the centre of k-space, and the second portion then repeats the gradient steps in the absence of RF excitation to encode the echo. The first two RF excitation time points are labelled as t_1, t_2.

The portion of the trajectory encoded by each RF excitation and accompanying gradient in 3D is referred to as a "spoke". As in RUFIS, Looping Star also involves ramping the gradients and, after ramping (i.e. when the gradients reach their required amplitude), then applying a hard, non-slice-selective, RF excitation (Wiesinger et al., 2019). However, the pulse sequence differs from standard RUFIS in how the gradients are applied. The number of gradient "spokes" chosen is applied in a "looping" directional sequence, making the net vector sum of the trajectory $\mathbf{k}$ equal to zero and their net amplitude is constant throughout the loop (Equation (3.1)).

$$\sum_{m=n+1}^{m=N_{SpkPerLoop}+n} \mathbf{k_m} = 0 \tag{3.1}$$

where $N_{SpkPerLoop}$ is the total number of spokes in a "loop", i.e. the total number of gradients applied for the "looping" trajectory (Wiesinger et al., 2019). $\mathbf{k_m}$ is the vector of the spoke trajectory with spoke index $\mathbf{m}$. For example, for $N_{SpkPerLoop} = 4$, the spoke indices will range from $\mathbf{k_{m=n+1}}$ to $\mathbf{k_{m=n+4}}$. If the trajectory from the first spoke $n = 1$ is studied, then it would be seen that the cumulative trajectory will return back to the point of the first spoke at $\mathbf{k_{m=4+1=5}}$ (i.e. $\mathbf{k_2 + k_3 + k_4 + k_5 = 0}$), meaning spoke $\mathbf{k_5}$ would begin the sampling of the echo.

As the cumulative trajectory returns to and crosses the centre of k-space, effectively self-refocusing, an echo is produced. The 'echo time' is given by the time it takes to apply the chosen number of gradient spokes. This "looping" gradient waveform can then be repeated without the RF excitation to produce gradient echoes separated by the same TE; hence the technique is inherently multi-echo.

These cumulative trajectory "loops" occur for each spoke, therefore multiple loops are co-occurring with each loop starting from each successive RF pulse (Figure 3.3A). It is for this reason that Looping Star is sometimes referred to as a 'time-multiplexed' technique (Ljungberg et al., 2021a; Wiesinger et al., 2019) since multiple coherences are excited and self-refocused simultaneously. The refocusing will occur at different time points for each RF excitation (Figure 3.3B).

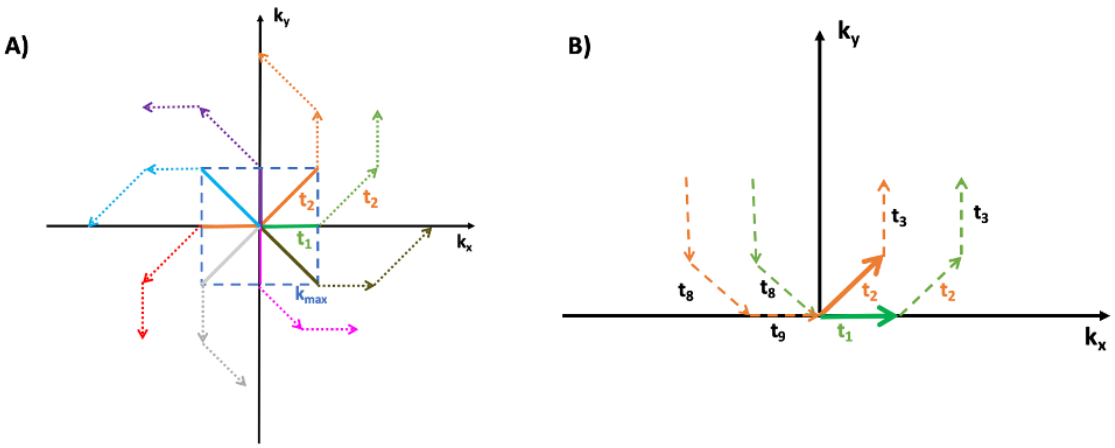

Figure 3.3: A) Cumulative trajectory for all eight spokes in k-space, colour coordinated with pulse sequence. The first two time points of the k-space trajectory evolution are shown (Figure 3.2). The central area k_{max} represents the matrix size and the encoding of the FID portion of the signal. It can be seen that continuing this cumulative trajectory for all spokes will result in refocusing, highlighting the management of multiple coherences. B) "Zoomed-in" version of cumulative trajectory for the first two RF excitations. It can be seen that the cumulative trajectory of the first excitation refocuses at t_8, and the second excitation will then refocus at t_9.

To summarise, the set of initial excitations produce the proton density-weighted image, referred to as the FID. After refocusing, producing the first trajectory "loop", the first echo is generated, and any following loops produce additional echoes. The total number of loops plus the initial excitation is equal to the FID plus the number of echo images. The number of spokes per loop determines how many coherences are simultaneously managed (Wiesinger et al., 2019). The refocusing nature occurs over multiple excitations,

similarly to PRinciples of Echo-Shifting with a Train of Observations (PRESTO) (Liu et al., 1993), and is therefore highly efficient. One of the consequences of this type of refocusing mechanism is echo-in/echo-out interference, whereby the spokes entering k_{max} at the end of the loop overlap with the first spoke of the following loop exiting k_{max}; this is discussed in more depth in Chapters 9 and 10.

3.2 Technical Considerations of Looping Star

In Section 3.1, the number of spokes per loop ($N_{SpkPerLoop}$) and the number of loops (N_{Loops}), i.e. the number of initial excitations and the number of echoes refocused plus the FID image, were used to describe the pulse sequence. In practice, Looping Star involves a segmented application in 3D, where "loops" occur in different conical planes (i.e. the plane being the flat portion of the cone, also known as the base) for full k-space coverage. The number of spokes in one segment ($N_{SpkPerSeg}$) therefore includes the total number of spokes within a conical plane, based on $N_{SpkPerLoop}$ and N_{Loops}.

$$N_{SpkPerSeg} = N_{SpkPerLoop} \times N_{Loops} \tag{3.2}$$

Hence one segment constitutes a conical plane of k-space coverage. This segmented structure is fundamental for describing trajectory generation, which is covered in Section 3.3.

The terms segments, spokes and loops describe the entire 3D encoding and sampling of k-space in the Looping Star acquisition. How the trajectory relates to the temporal parameters of the pulse sequence in Looping Star can now be addressed. A number of points along one radial spoke is collected for the duration of the gradient whilst the amplitude is "flat", i.e. after the ramping before the RF excitation and before ramping down for the next gradient step. The duration of the gradient is referred to as dt_{flat}.

The TE is therefore given by Equation (3.3), representing the time at which the echo is encoded at the centre of k-space

$$TE = dt_{flat} \times N_{SpkPerLoop} \tag{3.3}$$

The relationship between the duration of the "flat" portion of the applied gradients and the sampling time of each point along the spoke, also known as the dwell time (dt_{dwell}, which is proportional to the inverse of the readout bandwidth), depends on the number of sampling points acquired along the spoke ($N_{samples}$)

$$dt_{flat} = dt_{dwell} \times N_{samples} \tag{3.4}$$

The acquisition time for one volume (TR_{vol}), being equivalent to the repetition time in conventional single-shot fMRI since Looping Star is not slice-selective, is calculated based on the ramping times and the time required to acquire all of the segments within the volume (Equation (3.5)). The ramping times must be included; the readout gradients are ramped down and up in between segments. This is performed in a soft and unbalanced manner to reduce acoustic noise (Wiesinger et al., 2019) and effectively "gradient spoils" the signal.

$$TR_{vol} = ((TE \times N_{Loops}) + (2 \times T_{ramp})) \times N_{Segs} \tag{3.5}$$

N_{Segs} is the number of segments and T_{ramp} is the ramping time of the gradients.

The optimum number of spokes per volume can be determined from the image matrix size required. For example, for an isotropic FOV of 19.2 cm and a 3 mm isotropic spatial resolution, each line of k-space collected would need to consist of 64 samples. For full coverage of an equivalent 64 $\times$ 64 rectangular matrix size with 64 slices, 4096 spokes per

volume would be required, with each spoke collecting 64 samples. If it is assumed that a $dt_{flat} \approx 1024\mu s$, for a ±31.25 kHz bandwidth with 64 samples, this would produce $TR_{vol} = N_{SpokesPerVolume} \times dt_{flat} \approx 5.1s$.

This time can be shortened by increasing the readout bandwidth, but this will increase acoustic noise. Although the readout bandwidth is not inherently linked to acoustic noise, increasing the readout bandwidth in Looping Star produces both a shorter dt_{flat} and a higher gradient amplitude, which amounts to higher acoustic noise (see Section 2.1). This mechanism ensures the same extent of k-space is filled, i.e. maintaining the gradient integral in k-space (Section 1.6). One of the benefits of radial acquisition is the distinct impact of under-sampling on artefact production (compared with an equivalent Cartesian matrix), which can be used to accelerate imaging as discussed in Section 3.4.

Furthermore, it should be noted that given that the echo time and repetition time in Looping Star are dependent on the readout bandwidth and number of spokes per loop as described above, these timings cannot be arbitrarily selected. Therefore, the timing parameters must be carefully considered and calculated based on the parameters mentioned above for comparative studies with GRE-EPI.

3.3 K-space Trajectory of Looping Star

As described in Section 3.2, the Looping Star k-space trajectory has a segmented structure where one segment involves the number of spokes in a loop and the number of times these spokes are repeated. This structure provides an efficient method for generating full volume coverage in k-space, such that each segment is rotated relative to another until homogeneous k-space sampling of the volume is complete. In the case of Looping Star, this rotation can be generated analytically or in a random fashion depending on the type of k-space coverage desired. For the majority of the work in this thesis, a pseudo-random trajectory generation technique (Wiesinger et al., 2019) was used unless stated otherwise.

To produce the pseudo-random trajectory, an initial randomly-positioned loop is generated, and the second loop is then selected from an assigned number of random 'test' loops, equivalent to the first but in different spatial positions. The way this second loop is selected from the collection of test loops is determined using a model of charged point sources (Wiesinger et al., 2019). From fundamental physics principles, the electrical potential energy between charged point sources is dependent on their distance from one another (Grant and Phillips, 1990). By assuming the points on a trajectory loop are a distribution of charged point sources, the following loop can be specified to be at a distance that minimises the overall electrical potential between the two loops of charged points. The second loop in the generated collection of loops that minimises this electrical potential will then be selected (Wiesinger et al., 2019).

This calculation is performed iteratively until the necessary number of segments is produced for the number of spokes desired in the volume of interest. The number of test loops used to select the following loops can be chosen manually. Figure 3.4A demonstrates the trajectory "loop" of the endpoints for an 8 spokes per loop acquisition in their corresponding conical planes, and Figure 3.4B demonstrates the centre-out spokes of each loop.

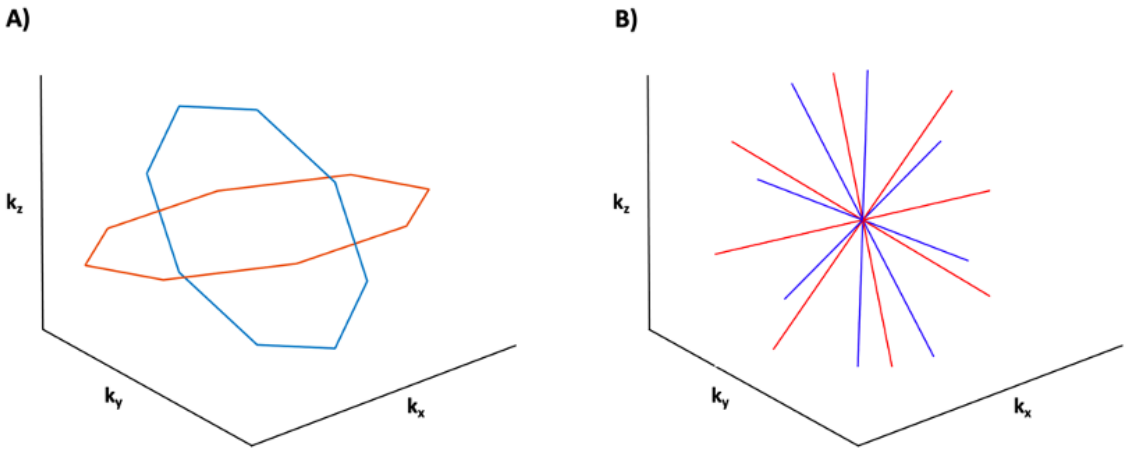

Figure 3.4: A volume of 16 spokes with 8 spokes per loop is shown in two formats. A) Blue and red lines represent "loops" (or joined endpoints) of the generated spokes. One segment corresponds to one loop, multiplied by the number of times the loop is repeated. B) Blue and red lines correspond to each loop, but with coverage of the spokes in centre-out format. A different, randomly selected starting loop is selected between A) and B), with the second loop being selected after 10 test loops.

In the above case, the spokes are 'straight' (i.e. linear from centre-out). However,

the spokes employed in Looping Star are not straight as Looping Star minimises the acoustic noise by employing gradient smoothing within the trajectory of each spoke. Gradient smoothing involves producing curved spokes to minimise the steps between gradients, hence minimising gradient switching. Smoothing the transition between spokes is performed similarly in variable density spiral sampling (Tsai and Nishimura, 2000). A higher GSF will produce more bending along the length of the spoke such that spoke endpoints are spatially nearer. RUFIS, on the other hand, uses a 'spiral phyllotaxis method', where spokes are applied from the centre out along the planes of a 3D spiral (Piccini et al., 2011). Figure 3.5 details the comparison for gradient smoothing factors for Looping Star.

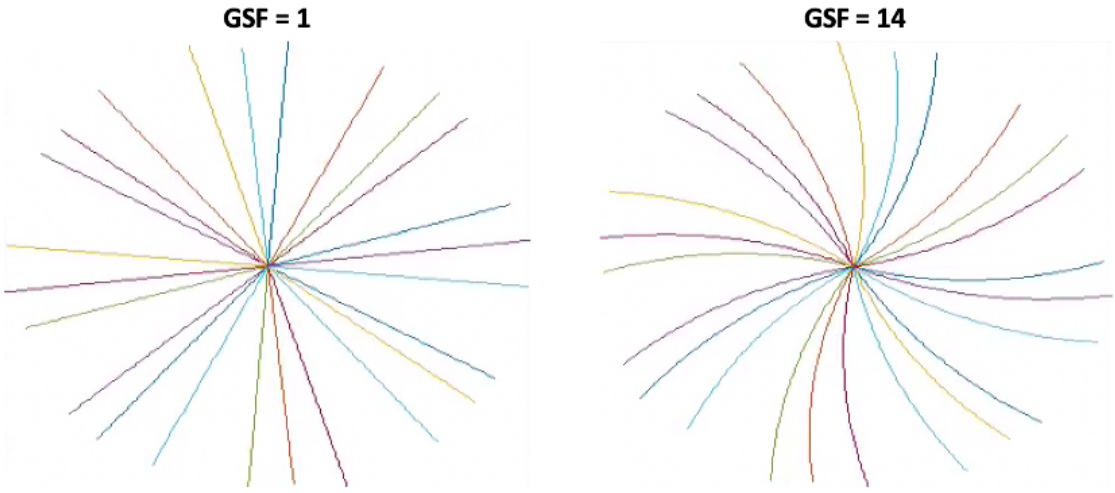

Figure 3.5: Comparison of centre-out spoke pattern for 32 spokes a GSF of (left) 1 and (right) 14.

This trajectory generation method is just one potential technique to determine the orientation of the loops analytically in order to gain homogenous k-space coverage. Alternative approaches can include, for example, computing the 'golden angle' between spokes or planes, which is a geometric principle related to the sectioning of a circle using the golden ratio (Benkert et al., 2018; Chan et al., 2009; Feng et al., 2014). There may also be scope for defining the endpoints of the spokes using hybrid cones for trajectory generation (Johnson, 2017).

Non-cartesian trajectories have attractive benefits to numerous acquisition methods. They are robust to respiratory motion due to the over-sampling of the centre of k-space

(Glover and Pauly, 1992), applied in lung imaging (Boucneau et al., 2021). They can also be useful for 'sensitivity-encoded reconstruction', i.e. for parallel imaging (Pruessmann et al., 2001). As Looping Star is not slice-selective and a single spoke will encode all three dimensions of k-space, there is also scope to employ under-sampling without the significant aliasing seen in Cartesian imaging, as discussed in Section 3.4.

3.4 Accelerating the Looping Star Acquisition

As described in Section 3.2, the number of spokes required to achieve the equivalent sampling density of conventional Cartesian methods can be high, posing issues in terms of both acquisition speed and data storage. One important constraint to evaluate when reducing the number of spokes is the Nyquist criterion. The Nyquist criterion dictates that in order to prevent aliasing of a signal of frequency v, the time between samples of the signal (Δt) should be at least

$$\Delta t = \frac{1}{2 \times (2\Delta v)} \tag{3.6}$$

where $2\Delta v$ is the total readout bandwidth for GE Healthcare scanners, accounting for the full diameter of k-space. The temporal Nyquist criterion also applies to k-space sampling, as described by Bernstein et al. (2004), such that the Nyquist requirement of the spacing between k-space points Δk links to the selected field-of-view (L)

$$\Delta k = \frac{1}{L} \tag{3.7}$$

However, in the case of Looping Star, bent radial spokes of data samples are acquired across a sphere, and the samples between spokes are more densely packed towards the centre of k-space than towards the edges of k-space. Computing the number of radial

spokes needed to meet the Nyquist criterion is therefore not trivial.

One approximate measure to compute the number of spokes required to fulfil the Nyquist criterion is to consider the azimuthal angle in k-space (Winkelmann et al., 2007). If the sampling interval along the length of the spoke ($\Delta k = \Delta k_L$) satisfies the field of view requirement of the Nyquist criterion in Equation (3.7), then the Nyquist criterion will be satisfied if the angular distance between spokes (Δk_θ) does not exceed this value. The spherical distance between two points is given as

$$\Delta k_\theta = r\Delta\theta \tag{3.8}$$

where r is the radius of the sphere and $\Delta\theta$ is the angle between two points. The radius of the sphere in k-space can be given as

$$r = \frac{\Delta k_L M}{2} \tag{3.9}$$

Where M is the matrix size (i.e. number of sampling points along the diameter of the sphere). As stated above, to satisfy the Nyquist criterion, the angle between spokes must be chosen such that

$$\Delta k_\theta = \frac{\Delta k_L M}{2}\Delta\theta \leq \Delta k_L \tag{3.10}$$

$$\Delta\theta \leq \frac{2}{M} \tag{3.11}$$

The number of spokes that fulfil this criterion depends on the surface area of the sphere sampled, whereby the number of spokes multiplied by the angular distance between

spokes should be equal to the surface area of the sphere at appropriate Nyquist sampling

$$N_{spk}\Delta k_\theta = 4\pi(\frac{\Delta k_L M}{2})^2 \tag{3.12}$$

$$N_{spk}\frac{\Delta k_L M}{2}\Delta\theta = 4\pi(\frac{\Delta k_L M}{2})^2 \tag{3.13}$$

$$\frac{2N_{spk}}{M} = 4\pi\frac{\Delta k_L M}{2} \tag{3.14}$$

$$N_{spk} = \frac{\pi M^2}{L} \tag{3.15}$$

For an fMRI image, where $M = 64$ and $L = 19.2cm$, the number of spokes required to satisfy the Nyquist criterion of the spherical acquisition is $N_{spk} \approx 670$. Compared with the requirement of 4096 spokes per volume derived in Section 3.2, 670 spokes is a much lower required number of spokes per volume and would constitute a $TR_{vol} \approx 0.7s$. These equations indicate that fewer spokes than required for full k-space sampling of the Cartesian grid can be employed without significant issues from aliasing, accelerating the acquisition substantially. Empirically, Maier et al. (2021) have shown that it is possible to acquire a smaller number of spokes without significant artefacts, and this has been further supported by 3D radial EPI imaging (Lee et al., 2010).

3.5 Bloch Simulation of the Longitudinal Magnetisation Evolution during Looping Star

3.5.1 Impact of Excitation Pulse Series

Bloch simulations are a valuable tool in MRI to determine the evolution of net magnetisation. Looping Star excites multiple coherences, is 3D, and the spokes have a curved trajectory, so calculating the evolution of the magnetisation of an entire volume, including the echoes, is not trivial. For simplicity, consider an example that includes only the first segment of a Looping Star pulse sequence. As stated previously, one segment is equal to one conical plane, consisting of a number of spokes per loop applied for a number of loops (i.e. FID plus echoes). In this section, the magnetisation evolution caused by eight sequential RF excitations, or spokes, in the absence of a gradient is shown.

Starting with the FID-portion of Looping Star, multiple RF pulses are applied sequentially with interleaved soft and unbalanced gradient ramping to spoil the signal (Wiesinger et al., 2019). Considering the evolution of the net magnetisation in the absence of the gradients, the longitudinal magnetisation after the first excitation pulse (M_{zB}) is given by Bernstein et al. (2004)

$$M_{zB} = M_{zA}cos(\alpha) \tag{3.16}$$

Where α is the FA of the RF pulse and M_{zA} is the longitudinal magnetisation prior to the excitation pulse. In between the application of the first and second RF pulse, T_1 relaxation occurs as defined by the Bloch equations (Bernstein et al., 2004; Bloch, 1946)

$$M_{zC} = M_{zB}e^{-\frac{TR_{rf}}{T_1}} + M_0(1 - e^{-\frac{TR_{rf}}{T_1}}) \tag{3.17}$$

Where M_0 is the initial net magnetisation, usually set as $M_0 = 1$, and TR_{rf} is then the time between RF pulses, approximately the duration of the spoke for Looping Star. Using this formula, the evolution after, for example, eight RF pulses, followed by iteratively calculating the net magnetisation until it enters the steady-state, can be determined. This is shown in Figure 3.6 (top).

By iteratively computing the magnetisation evolution of the RF pulses, the number of spokes required to reach steady-state can be found. From Figure 3.6 (bottom), it can be seen that steady-state is achieved by approximately 3000 RF excitations for these parameters, with an amplitude reduction of 50%, indicating significant T_1 saturation. It should be noted that the flip angles employed by Looping Star are very small, which drives the high number of spokes required.

Given that a conventional fMRI acquisition with Looping Star would consist of approximately 1000 spokes (or RF excitations) per volume, it can be assumed that steady-state will be reached after the first $\approx$ 5 - 10 volumes. These first volumes of any acquisition should therefore be investigated and discarded if necessary. However, as the decay is related to TR/T_1 and is affected by the number of spokes per volume, it is crucial to visually evaluate the number of volumes required for the longitudinal magnetisation to stabilise.

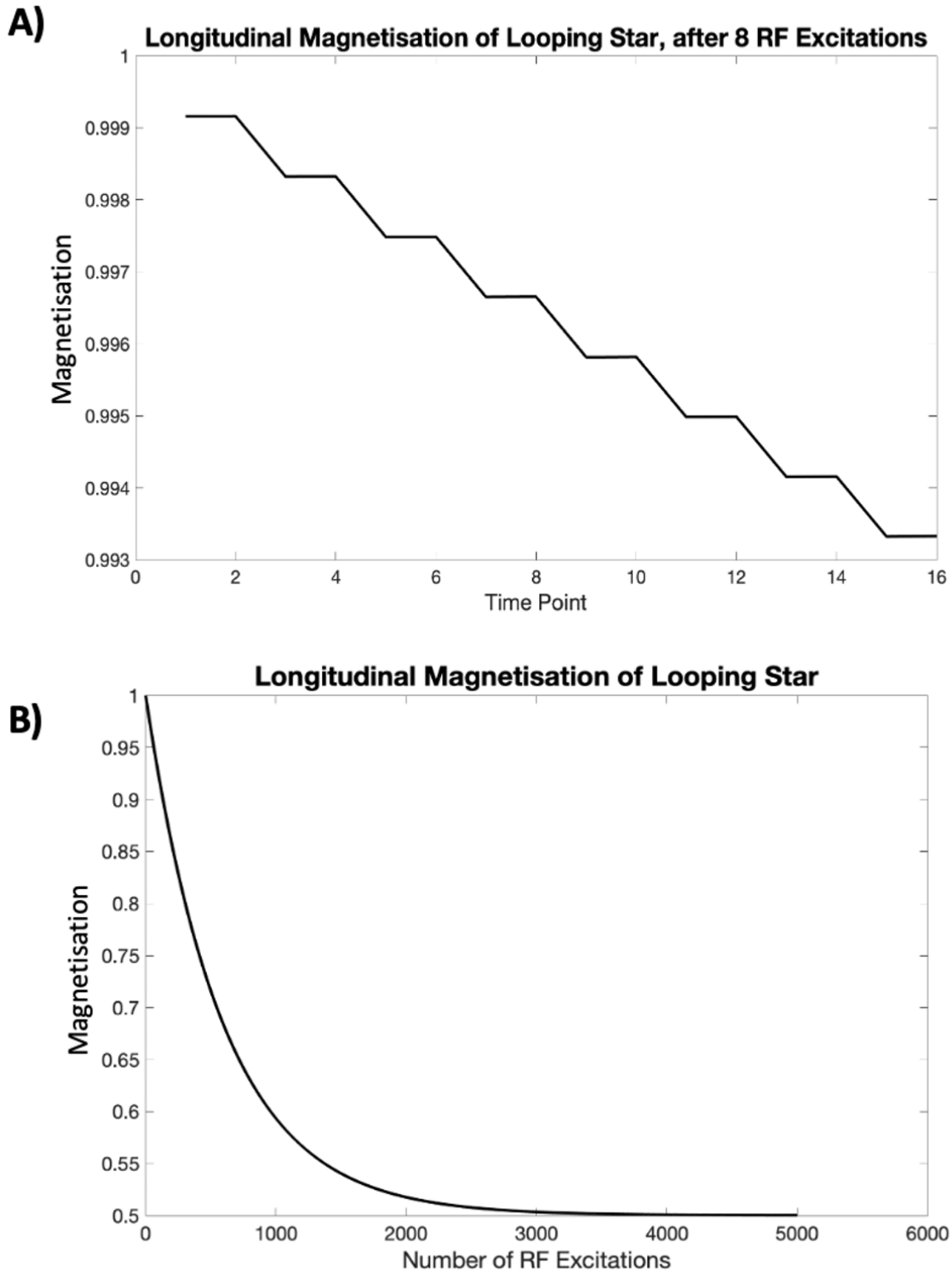

Figure 3.6: (top) Evolution of net longitudinal magnetisation at each time point, where odd time points are RF excitations and even time points are signal decay between spokes. (bottom) Evolution of net longitudinal magnetisation with number of excitations. Simulation performed using $FA = 3°$, $T_1 = 1000ms$, and $TR_{rf} = 840\mu s$.

3.5.2 Bloch Simulation of the Transverse Magnetisation Evolution during Looping Star

To evaluate the transverse component of the net magnetisation, consider the impact of the rotations produced by the net gradient at each time point. The effect of applying the gradients in the absence of RF excitations for the echo generation can be explored. The gradients do not effect the amplitude of the longitudinal magnetisation; they rotate the trajectory of the transverse magnetisation. This process can be crudely approximated iteratively: the rotation of the magnetisation produced from the first excitation can be combined with the rotation produced by the average gradient magnitude across the three dimensions.

The evolution of the transverse magnetisation after an 8 spoke per loop trajectory with no gradient smoothing is calculated. For compatibility with the units in the foundation scripts employed for Bloch simulations (Hargreaves, 2002), the average trajectory across the three dimensions was multiplied by the following conversion factor G_{conv}:

$$G_{conv} = \frac{4\pi \times BW}{\gamma \times FOV_x} \frac{T}{m} \tag{3.18}$$

$$G_{conv} = \frac{4\pi \times 62.5 \times 10^3}{42.58 \times 10^6 \times 0.192} \frac{T}{m} \tag{3.19}$$

Where γ is the gyromagnetic ratio $(4258 \times 10^4 Hz)$, BW is a typical full readout bandwidth employed for Looping Star, and FOV_x is a typical field of view in one direction. To move from T per metre (T/m) to Gauss per centimetre (G/cm)

$$1\frac{T}{m} = 100\frac{G}{cm} \tag{3.20}$$

$$\frac{G_{conv}}{100}\frac{T}{m} = G_{conv}\frac{G}{cm} \tag{3.21}$$

The conversion factor, to be multiplied with the net gradient, is therefore

$$G_{conv} = 9.60 \times 10^{-4}\frac{G}{cm} \tag{3.22}$$

Considering the net gradient at time point 1 ($t1$) ($\bar{G}_{t1}$)

$$\bar{G}_{t1} = \begin{bmatrix} 0 \\ 0 \\ 1 \end{bmatrix} \tag{3.23}$$

The net gradient at the first time point is, therefore, the conversion factor divided across the three directions

$$\bar{G}_{t1} = \frac{9.60 \times 10^{-4}}{3} = 3.20 \times 10^{-4}\frac{G}{cm} \tag{3.24}$$

Eight RF excitation pulses with FA $= 5°$ were designed in the Bloch simulation script, as this is the upper limit of hard pulses in ZTE imaging (Weiger et al., 2011). The T_1 and T_2 values were set to 1000 ms and 100 ms respectively, as approximate values, with the time between RF excitation pulses (TR_{rf}) as 840 μs (for a $\pm$31.25kHz readout bandwidth, commonly used for Looping Star).

To compute the rotation of the net magnetisation after the first RF excitation, both the precession about the z-axis (R_z) and the excitation into the transverse plane (R_x) must be considered. The latter involves using the RF excitation flip angle (φ), whereas the former involves the precession angle (θ). θ is set to zero to consider a static frame of

reference.

$$\varphi = \frac{\pi}{36} \tag{3.25}$$

$$\theta = 0 \tag{3.26}$$

Using the rotation matrices for the given directions R_z and R_x

$$R_z = \begin{bmatrix} cos(-\theta) & -sin(-\theta) & 0 \\ sin(-\theta) & cos(-\theta) & 0 \\ 0 & 0 & 1 \end{bmatrix} = \begin{bmatrix} 1 & 0 & 0 \\ 0 & 1 & 0 \\ 0 & 0 & 1 \end{bmatrix} \tag{3.27}$$

$$R_x = \begin{bmatrix} 1 & 0 & 0 \\ 0 & cos(\varphi) & -sin(\varphi) \\ 0 & sin(\varphi) & cos(\varphi) \end{bmatrix} = \begin{bmatrix} 1 & 0 & 0 \\ 0 & 0.996 & -0.087 \\ 0 & 0.087 & 0.996 \end{bmatrix} \tag{3.28}$$

The total rotation to the transverse plane (R_{th}) is then calculated

$$R_{th} = R_z^{-1} * R_x * R_z = \begin{bmatrix} 1 & 0 & 0 \\ 0 & 0.996 & -0.087 \\ 0 & 0.087 & 0.996 \end{bmatrix} \tag{3.29}$$

which is then used to calculate the magnetisation after the first RF pulse (M_{t1})

$$M_{t1} = M_0 * \begin{bmatrix} 1 & 0 & 0 \\ 0 & 0.996 & -0.087 \\ 0 & 0.087 & 0.996 \end{bmatrix} \tag{3.30}$$

$$M_{t1} = \begin{bmatrix} 1 & 0 & 0 \\ 0 & 0.996 & -0.087 \\ 0 & 0.087 & 0.996 \end{bmatrix} * \begin{bmatrix} 0 \\ 0 \\ 1 \end{bmatrix} = \begin{bmatrix} 0 \\ -0.087 \\ 0.996 \end{bmatrix} \tag{3.31}$$

The rotation (ϕ) from the net gradient applied simultaneously with this first excitation for the time between the RF pulses (TR_{rf}) is then calculated as

$$\phi = \gamma * 2\pi * \frac{TR_{rf}}{1000} * \bar{G_{t1}} \tag{3.32}$$

where $\bar{G_{t1}}$ is the net gradient at the first time point and the factor of 1000 converts the TR_{rf} to seconds. This angle was then used in the same equation for R_z above and multiplied with M_{t1}.

After these two rotations, one about the z-axis and one about the x-axis in the rotating reference frame, the free precession can be computed for the duration of the spoke. The net magnetisation at the time point of the next RF excitation (M_{t2}) is then defined by the transverse and longitudinal decay (A and B, respectively) using T_1 = 1000 ms and T_2 = 100 ms.

At this next time point, the transverse decay A is given by the T_2 decay multiplied by the rotation produced by the next net gradient at time point $t1$ (Equations (3.32) & (3.27))

$$A = \begin{bmatrix} e^{-\frac{t1}{T_2}} & 0 & 0 \\ 0 & e^{-\frac{t1}{T_2}} & 0 \\ 0 & 0 & e^{-\frac{t1}{T_1}} \end{bmatrix} * R_z(\phi = \frac{2\pi * t1}{1000}) = \begin{bmatrix} 0.992 & 0 & 0 \\ 0 & 0.992 & 0 \\ 0 & 0 & 0.999 \end{bmatrix} \tag{3.33}$$

$$B = \begin{bmatrix} 0 \\ 0 \\ 1 - e^{-\frac{t1}{T_1}} \end{bmatrix} = \begin{bmatrix} 0 \\ 0 \\ 0.00084 \end{bmatrix} \tag{3.34}$$

$$M_{t2} = (A * M_{t1}) + B \tag{3.35}$$

This series is then repeated for each of the RF pulses and corresponding gradients. The total evolution of the net transverse magnetisation across all eight repetitions of the RF pulse is seen in Figure 3.7 up to the dotted line. As small flip angles are used, it is unsurprising that such a small fractional signal intensity is produced. From the dotted line onwards, the only rotation applied to the magnetisation is that of the net gradient at each gradient step (i.e. 8 steps to match the 8 spokes per loop), which simulates how the accumulation of transverse magnetisation then changes in the absence of RF excitation, for a single spin with T_2* = 30 ms.

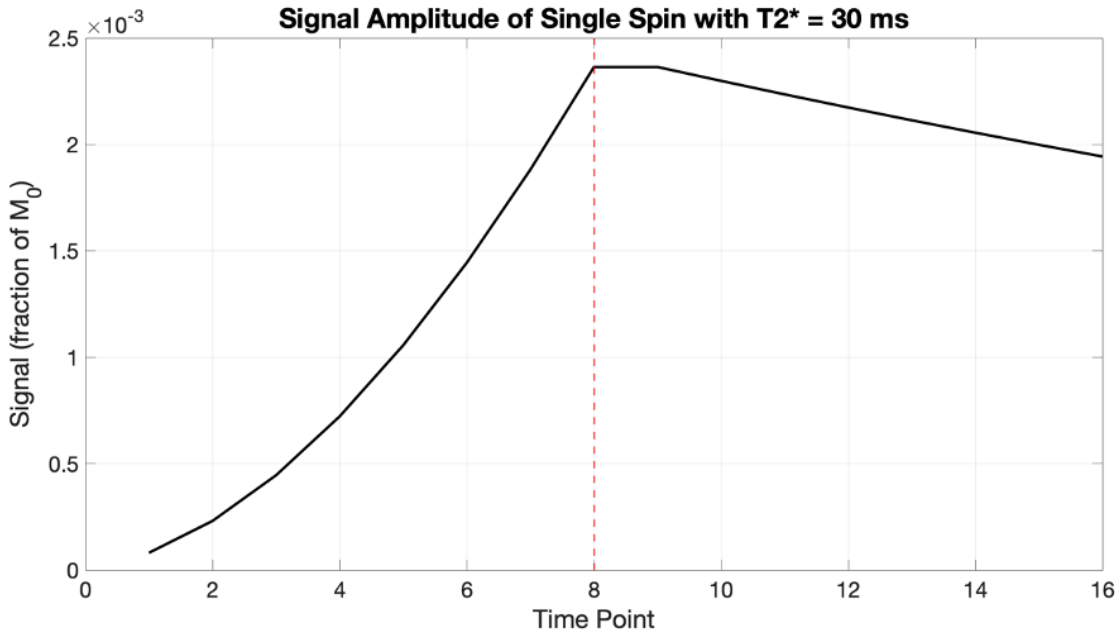

Figure 3.7: Bloch simulation of the evolution of the transverse magnetisation from the first eight RF spokes followed by eight consecutive gradients applied. Dotted line indicates point at which RF excitation stops and only gradients are applied.

3.6 Spatial Excitation Profile of Looping Star

In conventional imaging, the slice profile calculation evaluates the homogeneity of the signal intensity across the slice. In Looping Star, the RF excitation bandwidth encompasses the entire FOV. Although the RF bandwidth is broad, applying a pre-ramped gradient leads to a 3D slice selection effect that is dependent on the orientation and amplitude of the encoding gradients (Grodzki et al., 2012; Jang et al., 2016; Ljungberg et al., 2020).

As described by Ljungberg et al. (2020), the excitation profile across position x, for an RF pulse of amplitude $B_1(x)$, can be determined by the duration of the RF pulse (τ_{rf}) and the gradient magnitude (ω_G) via the normalised sinc function.

$$B_1(x) = sinc(\tau_{rf} * \omega_G) \tag{3.36}$$

where

$$\omega_G = \gamma * \bar{G} * x \tag{3.37}$$

$$max|\omega_G| = BW \tag{3.38}$$

$\bar{G}$ is a vector describing the gradient direction and $\gamma = 42.58MHz/T$. Figure 3.8 demonstrates the spatial excitation profile across the positions of -20 cm to 20 cm for a 20 μs hard pulse in one dimension.

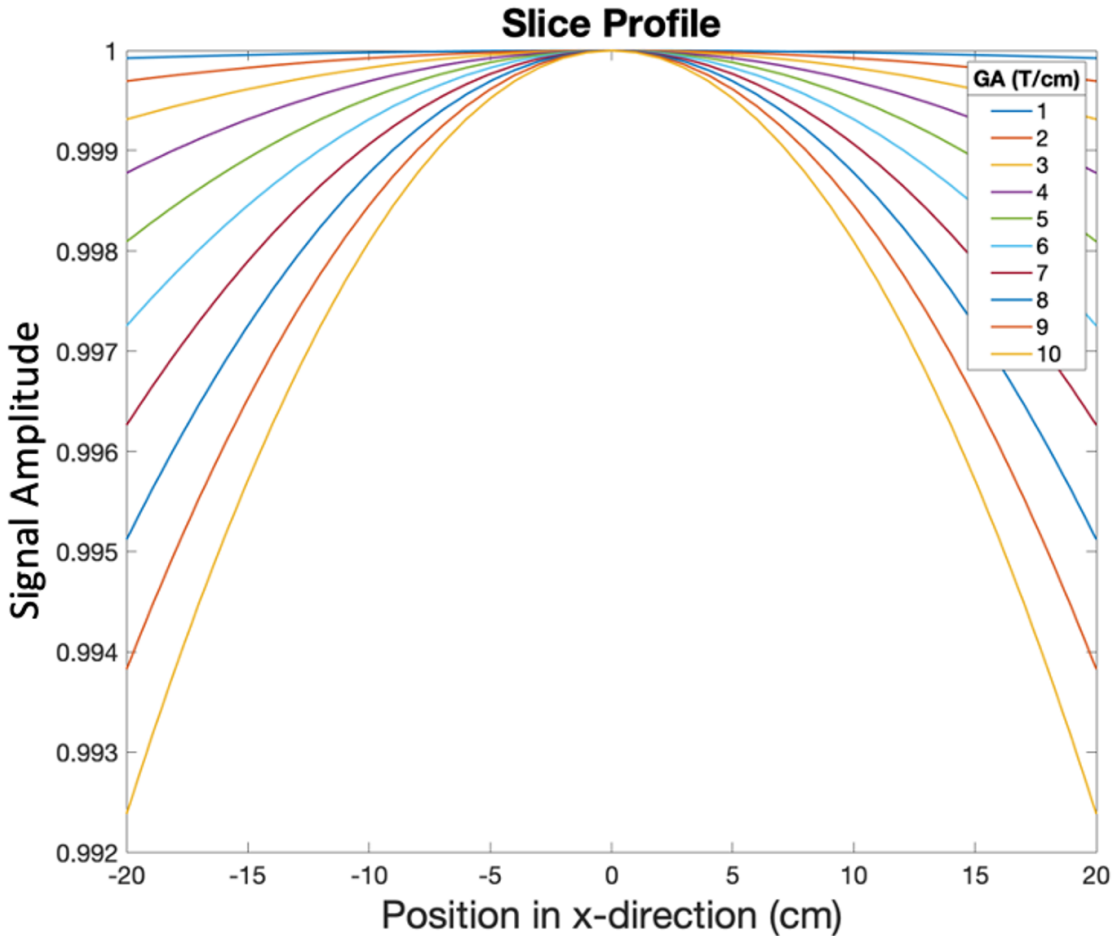

Figure 3.8: Spatial excitation profile in one dimension for a range of gradient amplitudes (GA) and 20μs hard pulse

The spatial excitation profile shows that the signal drops by less than 5 % over a 20 cm distance from the isocentre for Looping Star. The RF pulse flip angle most commonly employed in Looping Star is 2 °, which has an approximate duration of 8 - 12 μs

depending on specific absorption rate (SAR) limitations. Based on the above equations, this produces an even smaller amplitude change across the profile.

3.7 Looping Star Ernst Angle

Another consideration for Looping Star acquisitions is the optimum flip angle. This is typically known as the Ernst angle, which maximises the signal received for a train of pulses with constant TR, and is calculated as in Bernstein et al. (2004) (Equation (3.39)).

$$\alpha = arccos(e^{-\frac{TR_{rf}}{T_1}}) \tag{3.39}$$

where TR_{rf} is the time between RF excitations. For the initial part of Looping Star, i.e. the set of RF pulses, this is approximately equivalent to the duration of a single spoke. A value of 840μs was employed based on the typical value of a Looping Star protocol with 64 points and a bandwidth of $\pm$31.25 kHz. Figure 3.9 shows the effect of TR on the flip angle by selecting a range of values for the TR.

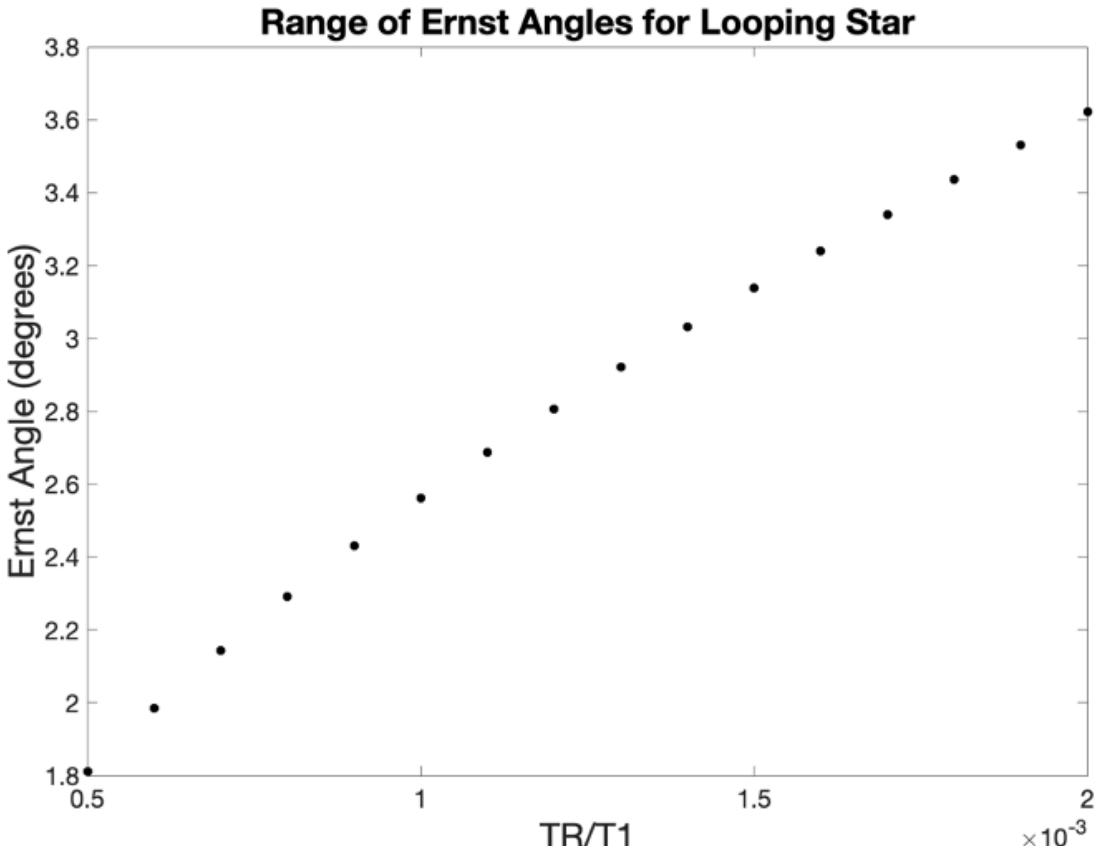

Figure 3.9: Ernst angle calculated for range 0.5 ms $< TR_{rf} <$ 2 ms and $T_1 = 1000$ ms.

However, Looping Star differs from conventional sequences as there is a period between sets of RF pulses where only gradients are applied. This increases the available longitudinal magnetisation as more T_1 recovery occurs in the "gradient-only" portion compared with the "RF plus gradient" portion. The optimum excitation angle therefore becomes dependent on the decay between the last RF excitation of the first set of RF pulses to the first RF excitation of the second set (TR_{sets}) (Equation (3.40))

$$\alpha_{sets} = arccos(e^{-\frac{TR_{sets}}{T_1}}) \tag{3.40}$$

As an example, for an 8 spoke per loop acquisition with a TR_{rf} of 840μs and $T_1 = 1000$ ms, the equivalent Ernst angle between RF pulses can be calculated as

$$\alpha = arccos(e^{-\frac{840\times10^{-6}}{1000\times10^{-3}}}) = 2.35^{\circ} \tag{3.41}$$

Whereas the optimum excitation angle between sets of RF pulses (i.e. after the 8 gradients applied between RF sets) is given as

$$\alpha_{sets} = arccos(e^{-\frac{8\times840\times10^{-6}}{1000\times10^{-3}}}) = 6.63^{\circ} \tag{3.42}$$

As it is not trivial to determine the impact of the two effects in combination, we employed a range of flip angles between 1 - 3 ° across this thesis and evaluated the tSNR of the images to justify the use of selected parameters.

3.8 Signal-to-Noise Efficiency of Looping Star

The efficiency of the SNR quantifies the relationship between SNR and acquisition speed. It has proven useful for diffusion imaging (Engström et al., 2015) and steady-state MRI (Weiger et al., 2005), to name two examples. SNR efficiency can be approximately characterised using the derivation by Reeder and McVeigh (1994) including using the repetition time and bandwidth

$$SNR_{efficiency}(\alpha) = \frac{SNR(\alpha)}{\sqrt{TR_{rf}}} \approx \frac{\frac{signal(\alpha)}{\sqrt{BW}}}{\sqrt{TR_{rf}}} = \frac{signal(\alpha)}{\sqrt{BW * TR_{rf}}} \tag{3.43}$$

Where α is the chosen flip angle. As Looping Star operates with short TRs and low flip angles, it is arguably highly SNR efficient (Miller et al., 2011). This is only the case if we consider the time between RF pulses, rather than the overall volume acquisition time.

To explore how the bandwidth can be used to make gains in SNR efficiency, if the Ernst angle (α) is used, then it can be stated that if the signal is at steady-state the SNR efficiency can be represented as

$$signal(\alpha) = \sqrt{\frac{1 - e^{-\frac{TR_{rf}}{T_1}}}{1 + e^{-\frac{TR_{rf}}{T_1}}}} \tag{3.44}$$

Knowing that $TR_{rf} << T_1$ and using the first order Taylor expansion, since $TR_{rf} << T_2, T_1$

$$signal(\alpha) = \sqrt{\frac{1 - e^{-\frac{TR_{rf}}{T_1}}}{1+1}} = \sqrt{\frac{1 - (1 - \frac{TR_{rf}}{T_1})}{1+1}} = \sqrt{\frac{\frac{TR_{rf}}{T_1}}{2}} = \sqrt{\frac{TR_{rf}}{2 * T_1}} \tag{3.45}$$

Then incorporating this back into the $SNR_{efficiency}$

$$SNR_{efficiency}(\alpha) = \frac{\sqrt{\frac{TR_{rf}}{2*T_1}}}{\sqrt{BW * TR_{rf}}} = \frac{1}{\sqrt{2 * BW * T_1}} \tag{3.46}$$

Therefore, a lower imaging bandwidth will lead to a gain in SNR efficiency, though this would come at the cost of acquisition speed. This relationship is consistent with all MR methods, i.e. the higher the bandwidth used, the more noise is introduced in the receiver.

3.9 Image Reconstruction of Non-Cartesian Acquisitions

Looping Star is a non-Cartesian acquisition technique; therefore, conventional reconstruction methods that rely on Fourier transforms alone cannot be used. There are three key considerations: moving from non-Cartesian to Cartesian coordinates for the Fourier transformation, density compensation for the changes in sampling density at different points in k-space and filling the central dead-time gap that leads to missed samples.

3.9.1 Gridding

One of the common methods for translating non-Cartesian data coordinates to Cartesian space, to ensure the Fourier transform can be used, is known as gridding. Gridding involves resampling the non-Cartesian coordinates to points on a Cartesian grid and Fourier transforming the data once interpolated to Cartesian space. As described by Bernstein et al. (2004), this method is time-efficient and can be simply computed by interpolating the data after convolution with a smooth function.

Prior to gridding, the influence of respiration on the signal phase in the centre of k-space is corrected via normalisation (Dionisio-Parra et al., 2020; Wiesinger et al., 2019). Looping Star uses one of the simplest gridding techniques, known as nearest-neighbour gridding, where the k-space coordinates are rounded to the nearest coordinate value of a two-fold oversampled Cartesian grid, and the signal intensity for the original k-space coordinate is assigned to this new coordinate. This is visualised in two dimensions in Figure 3.10.

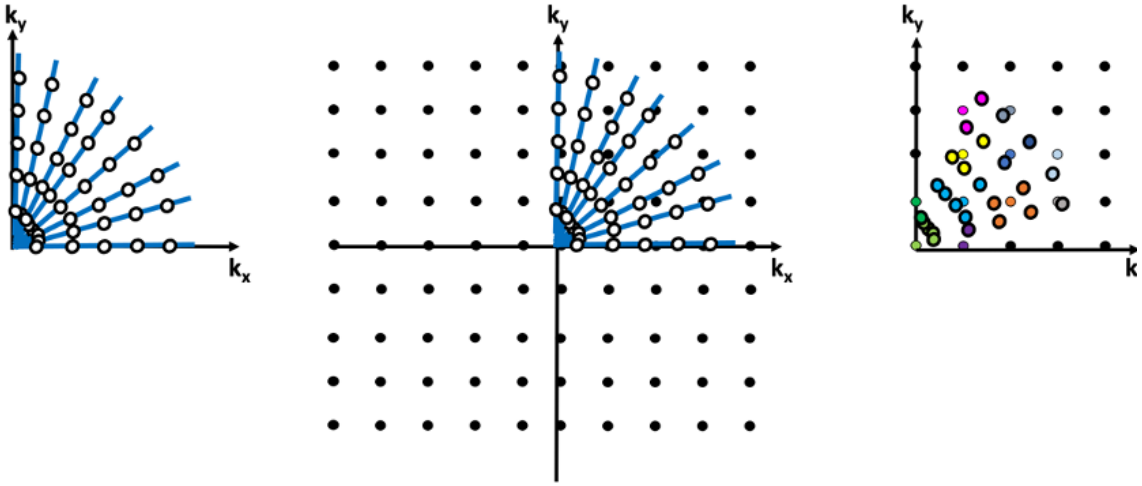

Figure 3.10: From (left) non-Cartesian to (middle) Cartesian grid, where it can be seen that the radial sampling points (white) may not necessarily align with the nearest Cartesian point (black). (right) Nearest neighbour gridding involves rounding the radial sampling points to the nearest Cartesian coordinate, demonstrated by colour coordination of k-space samples (circles with thick lines) with grid points (smaller circles with thin lines). As the k-space samples spread with distance from the centre, a one-to-one relationship begins to arise. At the centre, a many-to-one relationship exists.

The Cartesian grid used for nearest-neighbour gridding is twofold interpolated in order to reduce aliasing, avoiding the need for sinc interpolation to the grid (Bernstein et al., 2004). This technique is one of the simplest approaches, as weighting criteria are not

used to assign the intensity values from non-Cartesian to Cartesian coordinates. The k-space trajectory used in image reconstruction is derived from the nominal gradient waveform of the pulse sequence (Wiesinger et al., 2019). No additional k-space trajectory calibration is used. A simple sum of squares coil combination is then computed after the Fourier transform for each volume.

One important point to consider is that since the sampling trajectory is non-Cartesian, the matching coordinates with Cartesian space will not be produced and the signal intensity will not be gridded in a Cartesian manner, as described above. This leads to an inherent blurring in image space after Fourier transformation that becomes more obvious at lower spatial resolutions and lower spokes per volume, as fewer samples are collected and then interpolated in k-space. The degree of blurring can be quantified by point spread function simulations, however there are limitations to the accuracy of such simulations as discussed in Section 3.10.

Alternatively, iterative techniques can be used to determine the optimal grid interpolation (Benkert et al., 2018; Gabr et al., 2006; Lustig and Pauly, 2010; Smith et al., 2019; Song and Qing, 2006), but these come at the expense of reconstruction time. Section 11 will cover an advanced image reconstruction technique beyond nearest-neighbour gridding employed with Looping Star.

3.9.2 Density Compensation

Although gridding works well as a simple technique for image reconstruction of non-Cartesian data, it must be considered that there is not a simple one-to-one match in terms of the coordinates of the samples to the Cartesian grid. This is clearly shown by the oversampled centre in Figure 3.10, where one point in Cartesian space may be crossed by multiples points in non-Cartesian space (i.e. the centre of k-space is more densely sampled than the periphery of k-space). When the non-Cartesian data is then gridded, this will mean that lower spatial frequencies, nearer the centre (i.e. being a low contrast-based spatial frequency), will be more heavily sampled than others, producing

an imbalanced contrast.

A function is therefore necessary to compensate for this unequal contribution of the data for each coordinate in non-Cartesian to Cartesian space. This is the density compensation function, which weights the higher number of samples crossing different regions of k-space with the goal of effectively "flattening" the contributions of each sample point. For example, if five non-Cartesian points contribute to one Cartesian point, a density compensation function may be created that averages these points to account for this higher contribution.

In nearest-neighbour gridding, which is employed by Looping Star, a simple averaging method is used for density compensation. An example of the effect of density compensation on a gridded dataset is shown in Figure 3.11.

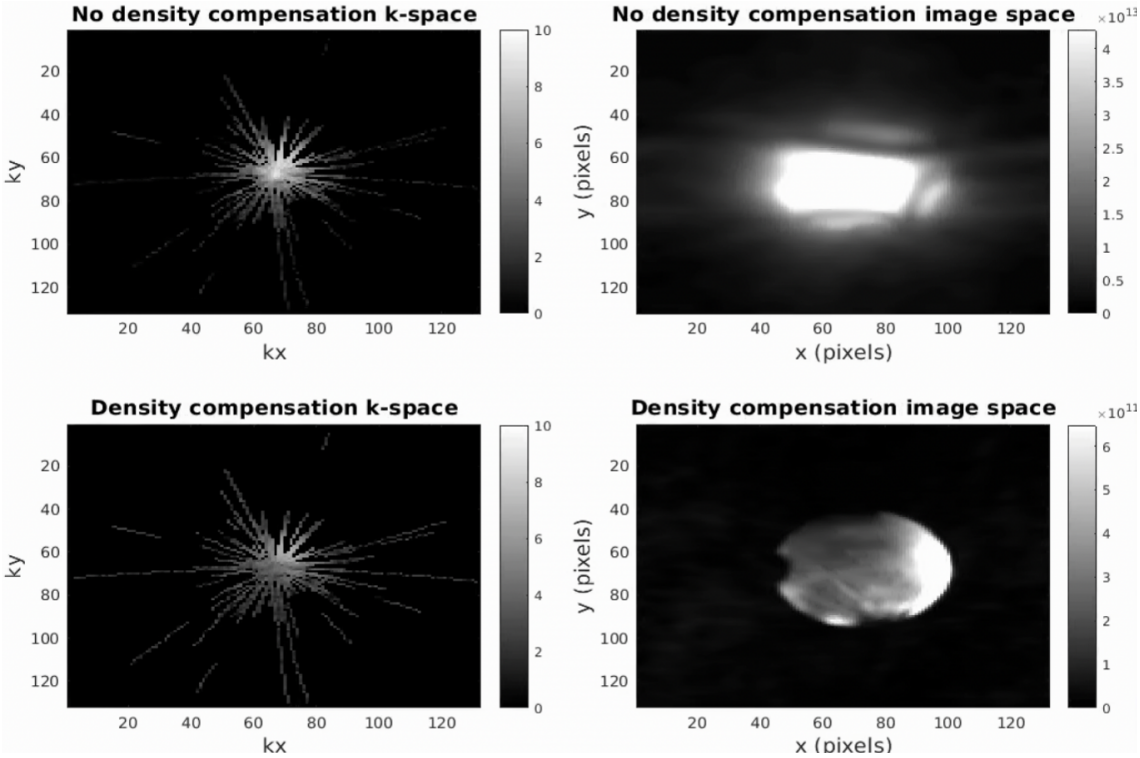

Figure 3.11: Example of image reconstruction for an 18 cm diameter homogeneous spherical pink ball phantom (GE Healthcare, Milwaukee, WI, USA) collected using the following parameters: ±31.25 kHz, GSF = 14, 32 spokes per loop, 1024 spokes per volume, 32-channel coil, 3 mm spatial resolution. (top) no density compensation and (bottom) density compensated, with (left) k-space at the log scale and (right) image space. k-space was thresholded at 0 - 10 and image space was thresholded at half the maximum amplitude.

More advanced methods, such as using a Kaiser-Bessel kernel to compute the optimal

weighting for each point rather than simply computing an average can be computationally expensive without much visual benefit to the image (Maier et al., 2021). In iterative reconstruction, on the other hand, a good density compensation function will lead to faster convergence and can facilitate a flexible compromise between image contrast and spatial resolution (Tan and Zheng, 2005). Another consideration with density compensation is that it can influence the intensity profile if inaccurate and downweighting the edges of k-space will produce blurred images.

Figures 3.12 - 3.13 demonstrate the impact of density compensation on the point spread function, with Figures 3.14 - 3.15 including temporal decay along the radial spokes. It can be seen that excluding density compensation leads to the highest signal intensity being in the centre of k-space, with little weighting towards the edges of k-space. This manifests as a blurred point spread function, as high spatial frequencies have little contribution to the image. Including T_2* decay during sampling along the spokes produces the same effect.

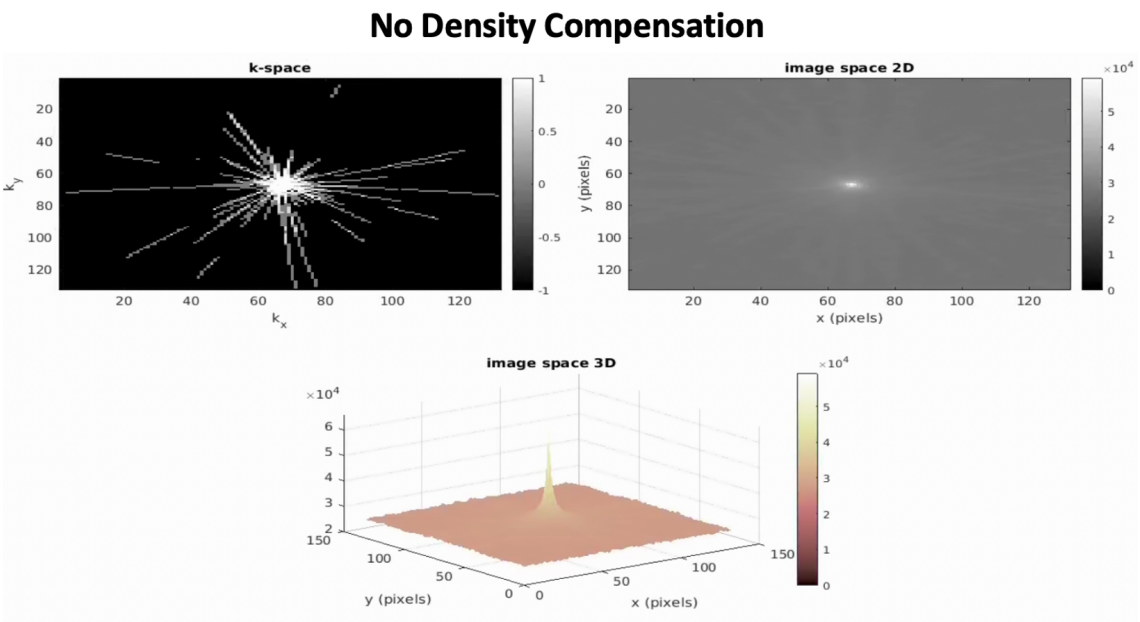

Figure 3.12: Impact of no density compensation without T_2* decay on k-space (top left), image space in 2D (top right) and image space in 3D (bottom) of point spread function from a single coil. $FWHM_x$ = 5 pixels, $FWHM_y$ = 4 pixels. Parameters were: ±31.25 kHz, GSF = 14, 32 spokes per loop, 1024 spokes per volume, 3 mm spatial resolution, time per spoke = 840 μs.

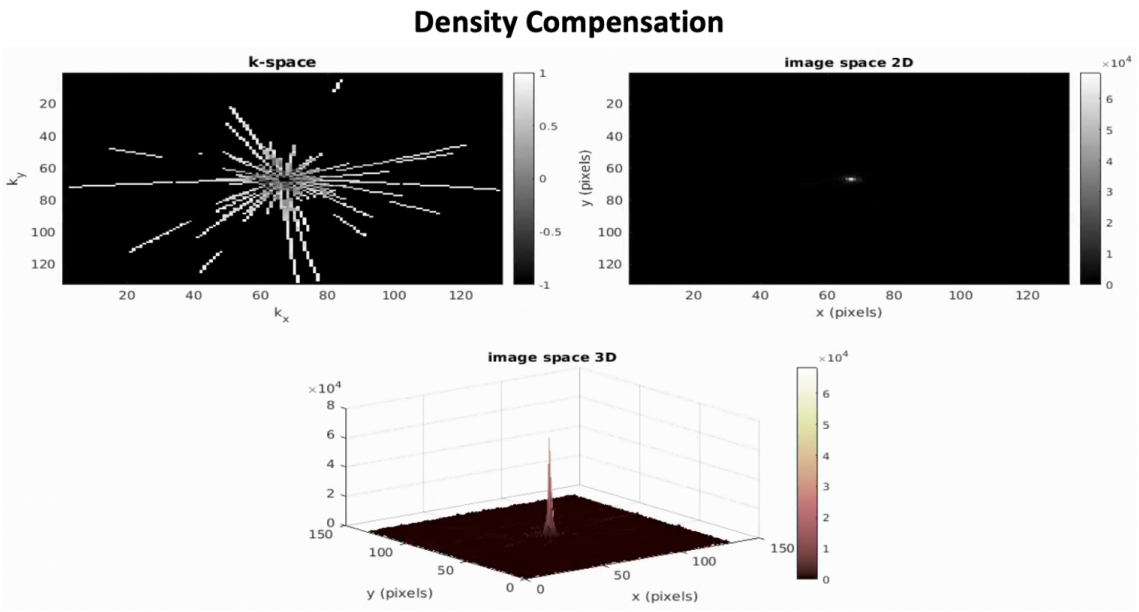

Figure 3.13: Impact of density compensation without T_2* decay on k-space (top left), image space in 2D (top right) and image space in 3D (bottom) of point spread function from a single coil with density compensation. $FWHM_x = 2$ pixels, $FWHM_y = 3$ pixels. Parameters were: $\pm$31.25 kHz, GSF = 14, 32 spokes per loop, 1024 spokes per volume, 3 mm spatial resolution, time per spoke = 840 μs.

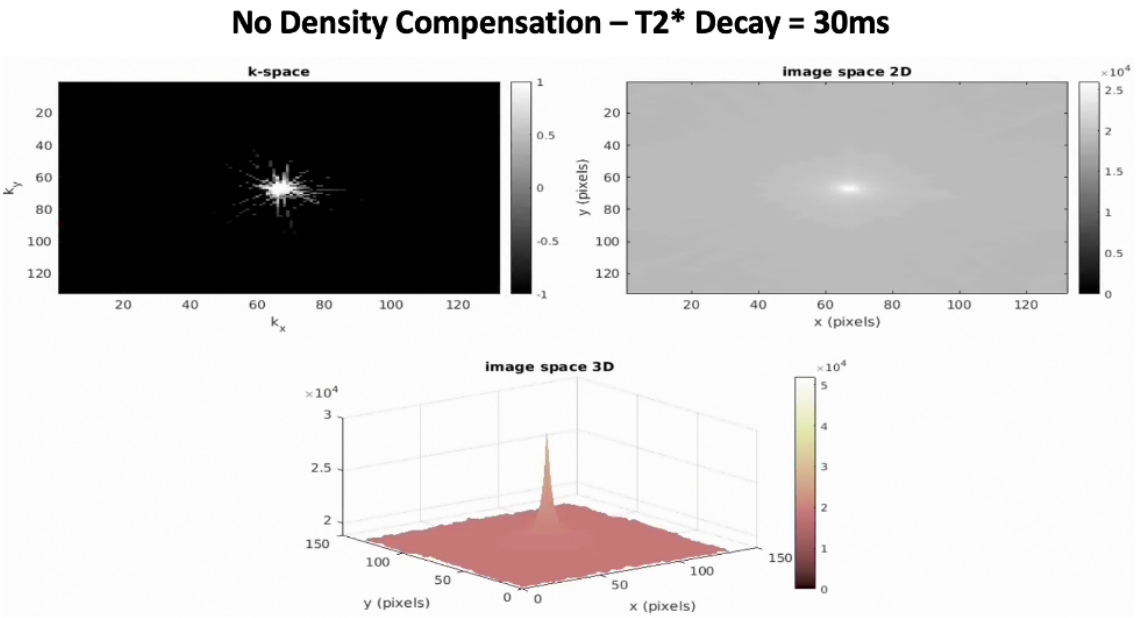

Figure 3.14: Impact of no density compensation on k-space (top left), image space in 2D (top right) and image space in 3D (bottom) of point spread function from a single coil with an added $T_{2*} = 30ms$ decay along the spokes. $FWHM_x = 5$ pixels, $FWHM_y = 6$ pixels. Parameters were: $\pm$31.25 kHz, GSF = 14, 32 spokes per loop, 1024 spokes per volume, 3 mm spatial resolution, time per spoke = 840 μs.

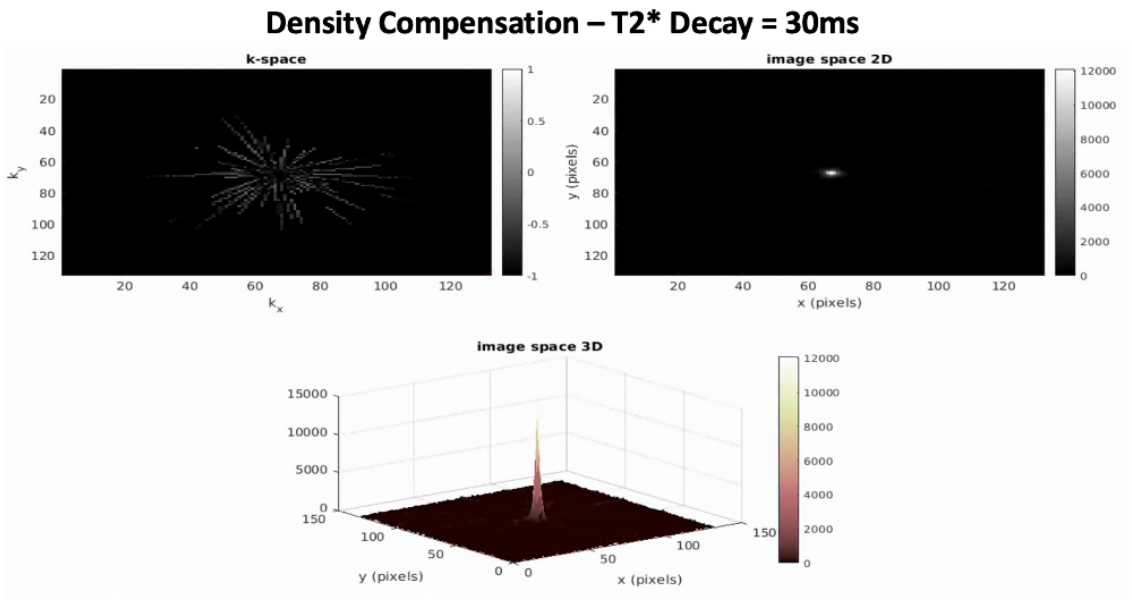

Figure 3.15: Impact of density compensation on k-space (top left), image space in 2D (top right) and image space in 3D (bottom) of point spread function from a single coil with density compensation and with an added $T_2* = 30ms$ decay along the spokes. $FWHM_x = 3$ pixels, $FWHM_y = 3$ pixels. Parameters were: $\pm$31.25 kHz, GSF = 14, 32 spokes per loop, 1024 spokes per volume, 3 mm spatial resolution, time per spoke = 840 μs.

3.9.3 Filling the Dead-time Gap

The final consideration for image reconstruction is that although the gradients and RF pulses may be applied at the same time point, there is an inherent delay before sampling begins known as dead-time where the coil transitions from "transmit" mode to "receive" mode. This means there are missing samples at the centre of k-space, though the delay also depends on the receiver coil used. For an 8-channel GE head coil this amounts to around 24 μs of missing data. This is shown in Figure 3.16, where it is clear that the centre of k-space is not sampled.

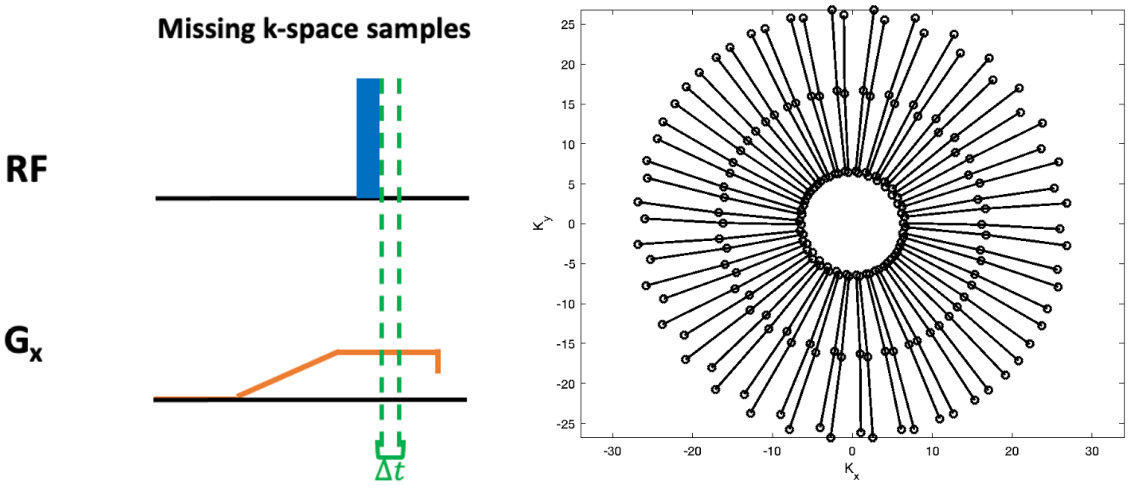

Figure 3.16: (left) Missing samples shown in pulse sequence, with (right) missing k-space samples in the centre

For effective image reconstruction of the FID, this gap must be filled, as a significant amount of signal evolution takes place that is unsampled. This results in missing data in the low spatial resolution regions of k-space, producing poor proton density-weighted contrast. This is not required for the echoes as the signal has been refocused at the point of sampling, meaning that the T_2*-weighted signal is fully sampled.

To address this missing data, a second acquisition can be incorporated into the pipeline to "fill" the missing samples. This was originally presented by Wu et al. (2007) through a technique known as Water and Fat Suppressed Proton Projection MRI (WASPI), which is incorporated into Looping Star image reconstruction (Wiesinger et al., 2019) (Figure 3.17). This is done by acquiring a single volume with lower gradient strength, as this allows samples to be collected from closer to the centre of k-space, followed by a simple addition of these samples into the reconstruction (Ljungberg et al., 2021a).

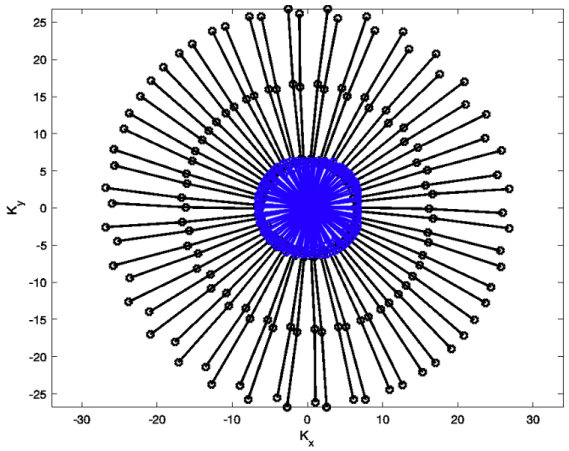

Figure 3.17: Visualisation of WASPI filling (blue) of missing k-space samples

WASPI differs from Pointwise Encoding Time Reduction with Radial Acquisition (PETRA) (Grodzki et al., 2012) as it involves consistently using a radial trajectory, whereas PETRA separates the k-space trajectory into radial imaging at the periphery and Cartesian filling at the centre. A full review on methods for filling the dead-time gap was presented by Froidevaux et al. (2018).

Furthermore, a technique known as HY-FI (Froidevaux et al., 2021) has been recently developed that retrieves the inner k-space data using a stack of shells technique. An example of the impact of including WASPI with Looping Star is shown in Figure 3.18, where it can be seen that the absence of k-space filling leads to loss of low spatial-frequency information.

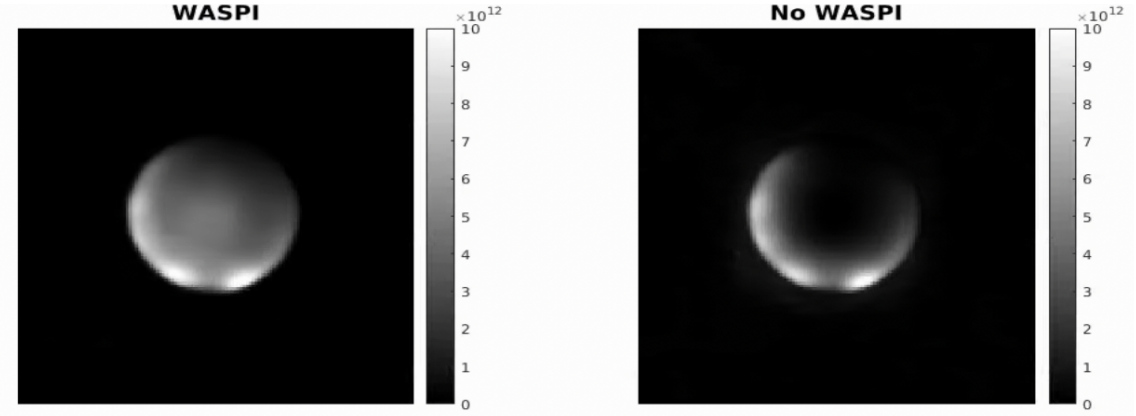

Figure 3.18: Example of FID image of an 18 cm diameter homogeneous spherical pink ball phantom (GE Healthcare, Milwaukee, WI, USA) reconstructed using the following parameters: $\pm$31.25 kHz, GSF = 14, 32 spokes per loop, 1024 spokes per volume, 32-channel coil, 3 mm spatial resolution, time per spoke = 840 μs. FID image with (left) dead-time filled and (right) no dead-time filling.

3.10 Point Spread Function of Looping Star

The point spread function is used to determine the smallest structure that can be resolved by an imaging system. It is more commonly used in methods that produce images known as 'linear' and unlikely to demonstrate shifts, for example in fluorescence microscopy. This assumption is not the case for MRI, as MRI is affected by time-dependent motion, time-varying magnetic fields and the relaxation effects of the tissue signal. However, it has been used to compute the theoretical spatial blurring of different techniques and the nature of spatial distortions (Robson et al., 1997; Tsao et al., 2006).

For Looping Star, the point spread function was defined by setting the k-space data to a value of one along all of the spokes and completing the defined gridding steps for a given trajectory and set of acquisition parameters. A direct Fourier transform was then applied to the data after interpolation to the oversampled grid (Section 3.9.1) to visualise the point spread function in image space.

Figures 3.19 - 3.21 show the point spread function and accompanying k-space for an acquisition sampled with 1024, 512 and 256 spokes per volume after the conventional nearest-neighbour gridding pipeline for Looping Star. In this case, alternate spokes were removed for the simulation, however in practice the under-sampling would involve removing entire segments rather than alternate spokes. It can be seen that streaking begins to appear in the side lobes of the point spread function with decreasing angular samples, however the full-width-half-maximum remains unchanged. This highlights the benefits of radial imaging, whereby the spatial resolution is not substantially affected by under-sampling as the length of the spoke and distance between k-space samples along the spoke are unchanged (Ljungberg et al., 2021a).

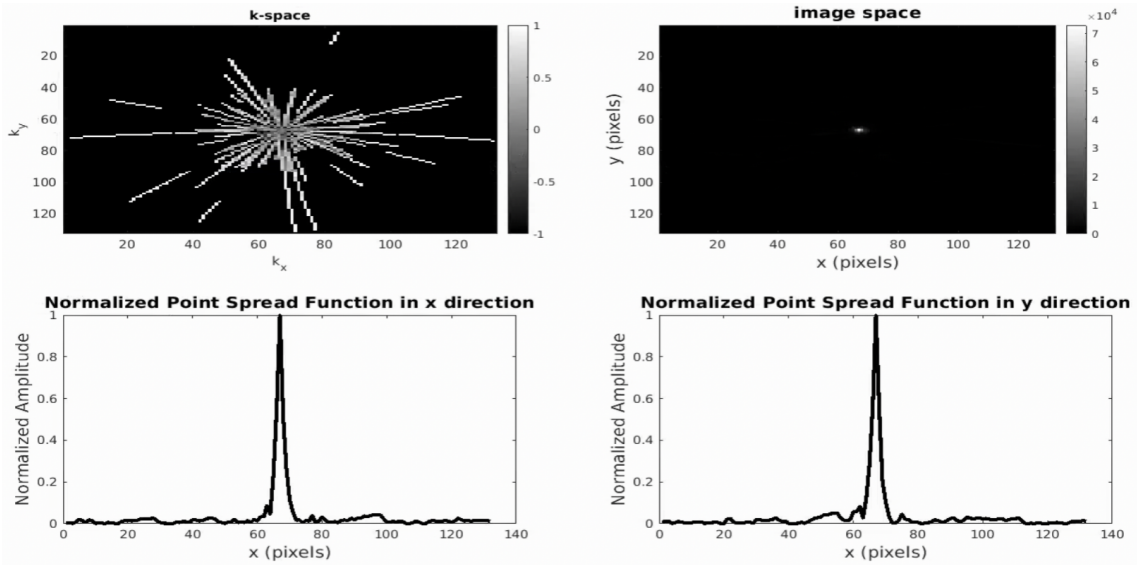

Figure 3.19: Point spread function for a 1024 spokes acquisition with one coil after standard nearest neighbour gridding at Z/2, including: (top left) density compensated image space at log-scale, (top right) image space of absolute value of point spread function, (bottom left) point spread function amplitude of image space in x-direction and (bottom right) point spread function amplitude of image space in y-direction ($FWHM_x$ = 3 pixels, $FWHM_y$ = 3 pixels). k-space thresholded from -1 to 1, image space thresholded from 0 to half FWHM amplitude, point spread function single dimension plots normalised to 0 to 1.

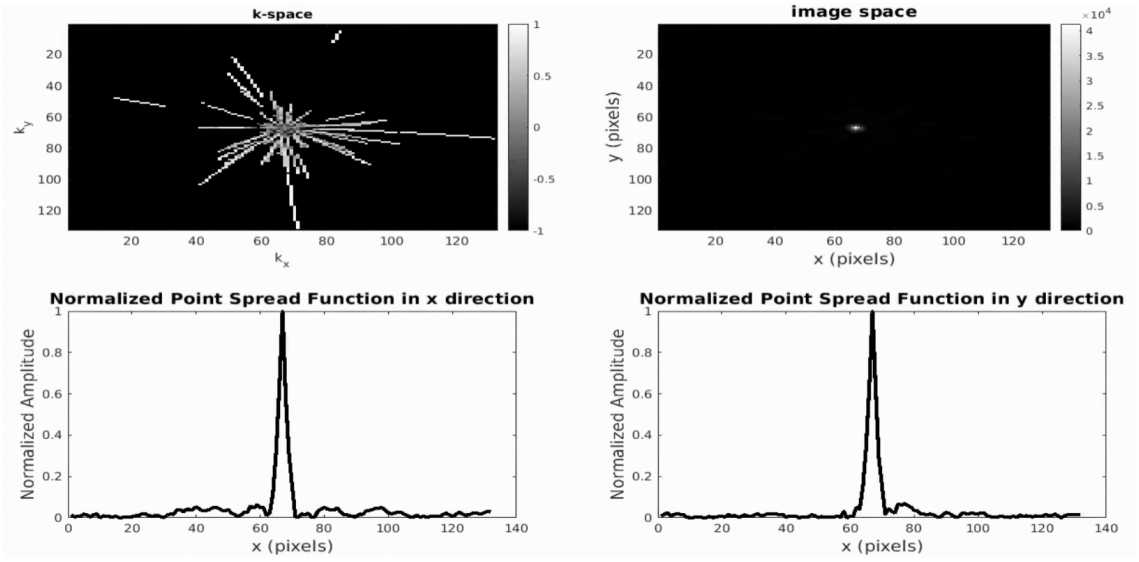

Figure 3.20: Point spread function for a 512 spokes acquisition with one coil after standard nearest neighbour gridding at Z/2, including: (top left) density compensated image space at log-scale, (top right) image space of absolute value of point spread function, (bottom left) point spread function amplitude of image space in x-direction and (bottom right) point spread function amplitude of image space in y-direction ($FWHM_x$ = 3 pixels, $FWHM_y$ = 3 pixels). k-space thresholded from -1 to 1, image space thresholded from 0 to half FWHM amplitude, point spread function single dimension plots normalised to 0 to 1.

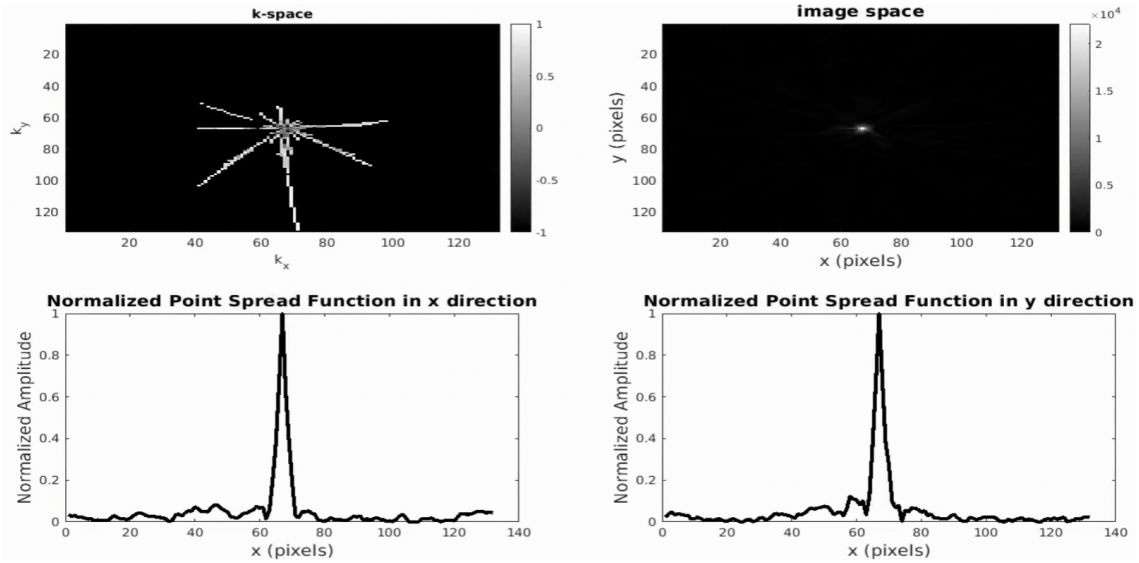

Figure 3.21: Point spread function for a 256 spokes acquisition with one coil after standard nearest neighbour gridding at Z/2, including: (top left) density compensated image space at log-scale, (top right) image space of absolute value of point spread function, (bottom left) point spread function amplitude of image space in x-direction and (bottom right) point spread function amplitude of image space in y-direction ($FWHM_x$ = 3 pixels, $FWHM_y$ = 3 pixels). k-space thresholded from -1 to 1, image space thresholded from 0 to half FWHM amplitude, point spread function single dimension plots normalised to 0 to 1.

To consider the impact of the sampling pattern with T_2* decay, T_2* = 10, 20, 30 ms decays were simulated along the length of each spoke using the Bloch equation (Equation (3.47))

$$M = M_0 e^{-\frac{t}{T_2*}} \tag{3.47}$$

Figures 3.22 - 3.24 demonstrate that changing the values of T_2* in calculating the point spread function has no impact on the full-width at half-maximum (FWHM) of the data, suggesting no changes to the spatial resolution of the point. However, there is an evident profile change with decreasing T_2* values, with more prominent side lobes arising for T_2* = 10 ms. This is due to the decay characteristics, whereby the 10 ms model decays much faster across the first half of the spokes than the 20 ms and 30 ms decay profiles. This means that most of the signal is near the centre of k-space for the 10 ms decay, producing more noise in the image background as there is a lower contribution to higher spatial frequencies.

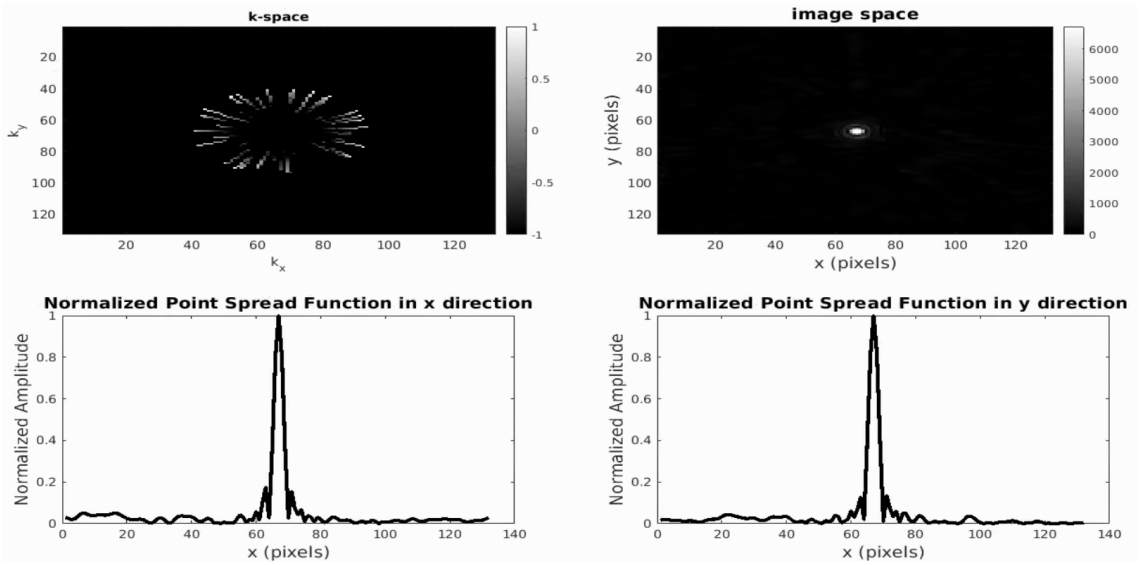

Figure 3.22: Point spread function for a 1024 spokes acquisition with one coil after standard nearest neighbour gridding at Z/2 with T_2* = 10 ms, including: (top left) density compensated image space at log-scale, (top right) image space of absolute value of point spread function, (bottom left) point spread function amplitude of image space in x-direction and (bottom right) point spread function amplitude of image space in y-direction ($FWHM_x$ = 3 pixels, $FWHM_y$ = 3 pixels). k-space thresholded from -1 to 1, image space thresholded from 0 to half FWHM amplitude, point spread function single dimension plots normalised to 0 to 1.

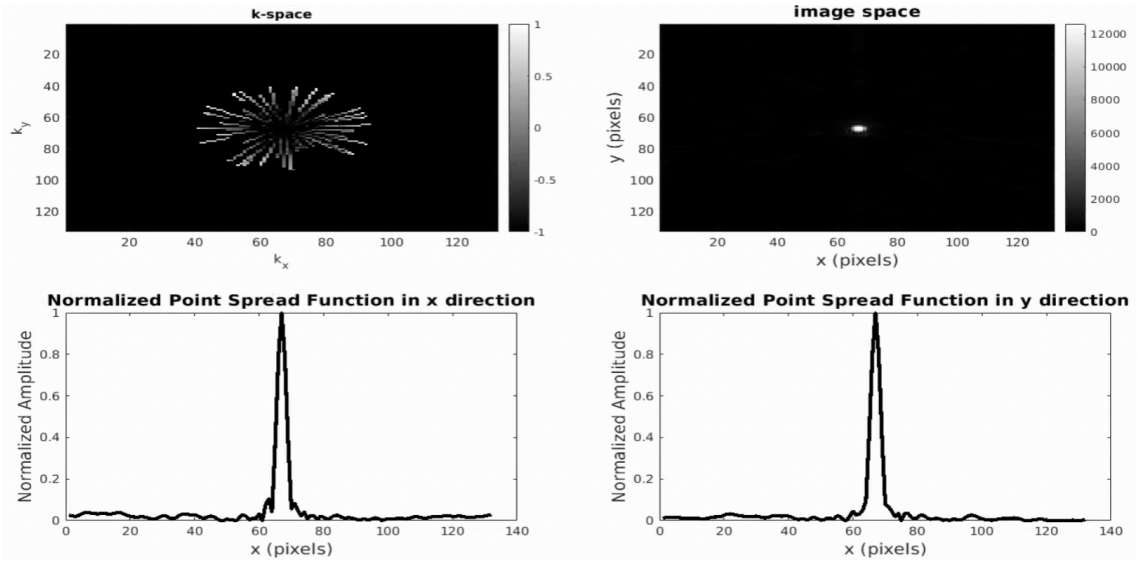

Figure 3.23: Point spread function for a 1024 spokes acquisition with one coil after standard nearest neighbour gridding at Z/2 with T_2* = 20 ms, including: (top left) density compensated image space at log-scale, (top right) image space of absolute value of point spread function, (bottom left) point spread function amplitude of image space in x-direction and (bottom right) point spread function amplitude of image space in y-direction ($FWHM_x$ = 3 pixels, $FWHM_y$ = 3 pixels). k-space thresholded from -1 to 1, image space thresholded from 0 to half FWHM amplitude, point spread function single dimension plots normalised to 0 to 1.

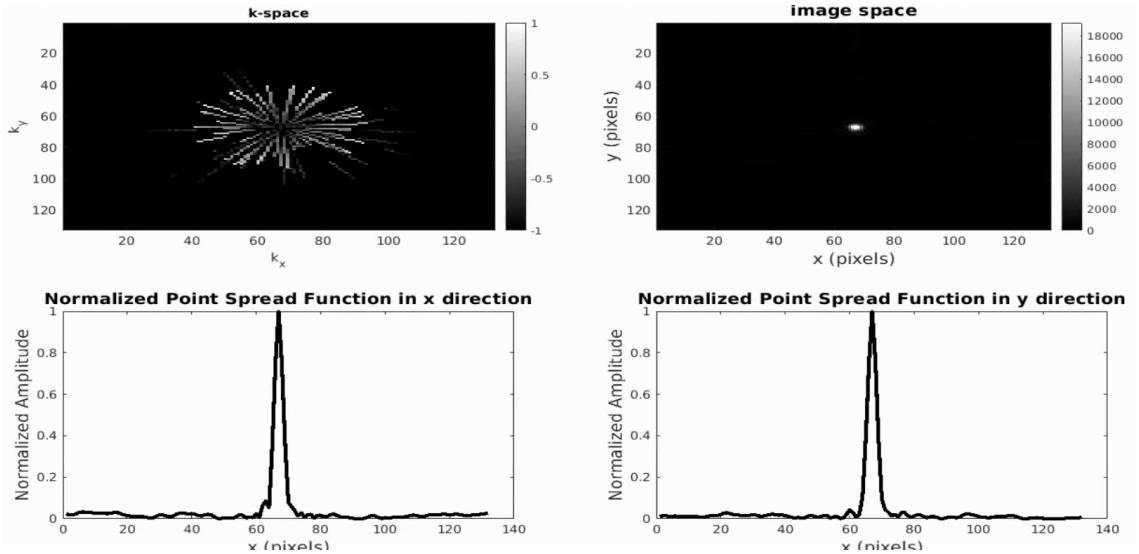

Figure 3.24: Point spread function for a 1024 spokes acquisition with one coil after standard nearest neighbour gridding at Z/2 with T_2* = 30 ms, including: (top left) density compensated image space at log-scale, (top right) image space of absolute value of point spread function, (bottom left) point spread function amplitude of image space in x-direction and (bottom right) point spread function amplitude of image space in y-direction ($FWHM_x$ = 3 pixels, $FWHM_y$ = 3 pixels). k-space thresholded from -1 to 1, image space thresholded from 0 to half FWHM amplitude, point spread function single dimension plots normalised to 0 to 1.

Another consideration for Looping Star is that radial sampling can lead to less localised aliasing in comparison with Cartesian methods (Weiger and Pruessmann, 2012). For example, if the edges of the brain are outside the FOV, then streaks will be generated at the distance of the effective field of view for each voxel and the amplitude of the streaks will be as high as the signal intensity (Bernstein et al., 2004). However, Looping Star is less susceptible to motion artefacts as motion will manifest as blur rather than phase wrapping due to its sampling characteristics (Wiesinger et al., 2019).

Chapter 4

Aims & Hypotheses

The key aims of this thesis are to:

1. Evaluate the acoustic noise and MR signal characteristics of single-echo and multi-echo Looping Star relative to GRE-EPI in phantoms.

2. Quantify the signal characteristics and functional sensitivity of single-echo and multi-echo Looping Star in vivo using a simple paradigm.

3. Explore the capabilities of Looping Star with auditory and resting-state paradigms in comparison with GRE-EPI.

4. Investigate the compatibility of Looping Star with conventional analysis and pre-processing techniques.

5. Evaluate further applications and areas of optimisation for Looping Star for future work.

It was hypothesised that Looping Star would provide adequate functional sensitivity to a range of functional paradigms, given its T_2* sensitivity. There is also scope for it to provide more meaningful information in auditory paradigms given the minimisation of acoustic noise. Distinct signal properties for Looping Star relative to GRE-EPI were also expected due to its 3D radial sampling nature.

Chapter 5

General Methods

Summary

This chapter details the following general methods for this thesis:

- Ethical approval and recruitment procedures.
- Scanners and paradigm equipment used.
- List of toolboxes employed.
- Technical descriptions of key methods.

Overview

This section describes the core general methods used in this thesis, particularly those that appear repetitively. The details and parameters used for specific techniques are included in each independent chapter. A list of toolboxes employed in this thesis and information regarding the ethical approval and recruitment procedures are also provided.

5.1 Ethical Approval and Recruitment

Ethical approval was obtained for physics development and testing of the Looping Star sequence under the following research ethic committee (REC) application details, unless stated otherwise:

- London - Camberwell St Giles REC: 04/Q0706/72 (Before 2020)
- King's College London REC: HR-20/21-21138 (From 2020)

In accordance with these ethics, participants were recruited from within the university based on whether they were deemed "MR-Knowledgeable". All data was stored on the Neuroimaging Analysis Network and pseudo-anonymised (i.e. all personal identifiers removed, no de-facing applied). Informed written consent was obtained from all participants.

5.2 Scanning Procedures

The scanners employed for the studies included in this thesis were:

- King's College London: Clinical Research Facility 3T GE Healthcare MR750 (Milwaukee, WI, USA)
- King's College London: Centre for Neuroimaging Sciences 3T GE Healthcare MR750 (Milwaukee, WI, USA)

The receive-only head coils used were:

- 32-channel Nova Medical receive-only head coil (Wilmington, MA, USA)
- 12-channel GE Healthcare receive-only head coil (Milwaukee, WI, USA)

All GRE-EPI and inversion-recovery prepared spoiled gradient echo (IR-SPGR) data were reconstructed with the standard image reconstruction used online for GE Healthcare scanners. All Looping Star datasets employed in this thesis were reconstructed with nearest neighbour gridding unless stated otherwise, with scripts provided by our collaborators at GE Healthcare (Section 3.9.1). The trajectories used were those generated pseudo-randomly, as described in Section 3.3, using scripts provided by our collaborators at GE Healthcare.

5.3 Paradigm Software

In house paradigm software was employed that included MR safe pneumatic headphones (MR Confon, Cambridge Research Systems, UK), a two-index button box, and an MR compatible projector with an accompanying screen. The screen was visible through a reflective mirror attached to the head coils, and it was ensured that the entire screen was encompassed by the mirror through communication with the participants. The tasks employed in this thesis were implemented via the local Microsoft VB.NET framework (Hill and Dalton, 2017). The screen distance was also adjusted to ensure the projector was correctly focused.

5.4 Physiological Recordings

An MR compatible pulse oximeter and respiratory belt were used to acquire physiological data. Analysis was conducted in SPM-12 (`https://www.fil.ion.ucl.ac.uk/spm/doc/`) using the TAPAS PhysIO toolbox (Kasper et al., 2017), with data cleaning performed in the Kubios Heart Rate Variability (HRV) software (Tarvainen et al., 2014, 2019).

5.5 Acoustic Recordings

Acoustic noise measures were collected using a Casella 62X (Casella Solutions, Bedfordshire, UK) sound meter in all cases in this thesis. The MR safe microphone for sound recording was positioned at the centre of the magnet bore through attachment to a phantom placed in the head coil and specifying a landmark that ensured it was central in the bore.

The Casella Insight software outputs Cumulative, Octave and Period data. An octave is defined as a range over which the frequency doubles. The Octave output includes the LA_{eq} measurements for the 1/1 octave, which contains 11 bands of centre frequencies from 16 Hz to 16 kHz. The LA_{eq} measure is weighted to the human ear and therefore measured in dB(A) (Casella Solutions, 2010, 2021).

5.6 Toolboxes and Software

Specific details of the software used are outlined in each methods section, and in some cases particular version numbers were used based on compatibility with toolboxes, though the following general tools were used:

- AFNI 17.2.17 (Cox, 1996)
- Anaconda (Anaconda Inc, 2020)
- BioImage Suite Web: MNI to Talairach Converter (BioImage Suite Web, 2021; Lacadie et al., 2008)
- Bland-Altman Analysis and Correlation Plot (Klein, 2021)

- BRAMILA (Power et al., 2012)
- Casella Insight (Casella Solutions, 2010, 2021)
- CONN, version 19.c (Whitfield-Gabrieli and Nieto-Castanon, 2012)
- conn tools (Vallat, 2017)
- FSL (most commonly version 5.0.11) (Jenkinson et al., 2012)
- G*Power 3.1 (Faul et al., 2007)
- IBM SPSS Statistics (IBM Corp, 2020)
- ICC Toolbox (Caceres et al., 2009)
- Kubios Heart Rate Variability Standard (Tarvainen et al., 2014, 2019)
- MarsBaR (Brett, 2016; Brett et al., 2002)
- MATLAB R2015 - R2021 (Mathworks, 2021)
- MRICRON 2019 (Rorden and Brett, 2000)
- N4 ITK Bias Field Correction (Tustison et al., 2010)
- Neurosynth (Yarkoni, 2011)
- NiLearn (The Nilearn developers, 2021)
- SEPIA Toolbox 0.8.1.1 (Chan and Marques, 2021)
- SPM-12 (most commonly version 7487) (FIL Methods Group, 2020)

- TAPAS PhysIO Toolbox, version 3.2.0 (Kasper et al., 2017)
- TEDANA (tedana community et al., 2021)
- Violinplot (Bechtold, 2016)

5.7 Technical Concepts

This section outlines the commonly employed technical concepts in this thesis.

5.7.1 Temporal Stability Measures

A 15 x 15 pixel ROI located at the centre of the image was used to compute the summary measures described below. An 18 cm diameter homogeneous spherical pink ball phantom (GE Healthcare, Milwaukee, WI, USA) was used. In-house scripts, a mixture of personally derived and those provided by Dr Brian Burns (GE Healthcare), of the following calculations were used to compute the Looping Star temporal stability measures, as defined by Friedman and Glover (2006). A 2D ROI was selected to ensure comparability with GRE-EPI.

5.7.1.1 Temporal Signal-to-Noise Ratio

The temporal signal-to-noise ratio (tSNR), referred to as the SFNR in Friedman and Glover (2006), is calculated for each voxel. This involves computing the temporal mean of the time series signal amplitude, then dividing the temporal mean by the temporal standard deviation of its residuals after second-order polynomial detrending, i.e. $\varepsilon = y - \hat{y}$ (Equation (5.1)), using the polyfit and polyval functions in MATLAB.

$$tSNR = \frac{\bar{y}}{\sigma_{\varepsilon}} \tag{5.1}$$

where $\bar{y}$ is the temporal mean of the signal $y(t)$, and σ_{ε} is the standard deviation of the residuals of $y(t)$ after detrending. A high tSNR would therefore indicate a high signal amplitude relative to its variability, indicating good temporal stability.

5.7.1.2 Static Spatial Noise

The static spatial noise (SSN) is computed by the sum of the even volumes subtracted by the sum of the odd volumes (Equation (5.2)).

$$SSN = \sum vol_{odd} - \sum vol_{even} \tag{5.2}$$

The number of odd and even volumes must be equal for an accurate SSN measure. A high SSN would further indicate variability between volumes, being particularly sensitive to drifts in amplitude and geometry (Friedman and Glover, 2006). Since Looping Star and GRE-EPI produce images of different image intensity values, via the scaling employed in image reconstruction, the SSN was normalised between -1 and 1.

5.7.1.3 Signal-to-Noise Ratio

The SNR is computed in the aforementioned ROI. First, an average temporal image is computed $\bar{vol}$. The average spatial amplitude across voxels in the ROI of the average temporal image is then computed $\bar{vol}_{ROI}$, as well as the spatial variance across this ROI ($\sigma^2_{vol_{ROI}}$). The spatial SNR for the ROI is then computed as (Equation (5.3))

$$SNR_{ROI} = \frac{\bar{vol}_{ROI}}{(\sigma_{vol_{ROI}}/N)} \tag{5.3}$$

where N is the number of volumes and $\sigma_{vol_{ROI}}$ is the square root of the variance, i.e. the standard deviation (Edelstein et al., 1986). The noise outside the image is not used given that this is not a reliable measure of noise for fMRI and can produce large variability (Goerner and Clarke, 2011; McCann et al., 2013; Welvaert and Rosseel, 2013). The noise outside the image would also not be consistent between GRE-EPI and Looping Star, given the different reconstruction schemes employed.

5.7.1.4 Percentage Signal Fluctuation and Drift

The percentage signal fluctuation (PSF) involves calculating the temporal mean of the spatially averaged time series across the ROI ($\bar{y_{ROI}}$), as well as the temporal standard deviation of the residuals ($\varepsilon_{ROI} = y_{ROI} - \hat{y}_{ROI}$) from the spatially averaged time series across the ROI ($\sigma_{\varepsilon_{ROI}}$). The PSF is then defined by Equation (5.4). This summary value quantifies the amount of signal fluctuation that takes place.

$$PSF = 100 \times \frac{\sigma_{\varepsilon_{ROI}}}{\bar{y_{ROI}}} \tag{5.4}$$

The percentage signal drift (PSD) is given by subtracting the minimum temporal signal fit value $min(\hat{y_{ROI}})$ from the maximum fit value $max(\hat{y_{ROI}})$. The fit described is from second order polynomial detrending. This is then divided by the temporal mean signal intensity across time for the spatially averaged time series of the ROI $\bar{y_{ROI}}$ (Equation (5.5)). This summary value quantifies how the signal linearly drifts in time.

$$PSD = 100 \times \frac{max(\hat{y_{ROI}}) - min(\hat{y_{ROI}})}{\bar{y_{ROI}}} \tag{5.5}$$

5.7.1.5 Weisskoff Analysis

Weisskoff analysis (Weisskoff, 1996) involves computing the spatially averaged time series across an ROI y_{ROI}, followed by calculating its temporal mean signal $y_{\bar{ROI}}$ and its temporal standard deviation $\sigma_{y_{ROI}}$. This is then calculated for incrementally increasing ROI sizes. The coefficient of variation (COV) (Equation (5.6)) for each ROI size is then plotted on a log scale.

$$COV = \frac{\sigma_{y_{ROI}}}{y_{\bar{ROI}}} \tag{5.6}$$

In theory, if there is no consistent noise present, then the relationship between the log of the coefficient of variation ($log(COV)$) and the log of the ROI size M ($log(M)$) should be linear and negative. This is because larger spatial averages across voxels should reduce the noise contribution, decreasing the coefficient of variance by the square root of the number of voxels in the volume.

The radius of decorrelation (RDC) is then determined as the ROI size at which the linear relationship is no longer present, with larger RDC values indicating better temporal stability. To compare this plot with the expected linear relationship, the first COV value is used and a linear relationship is extrapolated from this value. This is referred to in this thesis as the "expected" Weisskoff curve, compared with the "measured" curve calculated from each ROI size.

5.7.1.6 Fourier Analysis

Fourier analysis was also used to explore the main frequency components in the signal. This involved computing the power spectrum of the spatially averaged time series from the ROI after detrending with a second-order polynomial. This is done using the fast Fourier transform in MATLAB and the power is then plotted against the range of frequencies

determined from the TR.

High amplitude of a specific frequency can be useful for indicating the presence of fluctuations that may suggest the presence of natural frequencies that occur outside of the expected frequencies of the sequence. It can also be useful for identifying scanner instabilities.

5.7.2 Functional Sensitivity

The primary measure for functional sensitivity is the percentage signal change (PSC) when presenting a stimulus during the fMRI paradigm. This can either be measured from the beta parameters in the general linear model (Pernet, 2014), which describe the relative fit of the time series in a voxel to the model design, or directly from the time series as demonstrated in Solana et al. (2016) (Equation (5.7))

$$PSC = mean((\frac{max(fMRIsignal) - min(fMRIsignal)}{mean(fMRIsignal)})_{eachcycle}) \tag{5.7}$$

Measuring from the extracted time series is not recommended as overestimation of the change can occur in the case of the signal containing outliers (i.e. high maxima or low minima) (Pernet, 2014).

In the case of measuring the PSC from the beta parameters, the MarsBaR software can be used with the GLM (Brett, 2016; Brett et al., 2002). The functionality of this software is best described using an example, such as a simple ABAB block design (see Figure 1.8). In analysis, the design matrix would be set up such that the model is a HRF convolved with ABAB block design. The following columns in the model would be any additional regressors. The best estimate of the MR signal of interest for the response to the ABAB stimulus is the first β parameter multiplied by the set of regressors X (see Figure 1.8).

The first step is therefore to estimate the design but only in the ROI, producing a set of regressors and beta parameters only for the ROI (β_{ROI}, X_{ROI}). As mentioned previously, the first beta parameter in this design is the effect of interest ($\beta_{ROI_{HRF}}$).

To compute the percentage signal change in the ROI, MarsBaR creates a new regressor for a single block (X_A). The duration of the block is specified, matching that of the task (A), and this single block is run through the SPM design matrix to create the regressor of interest. This accounts for the scaling of the design matrix, i.e. the height of the regressors, to avoid exaggerating the percentage signal change (Pernet, 2014). Multiplying the average of the first beta parameter from the ROI ($\beta_{ROI_{HRF}}$) by X_A then produces the estimated response for the single event across the ROI, and the maximum height of the response is the signal change.

The signal change computed at this point will be scaled relative to the whole brain mean signal. To calculate the percentage signal change relative to the ROI baseline, the last β parameter of the ROI design matrix can be used as it represents the mean signal ($\beta_{ROI_{last}}$). The final percentage signal change is then given by

$$PSC_{ROI} = (\frac{\beta_{ROI_{HRF}} * X_A}{\beta_{ROI_{last}}}) \times 100 \tag{5.8}$$

5.7.3 Conventional Pre-processing

A standard SPM-12 pre-processing pipeline consists of realignment, co-registration to the T_1-weighted image, spatial normalisation to Montreal Neurological Institute (MNI) space (see Chau and McIntosh (2005) for further details) and spatial smoothing (FIL Methods Group, 2020). Slice timing correction is also included for GRE-EPI data, but is not required for Looping Star given that it is not slice-selective. Specific details are provided in relevant sections, and Poldrack et al. (2011) provide a useful review of pre-processing steps.

5.7.4 General Linear Model Analysis

A standard SPM-12 analysis pipeline consists of modelling the onsets of the task in the GLM (see Section 1.12 and Figure 1.8) and including the motion regressors at first-level, followed by taking the contrast file from first-level to second-level for group analysis (FIL Methods Group, 2020). Specific details are provided in relevant sections. Brodmann areas were used to determine cortical regions (for details see (Zilles and Amunts, 2010)).

Chapter 6

Characterisation of Looping Star in a Spherical Phantom

Summary

This chapter involves the following evaluations of Looping Star in a spherical phantom:

- Acoustic noise measures for different Looping Star acquisition parameters.
- A range of standard MRI temporal signal stability measures for characterising Looping Star.
- Comparisons of Looping Star with single echo and multi-echo GRE-EPI.

Overview

This chapter evaluates the signal stability produced by Looping Star acquisition parameters in a phantom. The sequence performance is characterised, independent of physiological noise and other subject-dependent factors. The acoustic noise levels for various parameters are also explored. The temporal stability of Looping Star is compared with single and multi-echo GRE-EPI acquisitions.

6.1 Chapter Introduction

Any potential source of temporal instability in the MR signal jeopardises the ability to detect the BOLD signal in vivo. This is because the percentage signal change of interest is incredibly small and can therefore be masked by non-BOLD related signal changes. To characterise signal changes that are independent of human contributions, imaging phantoms are frequently employed (Friedman and Glover, 2006). Since phantoms do not include any physiological noise sources, only scanner stability and the impact of the pulse sequence on the signal are evaluated.

Characterising the temporal stability of novel pulse sequences in phantoms can also help with disentangling noise sources from the BOLD signal during in vivo studies. This is since the MR signal in a phantom should be time-independent in the absence of any signal noise or instability (i.e. it should have low signal variance through time), differing from in vivo noise sources such as physiological noise. Physiological noise has been shown to affect sensitivity and statistical accuracy of fMRI analysis (Krüger and Glover, 2001; Triantafyllou et al., 2005, 2011; Wald and Polimeni, 2017) and different brain tissue types are also affected by physiological noise to different extents (Bodurka et al., 2007; Gonzalez-Castillo et al., 2011). Identifying and eliminating temporal instabilities prior to in vivo scanning therefore enables more accurate identification of in vivo noise sources and can streamline the pre-processing pipeline.

Phantoms have been employed across GRE-EPI studies to evaluate adaptations to pulse sequences (Giannelli et al., 2010; Van Der Zwaag et al., 2012) and changes in scanner stability that may occur day-to-day (Durand et al., 2001). One standard method for quantifying the variability in fMRI signal is to use the Functional Biomedical Informatics Research Network (FBIRN) consortium software suite (Friedman and Glover, 2006; Liu et al., 2015b). This includes measures of signal drift and fluctuation, temporal signal-to-noise ratio, frequency decomposition of the signal and 'Weisskoff analysis' (Weisskoff, 1996), all of which are described in depth in Section 5.7.1.

Given that acoustic noise can induce anxiety in participants (Quirk et al., 1989; van Minde et al., 2014) and anxiety can lead to additional head movement that affects fMRI data (Havsteen et al., 2017; Maknojia et al., 2019; Nguyen et al., 2020; Power et al., 2019), it is also important to characterise the acoustic noise levels of Looping Star. Different parameters affect not only the acoustic noise but also the temporal parameters of Looping Star (Section 3.2), hence both temporal stability and acoustic noise measures should be computed across different parameter combinations.

This chapter aims to fully characterise the Looping Star pulse sequence across a range of parameter combinations. Alongside these calculations, the acoustic noise measures of the different acquisitions are presented. GRE-EPI and Looping Star acquisitions were compared to validate the findings in an established modality. For this reason, only the gradient echo of Looping Star was investigated since the FID would not be comparable with GRE-EPI. The key methods used for the stability measures are described in Section 5.7.1. A 32-channel coil with an 18 cm diameter spherical GE Healthcare phantom was employed across all studies (Section 5.2 and 5.7.1).

6.2 Acoustic Noise Frequency Profile of Looping Star and GRE-EPI

6.2.1 Background

Understanding the acoustic noise level produced during scan acquisition is vital as discomfort could lead to head movement artefacts in vivo (Nguyen et al., 2020; van Minde et al., 2014). Furthermore, different acoustic noise characteristics can affect whether auditory stimuli are clearly heard in task-based fMRI paradigms (Perrachione and Ghosh, 2013) and therefore correctly attributed to brain regions of interest (Barker et al., 2012; Olulade et al., 2011). This section characterises the acoustic noise of Looping Star by exploring its frequency composition and peak amplitude across the frequency

spectra. Looping Star was expected to be quieter than GRE-EPI and that any change in Looping Star acquisition parameters that increase the distance between gradient steps will increase the acoustic noise (Section 2.1).

6.2.2 Methods

The data was collected from the 3 T scanner at the Centre for Neuroimaging Sciences (Section 5.2). Acoustic noise measures were recorded as detailed in Section 5.5 and the recorded scan durations were approximately 40 seconds. Table 6.1 describes the acquisition parameters used. All scans involved a FOV = 19.2 cm, isotropic voxel size = 3 mm, spokes per volume = 1024, and FA = 1°. The acquisition parameters used for GRE-EPI are taken from one of the most widely used GRE-EPI acquisition protocols at my institution.

Table 6.1: Looping Star acquisition parameters for acoustic noise frequency profile generation. All Looping Star scans involved a FOV = 19.2 cm, isotropic voxel size = 3 mm, spokes per volume = 1024, and FA = 1°.

Acquisition Parameters
FID + echo, ±31.25 kHz readout bandwidth (BW), 32 spokes per loop (spl), GSF = 14, TR = 2.13 s, TE = 26.88 ms
FID + echo, ±15.60 kHz BW, 32 spl, GSF = 14, TR = 3.19 s, TE = 43.0 ms
FID + 2 echoes, ±31.25 kHz BW, 32 spl, GSF = 12, TR = 2.91 s, ΔTE = 26.1 ms
FID + 2 echoes, ±46.88 kHz BW, 32 spl, GSF = 10, TR = 2.49 s, ΔTE = 21.8 ms
FID + 3 echoes, ±46.88 kHz BW, 16 spl, GSF = 8, TR = 3.55 s, ΔTE = 10.75 ms
FID + 3 echoes, ±62.5 kHz BW, 16 spl, GSF = 10, TR = 3.01 s, ΔTE = 8.70 ms
GRE-EPI, ±250 kHz BW [1], slice thickness = 3 mm, number of slices = 38, slice gap = 0.3 mm, TR = 2 s, TE = 28 ms, FA = 75°, FOV = 21.4 cm, dummy acquisitions (DDAs) = 0

[1] Ramp sampling used

6.2.3 Results

Figure 6.1 shows the acoustic noise profiles for the acquisitions in Table 6.1, displayed as the sound level amplitude (weighted to the human ear, i.e. A-weighted) relative to the frequency. The peak sound level occurs at frequency 1 kHz for GRE-EPI and exceeds 100 dB(A) in amplitude, whereas the highest amplitude of a Looping Star acquisition was 86 dB(A) at 125 Hz. All Looping Star scans presented peak amplitude at a lower frequency relative to GRE-EPI, indicating the dominant presence of low amplitude "rumbling" sounds in Looping Star compared with the high amplitude "drilling" of GRE-EPI.

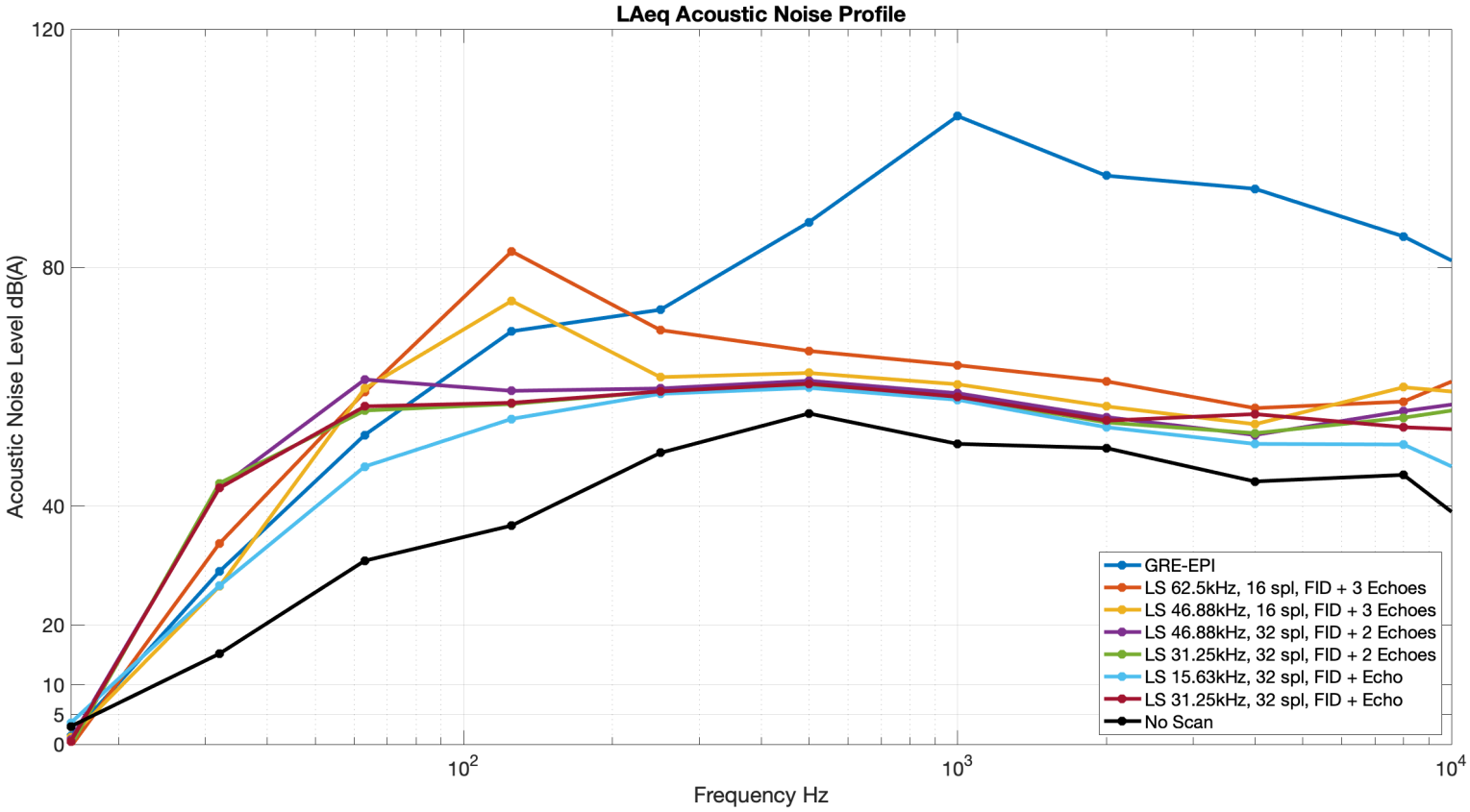

Figure 6.1: Acoustic noise frequency profile of Looping Star and GRE-EPI acquisitions in Table 6.1, plus the frequency profile of ambient noise.

6.2.4 Discussion

All Looping Star acquisitions presented a lower sound frequency at which the peak amplitude occurred, as well as a lower peak amplitude of acoustic noise, compared with GRE-EPI. These findings are consistent with expectations, as Looping Star demonstrated reduced acoustic noise relative to GRE-EPI. Additionally, the Looping Star scans that required larger gradient direction changes produced higher acoustic noise (i.e. 16 spokes per loop), as expected.

Looping Star may therefore improve the interpretation of studies of the auditory cortex, particularly for stimuli that have acoustic frequencies higher than 125 Hz (i.e. above the peak sound frequency for Looping Star). This is because different sound stimulus characteristics give rise to different neural responses (Brechmann et al., 2002; Hart et al., 2003; Langers et al., 2007), so removing as much background noise as possible will improve the specificity of the response.

6.3 Average Acoustic Noise of Looping Star and Conventional MRI across Parameters

6.3.1 Background

Characterising the acoustic noise of Looping Star across different parameters can guide parameter selection for future studies, particularly those prioritising sound reduction due to the inclusion of sound-averse participants. The impact of changing three core parameters expected to affect the average acoustic noise was explored whilst keeping all other parameters constant. These three parameters were spokes per loop, readout bandwidth and gradient smoothing factor. The effects of these parameters were also compared between high spatial resolution and low spatial resolution scans.

Looping Star acquisitions were also compared with those of conventional MRI, particularly GRE-EPI and IR-SPGR acquisitions. As the gradient amplitude increases with increasing readout bandwidth for Looping Star, to facilitate full k-space coverage (Section 3.2), higher readout bandwidths would increase the acoustic noise. It was expected that a higher gradient smoothing factor and a higher number of spokes per loop should reduce the acoustic noise, given that they reduce the distance between directional gradient steps.

6.3.2 Methods

The acoustic noise measures were collected from the 3 T scanner at the Centre for Neuroimaging Sciences (Section 5.2). The method for acoustic noise recording is given in Section 5.5. Static average LA_{eq} values were read from the device after 15 s of recording each scan and outputs were A-weighted, meaning they are weighted towards the sound heard by the human ear (Section 2.1).

Table 6.2 shows the fMRI acquisition parameters used for comparing the average acoustic noise. All scans involved a FOV = 19.2 cm, isotropic voxel size = 3 mm, spokes per volume = 1024, and a FA = 2° . All scans collected the FID plus a single echo. For the bandwidth comparison, the highest bandwidth (±62.5 kHz) required a lower GSF to avoid gradient smoothing exceeding the scanner capability.

Table 6.2: Looping Star acquisition parameters for average acoustic noise measurements, low resolution. All Looping Star scans involved a FOV = 19.2 cm, isotropic voxel size = 3 mm, spokes per volume = 1024, and a FA = 2°. All scans collected the FID plus a single echo.

Acquisition Parameters
±31.25 kHz BW, 32 spl, GSF = 1, TR = 1.97 s, TE = 25.4 ms
±31.25 kHz BW, 32 spl, GSF = 8, TR = 1.98 s, TE = 25.6 ms
±31.25 kHz BW, 32 spl, GSF = 10, TR = 1.98 s, TE = 25.6 ms
±31.25 kHz BW, 32 spl, GSF = 12, TR = 2.02 s, TE = 26.1 ms
±31.25 kHz BW, 32 spl, GSF = 14, TR = 2.07 s, TE = 26.9 ms
±15.625 kHz BW, 32 spl, GSF = 14, TR = 3.13 s, TE = 43.0 ms
±46.88 kHz BW, 32 spl, GSF = 14, TR = 1.71 s, TE = 21.5 ms
±62.5 kHz BW, 32 spl, GSF = 12, TR = 1.51 s, TE = 18.4 ms
±31.25 kHz BW, 8 spl, GSF = 14, TR = 3.10 s, TE = 6.72 ms
±31.25 kHz BW, 16 spl, GSF = 14, TR = 2.41 s, TE = 13.4 ms

Table 6.3 shows the acquisition parameters for high spatial resolution structural scans, likely to be used for T_2* imaging and quantitative susceptibility mapping (QSM). All acquisitions involved FOV = 19.2 cm, 1 mm isotropic voxel size, 36864 spokes per volume, FA = 2° and collected an FID plus echo image.

Table 6.3: Looping Star acquisition parameters for average acoustic noise measurements, high resolution. All Looping Star acquisitions involved FOV = 19.2 cm, 1 mm isotropic voxel size, 36864 spokes per volume, FA = 2° and collected an FID plus echo image. The TR is equivalent to the scan time.

Acquisition Parameters
±31.25 kHz BW, 8 spl, GSF = 1, TR = 101 s, TE = 14.6 ms
±31.25 kHz BW, 8 spl, GSF = 8, TR = 101 s, TE = 14.6 ms
±31.25 kHz BW, 8 spl, GSF = 10, TR = 102 s, TE = 14.7 ms
±31.25 kHz BW, 8 spl, GSF = 12, TR = 102 s, TE = 14.7 ms
±31.25 kHz BW, 8 spl, GSF = 14, TR = 102 s, TE = 14.8 ms
±15.625 kHz BW, 8 spl, GSF = 14, TR = 167 s, TE = 27.3 ms
±46.88 kHz BW, 8 spl, GSF = 14, TR = 86 s, TE = 11.6 ms
±62.5 kHz BW, 8 spl, GSF = 14, TR = 70 s, TE = 8.5 ms
±31.25 kHz BW, 4 spl, GSF = 8, TR = 135 s, TE = 7.3 ms
±31.25 kHz BW, 16 spl, GSF = 14, TR = 84 s, TE = 29 ms

For comparison, a multi-echo and a single echo GRE-EPI acquisitions, as well as an inversion-recovery spoiled gradient echo (IR-SPGR) (Alzheimer's Disease Neuroimaging Initiative, 2017; Leung et al., 2015) acquisition, were obtained (Table 6.4).

Table 6.4: Conventional MRI acquisition parameters for average acoustic noise measurements

Acquisition Parameters
GRE-EPI: ±250 kHz BW [1], slice thickness = 3 mm, number of slices = 39, slice gap = 0.3 mm, TR = 2 s, TE = 30 ms, FA = 75°, FOV = 21 cm, DDAs = 0, 100 volumes
Multi-echo GRE-EPI: TE = 12 ms, 28 ms, 44 ms, 60 ms, TR = 2.5 s, FA = 80°, slice thickness = 3 mm, 1 mm slice gap, FOV = 21 cm, number of slices = 32, DDAs = 4, ±250 kHz BW [1], 100 volumes
IR-SPGR: FOV = 27 cm, slice thickness 1.2 mm, 200 slices, 1.05 mm in plane resolution, TE = 3 ms, inversion time (TI) = 400 ms, FA = 11°, ±23 kHz BW, scan time = 5 mins 37 s

6.3.3 Results

Figures 6.2A-C demonstrate the impact of the number of spokes per loop, readout bandwidth and gradient smoothing factor on the average sound level in an fMRI acquisition (Table 6.2). Higher gradient smoothing factor and number of spokes per loop reduce the acoustic noise whereas higher readout bandwidth increases acoustic noise. Figure 6.2D shows that the GRE-EPI and IR-SPGR acquisition (Table 6.4) sound levels are much higher. The ±15.625 kHz Looping Star acquisition has a comparable noise level to ambient scanner room noise.

[1] Ramp sampling used

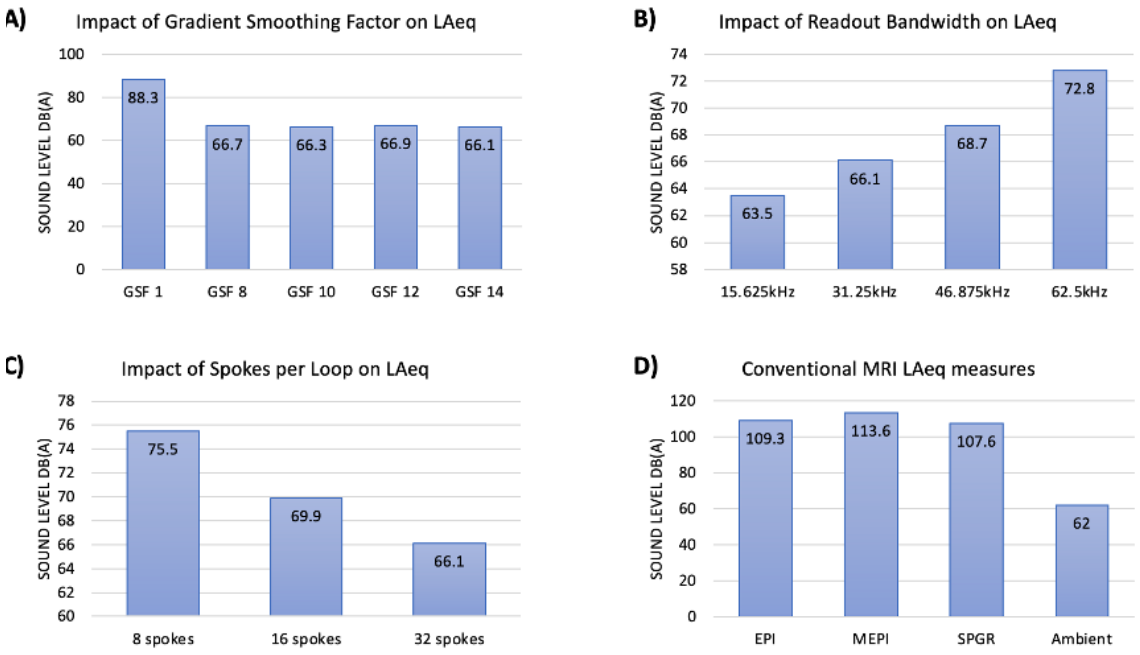

Figure 6.2: Acoustic noise levels (LA_{eq}) of acquisitions in Table 6.2 and Table 6.4. A) Impact of increasing gradient smoothing factor. B) Impact of increasing readout bandwidth. C) Impact of increasing spokes per loop. D) Conventional MRI acquisitions and ambient scanner room noise.

Figures 6.3A-C demonstrate the impact of spokes per loop, readout bandwidth and gradient smoothing factor on acoustic noise in a single volume high spatial resolution acquisition (Table 6.3). The same patterns are visible in comparison with the fMRI acquisitions, though are generally higher in amplitude.

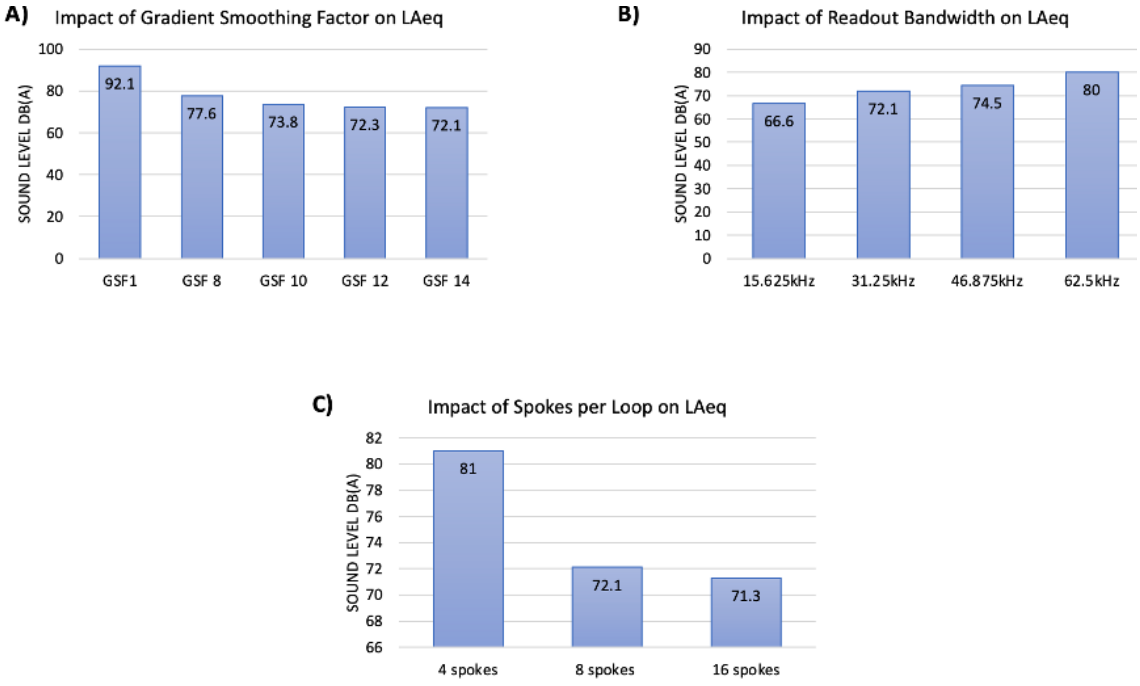

Figure 6.3: Acoustic noise levels (LA_{eq}) of acquisitions in Table 6.3. A) Impact of increasing gradient smoothing factor. B) Impact of increasing readout bandwidth. C) Impact of increasing spokes per loop.

6.3.4 Discussion

The average acoustic noise levels of Looping Star for a range of parameters were compared with conventional MRI acquisitions. The results demonstrate the patterns expected and highlight the importance of considering which acquisition parameters are selected given their impact on acoustic noise. These results should ideally be used in conjunction with an evaluation of signal stability (Sections 6.4 - 6.6) and the acoustic noise frequency characteristics (Section 6.2) to identify the best acquisition parameters for each study, based on the paradigm and cohort of interest. However, as different Looping Star acquisition parameters affect the TR and TE (Section 3.2), compromises on acoustic noise may be required to boost SNR or to use multi-echo acquisition with good temporal resolution.

6.4 Impact of Flip Angle on Temporal Stability with Looping Star

6.4.1 Background

Evidence has indicated that lower flip angles can be used in fMRI with GRE-EPI without significant impact on the tSNR in the case where SNR is high (Gonzalez-Castillo et al., 2011). To explore whether this is also true for Looping Star, particularly since it involves short, hard, RF pulses, the impact of flip angle on temporal stability was characterised. This is also crucial for ensuring sufficient signal amplitude for fMRI (Haase et al., 1986; Miller, 2012; Park et al., 2011). It was expected that increasing flip angle would increase the tSNR due to the increased signal amplitude, with no effect on temporal stability.

6.4.2 Methods

The spherical phantom data was collected from the 3 T scanner at the Clinical Research Facility (Section 5.2 and 5.7.1). Table 6.5 describes the acquisition parameters employed for Looping Star. All scans involved a FOV = 19.2 cm, isotropic voxel size = 3 mm, 50 volumes and spokes per volume = 1024. The temporal stability measures are described in Section 5.7.1. The first four volumes were neglected in analysis to allow the longitudinal magnetisation to reach steady-state, supported by the calculations in Section 3.5, which found that signal stability for Looping Star occurred after approximately 4000 spokes.

Table 6.5: Acquisition parameters for evaluation of flip angle impact on Looping Star signal stability. All scans involved a FOV = 19.2 cm, isotropic voxel size = 3 mm, and spokes per volume = 1024. 50 volumes were acquired per acquisition.

Acquisition Parameters
FID + 3 echoes, BW = $\pm$62.5 kHz, 16 spl, GSF = 8, TR = 3 s, ΔTE = 8.7 ms, FA = 1°
FID + 3 echoes, BW = $\pm$62.5 kHz, 16 spl, GSF = 8, TR = 3 s, ΔTE = 8.7 ms, FA = 2°
FID + 3 echoes, BW = $\pm$62.5 kHz, 16 spl, GSF = 8, TR = 3 s, ΔTE = 8.7 ms, FA = 3°

6.4.3 Results

The impact of increasing flip angle on the third gradient echo is shown in Table 6.6. Increasing flip angle correlates with increasing SNR and tSNR for all echoes acquired. Generally, there was little difference in PSD and PSF, and the highest RDC was for the third echo of flip angle 1° and the lowest for the first echo of flip angle 3°

Table 6.6: Temporal stability analysis of 2D ROI (15 x 15 pixel) for same acquisition with increasing flip angles. **Note:** GRE, GRE2, GRE3

Acquisition	SNR	tSNR	PSF (%)	PSD (%)	RDC
FA 1° GRE	120.32	141.57	0.099	-0.19	6.09
FA 1° GRE2	85.18	88.79	0.133	-0.17	9.16
FA 1° GRE3	57.80	58.68	0.176	-0.20	10.82
FA 2° GRE	142.63	141.82	0.070	0.08	9.71
FA 2° GRE2	90.49	90.61	0.121	0.02	8.66
FA 2° GRE3	61.39	58.02	0.205	-0.13	8.02
FA 3° GRE	265.55	259.59	0.062	-0.03	5.03
FA 3° GRE2	154.74	156.01	0.057	-0.04	9.88
FA 3° GRE3	94.81	97.01	0.130	0.01	9.74

Figure 6.4 shows that there were no major changes in tSNR characteristics across flip angles, beyond the correlation of higher flip angle producing higher tSNR values, which is to be expected with scaling signal amplitude. There were no differences for the SSN images, which produced values around zero across the image with no structural detail.

The appearance of an air bubble within the spherical phantom is visible in the tSNR images. Upon further investigation, the "hot spots" in the tSNR image appeared to be related to lower temporal standard deviation, increasing the tSNR in these regions. This could be linked to inhomogeneities in the phantom.

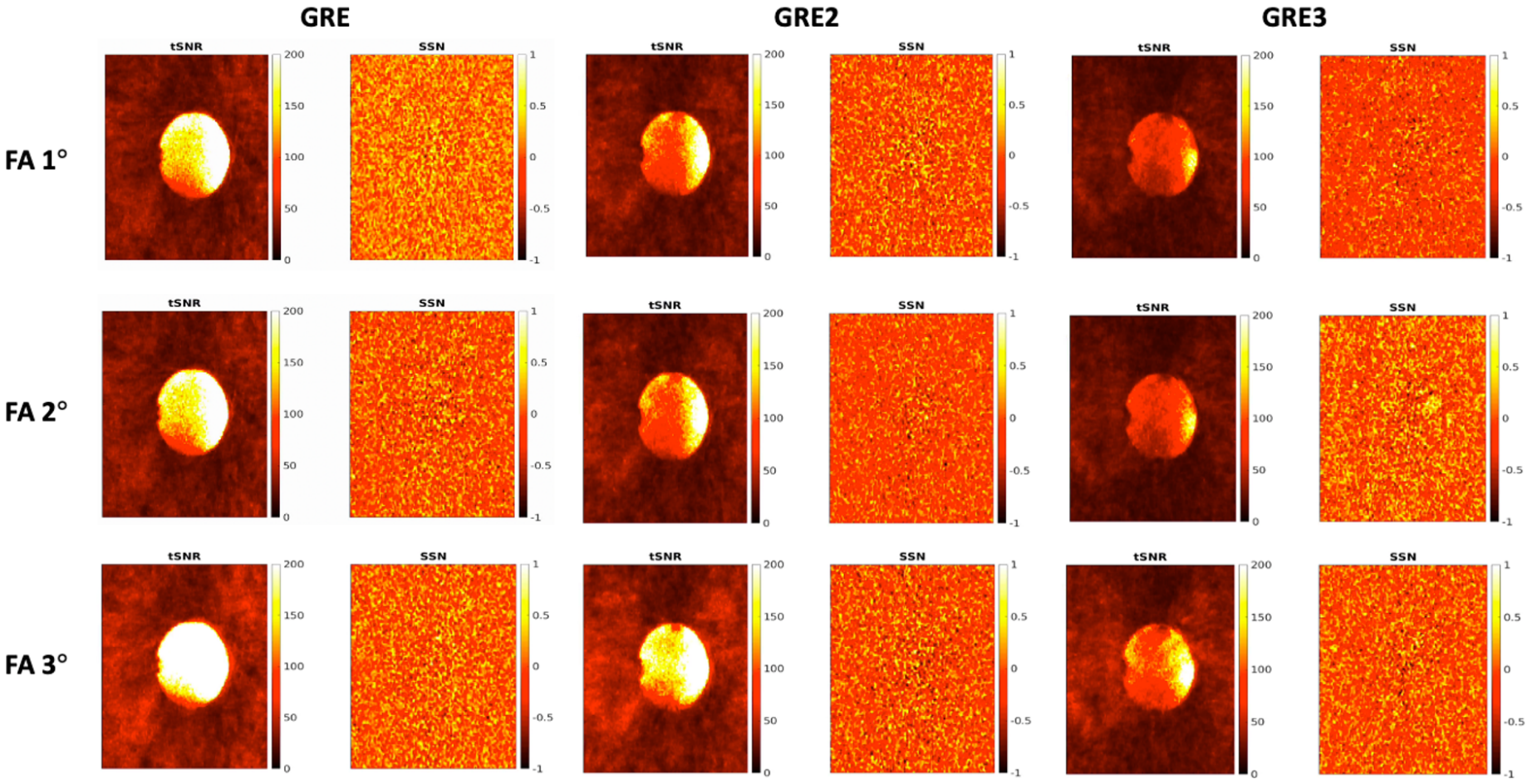

Figure 6.4: Impact of flip angle (FA) on tSNR and SSN for each echo (GRE, GRE2 and GRE3).

The Weisskoff curves are comparable between the curve measured from the data and the curve estimated assuming a linear relationship across all acquisitions (Figure 6.5), though with the earliest plateaus visible in the first gradient echo of the FA = 3° acquisition, as supported by Table 6.6.

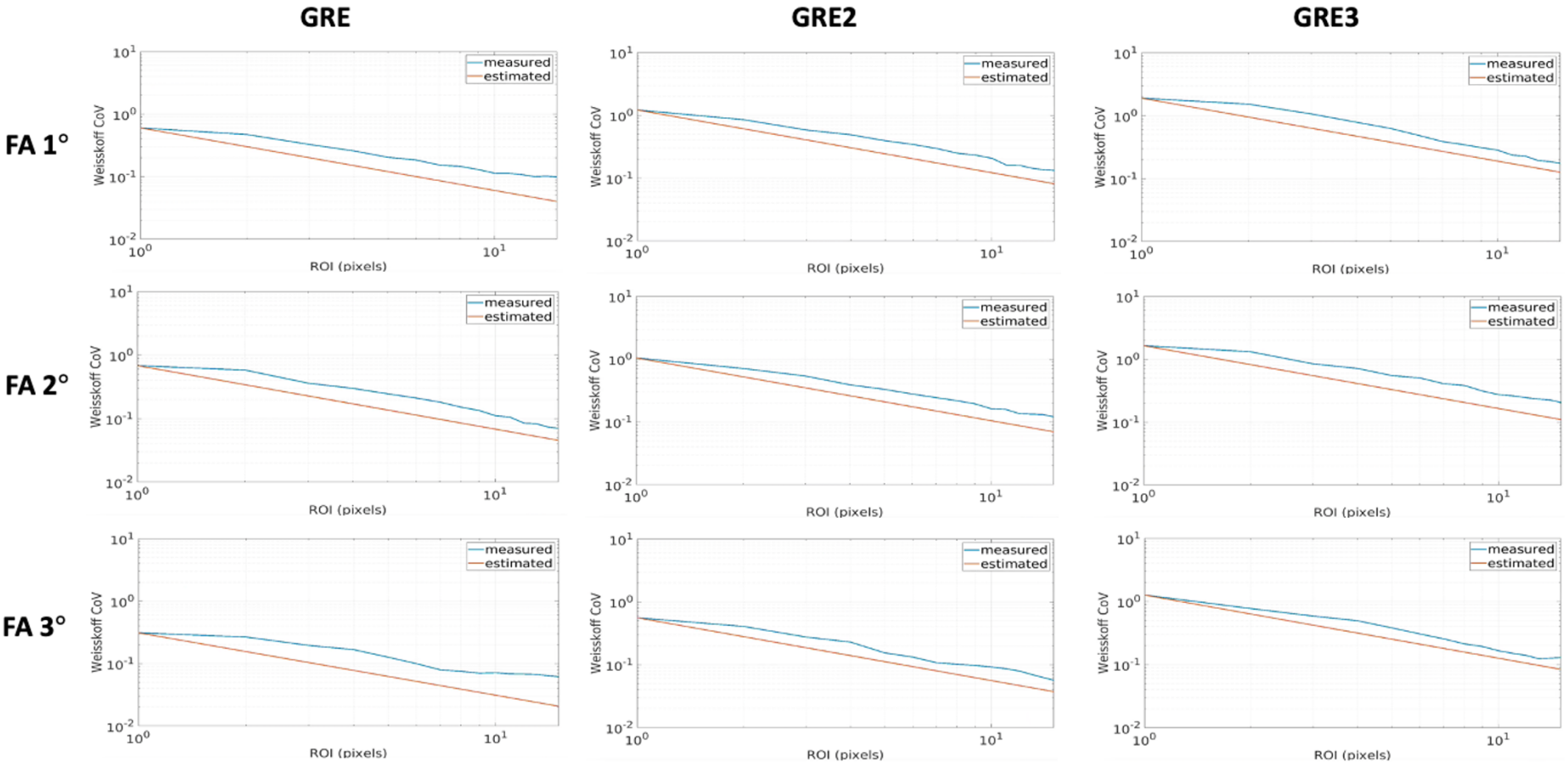

Figure 6.5: Weisskoff coefficient of variation (CoV) analysis for each flip angle (FA) across gradient echoes (GRE, GRE2 and GRE3).

Figure 6.6 also shows that there were no changes in dominant frequencies for increasing flip angles across echoes. The power in the frequency spectra was also low across all frequencies for all acquisitions.

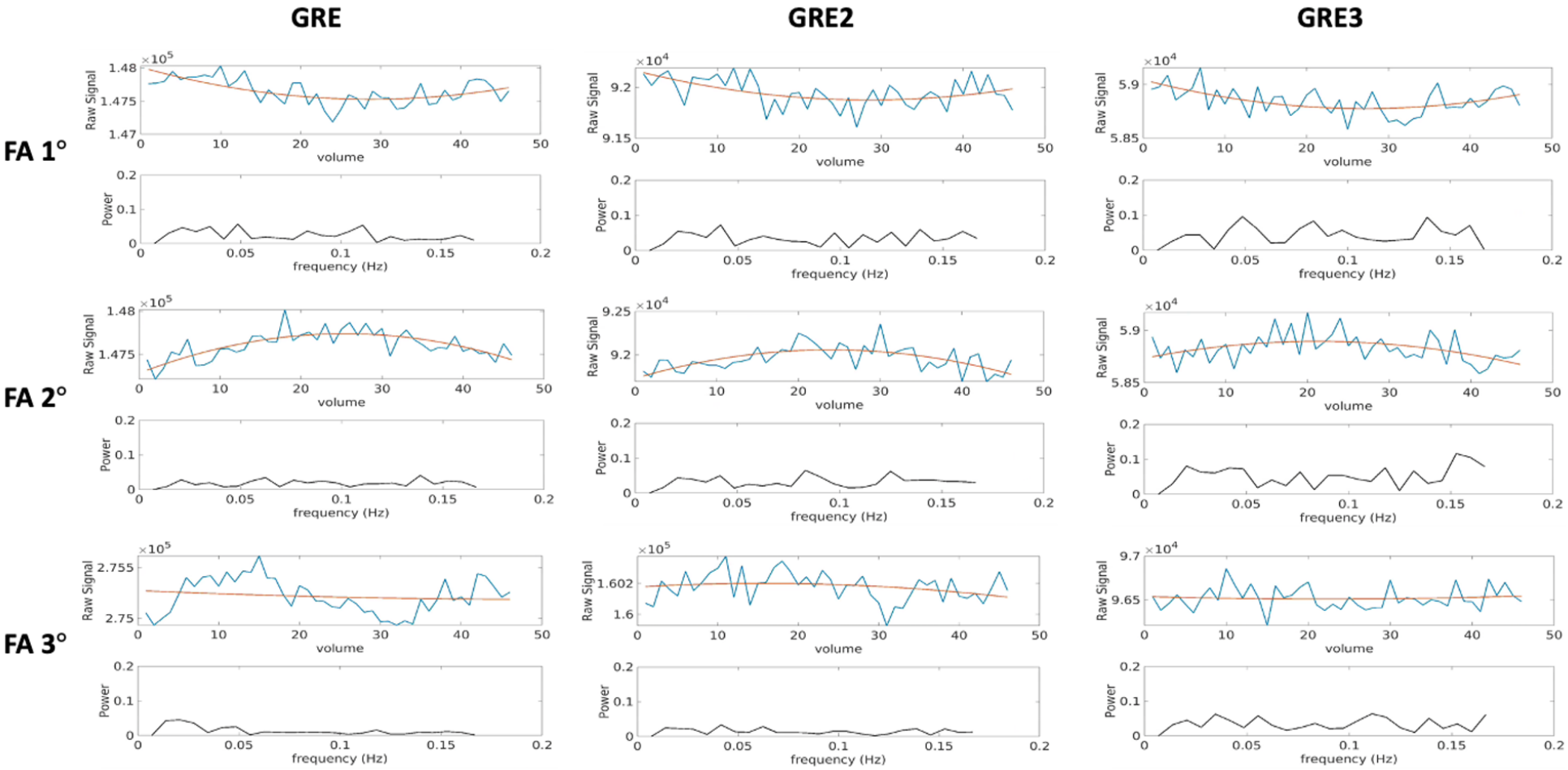

Figure 6.6: Frequency analysis and raw signal for each flip angle (FA) across gradient echoes (GRE) in 15 x 15 pixel ROI.

6.4.4 Discussion

Looping Star demonstrated the expected pattern of increasing tSNR with increasing flip angle, with no unexplained deviations in frequency or fluctuations. SNR and tSNR increased with flip angle, with the largest jump in values between FA = 2° and FA = 3°. This could indicate that FA = 3° is nearer to the optimal angle for the phantom, which would be the case for a TR_{rf} = 544 μs (for a ±62.5 kHz acquisition) and T_1 < 500 ms for the phantom. The T_1 value of the phantom requires further investigation. For future studies, the priority should be to employ the optimal angle and ensure maximal SNR efficiency (Section 3.8).

6.5 Impact of Readout Bandwidth on Temporal Stability with Looping Star

6.5.1 Background

For all MRI acquisitions, higher readout bandwidths lead to reductions in SNR as more noise is received in the larger readout frequency range, although the sampling time (TR) is reduced (Bernstein et al., 2004). As high temporal resolution is required in fMRI, characterising the extent of increasing signal noise for Looping Star with increasing readout bandwidth is essential for devising an optimal compromise during image acquisition. The impact of increasing readout bandwidth on Looping Star data was investigated, with an increase in temporal noise with increasing bandwidth expected. However, there may also be an impact due to the shortening of the echo time with increasing readout bandwidth (Section 3.2) that may counteract the temporal noise with higher signal amplitude.

6.5.2 Methods

The data was collected from a spherical phantom on the 3 T scanner at the Centre for Neuroimaging Sciences (Section 5.2 and Section 5.7.1). Table 6.7 describes the acquisition parameters employed for Looping Star. All scans involved a FOV = 19.2 cm, isotropic voxel size = 3 mm, spokes per volume = 1024, and a FA = 2° . All scans acquired the FID and one echo image and 100 volumes. The temporal stability measures are described in Section 5.7.1. The first four volumes were neglected in the Looping Star analysis for steady-state to be reached, supported by the calculations in Section 3.5.

Table 6.7: Acquisition parameters for increasing readout bandwidth. All Looping Star scans involved a FOV = 19.2 cm, isotropic voxel size = 3 mm, spokes per volume = 1024, and a FA = 2° , and acquired the FID and one echo image. 100 volumes were acquired per acquisition.

Acquisition parameters
±15.625 kHz BW, 32 spl, GSF = 12, TR = 3.13 s, TE = 43.0 ms
±31.25 kHz BW, 32 spl, GSF = 12, TR = 2.02 s, TE = 26.1 ms
±46.88 kHz BW, 32 spl, GSF = 12, TR = 1.71 s, TE = 21.5 ms
±62.5 kHz BW, 32 spl, GSF = 12, TR = 1.51 s, TE = 18.4 ms

6.5.3 Results

Table 6.8 compares the effects of incremental increases in readout bandwidth (Table 6.7). For the gradient echo (GRE), SNR and tSNR were highest for the ±46.88 kHz acquisition and lowest for the ±15.625 kHz acquisition. The percentage signal fluctuation and drift were low, with the highest RDC for the ±62.5 kHz gradient echo acquisition. Investigating the standard deviation of the temporal signal within the ROI, it can be seen that the signal variance increases with bandwidth.

Table 6.8: Temporal stability analysis of central 2D (15 x 15 pixel) ROI in gradient echo (GRE) for same acquisition with increasing bandwidths.

Acquisition	SNR	tSNR	PSF (%)	PSD (%)	RDC	$\sigma_{\varepsilon_{ROI}}$
±15.625 kHz GRE	99.29	96.41	0.147	0.08	5.84	2.18×10^7
±31.25 kHz GRE	119.61	121.15	0.104	-0.19	8.16	6.99×10^7
±46.88 kHz GRE	126.83	123.43	0.113	-0.14	7.98	1.33×10^8
±62.5 kHz GRE	120.60	107.57	0.115	-0.27	8.30	2.16×10^8

Figure 6.7 shows the tSNR and SSN images for each bandwidth. It can be seen that the tSNR is fairly consistent between the ±31.25 kHz, ±46.88 kHz and ±62.5 kHz acquisition. Lower mean signal appeared to be responsible for the "shadows" in the phantom tSNR images, likely linked to phantom inhomogeneities as seen previously. There appeared to be a more blurred structure in the ±15.625 kHz acquisition tSNR plot. The SSN values in the phantom structure were generally consistent across acquisitions.

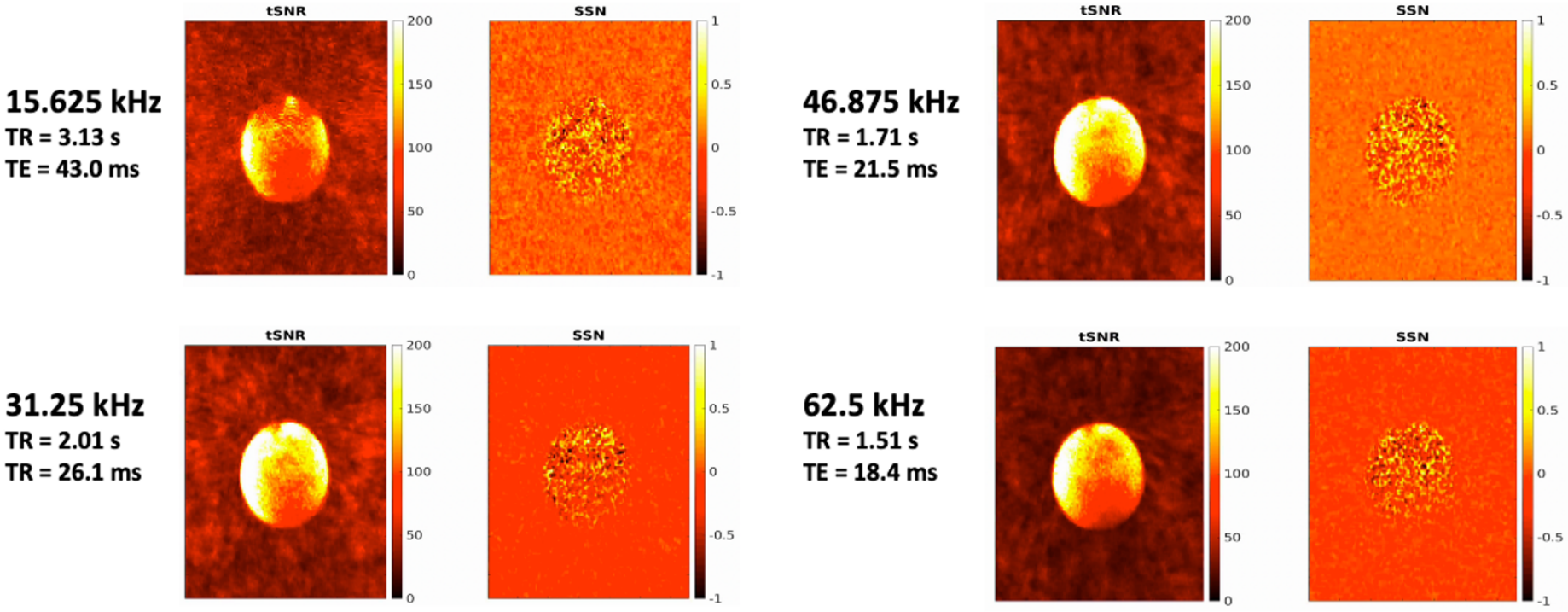

Figure 6.7: Impact of readout bandwidth for echo on tSNR and SSN for Looping Star.

Figure 6.8 shows the corresponding Weisskoff curves across readout bandwidths for the gradient echo images of Looping Star. All readout bandwidths produced Wiesskoff curves where the measured and estimated trends were consistently linear.

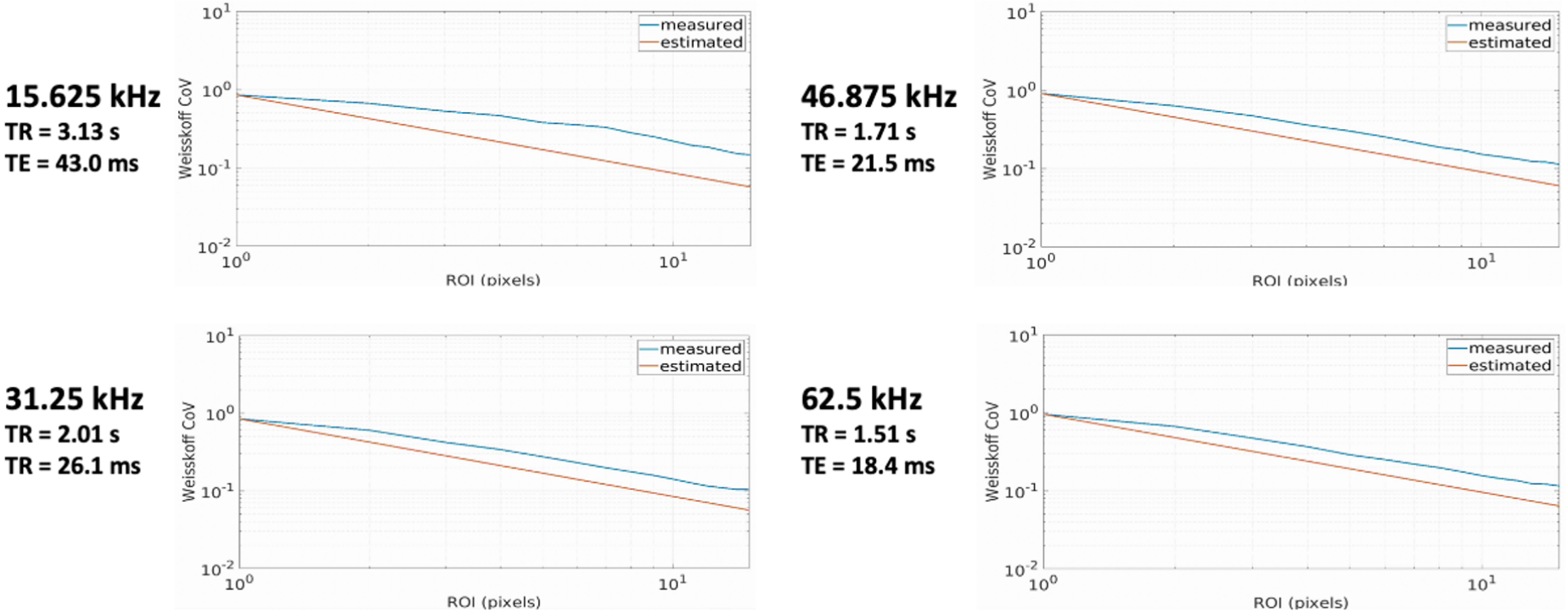

Figure 6.8: Impact of readout bandwidth on Wiesskoff analysis coefficient of variation (CoV) for gradient echo of Looping Star.

Figure 6.9 indicates the presence of a very low amplitude low frequency signal drift (i.e. < 0.05 Hz) across readout bandwidths and in the echo images, with marginally higher peak power in the $\pm$31.25 kHz (peak of 0.074 at 0.0152 Hz) and $\pm$62.5 kHz (peak of 0.0797 at 0.0203 Hz) datasets compared with the $\pm$15.625 kHz (peak of 0.065 at 0.0489 Hz) and $\pm$46.88 kHz data (peak of 0.0695 at 0.0179 Hz).

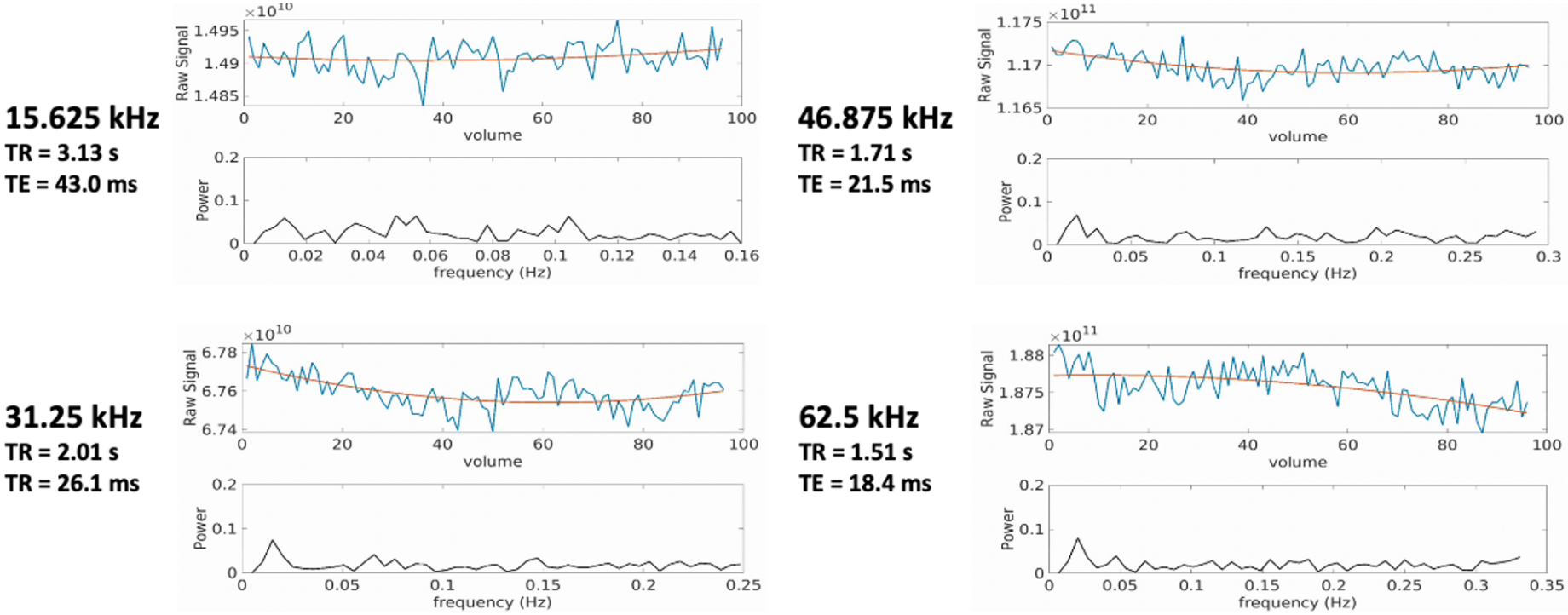

Figure 6.9: Impact of readout bandwidth on frequency spectrum profile and raw signal in 15 x 15 pixel ROI for gradient echo of Looping Star.

6.5.4 Discussion

As mentioned previously, the readout bandwidth is inherently linked to the echo time for Looping Star. This means that larger readout bandwidths produce shorter echo times, and so produce inherently higher signal amplitudes. As expected, higher tSNR and SNR were seen for larger bandwidths given their higher mean signal amplitudes. For this reason, it was essential to study the temporal variance of the data and it was found that there was increasingly higher signal standard deviation with increasing bandwidth. This suggests that although greater noise may be present at higher bandwidths, the entanglement of the echo time with the readout bandwidth inherently boosts the mean signal and therefore counteracts the acoustic noise, as expected. The prevalence of a low frequency peak in the power spectra across bandwidths was of substantially low amplitude that it was not deemed of concern.

6.6 Impact of Number of Spokes Per Loop on Temporal Stability with Looping Star

6.6.1 Background

The number of spokes per loop is another parameter that changes the TE and TR of Looping Star acquisitions. Though the SNR measures will predominantly be affected by the different signal intensities resulting from the different decay times, the temporal stability should be largely unaffected. Theoretically, any even number of spokes per loop would correctly refocus the signal, however imperfections in the gradients would produce phase errors; hence it is important to quantify the temporal stability of this parameter despite its entanglement with scan timings. It was expected that a higher number of spokes per loop would be more susceptible to phase errors and would therefore have worse temporal stability.

6.6.2 Methods

The data was collected from a spherical phantom on the 3 T scanner at the Centre for Neuroimaging Sciences (Section 5.2 and Section 5.7.1). Table 6.9 describes the acquisition parameters employed for Looping Star. All scans were acquired with a FOV = 19.2 cm, isotropic voxel size = 3 mm, spokes per volume = 1024, and FA = 2° . All scans acquired a FID and a single echo image and 100 volumes. The temporal stability measures are described in Section 5.7.1. The first four volumes were neglected in the Looping Star analysis, supported by the calculations in Section 3.5.

Table 6.9: Acquisition parameters for Looping Star with a range of number of spokes per loop. All scans were acquired with a FOV = 19.2 cm, isotropic voxel size = 3 mm, spokes per volume = 1024, and FA = 2°. All scans acquired a FID and a single echo image and 100 volumes.

Acquisition parameters
±31.25 kHz BW, 8 spl, GSF = 14, TR = 3.10 s, TE = 6.72 ms
±31.25 kHz BW, 16 spl, GSF = 14, TR = 2.41 s, TE = 13.4 ms
±31.25 kHz BW, 32 spl, GSF = 14, TR = 2.07 s, TE = 26.9 ms

6.6.3 Results

The impact of increasing the number of spokes per loop is shown in Table 6.10. The gradient echo for Looping Star demonstrated the highest SNR and tSNR in the 8 spokes per loop acquisition and the lowest SNR and tSNR in the 32 spokes per loop acquisition. Signal fluctuation and drift remained low across acquisitions, although the highest fluctuation and lowest drift were seen for the 32 spokes per loop acquisition. The standard deviation of the temporal signal was also lowest for the 32 spokes per loop acquisition.

Table 6.10: Temporal stability analysis of spokes per loop for 2D 15 x 15 pixel ROI.

Acquisition	SNR	tSNR	PSF (%)	PSD (%)	RDC	$\sigma_{\varepsilon_{ROI}}$
8 spl GRE	268.49	281.77	0.056	0.10	6.07	1.41×10^8
16 spl GRE	213.22	207.83	0.087	0.29	5.91	1.46×10^8
32 spl GRE	128.28	115.42	0.125	-0.03	6.67	7.59×10^7

The highest tSNR was observed for the 8 spokes per loop acquisition (Figure 6.10), compared with the higher number of spokes per loop acquisitions, and the lowest SSN appeared to be the 16 spokes per loop acquisition. Upon further investigation, once again, the lower mean signal was responsible for the "shadows" in the phantom tSNR images, likely linked to the phantom inhomogeneities mentioned previously.

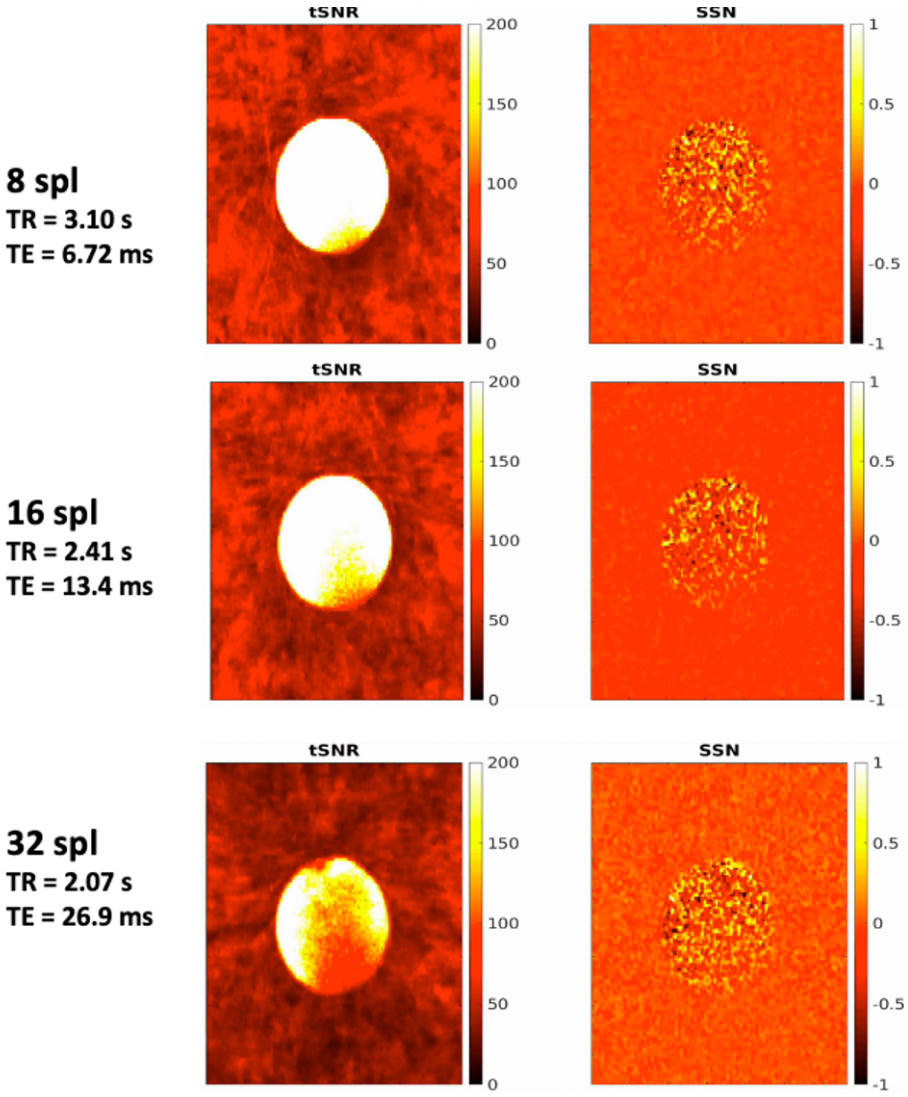

Figure 6.10: Impact of spokes per loop (spl) on tSNR and SSN for gradient echo of Looping Star.

Figure 6.11 shows the Weisskoff measures across spokes per loop, where the plateau began at a lower RDC value for the 8 spokes per loop acquisition.

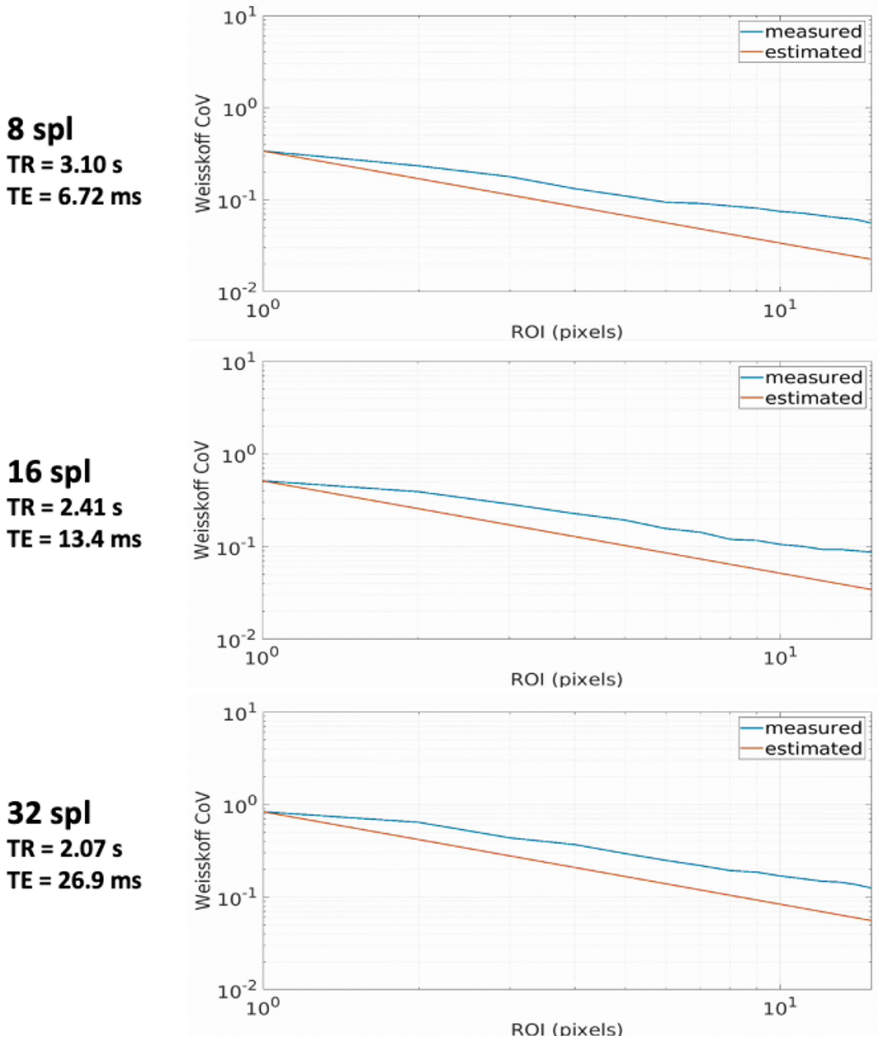

Figure 6.11: Impact of spokes per loop (spl) on Weisskoff coefficient of variance (CoV) analysis of gradient echo for Looping Star.

Figure 6.12 shows signal versus time plots and the power spectra for each number of spokes per loop. These demonstrate a peak low frequency (i.e. < 0.05 Hz) fluctuation in all acquisitions, with marginal differences between them: 8 spokes per loop (peak of 0.0368 at 0.0165 Hz), 16 spokes per loop (peak of 0.0616 at 0.017 Hz) and 32 spokes per loop (peak of 0.064 at 0.0148 Hz).

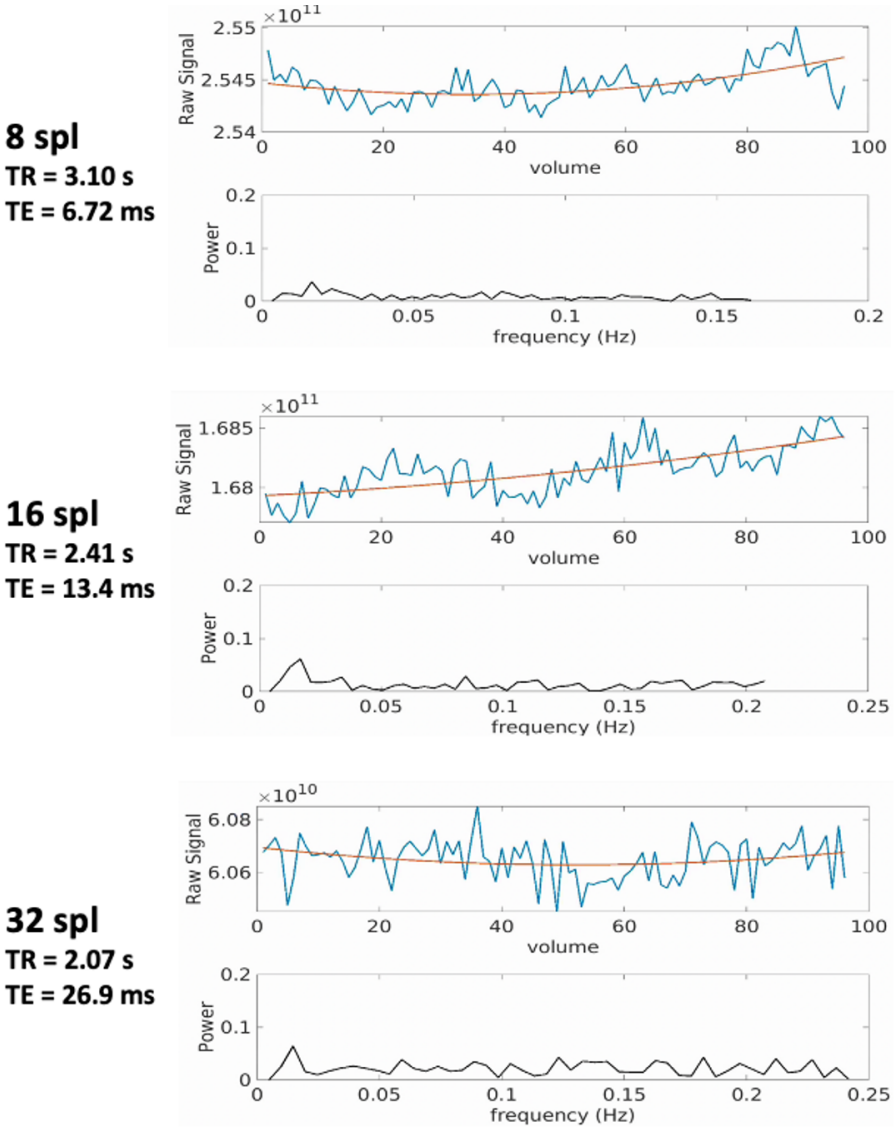

Figure 6.12: Impact of spokes per loop (spl) on frequency spectra and raw signal in 15 x 15 pixel ROI for gradient echo of Looping Star.

6.6.4 Discussion

As in Section 6.5, the number of spokes per loop is also inherently linked to the echo time for Looping Star. Fewer spokes per loop produce shorter echo times, producing higher signal amplitudes. This explains the higher tSNR and SNR for fewer spokes per loop, as well as the higher percentage signal fluctuation of the 32 spokes per loop acquisition given the dependence of the PSF measure on signal amplitude (see Section 5.7.1).

Alternatively, the 32 spokes per loop acquisition had the lowest temporal standard deviation

and percentage signal drift and highest RDC, suggesting greater signal stability. These results indicate that Looping Star is not especially susceptible to gradient imperfections in the phantom, given that the 32 spokes per loop acquisition provided good temporal stability in comparison with the 8 spokes per loop acquisition. Future studies should consider the required tSNR (and hence the necessary echo times) when deciding on the number of spokes per loop to use.

6.7 Comparing the Temporal Stabilities of Looping Star and GRE-EPI

6.7.1 Background

Evaluating the stability of Looping Star relative to GRE-EPI is important since GRE-EPI is the conventional technique used for functional MRI. Single and multi-echo GRE-EPI acquisitions were therefore compared with single-echo Looping Star of similar echo times. It was expected that since Looping Star involves very low flip angles, the tSNR would be lower.

6.7.2 Methods

The data was collected from a spherical phantom on the 3 T scanner at the Centre for Neuroimaging Sciences (Section 5.2 and Section 5.7.1). Table 6.11 describes the acquisition parameters employed for GRE-EPI, as well as the parameters of Looping Star acquisition. The acquisitions were collected on the same day in the same session.

The TE and TR were as closely matched between techniques as possible, given the technical implications of Looping Star that limit the flexibility of these timing parameters (Section 3.2, therefore only the second echo of the multi-echo GRE-EPI dataset was used.

The temporal stability measures are described in Section 5.7.1. The first four volumes were neglected in the Looping Star analysis, supported by the calculations in Section 3.5. The first four volumes from the single-echo GRE-EPI acquisition were also removed for consistency.

Table 6.11: Acquisition parameters of Looping Star and single and multi-echo GRE-EPI sequences, each collecting 100 volumes

Acquisition parameters for each modality
Single-echo GRE-EPI: ±250 kHz BW [1], slice thickness = 3 mm, number of slices = 39, slice gap = 0.3 mm, TR = 2 s, TE = 30 ms, FA = 75°, FOV = 21 cm, DDAs = 0
Multi-echo GRE-EPI: ±250 kHz BW [1], slice thickness = 3 mm, number of slices = 32, 1 mm slice gap, TR = 2.5 s, TE = 12 ms, 28 ms, 44 ms, 60 ms, FA = 80°, FOV = 21 cm, DDAs = 4
Looping Star: FID + echo, ±31.25 kHz BW, 32 spl, GSF 14, TR = 2.07 s, TE = 26.9 ms, FOV = 19.2 cm, isotropic voxel size = 3 mm, spokes per volume = 1024, FA = 2°

6.7.3 Results

The GRE-EPI results for both single and multi-echo acquisitions, as well as the Looping Star result, are shown in Table 6.12. Single echo GRE-EPI and the second echo of multi-echo GRE-EPI had higher SNR and tSNR than Looping Star. Looping Star had a shorter RDC and higher percentage signal fluctuation, though lower percentage signal drift.

[1] Ramp sampling used

Table 6.12: Temporal stability analysis of single echo and multi-echo GRE-EPI acquisitions and Looping Star of comparable echo time in 15 x 15 pixel ROI.

Acquisition	SNR	tSNR	PSF (%)	PSD (%)	RDC
EPI	168.62	155.54	0.087	-0.28	7.13
MEPI GRE2	131.55	143.38	0.070	-0.29	10.07
Looping Star GRE	128.28	115.42	0.125	-0.03	6.67

Figure 6.13 shows that, as expected, single-echo (SE) GRE-EPI and ME GRE-EPI have higher tSNR compared with Looping Star, although the ME GRE-EPI and Looping Star acquisitions had similar levels of SSN. The Looping Star images are not cropped compared with the GRE-EPI datasets. Additionally, the measured Weisskoff curves and frequency spectra were comparable across acquisitions.

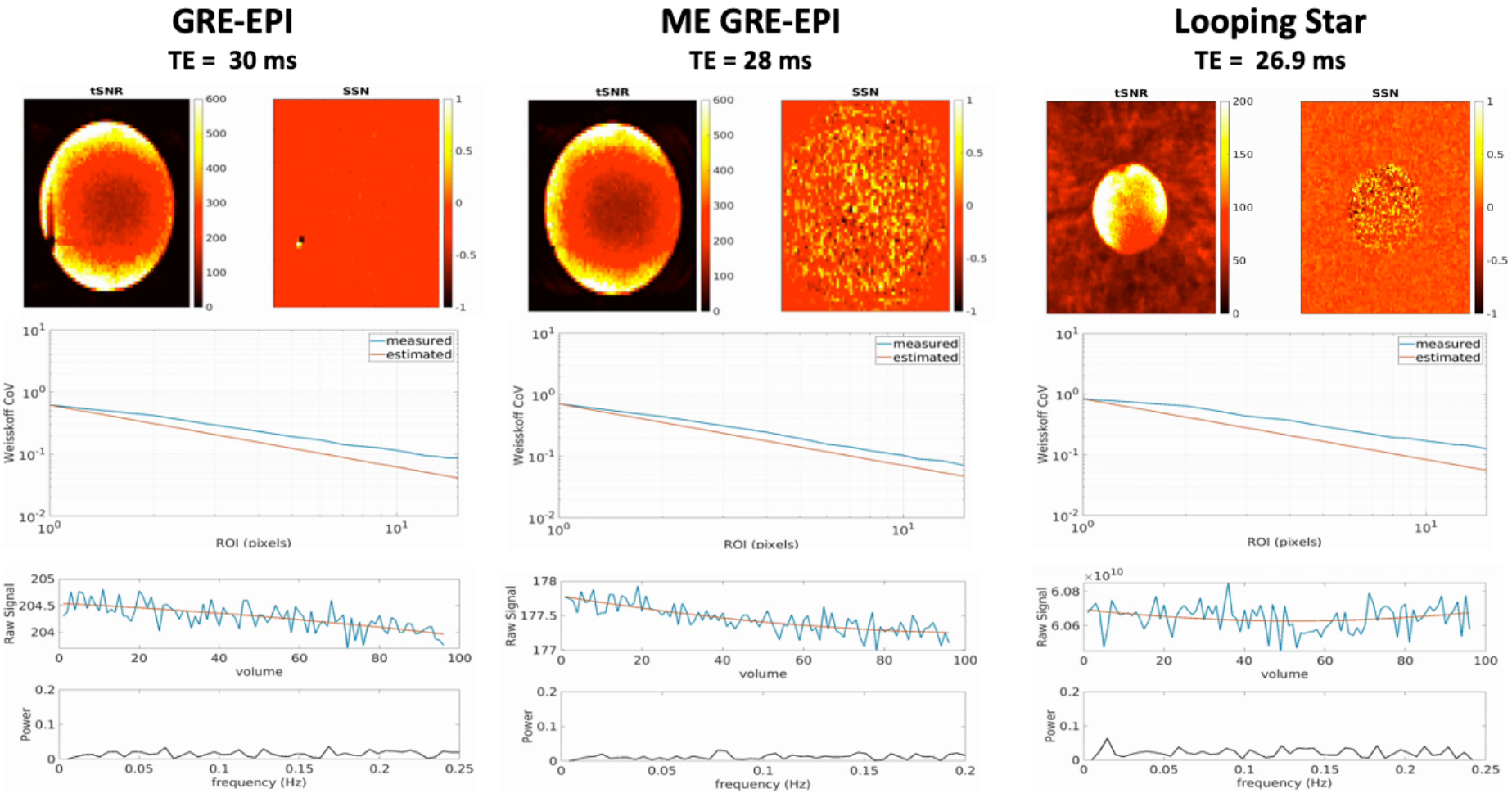

Figure 6.13: GRE-EPI, ME GRE-EPI and Looping Star stability measures. (top) tSNR and SSN, (middle) Weisskoff analysis, (bottom) frequency profile and raw signal in 15 x 15 pixel ROI

The relationship between tSNR and SNR between modalities for the range of acquisition parameters presented in this chapter (all echoes of Looping Star echoes, GRE-EPI and ME GRE-EPI) was also evaluated to ensure that the same relationship holds between modalities. This was found to be the case, as seen in Figure 6.14.

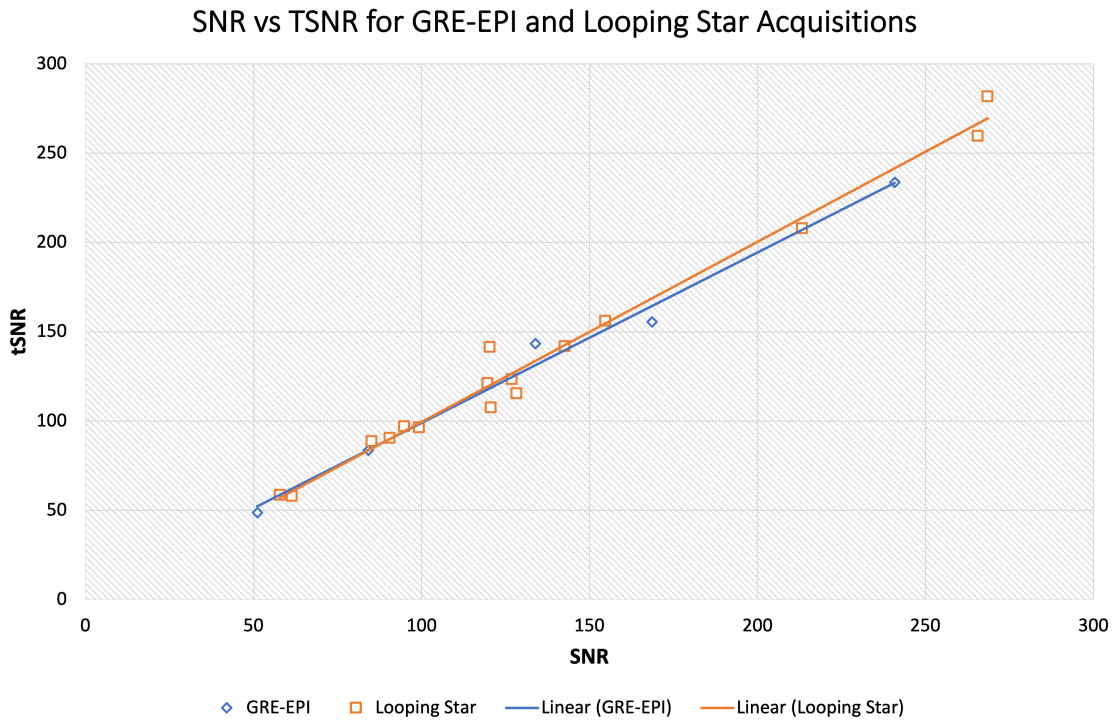

Figure 6.14: tSNR versus SNR for all Looping Star and GRE-EPI acquisitions in this chapter, with best fit line

6.7.4 Discussion

The temporal signal characteristics of Looping Star and the GRE-EPI datasets are similar, with little oscillation or impact of fluctuation and drift. However, the tSNR and SNR in the ROI are lower in Looping Star, likely due to the low flip angles used. For both datasets, minima were found in the tSNR that appeared to be linked to lower mean signal in these regions. This could indicate inhomogeneities in the spherical phantom, that produce different apparent spatial characteristics in each modality.

The higher SSN of Looping Star and ME GRE-EPI indicates that there are differences between odd and even volumes that are absent in single-echo GRE-EPI, which could

suggest higher sensitivity of these modalities to scanner instabilities. On the other hand, no highly-powered frequency oscillations were seen for any modality. These results can be used in conjunction with the acoustic noise measures to determine the optimal acquisition for the paradigm of interest.

6.8 Chapter Discussion

To summarise, this chapter sought to characterise the signal produced from Looping Star acquisitions in the context of a phantom i.e. in the absence of physiological noise. Understanding the temporal signal noise characteristics in a phantom is key for identifying requirements for pre- and post-processing to maximise the functional sensitivity of fMRI data. This may also affect the paradigm design employed, particularly when determining a compromise between tSNR and temporal resolution (Friman et al., 2004). The results were also compared with those of GRE-EPI and the acoustic noise properties of Looping Star were investigated. Together, the acoustic noise and temporal stability measures can be used to determine the optimal acquisition parameters for future studies.

The acoustic noise results indicated that lower readout bandwidths in combination with any method of reducing the distance between gradient steps (i.e. higher gradient smoothing factor or higher number of spokes per loop) would produce quieter acquisitions. Different readout bandwidths and number of spokes per loop, however, also affect the tSNR and temporal stability. Higher flip angles, longer readout bandwidths and lower spokes per loop shorten the echo time, which inherently boosts the tSNR. On the other hand, a higher number of spokes per loop and shorter readout bandwidths reduce the temporal instability. The differences between employed acquisition parameters were marginal, but are vital for future studies to consider depending on their priorities of tSNR, signal variance, acoustic noise and echo time.

It was found that the range of Looping Star acquisition parameters employed produced reliable temporal signal stability compared with single and multi-echo GRE-EPI, though

generally lower tSNR and SNR for the same echo time. The lower tSNR of Looping Star can largely be explained by the low flip angles employed by Looping Star. Although Looping Star did not demonstrate high signal fluctuation in the ROI, neither via the PSD, PSF nor temporal standard deviation, it was seen that Looping Star and ME GRE-EPI generally had higher SSN than single-echo GRE-EPI, which could indicate higher sensitivity to scanner instabilities.

Ultimately, Looping Star demonstrated good temporal stability both across parameters and in comparison with GRE-EPI. The acquisition method chosen for a study will depend on the importance of particular acquisition timing, tSNR and acoustic noise levels. To further support the use of Looping Star, the next chapter will demonstrate its functional sensitivity in vivo.

Chapter 7

In vivo Characterisation of Looping Star: Sensory Task Stimuli

Summary

In this chapter:

- Single and multi-echo Looping Star are characterised in vivo using a visual and an auditory blocked-design paradigm.
- Comparisons of power, percentage signal change and task-related functional correlations for both paradigms are computed.
- The impact of spatial smoothing and temporal autocorrelation correction functions is evaluated for Looping Star to identify whether alternative pre-processing steps are required relative to GRE-EPI.
- The functional sensitivity of Looping Star is compared with GRE-EPI.

Overview

An evaluation of the Looping Star pulse sequence in vivo is presented, characterising its signal properties using conventional blocked-design sensory paradigms. Whether there are specific spatial smoothing thresholds or temporal autocorrelation correction functions required for Looping Star that may differ from those employed in conventional fMRI was also evaluated. The results from both single and multi-echo Looping Star acquisitions were compared with closely temporally matched GRE-EPI acquisitions in small cohorts.

7.1 Chapter Introduction

Although phantom investigations are important for understanding non-physiological (i.e. scanner and pulse sequence-dependent) signal characteristics and artefacts, in vivo characterisation is essential. This is since the brain consists of tissues with distinct magnetic properties that can dramatically impact the sensitivity to the BOLD contrast (Hutton et al., 2002; Schwarzbauer and Porter, 2010). Understanding the complex effects of different tissues, resolving different structures, and obtaining functional sensitivity measures can provide insight into the practical capabilities of novel fMRI pulse sequences.

As previously shown, Looping Star produces good temporal stability alongside the reduced acoustic noise relative to GRE-EPI (Section 6.8). Computing the tSNR is helpful for in vivo studies, though characterising the sensitivity to the BOLD response is the most important evaluation of an fMRI pulse sequence in vivo. One primary measure of functional sensitivity is the percentage signal change (PSC) when presenting a stimulus during the fMRI paradigm. The methodology to derive this measurement is described in depth in Section 5.7.2. Investigating the fMRI time series can also be useful for evaluating the MR signal correlation with the task (Bandettini et al., 1993), as well as identifying temporally correlated brain regions as discussed in Section 8.1.

Functional sensitivity is not only dependent on the signal detected by the pulse sequence, but also on the pre-processing and analysis steps employed (Botvinik-Nezer et al., 2020; Bowring et al., 2019). Novel pulse sequences may require alternative pre-processing and analysis steps based on their signal characteristics, particularly given that most pipelines are designed for 2D EPI-based imaging and therefore may not generalise across acquisition methods. Exploring the impact of aspects of the pre-processing pipeline can therefore reveal further information on the signal characteristics of a pulse sequence. The following studies are particularly interested in characterising the presence of any inherent spatial smoothing of Looping Star, as well as its temporal autocorrelation characteristics, as these factors in the pre-processing and analysis pipeline affect functional sensitivity (Arbabshirani et al., 2014; Chen and Calhoun, 2018; Liu et al., 2017a; Molloy et al.,

2014; Olszowy et al., 2019; Pajula and Tohka, 2014).

In this chapter, the aforementioned pre-processing steps were investigated as well as the signal properties of both single and multi-echo Looping Star in the context of a simple visual checkerboard blocked-design paradigm and an auditory speech-processing blocked-design paradigm. The core signal characteristics were evaluated using the temporal signal-to-noise ratio, percentage signal change and time series correlations with the tasks employed. The data used for this chapter was collected using a 3 T MR750 GE Healthcare scanner based at the Centre for Neuroimaging Sciences (Section 5.2).

7.2 Visual Checkerboard blocked-design Paradigm

7.2.1 Task-related Signal Correlation of Looping Star

7.2.1.1 Background

A block-periodic, visual checkerboard paradigm is one of the most commonly used for signal characterisation in vivo, as the visual response is robust across participants and through the scan duration (DeYoe et al., 1994; Di and Biswal, 2017). In this study, the visual checkerboard paradigm was used to investigate the functional sensitivity of single-echo Looping Star relative to single-echo GRE-EPI. A standard pre-processing pipeline and GLM analysis was used and the resultant statistical maps were compared. This was followed by visual inspection of the extracted time series to evaluate the temporal correlation of the MR signal with the task. Part of this data was presented at the British and Irish Chapter of International Society for Magnetic Resonance in Medicine (ISMRM) Annual Meeting 2018 (Damestani et al., 2018).

7.2.1.2 Methods

Eight healthy participants (3 female; 1 left-handed) volunteered for the study, and were scanned using a 32-channel receive-only head coil (Section 5.2). Participants performed a visual paradigm involving an 8 Hz checkerboard (Figure 7.1) alternating with a fixation cross, encompassing the entire field of view of the screen via the mirror setup (Section 5.3). The visual checkerboard duration was 40 seconds and the rest duration was 32 seconds.

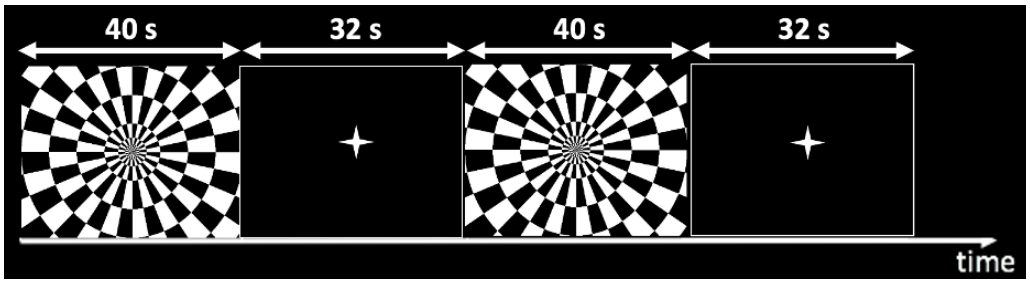

Figure 7.1: Visual checkerboard paradigm

The echo times acquired were matched between GRE-EPI and Looping Star as closely as was practically possible given the differences in the pulse sequence (see Section 3.2). The acquisition parameters for single-echo Looping Star were: spokes per loop = 32, FA = 1°, TR = 2410 ms, TE = 0 ms, 30.4 ms, 225 volumes, matrix size = 64 x 64 x 64, FOV = 19.2 cm, readout bandwidth ±31.25 kHz, GSF = 14, scan time 7 mins 49s.

The single-echo GRE-EPI acquisition was collected with the following parameters: FA = 75°, TR = 2000 ms, TE = 30 ms, 180 volumes, slice thickness = 3 mm, slice gap = 0.3 mm, matrix size = 64 x 64 x 38, FOV = 21.1 cm, scan time 6 mins. A 1.055 mm in-plane resolution IR-SPGR acquisition was also acquired, with TE = 3.016 ms, TR = 7.312 ms, TI = 400 ms, number of slices = 196, slice-gap = 1.2 mm, flip-angle = 11°, FOV = 27 cm.

The acoustic noise level was measured as described in Section 5.5 with the microphone placed at the centre of the scanner bore. The duration of recording was approximately 40 seconds.

The datasets were reconstructed separately (Section 5.2). The scanning order was single-echo Looping Star followed by single-echo GRE-EPI for all participants due to practical implementation requirements. Only the echo images for Looping Star were used for pre-processing and analysis. The final volumes of the Looping Star data were removed to equate the number of volumes between acquisitions at 170 volumes, to limit bias in the statistical power.

The first ten volumes were removed from GRE-EPI and Looping Star to allow the longitudinal component of the magnetisation to reach steady-state. Pre-processing in SPM-12 (FIL Methods Group, 2020) included bias field correction and segmentation of the T_1-weighted image, slice timing correction only for the GRE-EPI data, realignment, co-registration to the T_1-weighted image, spatial normalisation to MNI space with images saved at 2 mm isotropic resolution, and 8 mm FWHM smoothing. The tSNR was computed for the spatially normalised volumes of each participant after second-order polynomial de-trending of the signal in each voxel (Friedman and Glover, 2006), then averaged across participants.

The first level GLM included motion regressors and the visual onsets; the rest blocks were not modelled to avoid over-parametrisation (Pernet, 2014). A 128 s high-pass filter to reduce the presence of low frequency drift was included, and the standard canonical double-gamma haemodynamic response function was used. The autocorrelation AR(1) model was also used for Restricted Maximum Likelihood (ReML) parameter estimation (Poldrack et al., 2011). Cluster-level inference using a primary uncorrected cluster-forming threshold of $p < 0.001$ (Woo et al., 2014; Worsley et al., 1996) was employed at group level. Only clusters surviving family-wise error (FWE) correction at the cluster-level (i.e. $p_{FWE_c} < 0.05$) were deemed significant.

A spherical ROI of 10 mm radius was created for each participant in MarsBaR (Brett, 2016; Brett et al., 2002), centred on the voxel with the highest peak T-statistic, within the cluster with the highest significance (i.e. $p_{FWE_c} < 0.05$) for Looping Star. This ROI defined for Looping Star was also applied to GRE-EPI as different spatial localisation of peak T-statistics was identified between modalities (see Results; Figure 7.3, bottom),

which affected the comparison. A direct comparison of the functional sensitivity of the modalities was not computed using the percentage signal change as a result, though the normalised (i.e. scaling the signal to have a mean = 0 and standard deviation = 1) signal time series from the ROI for each modality and participant, after pre-processing, was plotted.

7.2.1.3 Results

The acoustic noise level (LA_{eq}) of Looping Star was 66.2 dB(A) compared with 106.8 dB(A) for GRE-EPI and 64.2 dB(A) for the ambient scan room noise. An example of raw Looping Star images in comparison with GRE-EPI can be seen in Figure 7.2, alongside the average tSNR maps. Looping Star generally had lower tSNR than GRE-EPI, and some frontal lobe dropout was visible relative to GRE-EPI.

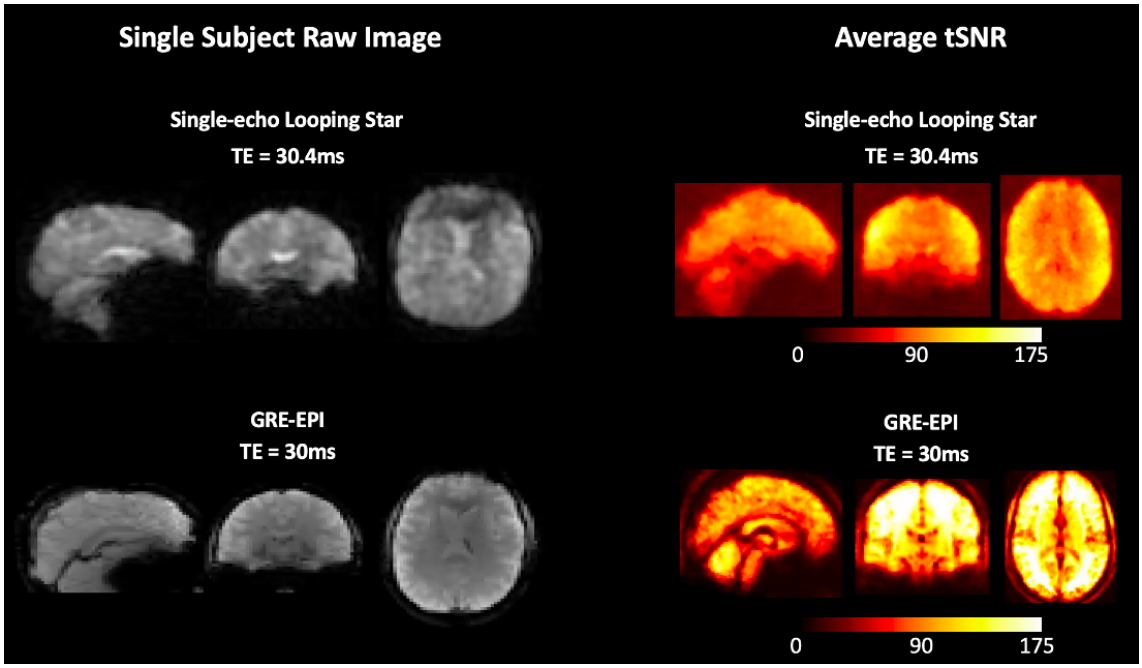

Figure 7.2: (left) Single subject raw image of each acquisition for equivalent echoes (right) Group averaged tSNR across spatially-normalised participant data. Images produced in FSL (Jenkinson et al., 2012).

The group level activity maps can be seen in Figure 7.3 (top), with accompanying statistics in Table 7.1. Both modalities presented statistically significant visual activity, although single-echo Looping Star had the largest cluster size and higher T-statistic.

Upon investigating the single-subject maps (Figure 7.3, bottom) it was found that the GRE-EPI acquisitions produced more spatially varied localisations, impacting the group level analysis given the small group size. Although there were statistically significant activations in the visual cortex for GRE-EPI single-subject maps, the peak T-statistic and most significant cluster occurred in regions such as the precuneus, which has been affiliated with episodic memory and visuospatial imagery (Cavanna and Trimble, 2006).

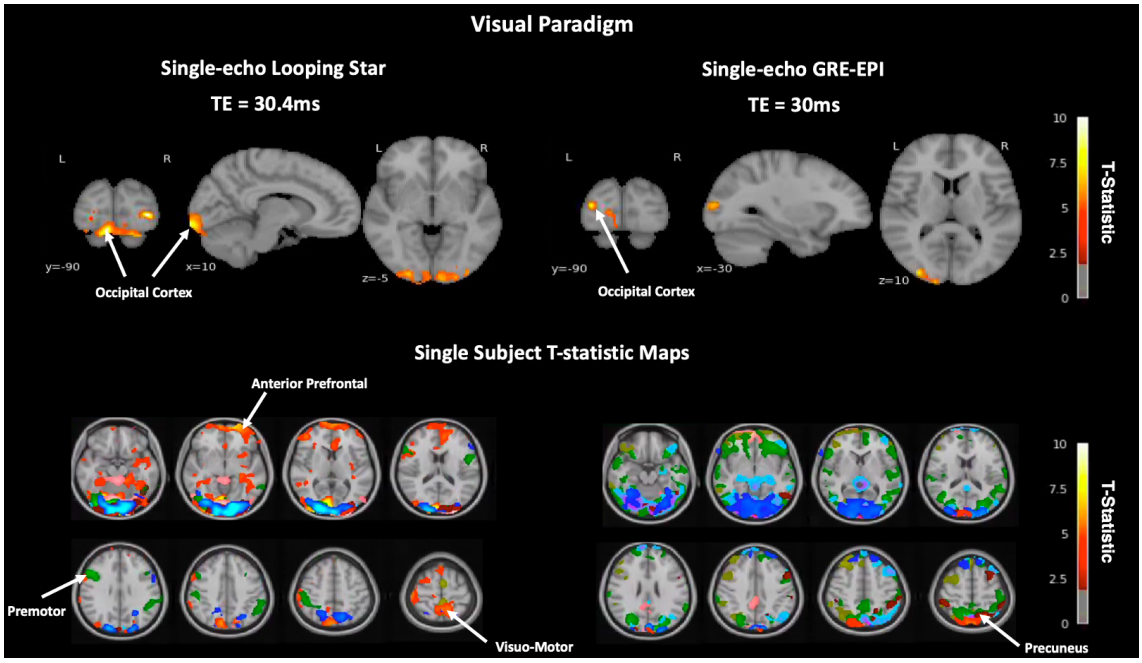

Figure 7.3: (top) Group level activity maps for Looping Star and GRE-EPI, with labelled T-statistic range. Images produced using NiLearn (The Nilearn developers, 2021). (bottom) Overlaid single subject activity maps for Looping Star and GRE-EPI in FSL (Jenkinson et al., 2012), with T-statistic range for all images in distinct colours. For both, images were thresholded for statistical significance using the appropriate cluster-extent threshold, and presented visually at threshold T-statistic = 2. Arrows indicate affiliated regions determined by Neurosynth (Yarkoni, 2011) and BioImage Suite Web (BioImage Suite Web, 2021).

Table 7.1: Cluster-level statistical results for group level activity during visual checkerboard paradigm for each modality. Brodmann areas defiined using BioImage Suite Web (BioImage Suite Web, 2021).

Acquisition	**Peak MNI coordinates (x,y,z mm)**	**Brodmann Area**	**Peak-level T-statistics**	**Cluster-level p_{FWE}**	**Cluster Size**
Single-echo Looping Star	32 -92 0	18 (R)	15.30	$< 10^{-3}$ **	2007
Single-echo GRE-EPI	26 -60 -24	N/A	8.88	0.028 *	211
	-32 -90 10	18 (L)	7.61	0.002 **	372

* = cluster-level p(FWE) < 0.05, ** = cluster-level p(FWE) < 0.001, N/A = outside of defined Brodmann Areas

Figure 7.4 highlights the extracted normalised signal time series from the defined 10 mm radius spherical ROI for each participant. As mentioned previously, the ROI was derived from the most significant Looping Star cluster given the apparent varied spatial localisation of GRE-EPI across participants. Both techniques demonstrated clear task-related correlations in the visual cortex. The percentage signal change was not computed to avoid bias, given the ROI was derived from Looping Star.

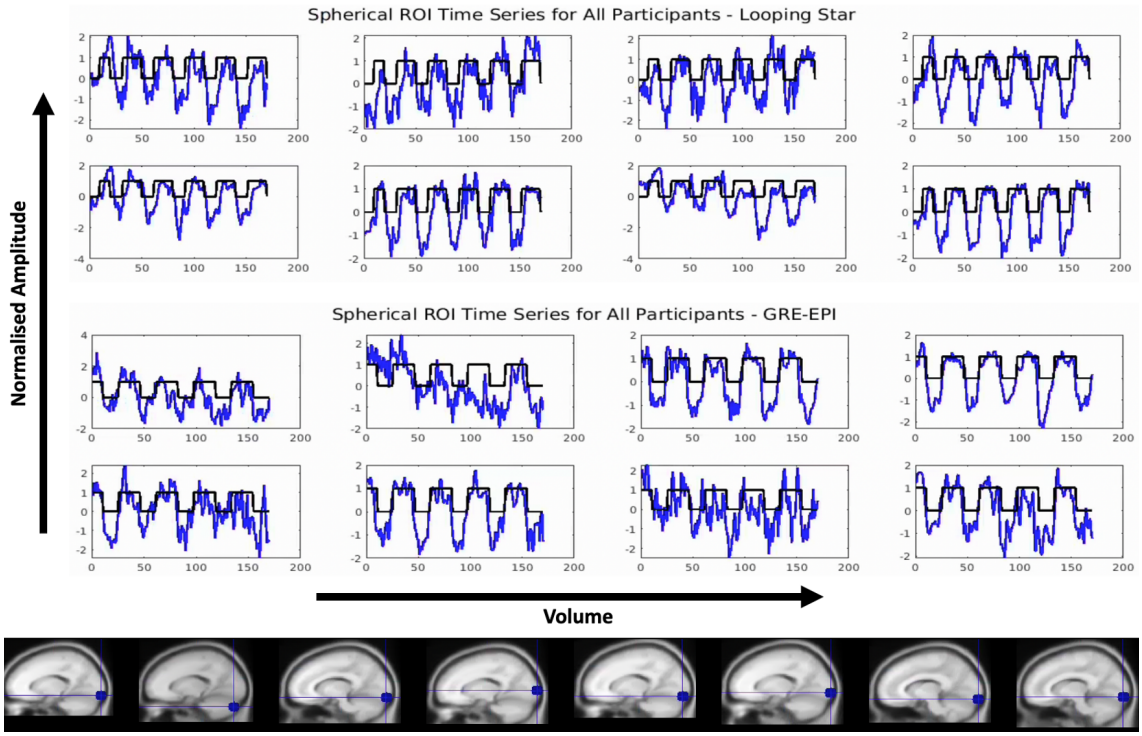

Figure 7.4: Extracted normalised signal time series from 10 mm radius spherical Looping Star ROI for each participant (blue) with task onsets (black). (top) Looping Star acquisitions and (bottom) GRE-EPI acquisitions. Looping Star ROIs shown at bottom of figure. Time series extraction and ROI display using MarsBaR (Brett, 2016; Brett et al., 2002).

7.2.1.4 Discussion

The results indicate that Looping Star produces good sensitivity to the BOLD response compared with GRE-EPI, evidenced by the temporal correlations of the MR signal with task onsets in the ROI within the visual cortex. Both modalities also produced statistically significant functional activity in the visual cortex. This is despite the lower tSNR of Looping Star, which is likely driven by the low flip angles included in the sequence.

Interestingly, both modalities at single-subject level presented significant activations outside the visual cortex, with GRE-EPI in particular demonstrating multiple subjects with significant activity in the precuneus. This could explain the smaller significant visual cluster identified at group level for GRE-EPI, and could be linked to an interaction effect with the acoustic noise as the precuneus has demonstrated higher BOLD responses during continuous sound fMRI (Haller et al., 2005). The practical limitations present in this study were addressed to better explore and directly compare the functional sensitivity

between modalities in Section 7.3.

7.2.2 Impact of Smoothing and Temporal Autocorrelation on Looping Star

7.2.2.1 Background

It has been demonstrated that a standard pre-processing pipeline in SPM-12 (FIL Methods Group, 2020) can be used with single-echo Looping Star data (Section 7.2), producing clear sensitivity to the BOLD response to the visual checkerboard paradigm. Previous studies have shown that the different steps in the pre-processing and analysis pipeline can affect the functional sensitivity detected in conventional fMRI (Botvinik-Nezer et al., 2020; Bowring et al., 2019). As Looping Star has different spatial characteristics driven by 3D radial sampling of non-constant density in k-space, it was expected that functional sensitivity may differ with distinct spatial smoothing thresholds in a unique manner relative to GRE-EPI.

Looping Star may also present different temporal characteristics and therefore distinct autocorrelation behaviour. Autocorrelation can be a product of non-neuronal noise sources, leading to the power spectrum of the fMRI signal having disproportionate power at low frequencies (Aguirre et al., 1997; Bullmore et al., 2001; Woolrich et al., 2001) and varying noise structure across brain regions (Zarahn et al., 1997). To avoid bias in the general linear model estimates, this autocorrelation must be removed from the data (Poldrack et al., 2011).

Autocorrelation is addressed by fitting the GLM to the data at each voxel to produce the residuals, and using these residuals to estimate the autocorrelation structure. Using this estimate of the autocorrelation structure, the data and design matrix implemented are then "pre-whitened", counter-balancing the variance and its structured noise with a known white noise source. The residuals are used to avoid affecting the task-related

signal (Poldrack et al., 2011)

However, the accuracy of autocorrelation correction depends on the correctness of the model. Two models are explored in this thesis: the auto-regressive, or AR(1), model, which assumes the variance of each time point is equal to one and that the correlation between data samples are spatially dependent and also incorporates white noise (Arbabshirani et al., 2014; Poldrack et al., 2011; Worsley et al., 2002), and the FAST algorithm, which involves a more complex dictionary of basis sets to estimate the serial correlations Bollmann et al. (2018); Corbin et al. (2018), both of which are implemented in SPM-12 (FIL Methods Group, 2020).

To evaluate the spatial characteristics of Looping Star, its functional sensitivity was explored at different smoothing thresholds in comparison with GRE-EPI. The impact of the autocorrelation functions was then assessed at each smoothing threshold. The power spectra of the residuals across participants after pre-whitening was also explored. Supposing that there are no differences in the group level results produced using the two autocorrelation models for both Looping Star and GRE-EPI, and similar power spectra for the residuals are seen, it can be deduced that the temporal autocorrelation structure of Looping Star can be well explained by both models typically used for GRE-EPI, suggesting similar temporal correlation behaviour.

7.2.2.2 Methods

The same Looping Star and GRE-EPI datasets were employed from Section 7.2. Standard SPM-12 (FIL Methods Group, 2020) pre-processing including bias field correction and segmentation of the T_1-weighted image, slice-timing correction for GRE-EPI, realignment, co-registration to the T_1 and spatial normalisation to MNI space with images saved at 2 mm isotropic resolution. The group level activity maps were calculated after no smoothing, 4 mm and 8 mm FWHM spatial smoothing for both modalities, with the first-level GLM including the motion regressors and visual onsets in the model as well as a 128 s high-pass filter and the standard canonical double-gamma haemodynamic

response function.

The FAST and AR(1) autocorrelation methods for ReML parameter estimation were explored at each smoothing level for both modalities. Cluster-level inference using a primary uncorrected cluster-forming threshold of $p < 0.001$ (Woo et al., 2014; Worsley et al., 1996) was employed. Only clusters surviving family-wise error correction at the cluster-level (i.e., $p_{FWE_c} < 0.05$) were deemed significant. The residuals after model estimation in the first level GLM were extracted for each participant, and its power spectrum was computed on average across the whole brain. The average power spectra across participants was then computed using the square of the discrete Fourier transform, whereby the time series of the residuals were normalised (i.e. variance = 1) to facilitate group level inference. These power spectra were produced using MATLAB scripts adapted from those provided by Olszowy et al. (2019).

The correlation scatter and Bland-Altman (Altman and Bland, 1983; Bland and Altman, 1999) plots were plotted to compare the group level T-maps produced between autocorrelation functions at each smoothing threshold for Looping Star and GRE-EPI. Bland-Altman analysis can be used to evaluate the correlation of results between two methods, assuming the same result should arise from both techniques (Altman and Bland, 1983; Giavarina, 2015). Explicitly, the absolute difference between the T-maps ($Diff_{BA}$) and their combined and averaged mean ($Mean_{BA}$) are computed and plotted against one another (Equations (7.1) - (7.2)).

$$Diff_{BA} = T_{FAST} - T_{AR(1)} \tag{7.1}$$

$$Mean_{BA} = \frac{T_{FAST} + T_{AR(1)}}{2} \tag{7.2}$$

Where T_{FAST} and $T_{AR(1)}$ are the group level T-maps for each respective autocorrelation correction function. To avoid skewing towards low T-statistics, only the group level

T-maps thresholded at the appropriate cluster-extent threshold for statistical significance were compared. Zero values (originating outside the brain) were removed to avoid biasing the result towards a zero mean.

The differences between the group level T-maps were tested using the Kolmogorov-Smirnov test and for 4 mm and 8 mm smoothing level; hence non-parametric Bland-Altman analysis was used (Klein, 2021). As the range of differences between T-maps was deemed non-Gaussian, the reproducibility coefficient was also computed based on the interquartile range of the differences (1.45 $\times$ IQR) rather than the standard deviation, to compare with the computed limit of agreement (1.96 $\times$ standard deviation of the differences) (Klein, 2021). The limits of agreement (LOA) are also given as a percentage (Equation (7.3))

$$LOA(\%) = 1.96 \times \sigma(\frac{Diff_{BA}}{Mean_{BA}}) \times 100 \tag{7.3}$$

where σ is the standard deviation for the fraction of the difference and the mean computations in Equations (7.1) - (7.2). The skewness of the differences and their coefficient of variation (Equation (7.4)) were also calculated. For the 0 mm smoothing level dataset, parametric statistics were used as the differences were Gaussian.

$$CV(\%) = \frac{\sigma(Diff_{BA})}{Mean_{BA}} \times 100 \tag{7.4}$$

7.2.2.3 Results

Figure 7.5 demonstrates the impact of different spatial smoothing levels for single-echo Looping Star with autocorrelation correction using the AR(1) function or FAST method. The GRE-EPI results are not shown as only the 8 mm smoothed dataset, shown in Section 7.2, produced statistically significant results. The accompanying group level statistics are

shown in Table 7.2. Group level significant activity was seen for all smoothing thresholds with Looping Star. For the FAST autocorrelation function the same effect was seen, where Looping Star produced significant activity at all smoothing thresholds whereas GRE-EPI only demonstrated significant visual activity with 8 mm smoothing, with accompanying statistics table shown in Table 7.3.

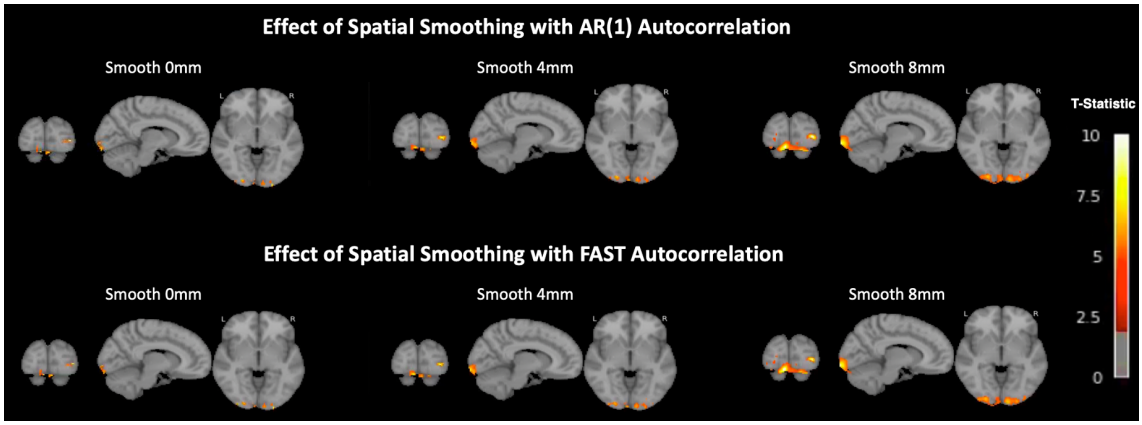

Figure 7.5: Group level activity maps for different smoothing thresholds for the autocorrelation functions AR(1) (top) and FAST (bottom) for single-echo Looping Star. GRE-EPI only demonstrated significant activity at 8 mm smoothing, producing the same result for both autocorrelation methods as seen in Section 7.2. Images produced using NiLearn (The Nilearn developers, 2021). Each image was thresholded at the appropriate cluster extent for significance, and each image is displayed at T-statistic threshold T = 2.

Table 7.2: Cluster-level statistical results for group level activity during visual checkerboard paradigm at each smoothing threshold using AR(1) autocorrelation correction.

Acquisition	**Peak MNI coordinates (x,y,z mm)**	**Brodmann Area**	**Peak-level T-statistics**	**Cluster-level p_{FWE}-value**	**Cluster Size**
Single-echo Looping Star, Smooth 0mm, AR(1)	2 -94 -20	N/A	14.88	$< 10^{-3}$ **	272
Single-echo Looping Star, Smooth 4mm, AR(1)	30 -94 6	18 (R)	15.16	$< 10^{-3}$ **	636
Single-echo Looping Star, Smooth 8mm, AR(1)	32 -92 0	18 (R)	15.30	$< 10^{-3}$ **	2007
Single-echo GRE-EPI, Smooth 0mm, AR(1)	48 20 48	N/A	10.67	0.528	8
Single-echo GRE-EPI, Smooth 4mm, AR(1)	-24 -34 -10	36 (L)	13.09	0.972	11
Single-echo GRE-EPI, Smooth 8mm, AR(1)	26 -60 -24	N/A	8.88	0.028 *	212

* = cluster-level p(FWE) < 0.05, ** = cluster-level p(FWE) < 0.001, N/A = outside of defined Brodmann Areas

Table 7.3: Cluster-level statistical results for group level activity during visual checkerboard paradigm at each smoothing threshold using FAST autocorrelation correction.

Acquisition	**Peak MNI coordinates (x,y,z mm)**	**Brodmann Area**	**Peak-level T-statistics**	**Cluster-level p_{FWE}-value**	**Cluster Size**
Single-echo Looping Star, Smooth 0mm, FAST	2 -94 -20	N/A	14.61	$< 10^{-3}$ **	277
Single-echo Looping Star, Smooth 4mm, FAST	30 -94 4	18 (R)	15.07	$< 10^{-3}$ **	616
Single-echo Looping Star, Smooth 8mm, FAST	-10 -88 -20	N/A	13.76	$< 10^{-3}$ **	1935
Single-echo GRE-EPI, Smooth 0mm, FAST	48 20 48	N/A	10.67	0.528	8
Single-echo GRE-EPI, Smooth 4mm, FAST	-24 -34 -10	36 (L)	13.09	0.972	11
Single-echo GRE-EPI, Smooth 8mm, FAST	26 -60 -24	N/A	8.88	0.028 *	212

* = cluster-level p(FWE) < 0.05, ** = cluster-level p(FWE) < 0.001, N/A = outside of defined Brodmann Areas

The differences between autocorrelation functions for Looping Star were explored in more depth at each smoothing level using correlation scatter and Bland-Altman plots (Figures 7.6 - 7.8). Only GRE-EPI at 8 mm smoothing presented significant results; hence Bland-Altman analysis was only performed on this GRE-EPI dataset. No differences were found between the group level maps with different applied autocorrelation functions for the 8 mm smoothed GRE-EPI dataset. High Pearson correlation coefficients were found across Looping Star smoothing levels indicating good agreement between the T-maps.

The Bland-Altman plots demonstrated that the majority of the data fell within the limits of agreement for all Looping Star smoothing levels. The reproducibility coefficient decreased and the coefficient of variation increased with increasing smoothing levels. Given that the differences were clustered around zero, and using the range of Bland-Altman differences found between fMRI analysis software methods by Bowring et al. (2019), it was determined that these differences between autocorrelation functions are not substantial.

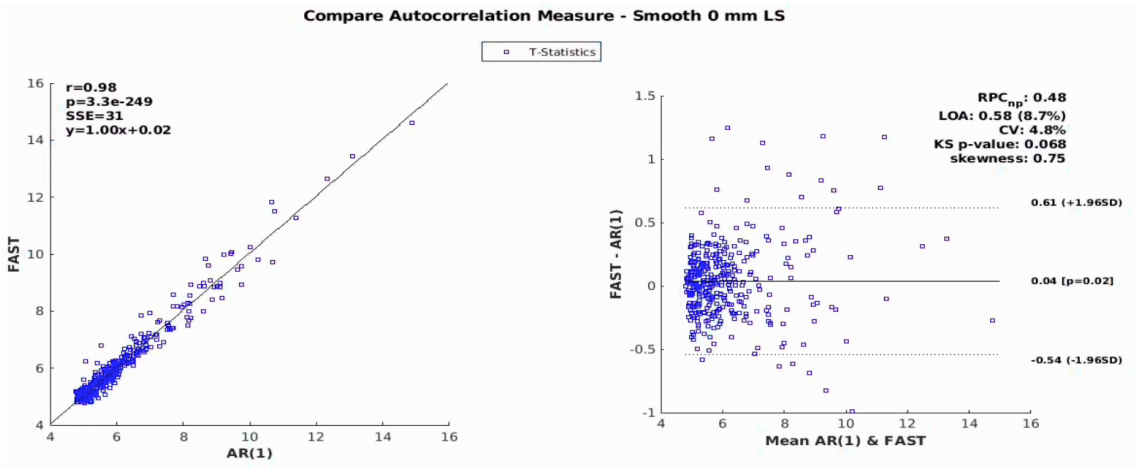

Figure 7.6: (left) Correlation scatter and (right) Bland-Altman plots comparing autocorrelation functions AR(1) and FAST for 0 mm FWHM smoothing. SSE = sum of squared error, r = Pearson correlation r-value, p = Pearson correlation p-value, RPC_{np} = non-parametric reproducibility coefficient, LOA (%) = limits of agreement, CV = coefficient of variation, KS p-value = Kolmogorov-Smirnov test p-value (Klein, 2021). The KS p-value indicated that the data is normally distributed.

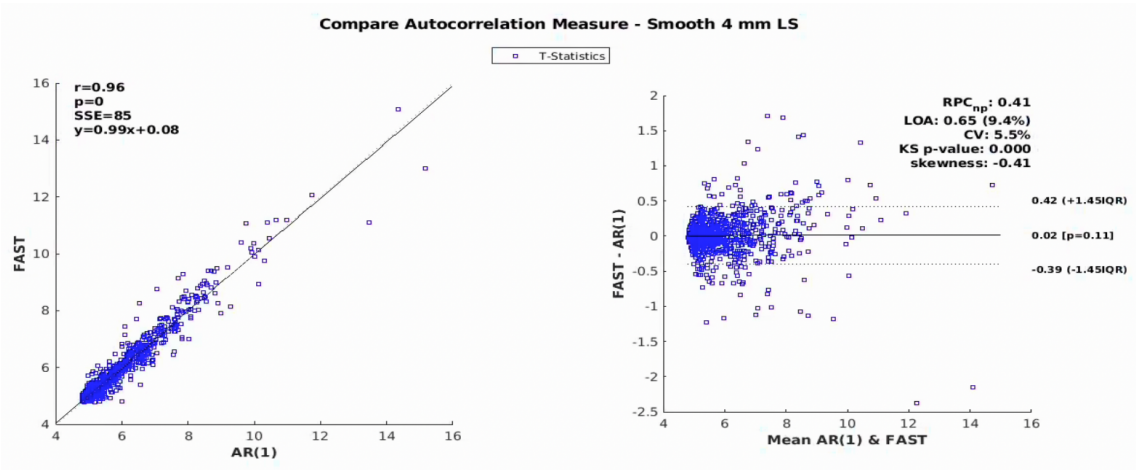

Figure 7.7: (left) Correlation scatter and (right) Bland-Altman plots comparing autocorrelation functions AR(1) and FAST for 4 mm FWHM smoothing. SSE = sum of squared error, r = Pearson correlation r-value, p = Pearson correlation p-value, RPC_{np} = non-parametric reproducibility coefficient, LOA (%) = limits of agreement, CV = coefficient of variation, KS p-value = Kolmogorov-Smirnov test p-value (Klein, 2021). The KS p-value indicated that the data is not normally distributed.

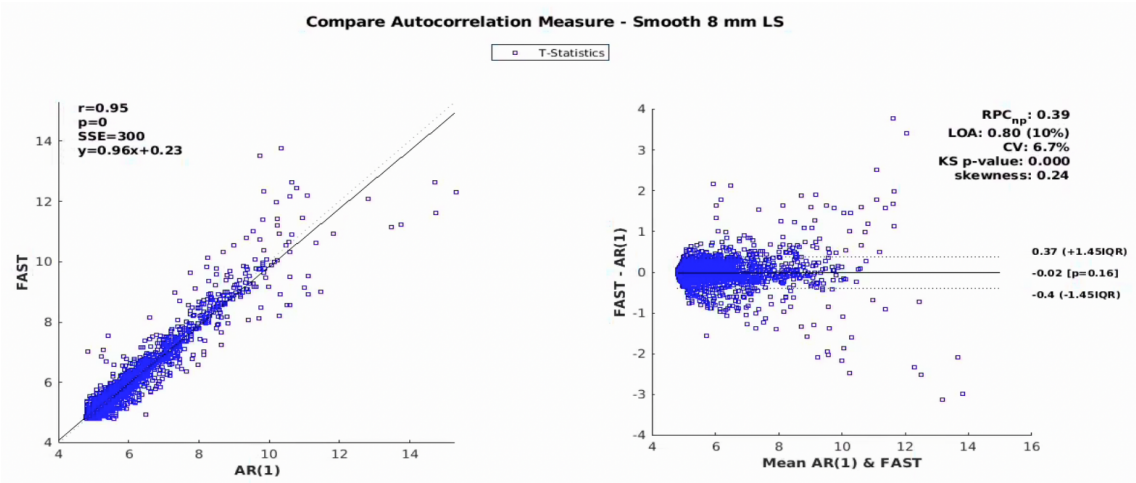

Figure 7.8: (left) Correlation scatter and (right) Bland-Altman plots comparing autocorrelation functions AR(1) and FAST for 8 mm FWHM smoothing. SSE = sum of squared error, r = Pearson correlation r-value, p = Pearson correlation p-value, RPC_{np} = non-parametric reproducibility coefficient, LOA (%) = limits of agreement, CV = coefficient of variation, KS p-value = Kolmogorov-Smirnov test p-value (Klein, 2021). The KS p-value indicated that the data is not normally distributed.

The average power spectra across the whole brain and all participants of the residuals after model estimation can be seen in Figure 7.9. This was only computed for the 8 mm smoothing levels of GRE-EPI and Looping Star as this was the only threshold at which GRE-EPI demonstrated significance. The expected pattern should be flat if all autocorrelation has been removed (Olszowy et al., 2019). It can be seen that Looping Star produced a flatter spectrum than GRE-EPI but both contained fluctuations, indicating that both would benefit from more accurate autocorrelation models.

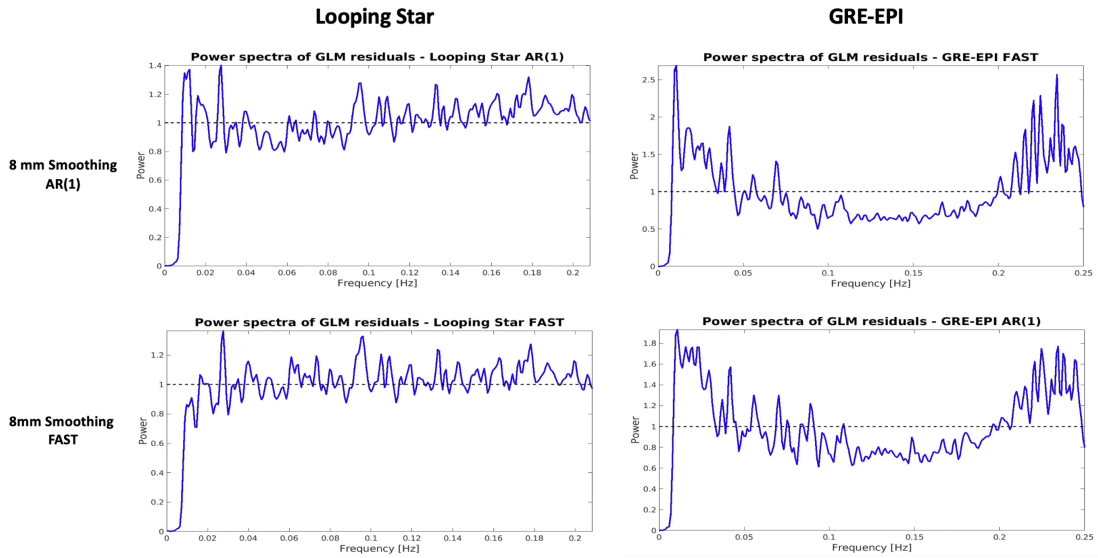

Figure 7.9: Power spectra (against frequency in Hz) of the residuals derived from the whole brain, averaged across participants of Looping Star and GRE-EPI for each autocorrelation function at 8 mm smoothing (Olszowy et al., 2019).

7.2.2.4 Discussion

Looping Star produces significant activity even in the absence of spatial smoothing in pre-processing, whereas GRE-EPI did not. This indicates that the Looping Star data is inherently smooth and therefore may already meet the requirements of random field theory (Nichols, 2012; Worsley et al., 1992). Kasper et al. (2014) showed that smoothing of 2D EPI data in k-space also improved the statistical sensitivity, supporting that inherent smoothing of Looping Star could be one of the mechanisms behind the functional sensitivity observed.

No differences were found between using the AR(1) or FAST autocorrelation models for the 8 mm smoothed GRE-EPI. However, for Looping Star, though the differences were small (based on the range of differences found in a previous study of conventional fMRI (Bowring et al., 2019)), differences were found between the T-maps produced using the two autocorrelation functions at all smoothing levels. The differences also increased for higher smoothing thresholds, indicated by the larger coefficient of variance and lower reproducibility coefficient with increasing smoothing. Furthermore, the FAST autocorrelation function produced smaller cluster sizes and lower T-statistics for all

smoothing thresholds relative to AR(1).

This could suggest that a more accurate autocorrelation model is required for Looping Star. On the other hand, neither Looping Star nor GRE-EPI produced completely pre-whitened data according to the average power spectra of the residuals. Future work should explore the autocorrelation functions used across analysis software to further characterise the temporal autocorrelation requirements of Looping Star.

7.2.3 Power Calculation for Visual Checkerboard

7.2.3.1 Background

Statistical power is defined as the probability of rejecting the null hypothesis when the alternative is true (Mumford, 2012). Power calculations can be helpful for determining the sample size required for a desired effect in future studies. Pilot data can be used to determine the power, using them as provision of a-priori knowledge. Most fMRI studies will aim for approximately 80 % power to allow for smaller sample sizes to be used for cost-efficiency (Mumford, 2012). This study provides a power calculation for GRE-EPI and Looping Star using the visual study presented in this chapter (Section 7.2). However, it must be acknowledged that power calculations are heavily dependent on the paradigm employed (Cremers et al., 2017).

7.2.3.2 Methods

A map of the effect size across voxels was calculated for each modality from the results of Section 7.2 by averaging the beta maps for the visual activation across subjects and dividing by their standard deviation across subjects (Geuter et al., 2018; Jackson et al., 2020). The effect size was then averaged across a 10 mm radius spherical ROI centred at x, y, z = 0, -86, 0 mm in MNI space. These coordinates were selected based on a

functional ROI derived from Neurosynth (Yarkoni, 2011), for a meta-analysis for the term "visual" thresholded at z-score = 7.92 (Figure 7.10). The average effect size from this ROI was then inputted into G*Power (Faul et al., 2007), for 8 subjects per modality using the post hoc power analysis for the difference between two dependent means (matched pairs) and an $\alpha = 0.05$.

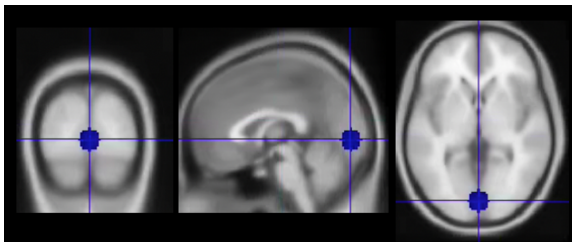

Figure 7.10: 10 mm spherical ROI employed in the visual cortex

7.2.3.3 Results

Figure 7.11 demonstrates the effect size map for both modalities. It can be seen that the spatial extent of higher effect sizes was larger for GRE-EPI than Looping Star.

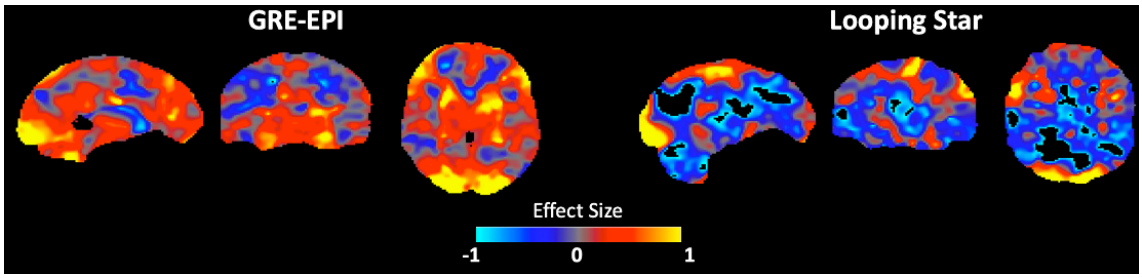

Figure 7.11: Effect size map for GRE-EPI and Looping Star in visual task

Table 7.4 shows the results of the effect size and power in the 10 mm spherical ROI centred on the visual cortex (Figure 7.10). Looping Star had lower power in the ROI, compared with GRE-EPI.

Table 7.4: Power calculation for eight subjects using average effect size from ROI for each modality, computed in G*Power (Faul et al., 2007).

Acquisition	Effect Size in ROI	Power in ROI (%)
Single-echo Looping Star	0.3666	23.9
Single-echo GRE-EPI	1.0901	86.9

7.2.3.4 Discussion

Looping Star produces lower statistical power in the chosen ROI than GRE-EPI for eight participants, which was expected given its lower tSNR. This suggests that to obtain comparable functional sensitivity to GRE-EPI, across either different conditions or different cohorts, more participants would be necessary for a study employing Looping Star. Future studies may benefit from these results for a-priori power calculations, although the sensitivity to the paradigm will also play a part given that this calculation originated from the beta parameters. Other methods of calculating power can also be explored in the future (Durnez et al., 2016; Joyce and Hayasaka, 2012; Ostwald et al., 2019).

7.3 Auditory Speech-processing Paradigm

7.3.1 Characterising the Functional Sensitivity of Looping Star

7.3.1.1 Background

Looping Star demonstrated sensitivity to significant functional activity during a visual paradigm, presenting clear temporal correlations to the task. To thoroughly validate its functional sensitivity, an auditory paradigm was employed and a direct comparison of the

percentage signal change of the BOLD response detected by Looping Star with that of GRE-EPI was computed. Auditory paradigms are crucial for evaluating any benefits of acoustic noise reduction for studying sound processing (see Section 2.4). This work was presented at the ISMRM Annual Meeting 2019 (Damestani et al., 2019b).

7.3.1.2 Methods

Eight healthy participants (two female; mean age = 35 ± 12 years; two left-handed; three native English speakers) were scanned whilst engaged in an auditory paradigm. English words were played through MR-compatible headphones during blocks of 24-second durations. The speed at which the words were played was different for each block (30, 60, 90 and 120 words per minute), and the order of the block was randomised (i.e. the speed did not steadily increase or decrease with consecutive blocks, but randomly changed). A fixation cross was displayed during the paradigm and participants were asked to keep their eyes open. Rest blocks of 24-second durations involved a fixation cross with no auditory stimulation (Figure 7.12). The paradigm set-up is described in Section 5.3.

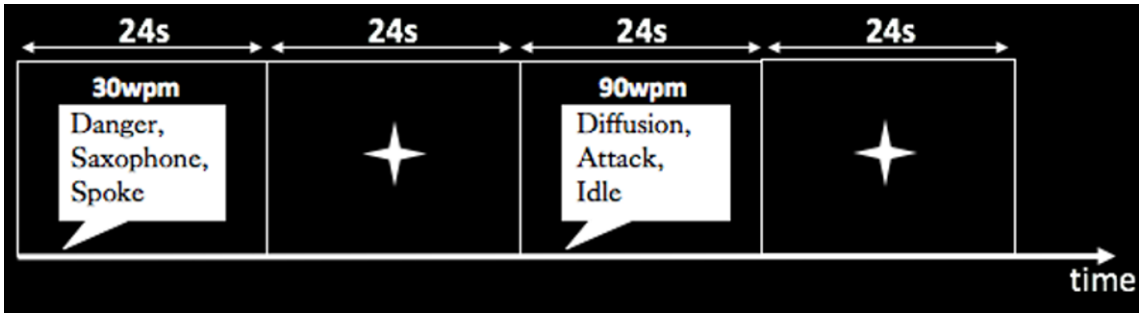

Figure 7.12: Auditory speech-processing paradigm, wpm = words per minute. The screen visually presented a fixation cross throughout the paradigm, the speech bubbles visualised here indicate the words being spoken.

The following acquisition parameters were used, closely matched between modalities given the practicalities of Looping Star (Section 3.2), using a 12-channel receive-only head coil (Section 5.2). Three echo GRE-EPI involved the parameters TE = 17 ms, 34 ms, 51 ms, TR = 2.1 s, 180 volumes, matrix size = 64 x 64 x 32, slice thickness = 3 mm, number of slices = 32, slice gap = 1 mm, FOV = 24 cm, FA = 80°.

FID + two echo Looping Star involved the parameters TE = 0 ms, 17.4 ms, 34.8 ms, TR = 1.87 s, number of volumes = 180, matrix size = 64 x 64 x 64, resolution = 3 mm, FOV = 19.2 cm, 32 spokes per echo, 96 spokes per segment, 960 spokes per volume, FA = 3°). The number of volumes was set to be equivalent between acquisitions, despite the different TRs. A structural IR-SPGR image was also acquired (TE = 3.016 ms, TR = 7.312 s, TI = 400 ms, matrix size = 256 x 256, in-plane resolution = 1.055 mm, 196 slices, FOV = 27 cm). Image reconstruction was performed as described in Section 5.2.

The acoustic noise level was measured as described in Section 5.5 for approximately one minute of scanning with each modality. To allow the longitudinal magnetisation component to reach the steady-state, the first ten volumes were removed from the Looping Star acquisition (see Section 3.5) and four volumes were removed from GRE-EPI. The acquisitions were randomised between participants to avoid bias from order effects.

A standard SPM-12 (FIL Methods Group, 2020) pipeline was used for single-echo pre-processing, including slice-timing correction for GRE-EPI, segmentation and bias field correction of the T_1-weighted image, realignment, co-registration with the T_1 image, spatial normalisation to MNI space with images saved at 2 mm spatial resolution, and smoothing with an 8 mm FWHM kernel.

For optimal echo combination, high frequency artefacts were removed (i.e. despiking). Optimal echo combination was performed after the realignment step for each echo within the multi-echo independent component analysis (ME-ICA) toolbox (Kundu et al., 2012), excluding Principal Component Analysis (PCA) de-noising and filtering. The optimal combination method used was that of T_2* weighting Posse et al. (1999). All three echoes for GRE-EPI and the FID + 2 echoes for Looping Star were combined using z-concatenation with AFNI (Cox, 1996), followed by employing the "opt _com" command from "tedana.py" (Kundu et al., 2012).

Co-registration of the optimally combined data with the T_1 image was then performed, followed by spatial normalisation to MNI space with images saved at 2 mm spatial resolution, and 8 mm FWHM spatial smoothing. The motion regressors were extracted

from the FID for Looping Star and the first echo of GRE-EPI.

Fixed-effects and group-level fMRI analyses were also conducted with SPM-12. The main effect of sound was evaluated through modelling the auditory blocks. The main effect of frequency of words spoken (or word frequency) was explored by modelling the parametric modulator with its first-order derivative. This model was used as it was expected that the required activation would increase with speed, though the volume of the words remains the same.

A 128 s high-pass filter was also included in the analysis to remve low frequency drifts, and the standard canonical double-gamma haemodynamic response function was used. The AR(1) autocorrelation correction function was also employed for ReML parameter estimation (Poldrack et al., 2011). Cluster-level inference using a primary uncorrected cluster-forming threshold of $p < 0.001$. (Woo et al., 2014; Worsley et al., 1996) was employed. Only clusters surviving family-wise error correction at the cluster-level (i.e., $p_{FWE_c} < 0.05$) were deemed significant.

A spherical ROI was produced with 10 mm radius for each subject using MarsBaR (Brett, 2016; Brett et al., 2002), centred on the cluster with highest significance (i.e. highest T-statistic and $p_{FWE_c} < 0.05$) for each modality. Where this cluster was outside the auditory cortex, the local maximum of the T-statistic within the auditory cortex was selected. Percentage signal change was calculated within the ROI for each participant (Section 5.7.2). The normalised time series (i.e. scaling the signal to have a mean = 0 and standard deviation = 1) for this ROI was then plotted to evaluate the correlation of the detected BOLD response with the task.

To further quantify the differences between modalities, a paired T-test between the contrast maps for both the contrast of the main effect of sound and the main effect of word frequency was computed. Cluster-level inference using a primary uncorrected cluster-forming threshold of $p < 0.001$ (Woo et al., 2014; Worsley et al., 1996) was employed. Only clusters surviving family-wise error correction at the cluster-level (i.e., $p_{FWE_c} < 0.05$) were deemed significant.

7.3.1.3 Results

Firstly, acoustic noise (LA_{eq}) was measured at 74.3dB (A) for Looping Star and 108 dB(A) for GRE-EPI. Figure 7.13 shows the tSNR of both modalities. The second echo of the Looping Star acquisition had much lower tSNR relative to GRE-EPI, though the tSNR was boosted by optimal-echo combination.

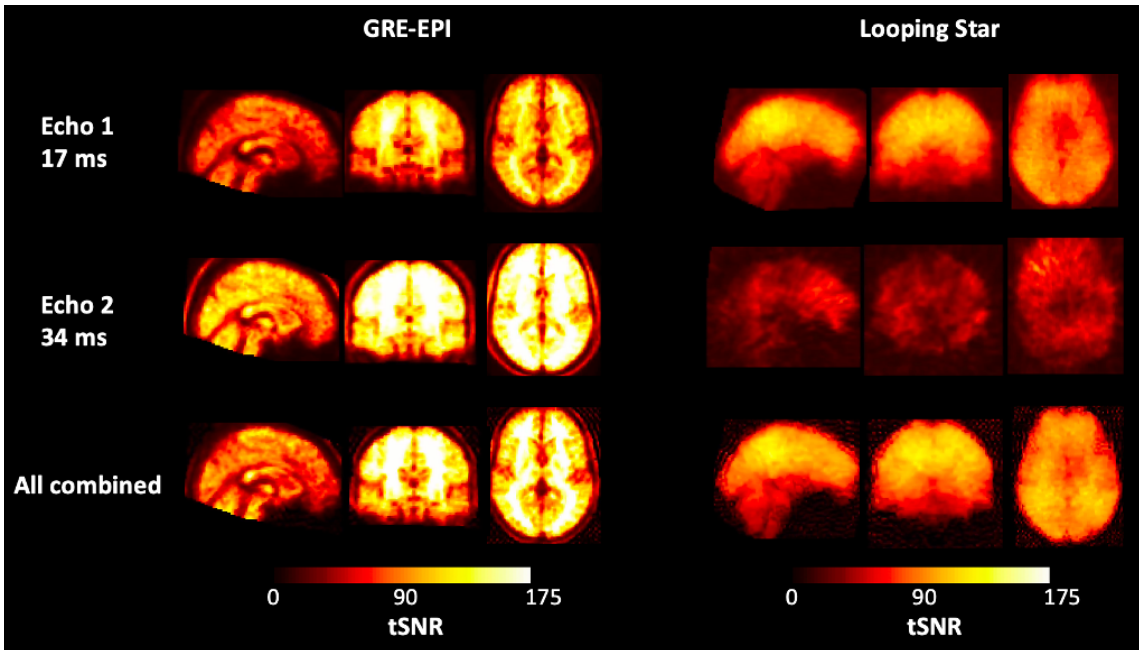

Figure 7.13: tSNR measures for GRE-EPI and Looping Star acquisitions at same echo times and optimally combined, displayed in FSL (Jenkinson et al., 2012).

The group-level activity maps for the main effect of sound (Figure 7.14) show that GRE-EPI produced significant bilateral activity for equivalent echoes and echo combined data. On the other hand, Looping Star only produced significant bilateral activity for the second echo and was otherwise significantly left-lateralised. Upon further investigation, this did not appear to be related to the tSNR. The accompanying statistical results are shown in Table 7.5.

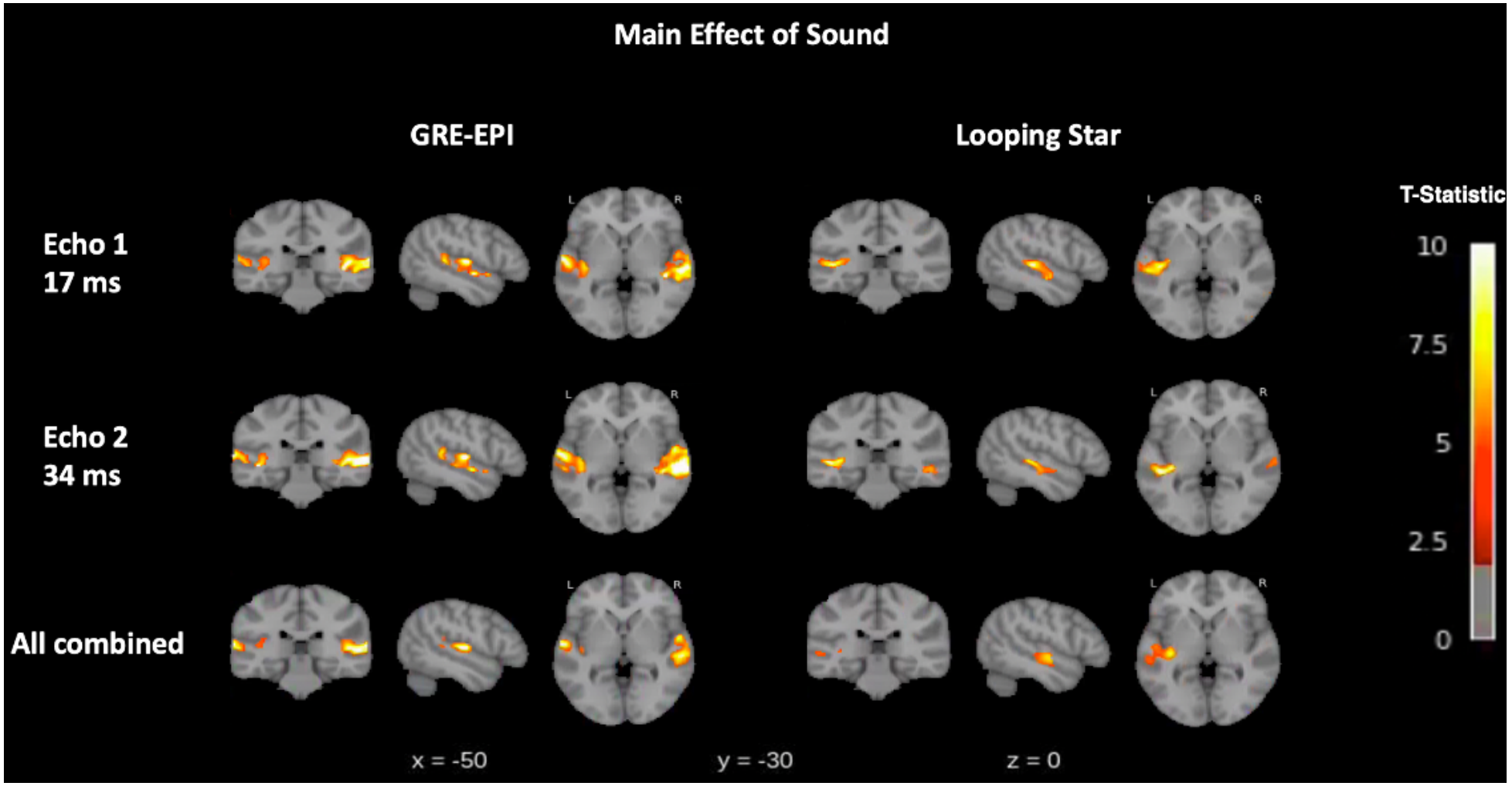

Figure 7.14: Group level activity maps for each acquisition at the same echo times, as well as for the echo combined datasets, for the main effect of sound. Images produced using NiLearn (The Nilearn developers, 2021). T-statistics were thresholded at T = 2, and each image was thresholded at the appropriate cluster extent to produce only the statistically significant clusters.

Table 7.5: Cluster-level statistical results for group level activity auditory paradigm for main effect of sound

Acquisition	**Peak MNI coordinates (x,y,z mm)**	**Brodmann Area**	**Peak-level T-statistics**	**Cluster-level p_{FWE}-value**	**Cluster Size**
Looping Star, Echo 1	-40 -24 6	41 (L)	18.94	$< 10^{-3}$ **	1034
Looping Star, Echo 2	58 -34 -12	21 (R)	20.36	0.001	285
Looping Star, All Comb	-36 -22 0	13 (L)	9.54	$< 10^{-3}$ **	525
GRE-EPI, Echo 1	62 -10 -6	22 (R)	28.09	$< 10^{-3}$ **	1998
GRE-EPI, Echo 2	44 -32 6	22 (R)	19.47	$< 10^{-3}$ **	1643
GRE-EPI, All Comb	-66 -34 12	22 (L)	17.86	$< 10^{-3}$ **	1049

* = cluster-level p(FWE) < 0.05, ** = cluster-level p(FWE) < 0.001, N/A = outside of defined Brodmann Areas

The group level activity maps for the effect of parametric modulation for the speed at which words were spoken showed that only Looping Star produced statistically significant activity (Figure 7.15), which was once again left-lateralised, with accompanying statistics shown in Table 7.6.

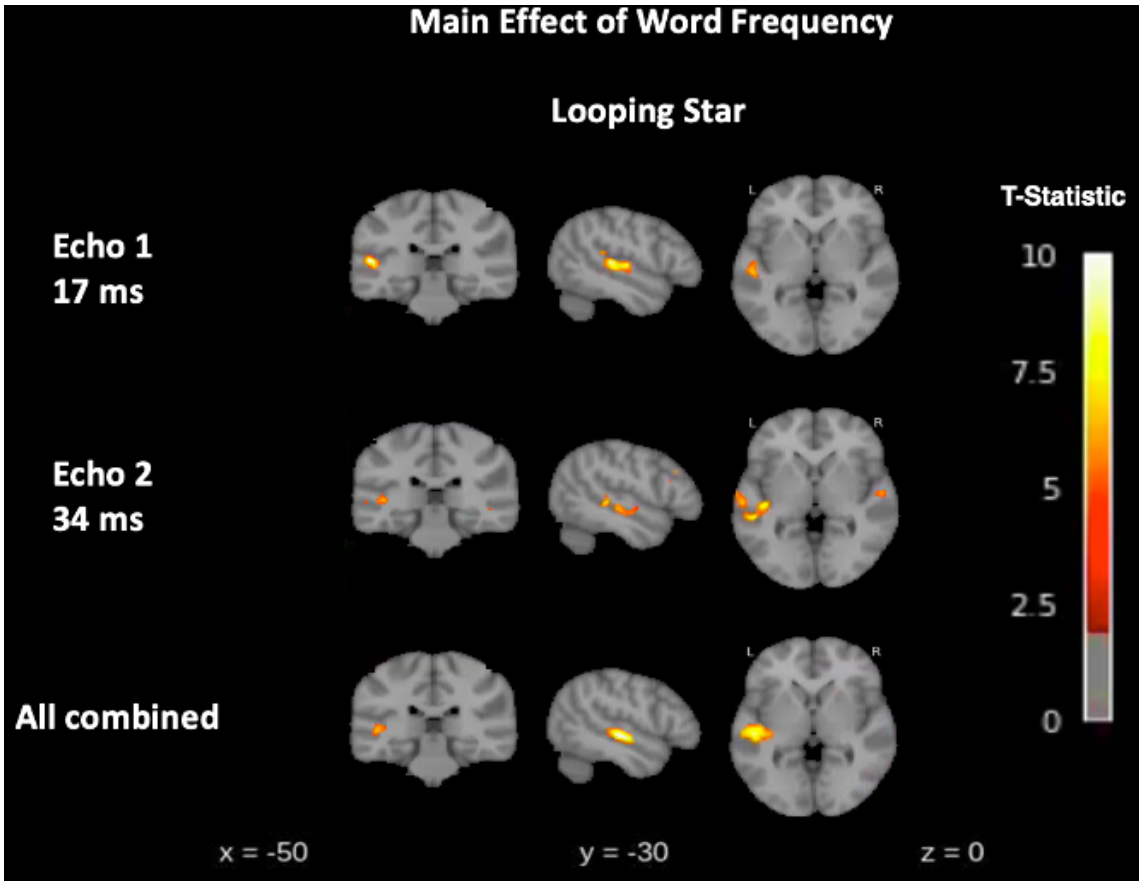

Figure 7.15: Group level activity maps for each acquisition at the same echo times, as well as for the echo combined datasets, for the main effect of word frequency. Only Looping Star demonstrated significant activity, hence GRE-EPI images are not shown. Images produced using NiLearn (The Nilearn developers, 2021). T-statistics were thresholded at T = 2, and each image was thresholded at the appropriate cluster extent to produce only the statistically significant clusters.

Table 7.6: Cluster-level statistical results for group level activity auditory paradigm for main effect of parametric modulation for word frequency

Acquisition	**Peak MNI coordinates (x,y,z mm)**	**Brodmann Area**	**Peak-level T-statistics**	**Cluster-level p_{FWE}-value**	**Cluster Size**
Looping Star, Echo 1	-54 -28 8	41 (L)	11.23	$< 10^{-3}$ **	368
Looping Star, Echo 2	-62 -24 -6	21 (L)	10.55	$< 10^{-3}$ **	523
Looping Star, All Comb	-48 -20 -2	22 (L)	11.03	$< 10^{-3}$ **	518
GRE-EPI, Echo 1	-54 -8 -6	22 (L)	7.64	0.352	95
GRE-EPI, Echo 2	-52 -12 4	41 (L)	7.02	0.402	86
GRE-EPI, All Comb	-52 -14 6	41 (L)	5.51	0.896	25

* = cluster-level p(FWE) < 0.05, ** = cluster-level p(FWE) < 0.001, N/A = outside of defined Brodmann Areas

The normalised time series extracted from the 10 mm radius spherical ROI for each participant and modality, for the optimally combined echo datasets, are shown in Figure 7.16. For both acquisitions there was high signal noise present for some participants, particularly for Looping Star, though generally a clear task-correlated pattern could be seen.

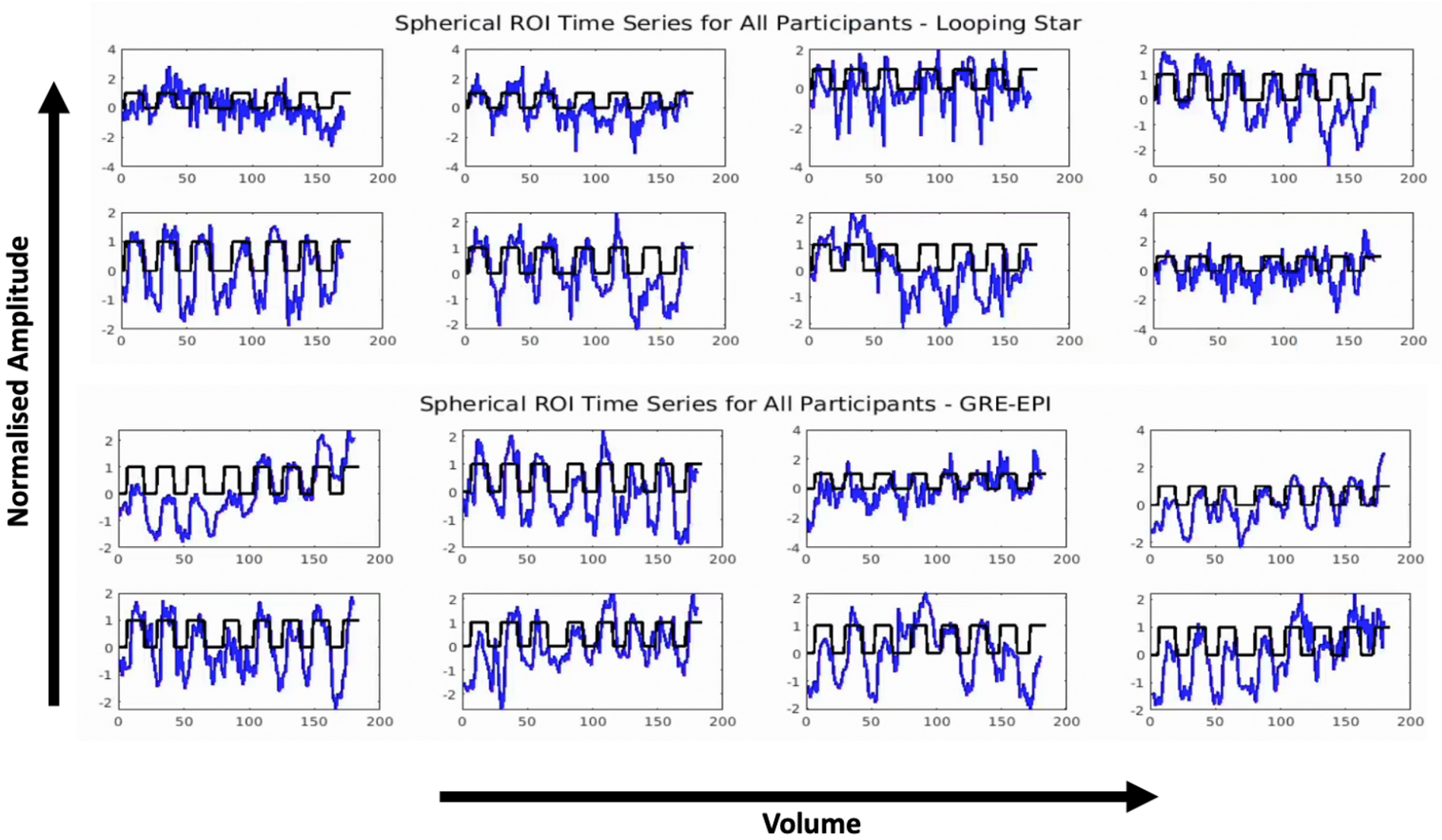

Figure 7.16: Normalised time series from 10 mm radius spherical ROI for each participant and each modality.

The percentage signal change on average was greater for optimally-combined GRE-EPI relative to optimally-combined Looping Star, demonstrated by the violin plots in Figure 7.17. Some participants produced similar percentage signal change for Looping Star with those in GRE-EPI.

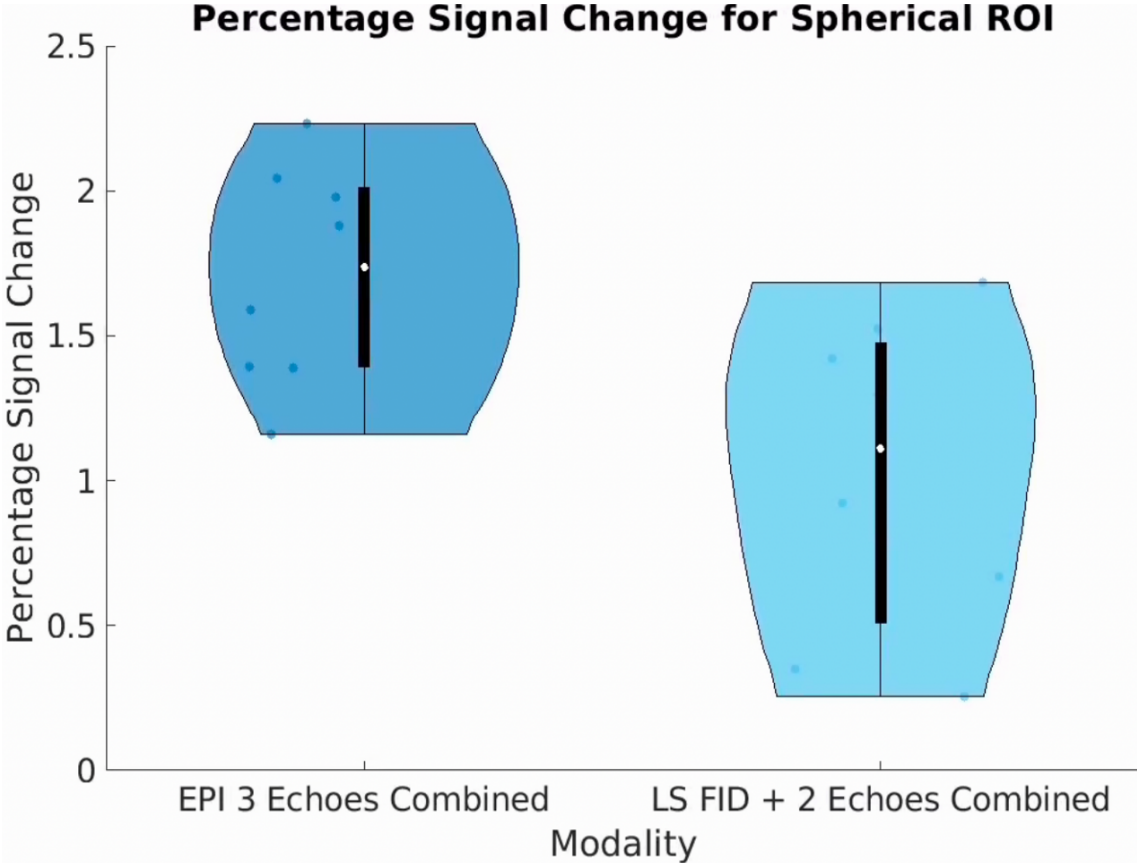

Figure 7.17: Violin plot for percentage signal change in 10 mm spherical ROI for each modality. Violinplot tool from github was used (Bechtold, 2016).

No significant differences were found using the paired T-test for the contrast of the main effect of word frequency, though GRE-EPI demonstrated significantly higher activity bilaterally in the auditory cortex for the main effect of sound (Table 7.7).

Table 7.7: Paired T-test for main effect of sound contrast between modalities

Comparison	Peak MNI coordinates (x,y,z mm)	Brodmann Area	Peak-level T-statistics	Cluster-level p_{FWE}-value	Cluster Size
GRE-EPI > LS	-60 -20 10 54 -14 8	1 (L) 41 (R)	13.40 11.49	$< 10^{-3}$ ** $< 10^{-3}$ **	460 488

* = cluster-level p(FWE) < 0.05, ** = cluster-level p(FWE) < 0.001, N/A = outside of defined Brodmann Areas

7.3.1.4 Discussion

GRE-EPI had a higher average percentage signal change, consistent with its higher tSNR, although there was substantial overlap with the percentage signal change identified for Looping Star for some participants. It was therefore determined that Looping Star and GRE-EPI had comparable functional sensitivity to the main effect of sound. A paired t-test showed that GRE-EPI produced significantly greater activity bilaterally relative to Looping Star for the main effect of sound. This could be due in part to an interaction effect with the background acoustic noise of scanning, as the background acoustic noise has been shown to affect activation in the auditory cortex (Gaab et al., 2007a,b; Ranaweera et al., 2016).

Interestingly, only Looping Star could identify significant auditory activity to the speed at which words were spoken. Importing the coordinates of the region identified as statistically significant into Neurosynth (Yarkoni, 2011) for the second echo of Looping Star, the peak coordinate of the most significant cluster was associated with the term "speech" for a meta-analysis with a z-score = 7.48 and "spoken" for a meta-analysis with z-score = 10.10. For the peak coordinate of the most significant cluster in the optimally combined Looping Star data, the term "speech" was affiliated for a meta-analysis with a z-score = 7.10.

There was also clear left lateralisation for Looping Star for the main effect of sound and the main effect of word frequency. The latter was unsurprising given the former and this was not produced by any tSNR assymetry. This lateralisation is characteristic of speech-processing (Boatman et al., 1995; Hickok and Poeppel, 2007; Narain et al., 2003), serving as a preliminary indicator that Looping Star may be more appropriate to investigate auditory processing. This is since it could disentangle effects from the background acoustic scanner noise that may mask the response of interest, driven by the

presented stimulus. De-noising strategies and investigations with larger cohorts should be explored to improve the specificity of these results.

7.3.2 Impact of Spatial Smoothing on Looping Star

7.3.2.1 Background

It was shown that Looping Star produces good functional sensitivity to an auditory speech-processing paradigm (Section 7.3), however Looping Star has demonstrated inherent smoothing characteristics that affect the results. The impact of spatial smoothing was therefore evaluated to further validate the functional sensitivity to auditory speech-processing.

7.3.2.2 Methods

The same acquisition, analysis and pre-processing was applied as in Section 7.3, however different spatial smoothing levels were applied to the optimally combined data. These included smoothing thresholds of 0 mm and 4 mm FWHM to evaluate the smoothness of the Looping Star data (e.g. Section 7.2). Only the group level activity maps were evaluated for the main effect of sound and the main effect of word frequency, analysed as described in the previous section.

7.3.2.3 Results

Both Looping Star and GRE-EPI identified statistically significant activity across all smoothing thresholds for the main effect of sound (Figure 7.18 and Table 7.8). This was surprising as GRE-EPI previously did not demonstrate statistically significant activity at this smoothing threshold for the visual paradigm (Section 7.2). However, this indicates

the strength of the auditory response in GRE-EPI, which could be amplified by interactions with the background acoustic noise.

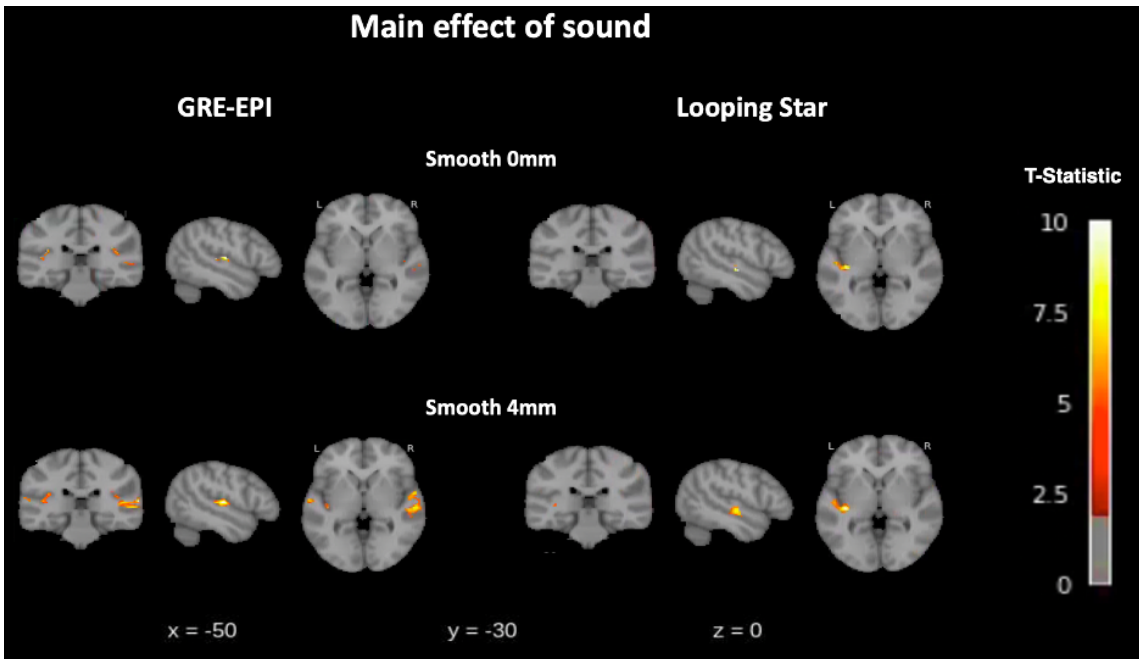

Figure 7.18: Main effect of sound for GRE-EPI and LS with all echoes + FID combined with 0mm and 4mm smoothing. Images produced using NiLearn (The Nilearn developers, 2021). The images were thresholded at the appropriate cluster-extent threshold to demonstrate only significant voxels. The T-statistics shown are thresholded at T = 2.

Table 7.8: Cluster-level statistical results of group level activity auditory paradigm for main effect of sound at each smoothing threshold. Optimally-combined echoes were employed.

Acquisition and Smoothing	Peak MNI coordinates (x,y,z mm)	Brodmann Area	Peak-level T-statistics	Cluster-level p_{FWE}-value	Cluster Size
Looping Star, 0 mm	-36 -24 2	N/A	15.29	$< 10^{-3}$ **	91
Looping Star, 4 mm	-36 -24 2	N/A	14.70	$< 10^{-3}$ **	222
GRE-EPI, 0 mm	-62 -10 4	41 (L)	13.09	$< 10^{-3}$ **	100
GRE-EPI, 4 mm	66 -28 10	22 (R)	15.03	$< 10^{-3}$ **	624

* = cluster-level p(FWE) < 0.05, ** = cluster-level p(FWE) < 0.001, N/A = outside of defined Brodmann Areas

For the main effect of word frequency, both smoothing thresholds of Looping Star identified significant auditory activity, whereas only GRE-EPI without any smoothing identified a significant activity pattern, localised to the auditory cortex. Once again, this was surprising as significant activity was not identified at 8 mm smoothing, though it could indicate that a very spatially specific response is identifiable with GRE-EPI that is masked upon smoothing (Mikl et al., 2008).

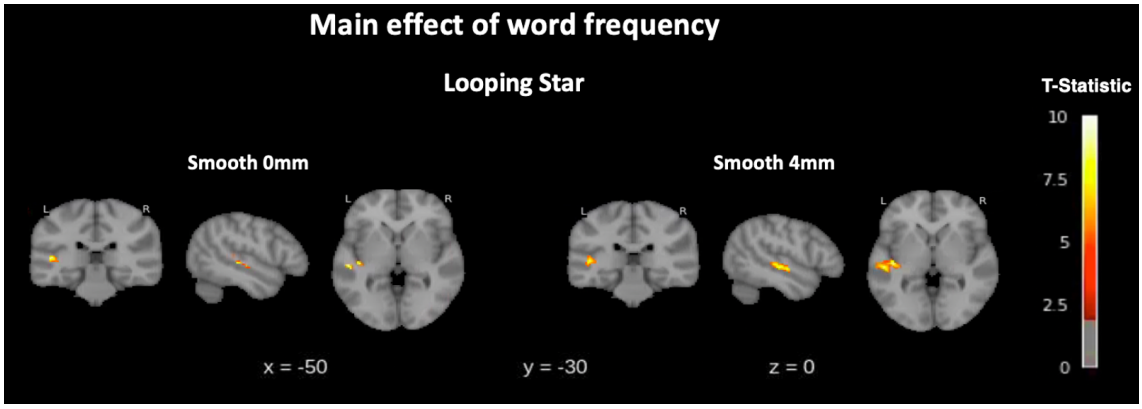

Figure 7.19: Main effect of word frequency for LS with all echoes + FID combined with 0 mm and 4 mm smoothing. Images produced using NiLearn (The Nilearn developers, 2021). Both images were thresholded at appropriate extent threshold for significant clusters only. Thresholded at T = 2.

Table 7.9: Cluster-level statistical results for group level activity auditory paradigm for main effect of word frequency at each smoothing threshold, for all echoes combined.

Acquisition and Smoothing	**Peak MNI coordinates (x,y,z mm)**	**Brodmann Area**	**Peak-level T-statistics**	**Cluster-level p_{FWE}-value**	**Cluster Size**
Looping Star, 0 mm	-52 -24 0	22 (L)	9.73	$< 10^{-3}$ **	86
Looping Star, 4 mm	-42 -20 0	41 (L)	10.47	$< 10^{-3}$ **	295
GRE-EPI, 0 mm	-58 -16 10	1 (L)	7.61	0.006 *	31
GRE-EPI, 4 mm	-58 -16 10	1 (L)	10.14	0.086	53

* = cluster-level p(FWE) < 0.05, ** = cluster-level p(FWE) < 0.001, N/A = outside of defined Brodmann Areas

7.3.2.4 Discussion

Significant auditory activity for both auditory effect contrasts was found in Looping Star across smoothing thresholds, further supporting its inherent smoothing. Curiously, this was also true for the GRE-EPI acquisition without any smoothing, though the identified cluster was smaller and produced a lower T-statistic. The significance of this response was lost at higher smoothing thresholds. This was also seen by Mikl et al. (2008) for the visual oddball task, who suggested that no spatial smoothing should be used if very accurate spatial localisation is required at the expense of functional sensitivity. This could suggest that a very specifically localised response is detectable with GRE-EPI, but the sensitivity will be diminished at higher smoothing thresholds. On the other hand, it remains difficult to disentangle this activity from interactions with the background acoustic noise, therefore further study is required.

7.4 Chapter Discussion

The studies in this chapter sought to validate the use of Looping Star in vivo, compared with GRE-EPI. For the first study, the robust visual checkerboard paradigm was employed and it was found that Looping Star produced good functional sensitivity relative to GRE-EPI. The first indicators towards benefits of the inherent smoothing of Looping Star were found, with even a 0 mm FWHM smoothing kernel producing significant results. Small differences in the group level activity maps were identified when applying the FAST versus the AR(1) autocorrelation correction functions, though further study is required of the temporal autocorrelation requirements of Looping Star. Additionally, Looping Star demonstrated lower power compared with GRE-EPI, which was expected, therefore future studies may need higher sample sizes.

The auditory paradigm study results provided the first indicator towards Looping Star being able to distinguish auditory processing more specifically than GRE-EPI, through the removal of acoustic noise. This was shown by left-lateralised significant auditory activity

that was identified only for Looping Star for sensitivity to the speed at which words were spoken, despite the tSNR being substantially lower for Looping Star relative to GRE-EPI. This was also independent of any heterogeneities in tSNR. Though a left-lateralised active cluster for GRE-EPI was also identified with no smoothing that disappears upon higher smoothing, it was not possible to disentangle the strength of this effect from interactions with the background acoustic noise. Furthermore, this result would not be valid under the requirements of random field theory. This highlights a key benefit to Looping Star.

Chapter 8

In vivo Characterisation of Looping Star: Resting-State

Summary

In this chapter:

- Two core resting-state networks are selected for investigation with multi-echo Looping Star
- The functional sensitivity of Looping Star to these two core resting-state networks is compared with multi-echo GRE-EPI.
- Signal characteristics of multi-echo Looping Star in vivo are investigated using independent component analysis.
- The impact of spatial smoothing and global signal regression on Looping Star resting-state network identification is evaluated.

Overview

In vivo investigations are continued by exploring the capabilities of multi-echo Looping Star for resting-state network identification using seed-based time series correlations, in comparison with multi-echo GRE-EPI. The impact of spatial smoothing and global signal regression on the identification of resting-state networks is characterised for both Looping Star and GRE-EPI. Finally, the independent components identified for a single subject at rest and at group level are examined to explore if these are spatially and temporally consistent between GRE-EPI and Looping Star.

8.1 Chapter Introduction

Though task stimuli are useful for identifying functional sensitivity via the BOLD response, resting-state fMRI (i.e. in the absence of external stimuli) can provide further insight into the spectral content of the MR signal. The core resting-state networks are well established, with resting-state oscillations typically occurring between 0.01 - 0.1 Hz (Damoiseaux et al., 2006; Fox and Raichle, 2007; Raichle et al., 2001). They are measured by assuming that separate regions with linearly correlated time series are functionally connected (Fox and Raichle, 2007; Friston et al., 1994; Hlinka et al., 2011). However, in order to accurately identify the resting-state networks, sources of noise outside the resting-state frequency range must be removed or filtered (Murphy et al., 2013).

Denoising of resting-state fMRI data has been extensively reviewed (De Blasi et al., 2020; Dipasquale et al., 2017; Kundu et al., 2017). One method of removing noise from resting-state fMRI data is global signal regression, whereby an average signal either from a region or from the whole brain is regressed from all voxels. However, this method is widely debated given that it could lead to loss of information from the signal (Liu et al., 2017b). Alternatively, ICA separates spatially independent time courses from the MR signal (Calhoun et al., 2001a, 2004; McKeown et al., 1998), allowing investigation of collective spatial and temporal dynamics. Upon identification of these components, they can be used to de-noise the MR signal to extract only resting-state correlations of interest.

On the other hand, signals typically identified as noise in resting-state data may be used to better understand underlying physiological processes occurring at rest (Chen et al., 2020a; Liu, 2016). The origins of signal noise in resting-state fMRI can vary from cerebral physiology to motion or non-neuronal sources, and can vary across participants (Gonzalez-Castillo et al., 2021; Griffanti et al., 2017; Tong et al., 2019). Group-level ICA can be used to identify consistent components across participants, although inferences are difficult to obtain given that each subject will have a different time course and spatial map across components (Erhardt et al., 2011). Temporal concatenation of the data is

one of the most common techniques for group ICA (Calhoun et al., 2001b, 2009) which involves performing one ICA that assumes common spatial maps for different temporal signal characteristics across participants. This is used if the temporal variability is larger than the spatial variability across subjects, which tends to be the case for fMRI data (Erhardt et al., 2011).

Furthermore, having shown the robust functional sensitivity of Looping Star to block design paradigms, Looping Star also presents an interesting new avenue for resting-state fMRI as studies have shown that acoustic noise can affect resting-state functional sensitivity (Andoh et al., 2017; Dionisio-Parra et al., 2020). This chapter therefore aims to better understand the signal and noise characteristics of Looping Star using resting-state fMRI. Two core resting-state networks are selected for investigation with seed-based time series correlation analysis, including and excluding global signal regression, and their appearance when identified with Looping Star is compared with GRE-EPI. Independent component analysis is also used at single subject and group level to investigate the spatial and temporal behaviour of resting-state components between modalities. The data used for this chapter was collected using a 3 T MR750 GE Healthcare scanner based at the Centre for Neuroimaging Sciences (Section 5.2).

8.2 Resting-State with Looping Star

8.2.1 Connectivity Analysis

8.2.1.1 Background

To investigate the spectral characteristics of Looping Star during rest, it is important to validate its functional sensitivity to the core resting-state networks. Multi-echo Looping Star for resting-state fMRI, with a standard pre-processing pipeline, was evaluated using seed-based correlation analysis. The seeds employed in analysis were affiliated with regions

that are part of two core resting-state networks. The resting state networks selected were the default mode network and the auditory network, as these should be identifiable by both Looping Star and GRE-EPI based on the literature (Andoh et al., 2017; Damoiseaux et al., 2006; Dionisio-Parra et al., 2020; Gaab et al., 2008; Gonzalez-Castillo et al., 2016).

A comparison with multi-echo GRE-EPI was also computed. It was expected that differences between modalities would be difficult to disentangle from effects of acoustic noise from the inherent functional sensitivity of Looping Star but that both modalities should identify correlated activity affiliated with the auditory and default mode networks. Parts of this work were presented at the Organisation for Human Brain Mapping (OHBM) Annual Meeting 2019 (Damestani et al., 2019a).

8.2.1.2 Methods

Eight healthy participants were recruited (6 male; mean age = 35 $\pm$ 12 years; 2 left-handed) for scanning during rest. The participants were asked to keep their eyes open and focused on a fixation cross centred on a screen, given that resting-state networks can differ between eyes open and closed conditions (Patriat et al., 2013). For full details of the paradigm set-up, see Section 5.3. A 12-channel receive-only head coil was used (Section 5.2).

The acquisition parameters for multi-echo GRE-EPI included: TE = 17 ms, 34 ms, 51 ms, TR = 2.1 s, 184 volumes, matrix size = 64 x 64 x 32, slice thickness = 3 mm, 32 slices, slice gap = 1 mm, FOV = 24 cm, FA = 80°.

For FID + 2 echo (multi-echo) Looping Star, the acquisition parameters were: TE = 0 ms, 17.4 ms, 34.8 ms, TR = 1.87 s, number of volumes = 180, matrix size = 64 x 64 x 64, isotropic resolution = 3 mm, FOV = 19.2 cm, 32 spokes per echo, 96 spokes per segment, 960 spokes per volume, FA = 3 °.

An IR-SPGR image (TE = 3.016 ms, TR = 7.312 s, TI = 400 ms, matrix size = 256

x 256, in-plane resolution = 1.055 mm, FOV = 27 cm, FA = 11°, 196 slices) was also acquired for spatial normalisation and co-registration. Image reconstruction was performed as described in Section 5.2.

The first ten volumes from the Looping Star series and four volumes from GRE-EPI were removed to ensure the longitudinal magnetisation had reached steady-state (Section 3.5). Scan order was randomised between participants. The acquisition parameters were the same as those from Section 7.3, therefore the acoustic noise measures were identical.

For pre-processing of both Looping Star and GRE-EPI, optimal echo combination involved T_2*-weighting of all echoes (including the FID for Looping Star) after realignment (Posse et al., 1999). This was performed using z-concatenation of the FID and echoes with AFNI (Cox, 1996), followed by employing the "opt _com" command from "tedana.py" (Kundu et al., 2012).

An SPM-12 (FIL Methods Group, 2020) pre-processing pipeline was then used on the optimally combined data, including bias field correction and segmentation of the T_1 image, co-registration of the optimally combined data with the T_1 image, spatial normalisation to MNI space with images saved at 2 mm spatial resolution, and 8 mm FWHM spatial smoothing.

The pre-processed data was imported into the CONN toolbox (Whitfield-Gabrieli and Nieto-Castanon, 2012). In the denoising step in CONN, only linear detrending was used and the regressor inputs were the motion regressors and their first-order temporal derivatives plus the effect of rest. The motion regressors were extracted from the FID for Looping Star and the first echo of GRE-EPI, and the data were bandpass filtered after regression between 0.01 – 0.1 Hz and no de-spiking was applied.

The extent of participant movement was evaluated using the motion regressors, derived from the FID for Looping Star and the first echo of GRE-EPI. The framewise displacement (FWD) was computed from the regressors, which produces a time series of the estimated movement as seen in Equation (8.1) (Power et al., 2012).

$$FWD(t) = \sum |d(t-1) - d(t)| + 50 \cdot (\pi/180) \cdot \sum |r(t-1) - r(t)| \quad (8.1)$$

where $FWD(t)$ is the framewise displacement at each time point t, d is the translation distances in the x, y, z directions and r is the rotation angles for yaw, pitch and roll for the surface of a sphere with radius 50 mm (considered as an average human head size). The root mean square (RMS) displacement for each direction was also computed for each participant. The average and the standard deviation across participants was then computed. The threshold for high motion for this study was determined as 0.3 mm, consistent with Power et al. (2012).

In the first level analysis in CONN, bivariate correlations were used. Both seed-to-voxel and ROI-to-ROI analyses were performed. For seed-to-voxel analysis, parametric statistics were employed (Worsley et al., 1996), with a two-sided uncorrected cluster-forming threshold of $p < 0.001$ (Woo et al., 2014; Worsley et al., 1996). Only clusters surviving cluster-level $p < 0.05$ were deemed significant, with the cluster-size p-FDR corrected. The seed-based connectivity maps were evaluated from a seed placed in the right side of Heschl's gyrus, which forms part of the auditory resting-state network, and the posterior cingulate, which is part of the default mode network (Damoiseaux et al., 2006). To directly compare the identified networks linked to these seeds between modalities, the group level correlation maps and correlation T-maps were subtracted from one another.

ROI-to-ROI analysis was computed in CONN between 25 atlas regions (described in Table 8.1), selected based on regions affiliated with the auditory and default mode network (Andoh et al., 2017; Damoiseaux et al., 2006; Davies et al., 2014). The connectivity wheels produced in CONN are thresholded for cluster-level inference using parametric multivariate statistics (Jafri et al., 2008), with a cluster threshold of $p < 0.05$ cluster level p-FDR corrected (MVPA omnibus test), and connection threshold $p < 0.05$ p-uncorrected. Correlation matrix plots for the ROI-to-ROI analysis were produced using the 'conn tools' toolbox (Vallat, 2017). h represents the beta values between ROIs, which corresponds to the average Fischer transformed pairwise correlations of specified contrast, F represents

the accompanying statistical values, and p represents the one-tailed p-values (Vallat, 2017).

Table 8.1: Key for the 25 atlas regions selected for ROI-to-ROI analysis in CONN

Acronym	Definition	Acronym	Definition
AC	Anterior Cingulate	IFG oper l	Inferior Frontal Gyrus, Opercular Left
PC	Posterior Cingulate	IFG oper r	Inferior Frontal Gyrus, Opercular Right
SFG l	Superior Frontal Gyrus Left	IFG tri l	Inferior Frontal Gyrus, Triangular Left
SFG r	Superior Frontal Gyrus Right	IFG tri r	Inferior Frontal Gyrus, Triangular Right
LG l	Lingual Gyrus Left	pSTG r	Posterior Superior Temporal Gyrus Right
LG r	Lingual Gyrus Right	aSTG r	Anterior Superior Temporal Gyrus Right
PreCG l	Precentral Gyrus Left	pSTG l	Posterior Superior Temporal Gyrus Left
PreCG r	Precentral Gyrus Right	aSTG l	Anterior Superior Temporal Gyrus Left
aSMG r	Anterior Supramarginal Gyrus Right	IC l	Insula Cortex Left
aSMG l	Anterior Supramarginal Gyrus Left	IC r	Insular Cortex Right
pSMG r	Posterior Supramarginal Gyrus Right	HG r	Heschl's Gyrus Right
pSMG l	Posterior Supramarginal Gyrus Left	HG l	Heschl's Gyrus Left
Med FC	Medial Frontal Cortex		

8.2.1.3 Results

As the acquisition parameters were the same as in Section 7.3, the tSNR and acoustic noise measures were also identical. Figure 8.1 shows that, on average, participants appeared to move slightly more during GRE-EPI than Looping Star, though no large movements were detected on average across participants for either modality.

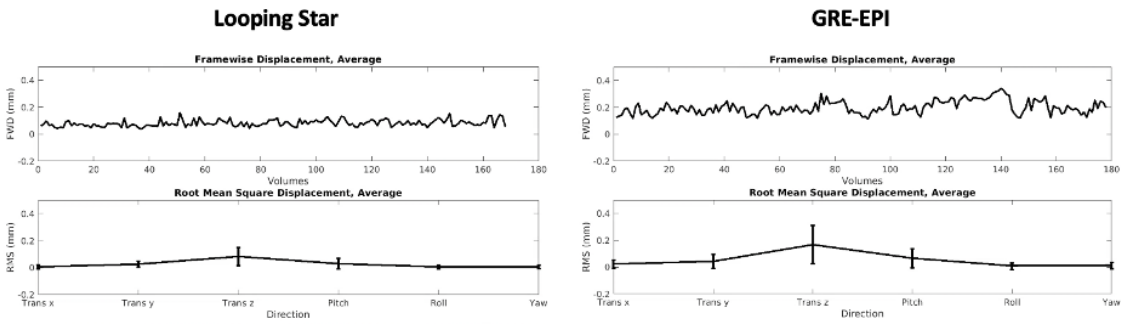

Figure 8.1: Framewise displacement (FWD) and root mean square (RMS) displacement on average across participants for each modality (Power et al., 2012).

Figure 8.2 demonstrates the regions with functional connectivity affiliated with the posterior cingulate and right Heschl's gyrus seeds. GRE-EPI has more spatially extensive statistically significant posterior cingulate connectivity, and both modalities identify significant bilateral Heschl's gyrus connectivity. The accompanying statistics can be seen in Table 8.2.

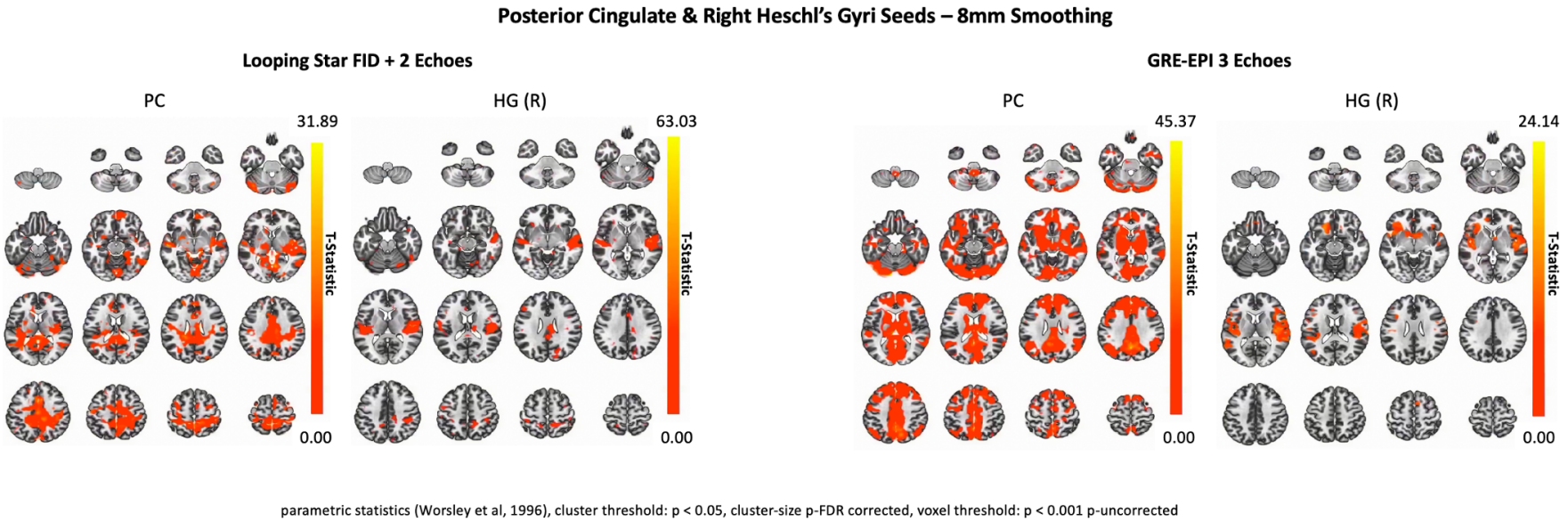

Figure 8.2: Identified regions that are temporally correlated with the time series in the posterior cingulate (PC) and right Heschl's gyrus (HG (R)) for each modality. The scale represents the T-score for the correlation. T-scores are unthresholded for visualisation, but the statistics shown have been thresholded as described in the Methods. Images produced using CONN (Whitfield-Gabrieli and Nieto-Castanon, 2012).

Table 8.2: Statistical results for 8 mm smoothing of resting-state acquisitions for right Heschl's gyri (HG (R)) and posterior cingulate (PC) in CONN (Whitfield-Gabrieli and Nieto-Castanon, 2012).

Acquisition and ROI	**MNI Co-ordinates (x,y,z mm)**	**Brodmann Area**	**Peak p_{FWE}**	**Cluster Size**
Looping Star, HG (R)	48 -16 6	41 (R)	$< 10^{-3}$ **	5299
	-50 -20 6	41 (L)	0.01	2604
GRE-EPI, HG (R)	-22 28 -14	41 (L)	$< 10^{-3}$ **	6427
	42 -18 8	41 (R)	0.012	5323
Looping Star, PC	-8 -40 34	23 (L)	0.022 *	2661
GRE-EPI, PC	-10 -88 -22	N/A	$< 10^{-3}$ **	87391

* = cluster-level p(FWE) < 0.05, ** = cluster-level p(FWE) < 0.001, N/A = outside of defined Brodmann Area

In the direct comparison of Looping Star and GRE-EPI (Figure 8.3 & Figure 8.4), it can be seen that GRE-EPI had higher correlation coefficients between the posterior cingulate and the anterior cingulate regions, indicative of a good functional sensitivity to the default mode network. Looping Star, on the other hand, demonstrated higher correlation coefficients between the posterior cingulate and the lingual gyrus. For the connectivity with Heschl's gyrus, Looping Star demonstrated higher correlations with the lateral occipital cortex and middle temporal gyrus relative to GRE-EPI. However, Looping Star produced higher correlations with the ventricles and white matter, indicating that additional denoising steps may be required.

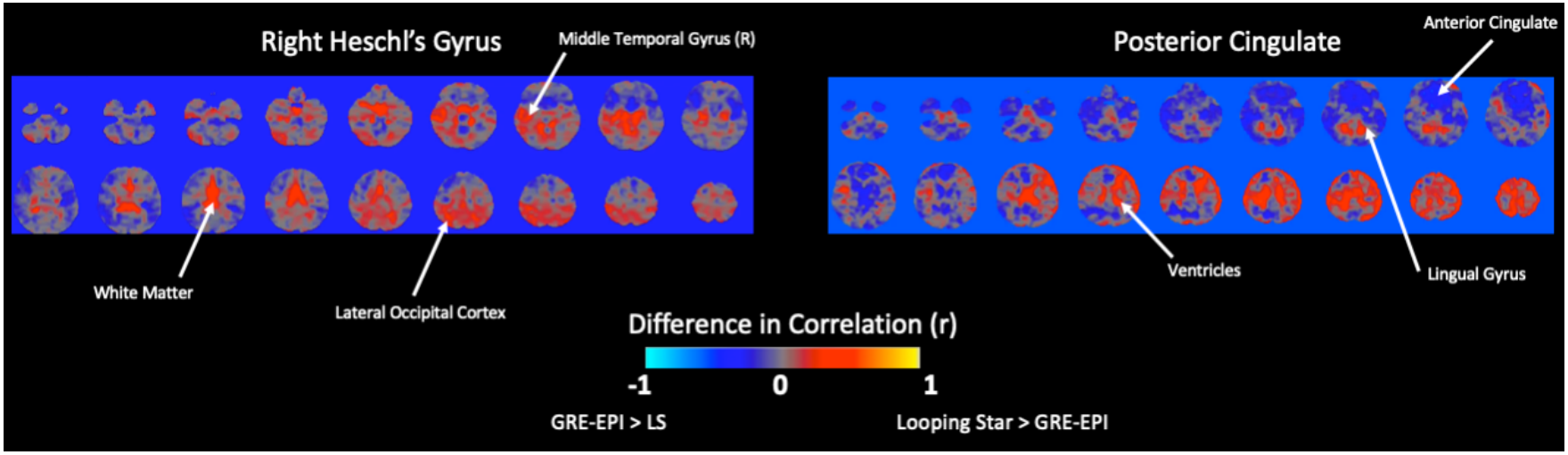

Figure 8.3: Difference between modalities of group level correlation (r) maps. Arrows indicate regions as defined by the Brodmann areas in BioImage Suite Web (BioImage Suite Web, 2021).

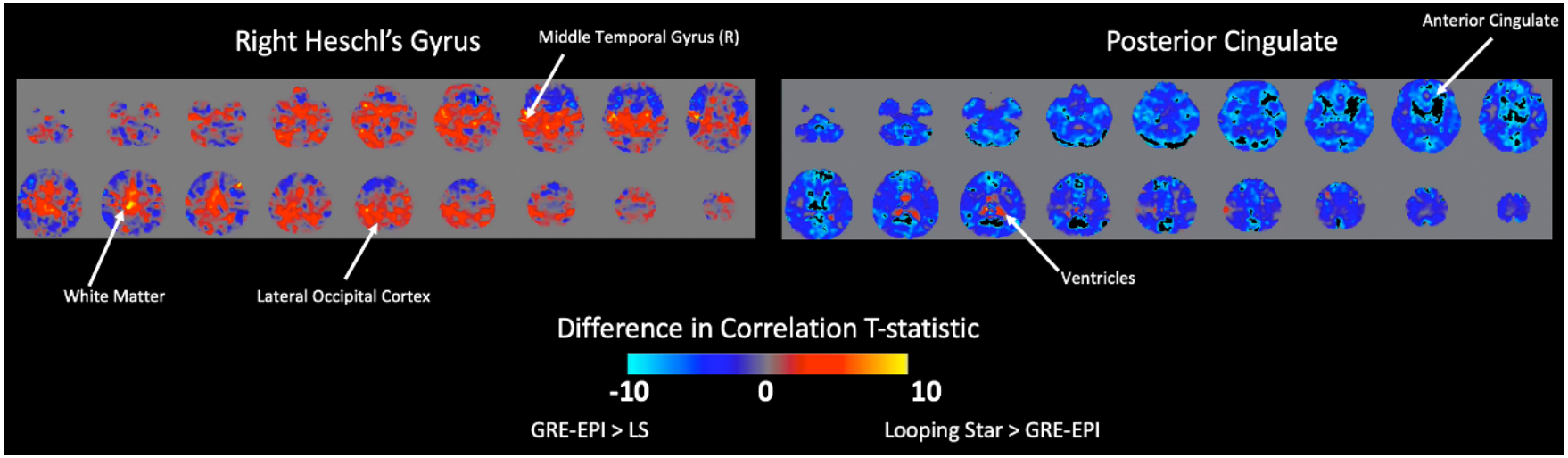

Figure 8.4: Difference between modalities of group level T-statistic maps of the correlations. Arrows indicate regions as defined by the Brodmann areas in BioImage Suite Web (BioImage Suite Web, 2021).

Investigating the differences in connectivity further, both the connectivity wheel (Figure 8.5) and connectivity matrices (Figures 8.6 - 8.8) were plotted for 25 atlas regions. It can be seen in the figures that GRE-EPI has a higher number of statistically significant connections between atlas regions compared with Looping Star. However, focusing on the connections with Heschl's gyri (bottom left of connectivity matrix, Figure 8.6), it can be seen that Looping Star produces statistically significant correlations with the lingual gyri, anterior cingulate and posterior cingulate where GRE-EPI does not.

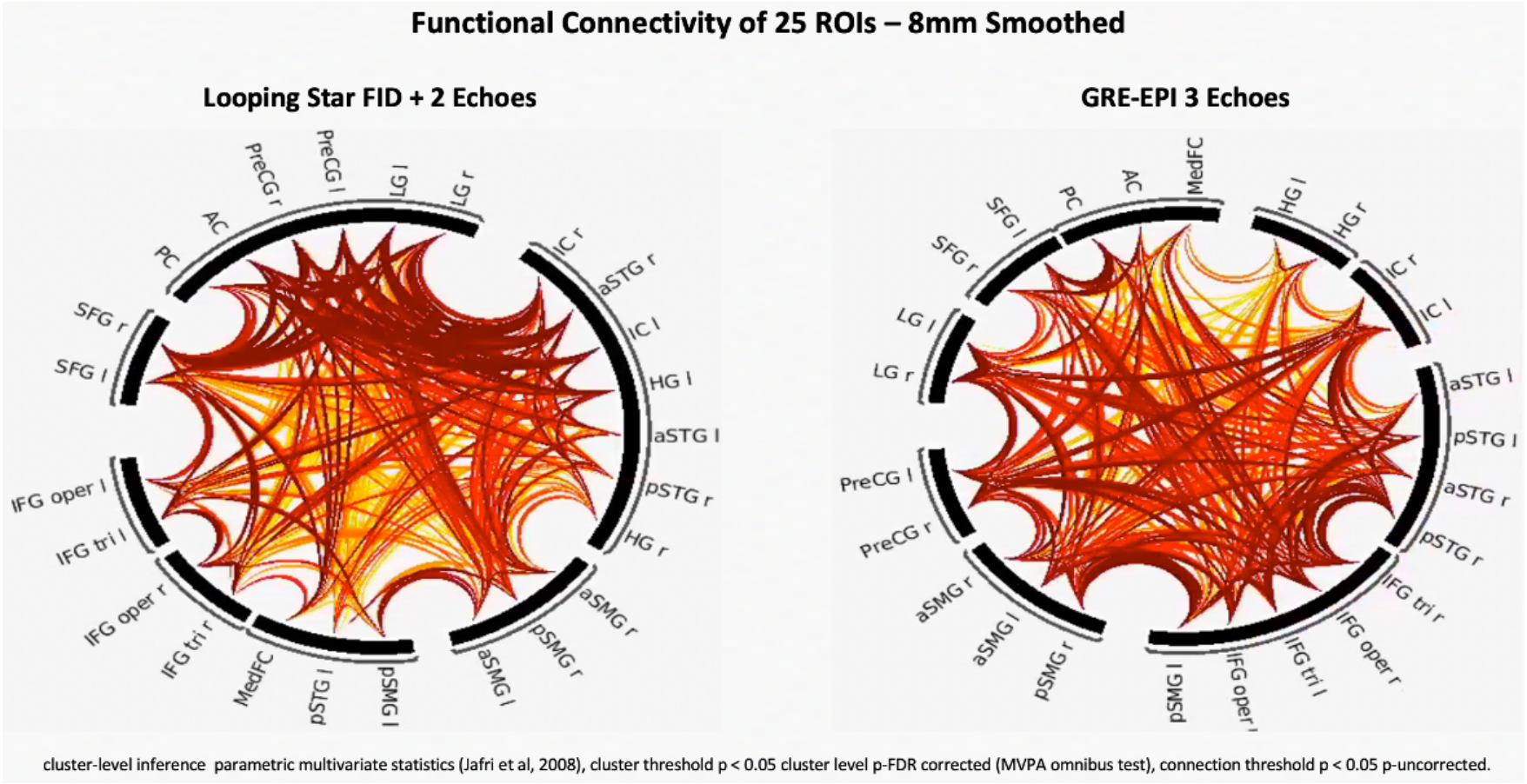

Figure 8.5: Connectivity wheel for each modality across 25 atlas regions (key for region names can be seen in Table 8.1). Line thickness and colour are proportional to the statistics (i.e. more red = higher correlation, thicker = higher correlation). Images produced using CONN (Whitfield-Gabrieli and Nieto-Castanon, 2012).

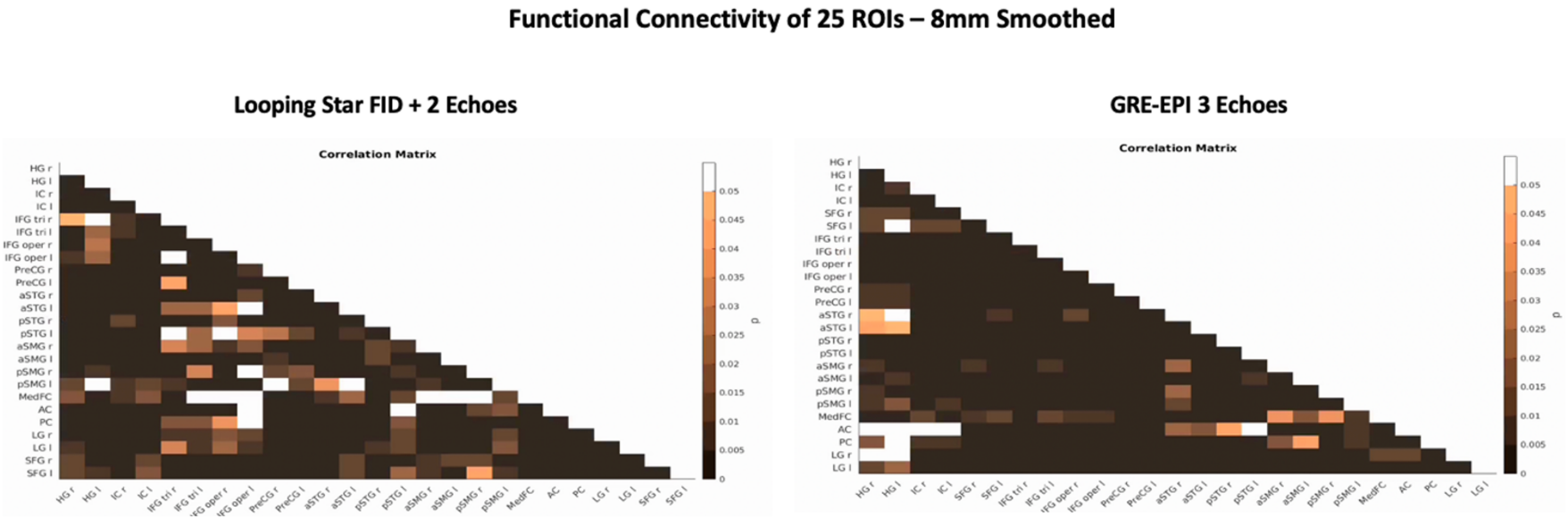

Figure 8.6: Connectivity matrix for each modality across 25 atlas regions (key for region names can be seen in Table 8.1). p represents the one-tailed p-values. Images produced using 'conn tools' (Vallat, 2017).

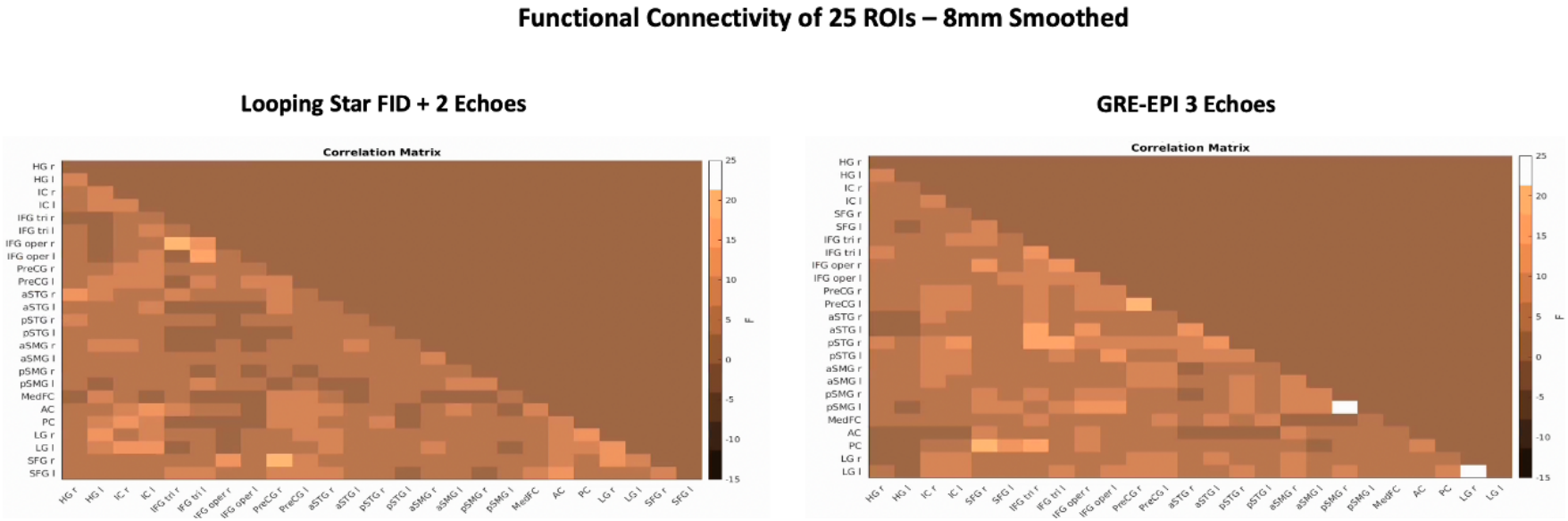

Figure 8.7: Connectivity matrix for each modality across 25 atlas regions (key for region names can be seen in Table 8.1). F represents the accompanying statistical values. Images produced using 'conn tools' (Vallat, 2017).

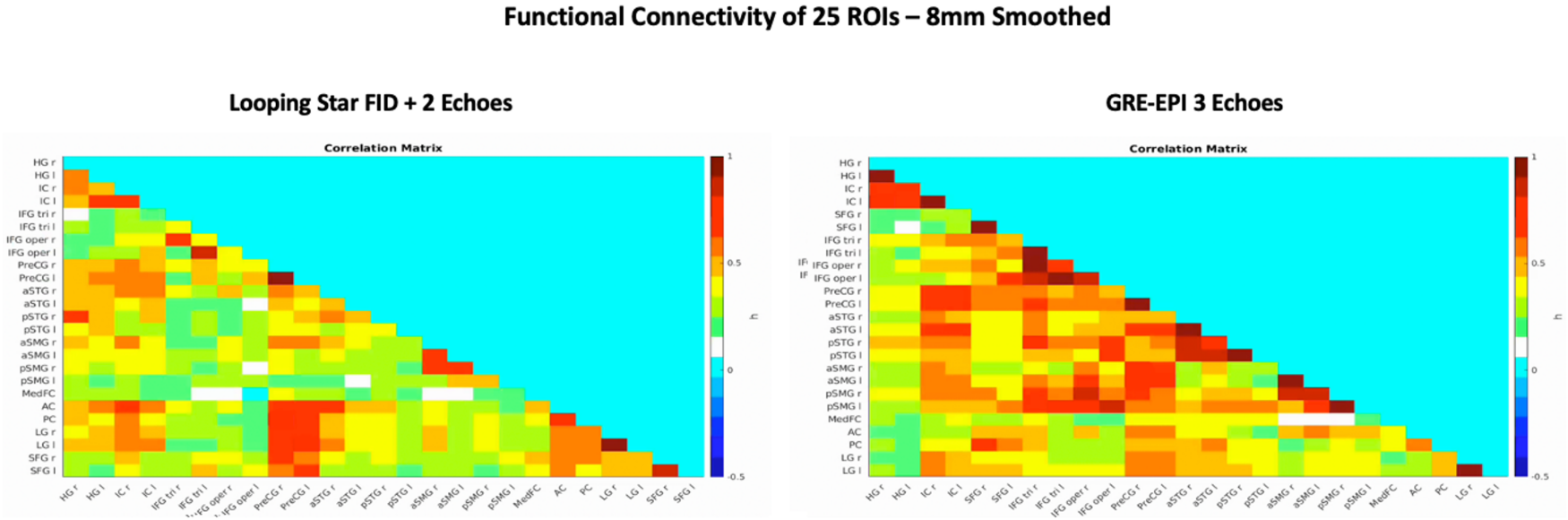

Figure 8.8: Connectivity matrix for each modality across 25 atlas regions (key for region names can be seen in Table 8.1). h represents the beta values between ROIs, which corresponds to the average Fischer transformed pairwise correlations of specified contrast. Images produced using 'conn tools' (Vallat, 2017)

The accompanying statistics tables for the ROI-to-ROI connectivity with right Heschl's gyrus for the top 10 out of the 25 atlas regions are seen in Tables 8.3 - 8.4 for each modality. GRE-EPI had the highest beta and T-statistic value for the connection between the left and right Heschl's gyrus. Looping Star not only had high beta and T-statistics for this connection pathway but also for the pathway between right Heschl's gyrus and the right anterior superior temporal gyrus.

Table 8.3: GRE-EPI group level statistical results for 8 mm smoothing threshold, evaluating connectivity with right Heschl's gyri in CONN (Whitfield-Gabrieli and Nieto-Castanon, 2012).

ROI	**Beta**	**T-statistic**	p_{FDR}**-value**
HG (L)	1.26	9.62	$< 10^{-3}$ **
IFG tri (L)	0.32	6.94	0.002 *
pSTG (R)	0.53	6.82	0.002 *
IC(L)	0.74	6.21	0.002 *
IFG tri (R)	0.43	6.18	0.002 *
pSTG (L)	0.42	5.55	0.003 *
IFG oper (L)	0.34	5.43	0.003 *
MedFC	0.30	5.17	0.004 *
IFG oper (R)	0.34	5.01	0.004 *
IC (r)	0.66	4.47	0.007 *

* = cluster-level p(FWE) < 0.05, ** = cluster-level p(FWE) < 0.001

Table 8.4: Looping Star group level statistical results for 8 mm smoothing threshold, evaluating connectivity with right Heschl's gyri in CONN (Whitfield-Gabrieli and Nieto-Castanon, 2012).

ROI	Beta	T-statistic	p_{FDR}-value
aSTG (R)	0.51	10.71	$< 10^{-3}$ **
HG (L)	0.60	9.18	$< 10^{-3}$ **
pSTG (R)	0.64	6.99	0.002 *
PC	0.47	6.17	0.003 *
IC(R)	0.59	5.66	0.003 *
IFG oper (R)	0.23	5.46	0.003 *
pSTG((L)	0.35	5.32	0.003 *
AC	0.51	4.96	0.004 *
pSMG (R)	0.37	4.95	0.004 *
aSMG (R)	0.47	4.90	0.004 *
aSTG(L)	0.45	4.80	0.004 *
IC (L)	0.47	4.52	0.005 *

* = cluster-level p(FWE) < 0.05, ** = cluster-level p(FWE) < 0.001

8.2.1.4 Discussion

The extracted motion regressors for Looping Star and GRE-EPI indicated that participants moved slightly less during the silent acquisition. As motion regressors are derived from the images, matching the volumes as closely as possible with the first volume using a cost function (Poldrack et al., 2011), it is not expected that this is mistaken as the image quality and contrast of the skull and background of the FID used was of a good standard. However, future work could use advanced methods for head motion detection to better evaluate the degree of motion in Looping Star (Fair et al., 2020; Power et al., 2020).

Both Looping Star and GRE-EPI could identify the default mode and auditory resting-state networks from an atlas seed within the networks, although differences in connectivity were found between techniques. GRE-EPI demonstrated the strongest default mode

network correlation map, whereas Looping Star presented weaker correlations between the anterior and posterior cingulate but higher correlations between the posterior cingulate and the lingual gyrus. For the auditory network, Looping Star identified higher correlations between Heschl's gyrus and the middle temporal gyrus and lateral occipital gyrus compared with GRE-EPI.

GRE-EPI also generally identified a higher number of statistically significant correlations across the 25 atlas regions selected, however stronger correlations were found between Heschl's gyrus and the anterior and posterior cingulate as well as the anterior superior temporal gyrus. Since there is evidence that auditory networks are lateralised (Andoh et al., 2015), the right lateralisation of the connectivity with right Heschl's gyrus identified by Looping Star might indicate that Looping Star can reveal the inherent lateralisation due to the removal of acoustic noise. However, high correlations were also found in Looping Star between the seeds and the ventricles and white matter, which warrants further investigation of denoising parameters.

8.2.2 Impact of Global Regression and Spatial Smoothing on Resting-State Network Identification

8.2.2.1 Background

As seen in the previous section, Looping Star can identify two core resting-state networks and detect clear functional correlations between atlas seeds. There were also subtle differences between modalities that could link to the acoustic noise levels. To validate these findings, the impact of different smoothing levels on resting-state network identification was evaluated. Denoising is also a vital step in the pre-processing pipeline for resting-state analysis, and one of the common regressors applied globally (i.e. to the whole brain) in this step is that of the signal detected from white matter and CSF, though its use is widely debated (Chai et al., 2012; Power, 2017; Vos De Wael et al., 2017; Weissenbacher et al., 2009). As a result, the impact of white matter and CSF regression on the networks

detect by both modalities was also explored.

8.2.2.2 Methods

The same Looping Star and GRE-EPI data from the previous section was employed, and the same initial pre-processing steps were applied. The smoothing kernel in pre-processing with SPM-12 (FIL Methods Group, 2020) was also evaluated at 3 mm and 5 mm FWHM for both modalities. These smoothing thresholds were selected to avoid an unfair comparison with GRE-EPI, given that GRE-EPI was previously shown to lose substantial functional sensitivity at 0mm FWHM smoothing (Section 7.2).

In the denoising step in CONN (Whitfield-Gabrieli and Nieto-Castanon, 2012), the impact of excluding all regressors (i.e. removing motion) was explored. The impact of including only the WM and CSF as regressors on analysis was also evaluated. Linear detrending and modelling the effect of rest was retained as part of the denoising pipeline in both cases. The data were bandpass filtered after regression between 0.01 – 0.1 Hz and no de-spiking was applied.

In first level analysis, bivariate correlations were used investigating the seed-based connectivity with the posterior cingulate and right Heschl's gyri. For seed-to-voxel analysis, parametric statistics were employed (Worsley et al., 1996), with a two-sided uncorrected cluster-forming threshold of $p < 0.001$ (Woo et al., 2014; Worsley et al., 1996). Only clusters surviving cluster-level $p < 0.05$ were deemed significant, with the cluster-size p-FDR corrected. The spatial extent of the networks for both analyses was visually qualitatively compared.

8.2.2.3 Results

Figure 8.9 shows the posterior cingulate and right Heschl's gyrus connectivity maps for 3 mm and 5 mm smoothing thresholds, which increase in spatial extent and significance

with increasing smoothing for both modalities. The spatial extent of GRE-EPI for the posterior cingulate network is consistently higher than Looping Star across smoothing thresholds. On the other hand, the spatial extent of the correlations with Heschl's gyri is higher for Looping Star. Tables 8.5 - 8.6 present the statistical results at each smoothing threshold. This was expected, given the lower tSNR for Looping Star and the previous findings for the task-based analysis.

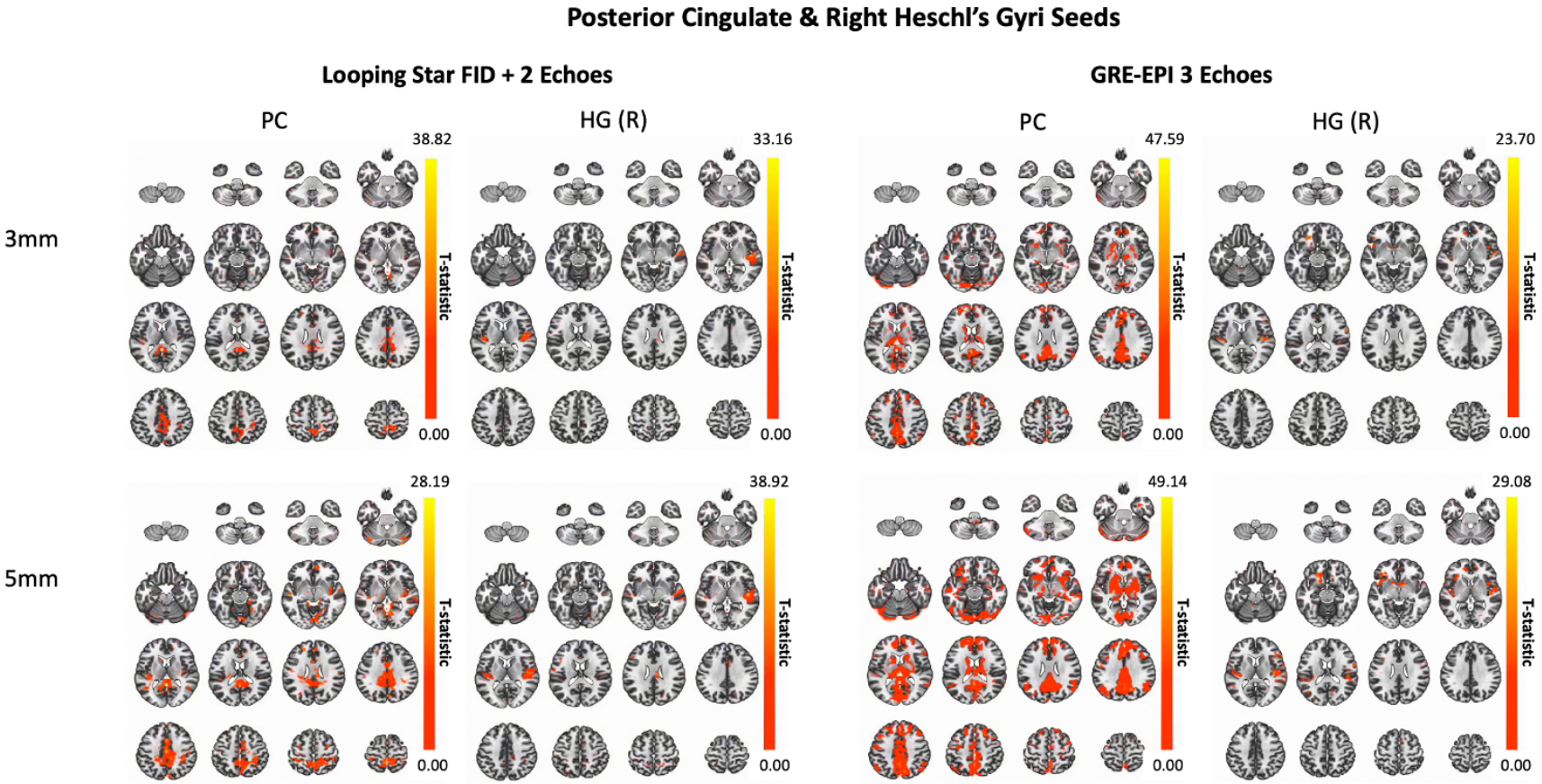

Figure 8.9: Posterior cingulate (PC) and right Heschl's gyrus (HG (R)) connectivity maps for each modality at different spatial smoothing thresholds.

Table 8.5: Statistical results for 3 mm smoothing of resting-state maps in CONN (Whitfield-Gabrieli and Nieto-Castanon, 2012), for seed-based connectivity with right Heschl's gyrus (HG (R)) and the posterior cingulate (PC).

Acquisition	**MNI Co-ordinates (x,y,z mm)**	**Brodmann Area**	**Cluster size p_{FWE}-value**	**Peak p_{FWE}-value**	**Cluster Size**
Looping Star, HG (R)	42 -16 4	41 (R)	$< 10^{-3}$ **	0.001 *	1599
	-46 -20 10	41 (L)	$< 10^{-3}$ **	0.194	502
GRE-EPI, HG (R)	42 -16 6	41 (R)	$< 10^{-3}$ **	0.014 *	1060
	-26 32 -12	47 (L)	$< 10^{-3}$ **	0.035 *	578
Looping Star, PC	-8 -40 24	23 (L)	$< 10^{-3}$ **	$< 10^{-3}$ **	9990
	36 -20 0	13 (R)	$< 10^{-3}$ **	0.044 *	486
GRE-EPI, PC	22 22 50	8 (R)	$< 10^{-3}$ **	$< 10^{-3}$ **	27146
	-52 -56 42	39 (L)	$< 10^{-3}$ **	0.145	1238

* = cluster-level p(FWE) < 0.05, ** = cluster-level p(FWE) < 0.001, N/A = outside of defined Brodmann Area

Table 8.6: Statistical results for 5 mm smoothing of resting-state maps in CONN (Whitfield-Gabrieli and Nieto-Castanon, 2012), for seed-based connectivity with right Heschl's gyrus (HG (R)) and the posterior cingulate (PC).

Acquisition	**MNI Co-ordinates (x,y,z mm)**	**Brodmann Area**	**Cluster size p_{FWE}-value**	**Peak p_{FWE}-value**	**Cluster Size**
Looping Star, HG (R)	46 -12 2	41 (R)	$< 10^{-3}$ **	$< 10^{-3}$ **	2555
	-46 -20 8	41 (L)	$< 10^{-3}$ **	0.008 *	1119
GRE-EPI, HG (R)	42 -16 6	41 (R)	$< 10^{-3}$ **	0.003 *	2703
	-22 32 -16	11 (L)	$< 10^{-3}$ **	0.012 *	2499
Looping Star, PC	20 -44 26	N/A	$< 10^{-3}$ **	0.004 *	22512
GRE-EPI, PC	12 -70 40	7 (R)	$< 10^{-3}$ **	$< 10^{-3}$ **	52607

* = cluster-level p(FWE) < 0.05, ** = cluster-level p(FWE) < 0.001, N/A = outside of defined Brodmann Area

The impact of excluding the motion regressors, therefore having no regressors included in analysis, was minimal for both modalities. However, white matter and CSF regression led to the removal of most of the resting-state correlations, relative to the previous analysis, for both modalities (Figure 8.10, Table 8.7). This suggests that the WM and CSF signals follow similar patterns to the grey matter correlations of interest, therefore alternative denoising strategies may be required in future work.

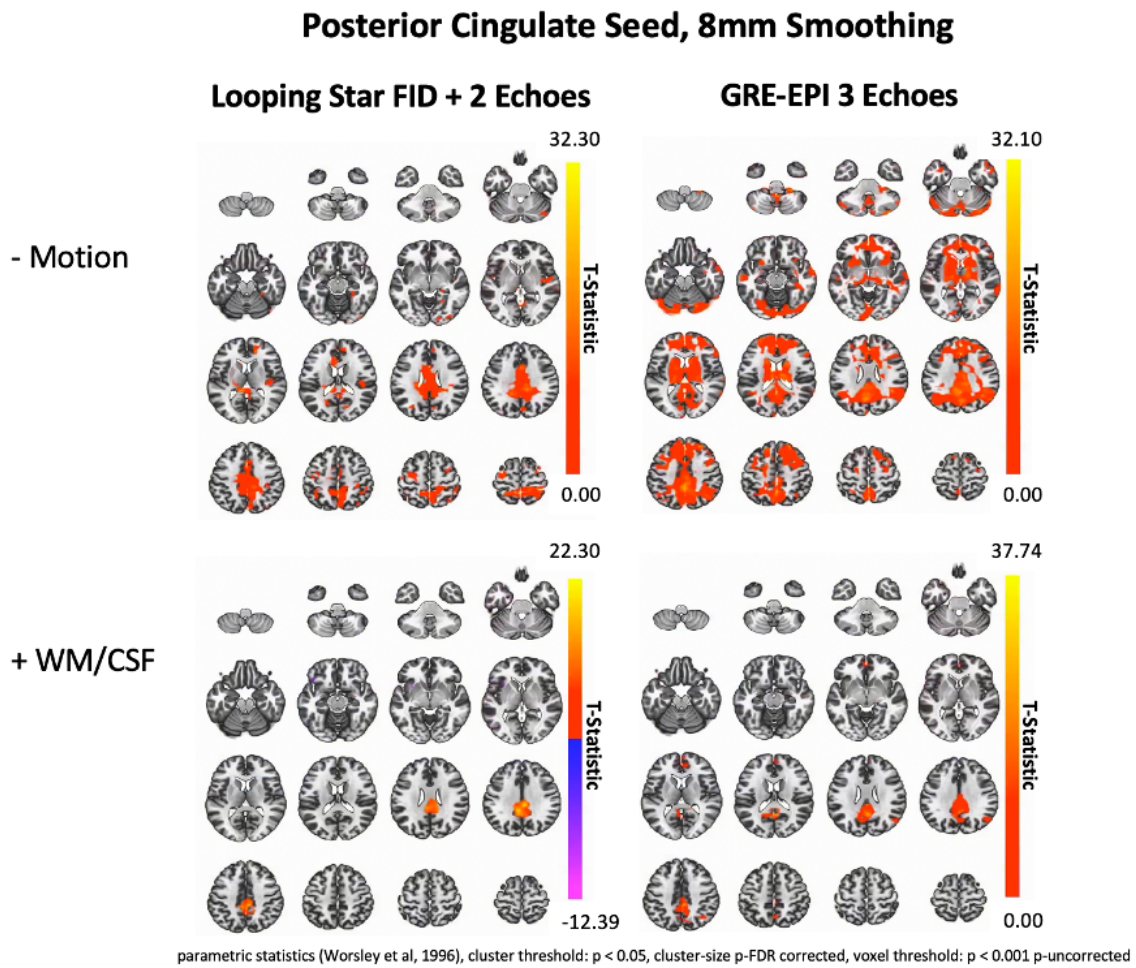

Figure 8.10: Exclusion of the motion regressors (top) and inclusion of the WM and CSF regressors (bottom) effect on the connectivity identified for the posterior cingulate seed

Table 8.7: Cluster-level statistical results for 8mm smoothing resting-state acquisitions with inclusion (+) and exclusion (-) of different regressors

Regressors	MNI Co-ordinates (x,y,z mm)	Brodmann Area	Cluster size p_{FWE}-value	Peak p_{FWE}-value	Cluster Size
Looping Star					
- Motion	-12 -36 16	N/A	$< 10^{-3}$ **	0.002 *	18652
+ WM/CSF	-8 -40 34	23 (L)	$< 10^{-3}$ **	0.022 *	2661
GRE-EPI					
- Motion	-8 -44 38	31 (L)	$< 10^{-3}$ **	0.002 *	62667
+ WM/CSF	2 -54 28	23 (R)	$< 10^{-3}$ **	$< 10^{-3}$ **	4264

* = cluster-level p(FWE) < 0.05, ** = cluster-level p(FWE) < 0.001, N/A = outside of defined

Brodmann Area

8.2.2.4 Discussion

These results indicate that different regressors and smoothing thresholds can affect the resultant resting-state networks, although this is not unique to Looping Star as it was also the case for GRE-EPI. Higher smoothing levels are preferred for both modalities to improve functional sensitivity, however alternative denoising strategies such as ICA may be preferred to WM or CSF global regression.

8.3 Identifying Independent Components with Looping Star

8.3.1 Introduction

The combination of principal and independent component analyses for noise detection is promising for strategically denoising multi-echo resting-state data (Kundu et al., 2017). This preliminary study involves qualitatively exploring the similarity of the spatial and temporal characteristics of independent components identified using the TE Dependent ANAlysis (TEDANA) software between Looping Star and GRE-EPI (tedana community et al., 2021). The frequency spectra of spatial components at single subject level was explored, as group level ICA methods only identify spatial patterns given that the time courses of participants will differ across subjects (Erhardt et al., 2011). The group level ICA spatial components identified in CONN were also investigated. The goal of this study was to identify components affiliated with physiological noise to determine whether denoising with TEDANA is feasible for Looping Star.

8.3.2 Methods

The GRE-EPI and Looping Star datasets described from the previous connectivity analysis were used, i.e. optimally-combined (Posse et al., 1999) FID + 2 echo Looping Star and 3-echo GRE-EPI resting-state acquisitions. The datasets were pre-processed as previously described in SPM-12 (FIL Methods Group, 2020) with an 8 mm FWHM spatial smoothing kernel. Group-level ICA was computed in CONN using voxel-to-voxel analysis with 15 components designated for G1 FastICA + GICA3 back-projection (Whitfield-Gabrieli and Nieto-Castanon, 2012). This terminology refers to the specific ICA algorithms employed. The number of 15 components was arbitrarily selected for group-level ICA though guided by the literature to avoiding over-fitting of noise (Correa et al., 2007; Griffanti et al., 2017; Li et al., 2007). Group-level ICA also included dimensionality reduction equal to 64 for each subject to reduce computational demand. The group ICA outputs for CONN include a spatial map of the components and a correlation plot of the identified components with 8 different resting-state networks.

To explore the frequency composition of identified components at single subject level, the independent components for one participant was extracted using the TEDANA software for both modalities (tedana community et al., 2021). TEDANA involves inputting each echo separately after realignment, and then computes optimal echo combination using the same T_2*-weighted combination method as applied previously (Posse et al., 1999). TEDANA outputs the frequency spectra and spatial component maps, which can then be used to guide denoising (tedana community et al., 2021). The TEDANA software includes a mono-exponential fit to the data for each voxel across the echoes, using log-linear regression to estimate T_2* and signal maps (tedana community et al., 2021).

As described by the software, principal component analysis is performed as part of the TEDANA pipeline using a moving average process Li et al. (2007), which reduces the dimensionality of the data by removing the least statistically significant principal components. This dimensionality reduction is performed to avoid overestimating the dimensions of the data, leading to overfitting, which would cause a poor ICA estimation

in the following step (Li et al., 2007; Ylipaavalniemi and Vigário, 2008). After PCA component estimation, ICA is then performed on the reduced dimensionality dataset.

For each voxel within each ICA component, the component time series were evaluated for TE-dependent signal changes (Kundu et al., 2012). This is determined by goodness of fit summary statistics based on the model for multi-echo data, as described in Section 1.10. The models for estimating BOLD changes (ΔR_2*) and noise changes (ΔS_0) are given as

$$\frac{\Delta S}{S} = \frac{\Delta S_0}{S_0} \tag{8.2}$$

$$\frac{\Delta S}{S} = -\Delta R_2^* \cdot TE \tag{8.3}$$

The goodness of fit statistics are computed separately for each sub-model, using a voxel-wise F-test that compares the residuals from the fit of a model with the null model (Kundu et al., 2012).

From these F-tests, summary statistics are produced: κ, which represents the goodness of fit to ΔR_2*, and ρ, representing goodness of fit to ΔS_0. A component with high κ and low ρ is considered to be BOLD-related (i.e. due to changes in neuronal activity), and vice versa if it is non-BOLD-related. Uncertain components are equivalent to low-variance components, where it is not possible to determine whether the signal is BOLD nor noise-related (Kundu et al., 2012).

Independent components can be rank-ordered based on their κ and ρ scores. A plot can be produced of the κ rank versus κ value and ρ rank versus ρ value for the range of identified components. In an ideal scenario, a clear "elbow" will exist in such plots, defining the point at which components have high or low scores for each and therefore being identified as noise-like or BOLD-like (Kundu et al., 2012).

8.3.3 Results

For the single subject, the κ and ρ rank plots can be seen for each modality in Figure 8.11. It can be seen that Looping Star has a slightly more apparent "elbow" in both plots (i.e. a clearer separation of ρ and κ), suggesting a clearer definition of BOLD versus non-BOLD components, relative to GRE-EPI.

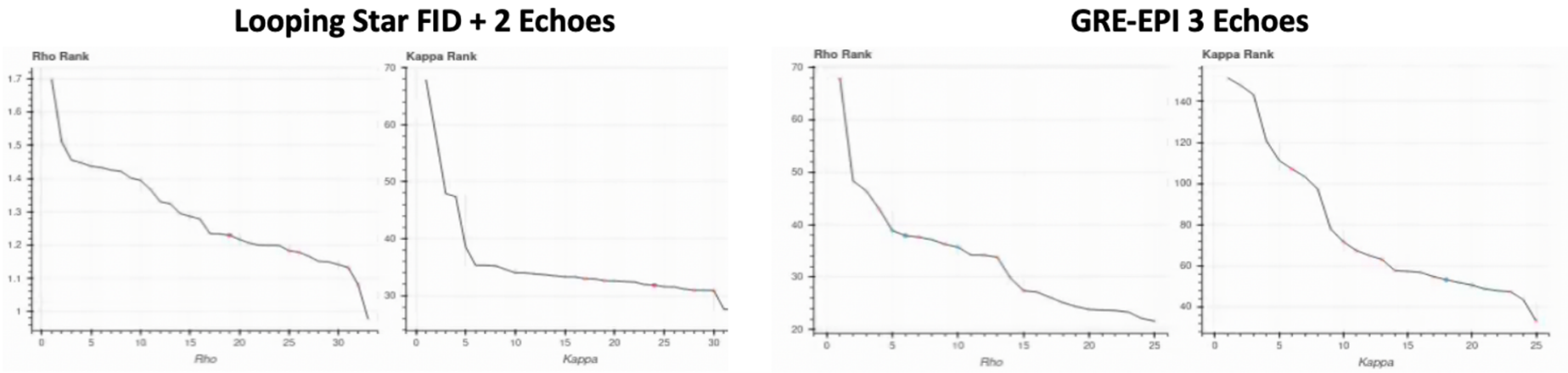

Figure 8.11: Kappa and rho goodness of fit statistic plots for the independent components identified in a single-subject with each modality. Produced by TEDANA (tedana community et al., 2021).

Exploring the components identified in more detail, the results of the single subject component analysis were grouped into spatially and temporally similar components, with behaviours including spiking, drifting, high frequency oscillation and pulsation, determined by eye based on the literature (Griffanti et al., 2017), as well as the components accepted as BOLD-like.

Firstly, drifting appears more prominently in GRE-EPI, with correlations primarily localised to the frontal cortex and edges of the brain. For Looping Star, the spatial distribution of these correlations is broad across the brain rather than localised. Drifting is likely related to scanner drift, and it could be of more benefit that this is present throughout the brain in Looping Star as it would be removed more generally rather than localised to a particular cortex (Figure 8.12).

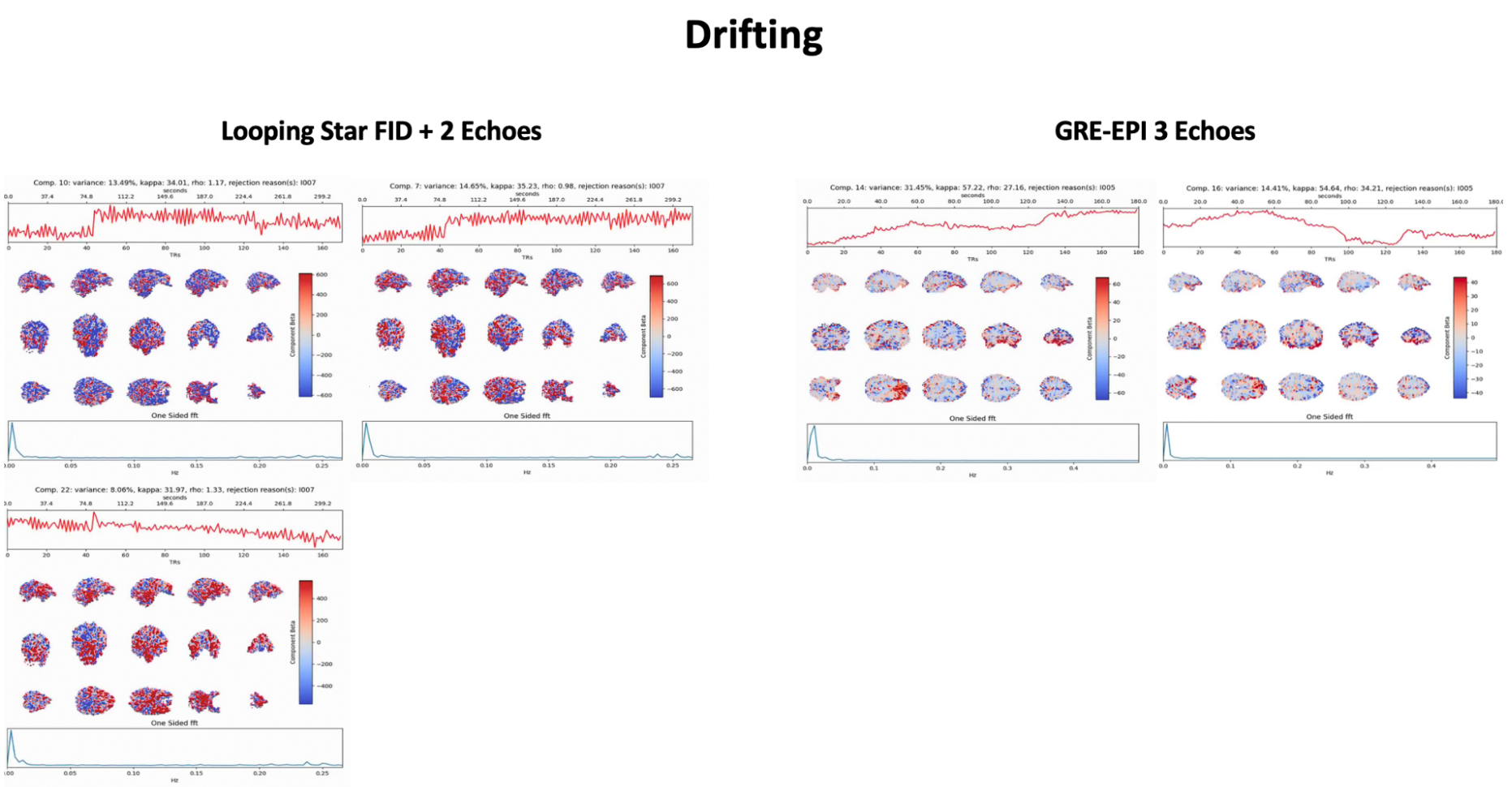

Figure 8.12: Identified independent components for Looping Star and GRE-EPI with temporal drifting behaviour. For each subfigure, (top) component time course, (middle) spatial distribution of component, and (bottom) one-sided fast fourier transform of time course. The accompanying scale shows the component beta. The variance, kappa and rho values are listed with each subfigure. Output from TEDANA (tedana community et al., 2021).

Spiking in the temporal signal has been affiliated with both motion and pulsing in the veins (Griffanti et al., 2017), with the spatial component aiding clarification between the two. It can be seen for GRE-EPI that the "downward" spiking is related to motion, whereas "upward" spiking is related to pulsing in the base of the brain. For Looping Star, predominantly "downward" spiking is seen, also localised to the base of the brain (Figure 8.13).

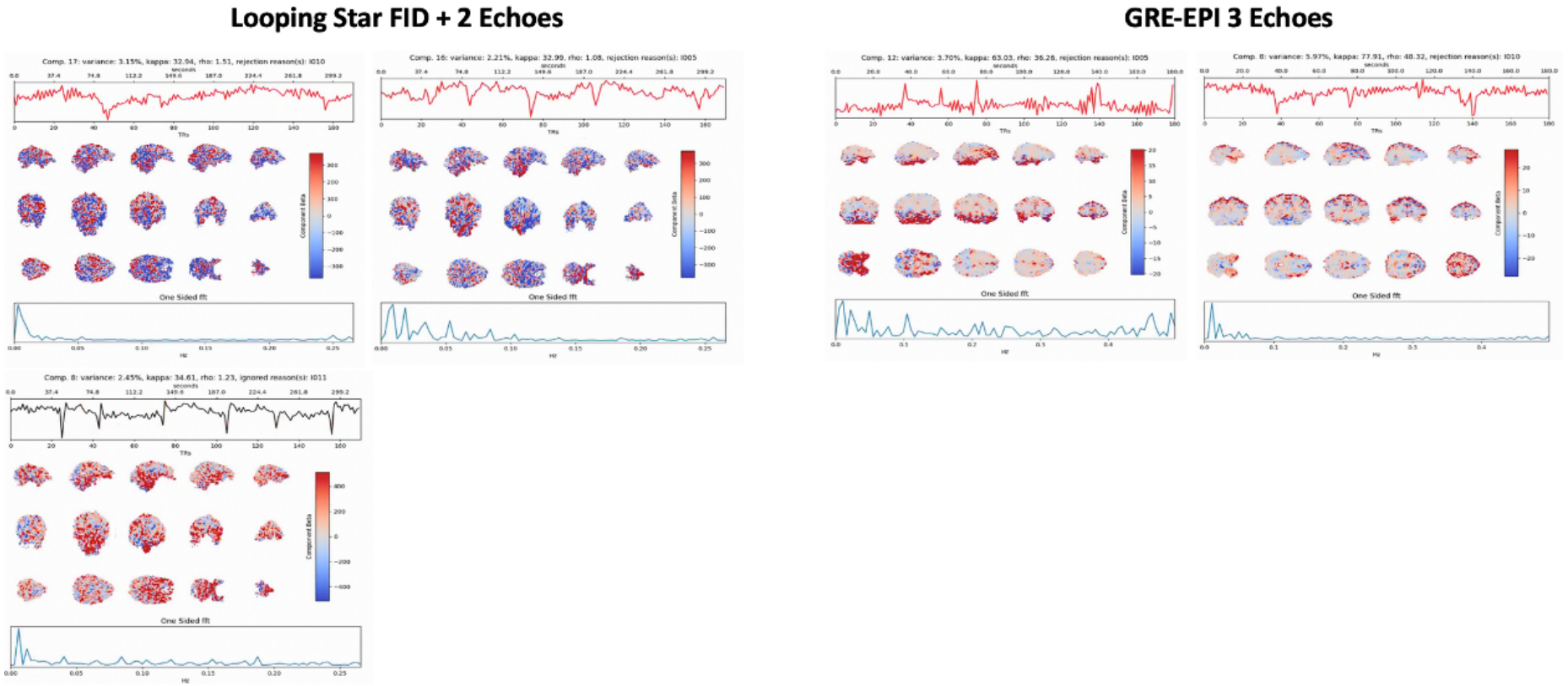

Figure 8.13: Identified independent components for Looping Star and GRE-EPI with spiking behaviour. For each subfigure, (top) component time course, (middle) spatial distribution of component, and (bottom) one-sided fast fourier transform of time course. The accompanying scale shows the component beta. The variance, kappa and rho values are listed with each subfigure. Output from TEDANA (tedana community et al., 2021).

Pulsating behaviour can be seen clearly in the ventricles and base of the brain for GRE-EPI, whereas it manifests more spatially widespread in Looping Star (Figure 8.14).

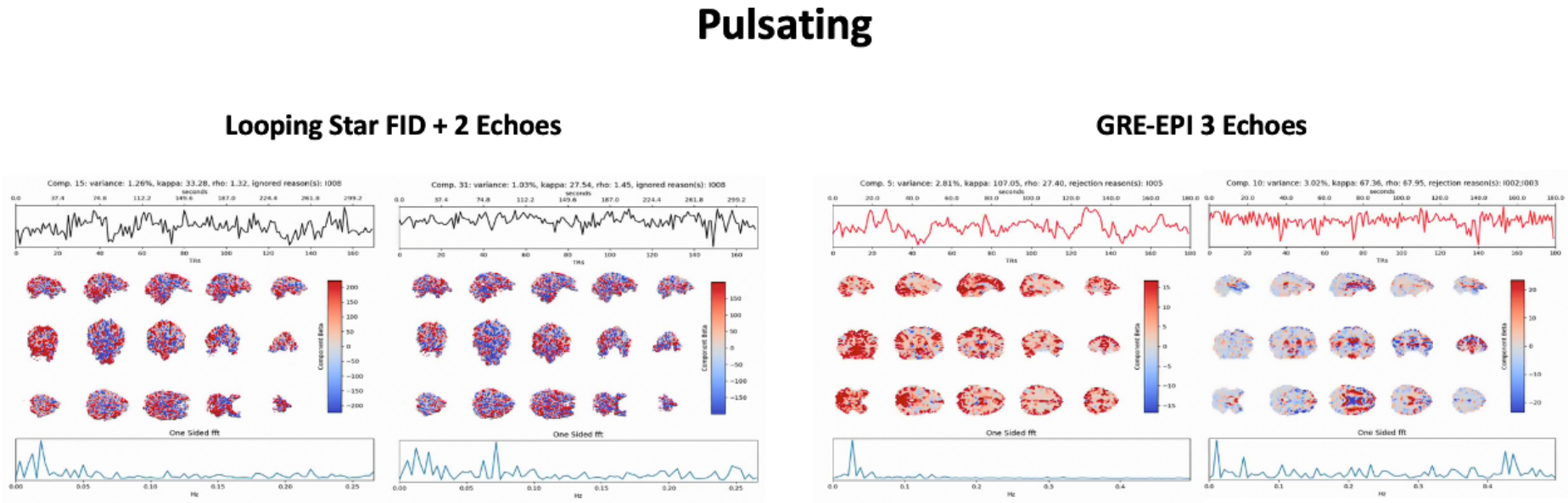

Figure 8.14: Identified independent components for Looping Star and GRE-EPI with pulsating behaviour. For each subfigure, (top) component time course, (middle) spatial distribution of component, and (bottom) one-sided fast fourier transform of time course. The accompanying scale shows the component beta. The variance, kappa and rho values are listed with each subfigure. Output from TEDANA (tedana community et al., 2021).

High frequency oscillation appears very specifically localised for GRE-EPI, but spatially very broad and high amplitude spatial characteristics for Looping Star (Figure 8.15).

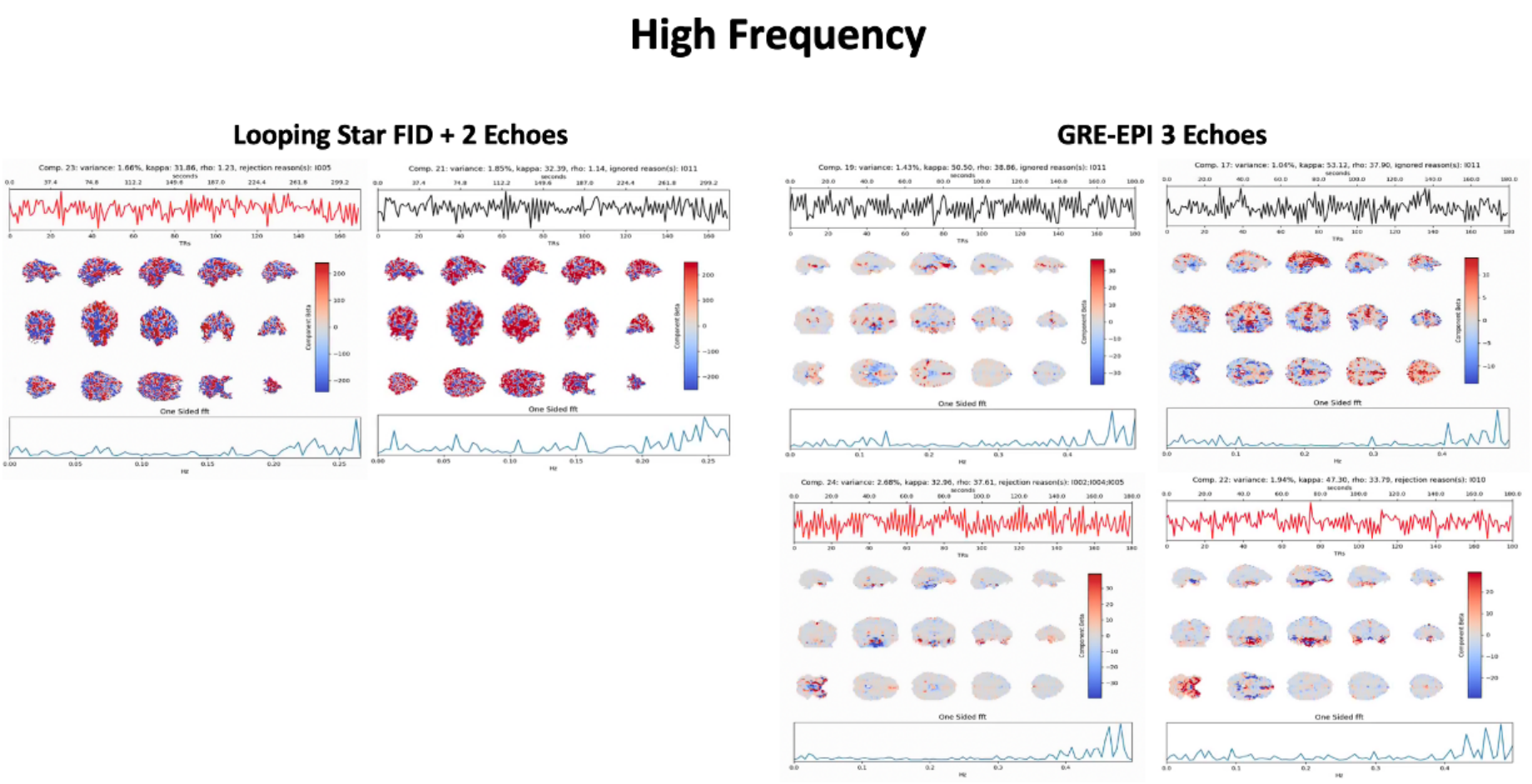

Figure 8.15: Identified independent components for Looping Star and GRE-EPI with high frequency behaviour. For each subfigure, (top) component time course, (middle) spatial distribution of component, and (bottom) one-sided fast fourier transform of time course. The accompanying scale shows the component beta. The variance, kappa and rho values are listed with each subfigure. Output from TEDANA (tedana community et al., 2021).

The accepted components for GRE-EPI and Looping Star both demonstrate a clear default mode network contribution, however once again there was also more spatial localisation for GRE-EPI relative to Looping Star (Figure 8.16).

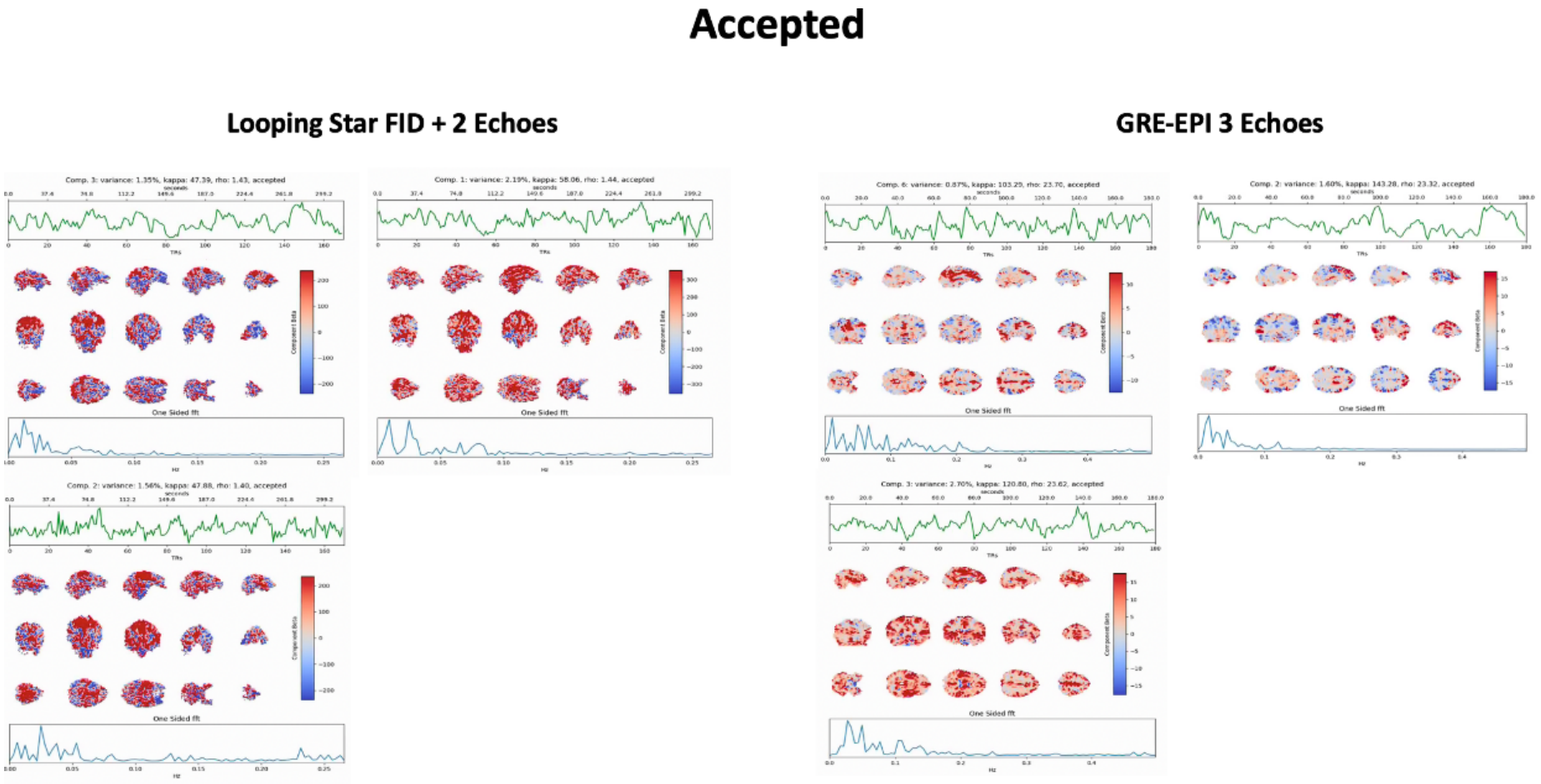

Figure 8.16: Identified independent components for Looping Star and GRE-EPI with BOLD-related behaviour. For each subfigure, (top) component time course, (middle) spatial distribution of component, and (bottom) one-sided fast fourier transform of time course. The accompanying scale shows the component beta. The variance, kappa and rho values are listed with each subfigure. Output from TEDANA (tedana community et al., 2021).

Finally, the group level ICA maps for GRE-EPI demonstrated higher spatial correlation values with the eight resting-state networks than Looping Star. However, Looping Star components had a higher number of components with spatial correlations that were low in value compared with GRE-EPI. This could be a result of the broad spatial distribution of noise sources seen in the previous figures (Figure 8.17).

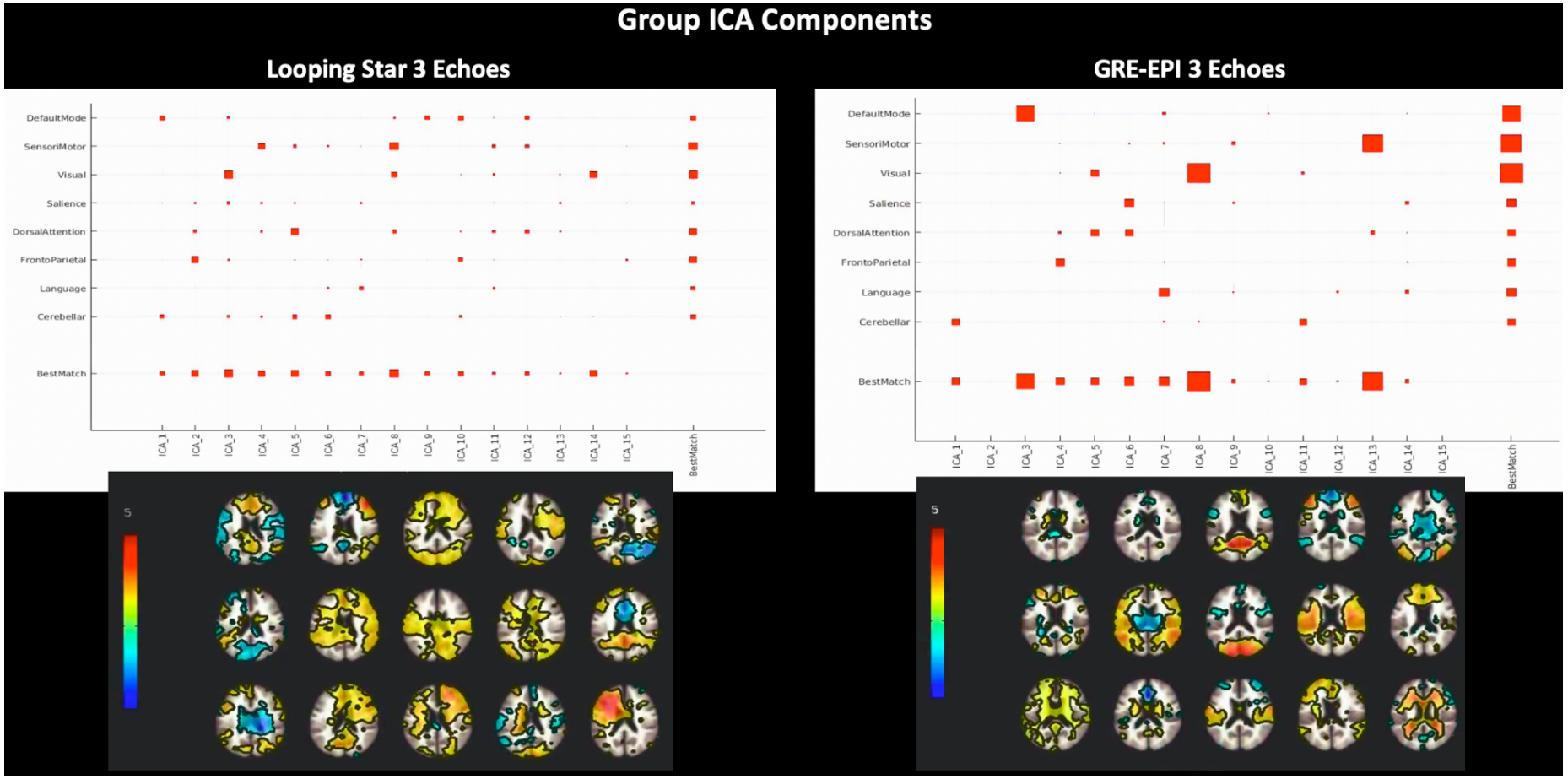

Figure 8.17: Group ICA outputs from CONN (Whitfield-Gabrieli and Nieto-Castanon, 2012) for each modality. (top) Spatial correlation coefficient of each component with eight resting-state networks, (bottom) spatial maps of independent components combined onto a single image, thresholded at component T-score = 1 with corresponding scale.

8.3.4 Discussion

Looping Star and GRE-EPI identified some temporally and spatially similar physiological components at single-subject level, however there were also entirely different spatial characteristics of the components that may link to the sampling pattern of Looping Star. For example, as mentioned previously, motion appears as general image blur and therefore this may be one explanation for why motion-related components are not seen with spatial localisation around the skull, typically seen in GRE-EPI. On the other hand, motion was found to be low across participants in the previous study and its exclusion from regression did not have a large affect on seed-based correlations; hence these signals could originate from other non-BOLD-related processes. In general, GRE-EPI located very spatially specific components, whereas Looping Star components were overall more spatially broad.

This study indicates that Looping Star may be more sensitive to particular noise characteristics, given that the four characteristics explored in this section were predominant across the brain. It was clear that the components were noise-related as the temporal characteristics between modalities were similar. This highlights that how these characteristics manifest should be carefully considered to accurately manually identify component sources, as removal of the more broadly spatially contributing components could lead to substantial removal of the desired functional signal. One approach in future could be to accurately retrieve the physiological measures and explore their correlation with the temporal signals of resting-state fMRI with Looping Star (Chen et al., 2020a; Chu et al., 2018).

In terms of group ICA, it was clear that the identified components were weakly correlated with the resting-state networks for Looping Star compared with GRE-EPI. This was expected given the lower tSNR of Looping Star, further indicating that it may benefit from additional denoising to better resolve the networks.

8.4 Chapter Discussion

Looping Star could extract the default mode and auditory networks from seed-based analyses, though with fewer significant ROI-to-ROI correlations identified across a range of atlas nodes. This could be due to the lower tSNR of Looping Star in this study, and denoising or advanced image reconstruction approaches could be explored to address this. Furthermore, the spatial characteristics of distinct noise-related components overlapped substantially, which could further affect the sensitivity of Looping Star to functional networks. Alternatively, this could be linked to the acoustic noise reduction of Looping Star as resting-state networks have demonstrated dependence on background acoustic noise (Andoh et al., 2017; Damoiseaux et al., 2006; Dionisio-Parra et al., 2020; Gaab et al., 2008; Gonzalez-Castillo et al., 2016), therefore further study is required.

Similarities were found in the temporal characteristics of physiological noise for Looping Star relative to GRE-EPI for a single subject. However, it was also found that the spatial characteristics of the noise differed substantially, likely due to the 3D radial sampling of Looping Star causing more image blur and therefore widespread spatial noise. This likely also contributes to the weaker correlation of group level ICA components with resting-state networks, as the spatial characteristics of components across the group will differ. It would be vital to explore the degree of denoising with ICA that can be applied without removing significant functional signals in future, particularly including accurate measures of physiology to better characterise Looping Star signal characteristics (Murphy et al., 2013). New directions in resting-state fMRI include novel analysis approaches that could be applied with Looping Star (Yang et al., 2020).

Chapter 9

In vivo Characterisation of Looping Star: Event-related Auditory Oddball Paradigm

Summary

This chapter includes:

- A peer-reviewed publication comparing Looping Star and GRE-EPI using an auditory oddball paradigm that I first-authored.
- The supplementary material for said publication.
- Expanded analysis and commentary on the publication.

Overview

The first part of this chapter incorporates a published peer-reviewed journal article (Damestani et al., 2021b), and is the exact copy of the publication. The title of the publication is "Revealing the mechanisms behind novel auditory stimuli discrimination: An evaluation of silent functional MRI using Looping Star." published by the journal "Human Brain Mapping" by Wiley Periodicals LLC, in which I, Nikou Louise Damestani, am listed as the first author. The full DOI for the article is doi.org/10.1002/hbm.25407.

I was the primary author of this publication, writing the first draft independently, and I declare this article as my own work. The full details of contributions by myself and my co-authors are listed in the following CRediT (Contributor Roles Taxonomy) authorship contribution statement (https://www.elsevier.com/authors/policies-and-guidelines/credit-author-statement):

Nikou Louise Damestani: Conceptualisation, Methodology, Software, Formal Analysis, Writing - Original Draft, Writing - Review & Editing, Project Administration, Visualisation, Data Curation, Investigation, Validation

Dr. Owen O'Daly: Methodology, Resources, Validation, Writing - Review & Editing

Dr. Ana Beatriz Solana: Methodology, Software, Resources, Writing - Review & Editing

Dr. Florian Wiesinger: Methodology, Software, Resources, Writing - Review & Editing

Dr. David John Lythgoe: Supervision, Conceptualisation, Writing - Review & Editing

Simon Hill: Software, Resources

Alfonso de la Rubio: Software, Resources

Dr. Elena Makovac: Resources, Writing - Review & Editing

Prof. Steven Charles Rees Williams: Funding acquisition, Writing - Review & Editing

Dr. Fernando Zelaya: Conceptualisation, Funding acquisition, Supervision, Writing - Review & Editing

The material in the content of the publication, i.e. Section 9.2, has not been changed. I have only added content around the paper for the purpose of contextualising its presence in the thesis, and the formatting was adapted in order to embed the publication so as to match the formatting of the rest of this thesis. Specifically, I include a chapter introduction, a section of expanded commentary and analysis after the section including

the publication, and chapter discussion.

9.1 Chapter Introduction

Looping Star has demonstrated good sensitivity to block design paradigms and can identify the resting-state networks in vivo (Sections 7.2, 7.3, 8.1). This chapter therefore focuses on an auditory paradigm with higher cognitive demand, the auditory oddball task, as we expect that Looping Star will be used for such studies in future. The functional sensitivity of Looping Star to this task was evaluated compared with GRE-EPI. The paradigm design and acquisition parameters for GRE-EPI were replicated from a previous study for validity. The paradigm was repeated by the same participants in a second session to evaluate the reliability of Looping Star. Further details on the background of this study are provided in the manuscript. Some expanded analysis at the end of this section to further support the content of the publication. The next section constitutes of the manuscript (Section 9.2).

9.2 Revealing the Mechanisms behind Novel Auditory Stimuli Discrimination: An Evaluation of Silent Functional MRI using Looping Star

9.2.1 Abstract

Looping Star is a near-silent, multi-echo, 3D functional magnetic resonance imaging (fMRI) technique. It reduces acoustic noise by at least 25dBA, with respect to gradient-recalled echo echo-planar imaging (GRE-EPI)-based fMRI. Looping Star has successfully demonstrated sensitivity to the cerebral blood-oxygen-level-dependent (BOLD) response during block design paradigms but has not been applied to event-related auditory perception tasks. Demonstrating Looping Star's sensitivity to such tasks could 1) provide new

insights into auditory processing studies, 2) minimise the need for invasive ear protection, and 3) facilitate the translation of numerous fMRI studies to investigations in sound-averse patients. We aimed to demonstrate, for the first time, that multi-echo Looping Star has sufficient sensitivity to the BOLD response, compared to that of GRE-EPI, during a well-established event-related auditory discrimination paradigm: the "oddball" task. We also present the first quantitative evaluation of Looping Star's test-retest reliability using the intra-class correlation coefficient. Twelve participants were scanned using single-echo GRE-EPI and multi-echo Looping Star fMRI in two sessions. Random-effects analyses were performed, evaluating the overall response to tones and differential tone recognition, and inter-modality analyses were computed. We found that multi-echo Looping Star exhibited consistent sensitivity to auditory stimulation relative to GRE-EPI. However, Looping Star demonstrated lower test-retest reliability in comparison with GRE-EPI. This could reflect differences in functional sensitivity between the techniques, though further study is necessary with additional cognitive paradigms as varying cognitive strategies between sessions may arise from elimination of acoustic scanner noise.

9.2.2 Introduction

The inherent acoustic noise of conventional functional magnetic resonance imaging (fMRI), carried out using gradient-recalled echo echo-planar imaging (GRE-EPI), is often intolerably high, commonly achieving sound levels greater than 100dBA (Price et al., 2001; Ravicz et al., 2000). At these levels, severe hearing damage can occur without ear protection. During GRE-EPI, this acoustic noise originates primarily from the rapid switching of the frequency encoding magnetic field gradient (from near maximum negative to near maximum positive and vice-versa), necessary for fast two-dimensional slice-by-slice imaging. This switching induces high-frequency mechanical vibrations in the scanner hardware, which fall within the acoustic spectrum (Price et al., 2001).

This high acoustic scanner noise impacts the interpretation of the mechanisms behind auditory processing in fMRI studies. For example, Yakunina et al. (2015) showed that the auditory connectivity network differed during a music listening task when a

quieter, sparse-sampling fMRI acquisition technique was used, in comparison with using conventional, noisy, continuous acquisition. Langers et al. (2005b) also showed the influence of background scanner noise on the haemodynamic response during auditory tone presentation, using a variable-length silent gap fMRI acquisition method. Moreover, Gaab et al. (2007a) demonstrated the masking effect of scanner background noise on blood-oxygen-level-dependent (BOLD) signal in response to word stimuli. The impact of acoustic scanner noise on auditory processes has been supported by further studies Healy et al. (2007); Scarff et al. (2004); Shah et al. (1999).

Background scanner noise can also impose limitations to the generalisability of studies across numerous cohorts. For example, conditions such as tinnitus can include symptoms of hypersensitivity to sound (or hyperacusis) (Baguley, 2003; Chen et al., 2015). fMRI studies have been performed with this cohort, however participants with hyperacusis are often excluded (Araneda et al., 2018; Golm et al., 2013; Han et al., 2018; Hofmeier et al., 2018; Leaver et al., 2011) and in some instances there is difficulty in disentangling whether activity patterns result from the stimulus or the acoustic scanner noise Ghazaleh et al. (2017); Gu et al. (2010); Husain and Schmidt (2014); Lanting et al. (2009); Leaver et al. (2016); Seydell-Greenwald et al. (2012). Given that hyperacusis is also heterogeneously prevalent in further cohorts, such as in individuals with autism spectrum disorder (Stiegler and Davis, 2010) and in children (Rosing et al., 2016), mitigating background scanner acoustic noise could greatly improve standardisation across numerous clinical groups.

To date, conventional methods for addressing this high acoustic scanner noise have revolved around the retention of GRE-EPI acquisition sequences, due to their functional sensitivity and spatiotemporal resolution. One example of this was presented by (Seifritz et al., 2006), where they tuned the GRE-EPI pulse sequence to alter the characteristics of the acoustic noise, but the noise amplitude remained comparable to conventional GRE-EPI. The primary strategy is to ask participants to employ earplugs during scanning, however effective sound attenuation relies on their correct application, hence there remains a risk of hearing damage (Salvi and Sheppard, 2018; Sheppard et al., 2018). Alternative strategies for scanner acoustic noise reduction involve adapting the GRE-EPI pulse sequence, for example via band-limited gradient pulses (Hennel et al., 1999) and

sparse temporal sampling (Hall et al., 1999). A number of early scanner noise reduction techniques were reviewed by Moelker and Pattynama (2003). Hardware improvements have also been explored, such as gradient coil isolation (Edelstein et al., 2002), and there has recently been increased use of active noise-cancelling headphones (Dewey et al., 2018; Gabrielsen et al., 2018), although these strategies can be financially costly and therefore not widely applicable across studies. Ultimately, there is no specific optimal workflow or acquisition technique applicable across sites and paradigms to reduce the potential confound and limitations of acoustic scanner noise at its source.

To address these issues, we present the application of a recently developed silent pulse sequence known as Looping Star (Wiesinger et al., 2019). This technique could mitigate the need for earplugs, improve accessibility to the scanning environment and remove the acoustic noise confound. Looping Star (LS) is based on a technique known as Rotating Ultra-Fast Imaging Sequence (RUFIS) (Madio and Lowe, 1995), which reduces the effect of vibrations induced by gradient switching by making small incremental changes in the direction (but not the amplitude) of the frequency encoding gradients of the readout. Looping Star is a modification of RUFIS in which a temporal-multiplexed gradient refocusing mechanism is employed (Wiesinger et al., 2019), allowing the transverse component of the magnetisation to evolve by returning periodically to the centre of k-space. As a result, it remains sensitive to static T2* dephasing as in GRE-EPI and can achieve multi-echo acquisition without the need for magnetisation preparation pulses (Solana et al., 2016). A detailed description of the Looping Star methodology can be found in Wiesinger et al. (2019).

To date, Looping Star has proven sensitive to the BOLD response evoked by periodic blocks of sensory stimuli (Damestani et al., 2019b; Wiesinger et al., 2019), visual working memory (Dionisio-Parra et al., 2020) and in the 'resting' state (Damestani et al., 2019a; Dionisio-Parra et al., 2020). However, Looping Star has not been evaluated using event-related fMRI paradigms, including those of an auditory nature, which are able to probe aspects of cognition in a manner not possible using block-designs. One such paradigm is the active "oddball" task (Squires et al., 1975), an important auditory discrimination paradigm that has been used extensively in several studies using both EEG (Barry et al.,

2000; Justen and Herbert, 2018; Wronka et al., 2008) and fMRI (Brázdil et al., 2005; Mangalathu-Arumana et al., 2012). It is particularly relevant in the study of cognitive deficits in participants with Autism Spectrum Disorder (ASD), as these individuals have shown reduced performance during similar tasks when compared with healthy controls (Dawson et al., 1986, 1988; Oades et al., 1988).

Importantly, a previous study also highlighted that alternative cognitive strategies were employed by children with ASD during an auditory "oddball" tone discrimination fMRI task (Gomot et al., 2006). This study used an adapted slice-onset version of conventional GRE-EPI to account for the acoustic noise limitations. The characterisation of responses to this task using Looping Star, in comparison with this adapted GRE-EPI acquisition, therefore has clear advantages with respect to its translation to studies involving individuals with ASD, as Looping Star would remove the acoustic noise confound. Demonstrating comparable test-retest reliability of Looping Star would further facilitate this translation. Furthermore, the multi-echo capabilities of Looping Star are worthy of investigation, given the benefits of echo combination to BOLD signal noise reduction (Kundu et al., 2012). These have not yet been evaluated for Looping Star using an event-related paradigm design.

Hence, our specific aims were:

1. To investigate whether multi-echo Looping Star is sensitive to the BOLD response elicited during the auditory "oddball" paradigm.

2. To quantitively compare the functional sensitivity of Looping Star with that of the adapted slice-onset single-echo GRE-EPI acquisition used in the original auditory tone discrimination study (Gomot et al., 2006).

3. To explore the test-retest reliability of the Looping Star and GRE-EPI acquisitions using two sessions.

We performed the following analyses to address the aims: a) group-level conventional

parametric general linear model (GLM) analyses b) inter-modality sensitivity comparisons using percentage signal change and parameter estimates and c) test-retest reliability analysis using intra-class correlation coefficients (ICC) for each modality between sessions.

9.2.3 Methods

9.2.3.1 Data Availability Statement

The scripts and toolboxes used in this research are available to download via the accompanying references. Please contact the corresponding author for access to specific scripts and data access, if collaboration is of interest.

9.2.3.2 Participants

Twelve healthy participants (6 female; mean $\pm$ standard deviation age = 31.5 $\pm$ 8.0 years; range = 25 years - 54 years) were scanned in two sessions. This number of participants was consistent with that of the healthy control group in the aforementioned study using the same paradigm (Gomot et al., 2006). These sessions were separated by at least one week and were no more than two weeks apart. All participants took part in both scanning sessions and for the full duration of both sessions. Exclusion criteria involved standard MRI contra-indications and participants were recruited from within the university (King's College London). Ethical approval was provided under London – Camberwell St Giles REC reference 04/Q0706/72, and informed written consent was obtained from all participants.

9.2.3.3 Oddball Paradigm

For consistency with Gomot et al. (2006), we decided to employ a paradigm with a design identical to that used in their study. The stimuli were presented through the pneumatic MR-compatible headphones (MR Confon, Cambridge Research Systems). The paradigm involved three tone types (P = probability of occurrence), Deviant (P = 0.09), Novel (P = 0.07) and Standard (P = 0.84), played with event duration 80ms and inter-stimulus interval 625ms. Deviant tones were simply frequency-shifted Standard tones, whereas Novel tones were completely Novel (in terms of pitch and frequency) relative to Standard and Deviant tones (Müller et al., 2002). The beginning of the paradigm was silent for a duration of ten volumes, then five Standard tones were played. After this, Novel and Deviant tones were played in random order with a minimum of three Standard tones between onsets.

Participants indicated with a button-box, in the right hand, when either a Deviant or Novel tone was detected, using the same button for both tones. Six silent rest blocks of 10-second duration were evenly distributed throughout the paradigm; and a video of neutral visual distractors, involving animals in natural habitats, was played throughout the paradigm as performed in the original study (Gomot et al., 2006). Deviant and Standard tones were swapped halfway through, as indicated by a screen displaying the command "Swap", whereby Standard tones became Deviant tones and vice versa, to prevent tone habituation and boredom. Although the Deviant and Standard tones were consistently the same tones when applied, the Novel tones differed for every onset. For further information on the paradigm and characteristics of the tones, we point towards the original study by Gomot et al. (2006), who kindly provided help with the implementation of the paradigm.

Participants' comprehension of the paradigm and hearing ability were tested outside of the scanning facility prior to the first session using a shorter version of the paradigm of frequency-shifted tones Standard and Deviant tones, to avoid conditioning effects. These tones were frequency-shifted by three semitones down from the original tone using

version 2.2.2. of the Audacity ®recording and editing software (Audacity Team, 2020). Within the scanning sessions, earplugs were provided beneath pneumatic MR-compatible headphones (MR Confon, Cambridge Research Systems). This was to prevent hearing damage during the loud GRE-EPI acquisition.

Participants self-reported whether they could hear stimuli presented through the pneumatic MR-compatible headphones based on whether they could clearly hear the voices of the radiographers through the headphones. The paradigm was then also played through these headphones. To avoid conditioning effects within the session, the tone order in the paradigm differed between Looping Star and GRE-EPI acquisitions (i.e. a unique paradigm was assigned to each modality, but not to each session nor each participant). Otherwise, the same paradigms were used for all participants and for both sessions. Participant responses were also monitored via a paradigm-linked computer to ensure they could consistently hear the paradigm.

9.2.3.4 fMRI Acquisition

Participants wore a pulse oximeter on their forefinger and respiratory belt around their waist to probe any possible differences in physiological parameters (heart rate and respiration rate). A 3T General Electric MR750 Discovery scanner (GE Healthcare, Chicago, IL) with a General Electric 12-channel receive-only head coil was used. A standard ADNI (Leung et al., 2015) 1.09 mm in-plane resolution structural IR-SPGR image was collected with acquisition parameters: TE = 3.016 ms, TR = 7.312 ms; TI = 400 ms, number of slices = 196, slice-gap = 1.2 mm, flip-angle = 11°.

For the fMRI modalities, the same acquisition parameters were used between sessions, and sequence order was pseudo-randomised between participants and sessions. Acquisition parameters for single-echo GRE-EPI were as follows: TE = 27.5 ms, TR = 2.5 s; slice thickness = 4 mm, number of slices = 20, slice-gap = 1 mm, in-plane resolution = 3.125 mm, flip-angle = 82°, 240 volumes, duration = 10 minutes. As in the case of the study of Gomot et al. (2006), our tone duration (80 ms) and the inter-trial time of 625

ms, ensured that the stimuli were audible in the time gap between slice read-outs of the multi-slice GRE-EPI scans. The field of view for the GRE-EPI acquisition did not cover the cerebellum.

To ensure k-space sampling uniformity in Looping Star, a pseudo-randomly ordered trajectory was applied (Dionisio-Parra et al., 2020; Wiesinger et al., 2019). The trajectory was calculated for a nominal spatial resolution of 3.2mm, including an acceleration factor to produce comparable TR with GRE-EPI (see Supplementary Material 9.3.1). This acceleration factor introduces blurring, reducing the effective resolution of the images (Maier et al., 2021), however this pattern is sufficient for fMRI as the centre of k-space is densely sampled (Kasper et al., 2014). This highlights a benefit of radial acquisition, as other artefacts typical of Cartesian under-sampling are not introduced.

As a result, the multi-echo Looping Star acquisition parameters were as follows: multi-echo TEs = 0 ms, 16.1 ms, 32.2 ms, TR = 2.648 s, equivalent spatial resolution = 3.2 mm, flip-angle = 3°, readout bandwidth = ±46.875 kHz, 24 spokes per loop, 72 spokes per segment, 1080 spokes per volume, 240 volumes, duration = 10 minutes 35 s. For reconstruction of the FID image (TE = 0 ms), missing centre of k-space samples due to the dead-time of the receiver were reacquired at the end of the scan by repeating the Looping Star k-space trajectory at reduced readout gradient amplitude, as described by (Wu et al., 2007) and Wiesinger et al. (2016), Wiesinger et al. (2019).

9.2.3.5 fMRI Pre-processing

Image reconstruction for Looping Star was conducted offline using a 'nearest-neighbour gridding' approach (Wiesinger et al., 2019), as the fast Fourier transform cannot be applied directly to non-Cartesian data. This included density compensation to account for oversampling of the centre of k-space (Hoge et al., 1997). Furthermore, an inherent property of Looping Star is that the signal from the spoke dephasing outwards is contaminated by the signal from the spoke refocusing inward. This is known as echo-in/echo-out interference (Wiesinger et al., 2019). Dionisio-Parra et al. (2020) demonstrated that

addressing this interference by applying a Fermi filter reduced the image resolution, and RF phase-cycling doubled acquisition time. Instead, optimal combination of the echoes was used to improve the temporal signal-to-noise ratio (tSNR) (Kundu et al., 2012).

After reconstruction, the first ten volumes were removed for both modalities to avoid the influence of effects due to non-steady state magnetisation. Looping Star images were rescaled by a factor of 105 post-reconstruction to avoid intensity capping. Looping Star images were cropped using the FSL (Jenkinson et al., 2012) command "fslroi" and re-oriented using SPM-12 (`fil.ion.ucl.ac.uk/spm/`). The origins were centred for the FID and echo images to lie on the anterior commissure. Looping Star and GRE-EPI pre-processing pipelines were almost identical: for single-echoes they followed the same pipeline, with Looping Star excluding slice-timing correction since it is a three-dimensional acquisition technique. For Looping Star, optimal echo-combination was included in the pipeline but TE-dependent denoising (DuPre et al., 2019; Kundu et al., 2012) was not applied to Looping Star to ensure consistency of the pre-processing pipelines between modalities. The pipelines are visualised in Supplementary Material 9.3.2, with further detail provided below.

Looping Star images were bias-field corrected with ANTS N4-ITK (Tustison et al., 2010). The high tSNR FID image was used to estimate the motion correction parameters, which were then applied to the multi-echo image time series. High frequency artefacts were removed from all of the time series, and concatenation of the FID and echoes was performed in the z-direction using AFNI (Cox, 1996). Optimal echo combination was applied using the "opt _com" command from "tedana.py" in the MEICA (Kundu et al., 2012) pipeline. The pipeline then continued with co-registration of the FID to the subject's own high-resolution T1-weighted scan, which was then applied to the optimally combined dataset, spatial normalisation using unified segmentation (as implemented in SPM-12) with images saved at 4mm isotropic resolution and smoothing with an 8 mm FWHM kernel. This smoothing kernel was used to ensure adequate signal-to-noise ratio for the Looping Star dataset and as a compromise between the minimum identifiable cluster size and satisfying the Gaussian random field approximation.

Following the same bias-field correction, the same standard SPM-12 pre-processing pipeline was applied adjusted for GRE-EPI, including slice-timing correction, co-registration to the subject high-resolution T1-weighted scan, spatial normalisation using unified segmentation (as implemented in SPM-12) with images normalised at 4mm isotropic resolution and smoothing with an 8 mm FWHM kernel.

9.2.3.6 fMRI Analysis - Group Level SPM

Single-subject fixed-effects and group-level random-effects analyses were conducted in SPM-12 with cluster-level inference using a primary uncorrected cluster-forming threshold of $p < 0.001$ (Woo et al., 2014; Worsley et al., 1996). Only results surviving family-wise error correction based on cluster extent (i.e. cluster-level $p(FWE) < 0.05$) were deemed significant. The baseline condition (Standard tones) was not modelled explicitly to avoid over-parameterisation of the general linear model (GLM) and thereby served as an implicit baseline. The first level GLM included modelling the motion parameters as nuisance regressors and modelling three conditions: Deviant, Novel and Silent periods, constructed by convolving regressors encoding the relevant trials with the standard canonical double-gamma hemodynamic response function. An autoregressive AR(1) model was also used for ReML parameter estimation, used as standard in SPM-12.

The contrasts interrogated in the first level model were:

i. Activity greater during both Novel and Deviant tones over Silent periods (Dev + Nov > Silent)

ii. Activity greater during both Novel and Deviant tones over Standard tones and Rest (Dev + Nov > All)

iii. Activity greater for Novel tones than Deviant tones (Nov > Dev) and vice versa (Dev > Nov)

iv. Activity greater for Novel tones over Deviant, Standard and Rest (Nov > All)

v. Activity greater for Deviant tones over Novel, Standard and Rest (Dev > All)

A 128s high-pass filter was applied during analysis. MNI co-ordinates, from the output of SPM-12, and Brodmann areas were compared using BioImage Suite (Lacadie et al., 2008).

9.2.3.7 fMRI Analysis - Between Modality Comparison

To quantitatively compare, in a general fashion, the functional sensitivity between techniques, a paired t-test was computed in SPM-12 between the first level contrast maps of Dev + Nov > Silent (contrast i., Section 9.2.3.6) in each session.

To further explore the inter-modality difference in functional sensitivity in auditory regions, given the nature of the task and the difference in acoustic load between acquisitions, a Neurosynth (Yarkoni, 2011)-derived auditory region of interest (ROI), using the term "auditory" thresholded at z = 8, was used as a mask. This mask was applied to the first level contrast maps of Dev + Nov > Silent (i, Section 9.2.3.6). The mean parameter estimates, or betas, of the Novel and Deviant tones modelled, as well as the T-scores of the activity maps (See Supplementary Material 9.3.3) were calculated in this region. The mean T-score and mean Novel and Deviant parameter estimates were computed across participants. The percentage signal change was also computed within this ROI using the MarsBaR toolbox of SPM-12; and its accompanying guidance for batch calculation of the percentage signal change (Brett et al., 2002). The event duration used was zero, and the computed scaling factor within the MarsBaR batch was dependent on the time-bin used for each modality as detailed in the aforementioned batch.

Normality was tested on the T-scores, beta parameters and percentage signal change values across participants via a Shapiro-Wilk test in version 27.0 of IBM SPSS Statistics. The percentage signal change results were therefore quantitatively compared using

Spearman's correlation in SPSS to evaluate the consistency of the participant responses between modalities. A Wilcoxon Signed Rank test was also computed in SPSS between modalities for the percentage signal change of each tone between modalities. For the beta parameters of each tone in the auditory ROI and the mean T-score in the auditory ROI, either a Wilcoxon Signed Rank or Paired T-test was computed based on the output of the normality test. All T-tests included a hypothesised mean/median difference of zero and $\alpha = 0.05$. Statistical significance was determined by a two-tailed test at a p-value threshold < 0.05.

9.2.3.8 fMRI Analysis - Between Session Differences

9.2.3.8.1 Group level Intra-class Correlation - Within Modality As is customary in quantitative assessments of reliability, the voxel-wise intra-class correlation (ICC) analysis (Caceres et al., 2009), using ICC index (3,1), was employed to evaluate between session characteristics for the contrast maps of Deviant + Novel > Silent at group level (i.e. across participants, between sessions, within modality). This was performed to establish the reliability of the activity maps between the scanning sessions, as this method is not sensitive to the mean difference between sessions but rather sheds light on the variability between sessions. The ICC (3,1) (Shrout and Fleiss, 1979) has been proposed specifically for this type of comparison. Its magnitude is calculated using the sum of squares between subjects (BMS) and between sessions (EMS), with k as the number of repeated sessions (Caceres et al., 2009), seen in Equation (1).

$$ICC(3,1) = \frac{BMS - EMS}{BMS + (k-1)EMS} \tag{9.1}$$

An ICC of 1 indicates exceptionally high reliability between sessions as the between session variability would be close to zero (i.e. the error sum of squares would be negligible). On the other hand, the ICC becomes negative as the size of the between-sessions variance regression becomes larger than the between-subject variance. An ICC close to -1 therefore,

(the other extreme), indicates exceptionally poor between session reliability; and that this term would be significantly larger than the variability between subjects (i.e. the between-subject sum of squares is close to zero).

The contrast maps were first masked with a grey matter mask (grey matter tissue prior from SPM-12, see Supplementary Material 9.3.3). A task-related network mask was then defined from the first session for each modality, by means of a low T-score threshold of 1. A low threshold was used to account for the difference in amplitude of the T-scores between techniques, preventing large clusters from being more prevalent in one modality than another. The median ICC score for all voxels within the mask was calculated. When calculating the network mask, grand mean scaling and global calculation were omitted.

9.2.3.8.2 Intra-voxel Reliability - Within Modality The ICC toolbox can also be applied to test the consistency of the signal distribution within an ROI across sessions. This produces a region ICC for each subject (i.e. across sessions, within modality) and is known as the intra-voxel reliability (ICC_v). This differs from a typical voxel-wise ICC where the reliability of the signal across sessions is determined separately for each voxel.

The intra-voxel reliability was calculated for each subject within an auditory ROI, generating an intra-voxel ICC_v value for each participant. This auditory ROI was computed across a Neurosynth (Yarkoni, 2011) -derived auditory ROI (See Supplementary Material 9.3.3), using the term "auditory" and thresholded at z = 5. In this case, Equation (1) is applied for each individual subject using the contrast values of the voxels within this auditory ROI as stated by Caceres et al. (2009). As this work suggests, the intra-voxel reliability then measures the total variance explained by the intra-voxel variance, testing the consistency of the spatial characteristics of the BOLD signal distribution in this ROI to infer differences between subjects. The ROI was applied to the contrast maps for Deviant + Novel > Silent for each participant and across sessions.

9.2.3.8.3 Comparison of Intra-voxel Reliability - Between Modality

To evaluate the differences in ICC_v between modalities, the mean and standard deviation of the outputted ICC_v from the intra-voxel reliability calculation was computed across participants. Upon computing a Shapiro-Wilk normality test, a Wilcoxon Signed Rank Test was computed between modalities to compare medians of the ICC_v values , given that the same population produced ICC_v scores for the two modalities, using SPSS. Statistical significance was determined by a two-tailed test at a p-value threshold < 0.05. Although Bland-Altman plots (Bland and Altman, 1999) have been used in some studies to explore reliability, these were not used in our work as the literature indicates that they are more appropriate when assessing direct replication of quantitative absolute measures, which is not the case of beta parameters in fMRI analysis.

9.2.3.9 Image Quality Measures

Temporal signal-to-noise ratio (tSNR) was calculated as outlined by (Friedman et al., 2006). The mean signal across time per voxel was computed and divided by its corresponding standard deviation after second-order polynomial de-trending (i.e. the standard deviation of the residuals). The images used were those pre-processed including all steps up to spatial normalisation (i.e. excluding smoothing), to produce the average tSNR value across participants. The tSNR was also calculated within a grey matter mask (grey matter tissue prior from SPM-12, see Supplementary Material Figure 9.3.3). This measure avoided artefacts in the average tSNR images that result from differences in brain structure. A difference map was produced by dividing the difference between the modality tSNR maps within-session by the sum of the maps and multiplying this result by 100.

9.2.3.10 Sound Level Measurements

A direct sound level measurement was taken by attaching the Casella 62X (Casella Solutions, UK) sound meter on a cylindrical phantom at the axial isocentre of the magnet

bore and taking the mean LCpeak and LAeq values across 15 seconds (approximately 5 volumes) for each scanning sequence.

9.2.4 Results

9.2.4.1 Looping Star Acoustic Noise and Image Quality Characteristics

Table 9.1 shows the in-bore sound amplitude measures inside the scanner, indicating that Looping Star was less than 10dBA louder than the ambient scan room noise and 27dBA quieter than GRE-EPI. This is a substantial difference, particularly since acoustic noise is measured on a logarithmic scale.

Table 9.1: Average sound level measures over a duration of 15 seconds of scanning from bore isocentre of each acquisition modality.

Acquisition	LAeq (dBA)	LCpeak (dBC)
GRE-EPI	98	112.9
Looping Star	71	102.8
Ambient scanner room, no scan	64	85.7

The tSNR results can be seen in Figure 9.1 for each individual echo and for the optimally combined temporal series from Looping Star, compared with GRE-EPI. tSNR overall was lower in Looping Star compared with GRE-EPI, evident both visually in the whole brain (Figure 9.1, top) and in the quantitative values in grey matter (Figure 9.1, bottom). The distribution of tSNR values was narrower for the echoes and optimally combined echoes of Looping Star than in GRE-EPI. The percentage difference map indicated less than 50% difference between optimally combined Looping Star and GRE-EPI, whereas higher differences could be seen in white matter, which is likely driven by the different tissue relaxation characteristics between techniques. A figure of the raw images has also been provided (Supplementary Material Figure 9.3.4).

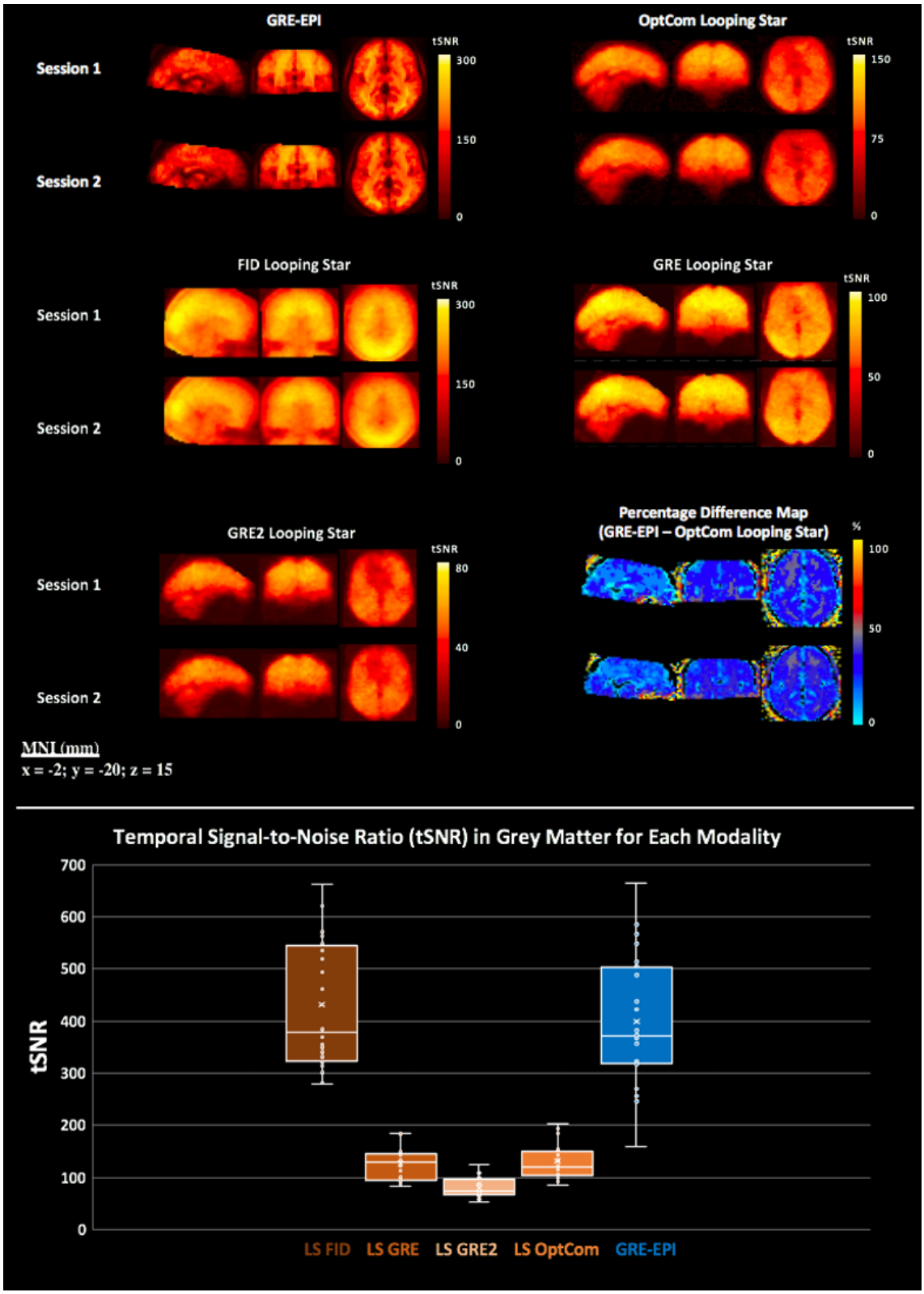

Figure 9.1: (top) Mean temporal signal-to-noise-ratio (tSNR) maps, calculated across participants for each modality and for separate echoes (free induction decay - FID, Echo 1 – GRE, Echo 2 – GRE2) and the optimally combined echoes (OptCom) in Looping Star (LS). Datasets have been realigned and spatially normalised prior to computation of the tSNR. Percentage difference maps between optimally combined Looping Star and GRE-EPI for each session are also shown at the bottom right. (bottom) tSNR values across subjects and both sessions within grey matter mask. S1 = Session 1, S2 = Session 2. Slice (mm = millimetres) in MNI space provided.

9.2.4.2 Physiological & Behavioural Responses

The mean heart rate and respiratory volume per time across the acquisition did not demonstrate any significant differences between modalities (Supplementary Material 9.3.5). Participants were over 86% accurate on average for both modalities and sessions, indicating satisfactory cognitive engagement with the paradigm. Only one participant had a lower than 86% accuracy during GRE-EPI Session 2, but they were still over 76% accurate. There was no evidence of poorer performance accuracy after the tones were swapped (Supplementary Material 9.3.5).

9.2.4.3 Whole-brain Voxel-wise GLM Random-effects Analysis

Since the Standard tone events served as an implicit baseline, we evaluated the overall sensitivity to auditory stimuli between modalities, using the contrasts: Deviant + Novel > Silent (rest blocks) and Deviant + Novel > All other blocks. Figures 9.2A and 9.2B show that Looping Star and GRE-EPI were both sensitive to the responses to non-Standard tones. Activation was observed in the same Brodmann areas (BA) identified by the original study (Gomot et al., 2006), namely the anterior transverse temporal area (BA 41) and the posterior superior temporal gyrus (BA 22) (Table 9.2). Significant activity was also identified in both modalities within the motor cortex (BA 6) and somatosensory cortex (BA 1). No significant results were identified for the contrast Deviant > Novel with either technique, however Figure 9.2C demonstrates the regions more responsive to Novel trials than Deviant trials. Only the Looping Star Session 1 data yielded a statistically significant BOLD response to this contrast in an auditory region.

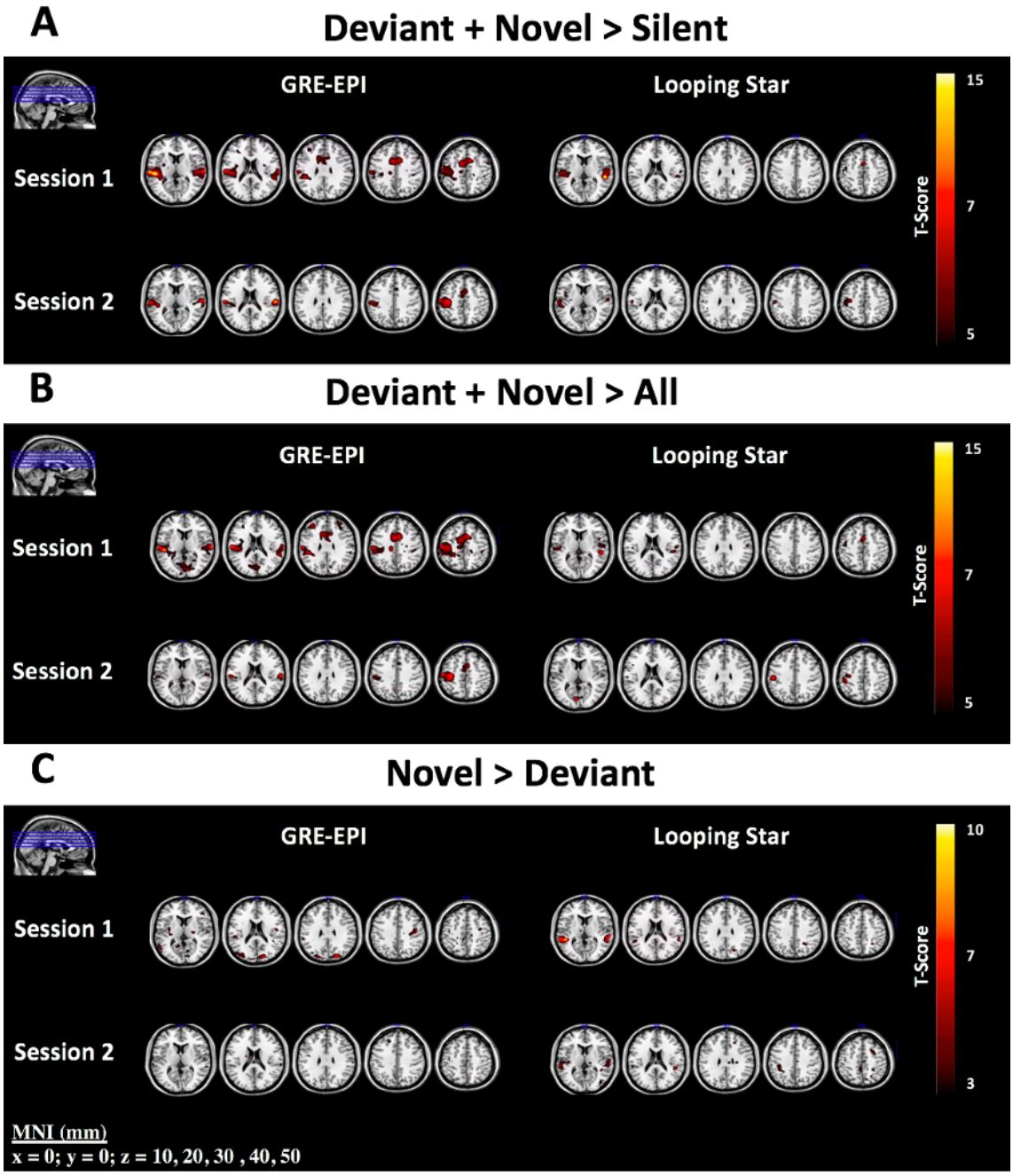

Figure 9.2: Parametric activity maps for the contrasts A) Deviant + Novel > Silent B) Deviant + Novel > All other onsets and C) Novel > Deviant. Comparable activity maps can be seen for A) and B), whereas C) highlights that only Looping Star Session 1 detects an auditory response for the contrast. Slices shown are also visualised in top left corner of images. Overlaid on ch2 image (Holmes et al., 1998) in MRICRON (Rorden and Brett, 2000). Statistics at $p < 0.001$ uncorrected can be seen in Table 9.2. Slice (mm = millimetres) in MNI space provided.

Table 9.2: SPM Statistics table of results for parametric analysis at cluster-level ($p < 0.001$ unc.) across different contrasts for each session and modality.

Contrast Name	Modality	MNI Co-ordinates (x,y,z in mm)	Brodmann area	Cluster-level p(FWE)-value	T-score	Cluster size
Deviant + Novel > Silent	GRE-EPI Session 1	-46 -28 10	41	$< 10^{-3}$ **	15.86	2325
		66 -20 10	41	$< 10^{-3}$ **	9.33	477
		42 -32 46	40	0.027 *	4.26	40
		34 28 26	9	0.003 *	4.06	67
	GRE-EPI Session 2	58 -20 18	40	$< 10^{-3}$ **	13.52	217
		-62 -20 18	1	$< 10^{-3}$ **	13.06	616
		-6 0 58	6	$< 10^{-3}$ **	9.56	278
		6 -84 -10	18	0.064	8.3	33
		-14 24 6	N/A	0.004 *	7.56	73
	Looping Star Session 1	50 -32 14	41	$< 10^{-3}$ **	16.91	242
		2 -76 -22	N/A	$< 10^{-3}$ **	11.15	130
		34 -52 -26	N/A	0.197	10.5	12
		-2 4 50	6	$< 10^{-3}$ **	9.16	91

		-34 -4 58	6	$< 10^{-3}$ **	8.33	127
		-46 6 -6	13	$< 10^{-3}$ **	7.77	222
	Looping Star Session 2	-58 -20 22	1	$< 10^{-3}$ **	9.6	542
		6 -64 -14	N/A	$< 10^{-3}$ **	10.02	329
		62 -12 6	41	0.006 *	8.96	36
		50 16 -10	N/A	0.001*	7.92	56
		2 4 66	6	0.010 *	5.73	32
Deviant > All	GRE-EPI Session 1	-50 -28 10	41	$< 10^{-3}$ **	14.43	3166
		34 8 34	13	$< 10^{-3}$ **	6.41	165
		54 8 -2	44	0.005 *	6.05	45
	GRE-EPI Session 2	62 -16 18	40	0.001 *	14.07	71
		10 -92 -6	17	$< 10^{-3}$ **	12.93	77
		-58 -16 50	N/A	$< 10^{-3}$ **	11.63	328
		2 12 58	6	$< 10^{-3}$ **	10.05	236
		-62 -20 22	1	0.001*	8.86	74
		10 28 -2	N/A	$< 10^{-3}$ **	7.92	123

	Looping Star Session 1	-2 0 66	6	$< 10^{-3}$ **	9.91	226
		-50 -24 10	40	$< 10^{-3}$ **	9.93	50
		-54 4 -2	6	0.014 *	8.48	26
		54 -20 22	N/A	$< 10^{-3}$ **	8.07	85
		30 0 -6	49	$< 10^{-3}$ **	7.52	120
		2 -76 -22	N/A	$< 10^{-3}$ **	7.48	134
	Looping Star Session 2	-50 -20 42	1	$< 10^{-3}$ **	9.2	130
		-6 -40 -22	N/A	0.121	7.9	15
		-6 -80 10	17	$< 10^{-3}$ **	7.6	95
Novel > All	GRE-EPI Session 1	-58 -20 18	1	$< 10^{-3}$ **	13.96	2775
		-10 -48 -2	N/A	$< 10^{-3}$ **	10.24	890
		-42 -36 -10	N/A	0.056	9.66	30
		-34 36 26	N/A	0.001 *	8.86	88
		30 32 26	9	$< 10^{-3}$ **	7.85	101
	GRE-EPI Session 2	-46 -20 58	1	$< 10^{-3}$ **	10.86	333

		-58 -24 14	40	0.004 *	10.15	89
		-2 0 62	N/A	$< 10^{-3}$ **	8.87	212
		62 -20 18	40	0.004 *	8.51	90
	Looping Star Session 1	54 -32 14	41	$< 10^{-3}$ **	11.55	255
		-92	N/A	$< 10^{-3}$ **	7.91	137
		-2 0 66	6	$< 10^{-3}$ **	7.43	72
		-43 4 -6	13	0.001*	6.88	52
		-62 -20 10	1	$< 10^{-3}$ **	6.7	98
		-14 -20 2	50	0.018*	6.55	26
		-18 -28 78	N/A	$< 10^{-3}$ **	6.31	186
	Looping Star Session 2	-54 -24 42	40	$< 10^{-3}$ **	12.15	455
		58 -16 6	41	0.001*	9.77	49
		14 -44 -14	N/A	$< 10^{-3}$ **	8.22	265
		54 12 -6	N/A	0.005*	7.44	37
		54 -24 30	40	0.044*	7.27	22
		-46 12 18	44	0.001*	7.11	49

Novel > Deviant	GRE-EPI Session 1	22 -84 26	19	0.009*	7.11	35
		-18 -92 26	18	0.022*	5.73	28
	GRE-EPI Session 2	-18 -8 22	48	0.907	5.7	2
	Looping Star Session 1	-46 -40 10	22	0.004 *	10.29	37
		58 -32 15	22	0.001 *	6.91	47
	Looping Star Session 2	42 -44 14	N/A	0.218	6.47	12
Deviant > Novel	GRE-EPI Session 1	14 -64 46	N/A	0.946	4.87	2
	GRE-EPI Session 2	NSC	NSC	NSC	NSC	NSC
	Looping Star Session 1	22 12 14	N/A	0.981	4.19	1
	Looping Star Session 2	-38 -36 -6	N/A	0.974	4.36	1
Deviant + Novel > All	GRE-EPI Session 1	-50 -28 10	41	$< 10^{-3}$ **	13.83	4099

			54 12 -2	44	0.039 *	6.5	32
			30 -4 18	N/A	0.036 *	5.73	33
		GRE-EPI Session 2	2 12 58	6	$< 10^{-3}$ **	11.88	261
			62 -20 18	40	$< 10^{-3}$ **	11.4	110
			-46 -20 58	1	$< 10^{-3}$ **	11.05	370
			2 -84 -10	18	0.11	10.4	57
			-6 28 2	N/A	0.001 *	9.24	90
			-62 -20 18	1	0.001 *	8.92	97
		Looping Star Session 1	-2 0 66	6	$< 10^{-3}$ **	12.54	313
			50 -32 14	41	$< 10^{-3}$ **	11.05	307
			2 -76 -22	N/A	$< 10^{-3}$ **	10.63	180
			-62 -20 6	41	$< 10^{-3}$ **	8.04	106
			-54 8 -6	22	$< 10^{-3}$ **	7.43	50
		Looping Star Session 2	-50 -20 42	1	$< 10^{-3}$ **	13.76	275
			-6 -80 10	17	$< 10^{-3}$ **	9.84	252
			50 16 -10	N/A	0.002 *	7.28	44

		-46 12 18 -6 -40 -22	44 N/A	0.003 * 0.035 *	6.96 6.55	41 23

* = cluster-level p(FWE) < 0.05, ** = cluster-level p(FWE) < 0.001, N/A = outside of defined Brodmann Area, NSC = no significant clusters

9.2.4.4 Quantitative comparison between modalities (within session)

Figure 9.3 demonstrates the results of the quantitative comparisons between modalities, within each session. The inter-modality paired t-tests of the statistical maps for each session (Figures 9.3A & 9.3B) highlight regions of differences in activity. Table 9.3 provides the accompanying statistics. Within Session 1, only motor cortices (i.e. BA 4 and BA 6) presented statistically significant higher activity for GRE-EPI relative to Looping Star.

The statistical comparisons of the different measures in an auditory ROI presented in Figures 9.3C-E are shown in Table 9.4. We found a statistically significant difference in the mean T-score within the auditory ROI between GRE-EPI and Looping Star for both sessions. We also found a statistically significant difference within the auditory ROI for the mean parameter estimates of the Deviant tones in Session 1. There was no significant difference for the parameter estimates of the Novel tones. This was also consistent with the percentage signal change results (Figures 9.3F-G). Table 9.5 shows the results of the inter-modality Spearman's correlation, which was between $0.08 < r < 0.32$, as well as the T-tests between the percentage signal change values. Only Deviant tones in Session 1 provided a statistically significant inter-modality difference in percentage signal change.

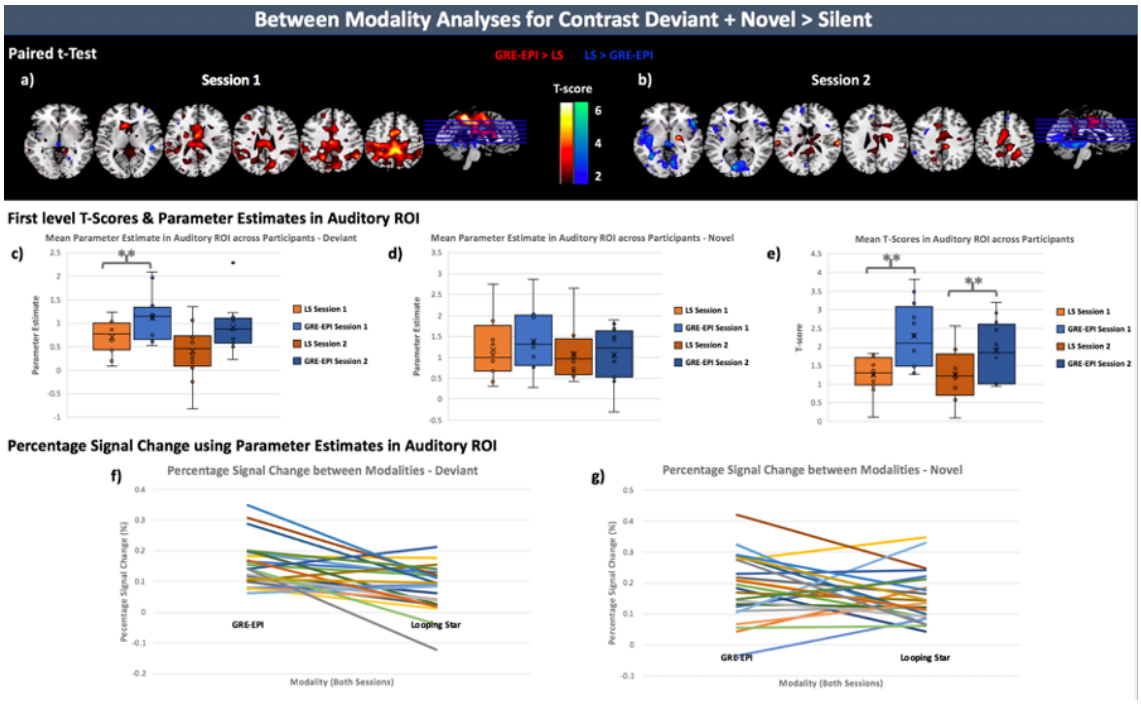

Figure 9.3: Between modality analyses using Deviant + Novel > Silent contrast maps. (top) Bidirectional results of paired T-test between first level contrast maps of all participants. a) Session 1 comparison and b) Session 2 comparison. Overlaid on ch2 image (Holmes et al., 1998) in MRICRON (Rorden and Brett, 2000). (middle) Auditory ROI was used to mask parameter estimate (beta) maps and mean parameter estimate calculated for regressors of c) Deviant onsets and d) Novel onsets as plotted for all participants. e) Mean T-score calculated from first level T-maps for the contrast, plotted for each participant after auditory ROI masking. (bottom) Percentage signal change computation based on parameter estimates in auditory ROI. All sessions included and plotted for each modality. Pattern of difference between modality shown for f) Deviant and g) Novel tones. LS = Looping Star. ** = p(two-tailed) < 0.05. Accompanying statistics seen in Tables 9.3-9.5.

Table 9.3: SPM Statistics table of results for parametric paired T-test at cluster-level ($p < 0.001$ unc.) for activity maps of contrast Deviant + Novel > Silent across participants for each session.

Paired T-Test	MNI Co-ordinates (x,y,z in mm)	Brodmann area	Cluster-level p(FWE)-value	T-score	Cluster size
GRE-EPI > LS Session 1	-34 -28 62	4	0.001*	8.72	50
	2 -44 58	N/A	$< 10^{-3}$ **	8.44	176
	6 4 46	6	0.002*	5.3	45
GRE-EPI > LS Session 2	62 –24 18	40	0.578	5.81	6
LS > GRE-EPI Session 1	14 -60 -10	17	0.299	4.69	10
LS > GRE-EPI Session 2	10 -52 -6	N/A	$< 10^{-3}$ **	6.54	79

* = cluster-level p(FWE) < 0.05, ** = cluster-level p(FWE) < 0.001, N/A = outside of defined Brodmann Area, NSC = no significant clusters

Table 9.4: Wilcoxon Signed Rank Test or Paired T-test results across different inter-modality measures within the auditory ROI.

Test Variables	**Wilcoxon Signed Rank/Paired T-test two-tailed p-value**	**Wilcoxon Signed Rank/Paired T-test T-score**
Mean T-Score in auditory ROI †, GRE-EPI - LS, Session 1	0.004 *	3.648
Mean T-Score in auditory ROI †, GRE-EPI - LS, Session 2	0.043 *	2.284
Mean Deviant beta parameter in auditory ROI †, GRE-EPI - LS, Session 1	0.022 *	2.677
Mean Deviant beta parameter in auditory ROI, GRE-EPI - LS, Session 2	0.060	-1.883
Mean Novel beta parameter in auditory ROI †, GRE-EPI - LS, Session 1	0.442	0.798
Mean Novel beta parameter in auditory ROI, GRE-EPI - LS, Session 2	0.814	-0.235

* = $p < 0.05$, † = Parametric paired T-test

Table 9.5: Inter-modality Spearman's correlation and Wilcoxon Signed Rank Test results between percentage signal change values within the auditory ROI

Correlation Pair	Spearman's r	Wilcoxon Signed Rank T-score	Wilcoxon Signed Rank two-tailed p-value
GRE-EPI - LS, Session 1, Deviant Tones	0.252	-2.510	0.012 *
GRE-EPI - LS, Session 2, Deviant Tones	0.133	-2.197	0.028
GRE-EPI - LS, Session 1, Novel Tones	-0.056	-1.334	0.182
GRE-EPI - LS, Session 2, Novel Tones	0.315	-0.471	0.638
GRE-EPI - LS, All Sessions, Deviant Tones	0.320	-3.343	$< 10^{-3}$ **
GRE-EPI - LS, All Sessions, Novel Tones	0.088	-1.257	0.209

* = p $<$ 0.05, ** = p $<$ 0.001

9.2.4.5 Quantitative comparison between sessions (within modality)

Inter-session differences, evident in the random-effects analyses, were more specifically characterised with an ICC analysis. Figure 9.4 (top) summarises the group level ICC results within modality, where the ICC values are consistently high in task-related regions, such as the auditory and motor cortices, in both modalities for the contrast maps of Deviant + Novel $>$ Silent. However, the spatial extent with high ICC, in the regions detected with Looping Star, was much smaller than in GRE-EPI and negative ICC values were seen in regions from the Looping Star data, outside of task-related regions. This was not the case in GRE-EPI data. A more skewed joint distribution (towards higher ICC values) was seen in GRE-EPI between activation T-score and ICC score in comparison

with Looping Star.

An independently derived functional ROI of the auditory cortex (Supplementary Material 9.3.3), was used to calculate the intra-voxel reliability (ICC_v) between sessions for each subject, specifically testing between session consistency in an auditory region in each individual. Significantly higher ICC_v values were identified using this method on average across subjects in this auditory ROI for GRE-EPI than Looping Star (Figure 9.4, centre), where p(two-tail) = 0.002. There was no evidence of one participant producing particularly low ICC_v values in both modalities (i.e. having low ICC_v in both modalities).

To further evaluate the ICC results, the between-subject sum of squares and between-session sum of squares outputs from the ICC analysis, which are calculated from the activity maps, were explored (Figure 9.4, bottom). Both modalities demonstrated clusters of low spatial extent with high between-session variance in the visual and auditory cortices. Although both modalities demonstrated high between-subject variance within the frontal lobe and auditory cortex, GRE-EPI demonstrated higher between-subject variance than Looping Star in the auditory cortex and along the longitudinal fissure.

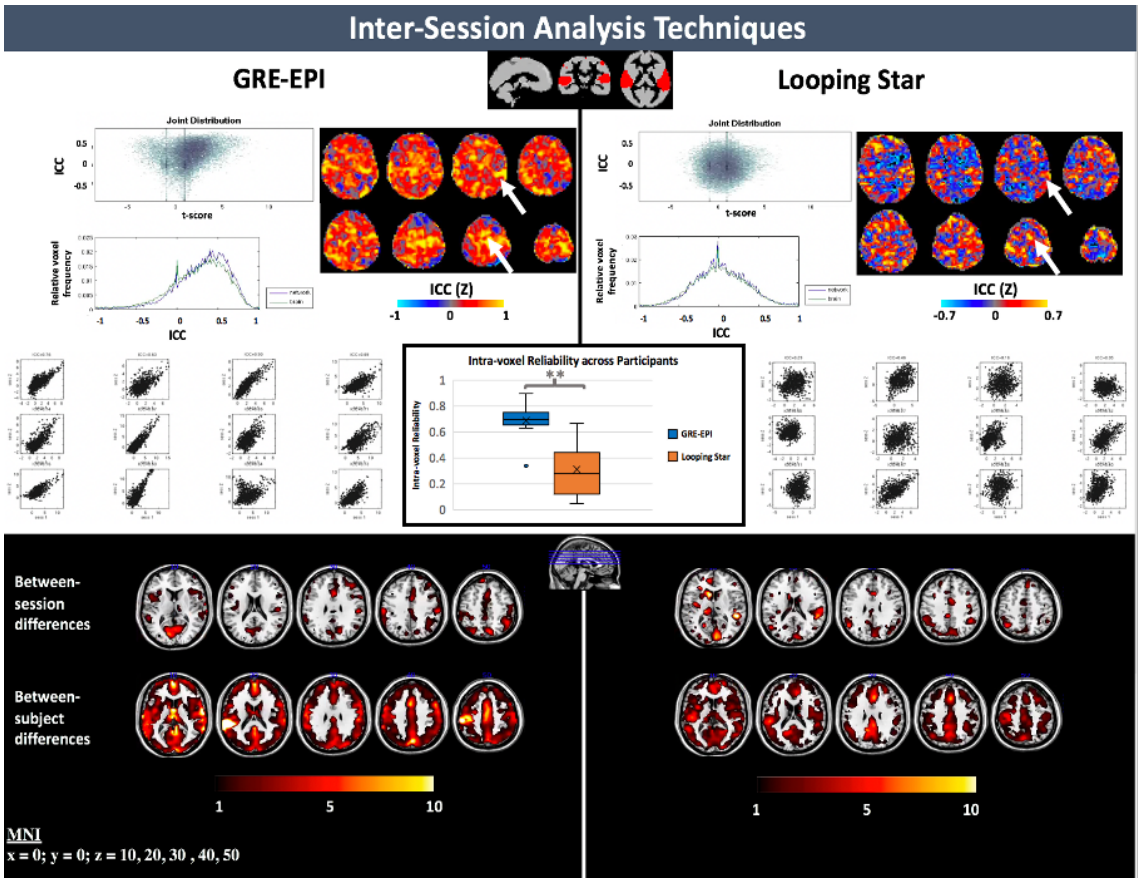

Figure 9.4: (top) Plots of intra-class correlation coefficient (ICC) vs T-score, relative voxel frequency vs ICC and ICC z-score map for each modality. (centre) Intra-voxel reliability (ICC_v) calculations with outputted score for each participant in an auditory region-of-interest (ROI) (overlaid on grey matter mask on top right) can be seen with accompanying box-and-whisker plot of the outputted ICC_v value for the auditory ROI across participants. Significant differences between inter-modality intra-voxel reliability was identified, where p(two-tailed) = 0.002 (** = $p < 0.05$). (bottom) Between-session and between-subject difference maps outputted from ICC analysis. Overlaid on ch2 image (Holmes et al., 1998) in MRICRON (Rorden and Brett, 2000). Slice (mm = millimetres) in MNI space provided. Scale of ICC z-score adjusted to account for functional sensitivity differences between modalities.

9.2.5 Discussion

9.2.5.1 Summary of Results

With respect to our key aims, we demonstrated that 1) multi-echo Looping Star is sensitive to the BOLD response elicited during the auditory oddball paradigm, 2) multi-echo Looping Star has comparable sensitivity for novel tone discrimination in auditory regions, relative to the GRE-EPI acquisition performed by Gomot et al. (2006), though inter-modality differences were also identified, and 3) multi-echo Looping Star has lower

test-retest reliability than GRE-EPI. We also observed some limitations in the Looping Star technique, such as its reduced tSNR, driven in part by the need to employ a very low excitation flip angle in this modality.

9.2.5.2 Physiological & Behavioural Data

On average, there were no differences in the mean heart rate and respiration volume per sampling time across participants for the duration of the different scans. This suggests that overall there were no additional systemic effects imposed by either imaging modality across the paradigm duration. Behaviourally, participants performed very well with regards to detecting the Deviant and Novel tones during both modalities. This is unsurprising as the GRE-EPI pulse sequence design used was identical to that used in the original study by Gomot et al. (2006), especially ensuring that the EPI slice acquisition train contained the appropriate delays for the tones to be heard by the participants. Our behavioural data also indicated that subjects remained attentive and alert throughout the scans.

9.2.5.3 Whole-brain Voxel-wise GLM Random-effects Analysis

In general, our results demonstrated good agreement with those of Gomot et al. (2006). The main effect of Deviant and Novel tones versus Silence demonstrated consistent bilateral activity in both GRE-EPI and Looping Star sessions, providing evidence that Looping Star is sensitive to the BOLD response in event-related auditory paradigms. Right hemisphere involvement of BA 41 was seen in both modalities, which may be linked to the right hemisphere involvement in attention processes (Müller et al., 2002; Stevens et al., 2005). Similar activity patterns were also seen in the response to Deviant + Novel > All, which addressed potential issues with the Silent condition likely being an unstable baseline due to its short duration.

The separate contrasts of Deviant > All and Novel > All also demonstrated significant results in auditory regions for both modalities, but there were no significant results for

the contrast Deviant > Novel. This could indicate that higher attention was paid to the Novel tones, eliciting a higher amplitude response in spatially overlapping regions relative to Deviant tones. This is supported by the functional overlap for Deviant and Novel tones seen here and by Gomot et al. (2006), alongside the proximity of the overlap of auditory loci and the prevalence of attention-driven modulations observed in a meta-analysis by (Alho et al., 2014). A key inter-modality difference that should be explored in depth with a larger cohort was that only Looping Star Session 1 revealed significantly greater activity in response to Novel trials compared to Deviant stimuli in the auditory regions. There were no behavioural motivations for this to be the case, therefore future studies may benefit from exploring potential differences in cognitive engagement, perhaps using a different oddball paradigm. This would inform whether the differences we observed are linked to the reduced auditory load in Looping Star.

9.2.5.4 Measurement of between modality differences

The inter-modality paired t-test for the contrast of Deviant and Novel tones over Silence indicated that there were no statistically significant differences in activity in auditory regions, but differences were present in motor cortices. However, significant activity in the motor cortex was indeed identified in both modalities, therefore these differences are likely related to functional sensitivity differences between techniques that lead to more localised responses in Looping Star. Significant differences in percentage signal change were only identified for the parameter estimate of the Deviant stimuli, which were much lower in Looping Star compared to GRE-EPI. To verify whether this could be linked to the difference in auditory demand, application of Looping Star with a paradigm exploring repetition priming (Bergerbest et al., 2004) may be of benefit.

9.2.5.5 Measurement of between-session reliability

The ICC results overall indicated lower reliability of Looping Star activity maps for the contrast Deviant + Novel > Silent compared with those of GRE-EPI. This was

demonstrated by the following: 1) the joint distribution indicated a strong relationship between T-score and ICC for GRE-EPI, i.e. a strong relationship between activity and repeatability, that was not apparent for Looping Star, 2) higher ICC values were seen in the auditory and motor cortex for GRE-EPI and Looping Star relative to the rest of the brain, though Looping Star demonstrated negative ICC values across the cortex, outside of the auditory regions, unlike GRE-EPI, suggesting high between-session variance, and 3) higher intra-voxel reliability (ICC_v) was seen in the auditory ROI for GRE-EPI than Looping Star on average across participants, therefore the signal distribution is more consistent in GRE-EPI than Looping Star within the auditory ROI. The lower tSNR and smaller identified clusters in Looping Star could be a contributing factor to this inter-session difference, though cognitive links to acoustic background noise have been identified in previous studies that could also contribute (Cho et al., 1998a; Kiehl and Liddle, 2003; Novitski et al., 2003; Seifritz et al., 2006; Wolak et al., 2016). Future replicability and repeatability studies should aim to disentangle these effects.

9.2.5.6 Limitations & Future Work

It is important to emphasise that our intention was to perform the first evaluation of multi-echo silent fMRI in an event-related context, and we acknowledge that a larger cohort would improve the generalisation of these findings. Limitations regarding the paradigm design, such as the duration of the resting blocks being barely longer than the haemodynamic response, were unavoidable as we aimed to replicate the paradigm used by Gomot et al. (2006). We did, however, adapt the original general linear model by deciding against modelling the Standard tones (Gomot et al., 2006) to avoid over-parametrisation. Our desire to reproduce the conditions of the study of Gomot et al. (2006) as much as possible, also meant that we did not acquire multi-echo GRE-EPI data and so were limited in our comparisons. There were also some inherent limitations in the pulse sequence design of the version of Looping Star that we employed, which prevented both faster imaging and higher tSNR. These have been outlined in detail by (Dionisio-Parra et al., 2020).

There is scope to further characterise Looping Star for targeting specific optimisation strategies. Such avenues include evaluating the impact of spatial blurring induced during acquisition, assessing whether anatomical configuration interacts with certain acquisition parameters, and exploring the impact of physiology on this three-dimensional acquisition. Future studies could also capitalise on the reduced impact of inflow effects in Looping Star given the absence of slice selection. Furthermore, alternative reconstruction schemes, beyond the one employed here for Looping Star, may be more appropriate in future studies. Such techniques include compressed sensing and low-rank reconstruction, which employ under-sampled k-space trajectories (Chiew et al., 2015; Holland et al., 2013; Zong et al., 2014).

9.2.6 Conclusions

Looping Star provides a useful, near-silent MRI acquisition alternative that mitigates the limitations produced by the high acoustic noise of GRE-EPI, providing a "real-world" scenario for functional neuroimaging. It also removes the reliance on strong ear protection and noise cancellation hardware by minimising acoustic noise at its source. Looping Star demonstrated sensitivity to the BOLD response in a complex, event-related auditory fMRI paradigm, supporting its extension from simple blocked designs to complex cognitive tasks that are more widely used across studies. Optimisation and further characterisation with a range of paradigms and acquisition parameters is required to identify whether it indeed reveals additional information on cognitive processes involved in auditory processing.Furthermore, our study evaluated, for the first time, the test-retest reliability of Looping Star, which warrants further study to understand the impact of reduced scanner acoustic noise on cognitive strategies between sessions. Ultimately, Looping Star is a promising technique that offers a useful alternative to study the mechanisms of brain activity in sound averse populations.

9.3 Supplementary Material

9.3.1 A: Under-sampling the multi-echo fMRI Looping Star trajectory

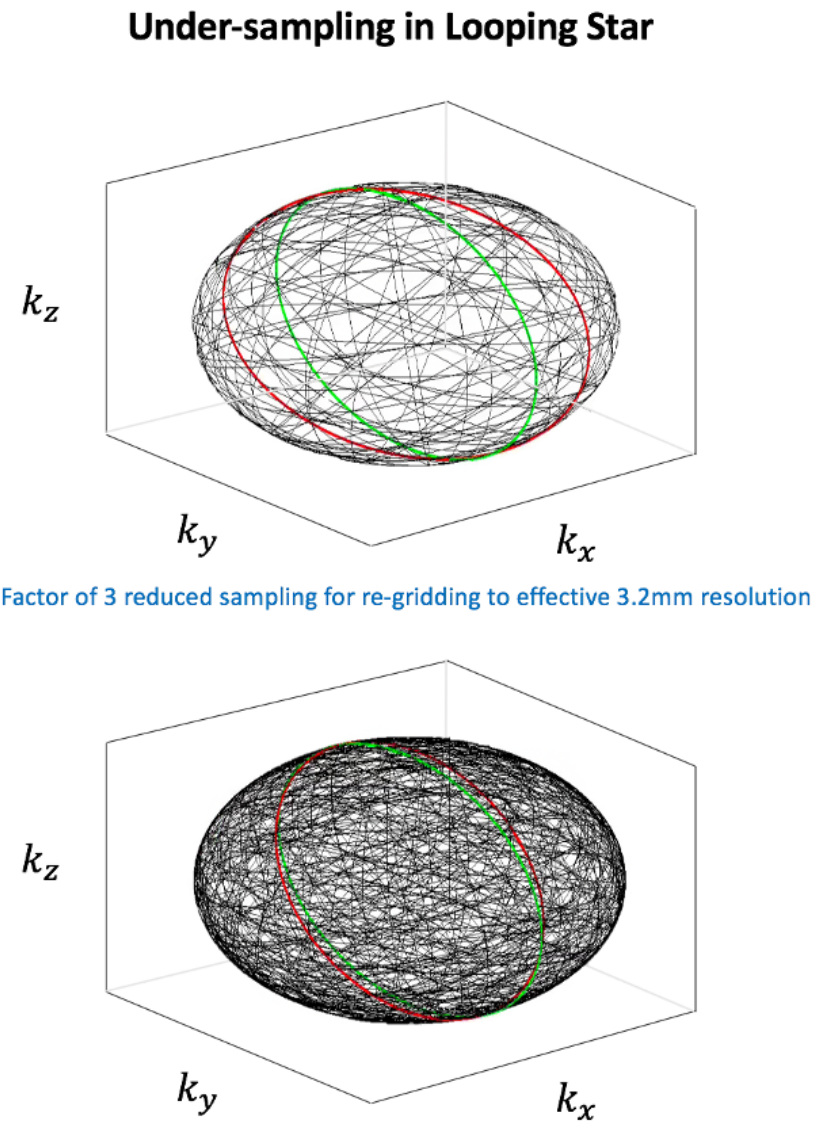

Figure 9.5: Under-sampled 1080 spoke per volume (top) vs fully sampled 3600 spokes per volume (bottom) trajectories that can be used for a 3.2 mm resolution and 19.2 cm field-of-view in Looping Star. kx, ky and kz indicate the three dimensions of k-space. The under-sampled trajectory was used in this study for Looping Star fMRI to reduce repetition time.

9.3.2 B: Pre-processing Pipeline

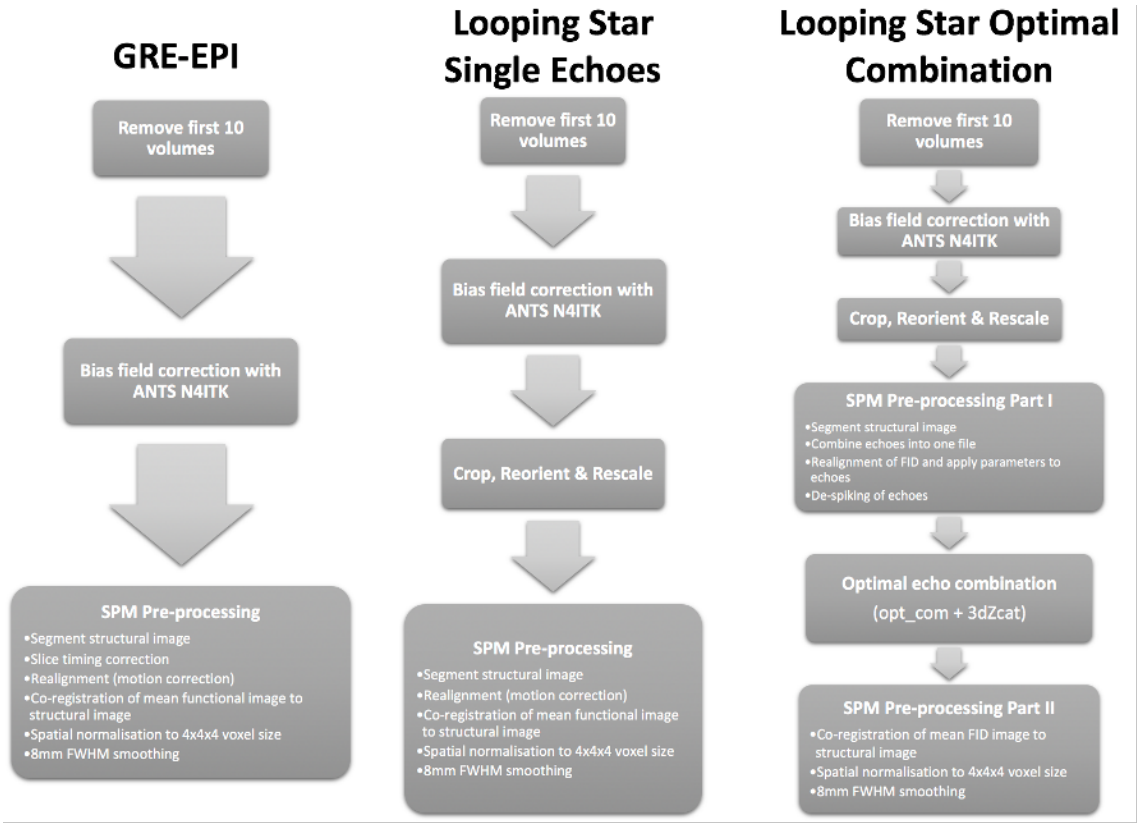

Figure 9.6: Pre-processing pipeline workflow for each modality, also detailed with accompanying references for software used in Methods (Section 9.2.3.5). FID = free induction decay, FWHM = full-width, half-maximum.

9.3.3 C: Regions of Interest Visualisation

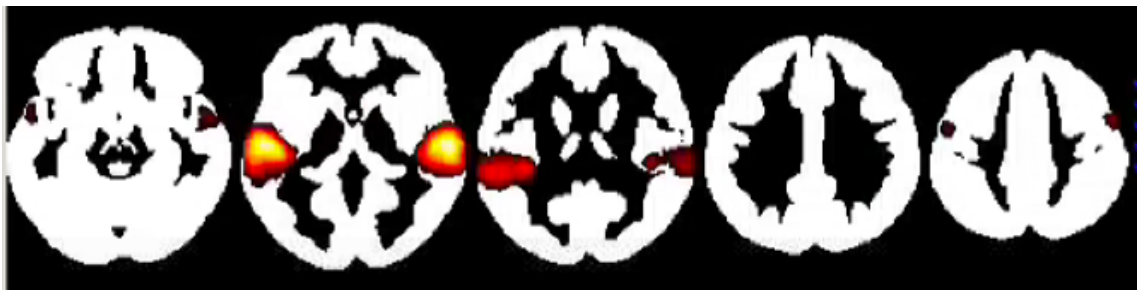

Figure 9.7: Grey matter mask (tissue prior template from SPM-12 software) with auditory region-of-interest (ROI) from Neurosynth for term "auditory" thresholded at z = 5 (Yarkoni, 2011) overlaid in red.

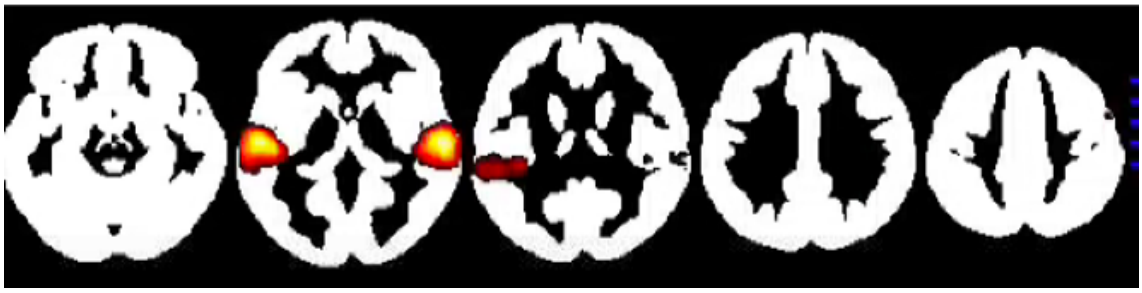

Figure 9.8: Grey matter mask (tissue prior template from SPM-12 software) with auditory region-of-interest (ROI) from Neurosynth for term "auditory" thresholded at z = 8 (Yarkoni, 2011) overlaid in red.

Figure 9.9: Grey matter mask (tissue prior template from SPM-12 software).

9.3.4 D: Raw Data Images

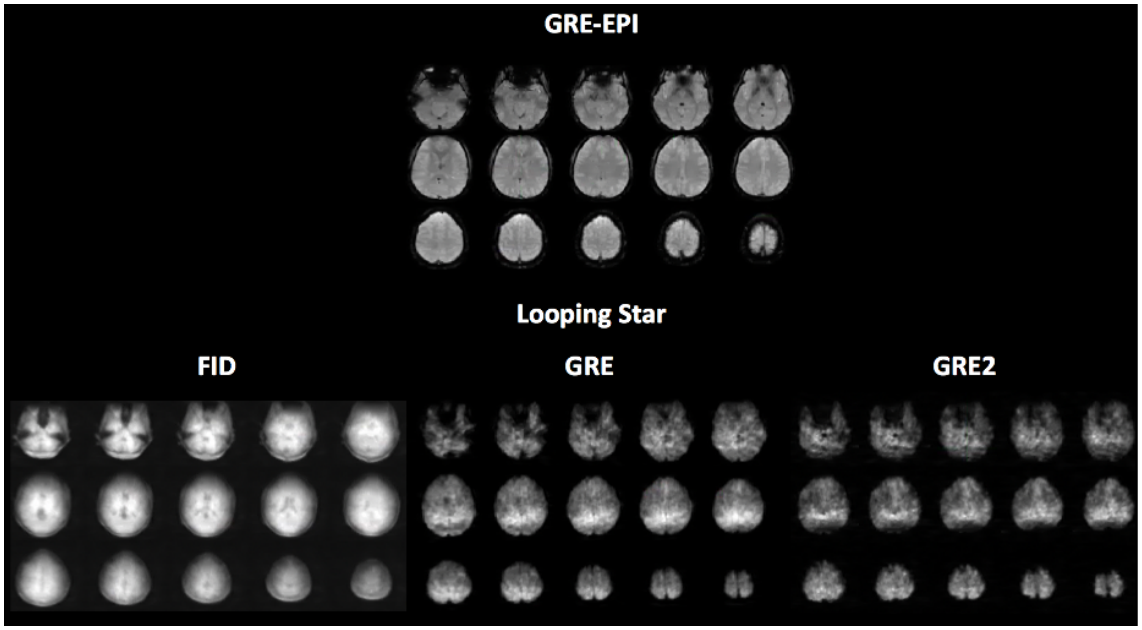

Figure 9.10: Raw images of Looping Star individual echoes (free induction decay – FID, echo 1 – GRE, echo 2 – GRE2) and GRE-EPI data for one participant.

9.3.5 E: Behavioural & Physiological Results

Methods - Physiology The physiological data from one participant in the second session was excluded due to severe artefacts in the pulse oximeter recording. First, an in-house MATLAB (Mathworks, 2021) script was used to locate the peaks in the pulse oximeter data and identify the inter-beat interval (IBI). The Kubios software (Tarvainen et al., 2014) was then used for threshold-based artefact correction, during which every IBI value is compared against a local average interval. If the IBI differed from the local average by more than 0.45 seconds ('very low' threshold in software), then it was identified as an artefact (Tarvainen et al., 2019). Kubios was also used to calculate the mean heart rate over a duration of 10 minutes, given these IBI values. The measure of interest was the mean heart rate over this duration, representative of the length of the paradigm, to identify any global changes in exertion.

Time per respiratory volume (or sampling period) was derived using the PhysIO toolbox within the TAPAS software in SPM-12 (Kasper et al., 2017). As stated in the software scripts and by Birn et al. (2006), this is computed using filtered respiratory readings; interpolating the maximum and minimum breathing amplitudes between detected peaks and dividing them by interpolated durations between the maximum amplitudes of the breathing signals. The inputs included the TR, sampling interval of the physiological recording and number of scans per modality, with the slice to slice timing set as the TR for Looping Star given its three-dimensional acquisition. The mean and standard deviation for the sampling period were computed across the time series. Differences in the mean physiological measures from the different modalities and sessions were deemed statistically significant based on a two-sample T-test with equal variances assumed and alpha = 0.05, if the p-value (one-tailed) < 0.05.

Methods - Behaviour Task performance accuracy was defined as whether a Novel or Deviant tone was correctly detected, according to the responses measured from the button box. Reaction time, between the onset of the tone and button press, was also recorded. The number of responses to Novel and Deviant tones that were accurate (<

625ms from onset) were summed with those that were late (> 625ms but < 1250ms). This was performed as the interval between tone onsets was very short, meaning fast reaction times were required: upon inspection of the behavioural data, we found many responses that appeared within the following onset (i.e. between 625ms and 1250ms after the previous onset), therefore indicating an accurate but delayed response. We also explored the accuracy before and after the Standard and Deviant tones were swapped.

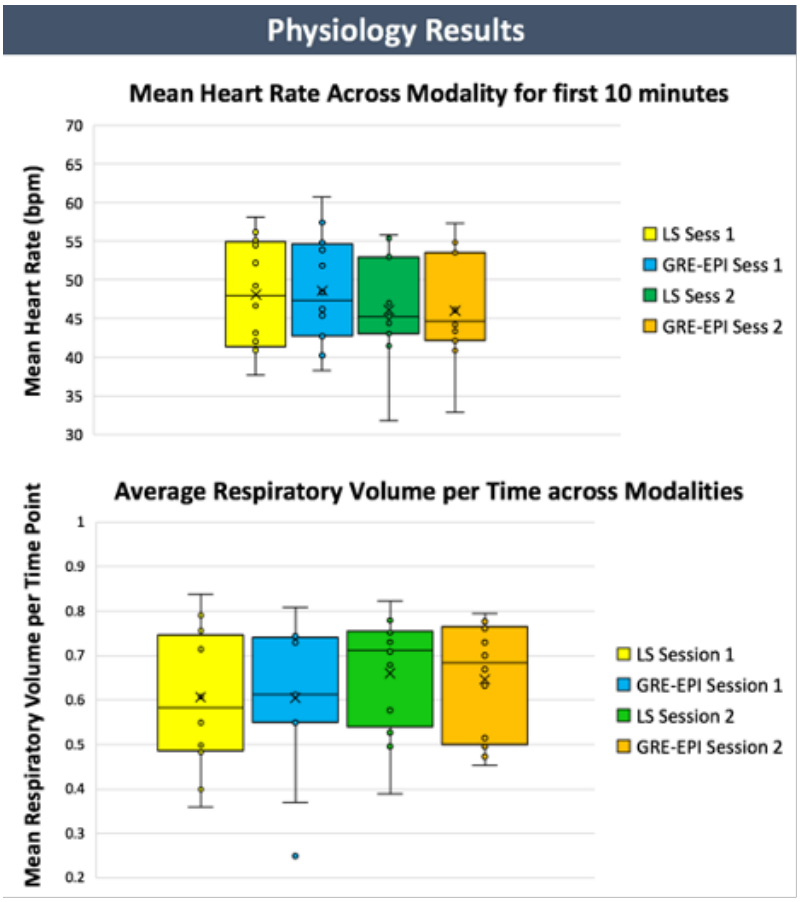

Figure 9.11: Physiology results for Looping Star (LS) and GRE-EPI. (top) Mean heart rate across modality for duration 10 minutes. (bottom) Average respiratory volume per time point for each modality. No significant differences identified. Methods for physiology measures available above.

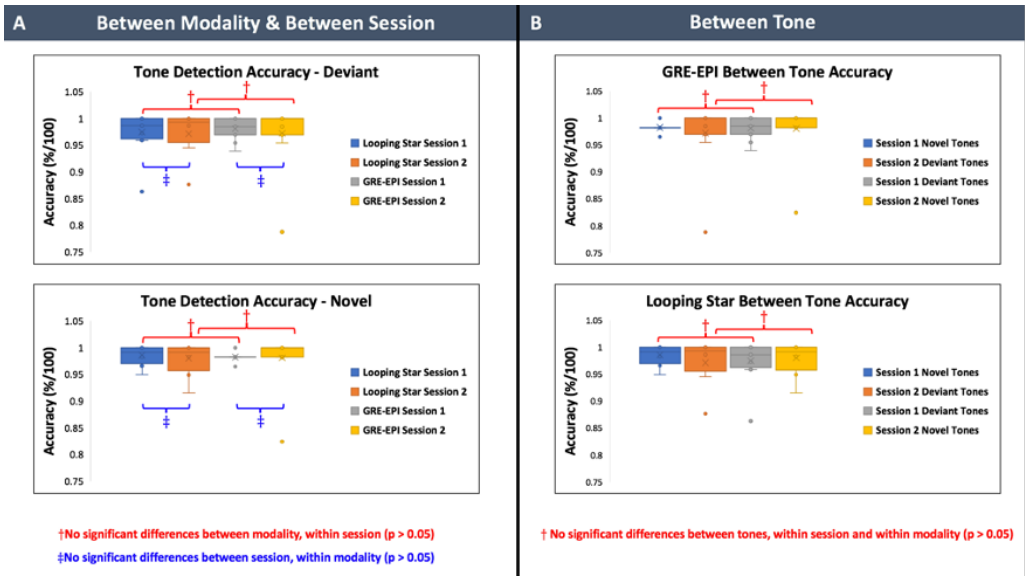

Figure 9.12: Behavioural results summarised for Looping Star and GRE-EPI. A) Between modality and between session tests are summarised. B) Between tone (Novel and Deviant) differences within session and within modality tests are summarised. No significant differences were found for any groups of tests (represented by parentheses).

Table 9.6: Behavioural results summary of accuracy values, bold font indicates highest percentage accuracy across modality and session for each tone.

Session Type	Number of Deviant Tones Accurately Detected	Number of Novel Tones Accurately Detected	Number of Deviant Tones Detected >625ms Late	Number of Novel Tones Detected >625ms Late	Total Deviant Tones Detected	Total Novel Tones Detected
GRE-EPI Session 1	56.8 ± 9.3 / 66	51.5 ± 7.0 / 57	7.1 ± 8.8 / 66	4.5 ± 7.2 / 57	64.8 ± 1.4 / 66 (**98.2 %**)	56.0 ± 0.6 / 57 (98.2 %)
Looping Star Session 1	67.3 ± 3.3 / 73	55.7 ± 2.6 / 59	3.9 ± 2.9 / 73	2.5 ± 2.2 / 59	71.2 ± 2.8 / 73 (97.5 %)	58.2 ± 1.0 / 59 (**98.6 %**)
GRE-EPI Session 2	58.0 ± 7.7 / 66	51.9 ± 8.0 / 57	6.2 ± 6.1 / 66	4.0 ± 7.2 / 57	64.1 ± 3.9 / 66 (97.2 %)	55.9 ± 2.8 / 57 (98.1 %)
Looping Star Session 2	65.2 ± 7.8 / 73	53.0 ± 6.4 / 59	5.8 ± 7.0 / 73	4.8 ± 6.0 / 59	70.9 ± 3.4 / 73 (97.1 %)	57.8 ± 1.6 / 59 (98.0 %)
Pre-scan Test (Session 1)	34.6 ± 6.4 / 41	22.6 ± 3.0 / 25	3.8 ± 3.4 / 41	1.9 ± 2.3 / 25	38.3 ± 3.7 / 41 (93.5 %)	24.5 ± 1.2 / 25 (98.0 %)

Table 9.7: Overall sum of the number of missed tones across participants for each modality and session, before and after the Standard and Deviant tones were swapped (half-way through the paradigm). There was no significant difference (i.e. p(one-tailed) > 0.05) between the overall number of tones missed before and after the swap for all modalities, using a paired T-test.

Session Type	Number of Novel Tones Missed Before Swap	Number of Novel Tones Missed After Swap	Number of Deviant Tones Missed Before Swap	Number of Deviant Tones Missed After Swap
GRE-EPI Session 1	5	8	1	8
Looping Star Session 1	4	6	12	10
GRE-EPI Session 2	4	7	8	11
Looping Star Session 2	8	2	14	8
Total number of missed tones across modality	21	23	35	37

9.4 Expanded Analysis and Further Commentary

This section includes analyses excluded from the manuscript that compares GRE-EPI and Looping Star, further establishing the validity of the results from the above manuscript.

9.4.1 Hyperintensities and tSNR

9.4.1.1 Background

Although tSNR is a helpful measure to evaluate the temporal stability of the fMRI signal, it can also be affected by regions having higher mean signal due to regional hyperintensities. In regions where the tSNR may be high, the functional response could be subject to exaggeration as the peak signal will be higher relative to other regions. To evaluate if there were hyperintensities of tSNR, as well as ensuring functional sensitivity was unaffected by the tSNR in our regions of interest, for both modalities, the relationship between tSNR and statistical T-scores was evaluated. The beta parameters within modality for the regions of interest in this study were also explored, particularly in the auditory and motor regions, to ensure that there was no differential sensitivity based on location.

9.4.1.2 Methods

tSNR images, as described in Section 9.2.3, were computed after pre-processing (up to spatial normalisation) but prior to smoothing. The resultant single-subject T-statistic maps were overlaid on the single-subject tSNR images to ascertain if the resultant tSNR related to the functional sensitivity, comparing the maps visually. To quantify this, a mask of each region of interest (motor and auditory) was computed using a functional ROI derived from Neurosynth Yarkoni (2011) to determine any patterns between T-statistics, tSNR and location.

The T-statistic maps for the contrast of Deviant + Novel > Silent were employed, assuming T-statistics as a measure of functional sensitivity given that they represent the best fit of the data to the GLM. The average T-statistic for the region was then plotted against the average tSNR for the region. The beta parameter measures for Looping Star and GRE-EPI were also extracted for the motor and auditory regions using MarsBaR (Section 5.7.2). A paired T-test was used (after normality testing) in IBM SPSS 27.0 (IBM Corp, 2020) to identify any statistically significant difference in beta parameters between regions of interest.

9.4.1.3 Results

Figure 9.13 shows an example of the T-statistics overlaid on the tSNR map for a single-subject, whereby there were no visible correlations between the tSNR and T-statistics. This was the case across all participants.

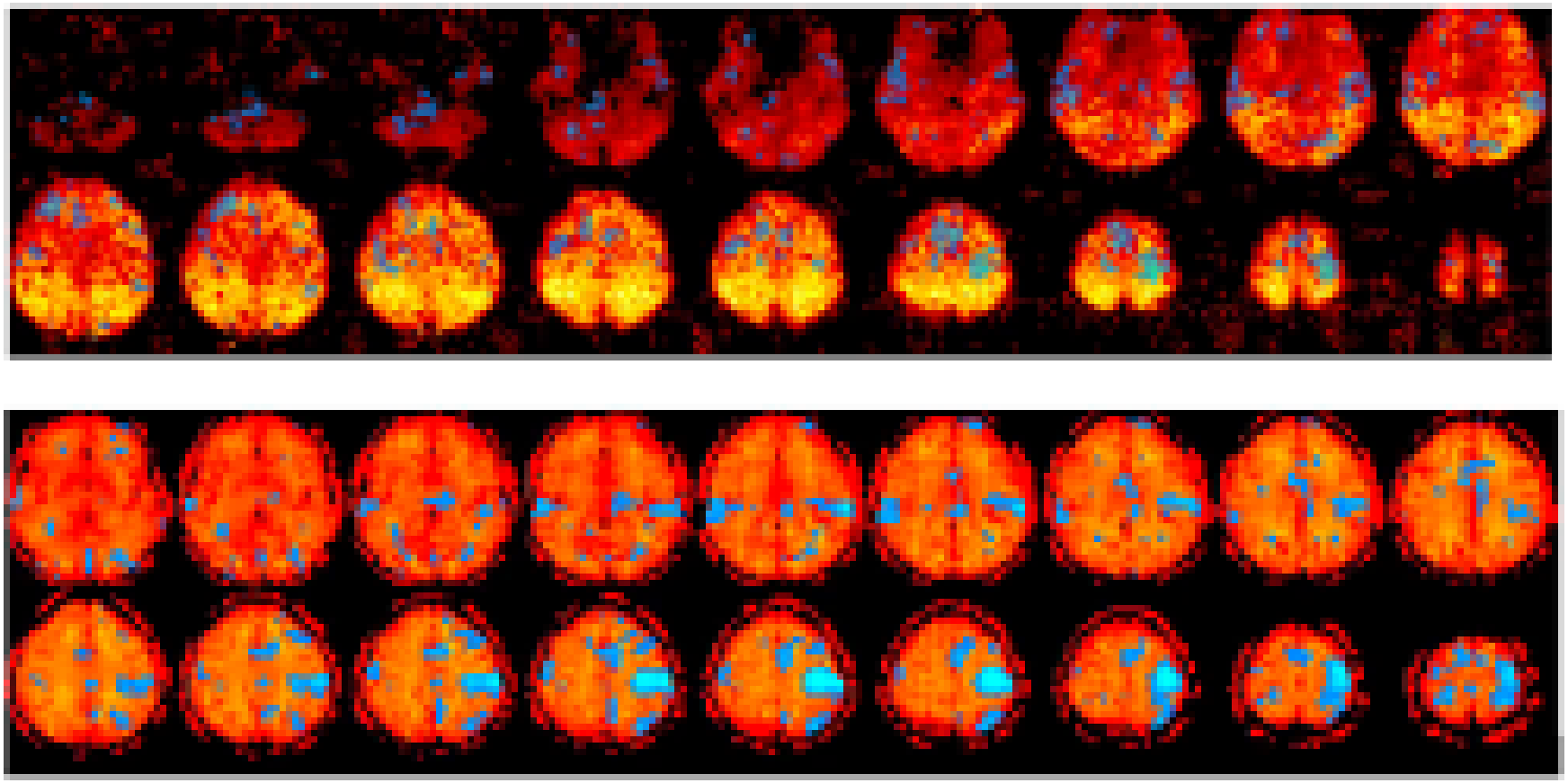

Figure 9.13: Single subject tSNR outputs overlaid with SPM T-score map, thresholded from $2 < T < 5$. Opacity increased for statistical overlay to visually demonstrate the absence of correlation of high tSNR regions with high T-score regions. (top) Looping Star, (bottom) GRE-EPI. Alternative slices shown to highlight active regions appropriately.

As expected, Figure 9.14 showed that tSNR did not impact the T-statistics of significant activity for either region of interest, as no correlations were found between tSNR and T-statistics for the ROIs.

Investigating the extracted beta parameter measures for each ROI, it can be seen that the beta parameters in general are lower in Looping Star, which is expected as our functional sensitivity is lower as described in Section 9.2.4. The result of the paired T-test showed that there was not a statistically significant difference in Deviant beta parameters within modality between regions but there was for Novel beta parameters for both modalities (Table 9.8). This does not indicate that Looping Star has differential sensitivity between regions any more so than GRE-EPI.

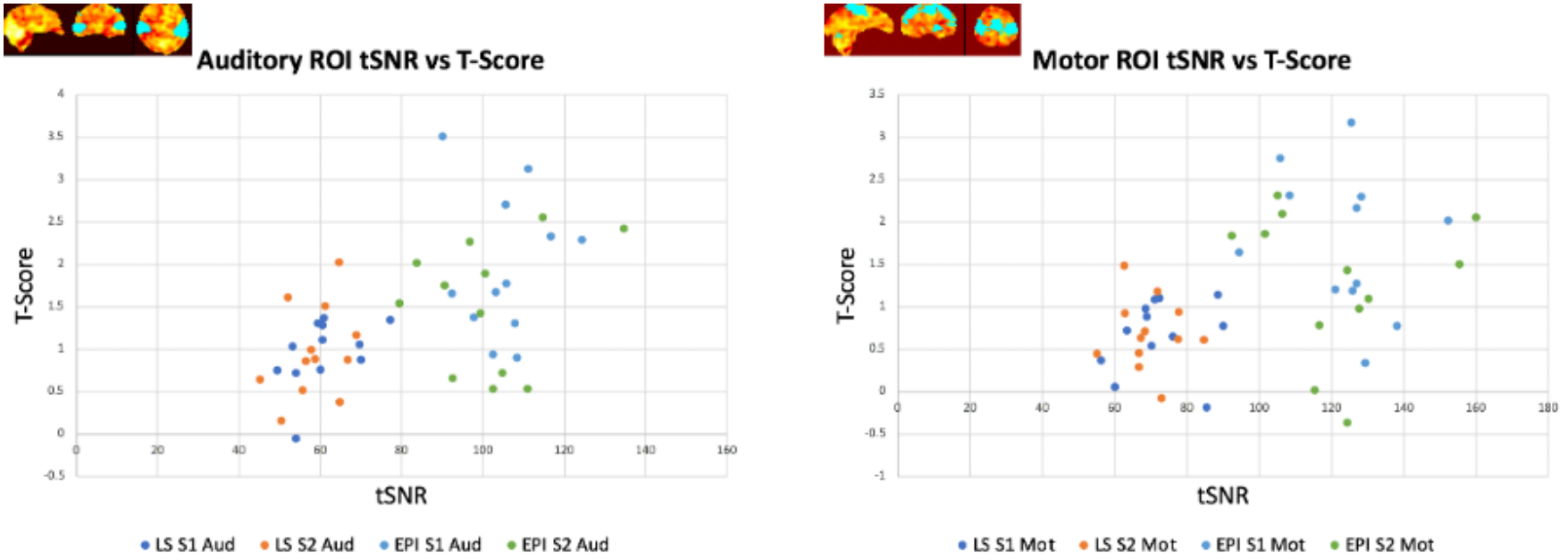

Figure 9.14: Average individual participant temporal signal to noise ratio (tSNR) and T-score, computed across an auditory and motor region of interest (ROI), plotted on the axes to identify any correlations. LS = Looping Star, S1 = Session 1, S2 = Session 2, Aud = Auditory ROI, Mot = Motor ROI. Each point represents a participant for the labelled session and modality. No clear correlations found between regions of higher tSNR and higher T-score for either modality. Example of mask applied on beta image demonstrated in top left corners of each plot.

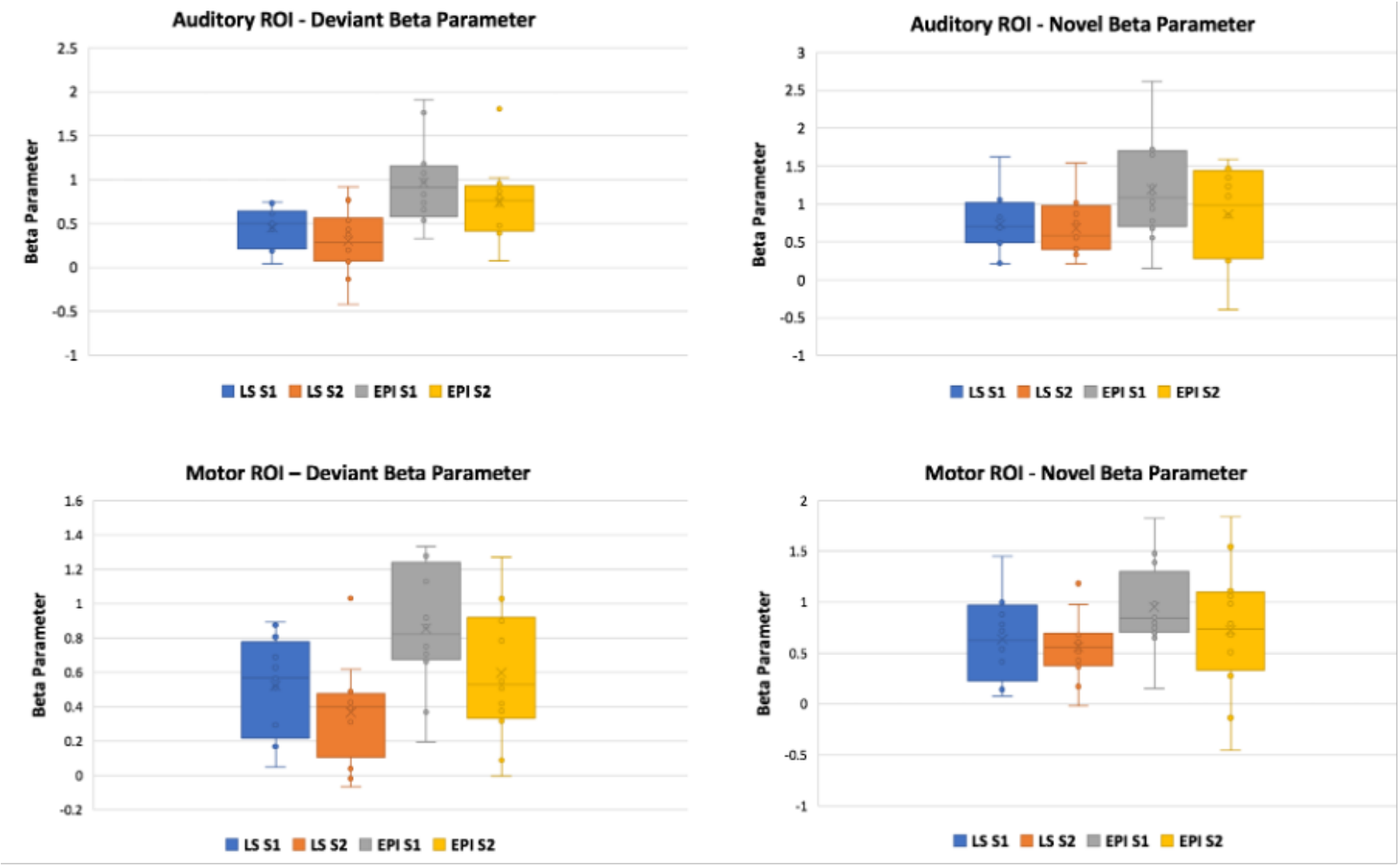

Figure 9.15: Average beta parameters for the modelled contrasts (Deviant and Novel Tones) extracted from auditory and motor regions of interest (ROI). Each point represents a single subject for the defined session and modality. LS = Looping Star, S1 = Session 1, S2 = Session 2. Beta maps for each participant were calculated at first level in SPM.

Table 9.8: Paired T-test results between ROIs for each modality and beta parameter.

Within-modality Paired T-test (Auditory ROI - Motor ROI)	**T-score**	**p-value (two-tailed)**
Looping Star Deviant Betas	-1.661	0.110
GRE-EPI Deviant Betas	1.777	0.089
Looping Star Novel Betas	2.615	0.015 *
GRE-EPI Novel Betas	2.387	0.026 *

* = $p < 0.05$

9.4.1.4 Discussion

Despite the hyperintensities seen in the raw images of Looping Star, visible in Supplementary Material Figure 9.10, regional tSNR did not appear to influence the resultant T-score. A possible explanation for the pattern of hyperintensities in the raw image may stem from motion as the patterns were not consistent across participants. Furthermore, the differences in the extracted beta parameters between regions of interest were consistent between GRE-EPI and Looping Star, supporting that there is no relationship between specific regions and having a higher beta parameter based on modality.

9.4.2 Impact of Smoothing

9.4.2.1 Background

As illustrated in Section 7.2, smoothing can affect the GRE-EPI acquisition however it tends not to affect Looping Star. The impact of lowering the smoothing threshold from 8 mm to 6 mm smoothing for both modalities was evaluated to investigate the robustness of the effects identified. The smoothing threshold was not lowered further

as this would likely lead to an unfair comparison with GRE-EPI given the voxel size and requirements for random field theory to hold (Worsley et al., 1996) alongside the findings of our previous investigations (Section 7.2).

9.4.2.2 Methods

The smoothing threshold for the data was lowered from 8 mm FWHM to 6 mm FWHM for both modalities; all other pre-processing and analysis remained consistent with Section 9.2.3. Only the statistical results for two contrasts are presented: Deviant + Novel > Silent and Novel > Deviant

9.4.2.3 Results

Robust results were found for Looping Star and GRE-EPI when lowering the smoothing threshold, whereby differential activation with Looping Star between tones was statistically significant in Session 1 but not in Session 2 or for GRE-EPI.

Table 9.9: Statistics table of results for parametric analysis at cluster-level ($p < 0.001$ unc.) across two contrasts for each session and modality at smoothing thresholds 6 mm and 8 mm.

Contrast Name	Modality	MNI Co-ordinates (x,y,z in mm)	Brodmann area	Cluster-level p(FWE)-value	T-score	Cluster size
Deviant + Novel > Silent	GRE-EPI Session 1 6 mm	-46 -28 10	41	$< 10^{-3}$ **	14.83	1612
		38 -32 -6	N/A	$< 10^{-3}$ **	8.7	289
	GRE-EPI Session 1 8 mm	-46 -28 10	41	$< 10^{-3}$ **	15.86	2325
		66 -20 10	41	$< 10^{-3}$ **	9.33	477
	GRE-EPI Session 2 6 mm	62 -20 14	40	$< 10^{-3}$ **	11.22	160
		-46 -20 58	1	$< 10^{-3}$ **	10.68	335
	GRE-EPI Session 2 8 mm	58 -20 18	40	$< 10^{-3}$ **	13.52	217
		-62 -20 18	1	$< 10^{-3}$ **	13.06	616
	Looping Star Session 1 6 mm	50 -32 14	41	$< 10^{-3}$ **	14.95	162
		2 -76 -22	N/A	$< 10^{-3}$ **	11.09	94

	Looping Star Session 1 8 mm	50 -32 14	41	$< 10^{-3}$ **	16.91	242
		2 -76 -22	N/A	$< 10^{-3}$ **	11.15	130
	Looping Star Session 2 6 mm	62 -12 6	40	0.006*	9.23	23
		-42 4 14	N/A	$< 10^{-3}$ **	9.16	369
	Looping Star Session 2 8 mm	-58 -20 22	1	$< 10^{-3}$ **	9.6	542
		6 -64 -14	N/A	$< 10^{-3}$ **	10.02	329
Novel > Deviant	GRE-EPI Session 1 6 mm	22 -84 30	19	0.002*	7.49	28
	GRE-EPI Session 1 8 mm	22 -84 26	19	0.009*	7.11	35
		-18 -92 26	18	0.022*	5.73	28
	GRE-EPI Session 2 6 mm	-18 -8 22	48	0.949	6.33	2

	GRE-EPI Session 2 8 mm	-18 -8 22	48	0.907	5.7	2
	Looping Star Session 1 6 mm	-46 -40 10	22	0.002*	13.62	27
		58 -32 14	22	0.002*	6.31	27
	Looping Star Session 1 8 mm	-46 -40 10	22	0.004*	10.29	37
		58 -32 15	22	0.001*	6.91	47
	Looping Star Session 2 6 mm	42 -44 14	N/A	0.202	6.36	9
	Looping Star Session 2 8 mm	42 -44 14	N/A	0.218	6.47	12

* = cluster-level p(FWE) < 0.05, ** = cluster-level p(FWE) < 0.001, N/A = outside of defined Brodmann Area, NSC = no significant clusters

9.4.2.4 Discussion

These results support the robustness of the Looping Star results to differentiating between auditory tones when using a different spatial smoothing kernel.

9.5 Chapter Discussion

This event-related design study, replicating a paradigm employed by Gomot et al. (2006), further indicates that despite the lower tSNR relative to GRE-EPI, Looping Star can be useful for auditory processing studies. The reliability requires further investigation to establish whether differences between sessions result from cognitive effects or acquisition effects. One promising avenue would be to compare with novel 3D radial GRE-EPI acquisition methods (Lee et al., 2010; Rettenmeier et al., 2021) to rule out the impact of non-Cartesian versus Cartesian sampling. The additional investigations and commentary showed that the results are robust to a lower smoothing threshold and are supported by inter-subject correlation analysis. It was also found that tSNR did not affect T-scores, with similar differences in T-scores between regions seen for both Looping Star and GRE-EPI.

Chapter 10

Coherence-Resolved Looping Star

In this chapter:

Summary

- A novel development of Looping Star is presented, involving temporally resolving the excited coherences in Looping Star.
- This technique is characterised in a phantom in comparison with original Looping Star.
- The application of this method is shown using an auditory speech processing task in a small cohort in comparison with original Looping Star.

Overview

This chapter describes the background and application of coherence-resolved Looping Star, a novel extension to Looping Star that involves temporally separating the excited coherences to reduce noise in the fMRI signal. This technique was characterised in phantoms and in vivo using an auditory speech processing paradigm. Its functional sensitivity and temporal stability were compared with original Looping Star.

10.1 Chapter Introduction

The original version of Looping Star, published by Wiesinger et al. (2019), exhibited echo-in echo-out mixing. This is caused by signal interference from the inwards refocusing and outwards dephasing coherences produced from the inherent 'looping' nature of the technique (Figure 10.1). In other words, the incoming echo and the start of the next echo overlap in the same acquisition window, which leads to artefacts in the MR signal.

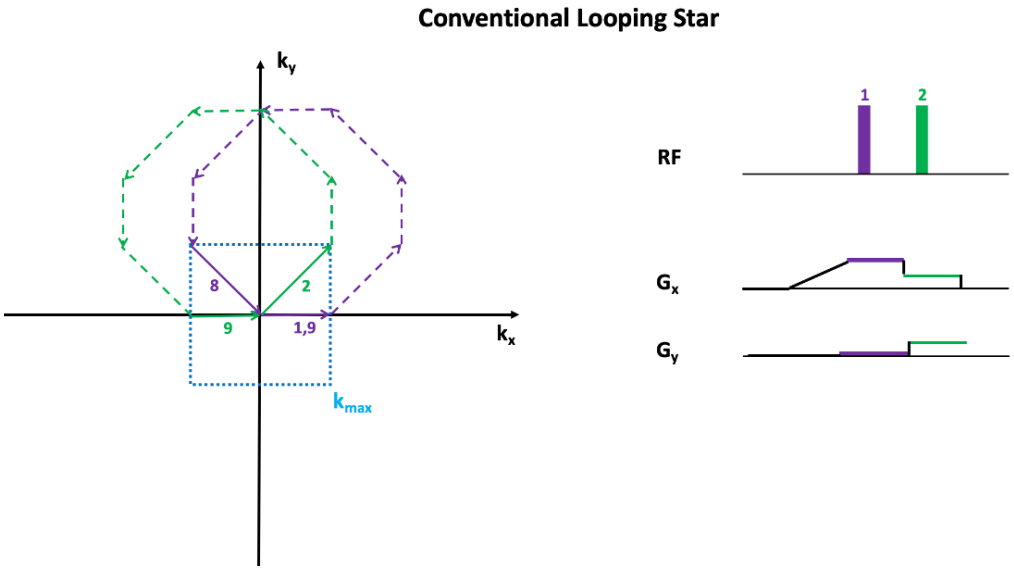

Figure 10.1: Conventional Looping Star in k-space with echo-in echo-out mixing (left), and short version of pulse sequence illustrating gradient (G_x, G_y) and RF application (i.e. first two spokes) at numbered time points (right). Overlapping coherences can be seen within the maximum k-space field of view (k_{max}), or acquisition window. This temporal interference is shown for the first two excitation loops (purple, green) in an 8 spokes per loop acquisition. At time point 9 there is signal present in the field of view from both the refocused incoming and excited outgoing coherences.

Initially, the main approaches for addressing this echo-in echo-out mixing have been focused on minimising the effects of this coherence overlap on the MR signal, for example by applying a Fermi filter (Wiesinger et al., 2019). As described by Caparelli and Tomasi (2008), Fermi filters smooth the fMRI data such that the high frequency components of k-space are attenuated. Therefore, they primarily eliminate noise in the MR signal but they can also remove signals of interest and reduce the SNR.

Although inappropriate for fMRI scanning as it doubles the scan time, RF phase cycling

is another method of addressing signal noise, whereby two volumes are acquired per required volume, with alternating transmit RF phases (by a factor of π). The two volumes acquired with alternating π phases are then linearly combined. This suppresses unwanted phase-dependent signal contributions (Tseytlin, 2017).

To improve the SNR and tSNR of the images, reducing the impact of noise in the MR signal, the multi-echo capability of Looping Star has primarily been exploited. Optimal multi-echo echo combination avoids removing signal or doubling the scan time, but does not address the signal noise from echo-interference unless de-noising strategies are then applied.

The signal interference has been effectively resolved by our collaborators at GE Healthcare through implementing temporal spaces between the RF excitations, producing diametric, rather than radial, spokes in k-space (Wiesinger and Solana, 2020). This means that although it reduces the number of overall excited coherences by half, the spokes are refocused with twice the length of the FID. This method is known as coherence-resolved Looping Star (CRLS).

Relative to the original Looping Star methodology, this can also be visualised as exciting every second radial spoke (Figure 10.2), allowing the cumulative trajectory to continue to develop via the next gradient application and therefore elongating the spoke. The coherences are therefore separated in time, preventing signal overlap.

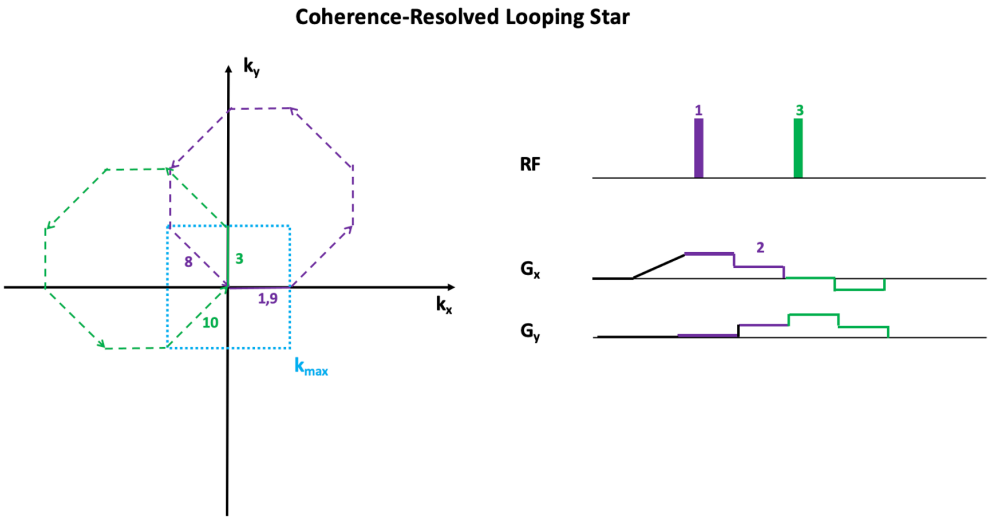

Figure 10.2: Coherence-resolved Looping Star in k-space (left), and pulse sequence illustrating gradient (G_x, G_y) and RF application of first two spokes (right) with numbered time points. Echo separation via coherence resolution can be seen for the first two excitations (purple, green), where each excitation has two accompanying gradient steps (right) and therefore produces diametric spokes, visible as the arrowheads (left). Since the second excitation (green) is applied at a later time point, temporal signal overlap in the field of view is avoided as indicated by the absence of overlapping time points. Although the FID is now only 4 spokes, the number of spokes per loop remains as 8 based on the number of gradient steps remaining the same.

The point spread function of CRLS after nearest-neighbour gridding and density compensation for a 24 spokes per loop fMRI acquisition can be seen in Figure 10.3, compared with a 32 spokes per loop acquisition with original Looping Star. The different spokes per loop were implemented as these parameters produce the same echo times in practice. CRLS produces a smaller FWHM compared with original Looping Star (Section 3.10), indicating improved spatial localisation.

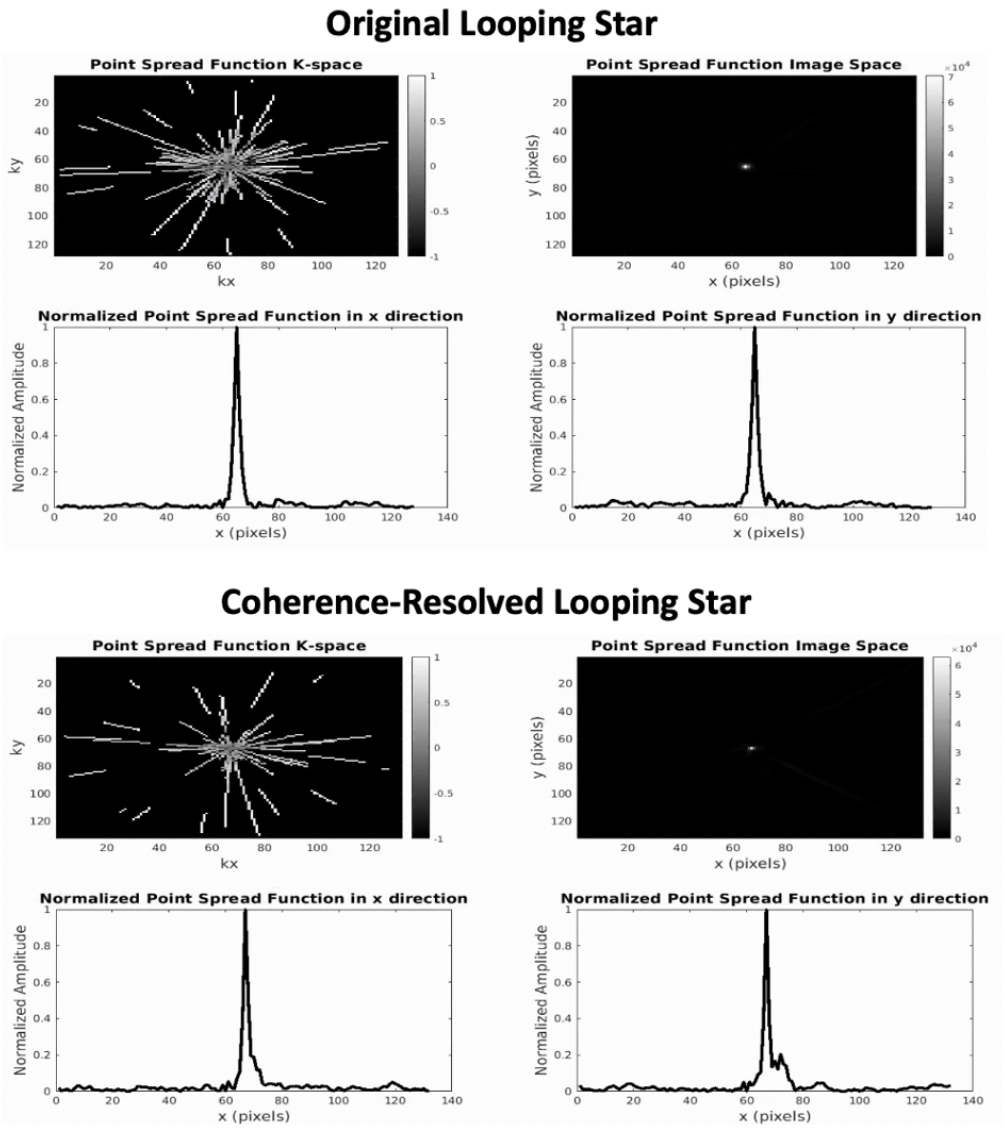

Figure 10.3: (top) Point spread function in k-space and image space, (bottom) profile of point spread function. (left) Original Looping Star with $FWHM_x = 3$ pixels, $FWHM_y = 3$ pixels, acquired with parameters 32 spokes per loop, 1024 spokes per volume, $\pm$ 31.25 kHz BW and (right) Coherence-resolved Looping Star with $FWHM_x = 1$ pixels, $FWHM_y = 2$ pixels, acquired with parameters 24 spokes per loop, 504 diametric spokes per volume, $\pm$ 31.25 kHz BW.

This chapter demonstrates the application of coherence-resolved Looping Star to an auditory speech-processing paradigm in vivo, including comparisons with conventional Looping Star. The sequence is also characterised in a phantom using temporal stability measures (Section 5.7.1). These studies were performed using the GE 3 T MR750 scanner at the Clinical Research Facility (Section 5.2). The original pseudo-random sampling trajectory generation method was used for both modalities (Wiesinger et al., 2019) (Section 3.3), and the trajectories used were produced by Dr Anabea Solana (GE Healthcare). Parts of this work were presented at the ISMRM Annual Meeting 2021 (Damestani et al., 2021c).

10.2 Phantom Characterisation of Coherence-Resolved Looping Star

10.2.1 Background

As discussed earlier, measuring the temporal stability of a pulse sequence in a phantom is key for identifying signal characteristics independent of tissue properties. High amplitude signal instabilities could mask the BOLD response in vivo, therefore it is important to characterise the pulse sequence in the phantom prior to in vivo evaluation. The impact of coherence resolution on temporal stability was evaluated in comparison with original Looping Star to identify whether noise in the MR signal was reduced in a phantom.

10.2.2 Methods

The spherical phantom previously described (Section 5.7.1) was used to evaluate the temporal stability. The data was collected using the parameters in Table 10.1, with the 32-channel coil (Section 5.2). The echo times were matched as closely as possible for the different parameters. Nearest neighbour gridding was used for both modalities (Section 5.2), and the stability measures from Section 5.7.1 were implemented. The first four volumes from analysis were neglected to allow the longitudinal magnetisation to reach steady-state.

Table 10.1: Acquisition parameters for single-echo coherence-resolved Looping Star

Acquisition Parameters
CRLS: 24 spokes per loop, FID + echo, ±31.25 kHz, GSF 14, 3 mm isotropic resolution, TR = 2.47 s, TE = 26.88 ms, factor of 2.5 undersampling, FOV = 19.2 cm, FA = 3°, 816 diametric spokes per echo volume, 100 volumes, 4 mins 24 s
CRLS: 24 spokes per loop, FID + echo, ±31.25 kHz, GSF 14, 3 mm isotropic resolution, TR = 1.53 s, TE = 26.88 ms, factor of 4 undersampling, FOV = 19.2 cm, FA = 3°, 504 diametric spokes per echo volume, 100 volumes, 2 mins 39 s
Original LS: 32 spokes per loop, FID + echo, ±31.25 kHz, GSF 14, 3 mm isotropic resolution, TR = 2.33 s, TE = 26.88 ms, factor of 4 undersampling, FOV = 19.2 cm, FA = 3°, 1024 spokes per echo volume, 100 volumes, 3 mins 52 s

10.2.3 Results

Table 10.2 shows the stability measures for each acquisition. It can be seen that the 24 spokes per loop CRLS acquisition with lower undersampling produces higher SNR and tSNR values than original Looping Star, which is expected, however it also produces the lowest RDC value. The amount of signal fluctuation and drift is similar across acquisitions. For the same undersampling factor, CRLS produces a lower tSNR and SNR, which is expected as the number of spokes per volume is lower.

Table 10.2: Temporal stability analysis of 2D ROI (15 x 15 pixel) for gradient echo of original (LS) and coherence-resolved Looping Star (CRLS). US = undersampling factor.

Acquisition	SNR	tSNR	PSF (%)	PSD (%)	RDC (pixels)
CRLS: 24 spl, x 2.5 US	268.49	248.98	0.108	-0.15	3.42
CRLS: 24 spl, x 4 US	195.72	200.69	-0.091	-0.13	5.70
Original LS: 32 spl, x 4 US	236.02	229.86	0.088	-0.07	5.16

Figure 10.4 demonstrates comparable SSN, Weiskoff curves and frequency profiles between acquisitions, with higher tSNR across the phantom for the 24 spokes per loop acquisition. The lower tSNR in the centre of the phantom was found to be related to lower average signal, which is likely linked to inhomogeneities in the spherical phantom as discussed previously (Section 6.1).

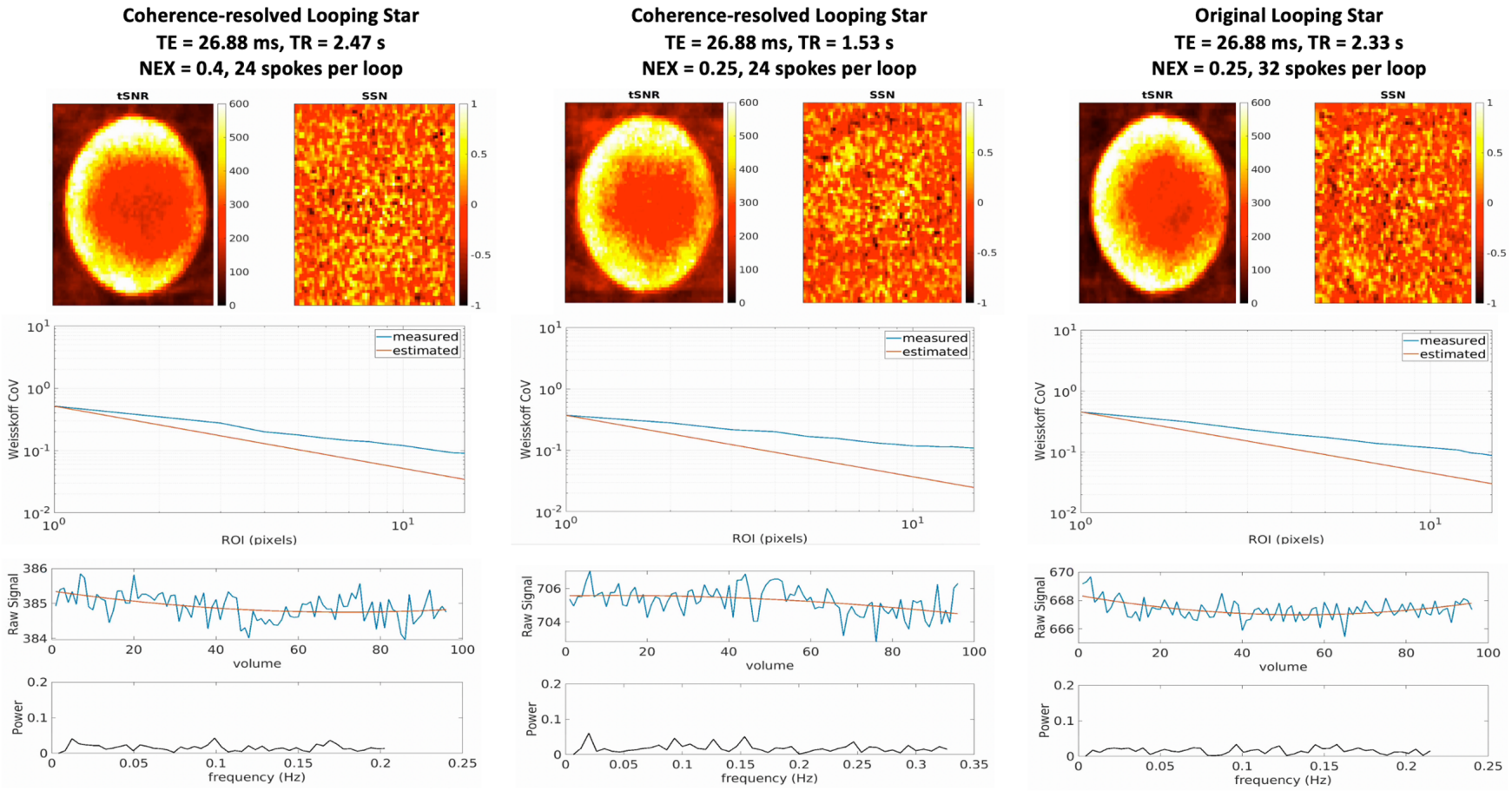

Figure 10.4: For each modality, (top) tSNR and SSN images (middle) Weisskoff curves and (bottom) raw signal with frequency profile in the 15 x 15 pixel ROI are shown.

10.2.4 Discussion

Coherence-resolved Looping Star demonstrated good tSNR and SNR for both acquisitions relative to original Looping Star, and a lower number of spokes per volume for coherence-resolved Looping Star can produce higher tSNR than original Looping Star, likely due to its diametric characteristics. Furthermore, the signal characteristics and temporal stability were similar between techniques, demonstrated by the power spectra and Weisskoff analysis. No significant pulse sequence-induced instabilities for CRLS were found and therefore in vivo characterisation of the functional sensitivity may be explored.

10.3 Comparing Conventional and Coherence-Resolved Looping Star In vivo

10.3.1 Background

This section directly compares conventional and coherence-resolved Looping Star using an auditory speech processing paradigm in a small cohort. Using an auditory paradigm for validation of both techniques is important given that their core benefit is acoustic noise reduction. This work can be used to evaluate whether future studies should prioritise the use of coherence-resolved Looping Star over its original iteration.

10.3.2 Methods

Five participants volunteered for this study. English words were played through MR-compatible headphones during blocks of 24 second durations. The speed at which the words were played was different for each block (30, 60, 90 and 120 words per minute), and the order of the block was randomised (i.e. the speed did not steadily increase or

decrease with consecutive blocks, but randomly changed). A fixation cross was displayed during the paradigm and participants were asked to keep their eyes open. Rest blocks of 24 seconds duration involved a fixation cross with no auditory stimulation (Figure 10.5). The paradigm set up is described in Section 5.3.

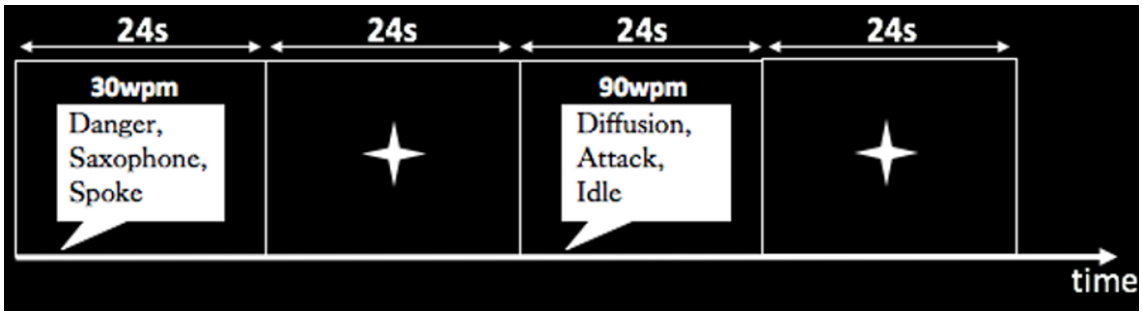

Figure 10.5: Auditory speech processing paradigm, wpm = words per minute. The fixation cross was displayed throughout the paradigm, the speech bubble in this visualisation indicates auditory words being spoken.

The acquisition parameters are detailed in Table 10.3, and were selected to closely match the TR and TE values between acquisitions. The number of volumes was selected to equalise the scan times for the two scans. The acoustic noise of each acquisition was measured in the centre of the scanner bore for a duration of 15 seconds (Section 5.5). Image reconstruction of both Looping Star datasets was performed using nearest-neighbour gridding. The scan order was randomised between participants to avoid order effects.

Table 10.3: Acquisition parameters for original and coherence-resolved Looping Star for fMRI.

Acquisition Parameters
Coherence-resolved Looping Star: FID + echo, $\pm$31.25 kHz BW, 24 spokes per loop, 816 spokes per volume, GSF = 14, TR = 2.47 s, TE = 26.9 ms, isotropic voxel resolution = 3 mm, FOV = 19.2 cm, FA = 3°, 142 volumes
Original Looping Star: FID + echo, $\pm$31.25 kHz BW, 32 spokes per loop, 1024 spokes per volume, GSF = 14, TR = 2.33 s, TE = 26.9 ms, isotropic voxel resolution = 3 mm, FOV = 19.2 cm, FA = 3°, 151 volumes

An anatomical image was acquired for each participant using a silent T_1 weighted

inversion recovery-prepared RUFIS acquisition for spatial normalisation of the fMRI datasets (Hollingsworth, 2015), with parameters: TI = 450 ms, 1 mm isotropic resolution, FOV = 22 cm, FA = 2°, ±15.6 kHz (Figure 10.6).

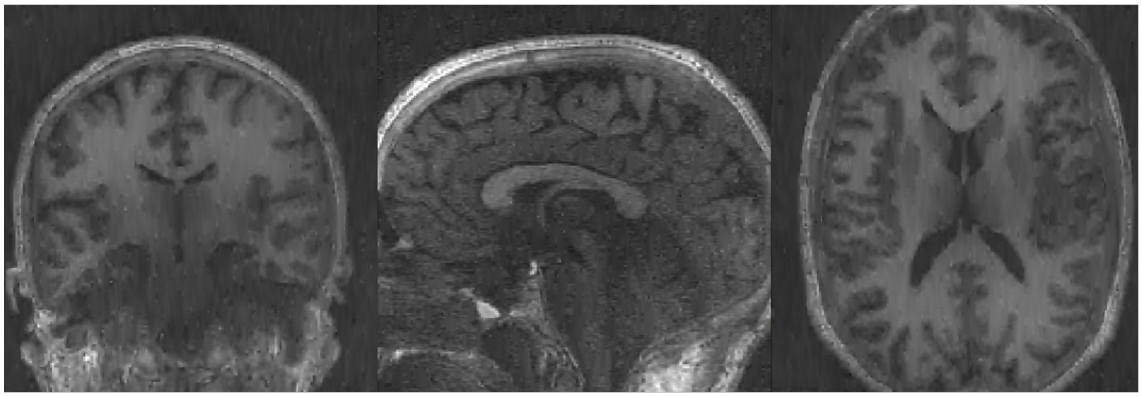

Figure 10.6: Example of single subject T_1 weighted inversion recovery-prepared RUFIS acquisition. Image presented using FSL (Jenkinson et al., 2012).

For one participant, a single volume with high number of spokes was additionally acquired to qualitatively compare image quality between coherence-resolved, original, RF cycled and filtered Looping Star acquisitions, highlighting whether benefits are clear when no additional undersampling effects are taking place. The acquisition parameters are given in Table 10.4. Both acquisitions were reconstructed with nearest-neighbour gridding, and the conventional Looping Star scans were also reconstructed with Fermi filtering and use of the RF-phase cycling for comparison with coherence-resolved Looping Star.

Table 10.4: Acquisition parameters for single-volume original and coherence-resolved Looping Star

Acquisition Parameters
Coherence-resolved Looping Star: FID + echo, ±31.25 kHz, 24 spokes per loop, 4176 spokes per volume, GSF = 14, TR = 7 s, TE = 26.88 ms, isotropic voxel resolution = 3 mm, FOV = 19.2 cm, FA = 3°, one volume
Original Looping Star: FID + echo, ±31.25 kHz, 32 spokes per loop, 4160 spokes per volume, GSF = 14, TR = 14 s, TE = 26.88 ms, isotropic voxel resolution = 3 mm, FOV = 19.2 cm, FA = 3°, RF phase cycling on, two volumes.

Steady-state signal stabilisation was ensured by removing the first four volumes of both

Looping Star datasets. tSNR was computed using second-order polynomial de-trending of the mean signal from the normalised datasets (Friedman and Glover, 2006), followed by averaging across participants.

The dataset was pre-processed with a standard SPM-12 pipeline (FIL Methods Group, 2020), including bias field correction and segmentation of the T_1-weighted RUFIS scan, realignment, co-registration of the FID and the T_1 image and application of the same transformation matrix to the other echo images, spatial normalisation to MNI space with images saved at 2 mm spatial resolution, and 6 mm FWHM smoothing.

First level and group level analyses were also performed in SPM-12. A 128 s high-pass filter was applied with motion regressors and the auditory stimuli modelled in the general linear model. The standard canonical double-gamma hemodynamic response function was employed. The AR(1) autocorrelation correction function was also employed for ReML parameter estimation (Poldrack et al., 2011). A first-order polynomial expansion of the parametric modulation for the speed at which words were spoken was also included in the general linear model. This model was used as the required activation was expected to increase with speed, though the volume of the words spoken remains the same. The contrast for the main effect of sound and the main effect of word frequency were modelled, as in Section 7.3.

Cluster-level inference using a primary uncorrected cluster-forming threshold of $p < 0.001$ uncorrected (Woo et al., 2014; Worsley et al., 1996) was employed. Only clusters surviving family-wise error correction at the cluster-level (i.e., $p_{FWE_c} < 0.05$) were deemed significant. A paired T-test between the contrast maps for the main effect of sound was also computed to directly compare modalities.

The normalised (i.e. scaling the signal to have a mean = 0 and standard deviation = 1) signal time series was extracted from the a 10 mm radius spherical ROI centred on the highest peak T-statistic within the most significant cluster (i.e. highest T-statistic in the cluster of $p_{FWE_c} < 0.005$) for each participant using MarsBaR (Brett, 2016; Brett et al., 2002). The percentage signal change was computed in this ROI for each participant as

described in Section 5.7.2.

10.3.3 Results

The improvements to image quality are qualitatively seen in Figure 10.7, whereby coherence-resolution can be seen to improve the identification of the ventricles relative to conventional Looping Star, regardless of filtering.

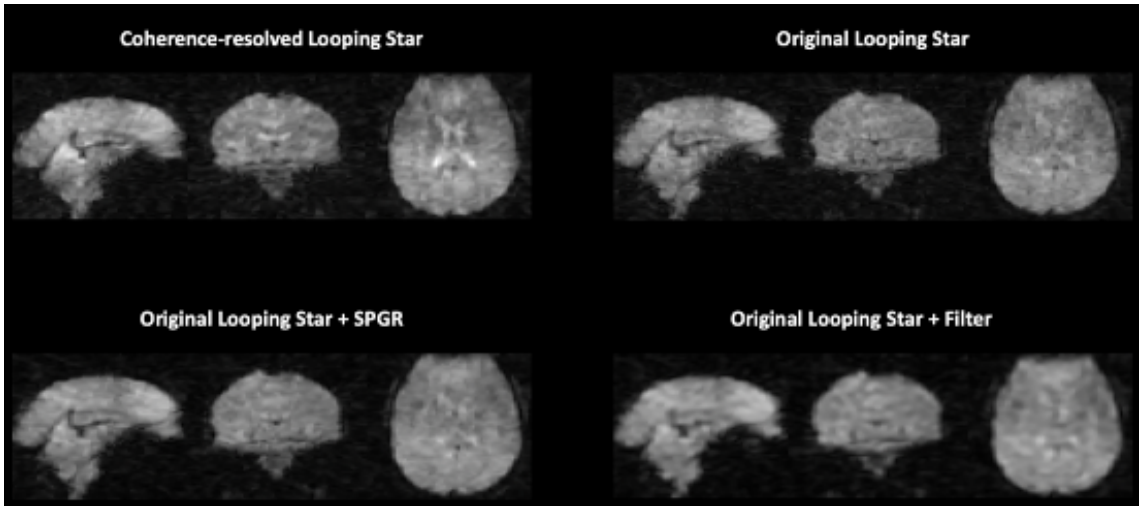

Figure 10.7: Image quality of single volume for the echo of acquisitions in Table 10.4, with reconstruction including averaging of the RF phases (+ SPGR) or Fermi filtering (+ filter). Image presented using FSL (Jenkinson et al., 2012).

The acoustic noise (LA_{eq}) for conventional Looping Star fMRI was 66.4 dB(A) and 66.3 dB(A) for CRLS fMRI, compared with the ambient scan room noise at 65 dB(A). The average tSNR across participants for conventional and coherence-resolved Looping Star was similar (Figure 10.8).

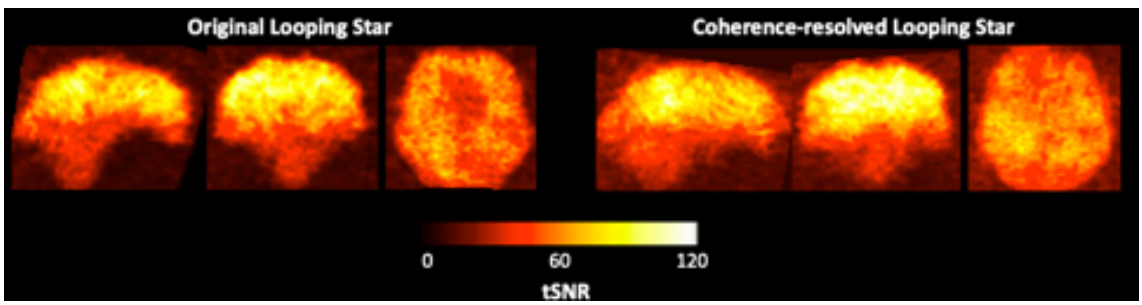

Figure 10.8: tSNR for original (left) and coherence-resolved (right) Looping Star echo data averaged across participants. Image presented using FSL (Jenkinson et al., 2012).

Both modalities identified significant activity related to the main effect of sound, with coherence-resolved Looping Star identifying more significant clusters of smaller spatial extent relative to the single larger cluster identified by original Looping Star (Figure 10.9, top). The statistics table accompanying these results can be seen in Table 10.5, where coherence-resolved Looping Star provided much higher T-scores but smaller cluster extent relative to original Looping Star. When investigating the single-subject statistical maps, varying lateralisation of the activity across participants was found for both modalities (Figure 10.9, bottom).

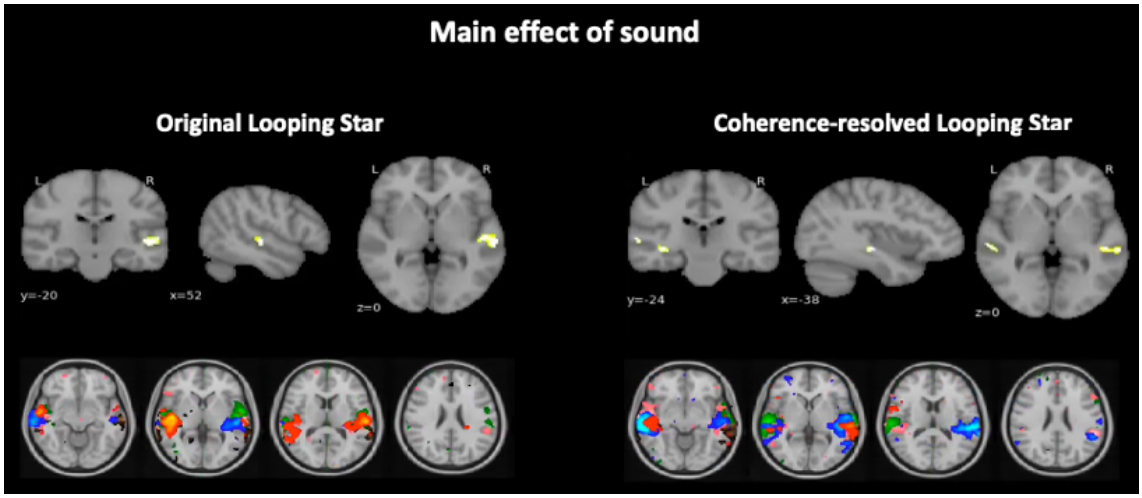

Figure 10.9: (top) Group-level T-statistic maps for the main effect of sound, thresholded at the appropriate cluster-extent for statistical significance. Visually demonstrated at $2 < T < 10$. Image produced using NiLearn (The Nilearn developers, 2021). (bottom) Single-subject T-statistic maps overlaid on for all participants, thresholded at $3 < T < 10$ without cluster-extent correction. Image presented using FSL (Jenkinson et al., 2012).

Table 10.5: Statistical results for group level activity for main effect of sound.

Acquisition	Peak MNI Co-ordinates (x,y,z mm)	Brodmann Area	Peak-level T-statistics	Cluster-level p_{FWE}-value	Cluster Size	Peak cluster MarsBaR PSC (%)
Coherence-resolved Looping Star	-38 -24 -8	N/A	60.98	0.037 *	32	0.9576
	-62 -24 2	22	21.09	$< 10^{-3}$ **	78	
	28 52 18	10	27.09	$< 10^{-3}$ **	83	
Original Looping Star	52 -20 -2	22	17.58	$< 10^{-3}$ **	152	0.9822

* = cluster-level p(FWE) < 0.05, ** = cluster-level p(FWE) < 0.001, N/A = outside of defined Brodmann Area

For the speed at which words were spoken, only original Looping Star identified significant activity and this was once again left-lateralised as in Section 7.3. Coherence-resolved Looping Star identified a left-lateralised non-significant cluster in the auditory cortex (Figure 10.10). A larger sample size may be required to better resolve this effect, given that Looping Star has demonstrated low power (Section 7.2.3). The accompanying statistical results can be seen in Table 10.6, where once again it can be seen that the cluster extent was lower but with a much higher T-statistic for coherence-resolved Looping Star.

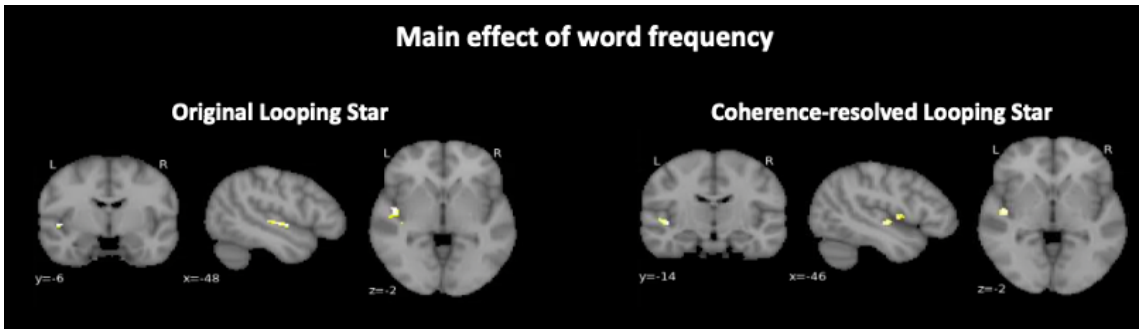

Figure 10.10: Main effect of word frequency for both modalities, thresholded at appropriate cluster-extent for statistical significance of original Looping Star. For coherence-resolved Looping Star, no significant activity was found so thresholding was performed for the cluster-extent of nearest statistical significance. The T-statistics were between $2 < T < 10$. Images were produced in Nilearn (The Nilearn developers, 2021).

Table 10.6: Statistical results for group level activity for main effect of word frequency

Acquisition	**Peak MNI Coordinates (x,y,z mm)**	**Brodmann Area**	**Peak-level T-statistics**	**Cluster-level p_{FWE}-value**	**Cluster Size**
Coherence-resolved Looping Star	-46 -14 -2	22 (L)	37.46	0.052	35
Original Looping Star	-48 -6 -2	N/A	17.54	0.008 *	54

* = cluster-level p(FWE) < 0.05, ** = cluster-level p(FWE) < 0.001, N/A = outside of defined Brodmann Area

Figure 10.11 demonstrates the time series extracted from the 10 mm radius spherical auditory ROI with the highest peak T-statistic for both modalities. Clear paradigm-related time series are seen in both modalities, with one participant demonstrating poor signal quality.

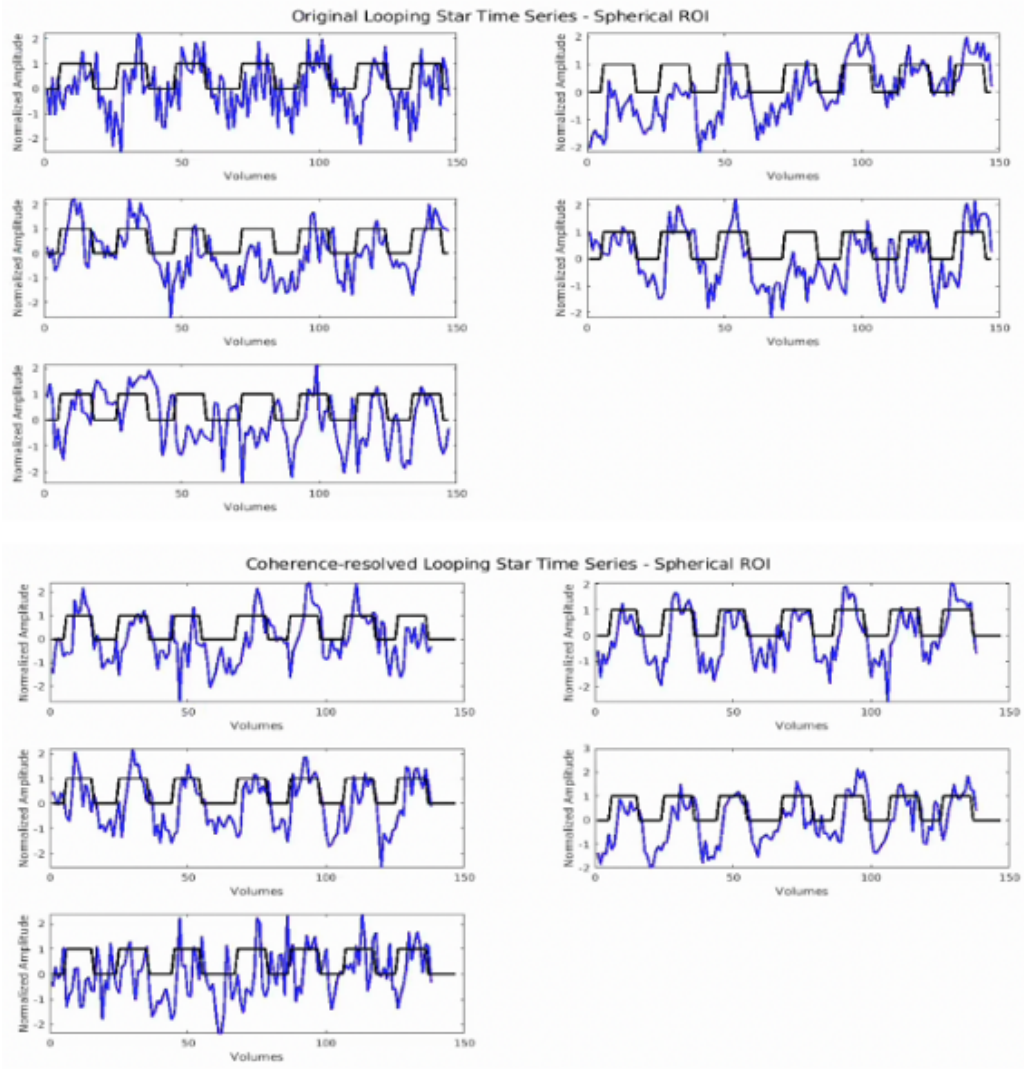

Figure 10.11: Extracted time series from 10 mm radius spherical ROIs in auditory cortex for each participant. (top) Original Looping Star, (bottom) Coherence-resolved Looping Star. Blue indicates the extracted signal and black indicates the task onsets.

Figure 10.12 demonstrates the range of percentage signal change extracted from the 10 mm radius auditory ROI with the highest peak T-statistic for both modalities. Table 10.7 details the mean beta and percentage signal change values, highlighting higher values for both from coherence-resolved Looping Star. However, the paired T-test between techniques indicated no statistically significant differences between modalities.

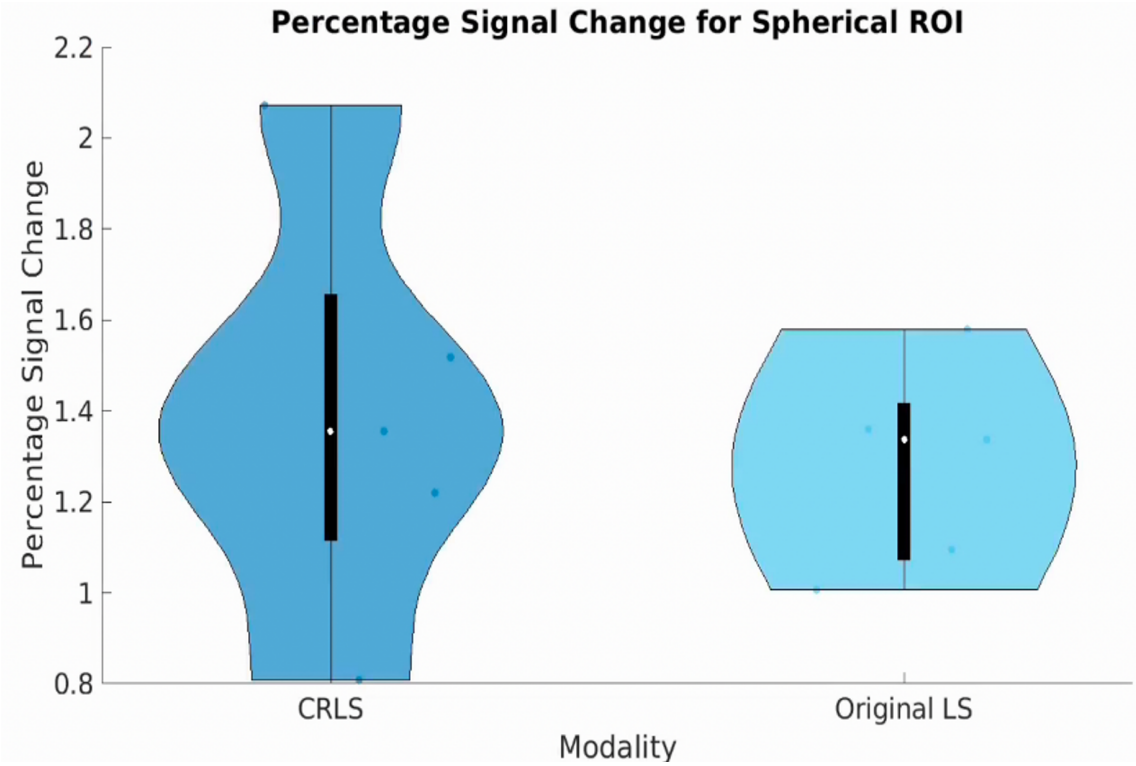

Figure 10.12: Percentage signal change violin plots across subjects from 10 mm radius spherical ROIs (Bechtold, 2016).

Table 10.7: Mean percentage signal change and mean beta parameter in spherical ROI for both modalities, extracted with MarsBaR (Brett, 2016; Brett et al., 2002).

Acquisition	Mean Beta in Spherical ROI	Mean PSC in Spherical ROI
Coherence-resolved Looping Star	2.14	1.39
Original Looping Star	1.79	1.28

10.3.4 Discussion

These results indicate that coherence-resolved Looping Star and original Looping Star produce similar results, with the key difference being that original Looping Star produces spatially larger clusters with lower T-scores whereas in coherence-resolved Looping Star the clusters are smaller with very high T-scores. As T-values result from the ratio between the parameter estimate and error variance (Pernet, 2014), this could indicate that coherence-resolved Looping Star has an advantage of smaller error variance, potentially due to reduced noise, although this requires validation in a larger cohort.

Interestingly, participants produced the distinct between-subject lateralisation, supporting studies of unique lateralisation of the auditory cortex between individuals (Burton et al., 2001; Langers et al., 2005a; Tervaniemi and Hugdahl, 2003). However, given that one participant demonstrated high noise in this small cohort and due to the low power of Looping Star, a larger cohort is crucial for better interpreting the benefits of coherence-resolved Looping Star.

10.4 Chapter Discussion

This chapter presented the successful application of coherence-resolved Looping Star, demonstrating improved image quality and good functional sensitivity relative to original Looping Star. The temporal stability of coherence-resolved Looping Star was also similar to original Looping Star, though coherence-resolved Looping Star was also capable of producing higher tSNR and SNR values for fewer spokes per volume. Though differences were not significant between techniques, the subtle difference at group level was that coherence-resolved Looping Star produces smaller clusters of higher peak T-statistic values in comparison with original Looping Star. This would be an important consideration for effect size calculations in future, if replicated in a larger cohort.

Chapter 11

Taking Looping Star Further

Summary

This chapter describes avenues for taking Looping Star further, including:

- A collaborative project involving a novel image reconstruction framework for accelerated coherence-resolved Looping Star
- Proof-of concept quantitative susceptibility mapping with coherence-resolved Looping Star
- Exploration of the functional sensitivity in free-induction decay images

Overview

This chapter highlights interesting future directions of Looping Star. A novel method for improving coherence-resolved Looping Star image quality and temporal resolution is demonstrated as a proof-of-concept study. A preliminary single subject investigation into susceptibility-weighted imaging with coherence-resolved Looping Star, compared for the first time with conventional MRI, is performed. Evaluation of the free-induction decay functional sensitivity is also explored with both original and coherence-resolved Looping Star.

11.1 Chapter Introduction

This thesis has so far demonstrated the successful applications of both original and coherence-resolved Looping Star across numerous functional paradigms and at rest. One of the primary limitations of Looping Star is the image quality, as Looping Star is susceptible to blurring due to its k-space sampling trajectory (i.e. the high spatial frequency regions of k-space are not densely sampled).

When the Looping Star trajectory is highly sampled, the presence of image blur is lower. However, the edges of k-space are always missed due to the spherical nature of acquisition (See Section 3.4). Blur is also further induced by motion, as motion manifests as radial smearing (Madio and Lowe, 1995).

High k-space sampling is not compatible with fMRI as further samples increase the acquisition time. The primary method for reducing the acquisition time is therefore to decrease the sampling density, which further affects the image quality. The impact of undersampling in original Looping Star is visualised both in vivo and in a phantom in Figure 11.1, where it can be seen that higher undersampling produces more image blur and streaking.

When undersampling is employed in Looping Star, entire segments (or conical planes) of k-space are not sampled, affecting both the image contrast and the resolution of finer details in the image. This could pose issues for future studies that require shorter repetition times, which are growing in popularity due to the benefits for detecting and removing physiological noise (Agrawal et al., 2020), gains in statistical power (Dowdle et al., 2021), as well as resolving neural activity (Lewis et al., 2016).

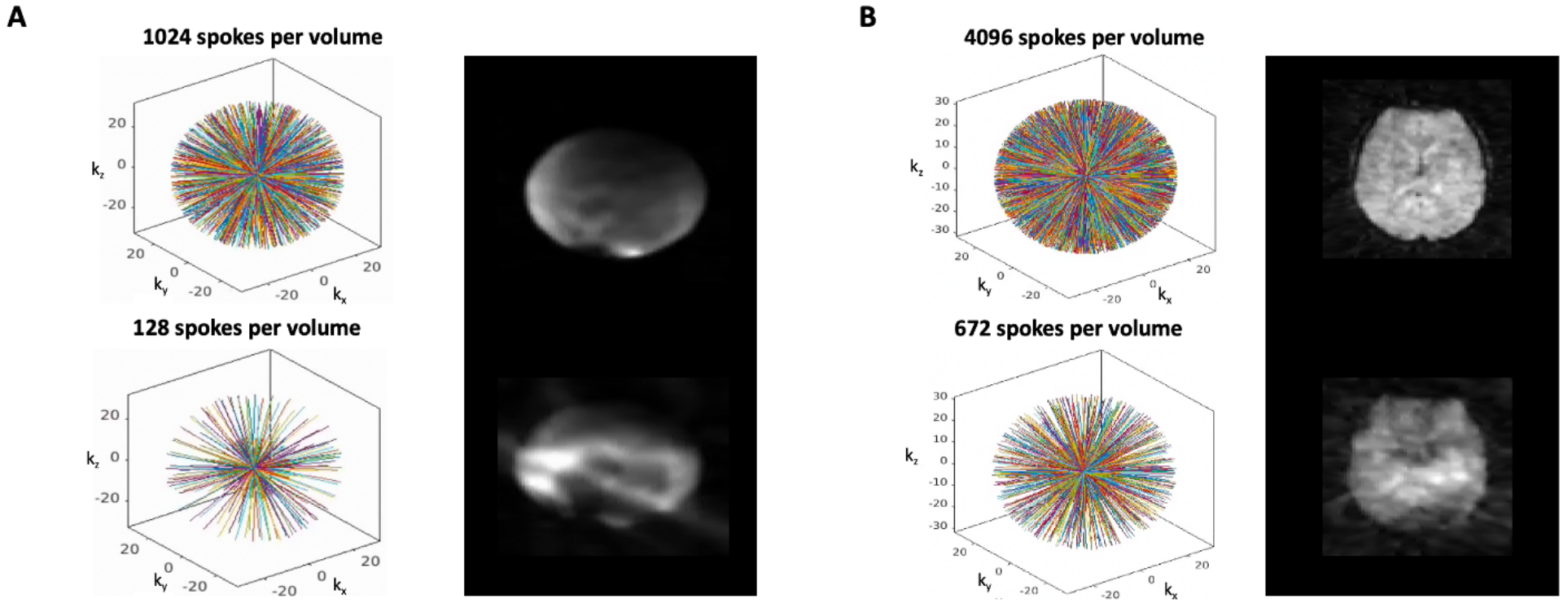

Figure 11.1: Impact of undersampling on an echo of original Looping Star acquisition A) in phantom and B) in vivo. For the phantom, 1024 spokes per volume (original acquisition) and 128 spokes per volume are shown, using a 32-channel coil and nearest-neighbour gridding. For the in vivo scan, 4096 spokes per volume (original acquisition) and 672 spokes per volume are shown, using a 12-channel coil and nearest-neighbour gridding. undersampling is produced by removing segments from the original acquisitions. Both datasets were acquired with acquisition parameters: 32 spokes per loop, 3 mm isotropic resolution, 19.2 cm FOV, GSF 14, ±31.25 kHz BW. Phantom data collected in spherical phantom, and both datasets were collected at the Clinical Research Facility (see Section 5.2).

A novel reconstruction method for accelerated non-Cartesian imaging is 'Extreme MRI', which is a low-rank image reconstruction technique. Low-rank methods have gained interest in recent years due to their potential for recovering fMRI signals from highly under-sampled data (Chiew et al., 2015, 2016; Mason et al., 2021). Extreme MRI involves adapting the Looping Star acquisition such that a single high resolution volume is acquired, and this volume is then separated into an fMRI time series consisting of randomly selected variable samples across the number of volumes of interest (Leynes et al., 2021; Ong et al., 2020). The redundancy present in fMRI data is exploited to fill missing k-space samples across volumes. To date, it has shown promising single subject results for fMRI with coherence-resolved Looping Star (Leynes et al., 2021), however the limitations of this method in terms of the accuracy of the signal detected with rapidly accelerated Looping Star data has not been thoroughly investigated.

Beyond improving image reconstruction, the application of coherence-resolved Looping Star to susceptibility-weighted imaging or quantitative susceptibility mapping has yet to be explored. Furthermore, the majority of this thesis has focused on the gradient echo, given its inherent T_2* sensitivity and therefore sensitivity to the BOLD contrast, in combination with its comparability with conventional GRE-EPI. However, there has been growing interest in the use of the free-induction decay image for fMRI acquisition, as some studies suggest that it may contain functional sensitivity to alternative physiological mechanisms linked to neural activity such as inflow effects (Lehto et al., 2017) and aspects of oxygen extraction (MacKinnon et al., 2020). It may therefore be of interest to investigate the functional sensitivity of the FID signal in Looping Star acquisitions to explore these findings. This chapter includes proof-of-concept and preliminary investigations into these future directions for Looping Star.

11.2 Extreme MRI with Coherence-Resolved Looping Star

11.2.1 Background

Extreme MRI is a low-rank image reconstruction method (Ong et al., 2020), where low-rank is a mathematical definition for a matrix structure that can be constrained (i.e. simplified). For fMRI, the data is considered low-rank as it is composed of a relatively small number of spatially coherent temporal processes (Chiew et al., 2015). In other words, fMRI data can be considered as a linear combination of a small number of principal components. This means there is a redundancy in fMRI data that can be exploited: as fMRI volumes contain generally similar information, the information in different volumes can fill missing information in other volumes.

By variably sampling the fMRI data, i.e. intentionally missing data but in a different way for each volume, low-rank reconstruction methods have been used to significantly accelerate fMRI acquisition without substantial loss of functional sensitivity (Chiew et al., 2015; Mason et al., 2021). For Extreme MRI with coherence-resolved Looping Star, rather than acquiring a variably sampled time series, a single trajectory is used to acquire one fully sampled volume (Feng et al., 2014), and this is then split into the number of volumes for the desired TR. The method therefore relies on the assumption that the participant remains still during scanning.

The Extreme MRI reconstruction framework also differs from other low-rank techniques as it employs a multi-scale representation of the data. This is useful as the underlying dynamics of the fMRI signal differ across spatial scales, so to capture these dynamics the acquired data is modelled by blocks of a range of sizes (Ong et al., 2020). To limit the amount of noise in the extracted time series during reconstruction, Extreme MRI relies on the specification of a low-rank regularisation parameter, which thresholds the signal noise in a manner similar to principal component analysis (i.e. by truncating the signal

components based on the threshold selected). This can be flexibly selected.

In the interest of relevance to this thesis, for further details on the technical functionality of the Extreme MRI framework I recommend the original paper (Ong et al., 2020) and our recent collaborative single subject study (Leynes et al., 2021). In our collaboration, we showed that Extreme MRI with coherence-resolved Looping Star could produce significant single-subject activity at high spatial and temporal resolution (Leynes et al., 2021).

In this section, a preliminary study investigating the limits of Extreme MRI by employing a heavily prospectively under-sampled multi-echo coherence-resolved Looping Star acquisition is presented. Parts of this work were presented at the OHBM Annual Meeting 2021 (Damestani et al., 2021a). Andrew P. Leynes developed and provided the Extreme MRI with CRLS reconstruction pipeline and also provided expertise on its functionality. I ran the reconstruction scheme on data that I collected and subsequently analysed in the following study.

11.2.2 Methods

Five participants (age range 25 – 58 years, one female) were scanned using the 3 T MR750 Clinical Research Facility scanner and 32-channel head coil (Section 5.2). The paradigm was a simple block design including an 8 Hz visual checkerboard, with the duration of the checkerboard as 10 s followed by 20 s rest consisting of a fixation cross. The shorter duration of the checkerboard allows us to explore the capabilities of a substantially accelerated acquisition.

The acquisition parameters for Extreme MRI with CRLS were 8 spokes per loop, FID + 3 echoes, $\pm$31.25 kHz readout bandwidth, FOV = 19.2 cm, 3 mm isotropic resolution, TE (ms) = 0, 8.96, 17.92, 26.88, scan duration 3 mins 49 s, FA = 2°, GSF = 20. The echo data was reconstructed with 1280 volumes, producing a TR = 0.18 s and approximate undersampling per volume of 0.01. The low-rank regularisation parameter that limits the amount of signal removed from the already under-sampled dataset $\lambda(LR)$ was selected

as 0.01. The block sizes were 16, 32, 64, representing the range of spatial scales to reconstruct where a "block" is a smaller sub-matrix. In the case of a block size of 16, the image matrix is decomposed into a number of 16 x 16 x 16 voxel matrices. This is repeated for a range of block sizes to better explore the data across space. JSENSE and SENSE were retained to iteratively reconstruct the images including coil combination with accompanying parameter $\lambda(JSENSE) = 1x10^{-12}$ (Leynes et al., 2021). An anatomical T_1-weighted RUFIS acquisition was also collected for each subject, with 1 mm slice thickness, TI = 450 ms, FA = 3°, FOV = 22 cm.

The first ten seconds worth of volumes were removed (i.e. 56 volumes), approximately equating to the first 2000 spokes. Upon investigation of the times series, it was found that the signal did not require any further volume removal as the signal appeared stable. Pre-processing in SPM-12 of each echo (FIL Methods Group, 2020) involved bias field correction and segmentation of the T_1-weighted RUFIS acquisition, re-centring of the origin, realignment, co-registration to the T_1-weighted RUFIS acquisition, spatial normalisation to MNI space with images saved at 2 mm spatial resolution and 6 mm FWHM smoothing.

The first-level GLM in SPM-12 included the visual onsets and motion regressors, as well as a 128 s high-pass filter and autocorrelation correction using the AR(1) function for ReML parameter estimation (Poldrack et al., 2011). The standard canonical double-gamma hemodynamic response function was used. Cluster-level inference using a primary uncorrected cluster-forming threshold of $p < 0.001$. (Woo et al., 2014; Worsley et al., 1996) was employed at group level. Only clusters surviving FWE correction at the cluster-level (i.e., $p_{FWE_c} < 0.05$) were deemed significant. Group level analyses were performed for each echo in SPM-12. The signal from the cluster with the highest peak T-statistic was extracted for each subject for the third echo, as it was expected to have highest functional sensitivity given its echo time. The tSNR for each participant was calculated from their spatially normalised image.

11.2.3 Results

The acoustic noise (LA_{eq}) of Extreme CRLS was 73 dB(A), compared with ambient noise at 64 dB(A). This is consistent with the acoustic noise expected from a single-volume acquisition (see Section 6.3). The image quality of an fMRI volume reconstructed with Extreme MRI image reconstruction in comparison with the fully sampled single-volume image can be seen in Figure 11.2 for a single subject. The heavily under-sampled dataset presents comparable image quality regarding anatomical detail, relative to the fully-sampled single volume CRLS with nearest-neighbour gridding.

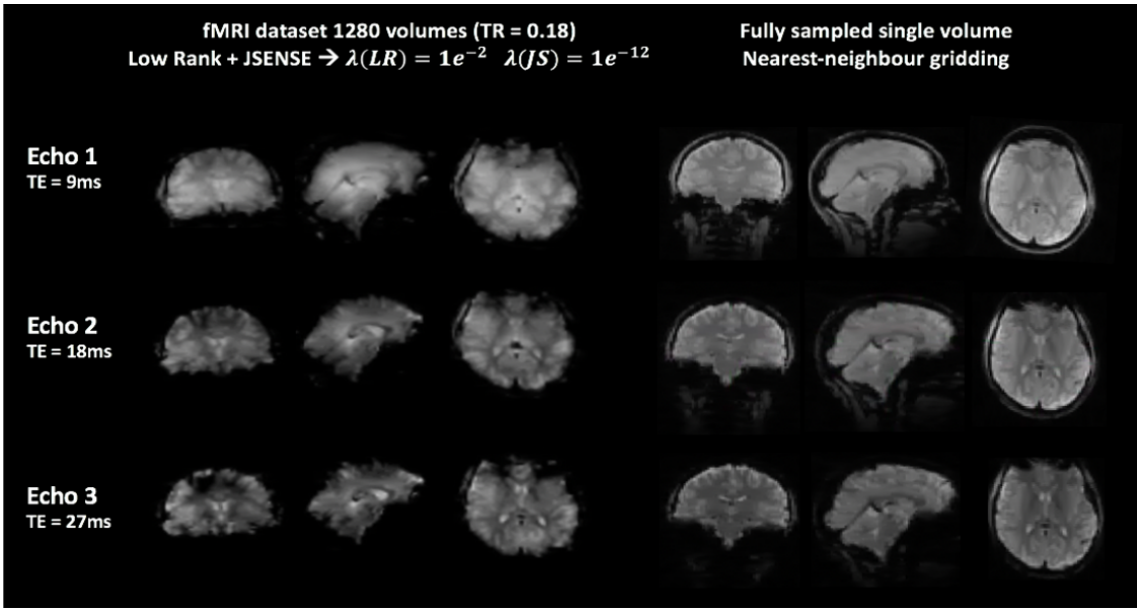

Figure 11.2: Image quality of each echo after reconstruction with Extreme MRI for a single volume of the fMRI time series (left) in comparison with the fully-sampled single volume reconstructed with nearest neighbour gridding (right) for a single subject (Damestani et al., 2021a).

No significant group level activity in response to the task was identified for any echo. This was unexpected, hence this outcome was investigated further by exploring the single subject results for the third echo. Figure 11.3 shows the single-subject tSNR and fMRI first-level results for two participants, with accompanying extracted time series. The tSNR pattern peaks at the centre of the image, which is the opposite to what is expected for the 32-channel coil.

The blocks are reconstructed individually; hence the blocking artefact in the tSNR can

be seen (Figure 11.3, left), produced by the spatially-dependent noise characteristics per block. Statistically significant visual voxels were found (Table 11.1), but not in the same spatial location between participants. The extracted time series does indicate task-correlated activity (Figure 11.3, right), however there is substantial high-frequency signal noise and an obvious loss of activity-related signal change.

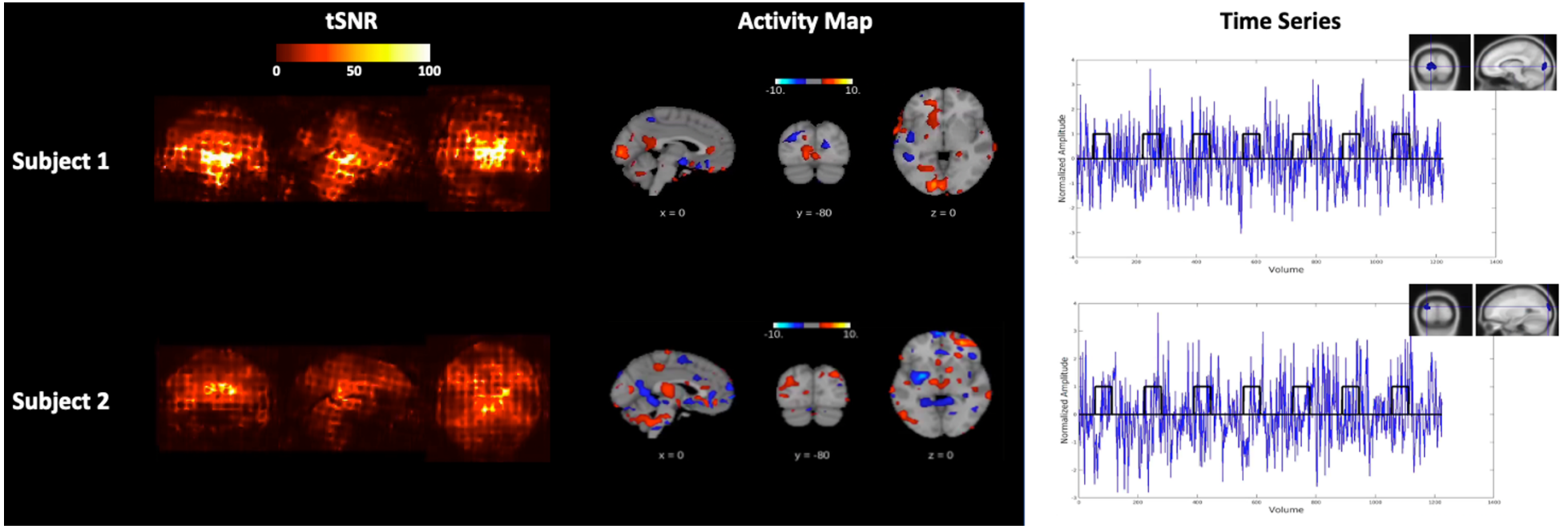

Figure 11.3: (left) tSNR map for the third echo of two subjects reconstructed with Extreme MRI. (middle) Single-subject activity maps for the third echo with accompanying statistics in Table 11.1. (right) Extracted time series from region-of-interest cluster containing peak T-statistic, indicated. tSNR map shown in FSL (Jenkinson et al., 2012), unthresholded activity map shown in NiLearn (The Nilearn developers, 2021).

Table 11.1: Statistical results for activity of each subject during visual checkerboard paradigm

Subject	**Peak MNI Co-ordinates (x,y,z mm)**	**Brodmann Area**	**Peak-level T-statistics**	**Cluster-level p_{FWE}-value**	**Cluster Size**
1	-10 -90 6	17 (L)	6.27	0.001 *	694
2	-22 -100 14	18 (L)	7.62	$0.033*$	374

* = cluster-level p(FWE) $<$ 0.05, ** = cluster-level p(FWE) $<$ 0.001, N/A = outside of defined Brodmann Area

11.2.4 Discussion

Although significant single subject functional activity was identified, in agreement with our previous study (Leynes et al., 2021), the spatial localisation was not consistent between participants and hence no significant activity at group level was found. Substantial signal noise in participant time series was also seen, as well as a blocking pattern in the tSNR originating from the standard deviation from the signal, related to the spatial scales of reconstruction. Low-rank reconstruction has parallels with PCA denoising, whereby a larger low-rank regularisation parameter removes additional noise as it effectively truncates the signal "components" according to the threshold used. It is therefore likely that the low-rank regularisation parameter needs optimising for each participant.

The tSNR pattern also indicated that there was higher signal noise removal in the centre of the image, causing a hyperintensity at the centre, further supporting that optimisation of the low-rank parameter is required. Despite being a promising method, there remains substantial loss in functional sensitivity and susceptibility to high frequency noise when heavily undersampling. This preliminary work indicates that further investigation is required into the parameter specification and functional limits of Extreme MRI image reconstruction.

11.3 Quantitative Susceptibility Mapping with Coherence-Resolved Looping Star

11.3.1 Background

Looping Star is a T_2*-weighted multi-gradient echo technique, which is not only of benefit to functional imaging but also for QSM and susceptibility-weighted imaging (SWI). This is because T_2*-weighted imaging provides sensitivity to magnetic field-induced de-phasing, the primary mechanism behind mapping the magnetic susceptibility of tissues in the brain. The original iteration of Looping Star demonstrated its capabilities of producing QSM and SWI images (Wiesinger et al., 2019), but this has not been carried out using CRLS.

QSM measures the magnetic field heterogeneity induced by the magnetic susceptibility of brain tissues, based on the phase of gradient echo data. As paramagnetic tissues locally enhance the magnetic field and diamagnetic tissues locally reduce the magnetic field, with different brain tissues housing different magnetic properties (Pauling and Coryell, 1936), the overall inhomogeneities that occur in the brain can be mapped. This is done by ultimately measuring the frequency shifts (and therefore the difference in phase accumulation) from the MR signal at different echo times (Chan and Marques, 2021).

Amongst many applications, QSM has been used to quantify the presence of iron in the brain, potentially induced by microbleeds (Wang and Liu, 2015). It can also be used to identify calcifications based on their diamagnetic properties (Wang and Liu, 2015). SWI is more commonly used to investigate intracranial haemorrhages or stroke. Various reviews have been conducted of both methods (Deistung et al., 2017; Haacke et al., 2015; Halefoglu and Yousem, 2018; Liu et al., 2015a), with applications demonstrated in multiple sclerosis (Barkhof and Thomas, 2018), Alzheimer's disease (Acosta-Cabronero et al., 2013), and brain arteriovenous malformations (Biondetti et al., 2019).

Imaging magnetic biomarkers with CRLS is therefore a vital development for facilitating

its clinical translatability for the benefit of patients who may be sound averse. This study is a proof-of-concept investigation demonstrating the use of CRLS for susceptibility-based imaging in a single subject in comparison with a conventional gradient echo susceptibility-weighted acquisition (SWAN).

11.3.2 Methods

A single-subject was scanned using a 12-channel coil with CRLS acquisition parameters: 2 spokes per loop, FID + 9 echoes, ±31.25 kHz readout bandwidth, GSF = 40, 1 mm isotropic resolution, no undersampling factor, FOV = 19.2 cm, ΔTE (ms) = 6.4 ms, FA = 2°, scan time 12 mins 58s. The gradient echo susceptibility-weighted angiography (SWAN) acquisition parameters were: 256 x 256 matrix size, ±62.5 kHz BW, 138 slices, 1 mm isotropic resolution, 13 echoes, FA = 20°, ΔTE (ms) = 3.3ms, scan time 9 mins 58 s.

Nearest-neighbour reconstruction was employed for CRLS, including coil combination using a simple sum of squares technique with the sensitivity maps calculated from a calibration region in the centre of k-space (McKenzie et al., 2002). The SWAN data were reconstructed using standard GE Healthcare online reconstruction.

The acoustic noise was measured at the centre of the scanner (see Section 5.5). Both datasets were processed using a pipeline in SuscEptibility mapping PIpeline tool for phAse images (SEPIA) (Chan and Marques, 2021), based on the recommended QSM pipeline by Wang et al. (2021). SEPIA is a novel post-processing pipeline tool for susceptibility imaging (Chan and Marques, 2021), connecting numerous toolboxes under one workflow. The workflow employed for this study included:

- Echo phase combination using optimum weights, meaning echo combination is based on SNR weighting

- Laplacian phase unwrapping via susceptibility tensor imaging (STI) suite Li et al.

(2014) to remove wrapping artefacts and obtain the true phase evolution

- Bipolar readout correction for CRLS, but not for SWAN as it is a unipolar acquisition, to correct for any eddy current-induced phase offsets

- Background field removal with VSHARP, a sophisticated harmonic artifact reduction for phase data (SHARP) method (Schweser et al., 2011) with a variable radius of the spherical kernel at the brain boundary, via STI suite Li et al. (2014), with spherical mean value (SMV) size 5mm to preserve the spatial boundaries, for removing magnetic fields contributed from external sources

- Removal of the residual using a 3D polynomial of order 4 to further correct any phase offsets

- QSM using iterative least squares (ILSQR) in STI suite for mapping the susceptibility sources based on the tissue fields computed via dipole inversion Li et al. (2015)

For the QSM, the default values provided by the software were used: a threshold on the dipole response of 0.01 (to avoid division by zeroes of the dipole kernel in k-space), maximum of 100 iterations with tolerances for error (i.e. streaking artefacts) specified at the first level as 0.01 and second level as 0.001. Two levels of least squares are performed to reduce the amount of streaking, first applied to the phase computation and then applied to the susceptibility computation Li et al. (2011b)

The zero-padding pad size was 5 x 5 x 5, which theoretically improves the numerical stability of the maps. CSF was used as the reference tissue. A mask was produced using FSL Brain Extraction Tool (Jenkinson et al., 2012). The inverse problem relating susceptibility to phase data was solved. The R_2* map was computed using the MEDI toolbox (Liu et al., 2011), which uses auto-regression on linear operations mono-exponential decay fitting function (ARLO; Pei et al. (2015)).

SEPIA was also used to produce the SWI images from the dataset, including contrast 4,

i.e. the power applied to the weighting maps prior to multiplying it to the magnitude data (Chan and Marques, 2021). The SWI implementation uses high-pass homodyne filtering (Chan and Marques, 2021; Noll et al., 1991), with the Hamming filter employed specified with kernel size 12 and the image contrast was specified at a threshold of π radians.

11.3.3 Results

The acoustic noise measures (LA_{eq}) for CRLS QSM were 81.9 dB(A) and for SWAN were 110.4 dB(A), compared with the ambient scan room noise at 65 dB(A). Figure 11.4 shows the raw magnitude and phase images at the specified echo time for each acquisition, as well as the susceptibility-weighted image.

There was good agreement between the SWAN and CRLS SWI images, although some frontal lobe dropout is visible in CRLS that may have affected the phase at the brain boundaries as indicated by the arrows. This was also indicated in the wrapped phase images, where there were some differences in phase jumps visible around the frontal lobe that propagate into the cortex. Equally, the acquisitions were collected at different echo times therefore different phase jumps can be expected.

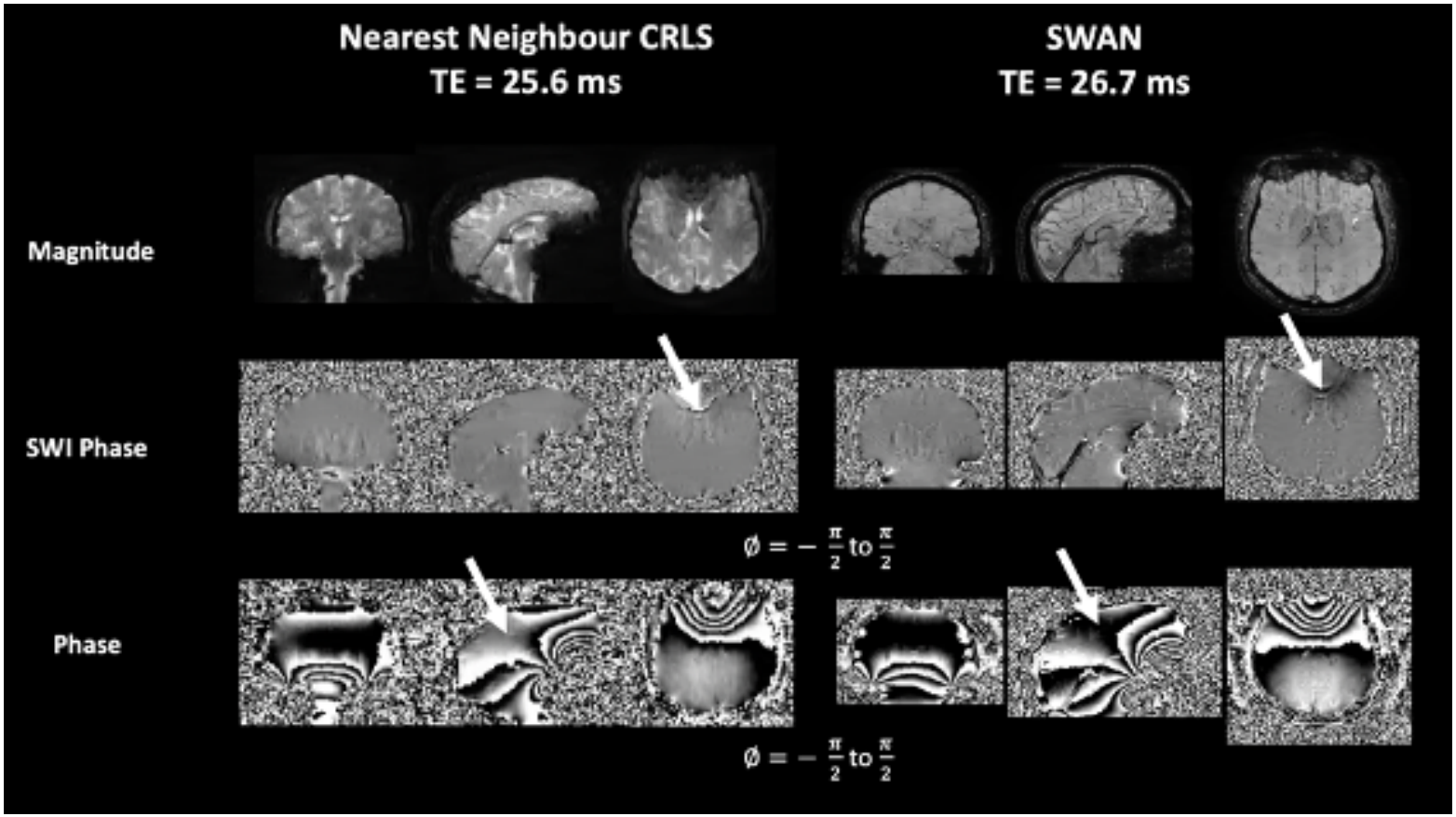

Figure 11.4: Raw magnitude, raw phase and susceptibility-weighted image (SWI) phase for coherence-resolved Looping Star and the SWAN acquisition. Arrows indicated regions of differences between images. Images produced in FSL (Jenkinson et al., 2012).

Figure 11.5 shows the QSM, R_2* map and local field image for coherence-resolved Looping Star and the SWAN acquisition. The local field map shows the magnetic field induced by the tissues, and the maps are consistent between modalities. Signal dropout is again seen in the frontal lobe of the CRLS acquisition, but otherwise good agreement is seen between techniques. The R_2* maps also show good consistency between techniques, with the arrow indicating a thalamic region in particular with similar values.

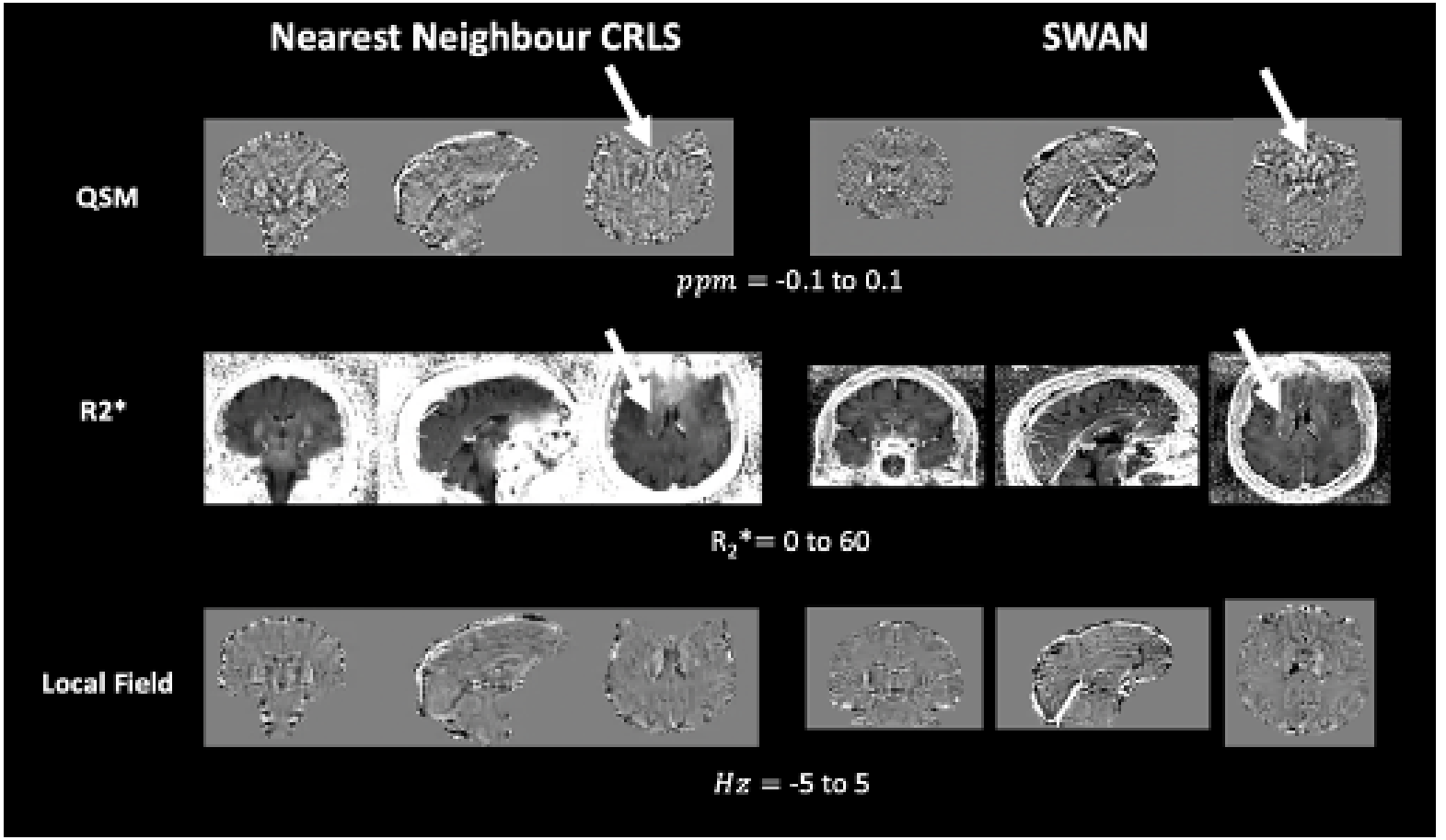

Figure 11.5: Quantitative susceptibility map (QSM), R_2* map and local field image for coherence-resolved Looping Star and the SWAN acquisition. Arrows indicate signal drop out in QSM image and thalamic region in R_2* map. Images produced in FSL (Jenkinson et al., 2012).

To investigate in more depth, Figure 11.6 shows the QSM and R_2* maps for the basal ganglia. Figure 11.6 specifically highlights the putamen as it contains the highest iron concentrations (Péran et al., 2009), which has good visibility and comparable R_2* and QSM values between both acquisitions. The substantia nigra and red nuclei are more visible in the SWAN acquisition than CRLS, though a potential artefact seen in SWAN is not seen in CRLS. The measurements agreed with those reported previously (Cohen-Adad, 2014).

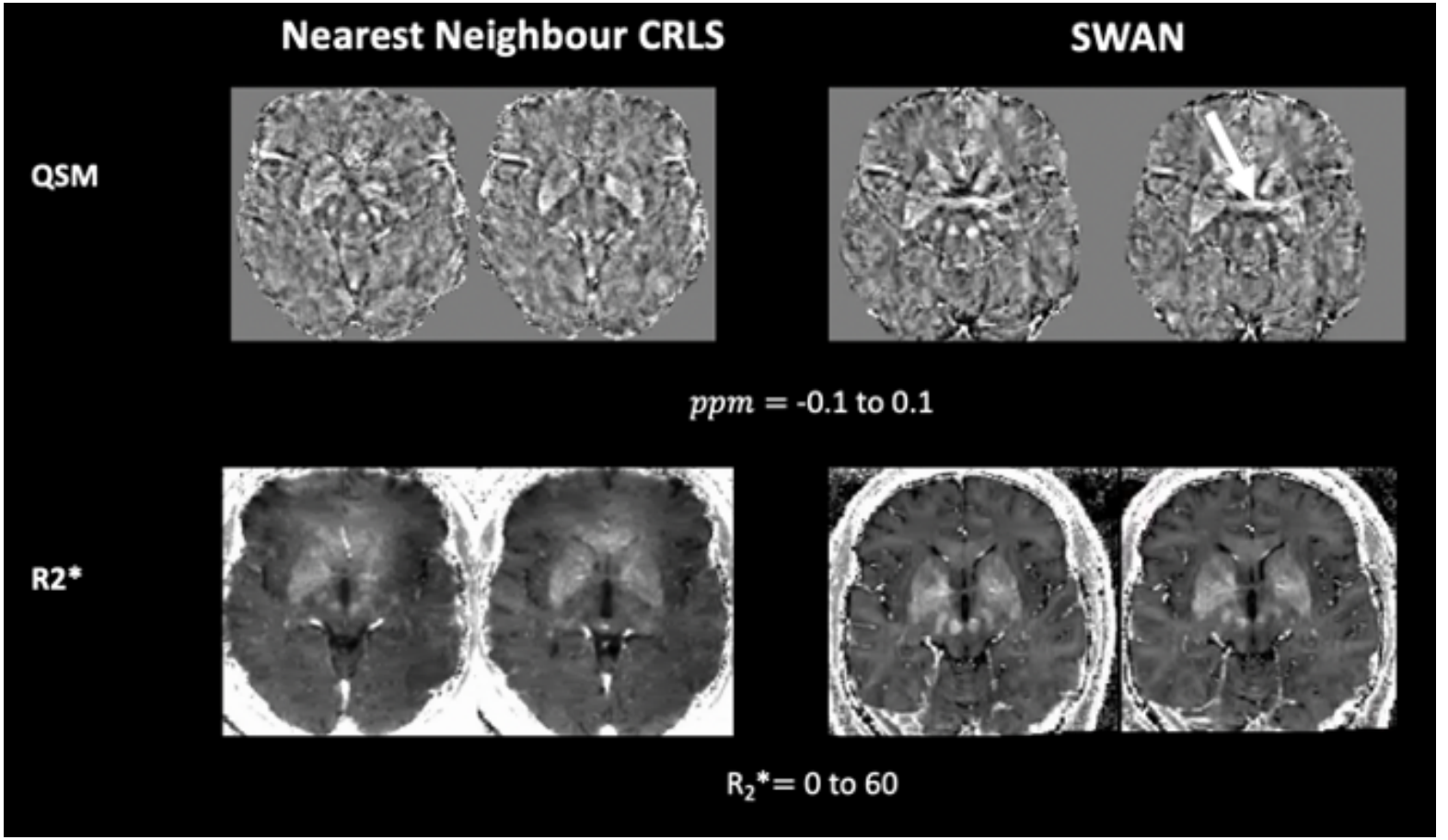

Figure 11.6: Quantitative susceptibility map (QSM) and R_2* map for coherence-resolved Looping Star and the SWAN acquisition, focusing on the basal ganglia. White arrow points towards potential artefact in the conventional SWAN scan that is not visible in Looping Star. Images produced in FSL (Jenkinson et al., 2012).

11.3.4 Discussion

This study has shown that coherence-resolved Looping Star can undoubtedly be used for QSM, SWI and R_2* mapping, and it is compatible with an exemplar SEPIA processing pipeline (Chan and Marques, 2021). Improvements to image quality via image reconstruction should be explored to improve the resolution of subcortical structures. Further optimisation of the QSM pre-processing pipeline should be explored. Upon optimisation, this work could also be extended to implementing Looping Star for functional QSM (Balla et al., 2014), given its multi-echo capability, or for biomarker detection.

11.4 Free-induction Decay fMRI

11.4.1 Background

The majority of this thesis has focused on comparing the gradient echoes of Looping Star and GRE-EPI, given that the BOLD contrast is produced from changes in T_2* (Section 1.7). However, Looping Star conveniently also collects the FID image, and recent studies have indicated that alternative mechanisms behind functional activity, such as inflow effects and oxygen extraction, can be detected from fMRI using the FID images (Lehto et al., 2017; MacKinnon et al., 2020; Paasonen et al., 2020).

This section details a preliminary investigation into the use of the FID for fMRI in both original and coherence-resolved Looping Star. The simultaneous collection of the FID and the echo allows direct comparison at the different echo times; hence Looping Star could be a promising technique for future FID functional sensitivity investigations.

11.4.2 Methods

Five participants volunteered for this study, which is the same study as in Section 10.3. As described previously, English words were played through pneumatic MR-compatible headphones during blocks of 24 second durations. The speed at which the words were played was different for each block (30, 60, 90 and 120 words per minute), and the order of the block was randomised (i.e. the speed did not steadily increase or decrease with consecutive blocks, but randomly changed). A fixation cross was displayed during the paradigm and participants were asked to keep their eyes open. Rest blocks of 24 second duration involved a fixation cross with no auditory stimulation (Figure 10.5). The paradigm set up is described in Section 5.3.

The acquisition parameters are detailed in Table 11.2, and were selected to closely match the TR and TE values between acquisitions and the number of volumes was selected to equalise the scan times for the two scans. The scan order was randomised between participants to avoid order effects. It can be seen that the coherence-resolved Looping Star FID acquisition produced half the number of spokes per volume relative to the echo due to the temporal excitation spacing (Wiesinger and Solana, 2020). An anatomical image was also acquired for each participant using a silent T_1 weighted IR-prepared RUFIS acquisition for spatial normalisation of the fMRI datasets, with parameters: TI = 450 ms, 1mm isotropic resolution, FOV = 22 cm, FA = 2°, ±15.6 kHz.

Table 11.2: Acquisition parameters for original and coherence-resolved Looping Star

Acquisition Parameters
Coherence-resolved Looping Star: FID + echo, ±31.25 kHz BW, 24 spokes per loop, 408 spokes per volume, GSF = 14, TR = 2.47 s, TE = 0 ms, isotropic voxel resolution = 3 mm, FOV = 19.2 cm, FA = 3°, 142 volumes
Original Looping Star: FID + echo, ±31.25 kHz BW, 32 spokes per loop, 1024 spokes per volume, GSF = 14, TR = 2.33 s, TE = 0 ms, isotropic voxel resolution = 3 mm, FOV = 19.2 cm, FA = 3°, 151 volumes

Image reconstruction of both Looping Star datasets was performed using nearest-neighbour gridding. The first four volumes of the Looping Star fMRI dataset were removed to facilitate the longitudinal magnetisation reaching the steady state. The FID datasets were pre-processed with a standard SPM-12 pipeline (FIL Methods Group, 2020), including segmentation of the T_1-weighted RUFIS scan, realignment, co-registration to the T_1 image, spatial normalisation to MNI space with images saved at 2mm spatial resolution and 6 mm FWHM smoothing.

First level and group level analyses were performed in SPM-12 (FIL Methods Group, 2020). A 128 s high-pass filter was applied with motion regressors and the auditory stimuli modelled in the general linear model. The standard canonical double-gamma hemodynamic response function was employed. The AR(1) autocorrelation correction function was also employed for ReML parameter estimation (Poldrack et al., 2011).

The contrast for the main effect of sound was modelled. Cluster-level inference using a primary uncorrected cluster-forming threshold of $p < 0.001$ unc. (Woo et al., 2014; Worsley et al., 1996) was employed. Only clusters surviving family-wise error correction at the cluster-level (i.e., $p_{FWE_c} < 0.05$) were deemed significant. The time series was extracted from a 5 mm radius spherical cluster centred on the peak voxel from the most significant cluster within the auditory cortex for each participant, or the cluster nearest to the auditory cortex in the event no significant responses were found.

11.4.3 Results

The group level activity maps can be seen in Figure 11.7 with accompanying statistics in Table 11.3. No significant auditory group level activity for coherence-resolved Looping Star was found, but significant auditory activity was identified with original Looping Star. Given that original Looping Star contains echo-in echo-out mixing, this could be due to signal interference.

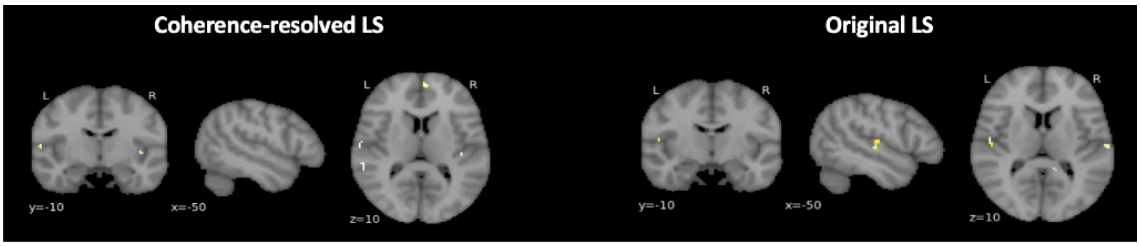

Figure 11.7: Group level results of FID datasets for each modality, thresholded for the appropriate cluster extent of significant voxels for original Looping Star and the cluster size near the auditory cortex for CRLS, and visualised between $2 < T < 10$. Visualised using Nilearn (The Nilearn developers, 2021).

Table 11.3: Statistical results of FID datasets

Acquisition	Peak MNI Co-ordinates (x,y,z mm)	Brodmann Area	Peak-level T-statistics	Cluster-level p_{FWE}-value	Cluster Size
Original LS	-36 -22 6	13 (L)	27.32	$< 10^{-3}$ **	81
CRLS	2 56 8 -58 -36 10	10 (R) 22 (L)	48.50 15.14	0.042 * 0.079	27 24

* = cluster-level p(FWE) < 0.05, ** = cluster-level p(FWE) < 0.001, N/A = outside of defined Brodmann Area

Upon further investigation, significant activity at single-subject level was present in some participants but not in others, with varying spatial localisation (Figure 11.8).

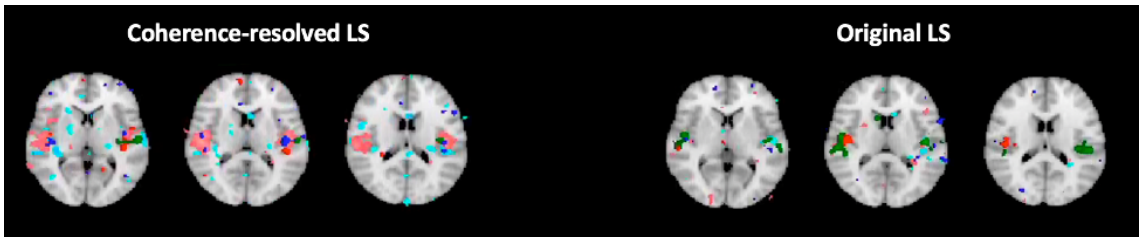

Figure 11.8: First level statistical maps overlaid for FID-only data for both modalities, thresholded at $T > 2$. Visualised in FSL (Jenkinson et al., 2012).

Furthermore, clear task-related time series correlations in the auditory ROI were only found for a few subjects (Figure 11.9).

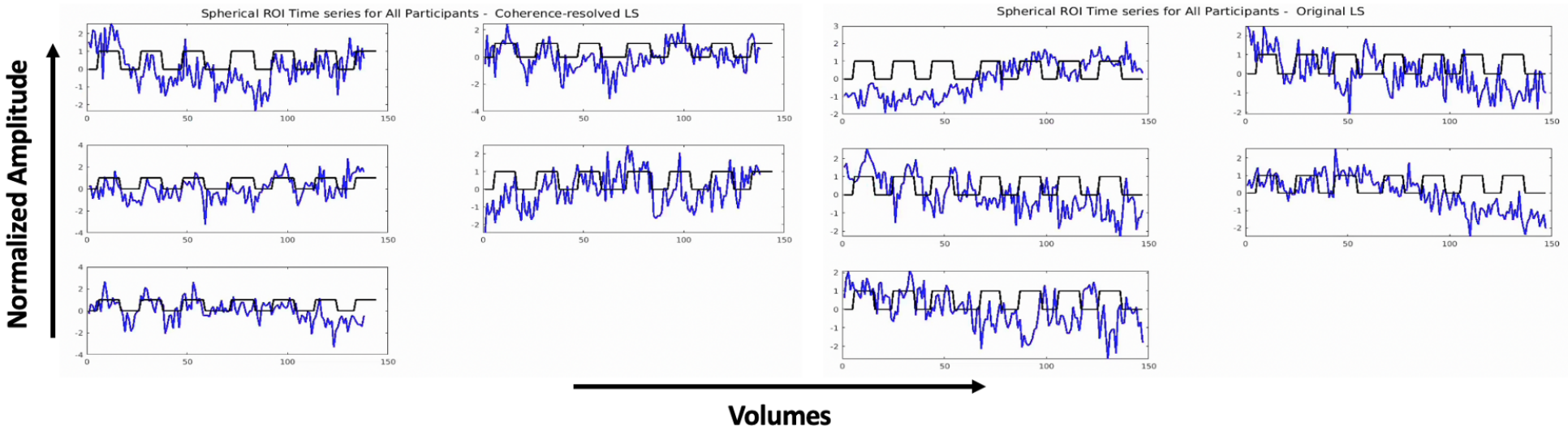

Figure 11.9: Normalised extracted time series for each participant in spherical 5 mm radius auditory ROI for FID-only data. (left) Coherence-resolved Looping Star and (right) Original Looping Star.

11.4.4 Discussion

Only original Looping Star identified significant peak auditory activity at group level, which could be confounded by echo-in echo-out signal interference. Furthermore, significant functional activity was not identified for all participants at single subject level in both original and coherence-resolved Looping Star. Further investigations should take place in coherence-resolved Looping Star in a bigger cohort to evaluate the reliability of functional sensitivity and the spatial localisation of activity in the FID image, particularly given the differences in lateralisation and image quality previously identified in this data (Section 10.3). Inflow effects are one potential mechanism behind this activity, though the presence of these effects are expected to be lower in Looping Star as it is not slice-selective and very small flip angles are employed, leading to a much smaller component of the longitudinal magnetisation (Duyn et al., 1994).

11.5 Chapter Discussion

This chapter highlighted a few interesting future directions for Looping Star that warrant further study. It was found that the Extreme MRI image reconstruction framework is compatible with heavily undersampled coherence-resolved Looping star, producing impressive image quality relative to fully-sampled coherence-resolved Looping Star. However, it also requires further evaluation and optimisation of the threshold at which noise removal is applied, via the low-rank parameter, as functional activity could be masked by the high noise present when using very high undersampling.

The viability for coherence-resolved Looping Star to be used in quantitative susceptibility mapping was also demonstrated, with good agreement demonstrated in comparison with conventional gradient echo imaging. Methods of improving the spatial resolution via image reconstruction is a further means to improve the identification of subcortical structures, for example by using alternative reconstruction tools such as the RIESLING

toolbox (Wood et al., 2021) being one promising avenue for future investigations. Finally, preliminary investigations were begun into the functional sensitivity of the free-induction decay image and initial indications that very localised activity may be identified were found, however a larger cohort is required to validate this finding.

Chapter 12

Thesis Discussion

This thesis sought to evaluate, optimise and apply a novel fMRI acquisition technique known as Looping Star. Looping Star was successfully characterised in a phantom, as well as across various task-based paradigms and resting-state in vivo. Looping Star was found to be capable of producing adequate functional sensitivity in both single-echo and multi-echo modes. Its use alongside different pre-processing and analysis schemes was also evaluated, determining that Looping Star is compatible with conventional pipelines.

Differences in functional sensitivity and image quality between Looping Star and GRE-EPI were identified, explained in part by the reduced tSNR achievable with Looping Star. However, questions remain regarding the degree to which reduced acoustic noise affects the functional responses measured and whether advanced reconstruction methods for 3D radial sampling are required to improve the quality of this method. Finally, areas were identified for further optimising the technique, including preliminary investigations into interesting routes for future research. This section returns to the five key aims outlined earlier that were addressed within the thesis, alongside the limitations of this work and avenues for future research.

Aim 1: Evaluate the acoustic noise and MR signal characteristics of single-echo and multi-echo Looping Star relative to GRE-EPI in phantoms.

The first evaluation performed was of the acoustic noise levels of Looping Star, where it was found that Looping Star consistently produced significantly lower peak acoustic noise amplitude and a lower peak frequency of acoustic noise relative to GRE-EPI, regardless of the parameters chosen. Any change of a parameter that led to a larger gradient step between samples also led to an increase in acoustic noise, as expected. It was crucial to evaluate the impact of these parameters on the acoustic noise as they are entangled with the timings of the sequence (i.e. the echo time and repetition time). These factors must be taken into account in future applications of this sequence.

In terms of the spatial characteristics of Looping Star, the initial evaluations showed that its point spread function was primarily affected by the density compensation step in reconstruction. This was expected as density compensation changes the MR signal intensity distribution in k-space as part of non-Cartesian gridding image reconstruction. It was also found that the full-width half-maximum of the point spread function of Looping Star was approximately 3 pixels, indicating image blur (Robson et al., 1997). This was expected based on the raw images produced by Looping Star. Image blur is typical of non-Cartesian methods due to the combination of the differing sampling characteristics employed and image reconstruction required (Hoge et al., 1997; Lee et al., 2010; Maier et al., 2021). Alternative methods to evaluate image quality and image blur could explore these findings in more depth (Chaimow and Shmuel, 2016).

The temporal stability of Looping Star was consistent with that of GRE-EPI in the spherical phantom employed. For example, similar spectral content of the time series in a central region of interest was seen between modalities, whereby Looping Star did not demonstrate any frequency bands with substantially higher amplitude relative to GRE-EPI. For the Weisskoff analysis (Weisskoff, 1996), the point at which the Weisskoff curves diverged (i.e. the RDC) was also consistent between techniques. This analysis suggested that Looping Star was not affected by different sources of noise when compared with GRE-EPI. Significant deviations in percentage signal drift or signal fluctuation between

techniques were also absent. However, Looping Star consistently demonstrated lower tSNR and SNR, likely related to the lower flip angles employed by the technique.

Evaluating the effect of flip angles, it was found that higher flip angles did not affect the temporal stability of Looping Star, as expected. Evaluating the impact of the number of spokes per loop and readout bandwidth in isolation proved difficult, given that these parameters inherently affect the echo time produced by Looping Star. It was expected that higher spokes per loop may be more susceptible to gradient imperfections, and that a higher readout bandwidth would introduce more noise, but minimal differences in image quality or temporal stability were seen in both cases. On the one hand, this is difficult to disentangle from the higher signal amplitude produced by shorter echo times, though on the other hand it also demonstrates a potential benefit of the entanglement of these parameters with the echo time.

Extracting the temporal stability based solely on the pulse sequence is not straightforward to evaluate as it is inherently entangled with scanner stability. For example, Greve et al. (2011) showed that system instabilities, i.e. multiplicative noise that originates from natural fluctuations in the gradients or RF pulses, produce lower magnitude noise in the image compared with background noise, i.e. additive noise from the phantom or external RF interference signals, and both produce noise within phantoms and different cortical tissues. Further investigations of temporal stability could include comparisons across different phantoms, including active phantoms that simulate functional activity (Chen et al., 2020b; Mattila et al., 2007; Olsrud et al., 2008; Renvall, 2009).

With wider use of Looping Star, it would be vital to explore the temporal stability across sites to establish a threshold for scanner stability at which it can be reliably used (Glover et al., 2012; Marcus et al., 2013; Stöcker et al., 2005). Future work may also consider estimating the noise-only image in order to obtain additional measures of SNR for further investigations (Bodurka et al., 2007; Hutton et al., 2012; Kellman and McVeigh, 2005; Triantafyllou et al., 2011).

Aim 2: Quantify the signal characteristics and functional sensitivity of single-echo and multi-echo Looping Star in vivo using a simple paradigm.

The functional sensitivity of single-echo Looping Star was evaluated qualitatively using a visual checkerboard block-design paradigm. Clear temporal correlations between the BOLD response detected by Looping Star and the paradigm onsets were found. Though this study could not directly compare the results quantitatively with those of the GRE-EPI acquisition due to limitations in the experimental design, this was a clear indicator towards good functional sensitivity of Looping Star. The power calculation for the task indicated that more participants would be needed for Looping Star than GRE-EPI due to the lower effect size calculated, which was expected given the lower tSNR.

For an auditory word-processing block-design paradigm, the comparison of multi-echo Looping Star with multi-echo GRE-EPI was quantified. It was found that Looping Star, though functionally sensitive, produced lower average percentage signal change compared with GRE-EPI for the main effect of sound. The study also found different lateralisation of the significant activity between modalities for the main effect of sound, which merits further investigation. Disentangling whether this originates from the acoustic noise or the lower tSNR of Looping Star is complex, however previous studies have supported asymmetry and lateralisation of the auditory cortex in response to auditory stimuli (Andoh et al., 2015; Brechmann et al., 2002; Devlin et al., 2003; Ren et al., 2020). Furthermore, the acoustic noise produced by GRE-EPI has been shown to interact with acoustic word stimuli (Mohr et al., 1999; Peelle et al., 2010; Schmidt et al., 2008). A future study could record the GRE-EPI acoustic noise and play this noise alongside an auditory stimulus during a Looping Star acquisition to further explore this interaction.

Interestingly, this study only found significant activity for the parametric modulation of the speed at which words were spoken when using Looping Star and not when using GRE-EPI. This activation was left lateralised and localised to the primary auditory cortex and medial temporal gyrus. Davis and Johnsrude (2003) found that the left lateral temporal cortex was related to the processing of degraded speech, which supports the findings as word comprehension is more difficult at higher speeds. This has also been supported by further

studies of degraded speech (Erb et al., 2013; Wild et al., 2012) as well as studies of the hierarchy of speech processing (Abrams et al., 2020; Zatorre et al., 2002). The findings for original Looping Star were also replicated using different acquisition parameters in a later study in this thesis, when comparing with coherence-resolved Looping Star. Further study with a larger cohort would enable the exploration of the auditory network in more depth, particularly given the importance of cognition in auditory processing (Peelle, 2018). Larger group sizes would also greatly benefit the statistical relevance of these results (Button et al., 2013).

Aim 3: Explore the capabilities of Looping Star with auditory and resting-state paradigms in comparison with GRE-EPI.

Looping Star identified the auditory resting-state network using a seed placed in Heschl's gyrus, as well as the default mode network using a seed placed in the posterior cingulate. Differences were found between Looping Star and GRE-EPI for these networks, most notably that GRE-EPI identified higher correlations between the posterior and anterior cingulate than Looping Star in the default mode network. On the other hand, Looping Star identified higher correlations bilaterally across the auditory cortices in the auditory network. The findings support those of Rondinoni et al. (2013), who showed that acoustic noise could suppress the auditory network and enhance the default mode network using a soft-tone parameter for imaging, although this was not supported by findings using sparse sampling (Gaab et al., 2008).

Exploring the ROI-to-ROI connectivity matrix, Looping Star produced fewer statistically significant inter-region correlations compared with GRE-EPI, supported by Dionisio-Parra et al. (2020). However, when focusing on correlations with Heschl's gyrus, it was seen that Looping Star had a higher number of regions with statistically significant correlations than GRE-EPI, which supports the findings of Andoh et al. (2017) using ISSS. One method of comparing these findings further would be to compute a comparison such as the receiver-operating characteristic curve Sorenson and Wang (1996) with an established network map, for example from Neurosynth (Yarkoni, 2011). However, the expectation would be for Looping Star to inherently differ more from such a map compared with

GRE-EPI given it is acoustically silent and the maps are derived from GRE-EPI data. A better alternative would be to replicate these findings in a separate larger cohort, particularly using a technique to improve the tSNR of Looping Star such as alternative acquisition parameters.

Furthermore, the noise components extracted using ICA (tedana community et al., 2021) for Looping Star were explored. Similar temporal characteristics of the independent components was found relative to GRE-EPI. However, the spatial distribution of the components for these temporal characteristics was different between modalities. This may be linked to the non-Cartesian sampling pattern of Looping Star, whereby noise sources affect the whole image via streaking rather than specific regions. This would be a core consideration for denoising pipelines, as component regression could lead to substantial signal removal across the brain.

Interestingly, signal regression using white matter and CSF regressors led to significant signal reduction for both modalities. Global signal regression, be it with the mean signal or from particular tissues, is extensively debated (Murphy and Fox, 2017); hence this is not unique to Looping Star. Equally, studies suggest that appropriate deconvolution models for the haemodynamic response are necessary for resting-state investigations, which would be one avenue for future research (Lanka et al., 2020; Rangaprakash et al., 2018; Wu et al., 2013). NOise reduction with DIstribution Corrected (NORDIC) PCA is another novel technique that should be explored for denoising Looping Star data, as it has been shown to substantially reduce the influence of thermal noise in fMRI (Moeller et al., 2021; Vizioli et al., 2021).

Using an event-related auditory paradigm in once-repeated sessions, it was shown that Looping Star could produce adequate functional sensitivity in comparison with GRE-EPI, though inter-session differences were apparent. The supporting analysis showed that the T-scores and beta parameters identified were independent of the tSNR of the modality. fMRI reliability can be affected by numerous factors, ranging from paradigm design to the duration of the interval between which the scans are performed, with the mean expected ICC for GRE-EPI being calculated as 0.5 (Bennett and Miller, 2010, 2013). The range

of ICC values for Looping Star in the study was between $\approx 0.1 - 0.6$, therefore some participants produced values within the range of adequate reliability. It could be that the lower mean ICC for Looping Star was driven by the tSNR, though this cannot be disentangled from cognitive differences due to reduced acoustic noise, therefore further study is warranted.

It would also be crucial to further explore the inter-modality differences of the auditory oddball paradigm, such as the significant activity identified by Looping Star in response to tone discrimination, in a larger cohort. Such a study could support the findings of auditory processing seen in previous auditory oddball studies (Justen and Herbert, 2018; Stevens et al., 2005). Additionally, higher spatial resolution acquisition could benefit identifying subcortical components of the auditory network such as the inferior colliculus (Gao et al., 2014).

Aim 4: Investigate the compatibility of Looping Star with conventional analysis and pre-processing techniques.

The compatibility of Looping Star with various conventional pre-processing and analysis software packages for both task and resting-state data was successfully demonstrated. The primary requirement when using conventional fMRI pre-processing pipelines with Looping Star is to remove slice timing correction, given that it is a non-slice selective technique. As mentioned previously, careful consideration should be taken for denoising via signal regression in analysis, given the differences in spatial characteristics of noise components found for Looping Star.

It was found that the average spectral profile of the residuals after GLM model estimation, using both FAST and AR(1) autocorrelation models, for Looping Star differed from that of GRE-EPI, though neither produced a completely pre-whitened power spectrum. This indicated that there might be more appropriate models for addressing serial correlations for Looping Star. Furthermore, Looping Star produced differences between the results from the FAST and AR(1) autocorrelation methods at all smoothing thresholds, with the differences increasing with smoothing level. This is not unique to Looping Star, as

Olszowy et al. (2019) also commented that smoothing confounds the autocorrelation result in GRE-EPI. In general, the area of autocorrelation in Looping Star requires further study with additional methods (Eklund et al., 2012; Friston et al., 2000a; Olszowy et al., 2019). Furthermore, if a study plans to accelerate Looping Star to sub-second temporal resolution, alternative temporal autocorrelation functions may be required (Bollmann et al., 2018; Chen et al., 2019; Corbin et al., 2018).

One of the core findings that was consistent across the studies in this thesis was that lower or no spatial smoothing in pre-processing can be applied to Looping Star without substantially affecting the significance of functional activity detected. The only effect seen was that of slightly reduced cluster sizes with lower smoothing levels. This is likely a result of the non-Cartesian characteristics of Looping Star that lead to signal blur discussed earlier. The production of spatial blur is also seen across spiral imaging methods, and improved density compensation functions have been shown to partly address this (Glover et al., 2012; Holland et al., 2013; Maier et al., 2021). Advanced techniques such as deep learning can also produce improvements (Jimeno et al., 2021).

Smoothing was retained in all of the studies for accurate comparisons with GRE-EPI (Worsley et al., 1996), though further study of the optimal size of the smoothing filter, as performed by Mikl et al. (2008), would be interesting to evaluate for a range of parameters. Such studies might reveal a preference for retaining the spatial blur and remove spatial smoothing in pre-processing, as performed by the "matched-filter theorem" (Kasper et al., 2014). As spatial averaging suppresses the thermal noise in conventional fMRI (Bodurka et al., 2007), future work could also explore the optimal voxel size at which physiological noise equates to thermal noise in Looping Star to better understand the impact of smoothing, particularly at higher spatial resolutions (Molloy et al., 2014).

A more appropriate EPI-based comparison with Looping Star might be the use of 3D radial GRE-EPI techniques that produce good functional sensitivity without significant time penalty (Rettenmeier et al., 2021). Alternatively, there are also numerous novel acquisition schemes, such as Oscillating Steady State Imaging (OSSI) (Guo and Noll, 2020), that have shown substantial boosts in SNR and tSNR with good functional

sensitivity, which would be interesting to compare with Looping Star.

Aim 5: Evaluate further applications and areas of optimisation for Looping Star for future work.

It was found that coherence-resolved Looping Star is one promising sequence modification, as it effectively temporally resolves the coherences that lead to the echo-in and echo-out signal interferences of Looping Star signals. However, it was interesting that although substantial improvements in the image quality were seen, huge differences were not seen for in vivo tSNR. It could be that the overlap between echoes of original Looping Star fortuitously boosts the tSNR. Coherence-resolved Looping Star also identified smaller clusters with larger T-scores compared with original Looping Star, which could be indicative of improved spatial localisation. This was supported by the smaller full-width half-maximum of the point spread function for coherence-resolved Looping Star.

The first main future direction of fMRI research is to produce higher spatial resolution, lowering the physiological-to-thermal noise ratio and improving statistical accuracy (Bollmann and Barth, 2020; Molloy et al., 2014). The second is to produce images at higher temporal resolution, acquiring more images at a faster rate to better characterise the haemodynamic response of interest and boost statistical power (Bollmann and Barth, 2020; Murphy et al., 2007). Advanced image reconstruction schemes, including low-rank methods such as Extreme MRI, can significantly boost the temporal and spatial resolution of Looping Star, though substantial work is required to improve its functional sensitivity and reduce reconstruction artefacts of the technique. Improvements to image reconstruction via parallel imaging could further facilitate accelerated, undersampled Looping Star acquisitions (Maier et al., 2021; Wright et al., 2014). The Radial Interstices Enable Speedy Low-Volume imagING (RIESLING) toolbox is of particular interest given that it has been optimised for centre-out radial imaging and includes flexible regularisation and density compensation methods (Wood et al., 2021).

Quantitative susceptibility mapping is an exciting new avenue for Looping Star, particularly as comparable resolution is achievable between Looping Star and conventional methods.

However, such mapping would also benefit from advanced image reconstruction to further improve the spatial resolution of subcortical structures. Motion navigators could also be used to limit the presence of motion artefacts in the images (Ljungberg et al., 2021b; Wallace et al., 2019, 2021).

There is also increasing interest in the neurobiological mechanisms behind functional activity detected with the free-induction decay especially in preclinical studies (MacKinnon et al., 2020), for which Looping Star could be a vital tool as it inherently collects the FID and the echo and therefore facilitates a direct comparison between the functional sensitivity of both echo times. Furthermore, Looping Star is inherently less sensitive to inflow effects, given the low flip angles and therefore minimal impact of T_1 on signal decay (Duyn et al., 1994; Gao and Liu, 2012; Kim and Ogawa, 2012). Promising indications towards functional sensitivity in the FID images were found, that could also be amplified with preparation pulses. In particular, Schulz et al. (2020) showed that magnetisation-preparation with GRE-EPI fMRI could localise arterial blood contributions to neural activity.

One useful application of Looping Star would be its integration with EEG-fMRI (Solana et al., 2014) due to the reduced influence of acoustic noise and gradient switching artefacts. It would also be particularly interesting to further explore the auditory oddball task with such a technique (Brázdil et al., 2005; Mangalathu-Arumana et al., 2012). Additionally, Looping Star is inherently more efficient than GRE-EPI given the higher number of points sampled per unit time, which could have interesting applications for further dynamic imaging. Finally, as discussed in previous chapters, the key application of Looping Star would be for clinical cohorts who are hypersensitive to acoustic noise in the hope of improving the accessibility of fMRI research across studies.

To conclude, confirming the hypotheses, I have successfully demonstrated adequate functional sensitivity of Looping Star relative to conventional GRE-EPI fMRI. I did so across a range of paradigms, including both tasks and rest. I have highlighted the core advantage of Looping Star, which is that its reduced background noise better represents "real-world" scenarios for fMRI research. I conclude that Looping Star is a promising new

imaging technique for functional MRI, with many avenues present for further improvement. These avenues include, but are not limited to, further validation in comparison with radial 3D GRE-EPI techniques, studies in larger cohorts, evaluation in more complex cognitive paradigms and in clinical groups, and technical advances in image reconstruction.

References

Abrams, D. A., Kochalka, J., Bhide, S., Ryali, S., and Menon, V. (2020). Intrinsic functional architecture of the human speech processing network. *Cortex*, 129:41–56. doi: 10.1016/j.cortex.2020.03.013.

Acosta-Cabronero, J., Williams, G. B., Cardenas-Blanco, A., Arnold, R. J., Lupson, V., and Nestor, P. J. (2013). In Vivo Quantitative Susceptibility Mapping (QSM) in Alzheimer's Disease. *PLoS ONE*, 8(11):e81093. doi: 10.1371/JOURNAL.PONE.0081093.

Agrawal, U., Brown, E. N., and Lewis, L. D. (2020). Model-based physiological noise removal in fast fMRI. *NeuroImage*, 205:116231. doi: 10.1016/j.neuroimage.2019.116231.

Aguirre, G., Zarahn, E., and D'Esposito, M. (1997). Empirical Analyses of BOLD fMRI Statistics. *NeuroImage*, 5(3):199–212. doi: 10.1006/nimg.1997.0264.

Aida, N., Niwa, T., Fujii, Y., Nozawa, K., Enokizono, M., Murata, K., and Obata, T. (2016). Quiet T1-Weighted pointwise encoding time reduction with radial acquisition for assessing myelination in the pediatric brain. *American Journal of Neuroradiology*, 37(8):1528–1534. doi: 10.3174/ajnr.A4747.

Alho, K., Rinne, T., Herron, T. J., and Woods, D. L. (2014). Stimulus-dependent activations and attention-related modulations inthe auditory cortex: A meta-analysis of fMRI studies. *Hearing Research*, 307:29–41. doi: 10.1016/j.heares.2013.08.001.

Alibek, S., Vogel, M., Sun, W., Winkler, D., Baker, C. A., Burke, M., and Gloger, H. (2014). Acoustic noise reduction in MRI using Silent Scan: An initial experience. *Diagnostic and Interventional Radiology*, 20(4):360–363. doi: 10.5152/dir.2014.13458.

Alsop, D. C. and Connick, T. J. (1996). Optimization of torque-balanced asymmetric head gradient coils. *Magnetic Resonance in Medicine*, 35(6):875–886. doi: 10.1002/mrm.1910350614.

Altman, D. G. and Bland, J. M. (1983). Measurement in Medicine: The Analysis of Method Comparison Studies. *The Statistician*, 32(3):307–317. doi: 10.2307/2987937.

Alzheimer's Disease Neuroimaging Initiative. (2017). Alzheimer's Disease Neuroimaging Initiative. http://adni.loni.usc.edu/methods/mri-tool/mri-analysis/.

Amaro, E. and Barker, G. J. (2006). Study design in fMRI: Basic principles. *Brain and Cognition*, 60(3):220–232. doi: 10.1016/j.bandc.2005.11.009.

Anaconda Inc. (2020). Anaconda Software Distribution, Anaconda Documentation. Version 3.7.

Ances, B. M. (2004). Coupling of Changes in Cerebral Blood Flow with Neural Activity: What Must Initially Dip Must Come Back Up. *Journal of Cerebral Blood Flow and Metabolism*, 24(1):1–6. doi: 10.1097/01.WCB.0000103920.96801.12.

Andoh, J., Ferreira, M., Leppert, I., Matsushita, R., Pike, B., and Zatorre, R. (2017). How restful is it with all that noise? Comparison of Interleaved silent steady state (ISSS) and conventional imaging in resting-state fMRI. *NeuroImage*, 147:726–735. doi: 10.1016/j.neuroimage.2016.11.065.

Andoh, J., Matsushita, R., and Zatorre, R. J. (2015). Asymmetric Interhemispheric Transfer in the Auditory Network: Evidence from TMS, Resting-State fMRI, and Diffusion Imaging. *Journal of Neuroscience*, 35(43):14602–14611. doi: 10.1523/JNEUROSCI.2333-15.2015.

Araneda, R., Renier, L., Dricot, L., Decat, M., Ebner-Karestinos, D., Deggouj, N., and De Volder, A. G. (2018). A key role of the prefrontal cortex in the maintenance of chronic tinnitus: An fMRI study using a Stroop task. *NeuroImage: Clinical*, 17:325–334. doi: 10.1016/j.nicl.2017.10.029.

Arbabshirani, M. R., Damaraju, E., Phlypo, R., Plis, S., Allen, E., Ma, S., Mathalon, D., Preda, A., Vaidya, J. G., Adali, T., and Calhoun, V. D. (2014). Impact of

autocorrelation on functional connectivity. *NeuroImage*, 102:294–308. doi: 10.1016/j.neuroimage.2014.07.045.

Attwell, D. and Iadecola, C. (2002). The neural basis of functional brain imaging signals. *Trends in Neurosciences*, 25(12):621–625. doi: 10.1016/S0166-2236(02)02264-6.

Audacity Team. (2020). Audacity ®software is copyright ©1999-2020 Audacity Team. It is free software distributed under the terms of the GNU General Public License. The name Audacity ®is a registered trademark of Dominic Mazzoni. https://audacityteam.org.

Badillo, S., Vincent, T., and Ciuciu, P. (2013). Group-level impacts of within- and between-subject hemodynamic variability in fMRI. *NeuroImage*, 82:433–448. doi: 10.1016/J.NEUROIMAGE.2013.05.100.

Baguley, D. M. (2003). Hyperacusis. *Journal of the Royal Society of Medicine*, 96: 582–585. doi: 10.1177/014107680309601203.

Baguley, D. M. and McFerran, D. J. (2011). Hyperacusis and disorders of loudness perception. In *Textbook of Tinnitus*, pages 13–23. Springer New York. doi: 10.1007/978-1-60761-145-5_3.

Balla, D. Z., Sanchez-Panchuelo, R. M., Wharton, S. J., Hagberg, G. E., Scheffler, K., Francis, S. T., and Bowtell, R. (2014). Functional quantitative susceptibility mapping (fQSM). *NeuroImage*, 100:112–124. doi: 10.1016/j.neuroimage.2014.06.011.

Bandettini, P. A., Jesmanowicz, A., Wong, E. C., and Hyde, J. S. (1993). Processing strategies for time-course data sets in functional mri of the human brain. *Magnetic Resonance in Medicine*, 30(2):161–173. doi: 10.1002/mrm.1910300204.

Bandettini, P. A., Jesmanowicz, A., Van Kylen, J., Birn, R. M., and Hyde, J. S. (1998). Functional MRI of brain activation induced by scanner acoustic noise. *Magnetic Resonance in Medicine*, 39(3):410–416. doi: 10.1002/mrm.1910390311.

Barker, D., Plack, C. J., and Hall, D. A. (2012). Reexamining the Evidence for a Pitch-Sensitive Region: A Human fMRI Study Using Iterated Ripple Noise. *Cerebral Cortex*, 22(4):745–753. doi: 10.1093/cercor/bhr065.

Barkhof, F. and Thomas, D. L. (2018). Mapping deep gray matter iron in multiple sclerosis by using quantitative magnetic susceptibility. *Radiology*, 289(2):497–498. doi: 10.1148/radiol.2018181274.

Barry, R. J., Kirkaikul, S., and Hodder, D. (2000). EEG alpha activity and the ERP to target stimuli in an auditory oddball paradigm. *International Journal of Psychophysiology*, 39(1):39–50. doi: 10.1016/S0167-8760(00)00114-8.

Bechtold, B. (2016). Violin Plots for Matlab, Accessed August 2021. https://github.com/bastibe/Violinplot-Matlab.

Beckett, A. J., Dadakova, T., Townsend, J., Huber, L., Park, S., and Feinberg, D. A. (2020). Comparison of BOLD and CBV using 3D EPI and 3D GRASE for cortical layer functional MRI at 7 T. *Magnetic Resonance in Medicine*, 84(6):3128–3145. doi: 10.1002/mrm.28347.

Benkert, T., Tian, Y., Huang, C., DiBella, E. V., Chandarana, H., and Feng, L. (2018). Optimization and validation of accelerated golden-angle radial sparse MRI reconstruction with self-calibrating GRAPPA operator gridding. *Magnetic Resonance in Medicine*, 80(1):286–293. doi: 10.1002/mrm.27030.

Bennett, C. M. and Miller, M. B. (2010). How reliable are the results from functional magnetic resonance imaging? *Annals of the New York Academy of Sciences*, 1191(1): 133–155. doi: 10.1111/j.1749-6632.2010.05446.x.

Bennett, C. M. and Miller, M. B. (2013). fMRI reliability: Influences of task and experimental design. *Cognitive, Affective and Behavioral Neuroscience*, 13(4):690–702. doi: 10.3758/s13415-013-0195-1.

Berens, P., Logothetis, N., and Tolias, A. (2010). Local field potentials, BOLD and spiking activity – relationships and physiological mechanisms. *Nature Precedings*. doi: 10.1038/npre.2010.5216.1.

Bergerbest, D., Ghahremani, D. G., and Gabrieli, J. D. (2004). Neural correlates of auditory repetition priming: Reduced fMRI activation in the auditory cortex. *Journal of Cognitive Neuroscience*, 16(6):966–977. doi: 10.1162/0898929041502760.

Bernstein, M. A., King, K. F., and Zhou, X. J. (2004). *Handbook of MRI Pulse Sequences*. Elsevier Academic Press.

BioImage Suite Web. (2021). The MNI - Talairach Tool, Accessed 2021. https://bioimagesuiteweb.github.io/webapp/mni2tal.html.

Biondetti, E., Rojas-Villabona, A., Sokolska, M., Pizzini, F. B., Jäger, H. R., Thomas, D. L., and Shmueli, K. (2019). Investigating the oxygenation of brain arteriovenous malformations using quantitative susceptibility mapping. *NeuroImage*, 199:440–453. doi: 10.1016/j.neuroimage.2019.05.014.

Birn, R. M., Diamond, J. B., Smith, M. A., and Bandettini, P. A. (2006). Separating respiratory-variation-related fluctuations from neuronal-activity-related fluctuations in fMRI. *NeuroImage*, 31(4):1536–1548. doi: 10.1016/j.neuroimage.2006.02.048.

Blackman, G. A. and Hall, D. A. (2011). Reducing the effects of background noise during auditory functional magnetic resonance imaging of speech processing: Qualitative and quantitative comparisons between two image acquisition schemes and noise cancellation. *Journal of Speech, Language, and Hearing Research*, 54(2):693–704. doi: 10.1044/1092-4388(2010/10-0143).

Bland, J. M. and Altman, D. G. (1999). Measuring agreement in method comparison studies. *Statistical Methods in Medical Research*, 8(2):135–160. doi: 10.1177/096228029900800204.

Bloch, F. (1946). Nuclear induction. *Physical Review*, 70(7-8):460–474. doi: 10.1103/PhysRev.70.460.

Boatman, D., Lesser, R. P., and Gordon, B. (1995). Auditory speech processing in the left temporal lobe: An electrical interference study. *Brain and Language*, 51(2):269–290. doi: 10.1006/brln.1995.1061.

Bodurka, J., Ye, F., Petridou, N., Murphy, K., and Bandettini, P. A. (2007). Mapping the MRI voxel volume in which thermal noise matches physiological noise-Implications for fMRI. *NeuroImage*, 34(2):542–549. doi: 10.1016/j.neuroimage.2006.09.039.

Bollmann, S. and Barth, M. (2020). New acquisition techniques and their prospects for the achievable resolution of fMRI. *Progress in Neurobiology*. doi: 10.1016/j.pneurobio.2020.101936.

Bollmann, S., Puckett, A. M., Cunnington, R., and Barth, M. (2018). Serial correlations in single-subject fMRI with sub-second TR. *NeuroImage*, 166:152–166. doi: 10.1016/j.neuroimage.2017.10.043.

Bongers, S., Slottje, P., and Kromhout, H. (2017). Hearing loss associated with repeated MRI acquisition procedure-related acoustic noise exposure: An occupational cohort study. *Occupational and Environmental Medicine*, 74:776–784. doi: 10.1136/oemed-2016-103750.

Boss, A., Weiger, M., and Wiesinger, F. (2015). Future image acquisition trends for PET/MRI. *Seminars in Nuclear Medicine*, 45(3):201–211. doi: 10.1053/j.semnuclmed.2014.12.002.

Botvinik-Nezer, R., Holzmeister, F., Camerer, C. F., ..., Nichols, T. E., Poldrack, R. A., and Schonberg, T. (2020). Variability in the analysis of a single neuroimaging dataset by many teams. *Nature*, 582:84–88. doi: 10.1038/s41586-020-2314-9.

Boucneau, T., Fernandez, B., Besson, F. L., Menini, A., Wiesinger, F., Durand, E., Caramella, C., Darrasse, L., and Maître, X. (2021). AZTEK: Adaptive zero TE k-space trajectories. *Magnetic Resonance in Medicine*, 85(2):926–935. doi: 10.1002/mrm.28483.

Bowring, A., Maumet, C., and Nichols, T. E. (2019). Exploring the impact of analysis software on task fMRI results. *Human Brain Mapping*, 40(11):3362–3384. doi: 10.1002/hbm.24603.

Bowtell, R. and Mansfield, P. (1991). Gradient coil design using active magnetic screening. *Magnetic Resonance in Medicine*, 17(1):15–21. doi: 10.1002/mrm.1910170105.

Boxerman, J. L., Hamberg, L. M., Rosen, B. R., and Weisskoff, R. M. (1995). Mr contrast due to intravascular magnetic susceptibility perturbations. *Magnetic Resonance in Medicine*, 34(4):555–566. doi: 10.1002/mrm.1910340412.

Boyacioğlu, R., Schulz, J., Koopmans, P. J., Barth, M., and Norris, D. G. (2015). Improved sensitivity and specificity for resting state and task fMRI with multiband multi-echo EPI compared to multi-echo EPI at 7T. *NeuroImage*, 119:352–361. doi: 10.1016/j.neuroimage.2015.06.089.

Boyacioğlu, R., Schulz, J., Müller, N. C., Koopmans, P. J., Barth, M., and Norris, D. G. (2014). Whole brain, high resolution multiband spin-echo EPI fMRI at 7T: A comparison with gradient-echo EPI using a color-word Stroop task. *NeuroImage*, 97: 142–150. doi: 10.1016/j.neuroimage.2014.04.011.

Boyle, Y., Bentley, D. E., Watson, A., and Jones, A. K. (2006). Acoustic noise in functional magnetic resonance imaging reduces pain unpleasantness ratings. *NeuroImage*, 31(3): 1278–1283. doi: 10.1016/j.neuroimage.2006.01.025.

Boynton, G. M., Engel, S. A., Glover, G. H., and Heeger, D. J. (1996). Linear systems analysis of functional magnetic resonance imaging in human V1. *Journal of Neuroscience*, 16(13):4207–4221. doi: 10.1523/jneurosci.16-13-04207.1996.

Boynton, G. M., Engel, S. A., and Heeger, D. J. (2012). Linear systems analysis of the fMRI signal. *NeuroImage*, 62(2):975–984. doi: 10.1016/j.neuroimage.2012.01.082.

Brázdil, M., Dobšík, M., Mikl, M., Hluštík, P., Daniel, P., Pažourková, M., Krupa, P., and Rektor, I. (2005). Combined event-related fMRI and intracerebral ERP study of an auditory oddball task. *NeuroImage*, 26(1):285–293. doi: 10.1016/j.neuroimage.2005.01.051.

Brechmann, A., Baumgart, F., and Scheich, H. (2002). Sound-Level-Dependent Representation of Frequency Modulations in Human Auditory Cortex: A Low-Noise fMRI Study. *Journal of Neurophysiology*, 87(1):423–433. doi: 10.1152/jn.00187.2001.

Brett, M. (2016). MarsBaR 0.44 Documentation Release, Accessed 2018 - 2021. https://marsbar-toolbox.github.io/faq.html.

Brett, M., Anton, J.-L., Valabregue, R., and Poline, J.-B. (2002). Region of interest analysis using an SPM toolbox, Available on CD-ROM in NeuroImage, 16(2). Presented at the 8th International Conference on Functional Mapping of the Human Brain, Abstract 497.

Brown, E. N. and Behrmann, M. (2017). Controversy in statistical analysis of functional magnetic resonance imaging data. *Proceedings of the National Academy of Sciences of the United States of America*, 114(17):E3368–E3369. doi: 10.1073/pnas.1705513114.

Brown, R. W., Cheng, Y.-C. N., Haacke, E., Thompson, M. R., and Venkatesan, R. (2014). *Magnetic Resonance Imaging: Physical Principles and Sequence Design*. John Wiley and Sons, Inc, second edition.

Brummett, R. E., Talbot, J. M., and Charuhas, P. (1988). Potential hearing loss resulting from MR imaging. *Radiology*, 169(2):539–540. doi: 10.1148/radiology.169.2.3175004.

Brunnquell, C. L., Hoff, M. N., Balu, N., Nguyen, X. V., Oztek, M. A., and Haynor, D. R. (2020). Making Magnets More Attractive: Physics and Engineering Contributions to Patient Comfort in MRI. *Topics in Magnetic Resonance Imaging*, 29(4):167–174. doi: 10.1097/RMR.0000000000000246.

Bullmore, E., Long, C., Suckling, J., Fadili, J., Calvert, G., Zelaya, F., Carpenter, T. A., and Brammer, M. (2001). Colored noise and computational inference in neurophysiological (fMRI) time series analysis: Resampling methods in time and wavelet domains. *Human Brain Mapping*, 12:61–78. doi: 10.1002/1097-0193(200102)12:2<61::AID-HBM1004>3.0.CO;2-W.

Burton, M. W., Noll, D. C., and Small, S. L. (2001). The anatomy of auditory word processing: Individual variability. *Brain and Language*, 77(1):119–131. doi: 10.1006/brln.2000.2444.

Bushberg, J. T., Seibert, J. A., Leidholdt, E. M., and Boone, J. M. (2012). *The Essential Physics of Medical Imaging*. Lippincott Williams and Wilkins, third edition.

Button, K. S., Ioannidis, J. P., Mokrysz, C., Nosek, B. A., Flint, J., Robinson, E. S., and Munafò, M. R. (2013). Power failure: Why small sample size undermines the reliability of neuroscience. *Nature Reviews Neuroscience*, 14(5):365–376. doi: 10.1038/nrn3475.

Buxton, R. B. (2013). The physics of functional magnetic resonance imaging (fMRI). *Reports on Progress in Physics*, 76(9):096601. doi: 10.1088/0034-4885/76/9/096601.

Buxton, R. B., Wong, E. C., and Frank, L. R. (1998). Dynamics of blood flow and oxygenation changes during brain activation: The balloon model. *Magnetic Resonance in Medicine*, 39(6):855–864. doi: 10.1002/mrm.1910390602.

Caballero-Gaudes, C., Moia, S., Panwar, P., Bandettini, P. A., and Gonzalez-Castillo, J. (2019). A deconvolution algorithm for multi-echo functional MRI: Multi-echo Sparse Paradigm Free Mapping. *NeuroImage*, 202:116081. doi: 10.1016/j.neuroimage.2019.116081.

Caceres, A., Hall, D. L., Zelaya, F. O., Williams, S. C., and Mehta, M. A. (2009). Measuring fMRI reliability with the intra-class correlation coefficient. *NeuroImage*, 45 (3):758–768. doi: 10.1016/j.neuroimage.2008.12.035.

Calhoun, V. D., Adali, T., McGinty, V. B., Pekar, J. J., Watson, T. D., and Pearlson, G. D. (2001)a. fMRI activation in a visual-perception task: Network of areas detected using the general linear model and independent components analysis. *NeuroImage*, 14 (5):1080–1088. doi: 10.1006/nimg.2001.0921.

Calhoun, V. D., Adali, T., Pearlson, G. D., and Pekar, J. J. (2001)b. A method for making group inferences from functional MRI data using independent component analysis. *Human Brain Mapping*, 14(3):140–151. doi: 10.1002/hbm.1048.

Calhoun, V. D., Adali, T., and Pekar, J. J. (2004). A method for comparing group fMRI data using independent component analysis: Application to visual, motor and visuomotor tasks. *Magnetic Resonance Imaging*, 22(9):1181–1191. doi: 10.1016/j.mri.2004.09.004.

Calhoun, V. D., Liu, J., and Adali, T. (2009). A review of group ICA for fMRI data and ICA for joint inference of imaging, genetic, and ERP data. *NeuroImage*, 45(1): S163–S172. doi: 10.1016/j.neuroimage.2008.10.057.

Caparelli, E. C. and Tomasi, D. (2008). k-Space spatial low-pass filters can increase signal loss artifacts in echo-planar imaging. *Biomedical Signal Processing and Control*, 3(1):107–114. doi: 10.1016/j.bspc.2007.11.003.

Casella Solutions. (2010). Cel-62X Series Sound Level Meter Operator's Manual.

Casella Solutions. (2021). Octave Definitions In CEL-63x Results.

Cavanna, A. E. and Seri, S. (2015). Misophonia: Current perspectives. *Neuropsychiatric Disease and Treatment*, 11:2117–2123. doi: 10.2147/NDT.S81438.

Cavanna, A. E. and Trimble, M. R. (2006). The precuneus: A review of its functional anatomy and behavioural correlates. *Brain*, 129(3):564–583. doi: 10.1093/brain/awl004.

Chai, X. J., Castañán, A. N., Öngür, D., and Whitfield-Gabrieli, S. (2012). Anticorrelations in resting state networks without global signal regression. *NeuroImage*, 59(2):1420–1428. doi: 10.1016/j.neuroimage.2011.08.048.

Chaimow, D. and Shmuel, A. (2016). A more accurate account of the effect of k-space sampling and signal decay on the effective spatial resolution in functional MRI. *bioRxiv*. doi: 10.1101/097154.

Chan, K. S. and Marques, J. P. (2021). SEPIA—Susceptibility mapping pipeline tool for phase images. *NeuroImage*, 227:117611. doi: 10.1016/j.neuroimage.2020.117611.

Chan, R. W., Ramsay, E. A., Cunningham, C. H., and Plewes, D. B. (2009). Temporal stability of adaptive 3D radial MRI using multidimensional golden means. *Magnetic Resonance in Medicine*, 61(2):354–363. doi: 10.1002/mrm.21837.

Chau, W. and McIntosh, A. R. (2005). The Talairach coordinate of a point in the MNI space: How to interpret it. *NeuroImage*, 25(2):408–416. doi: 10.1016/j.neuroimage.2004.12.007.

Chen, C. K., Chiueh, T. D., and Chen, J. H. (1999). Active cancellation system of acoustic noise in MR imaging. *IEEE Transactions on Biomedical Engineering*, 46(2):186–191. doi: 10.1109/10.740881.

Chen, J. and Cohen-Adad, J. (2019). Functional magnetic resonance imaging. In *Encyclopedia of Biomedical Engineering*, volume 2, pages 533–544. Elsevier. doi: 10.1016/B978-0-12-801238-3.99948-3.

Chen, J. E., Polimeni, J. R., Bollmann, S., and Glover, G. H. (2019). On the analysis of rapidly sampled fMRI data. *NeuroImage*, 188:807–820. doi: 10.1016/j.neuroimage.2019.02.008.

Chen, J. E., Lewis, L. D., Chang, C., Tian, Q., Fultz, N. E., Ohringer, N. A., Rosen, B. R., and Polimeni, J. R. (2020)a. Resting-state "physiological networks". *NeuroImage*, 213: 116707. doi: 10.1016/j.neuroimage.2020.116707.

Chen, T., Zhao, Y., Jia, C., Yuan, Z., and Qiu, J. (2020)b. BOLD signal simulation and fMRI quality control base on an active phantom: a preliminary study. *Medical and Biological Engineering and Computing*, 58(4):831–842. doi: 10.1007/s11517-020-02133-9.

Chen, Y. C., Li, X., Liu, L., Wang, J., Lu, C. Q., Yang, M., Jiao, Y., Zang, F. C., Radziwon, K., Chen, G. D., Sun, W., Muthaiah, V. P. K., Salvi, R., and Teng, G. J. (2015). Tinnitus and hyperacusis involve hyperactivity and enhanced connectivity in auditory-limbic-arousal-cerebellar network. *eLife*, 4:e06576. doi: 10.7554/eLife.06576.

Chen, Z. and Calhoun, V. (2018). Effect of spatial smoothing on task fMRI ICA and functional connectivity. *Frontiers in Neuroscience*, 12. doi: 10.3389/fnins.2018.00015.

Chiew, M., Smith, S. M., Koopmans, P. J., Graedel, N. N., Blumensath, T., and Miller, K. L. (2015). k-t FASTER: Acceleration of functional MRI data acquisition using low rank constraints. *Magnetic Resonance in Medicine*, 74(2):353–364. doi: 10.1002/mrm.25395.

Chiew, M., Graedel, N. N., McNab, J. A., Smith, S. M., and Miller, K. L. (2016). Accelerating functional MRI using fixed-rank approximations and radial-cartesian sampling. *Magnetic Resonance in Medicine*, 76(6):1825–1836. doi: 10.1002/mrm.26079.

Cho, Z. H., Chung, S. T., Chung, J. Y., Park, S. H., Kim, J. S., Moon, C. H., and Hong, I. K. (1998)a. A new silent magnetic resonance imaging using a rotating DC gradient. *Magnetic Resonance in Medicine*, 39(2):317–321. doi: 10.1002/MRM.1910390221.

Cho, Z. H., Chung, S. C., Lim, D. W., and Wong, E. K. (1998)b. Effects of the acoustic noise of the gradient systems on fMRI: A study on auditory, motor, and visual cortices. *Magnetic Resonance in Medicine*, 39(2):331–335. doi: 10.1002/mrm.1910390224.

Chonde, D. B., Abolmaali, N., Arabasz, G., Guimaraes, A. R., and Catana, C. (2013). Effect of MRI acoustic noise on cerebral fludeoxyglucose uptake in simultaneous MR-PET imaging. *Investigative Radiology*, 48(5):302–312. doi: 10.1097/RLI.0b013e3182839fbc.

Chu, P. P., Golestani, A. M., Kwinta, J. B., Khatamian, Y. B., and Chen, J. J. (2018). Characterizing the modulation of resting-state fMRI metrics by baseline physiology. *NeuroImage*, 173:72–87. doi: 10.1016/j.neuroimage.2018.02.004.

Cohen-Adad, J. (2014). What can we learn from T2* maps of the cortex? *NeuroImage*, 93(2):189–200. doi: 10.1016/j.neuroimage.2013.01.023.

Constable, R. T. (2006). Challenges in fMRI and its limitations. In Faro, S. and Mohamed, F., editors, *Functional MRI*, pages 75–98. Springer New York. doi: 10.1007/0-387-34665-1_4.

Corbin, N., Todd, N., Friston, K. J., and Callaghan, M. F. (2018). Accurate modeling of temporal correlations in rapidly sampled fMRI time series. *Human Brain Mapping*, 39 (10):3884–3897. doi: 10.1002/hbm.24218.

Correa, N., Adali, T., and Calhoun, V. D. (2007). Performance of blind source separation algorithms for fMRI analysis using a group ICA method. *Magnetic Resonance Imaging*, 25(5):684–694. doi: 10.1016/j.mri.2006.10.017.

Counter, S. A., Olofsson, A., Grahn, H. F., and Borg, E. (1997). MRI acoustic noise: Sound pressure and frequency analysis. *Journal of Magnetic Resonance Imaging*, 7(3): 606–611. doi: 10.1002/jmri.1880070327.

Cox, R. W. (1996). AFNI: Software for analysis and visualization of functional magnetic resonance neuroimages. *Computers and Biomedical Research*, 29(3):162–173. doi: 10.1006/cbmr.1996.0014.

Cremers, H. R., Wager, T. D., and Yarkoni, T. (2017). The relation between statistical power and inference in fMRI. *PLoS ONE*, 12(11):e0184923. doi: 10.1371/journal.pone.0184923.

Crémillieux, Y., Wheeler-Kingshott, C. A., Briguet, A., and Doran, S. J. (1997). STEAM-Burst: A single-shot, multi-slice imaging sequence without rapid gradient switching. *Magnetic Resonance in Medicine*, 38(4):645–652. doi: $10.1002/\mathrm{mrm}.1910380419$.

Dale, B. M., Brown, M. A., and Semelka, R. C. (2015). *MRI Basic Principles and Applications*. John Wiley and Sons, Ltd, fifth edition.

Damestani, N., Leynes, A., Solana, A. B., Lythgoe, D., Fernandez, B., Burns, B., Larson, P., Williams, S., Zelaya, F., and Wiesinger, F. (2021)a. Silent multi-echo fMRI at sub-second resolution using Extreme Coherence-Resolved Looping Star. Organisation for Human Brain Mapping 27th Annual Meeting, Abstract 1400.

Damestani, N. L., Lythgoe, D. J., and Zelaya, F. (2018). Looping Star - a novel silent approach to imaging brain function in health and disease. British Chapter of the International Society for Magnetic Resonance in Medicine Annual Meeting, Talk O8.

Damestani, N. L., Lythgoe, D. J., Wiesinger, F., Solana, A. B., Williams, S. C. R., and Zelaya, F. (2019)a. Identifying functional resting state networks in silence using Looping Star. Organisation for Human Brain Mapping 25th Annual Meeting, Abstract W364.

Damestani, N. L., O'Daly, O., Solana, A. B., Wiesinger, F., Lythgoe, D. J., Hill, S., de Lara Rubio, A., Makovac, E., Williams, S. C., and Zelaya, F. (2021)b. Revealing the mechanisms behind novel auditory stimuli discrimination: An evaluation of silent functional MRI using looping star. *Human Brain Mapping*, 42(9):2833–2850. doi: $10.1002/\mathrm{hbm}.25407$.

Damestani, N. L., Lythgoe, D. J., Wiesinger, F., Solana, A. B., Williams, S. C. R., and Zelaya, F. (2019)b. Looping Star silent fMRI: a platform for improving studies of auditory processing. International Society for Magnetic Resonance in Medicine 27th Annual Meeting, Abstract 0363.

Damestani, N. L., Lythgoe, D. J., Solana, A. B., Fernandez, B., Williams, S. C. R., Zelaya, F., and Wiesinger, F. (2021)c. Coherence-resolved Looping Star – improvements to image quality for silent structural and functional neuroimaging. International Society for Magnetic Resonance in Medicine 29th Annual Meeting, Abstract 2677.

Damoiseaux, J. S., Rombouts, S. A., Barkhof, F., Scheltens, P., Stam, C. J., Smith, S. M., and Beckmann, C. F. (2006). Consistent resting-state networks across healthy subjects. *Proceedings of the National Academy of Sciences of the United States of America*, 103(37):13848–13853. doi: 10.1073/pnas.0601417103.

Davies, J., Gander, P. E., Andrews, M., and Hall, D. A. (2014). Auditory network connectivity in tinnitus patients: A resting-state fMRI study. *International Journal of Audiology*, 53(3):192–198. doi: 10.3109/14992027.2013.846482.

Davis, M. H. and Johnsrude, I. S. (2003). Hierarchical processing in spoken language comprehension. *Journal of Neuroscience*, 23(8):3423–3431. doi: 10.1523/jneurosci.23-08-03423.2003.

Dawson, G., Finley, C., Phillips, S., and Galpert, L. (1986). Hemispheric Specialization and the Language Abilities of Autistic Children. *Child Development*, 57(6):1440. doi: 10.2307/1130422.

Dawson, G., Finley, C., Phillips, S., Galpert, L., and Lewy, A. (1988). Reduced P3 amplitude of the event-related brain potential: Its relationship to language ability in austism. *Journal of Autism and Developmental Disorders*, 18(4):493–504. doi: 10.1007/BF02211869.

De Blasi, B., Caciagli, L., Storti, S. F., Galovic, M., Koepp, M., Menegaz, G., Barnes, A., and Galazzo, I. B. (2020). Noise removal in resting-state and task fMRI: Functional connectivity and activation maps. *Journal of Neural Engineering*, 17(4). doi: 10.1088/1741-2552/aba5cc.

De Martino, F., Moerel, M., Ugurbil, K., Formisano, E., and Yacoub, E. (2015). Less noise, more activation: Multiband acquisition schemes for auditory functional MRI. *Magnetic Resonance in Medicine*, 74:462–467. doi: 10.1002/mrm.25408.

De Zwart, J. A., Van Gelderen, P., Kellman, P., and Duyn, J. H. (2002). Reduction of gradient acoustic noise in MRI using SENSE-EPI. *NeuroImage*, 16(4):1151–1155. doi: 10.1006/nimg.2002.1119.

Deistung, A., Schweser, F., and Reichenbach, J. R. (2017). Overview of quantitative susceptibility mapping. *NMR in Biomedicine*, 30(4):e3569. doi: 10.1002/nbm.3569.

Devlin, J. T., Raley, J., Tunbridge, E., Lanary, K., Floyer-Lea, A., Narain, C., Cohen, I., Behrens, T., Jezzard, P., Matthews, P. M., and Moore, D. R. (2003). Functional Asymmetry for Auditory Processing in Human Primary Auditory Cortex. *Journal of Neuroscience*, 23(37):11516–11522. doi: 10.1523/jneurosci.23-37-11516.2003.

Dewey, M., Schink, T., and Dewey, C. F. (2007). Claustrophobia during magnetic resonance imaging: Cohort study in over 55,000 patients. *Journal of Magnetic Resonance Imaging*, 26(5):1322–1327. doi: 10.1002/jmri.21147.

Dewey, R. S., Francis, S. T., Guest, H., Prendergast, G., Millman, R. E., Plack, C. J., and Hall, D. A. (2020). The association between subcortical and cortical fMRI and lifetime noise exposure in listeners with normal hearing thresholds. *NeuroImage*, 204: 116239. doi: 10.1016/j.neuroimage.2019.116239.

Dewey, R. S., Hall, D. A., Plack, C. J., and Francis, S. T. (2021). Comparison of continuous sampling with active noise cancelation and sparse sampling for cortical and subcortical auditory functional MRI. *Magnetic Resonance in Medicine*, 00:1–12. doi: 10.1002/mrm.28902.

Dewey, R. S., Hall, D. A., Guest, H., Prendergast, G., Plack, C. J., and Francis, S. T. (2018). The physiological bases of hidden noise-induced hearing loss: Protocol for a functional neuroimaging study. *JMIR Research Protocols*, 7(3). doi: 10.2196/resprot.9095.

DeYoe, E. A., Bandettini, P., Neitz, J., Miller, D., and Winans, P. (1994). Functional magnetic resonance imaging (FMRI) of the human brain. *Journal of Neuroscience Methods*, 54(2):171–187. doi: 10.1016/0165-0270(94)90191-0.

Di, X. and Biswal, B. B. (2017). Psychophysiological interactions in a visual checkerboard task: Reproducibility, reliability, and the effects of deconvolution. *Frontiers in Neuroscience*, 11:573. doi: 10.3389/fnins.2017.00573.

Di Salle, F., Formisano, E., Seifritz, E., Linden, D. E., Scheffler, K., Saulino, C., Tedeschi, G., Zanella, F. E., Pepino, A., Goebel, R., and Marciano, E. (2001). Functional fields in human auditory cortex revealed by time-resolved fMRI without interference of EPI noise. *NeuroImage*, 13(2):328–338. doi: 10.1006/nimg.2000.0683.

Di Salle, F., Esposito, F., Scarabino, T., Formisano, E., Marciano, E., Saulino, C., Cirillo, S., Elefante, R., Scheffler, K., and Seifritz, E. (2003). fMRI of the auditory system: Understanding the neural basis of auditory gestalt. *Magnetic Resonance Imaging*, 21 (10):1213–1224. doi: 10.1016/j.mri.2003.08.023.

Dionisio-Parra, B., Wiesinger, F., Sämann, P. G., Czisch, M., and Solana, A. B. (2020). Looping Star fMRI in Cognitive Tasks and Resting State. *Journal of Magnetic Resonance Imaging*, 52(3):739–751. doi: 10.1002/jmri.27073.

Dipasquale, O., Sethi, A., Lagan, M. M., Baglio, F., Baselli, G., Kundu, P., Harrison, N. A., and Cercignani, M. (2017). Comparing resting state fMRI de-noising approaches using multi-and single-echo acquisitions. *PLoS ONE*, 12(3):e0173289. doi: 10.1371/journal.pone.0173289.

Dowdle, L. T., Ghose, G., Ugurbil, K., Yacoub, E., and Vizioli, L. (2021). Statistical Power or More Precise Insights into Neuro-Temporal Dynamics? Assessing the Benefits of Rapid Temporal Sampling in fMRI. *bioRxiv*. doi: 10.1101/2021.06.05.447164.

Drew, P. J. (2019). Vascular and neural basis of the BOLD signal. *Current Opinion in Neurobiology*, 58:61–69. doi: 10.1016/j.conb.2019.06.004.

Duong, T. Q., Yacoub, E., Adriany, G., Hu, X., Uğurbil, K., and Kim, S. G. (2003). Microvascular BOLD contribution at 4 and 7 T in the human brain: Gradient-echo and spin-echo fMRI with suppression of blood effects. *Magnetic Resonance in Medicine*, 49(6):1019–1027. doi: 10.1002/mrm.10472.

DuPre, E., Salo, T., Markello, R., Kundu, P., Whitaker, K., and Handwerker, D. (2019). ME-ICA/tedana: 0.0.6. *Zenodo*. doi: 10.5281/ZENODO.2558498.

Durand, E., Van Moortele, P. F. D., Pachot-Clouard, M., and Bihan, D. L. (2001). Artifact due to B0 fluctuations in fMRI: Correction using the k-space central line. *Magnetic Resonance in Medicine*, 46(1):198–201. doi: 10.1002/mrm.1177.

Durnez, J., Degryse, J., Moerkerke, B., Seurinck, R., Sochat, V., Poldrack, R., and Nichols, T. (2016). Power and sample size calculations for fMRI studies based on the prevalence of active peaks. *bioRxiv*. doi: 10.1101/049429.

Duyn, J. H., Moonen, C. T., van Yperen, G. H., de Boer, R. W., and Luyten, P. R. (1994). Inflow versus deoxyhemoglobin effects in bold functional MRI using gradient echoes at 1.5 T. *NMR in Biomedicine*, 7(1-2):83–88. doi: 10.1002/nbm.1940070113.

Edelstein, M., Brang, D., Rouw, R., and Ramachandran, V. S. (2013). Misophonia: Physiological investigations and case descriptions. *Frontiers in Human Neuroscience*, 7. doi: 10.3389/fnhum.2013.00296.

Edelstein, W. A., Glover, G. H., Hardy, C. J., and Redington, R. W. (1986). The intrinsic signal-to-noise ratio in NMR imaging. *Magnetic Resonance in Medicine*, 3(4):604–618. doi: 10.1002/mrm.1910030413.

Edelstein, W. A., Hedeen, R. A., Mallozzi, R. P., El-Hamamsy, S. A., Ackermann, R. A., and Havens, T. J. (2002). Making MRI quieter. *Magnetic Resonance Imaging*, 20(2): 155–163. doi: 10.1016/S0730-725X(02)00475-7.

Edelstein, W. A., Kidane, T. K., Taracila, V., Baig, T. N., Eagan, T. P., Cheng, Y. C. N., Brown, R. W., and Mallick, J. A. (2005). Active-passive gradient shielding for MRI acoustic noise reduction. *Magnetic Resonance in Medicine*, 53(5):1013–1017. doi: 10.1002/mrm.20472.

Eden, G. F., Joseph, J. E., Brown, H. E., Brown, C. P., and Zeffiro, T. A. (1999). Utilizing hemodynamic delay and dispersion to detect fMRI signal change without auditory interference: The behavior interleaved gradients technique. *Magnetic Resonance in Medicine*, 41(1):13–20. doi: 10.1002/(SICI)1522-2594(199901)41:1<13::AID-MRM4>3.0.CO;2-T.

Edmister, W. B., Talavage, T. M., Ledden, P. J., and Weisskoff, R. M. (1999). Improved auditory cortex imaging using clustered volume acquisitions. *Human Brain Mapping*, 7 (2):89–97. doi: 10.1002/(SICI)1097-0193(1999)7:2<89::AID-HBM2>3.0.CO;2-N.

Eklund, A., Andersson, M., Josephson, C., Johannesson, M., and Knutsson, H. (2012). Does parametric fMRI analysis with SPM yield valid results? An empirical study of 1484 rest datasets. *NeuroImage*, 61(3):565–578. doi: 10.1016/j.neuroimage.2012.03.093.

Eklund, A., Nichols, T. E., and Knutsson, H. (2016). Cluster failure: Why fMRI inferences for spatial extent have inflated false-positive rates. *Proceedings of the*

National Academy of Sciences of the United States of America, 113(28):7900–7905. doi: 10.1073/pnas.1602413113.

Elliott, M. R., Bowtell, R. W., and Morris, P. G. (1999). The effect of scanner sound in visual, motor, and auditory functional MRI. *Magnetic Resonance in Medicine*, 41(6): 1230–1235. doi: 10.1002/(SICI)1522-2594(199906)41:6<1230::AID-MRM20>3.0.CO;2-1.

Engström, M., Mårtensson, M., Avventi, E., and Skare, S. (2015). On the signal-to-noise ratio efficiency and slab-banding artifacts in three-dimensional multislab diffusion-weighted echo-planar imaging. *Magnetic Resonance in Medicine*, 73(2):718–725. doi: 10.1002/mrm.25182.

Erb, J., Henry, M. J., Eisner, F., and Obleser, J. (2013). The brain dynamics of rapid perceptual adaptation to adverse listening conditions. *Journal of Neuroscience*, 33(26): 10688–10697. doi: 10.1523/JNEUROSCI.4596-12.2013.

Erhardt, E. B., Rachakonda, S., Bedrick, E. J., Allen, E. A., Adali, T., and Calhoun, V. D. (2011). Comparison of multi-subject ICA methods for analysis of fMRI data. *Human Brain Mapping*, 32(12):2075–2095. doi: 10.1002/hbm.21170.

Evans, J. W., Kundu, P., Horovitz, S. G., and Bandettini, P. A. (2015). Separating slow BOLD from non-BOLD baseline drifts using multi-echo fMRI. *NeuroImage*, 105: 189–197. doi: 10.1016/j.neuroimage.2014.10.051.

Fair, D. A., Miranda-Dominguez, O., Snyder, A. Z., Perrone, A., Earl, E. A., Van, A. N., Koller, J. M., Feczko, E., Tisdall, M. D., van der Kouwe, A., Klein, R. L., Mirro, A. E., Hampton, J. M., Adeyemo, B., Laumann, T. O., Gratton, C., Greene, D. J., Schlaggar, B. L., Hagler, D. J., Watts, R., Garavan, H., Barch, D. M., Nigg, J. T., Petersen, S. E., Dale, A. M., Feldstein-Ewing, S. W., Nagel, B. J., and Dosenbach, N. U. (2020). Correction of respiratory artifacts in MRI head motion estimates. *NeuroImage*, 208: 116400. doi: 10.1016/j.neuroimage.2019.116400.

Faul, F., Erdfelder, E., Lang, A. G., and Buchner, A. (2007). G*Power 3: A flexible statistical power analysis program for the social, behavioral, and biomedical sciences. *Behavior Research Methods*, 39(2):175–191. doi: 10.3758/BF03193146.

Feinberg, D. A. and Yacoub, E. (2012). The rapid development of high speed, resolution and precision in fMRI. *NeuroImage*, 62(2):720–725. doi: 10.1016/j.neuroimage.2012.01.049.

Feng, L., Grimm, R., Block, K. T. T., Chandarana, H., Kim, S., Xu, J., Axel, L., Sodickson, D. K., and Otazo, R. (2014). Golden-angle radial sparse parallel MRI: Combination of compressed sensing, parallel imaging, and golden-angle radial sampling for fast and flexible dynamic volumetric MRI. *Magnetic Resonance in Medicine*, 72(3):707–717. doi: 10.1002/mrm.24980.

FIL Methods Group. (2020). SPM-12 Manual (Various Versions, Accessed 2017 - 2021). https://www.fil.ion.ucl.ac.uk/spm/.

Fjaeldstad, A. W., Nørgaard, H. J., and Fernandes, H. M. (2019). The Impact of Acoustic fMRI-Noise on Olfactory Sensitivity and Perception. *Neuroscience*, 406:262–267. doi: 10.1016/j.neuroscience.2019.03.028.

Forbes, L. K., Brideson, M. A., Crozier, S., and While, P. T. (2007). An analytical approach to the design of quiet cylindrical asymmetric gradient coils in MRI. *Concepts in Magnetic Resonance Part B: Magnetic Resonance Engineering*, 31(4):218–236. doi: 10.1002/cmr.b.20095.

Foster, J. R., Hall, D. A., Summerfield, A. Q., Palmer, A. R., and Bowtell, R. W. (2000). Sound-level measurements and calculations of safe noise dosage during EPI at 3 T. *Journal of Magnetic Resonance Imaging*, 12(1):157–163. doi: 10.1002/1522-2586(200007)12:1<157::AID-JMRI17>3.0.CO;2-M.

Fox, M. D. and Raichle, M. E. (2007). Spontaneous fluctuations in brain activity observed with functional magnetic resonance imaging. *Nature Reviews Neuroscience*, 8(9):700–711. doi: 10.1038/nrn2201.

Francis, S. and Panchuelo, R. S. (2014). Physiological measurements using ultra-high field fMRI: A review. *Physiological Measurement*, 35(9):R167–185. doi: 10.1088/0967-3334/35/9/R167.

Friedman, L. and Glover, G. H. (2006). Report on a multicenter fMRI quality assurance

protocol. *Journal of Magnetic Resonance Imaging*, 23(6):827–839. doi: 10.1002/jmri.20583.

Friedman, L., Glover, G. H., and The FBIRN Consortium. (2006). Reducing inter-scanner variability of activation in a multicenter fMRI study: Controlling for signal-to-fluctuation-noise-ratio (SFNR) differences. *NeuroImage*, 33(2):471–481. doi: 10.1016/j.neuroimage.2006.07.012.

Friman, O., Borga, M., Lundberg, P., and Knutsson, H. (2004). Detection and detrending in fMRI data analysis. *NeuroImage*, 22(2):645–655. doi: 10.1016/j.neuroimage.2004.01.033.

Friston, K. J., Jezzard, P., and Turner, R. (1994). Analysis of Functional MRI Time-Series. *Human Brain Mapping*, 1:153–171. doi: 10.1002/hbm.460010207.

Friston, K. J., Josephs, O., Zarahn, E., Holmes, A. P., Rouquette, S., and Poline, J. B. (2000)a. To smooth or not to smooth? Bias and efficiency in fMRI time-series analysis. *NeuroImage*, 12(2):196–208. doi: 10.1006/nimg.2000.0609.

Friston, K. J., Mechelli, A., Turner, R., and Price, C. J. (2000)b. Nonlinear responses in fMRI: The balloon model, Volterra kernels, and other hemodynamics. *NeuroImage*, 12 (4):466–477. doi: 10.1006/nimg.2000.0630.

Froidevaux, R., Weiger, M., Brunner, D. O., Dietrich, B. E., Wilm, B. J., and Pruessmann, K. P. (2018). Filling the dead-time gap in zero echo time MRI: Principles compared. *Magnetic Resonance in Medicine*, 79(4):2036–2045. doi: 10.1002/mrm.26875.

Froidevaux, R., Weiger, M., Rösler, M., Brunner, D., and Pruessmann, K. (2021). HYFI: Hybrid filling of the dead-time gap for faster zero echo time imaging. *NMR in Biomedicine*, 34(6). doi: 10.1002/nbm.4493.

Fuelkell, P., Langner, S., Friedrich, N., Kromrey, M. L., Radosa, C. G., Platzek, I., Mensel, B., and Kühn, J. P. (2018). Software-based noise reduction in cranial magnetic resonance imaging: Influence on image quality. *PLoS ONE*, 13(11):e0206196. doi: 10.1371/journal.pone.0206196.

Gaab, N., Gaser, C., Zaehle, T., Jancke, L., and Schlaug, G. (2003). Functional anatomy of pitch memory - An fMRI study with sparse temporal sampling. *NeuroImage*, 19(4): 1417–1426. doi: 10.1016/S1053-8119(03)00224-6.

Gaab, N., Gabrieli, J. D., and Glover, G. H. (2007)a. Assessing the influence of scanner background noise on auditory processing. II. An fMRI study comparing auditory processing in the absence and presence of recorded scanner noise using a sparse design. *Human Brain Mapping*, 28(8):721–732. doi: 10.1002/hbm.20299.

Gaab, N., Gabrieli, J. D., and Glover, G. H. (2007)b. Assessing the influence of scanner background noise on auditory processing. I. An fMRI study comparing three experimental designs with varying degrees of scanner noise. *Human Brain Mapping*, 28(8):703–720. doi: 10.1002/hbm.20298.

Gaab, N., Gabrieli, J. D., and Glover, G. H. (2008). Resting in peace or noise: Scanner background noise suppresses default-mode network. *Human Brain Mapping*, 29(7): 858–867. doi: 10.1002/hbm.20578.

Gabr, R. E., Aksit, P., Bottomley, P. A., Youssef, A. B. M., and Kadah, Y. M. (2006). Deconvolution-interpolation gridding (DING): Accurate reconstruction for arbitrary k-space trajectories. *Magnetic Resonance in Medicine*, 56(6):1182–1191. doi: 10.1002/mrm.21095.

Gabrielsen, T. P., Anderson, J. S., Stephenson, K. G., Beck, J., King, J. B., Kellems, R., Top, D. N., Russell, N. C., Anderberg, E., Lundwall, R. A., Hansen, B., and South, M. (2018). Functional MRI connectivity of children with autism and low verbal and cognitive performance. *Molecular Autism*, 9(1):67. doi: 10.1186/s13229-018-0248-y.

Gao, J. H. and Liu, H. L. (2012). Inflow effects on functional MRI. *NeuroImage*, 62(2): 1035–1039. doi: 10.1016/j.neuroimage.2011.09.088.

Gao, P. P., Zhang, J. W., Cheng, J. S., Zhou, I. Y., and Wu, E. X. (2014). The inferior colliculus is involved in deviant sound detection as revealed by BOLD fMRI. *NeuroImage*, 91:220–227. doi: 10.1016/j.neuroimage.2014.01.043.

Gerhardt, K. J. and Abrams, R. M. (2000). Fetal Exposures to Sound and Vibroacoustic Stimulation. *Journal of Perinatology*, 20(1):S21–S30. doi: 10.1038/sj.jp.7200446.

Geuter, S., Qi, G., Welsh, R. C., Wager, T. D., and Lindquist, M. A. (2018). Effect Size and Power in fMRI Group Analysis. *bioRxiv*. doi: 10.1101/295048.

Ghazaleh, N., van der Zwaag, W., Clarke, S., Ville, D. V. D., Maire, R., and Saenz, M. (2017). High-Resolution fMRI of Auditory Cortical Map Changes in Unilateral Hearing Loss and Tinnitus. *Brain Topography*, 30(5):685–697. doi: 10.1007/s10548-017-0547-1.

Giannelli, M., Diciotti, S., Tessa, C., and Mascalchi, M. (2010). Effect of echo spacing and readout bandwidth on basic performances of EPI-fMRI acquisition sequences implemented on two 1.5 T MR scanner systems. *Medical Physics*, 37(1):303–310. doi: 10.1118/1.3271130.

Giavarina, D. (2015). Understanding Bland Altman analysis. *Biochemia Medica*, 25(2): 141–151. doi: 10.11613/BM.2015.015.

Glover, G. H. and Pauly, J. M. (1992). Projection Reconstruction Techniques for Reduction of Motion Effects in MRI. *Magnetic Resonance in Medicine*, 28(2):275–289. doi: 10.1002/mrm.1910280209.

Glover, G. H., Mueller, B. A., Turner, J. A., van Erp, T. G., Liu, T. T., Greve, D. N., Voyvodic, J. T., Rasmussen, J., Brown, G. G., Keator, D. B., Calhoun, V. D., Jong Lee, H., Ford, J. M., Mathalon, D. H., Diaz, M., O, D. S., Gadde, S., Preda, A., Lim, K. O., Wible, C. G., Stern, H. S., Belger, A., McCarthy, G., Ozyurt, B., and Potkin, S. G. (2012). Function Biomedical Informatics Research Network Recommendations for Prospective Multi-Center Functional Magnetic Resonance Imaging Studies. *Function Biomedical Informatics Research Network J Magn Reson Imaging*, 36(1):39–54. doi: 10.1002/jmri.23572.

Goerke, U., Möller, H. E., Norris, D. G., and Schwarzbauer, C. (2005). A comparison of signal instability in 2D and 3D EPI resting-state fMRI. *NMR in Biomedicine*, 18(8): 534–542. doi: 10.1002/nbm.987.

Goerner, F. L. and Clarke, G. D. (2011). Measuring signal-to-noise ratio in partially parallel imaging MRI. *Medical Physics*, 38(9):5049–5057. doi: 10.1118/1.3618730.

Golm, D., Schmidt-Samoa, C., Dechent, P., and Kröner-Herwig, B. (2013). Neural correlates of tinnitus related distress: An fMRI-study. *Hearing Research*, 295:87–99. doi: 10.1016/j.heares.2012.03.003.

Gomot, M., Bernard, F. A., Davis, M. H., Belmonte, M. K., Ashwin, C., Bullmore, E. T., and Baron-Cohen, S. (2006). Change detection in children with autism: An auditory event-related fMRI study. *NeuroImage*, 29(2):475–484. doi: 10.1016/j.neuroimage.2005.07.027.

Gonzalez-Castillo, J., Roopchansingh, V., Bandettini, P. A., and Bodurka, J. (2011). Physiological noise effects on the flip angle selection in BOLD fMRI. *NeuroImage*, 54 (4):2764–2778. doi: 10.1016/j.neuroimage.2010.11.020.

Gonzalez-Castillo, J., Panwar, P., Buchanan, L. C., Caballero-Gaudes, C., Handwerker, D. A., Jangraw, D. C., Zachariou, V., Inati, S., Roopchansingh, V., Derbyshire, J. A., and Bandettini, P. A. (2016). Evaluation of multi-echo ICA denoising for task based fMRI studies: Block designs, rapid event-related designs, and cardiac-gated fMRI. *NeuroImage*, 141:452–468. doi: 10.1016/j.neuroimage.2016.07.049.

Gonzalez-Castillo, J., Kam, J. W., Hoy, C. W., and Bandettini, P. A. (2021). How to Interpret Resting-State fMRI: Ask Your Participants. *Journal of Neuroscience*, 41(6): 1130–1141. doi: 10.1523/JNEUROSCI.1786-20.2020.

Govindaraju, R., Omar, R., Rajagopalan, R., Norlisah, R., and Kwan-Hoong, N. (2011). Hearing loss after noise exposure. *Auris Nasus Larynx*, 38(4):519–522. doi: 10.1016/j.anl.2010.12.006.

Gowland, P. A. and Bowtell, R. (2007). Theoretical optimization of multi-echo fMRI data acquisition. *Physics in Medicine and Biology*, 52(7):1801–1813. doi: 10.1088/0031-9155/52/7/003.

Graedel, N. N., McNab, J. A., Chiew, M., and Miller, K. L. (2017). Motion correction for functional MRI with three-dimensional hybrid radial-Cartesian EPI. *Magnetic Resonance in Medicine*, 78(2):527–540. doi: 10.1002/mrm.26390.

Graedel, N. N., Kasper, L., Engel, M., Nussbaum, J., Wilm, B. J., Pruessmann, K. P.,

and Johanna Vannesjo, S. (2019). Feasibility of spiral fMRI based on an LTI gradient model. *bioRxiv*, page 805580. doi: 10.1101/805580.

Grant, I. and Phillips, W. (1990). *Electromagnetism*. John Wiley and Sons Inc., second edition.

Graven, S. N. and Browne, J. V. (2008)a. Auditory Development in the Fetus and Infant. *Newborn and Infant Nursing Reviews*, 8(4):187–193. doi: 10.1053/j.nainr.2008.10.010.

Graven, S. N. and Browne, J. V. (2008)b. Sensory Development in the Fetus, Neonate, and Infant: Introduction and Overview. *Newborn and Infant Nursing Reviews*, 8(4): 169–172. doi: 10.1053/j.nainr.2008.10.007.

Greve, D. N., Mueller, B. A., Liu, T., Turner, J. A., Voyvodic, J., Yetter, E., Diaz, M., McCarthy, G., Wallace, S., Roach, B. J., Ford, J. M., Mathalon, D. H., Calhoun, V. D., Wible, C. G., Brown, G. G., Potkin, S. G., and Glover, G. (2011). A novel method for quantifying scanner instability in fMRI. *Magnetic Resonance in Medicine*, 65(4): 1053–1061. doi: 10.1002/mrm.22691.

Griffanti, L., Douaud, G., Bijsterbosch, J., Evangelisti, S., Alfaro-Almagro, F., Glasser, M. F., Duff, E. P., Fitzgibbon, S., Westphal, R., Carone, D., Beckmann, C. F., and Smith, S. M. (2017). Hand classification of fMRI ICA noise components. *NeuroImage*, 154:188–205. doi: 10.1016/j.neuroimage.2016.12.036.

Grodzki, D. M., Jakob, P. M., and Heismann, B. (2012). Correcting slice selectivity in hard pulse sequences. *Journal of Magnetic Resonance*, 214:61–67. doi: 10.1016/j.jmr.2011.10.005.

Gu, J. W., Halpin, C. F., Nam, E. C., Levine, R. A., and Melcher, J. R. (2010). Tinnitus, diminished sound-level tolerance, and elevated auditory activity in humans with clinically normal hearing sensitivity. *Journal of Neurophysiology*, 104(6):3361–3370. doi: 10.1152/jn.00226.2010.

Guo, S. and Noll, D. C. (2020). Oscillating steady-state imaging (OSSI): A novel method for functional MRI. *Magnetic Resonance in Medicine*, 84(2):698–712. doi: 10.1002/mrm.28156.

Haacke, E. M., Liu, S., Buch, S., Zheng, W., Wu, D., and Ye, Y. (2015). Quantitative susceptibility mapping: Current status and future directions. *Magnetic Resonance Imaging*, 33(1):1–25. doi: 10.1016/j.mri.2014.09.004.

Haase, A., Frahm, J., Matthaei, D., Hanicke, W., and Merboldt, K. D. (1986). FLASH imaging. Rapid NMR imaging using low flip-angle pulses. *Journal of Magnetic Resonance (1969)*, 67(2):258–266. doi: 10.1016/0022-2364(86)90433-6.

Hahn, E. L. (1950). Spin echoes. *Physical Review*, 80(4):580–594. doi: 10.1103/PhysRev.80.580.

Haigh, S. M., Cooper, N. R., and Wilkins, A. J. (2015). Cortical excitability and the shape of the haemodynamic response. *NeuroImage*, 111:379–384. doi: 10.1016/j.neuroimage.2015.02.034.

Halai, A. D., Welbourne, S. R., Embleton, K., and Parkes, L. M. (2014). A comparison of dual gradient-echo and spin-echo fMRI of the inferior temporal lobe. *Human Brain Mapping*, 35(8):4118–4128. doi: 10.1002/hbm.22463.

Halefoglu, A. M. and Yousem, D. M. (2018). Susceptibility weighted imaging: Clinical applications and future directions. *World Journal of Radiology*, 10(4):30–45. doi: 10.4329/wjr.v10.i4.30.

Hall, D. A., Haggard, M. P., Akeroyd, M. A., Palmer, A. R., Summerfield, A. Q., Elliott, M. R., Gurney, E. M., and Bowtell, R. W. (1999). Sparse temporal sampling in auditory fMRI. *Human Brain Mapping*, 7(3):213–223. doi: 10.1002/(SICI)1097-0193(1999)7:3<213::AID-HBM5>3.0.CO;2-N.

Hall, D. A., Summerfield, A. Q., Gonçalves, M. S., Foster, J. R., Palmer, A. R., and Bowtell, R. W. (2000). Time-course of the auditory BOLD response to scanner noise. *Magnetic Resonance in Medicine*, 43(4):601–606. doi: 10.1002/(SICI)1522-2594(200004)43:4<601::AID-MRM16>3.0.CO;2-R.

Hall, D. A., Chambers, J., Akeroyd, M. A., Foster, J. R., Coxon, R., and Palmer, A. R. (2009). Acoustic, psychophysical, and neuroimaging measurements of the effectiveness of active cancellation during auditory functional magnetic resonance imaging. *The Journal of the Acoustical Society of America*, 125(1):347–359. doi: 10.1121/1.3021437.

Haller, S. and Bartsch, A. J. (2009). Pitfalls in fMRI. *European Radiology*, 19(11): 2689–2706. doi: 10.1007/s00330-009-1456-9.

Haller, S., Bartsch, A. J., Radue, E. W., Klarhöfer, M., Seifritz, E., and Scheffler, K. (2005). Effect of fMRI acoustic noise on non-auditory working memory task: Comparison between continuous and pulsed sound emitting EPI. *Magnetic Resonance Materials in Physics, Biology and Medicine*, 18(5):263–271. doi: 10.1007/s10334-005-0010-2.

Hamilton, J., Franson, D., and Seiberlich, N. (2017). Recent advances in parallel imaging for MRI. *Progress in Nuclear Magnetic Resonance Spectroscopy*, 101:71–95. doi: 10.1016/j.pnmrs.2017.04.002.

Han, Y., Yoo, J., Kim, H. H., Shin, H. J., Sung, K., and Ye, J. C. (2018). Deep learning with domain adaptation for accelerated projection-reconstruction MR. *Magnetic Resonance in Medicine*, 80(3):1189–1205. doi: 10.1002/mrm.27106.

Handwerker, D. A., Gonzalez-Castillo, J., D'Esposito, M., and Bandettini, P. A. (2012). The continuing challenge of understanding and modeling hemodynamic variation in fMRI. *NeuroImage*, 62(2):1017–1023. doi: 10.1016/j.neuroimage.2012.02.015.

Hanson, L. G. (2008). Is quantum mechanics necessary for understanding magnetic resonance? *Concepts in Magnetic Resonance Part A*, 32A(5):329–340. doi: 10.1002/cmr.a.20123.

Hargreaves, B. (2002). Bloch Equation Simulation, Accessed 2021. http://mrsrl.stanford.edu/$\sim$brian/bloch/.

Hart, H. C., Hall, D. A., and Palmer, A. R. (2003). The sound-level-dependent growth in the extent of fMRI activation in Heschl's gyrus is different for low- and high-frequency tones. *Hearing Research*, 179(1-2):104–112. doi: 10.1016/S0378-5955(03)00100-X.

Havsteen, I., Ohlhues, A., Madsen, K. H., Nybing, J. D., Christensen, H., and Christensen, A. (2017). Are movement artifacts in magnetic resonance imaging a real problem?-a narrative review. *Frontiers in Neurology*, 8. doi: 10.3389/fneur.2017.00232.

Haywood, B., Chapman, B., and Mansfield, P. (2007). Model gradient coil employing

active acoustic control for MRI. *Magnetic Resonance Materials in Physics, Biology and Medicine*, 20(5-6):223–231. doi: 10.1007/s10334-007-0086-y.

Healy, E. W., Moser, D. C., Morrow-Odom, K. L., Hall, D. A., and Fridriksson, J. (2007). Speech perception in MRI scanner noise by persons with aphasia. *Journal of Speech, Language, and Hearing Research*, 50(2):323–334. doi: 10.1044/1092-4388(2007/023).

Hedeen, R. A. and Edelstein, W. A. (1997). Characterization and prediction of gradient acoustic noise in MR imagers. *Magnetic Resonance in Medicine*, 37(1):7–10. doi: 10.1002/mrm.1910370103.

Hennel, F., Girard, F., and Loenneker, T. (1999). 'Silent' MRI with soft gradient pulses. *Magnetic Resonance in Medicine*, 42(1):6–10. doi: 10.1002/(SICI)1522-2594(199907)42:1<6::AID-MRM2>3.0.CO;2-D.

Hennig, J. and Hodapp, M. (1993). Burst imaging. *Magnetic Resonance Materials in Physics, Biology, and Medicine*, 1(1):39–48. doi: 10.1007/BF02660372.

Hickok, G. and Poeppel, D. (2007). The cortical organization of speech processing. *Nature Reviews Neuroscience*, 8(5):393–402. doi: 10.1038/nrn2113.

Hidalgo-Tobon, S. S. (2010). Theory of gradient coil design methods for magnetic resonance imaging. *Concepts in Magnetic Resonance Part A*, 36A(4):223–242. doi: 10.1002/cmr.a.20163.

Hill, S. and Dalton, J. (2017). FearFaces and VisAural. Centre for Neuroimaging Sciences, Kings College London.

Hlinka, J., Paluš, M., Vejmelka, M., Mantini, D., and Corbetta, M. (2011). Functional connectivity in resting-state fMRI: Is linear correlation sufficient? *NeuroImage*, 54(3):2218–2225. doi: 10.1016/j.neuroimage.2010.08.042.

Hofmeier, B., Wolpert, S., Aldamer, E. S., Walter, M., Thiericke, J., Braun, C., Zelle, D., Rüttiger, L., Klose, U., and Knipper, M. (2018). Reduced sound-evoked and resting-state BOLD fMRI connectivity in tinnitus. *NeuroImage: Clinical*, 20:637–649. doi: 10.1016/j.nicl.2018.08.029.

Hoge, R. D., Kwan, R. K., and Pike, G. B. (1997). Density compensation functions for spiral MRI. *Magnetic Resonance in Medicine*, 38(1):117–128. doi: 10.1002/mrm.1910380117.

Holland, D. J., Liu, C., Song, X., Mazerolle, E. L., Stevens, M. T., Sederman, A. J., Gladden, L. F., D'Arcy, R. C. N., Bowen, C. V., and Beyea, S. D. (2013). Compressed sensing reconstruction improves sensitivity of variable density spiral fMRI. *Magnetic Resonance in Medicine*, 70(6):1634–1643. doi: 10.1002/MRM.24621.

Hollingsworth, K. G. (2015). Reducing acquisition time in clinical MRI by data undersampling and compressed sensing reconstruction. *Physics in Medicine and Biology*, 60 (21):R297–R322. doi: 10.1088/0031-9155/60/21/R297.

Holmes, C. J., Hoge, R., Collins, L., Woods, R., Toga, A. W., and Evans, A. C. (1998). Enhancement of MR Images Using Registration for Signal Averaging. *Journal of Computer Assisted Tomography*, 22(2):324–333. doi: 10.1097/00004728-199803000-00032.

Huber, L., Ivanov, D., Handwerker, D. A., Marrett, S., Guidi, M., Uludağ, K., Bandettini, P. A., and Poser, B. A. (2018). Techniques for blood volume fMRI with VASO: From low-resolution mapping towards sub-millimeter layer-dependent applications. *NeuroImage*, 164:131–143. doi: 10.1016/j.neuroimage.2016.11.039.

Huettel, S. A., Song, A. W., and McCarthy, G. (2014). *Functional Magnetic Resonance Imaging*. Sinauer Associates, Inc, third edition.

Husain, F. T. and Schmidt, S. A. (2014). Using resting state functional connectivity to unravel networks of tinnitus. *Hearing Research*, 307:153–162. doi: 10.1016/j.heares.2013.07.010.

Hutton, C., Bork, A., Josephs, O., Deichmann, R., Ashburner, J., and Turner, R. (2002). Image distortion correction in fMRI: A quantitative evaluation. *NeuroImage*, 16(1): 217–240. doi: 10.1006/nimg.2001.1054.

Hutton, C., Balteau, E., Lutti, A., Josephs, O., and Weiskopf, N. (2012). Modelling Temporal Stability of EPI Time Series Using Magnitude Images Acquired with Multi-Channel Receiver Coils. *PLoS ONE*, 7(12):e52075. doi: 10.1371/journal.pone.0052075.

IBM Corp. (2020). IBM SPSS Statistics for Mac Version 27.0. Armonk, NY: IBM Corp.

Ida, M., Wakayama, T., Nielsen, M. L., Abe, T., and Grodzki, D. M. (2015). Quiet T1-weighted imaging using PETRA: Initial clinical evaluation in intracranial tumor patients. *Journal of Magnetic Resonance Imaging*, 41(2):447–453. doi: 10.1002/jmri.24575.

Idiyatullin, D., Corum, C. A., and Garwood, M. (2015). Multi-Band-SWIFT. *Journal of Magnetic Resonance*, 251(1):19–25. doi: 10.1016/j.jmr.2014.11.014.

Jabehdar Maralani, P., Kapadia, A., Liu, G., Moretti, F., Ghandehari, H., Clarke, S. E., Wiebe, S., Garel, J., Ertl-Wagner, B., Hurrell, C., and Schieda, N. (2021). Canadian Association of Radiologists Recommendations for the Safe Use of MRI During Pregnancy. *Canadian Association of Radiologists Journal*. doi: 10.1177/08465371211015657.

Jackson, J. B., O'Daly, O., Makovac, E., Medina, S., Rubio, A. d. L., McMahon, S. B., Williams, S. C., and Howard, M. A. (2020). Noxious pressure stimulation demonstrates robust, reliable estimates of brain activity and self-reported pain. *NeuroImage*, 221: 117178. doi: 10.1016/j.neuroimage.2020.117178.

Jafri, M. J., Pearlson, G. D., Stevens, M., and Calhoun, V. D. (2008). A method for functional network connectivity among spatially independent resting-state components in schizophrenia. *NeuroImage*, 39(4):1666–1681. doi: 10.1016/j.neuroimage.2007.11.001.

Jakob, P. M., Griswold, M. A., Lovblad, K. O., Chen, Q., and Edelman, R. R. (1997). Half-Fourier BURST imaging on a clinical scanner. *Magnetic Resonance in Medicine*, 38(4):534–540. doi: 10.1002/mrm.1910380405.

Jäncke, L., Shah, N. J., Posse, S., Grosse-Ryuken, M., and Müller-Gärtner, H. W. (1998). Intensity coding of auditory stimuli: An fMRI study. *Neuropsychologia*, 36(9):875–883. doi: 10.1016/S0028-3932(98)00019-0.

Jang, H., Wiens, C. N., and McMillan, A. B. (2016). Ramped hybrid encoding for improved ultrashort echo time imaging. *Magnetic Resonance in Medicine*, 76(3): 814–825. doi: 10.1002/mrm.25977.

Jenkinson, M., Beckmann, C. F., Behrens, T. E., Woolrich, M. W., and Smith, S. M. (2012). FSL. *NeuroImage*, 62(2):782–790. doi: 10.1016/J.NEUROIMAGE.2011.09.015.

Jenkinson, M., Bijsterbosch, J., Chappell, M., and Winkler, A. (2017). *Short Introduction to the General Linear Model for Neuroimaging*. Oxford University Press.

Jezzard, P. and Balaban, R. S. (1995). Correction for geometric distortion in echo planar images from B0 field variations. *Magnetic Resonance in Medicine*, 34(1):65–73. doi: 10.1002/mrm.1910340111.

Jezzard, P. and Clare, S. (1999). Sources of distortion in functional MRI data. *Human Brain Mapping*, 8(2-3):80–85. doi: 10.1002/(SICI)1097-0193(1999)8:2/3<80::AID-HBM2>3.0.CO;2-C.

Jimeno, M. M., Jr., J. T. V., and Geethanath, S. (2021). Deblurring of spiral fMRI images using deep learning. International Society for Magnetic Resonance in Medicine 29th Annual Meeting, Abstract 2414.

Johnson, K. M. (2017). Hybrid radial-cones trajectory for accelerated MRI. *Magnetic Resonance in Medicine*, 77(3):1068–1081. doi: 10.1002/mrm.26188.

Jorge, J., Figueiredo, P., van der Zwaag, W., and Marques, J. P. (2013). Signal fluctuations in fMRI data acquired with 2D-EPI and 3D-EPI at 7 Tesla. *Magnetic Resonance Imaging*, 31(2):212–220. doi: 10.1016/j.mri.2012.07.001.

Joyce, K. E. and Hayasaka, S. (2012). Development of PowerMap: A software package for statistical power calculation in neuroimaging studies. *Neuroinformatics*, 10(4):351–365. doi: 10.1007/s12021-012-9152-3.

Justen, C. and Herbert, C. (2018). The spatio-temporal dynamics of deviance and target detection in the passive and active auditory oddball paradigm: A sLORETA study. *BMC Neuroscience*, 19(25):1–18. doi: 10.1186/s12868-018-0422-3.

Kanakri, S. M., Shepley, M., Varni, J. W., and Tassinary, L. G. (2017). Noise and autism spectrum disorder in children: An exploratory survey. *Research in Developmental Disabilities*, 63:85–94. doi: 10.1016/j.ridd.2017.02.004.

Kannan, G., Milani, A. A., Panahi, I. M., and Briggs, R. W. (2011). An efficient feedback active noise control algorithm based on reduced-order linear predictive modeling of fMRI acoustic noise. *IEEE Transactions on Biomedical Engineering*, 58(12):3303–3309. doi: 10.1109/TBME.2010.2096423.

Kasper, L., Haeberlin, M., Dietrich, B. E., Gross, S., Barmet, C., Wilm, B. J., Vannesjo, S. J., Brunner, D. O., Ruff, C. C., Stephan, K. E., and Pruessmann, K. P. (2014). Matched-filter acquisition for bold fMRI. *NeuroImage*, 100:145–160. doi: 10.1016/j.neuroimage.2014.05.024.

Kasper, L., Bollmann, S., Diaconescu, A. O., Hutton, C., Heinzle, J., Iglesias, S., Hauser, T. U., Sebold, M., Manjaly, Z. M., Pruessmann, K. P., and Stephan, K. E. (2017). The PhysIO Toolbox for Modeling Physiological Noise in fMRI Data. *Journal of Neuroscience Methods*, 276:56–72. doi: 10.1016/j.jneumeth.2016.10.019.

Katsunuma, A., Takamori, H., Sakakura, Y., Hamamura, Y., Ogo, Y., Katayama, R., Katsunuma Takamori Sakakura, A. H., and Ogo Katayama, H. R. (2002). Quiet MRI with novel acoustic noise reduction. *Magnetic Resonance Materials in Physics, Biology and Medicine*, 13(3):139–144. doi: 10.1016/S1352-8661(01)00142-9.

Kellman, P. and McVeigh, E. R. (2005). Image reconstruction in SNR units: A general method for SNR measurement. *Magnetic Resonance in Medicine*, 54(6):1439–1447. doi: 10.1002/mrm.20713.

Kessler, D., Angstadt, M., and Sripada, C. S. (2017). Reevaluating "cluster failure" in fMRI using nonparametric control of the false discovery rate. *Proceedings of the National Academy of Sciences of the United States of America*, 114(17):E3372–E3373. doi: 10.1073/pnas.1614502114.

Kiehl, K. A. and Liddle, P. F. (2003). Reproducibility of the hemodynamic response to auditory oddball stimuli: A six-week test-retest study. *Human Brain Mapping*, 18(1): 42–52. doi: 10.1002/hbm.10074.

Kim, S. G. and Ogawa, S. (2012). Biophysical and physiological origins of blood oxygenation level-dependent fMRI signals. *Journal of Cerebral Blood Flow and Metabolism*, 32(7):1188–1206. doi: 10.1038/jcbfm.2012.23.

Klein, R. (2021). Bland-Altman and Correlation Plot, MATLAB Central File Exchange, Accessed June-August 2021. https://www.mathworks.com/matlabcentral/fileexchange/45049-bland-altman-and-correlation-plot.

Koops, E. A. and van Dijk, P. (2021). Hyperacusis in tinnitus patients relates to enlarged subcortical and cortical responses to sound except at the tinnitus frequency. *Hearing Research*, 401:108158. doi: 10.1016/j.heares.2020.108158.

Krämer, M., Jochimsen, T. H., and Reichenbach, J. R. (2012). Functional magnetic resonance imaging using PROPELLER-EPI. *Magnetic Resonance in Medicine*, 68(1): 140–151. doi: 10.1002/mrm.23220.

Krüger, G. and Glover, G. H. (2001). Physiological noise in oxygenation-sensitive magnetic resonance imaging. *Magnetic Resonance in Medicine*, 46(4):631–637. doi: 10.1002/mrm.1240.

Kundu, P., Inati, S. J., Evans, J. W., Luh, W. M., and Bandettini, P. A. (2012). Differentiating BOLD and non-BOLD signals in fMRI time series using multi-echo EPI. *NeuroImage*, 60(3):1759–1770. doi: 10.1016/j.neuroimage.2011.12.028.

Kundu, P., Voon, V., Balchandani, P., Lombardo, M. V., Poser, B. A., and Bandettini, P. A. (2017). Multi-echo fMRI: A review of applications in fMRI denoising and analysis of BOLD signals. *NeuroImage*, 154:59–80. doi: 10.1016/j.neuroimage.2017.03.033.

Kwong, K. K., Belliveau, J. W., Chesler, D. A., Goldberg, I. E., Weisskoff, R. M., Poncelet, B. P., Kennedy, D. N., Hoppel, B. E., Cohen, M. S., Turner, R., Cheng -, H. M., Brady, T. J., and Rosen, B. R. (1992). Dynamic magnetic resonance imaging of human brain activity during primary sensory stimulation. *Proceedings of the National Academy of Sciences of the United States of America*, 89(12):5675–5679. doi: 10.1073/pnas.89.12.5675.

Lacadie, C. M., Fulbright, R. K., Rajeevan, N., Constable, R. T., and Papademetris, X. (2008). More accurate Talairach coordinates for neuroimaging using non-linear registration. *NeuroImage*, 42(2):717–725. doi: 10.1016/j.neuroimage.2008.04.240.

Lancione, M., Buonincontri, G., Cecchetti, L., Costagli, M., Kurzawski, J. W., Ricciardi, E., Schulte, R. F., Solana Sanchez, B. A., and Tosetti, M. (2019). Silent fMRI with

visual and auditory stimulation using 3D radial T2*-weighted ZTE-BURST sequence. International Society for Magnetic Resonance in Medicine 27th Annual Meeting, Abstract 3944.

Langers, D. R. and Van Dijk, P. (2012). Mapping the tonotopic organization in human auditory cortex with minimally salient acoustic stimulation. *Cerebral Cortex*, 22(9): 2024–2038. doi: 10.1093/cercor/bhr282.

Langers, D. R., Van Dijk, P., and Backes, W. H. (2005)a. Lateralization, connectivity and plasticity in the human central auditory system. *NeuroImage*, 28(2):490–499. doi: 10.1016/j.neuroimage.2005.06.024.

Langers, D. R., van Dijk, P., Schoenmaker, E. S., and Backes, W. H. (2007). fMRI activation in relation to sound intensity and loudness. *NeuroImage*, 35(2):709–718. doi: 10.1016/j.neuroimage.2006.12.013.

Langers, D. R. M., Van Dijk, P., and Backes, W. H. (2005)b. Interactions between hemodynamic responses to scanner acoustic noise and auditory stimuli in functional magnetic resonance imaging. *Magnetic Resonance in Medicine*, 53(1):49–60. doi: 10.1002/mrm.20315.

Lanka, P., Rangaprakash, D., Gotoor, S. S. R., Dretsch, M. N., Katz, J. S., Denney, T. S., and Deshpande, G. (2020). MALINI (Machine Learning in NeuroImaging): A MATLAB toolbox for aiding clinical diagnostics using resting-state fMRI data. *Data in Brief*, 29:105213. doi: 10.1016/j.dib.2020.105213.

Lanting, C. P., de Kleine, E., and van Dijk, P. (2009). Neural activity underlying tinnitus generation: Results from PET and fMRI. *Hearing Research*, 255(1-2):1–13. doi: 10.1016/j.heares.2009.06.009.

Lauer, A. M., El-Sharkawy, A.-M. M. M., Kraitchman, D. L., and Edelstein, W. A. (2012). MRI acoustic noise can harm experimental and companion animals. *Journal of Magnetic Resonance Imaging*, 36(3):743–747. doi: 10.1002/jmri.23653.

Laurell, G. F. (1992). Combined effects of noise and cisplatin: Short- and long-term follow-up. *Annals of Otology, Rhinology and Laryngology*, 101(12):969–976. doi: 10.1177/000348949210101202.

Leaver, A. M., Renier, L., Chevillet, M. A., Morgan, S., Kim, H. J., and Rauschecker, J. P. (2011). Dysregulation of Limbic and Auditory Networks in Tinnitus. *Neuron*, 69 (1):33–43. doi: 10.1016/j.neuron.2010.12.002.

Leaver, A. M., Seydell-Greenwald, A., and Rauschecker, J. P. (2016). Auditory-limbic interactions in chronic tinnitus: Challenges for neuroimaging research. *Hearing Research*, 334:49–57. doi: 10.1016/j.heares.2015.08.005.

Lee, G. R., Griswold, M. A., and Tkach, J. A. (2010). Rapid 3D radial multi-echo functional magnetic resonance imaging. *NeuroImage*, 52(4):1428–1443. doi: 10.1016/j.neuroimage.2010.05.004.

Lee, M. H., Smyser, C. D., and Shimony, J. S. (2013). Resting-state fMRI: A review of methods and clinical applications. *American Journal of Neuroradiology*, 34(10): 1866–1872. doi: 10.3174/ajnr.A3263.

Lee, N., Park, Y., and Lee, G. W. (2017). Frequency-domain active noise control for magnetic resonance imaging acoustic noise. *Applied Acoustics*, 118:30–38. doi: 10.1016/j.apacoust.2016.11.003.

Lehto, L. J., Idiyatullin, D., Zhang, J., Utecht, L., Adriany, G., Garwood, M., Gröhn, O., Michaeli, S., and Mangia, S. (2017). MB-SWIFT functional MRI during deep brain stimulation in rats. *NeuroImage*, 159:443–448. doi: 10.1016/j.neuroimage.2017.08.012.

Leung, K. K., Malone, I. M., Ourselin, S., Gunter, J. L., Bernstein, M. A., Thompson, P. M., Jack, C. R., Weiner, M. W., and Fox, N. C. (2015). Effects of changing from non-accelerated to accelerated MRI for follow-up in brain atrophy measurement. *NeuroImage*, 107:46–53. doi: 10.1016/j.neuroimage.2014.11.049.

Lewis, L. D., Setsompop, K., Rosen, B. R., and Polimeni, J. R. (2016). Fast fMRI can detect oscillatory neural activity in humans. *Proceedings of the National Academy of Sciences of the United States of America*, 113(43):E6679–E6685. doi: 10.1073/pnas.1608117113.

Leynes, A., Damestani, N., Lythgoe, D., Solana, A. B., Fernandez, B., Burns, B., Williams, S., Zelaya, F., Larson, P., and Wiesinger, F. (2021). Extreme Looping Star: Quiet

fMRI at high spatiotemporal resolution. International Society for Magnetic Resonance in Medicine 29th Annual Meeting, Abstract 0458.

Li, G. and Mechefske, C. K. (2010). A comprehensive experimental study of micro-perforated panel acoustic absorbers in MRI scanners. *Magnetic Resonance Materials in Physics, Biology and Medicine*, 23(3):177–185. doi: 10.1007/s10334-010-0216-9.

Li, M., Rudd, B., Lim, T. C., and Lee, J.-H. H. (2011)a. In situ active control of noise in a 4 T MRI scanner. *Journal of Magnetic Resonance Imaging*, 34(3):662–669. doi: 10.1002/jmri.22694.

Li, W., Wu, B., and Liu, C. (2011)b. Quantitative susceptibility mapping of human brain reflects spatial variation in tissue composition. *NeuroImage*, 55(4):1645–1656. doi: 10.1016/j.neuroimage.2010.11.088.

Li, W., Avram, A. V., Wu, B., Xiao, X., and Liu, C. (2014). Integrated Laplacian-based phase unwrapping and background phase removal for quantitative susceptibility mapping. *NMR in Biomedicine*, 27(2):219–227. doi: 10.1002/nbm.3056.

Li, W., Wang, N., Yu, F., Han, H., Cao, W., Romero, R., Tantiwongkosi, B., Duong, T. Q., and Liu, C. (2015). A method for estimating and removing streaking artifacts in quantitative susceptibility mapping. *NeuroImage*, 108:111–122. doi: 10.1016/J.NEUROIMAGE.2014.12.043.

Li, Y. O., Adali, T., and Calhoun, V. D. (2007). Estimating the number of independent components for functional magnetic resonance imaging data. *Human Brain Mapping*, 28(11):1251–1266. doi: 10.1002/hbm.20359.

Liem, F., Lutz, K., Luechinger, R., Jäncke, L., Meyer, M., Liem, F., Lutz Á L Jäncke Á M Meyer, Á. K., Lutz, K., Jäncke, L., Meyer, M., Luechinger, R., and Jäncke Á Meyer, L. M. (2012). Reducing the Interval Between Volume Acquisitions Improves "Sparse" Scanning Protocols in Event-related Auditory fMRI. *Brain Topography*, 25(2): 182–193. doi: 10.1007/s10548-011-0206-x.

Lin, T. R., O'Shea, P., and Mechefske, C. (2009). Reducing MRI gradient coil vibration with rib stiffeners. *Concepts in Magnetic Resonance Part B: Magnetic Resonance Engineering*, 35(4):198–209. doi: 10.1002/cmr.b.20148.

Lindquist, M. A. and Mejia, A. (2015). Zen and the art of multiple comparisons. *Psychosomatic Medicine*, 77(2):114–125. doi: 10.1097/PSY.0000000000000148.

Liu, C., Li, W., Tong, K. A., Yeom, K. W., and Kuzminski, S. (2015)a. Susceptibility-weighted imaging and quantitative susceptibility mapping in the brain. *Journal of Magnetic Resonance Imaging*, 42(1):23–41. doi: 10.1002/jmri.24768.

Liu, G., Sobering, G., Duyn, J., and Moonen, C. T. (1993). A. functional MRI technique combining principles of echo-shifting with a train of observations (PRESTO). *Magnetic Resonance in Medicine*, 30(6):764–768. doi: 10.1002/mrm.1910300617.

Liu, P., Calhoun, V., and Chen, Z. (2017)a. Functional overestimation due to spatial smoothing of fMRI data. *Journal of Neuroscience Methods*, 291:1–12. doi: 10.1016/j.jneumeth.2017.08.003.

Liu, T. T. (2016). Noise contributions to the fMRI signal: An overview. *NeuroImage*, 143:141–151. doi: 10.1016/j.neuroimage.2016.09.008.

Liu, T. T., Glover, G. H., Mueller, B. A., Greve, D. N., Rasmussen, J., Voyvodic, J. T., Turner, J. A., Erp, T. G. M., Mathalon, D. H., Andersen, K., Lu, K., Brown, G. G., Keator, D. B., Calhoun, V. D., Lee, H. J., Ford, J. M., Diaz, M., O'Leary, D. S., Gadde, S., Preda, A., Lim, K. O., Wible, C. G., Stern, H. S., Belger, A., McCarthy, G., Ozyurt, B., Potkin, S. G., and FBIRN. (2015)b. Quality assurance in functional MRI. In *fMRI: From Nuclear Spins to Brain Functions*, pages 245–270. Springer, Boston, MA. doi: 10.1007/978-1-4899-7591-1_10.

Liu, T. T., Nalci, A., and Falahpour, M. (2017)b. The global signal in fMRI: Nuisance or Information? *NeuroImage*, 150:213–229. doi: 10.1016/j.neuroimage.2017.02.036.

Liu, T., Liu, J., De Rochefort, L., Spincemaille, P., Khalidov, I., Ledoux, J. R., and Wang, Y. (2011). Morphology enabled dipole inversion (MEDI) from a single-angle acquisition: Comparison with COSMOS in human brain imaging. *Magnetic Resonance in Medicine*, 66(3):777–783. doi: 10.1002/mrm.22816.

Ljungberg, E., Wood, T., Solana, A. B., Kolind, S., Williams, S. C., Wiesinger, F., and Barker, G. J. (2020). Silent T1 mapping using the variable flip angle method with B1 correction. *Magnetic Resonance in Medicine*, 84(2):813–824. doi: 10.1002/mrm.28178.

Ljungberg, E., Damestani, N. L., Wood, T. C., Lythgoe, D. J., Zelaya, F., Williams, S. C., Solana, A. B., Barker, G. J., and Wiesinger, F. (2021)a. Silent zero TE MR neuroimaging: Current state-of-the-art and future directions. *Progress in Nuclear Magnetic Resonance Spectroscopy*, 123:73–93. doi: 10.1016/J.PNMRS.2021.03.002.

Ljungberg, E., Wood, T., Solana, A. B., Williams, S. C., Barker, G. J., and Wiesinger, F. (2021)b. MERLIN: Motion Insensitive Silent Neuroimaging. International Society for Magnetic Resonance in Medicine 29th Annual Meeting, Abstract 0120.

Loenneker, T., Hennel, F., Ludwig, U., and Hennig, J. (2001). Silent BOLD imaging. *Magnetic Resonance Materials in Physics, Biology and Medicine*, 13(2):76–81. doi: 10.1016/S1352-8661(01)00131-4.

Logothetis, N. K., Pauls, J., Augath, M., Trinath, T., and Oeltermann, A. (2001). Neurophysiological investigation of the basis of the fMRI signal. *Nature*, 412(6843): 150–157. doi: 10.1038/35084005.

Logothetis, N. K. (2008). What we can do and what we cannot do with fMRI. Nature Publishing Group.

Logothetis, N. K. and Wandell, B. A. (2004). Interpreting the BOLD Signal. *Annual Review of Physiology*, 66(1):735–769. doi: 10.1146/annurev.physiol.66.082602.092845.

Lorentzen, K. L., Nørgaard, H. J., Thrane, J. F., and Fjaeldstad, A. W. (2021). Effects of acoustic fMRI-noise on taste identification, liking, and intensity. *Current Research in Behavioral Sciences*, 2:100054. doi: 10.1016/j.crbeha.2021.100054.

Loring, D. W., Meador, K. J., Allison, J. D., Pillai, J. J., Lavin, T., Lee, G. P., Balan, A., and Dave, V. (2002). Now you see it, now you don't: Statistical and methodological considerations in fMRI. *Epilepsy and Behavior*, 3(6):539–547. doi: 10.1016/S1525-5050(02)00558-9.

Lu, H., Golay, X., Pekar, J. J., and Van Zijl, P. C. (2003). Functional magnetic resonance imaging based on changes in vascular space occupancy. *Magnetic Resonance in Medicine*, 50(2):263–274. doi: 10.1002/mrm.10519.

Lu, H., Nagae-Poetscher, L. M., Golay, X., Lin, D., Pomper, M., and Van Zijl, P. C. (2005). Routine clinical brain MRI sequences for use at 3.0 tesla. *Journal of Magnetic Resonance Imaging*, 22(1):13–22. doi: 10.1002/jmri.20356.

Lustig, M. and Pauly, J. M. (2010). SPIRiT: Iterative self-consistent parallel imaging reconstruction from arbitrary k-space. *Magnetic Resonance in Medicine*, 64(2):457–471. doi: 10.1002/mrm.22428.

Lynch, C. J., Power, J. D., Scult, M. A., Dubin, M., Gunning, F. M., and Liston, C. (2020). Rapid Precision Functional Mapping of Individuals Using Multi-Echo fMRI. *Cell Reports*, 33(12). doi: 10.1016/j.celrep.2020.108540.

MacKinnon, M. J., Song, S., Hsu, L.-M., Lee, S.-H., Johnson, G. A., and Shih, Y.-Y. I. (2020). iZTE-fMRI. International Society for Magnetic Resonance in Medicine 28th Annual Meeting, Abstract 1221.

MacSweeney, M., Amaro, E., Calvert, G. A., Campbell, R., David, A. S., McGuire, P., Williams, S. C., Woll, B., and Brammer, M. J. (2000). Silent speechreading in the absence of scanner noise: An event-related fMRI study. *NeuroReport*, 11(8):1729–1733. doi: 10.1097/00001756-200006050-00026.

Madio, D. P. and Lowe, I. J. (1995). Ultra-fast imaging using low flip angles and fids. *Magnetic Resonance in Medicine*, 34(4):525–529. doi: 10.1002/mrm.1910340407.

Maier, O., Baete, S. H., Fyrdahl, A., Hammernik, K., Harrevelt, S., Kasper, L., Karakuzu, A., Loecher, M., Patzig, F., Tian, Y., Wang, K., Gallichan, D., Uecker, M., and Knoll, F. (2021). CG-SENSE revisited: Results from the first ISMRM reproducibility challenge. *Magnetic Resonance in Medicine*, 85(4):1821–1839. doi: 10.1002/mrm.28569.

Maknojia, S., Churchill, N. W., Schweizer, T. A., and Graham, S. J. (2019). Resting state fMRI: Going through the motions. *Frontiers in Neuroscience*, 13. doi: 10.3389/fnins.2019.00825.

Mangalathu-Arumana, J., Beardsley, S., and Liebenthal, E. (2012). Within-subject joint independent component analysis of simultaneous fMRI/ERP in an auditory oddball paradigm. *NeuroImage*, 60(4):2247–2257. doi: 10.1016/j.neuroimage.2012.02.030.

Mansfield, P. (1977). Multi-planar image formation using NMR spin echoes. *Journal of Physics C: Solid State Physics*, 10(3). doi: 10.1088/0022-3719/10/3/004.

Mansfield, P., Howseman, A. M., and Ordidge, R. J. (1989). Volumar imaging using NMR spin echoes: Echo-volumar imaging (EVI) at 0.1 T. *Journal of Physics E: Scientific Instruments*, 22(5):324–330. doi: 10.1088/0022-3735/22/5/012.

Mansfield, P., Glover, P., and Bowtell, R. (1994). Active acoustic screening: Design principles for quiet gradient coils in MRI. *Measurement Science and Technology*, 5(8): 1021–1025. doi: 10.1088/0957-0233/5/8/026.

Mansfield, P., Haywood, B., and Coxon, R. (2001). Active acoustic control in gradient coils for MRI. *Magnetic Resonance in Medicine*, 46(4):807–818. doi: 10.1002/mrm.1261.

Mansfield, P., Chapman, B. L. W., Bowtell, R., Glover, P., Coxon, R., and Harvey, P. R. (1995)a. Active Acoustic Screening: Reduction of Noise in Gradient Coils by Lorentz Force Balancing. *Magnetic Resonance in Medicine*, 33(2):276–281. doi: 10.1002/mrm.1910330220.

Mansfield, P., Coxon, R., and Hykin, J. (1995)b. Echo-volumar imaging (evi) of the brain at 3.0 t: First normal volunteer and functional imaging results. *Journal of Computer Assisted Tomography*, 19(6):847–852. doi: 10.1097/00004728-199511000-00002.

Marcus, D. S., Harms, M. P., Snyder, A. Z., Jenkinson, M., Wilson, J. A., Glasser, M. F., Barch, D. M., Archie, K. A., Burgess, G. C., Ramaratnam, M., Hodge, M., Horton, W., Herrick, R., Olsen, T., McKay, M., House, M., Hileman, M., Reid, E., Harwell, J., Coalson, T., Schindler, J., Elam, J. S., Curtiss, S. W., and Van Essen, D. C. (2013). Human Connectome Project informatics: Quality control, database services, and data visualization. *NeuroImage*, 80:202–219. doi: 10.1016/j.neuroimage.2013.05.077.

Mason, H. T., Graedel, N. N., Miller, K. L., and Chiew, M. (2021). Subspace-constrained approaches to low-rank fMRI acceleration. *NeuroImage*, 238:118235. doi: 10.1016/j.neuroimage.2021.118235.

Mathworks. (2021). Matlab (Various Versions, Accessed 2017 - 2021).

Matsuo-Hagiyama, C., Watanabe, Y., Tanaka, H., Takahashi, H., Arisawa, A., Yoshioka, E., Nabatame, S., Nakano, S., and Tomiyama, N. (2016). Comparison of Silent and Conventional MR Imaging for the Evaluation of Myelination in Children. *Magnetic Resonance in Medical Sciences*, 16(3):209–216. doi: 10.2463/mrms.mp.2016-0045.

Mattila, S., Renvall, V., Hiltunen, J., Kirven, D., Sepponen, R., Hari, R., and Tarkiainen, A. (2007). Phantom-based evaluation of geometric distortions in functional magnetic resonance and diffusion tensor imaging. *Magnetic Resonance in Medicine*, 57(4): 754–763. doi: 10.1002/mrm.21218.

Mazard, A., Mazoyer, B., Etard, O., Tzourio-mazoyer, N., Kosslyn, S. M., and Mellet, E. (2002). Impact of fMRI acoustic noise on the functional anatomy of visual mental imagery. *Journal of Cognitive Neuroscience*, 14(2):172–186. doi: 10.1162/089892902317236821.

McCann, A. J., Workman, A., and McGrath, C. (2013). A quick and robust method for measurement of signal-to-noise ratio in MRI. *Physics in Medicine and Biology*, 58(11): 3775–3790. doi: 10.1088/0031-9155/58/11/3775.

McJury, M., Stewart, R. W., Crawford, D., and Toma, E. (1997). The use of active noise control (ANC) to reduce acoustic noise generated during MRI scanning: Some initial results. *Magnetic Resonance Imaging*, 15(3):319–322. doi: 10.1016/S0730-725X(96)00337-2.

McJury, M. and Shellock, F. G. (2000). Auditory noise associated with MR procedures: A review. *Journal of Magnetic Resonance Imaging*, 12(1):37–45. doi: 10.1002/1522-2586(200007)12:1<37::AID-JMRI5>3.0.CO;2-I.

McJury, M. J. (2021). Acoustic Noise and Magnetic Resonance Imaging: A Narrative/Descriptive Review. *Journal of Magnetic Resonance Imaging*. doi: 10.1002/jmri.27525.

McKenzie, C. A., Yeh, E. N., Ohliger, M. A., Price, M. D., and Sodickson, D. K. (2002). Self-calibrating parallel imaging with automatic coil sensitivity extraction. *Magnetic Resonance in Medicine*, 47(3):529–538. doi: 10.1002/mrm.10087.

McKeown, M. J., Makeig, S., Brown, G. G., Jung, T. P., Kindermann, S. S., Bell, A. J., and Sejnowski, T. J. (1998). Analysis of fMRI data by blind separation into independent spatial components. *Human Brain Mapping*, 6(3):160–188. doi: 10.1002/(SICI)1097-0193(1998)6:3<160::AID-HBM5>3.0.CO;2-1.

McNulty, J. P. and McNulty, S. (2009). Acoustic noise in magnetic resonance imaging: An ongoing issue. *Radiography*, 15(4):320–326. doi: 10.1016/j.radi.2009.01.001.

McRobbie, D. W., Moore, E. A., Graves, M. J., and Prince, M. R. (2017). *MRI from Picture to Proton*. Cambridge University Press, third edit edition. doi: 10.1017/9781107706958.

Mechefske, C. K., Geris, R., Gati, J. S., and Rutt, B. K. (2002). Acoustic noise reduction in a 4T MRI scanner. *Magnetic Resonance Materials in Physics, Biology and Medicine*, 13:172–176. doi: 10.1016/S1352-8661(01)00146-6.

Menon, R. S., Thomas, C. G., and Gati, J. S. (1997). Investigation of BOLD contrast in fMRI using multi-shot EPI. *NMR in Biomedicine*, 10(4-5):179–182. doi: 10.1002/(SICI)1099-1492(199706/08)10:4/5<179::AID-NBM463>3.0.CO;2-X.

Mervak, B. M., Altun, E., McGinty, K. A., Hyslop, W. B., Semelka, R. C., and Burke, L. M. (2019). MRI in pregnancy: Indications and practical considerations. *Journal of Magnetic Resonance Imaging*, 49(3):621–631. doi: 10.1002/jmri.26317.

Mikl, M., Mareček, R., Hluštík, P., Pavlicová, M., Drastich, A., Chlebus, P., Brázdil, M., and Krupa, P. (2008). Effects of spatial smoothing on fMRI group inferences. *Magnetic Resonance Imaging*, 26(4):490–503. doi: 10.1016/J.MRI.2007.08.006.

Miller, K. L. (2012). fMRI using balanced steady-state free precession (SSFP). *NeuroImage*, 62(2):713–719. doi: 10.1016/j.neuroimage.2011.10.040.

Miller, K. L., Tijssen, R. H. H., Stikov, N., and Okell, T. W. (2011). Steady-state MRI: Methods for neuroimaging. *Imaging in Medicine*, 3(1):93–105. doi: 10.2217/iim.10.66.

Moelker, A. and Pattynama, P. M. (2003). Acoustic noise concerns in functional magnetic resonance imaging. *Human Brain Mapping*, 20(3):123–141. doi: 10.1002/hbm.10134.

Moelker, A., Wielopolski, P. A., and Pattynama, P. M. (2003). Relationship between magnetic field strength and magnetic-resonance-related acoustic noise levels. *Magnetic Resonance Materials in Physics, Biology and Medicine*, 16(1):52–55. doi: 10.1007/s10334-003-0005-9.

Moeller, S., Pisharady, P. K., Ramanna, S., Lenglet, C., Wu, X., Dowdle, L., Yacoub, E., Uğurbil, K., and Akçakaya, M. (2021). NOise reduction with DIstribution Corrected (NORDIC) PCA in dMRI with complex-valued parameter-free locally low-rank processing. *NeuroImage*, 226:117539. doi: 10.1016/j.neuroimage.2020.117539.

Mohr, C. M., King, W. M., Freeman, A. J., Briggs, R. W., and Leonard, C. M. (1999). Influence of speech stimuli intensity on the activation of auditory cortex investigated with functional magnetic resonance imaging. *The Journal of the Acoustical Society of America*, 105(5):2738–2745. doi: 10.1121/1.426942.

Moia, S., Termenon, M., Uruñuela, E., Chen, G., Stickland, R. C., Bright, M. G., and Caballero-Gaudes, C. (2021). ICA-based denoising strategies in breath-hold induced cerebrovascular reactivity mapping with multi echo BOLD fMRI. *NeuroImage*, 233:117914. doi: 10.1016/j.neuroimage.2021.117914.

Molloy, E. K., Meyerand, M. E., and Birn, R. M. (2014). The influence of spatial resolution and smoothing on the detectability of resting-state and task fMRI. *NeuroImage*, 86:221–230. doi: 10.1016/J.NEUROIMAGE.2013.09.001.

Monti, M. (2011). Statistical Analysis of fMRI Time-Series: A Critical Review of the GLM Approach. *Frontiers in Human Neuroscience*, 5:1–13. doi: 10.3389/fnhum.2011.00028.

More, S. R., Lim, T. C., Li, M., Holland, C. K., Boyce, S. E., and Lee, J. H. (2006). Acoustic noise characteristics of a 4 Telsa MRI scanner. *Journal of Magnetic Resonance Imaging*, 23(3):388–397. doi: 10.1002/jmri.20526.

Mueller, K., Mildner, T., Fritz, T., Lepsien, J., Schwarzbauer, C., Schroeter, M. L., and Möller, H. E. (2011). Investigating brain response to music: A comparison of different fMRI acquisition schemes. *NeuroImage*, 54(1):337–343. doi: 10.1016/j.neuroimage.2010.08.029.

Mukamel, R., Gelbard, H., Arieli, A., Hasson, U., Fried, I., and Malach, R. (2005). Neuroscience: Coupling between neuronal firing, field potentials, and fMRI in human auditory cortex. *Science*, 309(5736):951–954. doi: 10.1126/science.1110913.

Müller, B. W., Jüptner, M., Jentzen, W., and Müller, S. P. (2002). Cortical activation to auditory mismatch elicited by frequency deviant and complex novel sounds: A PET study. *NeuroImage*, 17(1):231–239. doi: 10.1006/nimg.2002.1176.

Mumford, J. A. (2012). A power calculation guide for FMRI studies. *Social Cognitive and Affective Neuroscience*, 7(6):738–742. doi: 10.1093/scan/nss059.

Murphy, K. and Fox, M. D. (2017). Towards a consensus regarding global signal regression for resting state functional connectivity MRI. *NeuroImage*, 154:169–173. doi: 10.1016/j.neuroimage.2016.11.052.

Murphy, K., Bodurka, J., and Bandettini, P. A. (2007). How long to scan? The relationship between fMRI temporal signal to noise ratio and necessary scan duration. *NeuroImage*, 34(2):565–574. doi: 10.1016/j.neuroimage.2006.09.032.

Murphy, K., Birn, R. M., and Bandettini, P. A. (2013). Resting-state fMRI confounds and cleanup. *NeuroImage*, 80:349–359. doi: 10.1016/j.neuroimage.2013.04.001.

Mutschler, I., Wieckhorst, B., Meyer, A. H., Schweizer, T., Klarhöfer, M., Wilhelm, F. H., Seifritz, E., and Ball, T. (2014). Who gets afraid in the MRI-scanner? Neurogenetics of state-anxiety changes during an fMRI experiment. *Neuroscience Letters*, 583:81–86. doi: 10.1016/j.neulet.2014.09.021.

Narain, C., Scott, S. K., Wise, R. J., Rosen, S., Leff, A., Iversen, S. D., and Matthews, P. M. (2003). Defining a Left-lateralized Response Specific to Intelligible Speech Using fMRI. *Cerebral Cortex*, 13(12):1362–1368. doi: 10.1093/cercor/bhg083.

Narsude, M., Van Der Zwaag, W., Kober, T., Gruetter, R., and Marques, J. P. (2014). Improved temporal resolution for functional studies with reduced number of segments with three-dimensional echo planar imaging. *Magnetic Resonance in Medicine*, 72(3): 786–792. doi: 10.1002/mrm.24975.

Narsude, M., Gallichan, D., Van Der Zwaag, W., Gruetter, R., and Marques, J. P. (2016). Three-dimensional echo planar imaging with controlled aliasing: A sequence for high temporal resolution functional MRI. *Magnetic Resonance in Medicine*, 75(6): 2350–2361. doi: 10.1002/mrm.25835.

Nguyen, X. V., Tahir, S., Bresnahan, B. W., Andre, J. B., Lang, E. V., Mossa-Basha, M., Mayr, N. A., and Bourekas, E. C. (2020). Prevalence and Financial Impact of Claustrophobia, Anxiety, Patient Motion, and Other Patient Events in Magnetic Resonance Imaging. *Topics in magnetic resonance imaging*, 29(3):125–130. doi: 10.1097/RMR.0000000000000243.

Nichols, T. E. (2012). Multiple testing corrections, nonparametric methods, and random field theory. *NeuroImage*, 62(2):811–815. doi: 10.1016/J.NEUROIMAGE.2012.04.014.

Noll, D. C., Nishimura, D. G., and Macovski, A. (1991). Homodyne Detection in Magnetic Resonance Imaging. *IEEE Transactions on Medical Imaging*, 10(2):154–163. doi: 10.1109/42.79473.

Nordell, A., Lundh, M., Horsch, S., Hallberg, B., Åden, U., Nordell, B., and Blennow, M. (2009). The acoustic hood: A patient-independent device improving acoustic noise protection during neonatal magnetic resonance imaging. *Acta Paediatrica, International Journal of Paediatrics*, 98(8):1278–1283. doi: 10.1111/j.1651-2227.2009.01339.x.

Norris, D. G. (2012). Spin-echo fMRI: The poor relation? *NeuroImage*, 62(2):1109–1115. doi: 10.1016/j.neuroimage.2012.01.003.

Novitski, N., Maess, B., and Tervaniemi, M. (2006). Frequency specific impairment of automatic pitch change detection by fMRI acoustic noise: An MEG study. *Journal of Neuroscience Methods*, 155(1):149–159. doi: 10.1016/j.jneumeth.2006.01.030.

Novitski, N., Anourova, I., Martinkauppi, S., Aronen, H. J., Näätänen, R., and Carlson, S. (2003). Effects of noise from functional magnetic resonance imaging on auditory event-related potentials in working memory task. *NeuroImage*, 20(2):1320–1328. doi: 10.1016/S1053-8119(03)00390-2.

Oades, R. D., Walker, M. K., Geffen, L. B., and Stern, L. M. (1988). Event-related potentials in autistic and healthy children on an auditory choice reaction time task. *International Journal of Psychophysiology*, 6(1):25–37. doi: 10.1016/0167-8760(88)90032-3.

Oesterle, C., Hennel, F., and Hennig, J. (2001). Quiet imaging with interleaved spiral readout. *Magnetic Resonance Imaging*, 19(10):1333–1337. doi: 10.1016/S0730-725X(01)00458-1.

Ogawa, S., Tank, D. W., Menon, R., Ellermann, J. M., Kim, S. G., Merkle, H., and Ugurbil, K. (1992). Intrinsic signal changes accompanying sensory stimulation: Functional brain mapping with magnetic resonance imaging. *Proceedings of the National Academy of Sciences of the United States of America*, 89(13):5951–5955. doi: 10.1073/pnas.89.13.5951.

Ogawa, S., Lee, T. M., Nayak, A. S., and Glynn, P. (1990). Oxygenation-sensitive contrast in magnetic resonance image of rodent brain at high magnetic fields. *Magnetic Resonance in Medicine*, 14(1):68–78. doi: 10.1002/mrm.1910140108.

Okada, T. and Nakai, T. (2003). Silent fMRI acquisition methods for large acoustic noise during scan. *Magnetic resonance in medical sciences : MRMS : an official journal of Japan Society of Magnetic Resonance in Medicine*, 2(4):181–7. doi: 10.2463/mrms.2.181.

Olafsson, V., Kundu, P., Wong, E. C., Bandettini, P. A., and Liu, T. T. (2015). Enhanced identification of BOLD-like components with multi-echo simultaneous multi-slice (MESMS) fMRI and multi-echo ICA. *NeuroImage*, 112:43–51. doi: 10.1016/j.neuroimage.2015.02.052.

Olsrud, J., Nilsson, A., Mannfolk, P., Waites, A., and Ståhlberg, F. (2008). A two-compartment gel phantom for optimization and quality assurance in clinical BOLD fMRI. *Magnetic Resonance Imaging*, 26(2):279–286. doi: 10.1016/j.mri.2007.06.010.

Olszowy, W., Aston, J., Rua, C., and Williams, G. B. (2019). Accurate autocorrelation modeling substantially improves fMRI reliability. *Nature Communications 2019 10:1*, 10(1):1–11. doi: 10.1038/s41467-019-09230-w.

Olulade, O., Hu, S., Gonzalez-Castillo, J., Tamer, G. G., Luh, W. M., Ulmer, J. L., and Talavage, T. M. (2011). Assessment of temporal state-dependent interactions between auditory fMRI responses to desired and undesired acoustic sources. *Hearing Research*, 277(1-2):67–77. doi: 10.1016/j.heares.2011.03.008.

Ong, F., Zhu, X., Cheng, J. Y., Johnson, K. M., Larson, P. E., Vasanawala, S. S., and Lustig, M. (2020). Extreme MRI: Large-scale volumetric dynamic imaging from continuous non-gated acquisitions. *Magnetic Resonance in Medicine*, 84(4):1763–1780. doi: 10.1002/mrm.28235.

Ostwald, D., Schneider, S., Bruckner, R., and Horvath, L. (2019). Power, positive predictive value, and sample size calculations for random field theory-based fMRI inference. *bioRxiv*. doi: 10.1101/613331.

Ott, M., Blaimer, M., Breuer, F., Grodzki, D., Heismann, B., and Jakob, P. (2016). Acoustic noise reduction in T 1- and proton-density-weighted turbo spin-echo imaging. *Magnetic Resonance Materials in Physics, Biology and Medicine*, 29(1):5–15. doi: 10.1007/s10334-015-0502-7.

Oztek, M. A., Brunnquell, C. L., Hoff, M. N., Boulter, D. J., Mossa-Basha, M., Beauchamp, L. H., Haynor, D. L., and Nguyen, X. V. (2020). Practical Considerations for Radiologists in Implementing a Patient-friendly MRI Experience. *Topics in magnetic resonance imaging*, 29(4):181–186. doi: 10.1097/RMR.0000000000000247.

Paasonen, J., Laakso, H., Pirttimäki, T., Stenroos, P., Salo, R. A., Zhurakovskaya, E., Lehto, L. J., Tanila, H., Garwood, M., Michaeli, S., Idiyatullin, D., Mangia, S., and Gröhn, O. (2020). Multi-band SWIFT enables quiet and artefact-free EEG-fMRI and awake fMRI studies in rat. *NeuroImage*, 206:116338. doi: 10.1016/j.neuroimage.2019.116338.

Pajula, J. and Tohka, J. (2014). Effects of spatial smoothing on inter-subject correlation based analysis of FMRI. *Magnetic Resonance Imaging*, 32(9):1114–1124. doi: 10.1016/j.mri.2014.06.001.

Park, S. H., Kim, T., Wang, P., and Kim, S. G. (2011). Sensitivity and specificity

of high-resolution balanced steady-state free precession fMRI at high field of 9.4T. *NeuroImage*, 58(1):168–176. doi: 10.1016/j.neuroimage.2011.06.010.

Patriat, R., Molloy, E. K., Meier, T. B., Kirk, G. R., Nair, V. A., Meyerand, M. E., Prabhakaran, V., and Birn, R. M. (2013). The effect of resting condition on resting-state fMRI reliability and consistency: A comparison between resting with eyes open, closed, and fixated. *NeuroImage*, 78:463–473. doi: 10.1016/j.neuroimage.2013.04.013.

Pauling, L. and Coryell, C. D. (1936). The Magnetic Properties and Structure of Hemoglobin, Oxyhemoglobin and Carbonmonoxyhemoglobin. *Proceedings of the National Academy of Sciences of the United States of America*, 22(4):210–216. doi: 10.1073/pnas.22.4.210.

Peelle, J. E. (2014). Methodological challenges and solutions in auditory functional magnetic resonance imaging. *Frontiers in Neuroscience*, 8(8 JUL):1–13. doi: 10.3389/fnins.2014.00253.

Peelle, J. E. (2018). Listening effort: How the cognitive consequences of acoustic challenge are reflected in brain and behavior. *Ear and Hearing*, 39(2):204–214. doi: 10.1097/AUD.0000000000000494.

Peelle, J. E., Eason, R. J., Schmitter, S., Schwarzbauer, C., and Davis, M. H. (2010). Evaluating an acoustically quiet EPI sequence for use in fMRI studies of speech and auditory processing. *NeuroImage*, 52(4):1410–1419. doi: 10.1016/j.neuroimage.2010.05.015.

Pei, M., Nguyen, T. D., Thimmappa, N. D., Salustri, C., Dong, F., Cooper, M. A., Li, J., Prince, M. R., and Wang, Y. (2015). Algorithm for fast monoexponential fitting based on Auto-Regression on Linear Operations (ARLO) of data. *Magnetic Resonance in Medicine*, 73(2):843–850. doi: 10.1002/mrm.25137.

Péran, P., Cherubini, A., Luccichenti, G., Hagberg, G., Démonet, J. F., Rascol, O., Celsis, P., Caltagirone, C., Spalletta, G., and Sabatini, U. (2009). Volume and iron content in basal ganglia and thalamus. *Human Brain Mapping*, 30(8):2667–2675. doi: 10.1002/hbm.20698.

Pernet, C. R. (2014). Misconceptions in the use of the General Linear Model applied to functional MRI: A tutorial for junior neuro-imagers. *Frontiers in Neuroscience*, 8:1–12. doi: 10.3389/fnins.2014.00001.

Perrachione, T. K. and Ghosh, S. S. (2013). Optimized Design and Analysis of Sparse-Sampling fMRI Experiments. *Frontiers in Neuroscience*, 7:55. doi: 10.3389/fnins.2013.00055.

Philbin, K. M., Taber, K. H., and Hayman, L. A. (1996). Preliminary report: Changes in vital signs of term newborns during MR. *American Journal of Neuroradiology*, 17(6): 1033–1036.

Phillips, A. A., Chan, F. H., Zheng, M. M. Z., Krassioukov, A. V., and Ainslie, P. N. (2015). Neurovascular coupling in humans: Physiology, methodological advances and clinical implications. *Journal of Cerebral Blood Flow and Metabolism*, 36(4):647–664. doi: 10.1177/0271678X15617954.

Piccini, D., Littmann, A., Nielles-Vallespin, S., and Zenge, M. O. (2011). Spiral phyllotaxis: The natural way to construct a 3D radial trajectory in MRI. *Magnetic Resonance in Medicine*, 66(4):1049–1056. doi: 10.1002/mrm.22898.

Piechnik, S. S. K., Evans, J., Bary, L. H., Wise, R. G., and Jezzard, P. (2009). Functional changes in CSF volume estimated using measurement of water T2 relaxation. *Magnetic Resonance in Medicine*, 61(3):579–586. doi: 10.1002/mrm.21897.

Poldrack, R. A., Fletcher, P. C., Henson, R. N., Worsley, K. J., Brett, M., and Nichols, T. E. (2008). Guidelines for reporting an fMRI study. *NeuroImage*, 40(2):409–414. doi: 10.1016/j.neuroimage.2007.11.048.

Poldrack, R. A., Mumford, J. A., and Nichols, T. E. (2011). *Handbook of Functional MRI Data Analysis*. Cambridge University Press, fourth edition.

Poser, B. A. and Norris, D. G. (2009). Investigating the benefits of multi-echo EPI for fMRI at 7 T. *NeuroImage*, 45(4):1162–1172. doi: 10.1016/J.NEUROIMAGE.2009.01.007.

Poser, B. A., Versluis, M. J., Hoogduin, J. M., and Norris, D. G. (2006). BOLD contrast sensitivity enhancement and artifact reduction with multiecho EPI: Parallel-acquired

inhomogeneity-desensitized fMRI. *Magnetic Resonance in Medicine*, 55(6):1227–1235. doi: 10.1002/mrm.20900.

Posse, S. (2012). Multi-echo acquisition. *NeuroImage*, 62(2):665–671. doi: 10.1016/j.neuroimage.2011.10.057.

Posse, S., Wiese, S., Gembris, D., Mathiak, K., Kessler, C., Grosse-Ruyken, M.-L. L., Elghahwagi, B., Richards, T., Dager, S. R., and Kiselev, V. G. (1999). Enhancement of BOLD-contrast sensitivity by single-shot multi-echo functional MR imaging. *Magnetic Resonance in Medicine*, 42(1):87–97. doi: 10.1002/(SICI)1522-2594(199907)42:1<87::AID-MRM13>3.0.CO;2-O.

Posse, S., Ackley, E., Mutihac, R., Rick, J., Shane, M., Murray-Krezan, C., Zaitsev, M., and Speck, O. (2012). Enhancement of temporal resolution and BOLD sensitivity in real-time fMRI using multi-slab echo-volumar imaging. *NeuroImage*, 61(1):115–130. doi: 10.1016/j.neuroimage.2012.02.059.

Power, J. D. (2017). A simple but useful way to assess fMRI scan qualities. *NeuroImage*, 154:150–158. doi: 10.1016/j.neuroimage.2016.08.009.

Power, J. D., Barnes, K. A., Snyder, A. Z., Schlaggar, B. L., and Petersen, S. E. (2012). Spurious but systematic correlations in functional connectivity MRI networks arise from subject motion. *NeuroImage*, 59(3):2142–2154. doi: 10.1016/j.neuroimage.2011.10.018.

Power, J. D., Lynch, C. J., Silver, B. M., Dubin, M. J., Martin, A., and Jones, R. M. (2019). Distinctions among real and apparent respiratory motions in human fMRI data. *NeuroImage*, 201. doi: 10.1016/j.neuroimage.2019.116041.

Power, J. D., Lynch, C. J., Adeyemo, B., and Petersen, S. E. (2020). A critical, event-related appraisal of denoising in resting-state fMRI studies. *Cerebral Cortex*, 30(10):5544–5559. doi: 10.1093/cercor/bhaa139.

Preibisch, C., Castrillón G., J. G., Bührer, M., and Riedl, V. (2015). Evaluation of multiband EPI acquisitions for resting state fMRI. *PLoS ONE*, 10(9). doi: 10.1371/journal.pone.0136961.

Price, D. L., De Wilde, J. P., Papadaki, A. M., Curran, J. S., and Kitney, R. I. (2001). Investigation of acoustic noise on 15 MRI scanners from 0.2 T to 3 T. *Journal of Magnetic Resonance Imaging*, 13(2):288–293. doi: 10.1002/1522-2586(200102)13:2<288::AID-JMRI1041>3.0.CO;2-P.

Pripfl, J., Robinson, S., Leodolter, U., Moser, E., and Bauer, H. (2006). EEG reveals the effect of fMRI scanner noise on noise-sensitive subjects. *NeuroImage*, 31(1):332–341. doi: 10.1016/j.neuroimage.2005.11.031.

Pruessmann, K. P., Weiger, M., Börnert, P., and Boesiger, P. (2001). Advances in sensitivity encoding with arbitrary k-space trajectories. *Magnetic Resonance in Medicine*, 46(4):638–651. doi: 10.1002/mrm.1241.

Published by the Medicines and Healthcare products Regulatory Agency. (2021). Safety Guidelines for Magnetic Resonance Imaging Equipment in Clinical Use, Accessed September 2021. https://assets.publishing.service.gov.uk/government/uploads/system/uploads/attachment_data/file/958486/MRI_guidance_2021-4-03c.pdf.

Pulkki, V. and Karjalainen, M. (2014). *Communication Acoustics: An Introduction to Speech, Audio and Psychoacoustics*. John Wiley and Sons Inc., first edition.

Quirk, M. E., Letendre, A. J., Ciottone, R. A., and Lingley, J. F. (1989). Anxiety in patients undergoing MR imaging. *Radiology*, 170(2):463–466. doi: 10.1148/radiology.170.2.2911670.

Rabrait, C., Ciuciu, P., Ribés, A., Poupon, C., Le Roux, P., Dehaine-Lambertz, G., Le Bihan, D., and Lethimonnier, F. (2008). High temporal resolution functional MRI using parallel echo volumar imaging. *Journal of Magnetic Resonance Imaging*, 27(4):744–753. doi: 10.1002/jmri.21329.

Radomskij, P., Schmidt, M. A., Heron, C. W., and Prasher, D. (2002). Effect of MRI noise on cochlear function. *Lancet*, 359(9316):1485–1486. doi: 10.1016/S0140-6736(02)08423-4.

Raichle, M. E., MacLeod, A. M., Snyder, A. Z., Powers, W. J., Gusnard, D. A., and Shulman, G. L. (2001). A default mode of brain function. *Proceedings of the*

National Academy of Sciences of the United States of America, 98(2):676–682. doi: 10.1073/pnas.98.2.676.

Ranaweera, R. D., Kwon, M., Hu, S., Tamer, G. G., and Talavage, T. M. (2011). Measurement of auditory hemodynamic response function due to different temporal patterns of imaging acoustic noise using functional magnetic resonance imaging. *6th International Conference on Industrial and Information Systems*, pages 239–243. doi: 10.1109/ICIINFS.2011.6038073.

Ranaweera, R. D., Kwon, M., Hu, S., Tamer, G. G., Luh, W. M., and Talavage, T. M. (2016). Temporal pattern of acoustic imaging noise asymmetrically modulates activation in the auditory cortex. *Hearing Research*, 331:57–68. doi: 10.1016/j.heares.2015.09.017.

Rangaprakash, D., Wu, G.-R. R., Marinazzo, D., Hu, X., and Deshpande, G. (2018). Hemodynamic response function (HRF) variability confounds resting-state fMRI functional connectivity. *Magnetic Resonance in Medicine*, 80(4):1697–1713. doi: 10.1002/mrm.27146.

Ravicz, M. E. and Melcher, J. R. (2001). Isolating the auditory system from acoustic noise during functional magnetic resonance imaging: Examination of noise conduction through the ear canal, head, and body. *The Journal of the Acoustical Society of America*, 109(1):216–231. doi: 10.1121/1.1326083.

Ravicz, M. E., Melcher, J. R., and Kiang, N. Y.-S. (2000). Acoustic noise during functional magnetic resonance imaging. *The Journal of the Acoustical Society of America*, 108(4):1683–1696. doi: 10.1121/1.1310190.

Reddy, R. M., Panahi, I. M., and Briggs, R. (2011). Hybrid FxRLS-FxNLMS adaptive algorithm for active noise control in fMRI application. *IEEE Transactions on Control Systems Technology*, 19(2):474–480. doi: 10.1109/TCST.2010.2042599.

Reeder, S. B. and McVeigh, E. R. (1994). The effect of high performance gradients on fast gradient echo imaging. *Magnetic Resonance in Medicine*, 32(5):612–621. doi: 10.1002/mrm.1910320510.

Ren, J., Liu, H., Xu, T., Wang, D., Li, M., Lin, Y., Ramirez, J. S., Lu, J., Li, L., and Ahveninen, J. (2020). Individual variability in functional organization of the human and monkey auditory cortex. *bioRxiv*. doi: 10.1101/2020.01.06.895474.

Renvall, V. (2009). Functional magnetic resonance imaging reference phantom. *Magnetic Resonance Imaging*, 27(5):701–708. doi: 10.1016/j.mri.2008.11.007.

Rettenmeier, C. A., Maziero, D., and Stenger, V. A. (2021). Three dimensional radial echo planar imaging for functional MRI. *Magnetic Resonance in Medicine*. doi: 10.1002/mrm.28980.

Rizzo Sierra, C. V., Versluis, M. J., Hoogduin, J. M., and Duifhuis, H. (2008). Acoustic fMRI noise: Linear time-invariant system model. *IEEE Transactions on Biomedical Engineering*, 55(9):2115–2123. doi: 10.1109/TBME.2008.923112.

Robson, M. D., Gore, J. C., and Constable, R. T. (1997). Measurement of the point spread function in MRI using constant time imaging. *Magnetic Resonance in Medicine*, 38(5):733–740. doi: 10.1002/mrm.1910380509.

Rondinoni, C., Amaro, E., Cendes, F., dos Santos, A. C., and Salmon, C. E. (2013). Effect of scanner acoustic background noise on strict resting-state fMRI. *Brazilian Journal of Medical and Biological Research*, 46(4):359–367. doi: 10.1590/1414-431X20132799.

Roozen, N. B., Koevoets, A. H., and den Hamer, A. J. (2008). Active vibration control of gradient coils to reduce acoustic noise of MRI systems. *IEEE/ASME Transactions on Mechatronics*, 13(3):325–334. doi: 10.1109/TMECH.2008.924111.

Rorden, C. and Brett, M. (2000). Stereotaxic display of brain lesions. *Behavioural Neurology*, 12(4):191–200. doi: 10.1155/2000/421719.

Rosing, S. N., Schmidt, J. H., Wedderkopp, N., and Baguley, D. M. (2016). Prevalence of tinnitus and hyperacusis in children and adolescents: A systematic review. *BMJ Open*, 6(6). doi: 10.1136/bmjopen-2015-010596.

Salvi, R. and Sheppard, A. (2018). Is noise in the MR imager a significant risk factor for hearing loss? *Radiology*, 286(2):609–610. doi: 10.1148/radiol.2017172221.

Sartoretti, E., Sartoretti, T., Wyss, M., van Smoorenburg, L., Eichenberger, B., van der Duim, S., Cereghetti, D., Binkert, C. A., Sartoretti-Schefer, S., and Najafi, A. (2020). Impact of Acoustic Noise Reduction on Patient Experience in Routine Clinical Magnetic Resonance Imaging. *Academic Radiology*, pages 1–8. doi: 10.1016/j.acra.2020.10.012.

Scarff, C. J., Dort, J. C., Eggermont, J. J., and Goodyear, B. G. (2004). The effect of MR scanner noise on auditory cortex activity using fMRI. *Human Brain Mapping*, 22 (4):341–349. doi: 10.1002/hbm.20043.

Schmidt, C. F., Zaehle, T., Meyer, M., Geiser, E., Boesiger, P., and Jancke, L. (2008). Silent and continuous fMRI scanning differentially modulate activation in an auditory language comprehension task. *Human Brain Mapping*, 29(1):46–56. doi: 10.1002/hbm.20372.

Schmithorst, V. J. and Holland, S. K. (2004). Event-Related fMRI Technique for Auditory Processing with Hemodynamics Unrelated to Acoustic Gradient Noise. *Magnetic Resonance in Medicine*, 51(2):399–402. doi: 10.1002/mrm.10706.

Schmitter, S., Diesch, E., Amann, M., Kroll, A., Moayer, M., and Schad, L. R. (2008). Silent echo-planar imaging for auditory FMRI. *Magnetic Resonance Materials in Physics, Biology and Medicine*, 21(5):317–325. doi: 10.1007/s10334-008-0132-4.

Schulte, R. F., Buonincontri, G., Costagli, M., Menini, A., Wiesinger, F., and Solana, A. B. (2019). Silent T2* and T2 encoding using ZTE combined with BURST. *Magnetic Resonance in Medicine*, 81(4):2277–2287. doi: 10.1002/mrm.27552.

Schulz, J., Fazal, Z., Metere, R., Marques, J., and Norris, D. (2020). Arterial blood contrast (ABC) enabled by magnetization transfer (MT): a novel MRI technique for enhancing the measurement of brain activation changes. *bioRxiv*. doi: 10.1101/2020.05.20.106666.

Schwarzbauer, C. and Porter, D. A. (2010). Single shot partial dual echo (SPADE) EPI-an efficient acquisition scheme for reducing susceptibility artefacts in fMRI. *NeuroImage*, 49(3):2234–2237. doi: 10.1016/j.neuroimage.2009.10.059.

Schwarzbauer, C., Davis, M. H., Rodd, J. M., and Johnsrude, I. (2006). Interleaved

silent steady state (ISSS) imaging: A new sparse imaging method applied to auditory fMRI. *NeuroImage*, 29(3):774–782. doi: 10.1016/j.neuroimage.2005.08.025.

Schweser, F., Deistung, A., Lehr, B. W., and Reichenbach, J. R. (2011). Quantitative imaging of intrinsic magnetic tissue properties using MRI signal phase: An approach to in vivo brain iron metabolism? *NeuroImage*, 54(4):2789–2807. doi: 10.1016/j.neuroimage.2010.10.070.

Seifritz, E., Di Salle, F., Esposito, F., Herdener, M., Neuhoff, J. G., and Scheffler, K. (2006). Enhancing BOLD response in the auditory system by neurophysiologically tuned fMRI sequence. *NeuroImage*, 29(3):1013–1022. doi: 10.1016/j.neuroimage.2005.08.029.

Seydell-Greenwald, A., Leaver, A. M., Turesky, T. K., Morgan, S., Kim, H. J., and Rauschecker, J. P. (2012). Functional MRI evidence for a role of ventral prefrontal cortex in tinnitus. *Brain Research*, 1485:22–39. doi: 10.1016/j.brainres.2012.08.052.

Shah, N. J., Steinhoff, S., Mirzazade, S., Zafiris, O., Grosse-Ruyken, M. L., Jäncke, L., and Zilles, K. (2000). The effect of sequence repeat time on auditory cortex stimulation during phonetic discrimination. *NeuroImage*, 12(1):100–108. doi: 10.1006/nimg.2000.0588.

Shah, N. J., Jäncke, L., Grosse-Ruyken, M. L., and Müller-Gärtner, H. W. (1999). Influence of acoustic masking noise in fMRI of the auditory cortex during phonetic discrimination. *Journal of Magnetic Resonance Imaging*, 9(1):19–25. doi: 10.1002/(SICI)1522-2586(199901)9:1<19::AID-JMRI3>3.0.CO;2-K.

Shellock, F., Mokhtar, Z., Atkinson, D., and Dar-Yeong, C. (1998). Gradient Magnetic Field-Induced Acoustic Noise Associated with the Use of Echo Planar and Three-Dimensional, Fast Spin Echo Techniques. *Journal of Magnetic Resonance Imaging*, 8 (5):1154–1157. doi: 10.1002/jmri.1880080522.

Sheppard, A., Chen, Y.-C. C., and Salvi, R. (2018). MRI Noise and Hearing Loss. *The Hearing Journal*, 71(4):30. doi: 10.1097/01.HJ.0000532395.75558.2d.

Shrout, P. E. and Fleiss, J. L. (1979). Intraclass Correlations : Uses in Assessing Rater Reliability. *Psychological Bulletin*, 86(2):420–428. doi: 10.1037/0033-2909.86.2.420.

Sigalovsky, I. S. and Melcher, J. R. (2006). Effects of sound level on fMRI activation in human brainstem, thalamic and cortical centers. *Hearing Research*, 215(1-2):67–76. doi: 10.1016/j.heares.2006.03.002.

Silva, A. C., Barbier, E. L., Lowe, I. J., and Koretsky, A. P. (1998). Radial Echo-Planar Imaging. *Journal of Magnetic Resonance*, 135(1):242–247. doi: 10.1006/jmre.1998.1547.

Skouras, S., Gray, M., Critchley, H., and Koelsch, S. (2013). fMRI scanner noise interaction with affective neural processes. *PLoS ONE*, 8(11):e80564. doi: 10.1371/journal.pone.0080564.

Smith, D. S., Sengupta, S., Smith, S. A., and Brian Welch, E. (2019). Trajectory optimized NUFFT: Faster non-Cartesian MRI reconstruction through prior knowledge and parallel architectures. *Magnetic Resonance in Medicine*, 81(3):2064–2071. doi: 10.1002/mrm.27497.

Solana, A. B., Hernández-Tamames, J. A., Manzanedo, E., García-Álvarez, R., Zelaya, F. O., and Del Pozo, F. (2014). Gradient induced artifacts in simultaneous EEG-fMRI: Effect of synchronization on spiral and EPI k-space trajectories. *Magnetic Resonance Imaging*, 32(6):684–692. doi: 10.1016/j.mri.2014.03.008.

Solana, A. B., Menini, A., Sacolick, L. I., Hehn, N., and Wiesinger, F. (2016). Quiet and distortion-free, whole brain BOLD fMRI using T2-prepared RUFIS. *Magnetic Resonance in Medicine*, 75(4):1402–1412. doi: 10.1002/mrm.25658.

Song, J. and Qing, H. L. (2006). Improving non-cartesian MRI reconstruction through discontinuity subtraction. *International Journal of Biomedical Imaging*, 2006:1–9. doi: 10.1155/IJBI/2006/87092.

Sorenson, J. A. and Wang, X. (1996). ROC methods for evaluation of fMRI techniques. *Magnetic Resonance in Medicine*, 36(5):737–744. doi: 10.1002/mrm.1910360512.

Speck, O. and Hennig, J. (2005). Functional imaging by I0- and T2*-parameter mapping using multi- image EPI. *Magnetic Resonance in Medicine*, 40(2):243–248. doi: 10.1002/mrm.1910400210.

Squires, N. K., Squires, K. C., and Hillyard, S. A. (1975). Two varieties of long-latency positive waves evoked by unpredictable auditory stimuli in man. *Electroencephalography and Clinical Neurophysiology*, 38(4):387–401. doi: 10.1016/0013-4694(75)90263-1.

Stanisz, G. J., Odrobina, E. E., Pun, J., Escaravage, M., Graham, S. J., Bronskill, M. J., and Henkelman, R. M. (2005). T1, T2 relaxation and magnetization transfer in tissue at 3T. *Magnetic Resonance in Medicine*, 54(3):507–512. doi: 10.1002/mrm.20605.

Stehling, M. K., Turner, R., and Mansfield, P. (1991). Echo-planar imaging: Magnetic resonance imaging in a fraction of a second. *Science*, 254:43–50. doi: 10.1126/science.1925560.

Stenger, V. A., Noll, D. C., and Boada, F. E. (1998). Partial fourier reconstruction for three-dimensional gradient echo functional MRI: Comparison of phase correction methods. *Magnetic Resonance in Medicine*, 40(3):481–490. doi: 10.1002/mrm.1910400320.

Stevens, M. C., Calhoun, V. D., and Kiehl, K. A. (2005). Hemispheric differences in hemodynamics elicited by auditory oddball stimuli. *NeuroImage*, 26(3):782–792. doi: 10.1016/j.neuroimage.2005.02.044.

Stiegler, L. N. and Davis, R. (2010). Understanding sound sensitivity in individuals with autism spectrum disorders. *Focus on Autism and Other Developmental Disabilities*, 25 (2):67–75. doi: 10.1177/1088357610364530.

Stöcker, T., Schneider, F., Klein, M., Habel, U., Kellermann, T., Zilles, K., and Shah, N. J. (2005). Automated quality assurance routines for fMRI data applied to a multicenter study. *Human Brain Mapping*, 25(2):237–246. doi: 10.1002/hbm.20096.

Talavage, T. M. and Hall, D. A. (2012). How challenges in auditory fMRI led to general advancements for the field. *NeuroImage*, 62(2):641–647. doi: 10.1016/j.neuroimage.2012.01.006.

Talavage, T. M., Edmister, W. B., Ledden, P. J., and Weisskoff, R. M. (1999). Quantitative assessment of auditory cortex responses induced by imager acoustic noise. *Human Brain Mapping*, 7(2):79–88. doi: 10.1002/(SICI)1097-0193(1999)7:2<79::AID-HBM1>3.0.CO;2-R.

Talavage, T. M., Gonzalez-Castillo, J., and Scott, S. K. (2014). Auditory neuroimaging with fMRI and PET. *Hearing Research*, 307:4–15. doi: 10.1016/j.heares.2013.09.009.

Tamer, G. G., Luh, W. M., and Talavage, T. M. (2009). Characterizing response to elemental unit of acoustic imaging noise: An fMRI study. *IEEE Transactions on Biomedical Engineering*, 56(7):1919–1928. doi: 10.1109/TBME.2009.2016573.

Tan, E. T., Hardy, C. J., Shu, Y., In, M.-H. H., Guidon, A., Huston, J., Bernstein, M. A., and K.F. Foo, T. (2018). Reduced acoustic noise in diffusion tensor imaging on a compact MRI system. *Magnetic Resonance in Medicine*, 79(6):2902–2911. doi: 10.1002/mrm.26949.

Tan, H. and Zheng, Y. (2005). Point spread function optimization for MRI reconstruction. In *IEEE International Conference on Acoustics, Speech and Signal Processing*. Institute of Electrical and Electronics Engineers Inc. doi: 10.1109/ICASSP.2005.1415445.

Taracila, V., Edelstein, W. A., Kidane, T. K., Eagan, T. P., Baig, T. N., and Brown, R. W. (2005). Analytical calculation of cylindrical shell modes: Implications for MRI acoustic noise. *Concepts in Magnetic Resonance Part B: Magnetic Resonance Engineering*, 25 (1):60–64. doi: 10.1002/cmr.b.20031.

Tarvainen, M. P., Niskanen, J. P., Lipponen, J. A., Ranta-aho, P. O., and Karjalainen, P. A. (2014). Kubios HRV - Heart rate variability analysis software. *Computer Methods and Programs in Biomedicine*, 113(1):210–220. doi: 10.1016/j.cmpb.2013.07.024.

Tarvainen, M., Niskanen, J., Lipponen, J., and Ranta-Aho, P. (2019). Kubios HRV (version 3.3) User's Guide. https://www.kubios.com/support/.

Taylor, A. J., Kim, J. H., and Ress, D. (2018). Characterization of the hemodynamic response function across the majority of human cerebral cortex. *NeuroImage*, 173: 322–331. doi: 10.1016/j.neuroimage.2018.02.061.

tedana community, T., Ahmed, Z., Bandettini, P. A., Bottenhorn, K. L., Caballero-Gaudes, C., Dowdle, L. T., DuPre, E., Gonzalez-Castillo, J., Handwerker, D., Heunis, S., Kundu, P., Laird, A. R., Markello, R., Markiewicz, C. J., Maullin-Sapey, T., Moia, S., Salo, T., Staden, I., Teves, J., Uruñuela, E., Vaziri-Pashkam, M., and Whitaker, K.

(2021). TEDANA version 0.0.10 (Accessed 2021). https://tedana.readthedocs.io/en/stable/index.html.

Tervaniemi, M. and Hugdahl, K. (2003). Lateralization of auditory-cortex functions. *Brain Research Reviews*, 43(3):231–246. doi: 10.1016/j.brainresrev.2003.08.004.

The Nilearn developers. (2021). NiLearn, Version 0.8.0 (Accessed 2021). https://nilearn.github.io/.

Tkach, J. A., Li, Y., Pratt, R. G., Baroch, K. A., Loew, W., Daniels, B. R., Giaquinto, R. O., Merhar, S. L., Kline-Fath, B. M., and Dumoulin, C. L. (2014). Characterization of acoustic noise in a neonatal intensive care unit MRI system. *Pediatric Radiology*, 44 (8):1011–1019. doi: 10.1007/s00247-014-2909-0.

Tomasi, D., Caparelli, E. C., Chang, L., and Ernst, T. (2005). fMRI-acoustic noise alters brain activation during working memory tasks. *NeuroImage*, 27(2):377–386. doi: 10.1016/j.neuroimage.2005.04.010.

Tomasi, D. G. and Ernst, T. (2003). Echo planar imaging at 4 Tesla with minimum acoustic noise. *Journal of Magnetic Resonance Imaging*, 18(1):128–130. doi: 10.1002/jmri.10326.

Tong, Y., Hocke, L. M., and Frederick, B. B. (2019). Low frequency systemic hemodynamic "noise" in resting state BOLD fMRI: Characteristics, causes, implications, mitigation strategies, and applications. *Frontiers in Neuroscience*, 13(JUL). doi: 10.3389/fnins.2019.00787.

Toshiba America Medical Systems. (2014). Improved auditory fMRI imaging using Toshiba scanner with pianissimo. Patent Number MRWP12219US. 2014.

Triantafyllou, C., Hoge, R. D., Krueger, G., Wiggins, C. J., Potthast, A., Wiggins, G. C., and Wald, L. L. (2005). Comparison of physiological noise at 1.5 T, 3 T and 7 T and optimization of fMRI acquisition parameters. *NeuroImage*, 26(1):243–250. doi: 10.1016/j.neuroimage.2005.01.007.

Triantafyllou, C., Polimeni, J. R., and Wald, L. L. (2011). Physiological noise and signal-

to-noise ratio in fMRI with multi-channel array coils. *NeuroImage*, 55(2):597–606. doi: 10.1016/j.neuroimage.2010.11.084.

Tsai, C. M. and Nishimura, D. G. (2000). Reduced aliasing artifacts using variable-density k-space sampling trajectories. *Magnetic Resonance in Medicine*, 43(3):452–458. doi: 10.1002/(SICI)1522-2594(200003)43:3<452::AID-MRM18>3.0.CO;2-B.

Tsao, J., Boesiger, P., and Pruessmann, K. P. (2006). Lattice permutation for reducing motion artifacts in radial and spiral dynamic imaging. *Magnetic Resonance in Medicine*, 55(1):116–125. doi: 10.1002/mrm.20743.

Tseytlin, M. (2017). Concept of Phase Cycling in Pulsed Magnetic Resonance Using Sinusoidal Magnetic Field Modulation. *Zeitschrift fur Physikalische Chemie*, 231(3): 689–703. doi: 10.1515/zpch-2016-0843.

Tustison, N. J., Avants, B. B., Cook, P. A., Zheng, Y., Egan, A., Yushkevich, P. A., and Gee, J. C. (2010). N4ITK: Improved N3 bias correction. *IEEE Transactions on Medical Imaging*, 29(6):1310–1320. doi: 10.1109/TMI.2010.2046908.

Ulmer, J. L., Biswal, B. B., Yetkin, F. Z., Mark, L. P., Mathews, V. P., Prost, R. W., Estkowski, L. D., McAuliffe, T. L., Haughton, V. M., and Daniels, D. L. (1998). Cortical activation response to acoustic echo planar scanner noise. *Journal of Computer Assisted Tomography*, 22(1):111–119. doi: 10.1097/00004728-199801000-00021.

Uludağ, K., Uğurbil, K., Berliner, L., Urgurbil, K., Berliner, L., Uğurbil, K., and Berliner, L. (2015). fMRI: From Nuclear Spins to Brain Functions. In *fMRI: From Nuclear Spins to Brain Functions*, pages 1–929. Springer New York, first edit edition. doi: https://doi.org/10.1007/978-1-4899-7591-1.

Vallat, R. (2017). conn tools. https://github.com/raphaelvallat/conn_tools.

Van Der Zwaag, W., Marques, J. P., Kober, T., Glover, G., Gruetter, R., and Krueger, G. (2012). Temporal SNR characteristics in segmented 3D-EPI at 7T. *Magnetic Resonance in Medicine*, 67(2):344–352. doi: 10.1002/mrm.23007.

Van Der Zwaag, W., Francis, S., and Bowtell, R. (2006). Improved Echo Volumar

Imaging (EVI) for functional MRI. *Magnetic Resonance in Medicine*, 56(6):1320–1327. doi: 10.1002/mrm.21080.

van der Zwaag, W., Schäfer, A., Marques, J. P., Turner, R., and Trampel, R. (2016). Recent applications of UHF-MRI in the study of human brain function and structure: a review. *NMR in Biomedicine*, 29(9):1274–1288. doi: 10.1002/nbm.3275.

van Minde, D., Klaming, L., and Weda, H. (2014). Pinpointing moments of high anxiety during an MRI examination. *International journal of behavioral medicine*, 21 (3):487–495. doi: 10.1007/s12529-013-9339-5.

Vazquez, A. L. and Noll, D. C. (1998). Nonlinear aspects of the BOLD response in functional MRI. *NeuroImage*, 7(2):108–118. doi: 10.1006/nimg.1997.0316.

Versteeg, E., Van der Velden, T., Hendrikse, J., Klomp, D., and Siero, J. (2020). Dual axis gradient insert for supersonic MRI. International Society for Magnetic Resonance in Medicine 28th Annual Meeting, Abstract 0617.

Viallet, G., Sgard, F., Laville, F., and Nélisse, H. (2015). Investigation of the variability in earplugs sound attenuation measurements using a finite element model. *Applied Acoustics*, 89:333–344. doi: 10.1016/j.apacoust.2014.10.007.

Vizioli, L., Moeller, S., Dowdle, L., Akçakaya, M., Martino, F. D., Yacoub, E., and Ugurbil, K. (2021). A Paradigm Change in Functional Brain Mapping: Suppressing the Thermal Noise in fMRI. *bioRxiv*. doi: 10.1101/2020.11.04.368357.

Vos De Wael, R., Hyder, F., and Thompson, G. J. (2017). Effects of Tissue-Specific Functional Magnetic Resonance Imaging Signal Regression on Resting-State Functional Connectivity. *Brain Connectivity*, 7(8):482–490. doi: 10.1089/brain.2016.0465.

Wald, L. L. and Polimeni, J. R. (2017). Impacting the effect of fMRI noise through hardware and acquisition choices – Implications for controlling false positive rates. *NeuroImage*, 154:15–22. doi: 10.1016/j.neuroimage.2016.12.057.

Wallace, T. E., Afacan, O., Waszak, M., Kober, T., and Warfield, S. K. (2019). Head motion measurement and correction using FID navigators. *Magnetic Resonance in Medicine*, 81(1):258–274. doi: 10.1002/mrm.27381.

Wallace, T. E., Polimeni, J. R., Stockmann, J. P., Hoge, W. S., Kober, T., Warfield, S. K., and Afacan, O. (2021). Dynamic distortion correction for functional MRI using FID navigators. *Magnetic Resonance in Medicine*, 85(3):1294–1307. doi: 10.1002/mrm.28505.

Waltmann, M., O'Daly, O., Egerton, A., McMullen, K., Kumari, V., Barker, G. J., Williams, S. C., and Modinos, G. (2019). Multi-echo fMRI, resting-state connectivity, and high psychometric schizotypy. *NeuroImage: Clinical*, 21. doi: 10.1016/j.nicl.2018.11.013.

Wang, C., Martins-Bach, A. B., Alfaro-Almagro, F., Douaud, G., Klein, J. C., Llera, A., Fiscone, C., Bowtell, R., Elliott, L. T., Smith, S. M., Tendler, B. C., and Miller, K. L. (2021). Phenotypic and genetic associations of quantitative magnetic susceptibility in UK Biobank brain imaging. *bioRxiv*. doi: 10.1101/2021.06.28.450248.

Wang, Y. and Liu, T. (2015). Quantitative susceptibility mapping (QSM): Decoding MRI data for a tissue magnetic biomarker. *Magnetic Resonance in Medicine*, 73(1):82–101. doi: 10.1002/mrm.25358.

Watanabe, M., Bartels, A., Macke, J., Murayama, Y., and Logothetis, N. (2013). Temporal Jitter of the BOLD Signal Reveals a Reliable Initial Dip and Improved Spatial Resolution. *Current Biology*, 23(21):2146–2150. doi: 10.1016/J.CUB.2013.08.057.

Watson, S. R., Halmagyi, G. M., and Colebatch, J. G. (2000). Vestibular hypersensitivity to sound (Tullio phenomenon): Structural and functional assessment. *Neurology*, 54(3):722–728. doi: 10.1212/wnl.54.3.722.

Weiger, M. and Pruessmann, K. P. (2012). MRI with Zero Echo Time. *Encyclopedia of Magnetic Resonance*, 1:311–322. doi: 10.1002/9780470034590.emrstm1292.

Weiger, M., Boesiger, P., Hilfiker, P. R., Weishaupt, D., and Pruessmann, K. P. (2005). Sensitivity encoding as a means of enhancing the SNR efficiency in steady-state MRI. *Magnetic Resonance in Medicine*, 53(1):177–185. doi: 10.1002/mrm.20322.

Weiger, M., Pruessmann, K. P., and Hennel, F. (2011). MRI with zero echo time: Hard versus sweep pulse excitation. *Magnetic Resonance in Medicine*, 66(2):379–389. doi: 10.1002/mrm.22799.

Weissenbacher, A., Kasess, C., Gerstl, F., Lanzenberger, R., Moser, E., and Windischberger, C. (2009). Correlations and anticorrelations in resting-state functional connectivity MRI: A quantitative comparison of preprocessing strategies. *NeuroImage*, 47(4):1408–1416. doi: 10.1016/j.neuroimage.2009.05.005.

Weisskoff, R. M. (1996). Simple measurement of scanner stability for functional NMR imaging of activation in the brain. *Magnetic Resonance in Medicine*, 36(4):643–645. doi: 10.1002/mrm.1910360422.

Welvaert, M. and Rosseel, Y. (2013). On the definition of signal-to-noise ratio and contrast-to-noise ratio for fMRI data. *PLoS ONE*, 8(11):e77089. doi: 10.1371/journal.pone.0077089.

Whitfield-Gabrieli, S. and Nieto-Castanon, A. (2012). Conn: A Functional Connectivity Toolbox for Correlated and Anticorrelated Brain Networks. *Brain Connectivity*, 2(3):125–141. doi: 10.1089/brain.2012.0073.

Wiesinger, F. and Solana, A. B. (2020). Looping Star: Revisiting echo in/out separation. International Society for Magnetic Resonance in Medicine 28th Annual Meeting, Abstract 3733.

Wiesinger, F., Sacolick, L. I., Menini, A., Kaushik, S. S., Ahn, S., Veit-Haibach, P., Delso, G., and Shanbhag, D. D. (2016). Zero TE MR bone imaging in the head. *Magnetic Resonance in Medicine*, 75(1):107–114. doi: 10.1002/mrm.25545.

Wiesinger, F., Menini, A., and Solana, A. B. (2019). Looping Star. *Magnetic Resonance in Medicine*, 81(1):57–68. doi: 10.1002/mrm.27440.

Wild, C. J., Yusuf, A., Wilson, D. E., Peelle, J. E., Davis, M. H., and Johnsrude, I. S. (2012). Effortful listening: The processing of degraded speech depends critically on attention. *Journal of Neuroscience*, 32(40):14010–14021. doi: 10.1523/JNEUROSCI.1528-12.2012.

Winkelmann, S., Schaeffter, T., Koehler, T., Eggers, H., and Doessel, O. (2007). An optimal radial profile order based on the golden ratio for time-resolved MRI. *IEEE Transactions on Medical Imaging*, 26(1):68–76. doi: 10.1109/TMI.2006.885337.

Winkler, A. M., Webster, M. A., Brooks, J. C., Tracey, I., Smith, S. M., and Nichols, T. E. (2016). Non-parametric combination and related permutation tests for neuroimaging. *Human Brain Mapping*, 37(4):1486–1511. doi: 10.1002/hbm.23115.

Winkler, S. A., Schmitt, F., Landes, H., DeBever, J., Wade, T., Alejski, A., and Rutt, B. K. (2018). Gradient and shim technologies for ultra high field MRI. *NeuroImage*, 168:59–70. doi: 10.1016/j.neuroimage.2016.11.033.

Wolak, T., Cieśla, K., Rusiniak, M., Piłka, A., Lewandowska, M., Pluta, A., Skarżyński, H., and Skarżyński, P. H. (2016). Influence of Acoustic Overstimulation on the Central Auditory System: An Functional Magnetic Resonance Imaging (fMRI) Study. *Medical Science Monitor : International Medical Journal of Experimental and Clinical Research*, 22:4623. doi: 10.12659/MSM.897929.

Woo, C. W., Krishnan, A., and Wager, T. D. (2014). Cluster-extent based thresholding in fMRI analyses: Pitfalls and recommendations. *NeuroImage*, 91:412–419. doi: 10.1016/j.neuroimage.2013.12.058.

Wood, T. C., Ljungberg, E., and Wiesinger, F. (2021). Radial Interstices Enable Speedy Low-Volume imagING. https://github.com/spinicist/riesling.

Woolrich, M. W., Ripley, B. D., Brady, M., and Smith, S. M. (2001). Temporal autocorrelation in univariate linear modeling of FMRI data. *NeuroImage*, 14(6): 1370–1386. doi: 10.1006/nimg.2001.0931.

Worsley, K. J., Evans, A. C., Marrett, S., and Neelin, P. (1992). A three-dimensional statistical analysis for CBF activation studies in human brain. *Journal of Cerebral Blood Flow and Metabolism*, 12(6):900–918. doi: 10.1038/jcbfm.1992.127.

Worsley, K. J., Marrett, S., Neelin, P., Vandal, A. C., Friston, K. J., and Evans, A. C. (1996). A unified statistical approach for determining significant signals in images of cerebral activation. *Human Brain Mapping*, 4(1):58–73. doi: 10.1002/(SICI)1097-0193(1996)4:1<58::AID-HBM4>3.0.CO;2-O.

Worsley, K. J., Liao, C. H., Aston, J., Petre, V., Duncan, G. H., Morales, F., and Evans, A. C. (2002). A general statistical analysis for fMRI data. *NeuroImage*, 15(1):1–15. doi: 10.1006/nimg.2001.0933.

Wright, B., Peters, E., Ettinger, U., Kuipers, E., and Kumari, V. (2014). Understanding noise stress-induced cognitive impairment in healthy adults and its implications for schizophrenia. *Noise and Health*, 16(70):166–176. doi: 10.4103/1463-1741.134917.

Wright, P. J., Mougin, O. E., Totman, J. J., Peters, A. M., Brookes, M. J., Coxon, R., Morris, P. E., Clemence, M., Francis, S. T., Bowtell, R. W., and Gowland, P. A. (2008). Water proton T1 measurements in brain tissue at 7, 3, and 1.5T using IR-EPI, IR-TSE, and MPRAGE: Results and optimization. *Magnetic Resonance Materials in Physics, Biology and Medicine*, 21(1-2):121–130. doi: 10.1007/s10334-008-0104-8.

Wronka, E., Kaiser, J., and Coenen, A. M. (2008). The auditory P3 from passive and active three-stimulus oddball paradigm. *Acta Neurobiologiae Experimentalis*, 68(3): 362–372.

Wu, G. R., Liao, W., Stramaglia, S., Ding, J. R., Chen, H., and Marinazzo, D. (2013). A blind deconvolution approach to recover effective connectivity brain networks from resting state fMRI data. *Medical Image Analysis*, 17(3):365–374. doi: 10.1016/j.media.2013.01.003.

Wu, Y., Dai, G., Ackerman, J. L., Hrovat, M. I., Glimcher, M. J., Snyder, B. D., Nazarian, A., and Chesler, D. A. (2007). Water- and fat-suppressed proton projection MRI (WASPI) of rat femur bone. *Magnetic Resonance in Medicine*, 57(3):554–567. doi: 10.1002/mrm.21174.

Yakunina, N., Kang, E. K., Tae, ., Kim, S. S. S., Min, J.-H. H., Kim, S. S. S., Nam, E.-C. C., Kim, T. S., Min, J.-H. H., Kim, S. S. S., and Nam, E.-C. C. (2015). Effects of scanner acoustic noise on intrinsic brain activity during auditory stimulation. *Neuroradiology Journal*, 57(10):1063–1073. doi: 10.1007/s00234-015-1561-1.

Yamashiro, T., Morita, K., and Nakajima, K. (2019). Evaluation of magnetic resonance imaging acoustic noise reduction technology by magnetic gradient waveform control. *Magnetic Resonance Imaging*, 63:170–177. doi: 10.1016/j.mri.2019.08.015.

Yancey, S. E., Rotenberg, D. J., Tam, F., Chiew, M., Ranieri, S., Biswas, L., Anderson, K. J., Nicole Baker, S., Wright, G. A., and Graham, S. J. (2011). Spin-history artifact

during functional MRI: Potential for adaptive correction. *Medical Physics*, 38(8): 4634–4646. doi: 10.1118/1.3583814.

Yang, J., Gohel, S., and Vachha, B. (2020). Current methods and new directions in resting state fMRI. *Clinical Imaging*, 65:47–53. doi: 10.1016/J.CLINIMAG.2020.04.004.

Yang, Y., Engelien, A., Engelien, W., Xu, S., Stern, E., and Silbersweig, D. A. (2000). A silent event-related functional MRI technique for brain activation studies without interference of scanner acoustic noise. *Magnetic Resonance in Medicine*, 43(2):185–190. doi: 10.1002/(SICI)1522-2594(200002)43:2<185::AID-MRM4>3.0.CO;2-3.

Yarkoni, T. (2011). Neurosynth (Accessed 2018 - 2021). https://neurosynth.org/.

Ye, Y., Zhuo, Y., Xue, R., and Zhou, X. J. (2010). BOLD fMRI using a modified HASTE sequence. *NeuroImage*, 49(1):457–466. doi: 10.1016/j.neuroimage.2009.07.044.

Ylipaavalniemi, J. and Vigário, R. (2008). Analyzing consistency of independent components: An fMRI illustration. *NeuroImage*, 39(1):169–180. doi: 10.1016/j.neuroimage.2007.08.027.

Zapp, J., Schmitter, S., and Schad, L. R. (2012). Sinusoidal echo-planar imaging with parallel acquisition technique for reduced acoustic noise in auditory fMRI. *Journal of Magnetic Resonance Imaging*, 36(3):581–588. doi: 10.1002/jmri.23699.

Zarahn, E., Aguirre, G. K., and D'Esposito, M. (1997). Empirical analyses of BOLD fMRI statistics. I. Spatially unsmoothed data collected under null-hypothesis conditions. *NeuroImage*, 5(3):179–197. doi: 10.1006/nimg.1997.0263.

Zatorre, R. J., Belin, P., and Penhune, V. B. (2002). Structure and function of auditory cortex: music and speech. *Trends in Cognitive Sciences*, 6(1):37–46. doi: 10.1016/S1364-6613(00)01816-7.

Zhang, N., Zhu, X. H., and Chen, W. (2005). Influence of gradient acoustic noise on fMRI response in the human visual cortex. *Magnetic Resonance in Medicine*, 54(2): 258–263. doi: 10.1002/mrm.20512.

Zhao, F., Wang, P., and Kim, S. G. (2004). Cortical Depth-Dependent Gradient-Echo and Spin-Echo BOLD fMRI at 9.4T. *Magnetic Resonance in Medicine*, 51(3):518–524. doi: 10.1002/mrm.10720.

Zilles, K. and Amunts, K. (2010). Centenary of Brodmann's map — conception and fate. *Nature Reviews Neuroscience 2010 11:2*, 11(2):139–145. doi: 10.1038/nrn2776.

Zong, X., Lee, J., John Poplawsky, A., Kim, S. G., and Ye, J. C. (2014). Compressed sensing fMRI using gradient-recalled echo and EPI sequences. *NeuroImage*, 92:312–321. doi: 10.1016/j.neuroimage.2014.01.045.